Lecture Notes in Networks and Systems 33

H. S. Saini · Ravi Kishore Singh
Vishal M. Patel · K. Santhi
S. V. Ranganayakulu *Editors*

Innovations in Electronics and Communication Engineering

Proceedings of the 6th ICIECE 2017

Springer

Lecture Notes in Networks and Systems

Volume 33

Series editor

Janusz Kacprzyk, Polish Academy of Sciences, Warsaw, Poland
e-mail: kacprzyk@ibspan.waw.pl

The series "Lecture Notes in Networks and Systems" publishes the latest developments in Networks and Systems—quickly, informally and with high quality. Original research reported in proceedings and post-proceedings represents the core of LNNS.

Volumes published in LNNS embrace all aspects and subfields of, as well as new challenges in, Networks and Systems.

The series contains proceedings and edited volumes in systems and networks, spanning the areas of Cyber-Physical Systems, Autonomous Systems, Sensor Networks, Control Systems, Energy Systems, Automotive Systems, Biological Systems, Vehicular Networking and Connected Vehicles, Aerospace Systems, Automation, Manufacturing, Smart Grids, Nonlinear Systems, Power Systems, Robotics, Social Systems, Economic Systems and other. Of particular value to both the contributors and the readership are the short publication timeframe and the world-wide distribution and exposure which enable both a wide and rapid dissemination of research output.

The series covers the theory, applications, and perspectives on the state of the art and future developments relevant to systems and networks, decision making, control, complex processes and related areas, as embedded in the fields of interdisciplinary and applied sciences, engineering, computer science, physics, economics, social, and life sciences, as well as the paradigms and methodologies behind them.

Advisory Board

More information about this series at http://www.springer.com/series/15179

H. S. Saini · Ravi Kishore Singh
Vishal M. Patel · K. Santhi
S. V. Ranganayakulu
Editors

Innovations in Electronics and Communication Engineering

Proceedings of the 6th ICIECE 2017

Springer

Editors
H. S. Saini
Guru Nanak Institutions
Ibrahimpatnam, Telangana
India

Ravi Kishore Singh
Guru Nanak Institutions Technical Campus
Ibrahimpatnam, Telangana
India

Vishal M. Patel
Department of Electrical
and Computer Engineering
Rutgers University
New Brunswick, NJ
USA

K. Santhi
Department of Electronics and
Communication Engineering
Guru Nanak Institutions Technical Campus
Ibrahimpatnam, Telangana
India

S. V. Ranganayakulu
Research and Development
Guru Nanak Institutions Technical Campus
Ibrahimpatnam, Telangana
India

ISSN 2367-3370 ISSN 2367-3389 (electronic)
Lecture Notes in Networks and Systems
ISBN 978-981-10-8203-0 ISBN 978-981-10-8204-7 (eBook)
https://doi.org/10.1007/978-981-10-8204-7

Library of Congress Control Number: 2018939002

This Springer imprint is published by the registered company Springer Nature Singapore Pte Ltd.
The registered company address is: 152 Beach Road, #21-01/04 Gateway East, Singapore 189721, Singapore

Preface

The Sixth International Conference on Innovations in Electronics and Communication Engineering (ICIECE) by the Department of Electronics and Communication Engineering, Guru Nanak Institutions Technical Campus, was conducted in association with Defense Research and Development Organisation and the Department of Science and Technology on July 21 and 22, 2017. The conference has grown exponentially over the years and has become a platform for scientists, researchers, academicians, and students to present their ideas and share their research in various fields of Electronics and Communication Engineering. The focus for this year conference was 'Innovation,' and we had distinguished speakers from India and abroad who shared innovative solutions and technologies.

Over 230 papers were received, of which 49 papers have been selected for Lecture Notes in Networks and Systems. The papers selected were presented by the authors during the conference. Various parallel sessions accommodate all the authors to discuss their ideas. We were happy to note that all the authors were satisfied with the arrangements and encouraged us to continue to conduct such conferences in the future as well.

We would like to thank all the participants, speakers, session chairs, committee members, and reviewers, international and national board members, Guru Nanak Institutions Management, and all the people who have directly or indirectly contributed to the success of this conference. The editors would also like to thank Springer Editorial Team for their support and for publishing the papers as part of the 'Lecture Notes in Networks and Systems' series.

Ibrahimpatnam, India — H. S. Saini
Ibrahimpatnam, India — Ravi Kishore Singh
New Brunswick, USA — Vishal M. Patel
Ibrahimpatnam, India — K. Santhi
Ibrahimpatnam, India — S. V. Ranganayakulu

Editorial Board Members

Patrons

Sardar Tavinder Singh Kohli, Chairman, Guru Nanak Institutions
Sardar Gagandeep Singh Kohli, Vice-Chairman, Guru Nanak Institutions

Conference Chair

Dr. H. S. Saini, Managing Director, Guru Nanak Institutions

Conference Co-chairs

Prof. Ravi Kishore Singh, Associate Director, GNITC
Dr. S. V. Ranganayakulu, Dean (R&D), GNITC

Steering Committee

Dr. M. Ramalinga Reddy, Director, GNITC
Dr. S. Sreenatha Reddy, Principal, GNIT
Prof. Parthsaradhy, Associate Director, GNITC
Dr. Rishi Sayal, Associate Director, GNITC
Dr. K. Chanthirasekaran, Dean (Academics), ECE

Conveners

Dr. K. Santhi, Professor, GNITC
Dr. S. Sugumar, Professor, GNITC
Dr. Syed Jalal Ahmad, Professor, GNITC

Committee Members

Prof. S. Maheshwara Reddy, HOD, ECE
Prof. B. Kedarnath, HOD, ECE, GNIT
Prof. Anithaswamidas, Professor
Prof. Hemasundara Rao, Professor

Prof. A. Mohan, Professor
Prof. K. Nagaiah, Professor
Prof. E. N. V. Purna Chandra Rao, Professor
Prof. V. Bhagya Raju, Associate Professor
Mr. B. Sridhar, Associate Professor
Mr. Sandeep Patil, Associate Professor

Advisory Board—International

Dr. Xiao-Zhi Gao, Finland University
Prof. Libor Rufer, CIMA, Micro and Nano Systems Groups, France
Dr. Vishal M. Patel, State University of New Jersey, USA
Dr. Savatri Bevinakopp, MIT Australia
Dr. C. H. Suresh Babu, K.K. University, Abha KSA
Shri. Rajashekhar N., INPHI, UK
Dr. Surgey Mosin, Vladimir State University, Russia
Dr. Katina Michael, University of Wollongong, Australia
Dr. Ahmed Faheem Zobaa, BU, UK
Dr. Akhtar Kalam, VU, Australia
Dr. Alfredo Vaccaro, US, Italy
Dr. David Yu, UMW, USA
Dr. Dimitri Vinnikov, TUT, Estonia
Dr. Gorazad Stumberger, UM, Slovenia
Dr. Jagadish Nayak, BITS Pilani, Dubai Campus
Dr. Lausiong Hoe, Multimedia University, Malaysia
Dr. Hussian Shareef, UK, Malaysia
Dr. Murad Al-Shibli, Head, EMET, Abu Dhabi
Dr. Nesimi Ertugrul, UA, Australia
Dr. Richarad Blanchard, LBU, UK
Dr. Shashi Paul, DM, UK
Dr. Zhao Xu, HKPU, Hong Kong
Dr. Ahmed Zobaa, Brunel University London, UK
Dr. Adel Nasiri, UMW, USA
Dr. P. N. Sugunathan, NTU, Singapore
Dr. Hiroya Fuji Saki, University of Tokyo
Dr. Fawnizu Azmadi Hussin, Universiti Teknologi Petronas, Malaysia
Dimov Stojce Ilcev, DUT, Durban, South Africa

Advisory Board—National

Dr. Mohammed Zafar Ali Khan, Associate Professor and HOD, EE Department, IIT Hyderabad
Dr. Gulam Mohammed Rather, Professor, ECE, NIT Srinagar
Dr. N. Bheem Rao, Associate Professor, NIT Warangal

Conference Committee Members

Conference Co-chair

Prof. Ravi Kishore Singh, Associate Director
Dr. S. V. Ranganayakulu, Dean, R&FD

Conveners

Dr. K. Santhi
Dr. S. J. Sugumar
Dr. Syed Jalal Ahmad

S.No.	Name of committee	Faculty in charge	Faculty
1	Budget	Prof. Ravi Kishore Singh	Mr. Sandeep Patil
2	Conference team	Prof. Ravi Kishore Singh	
3	Conference dates	Prof. Ravi Kishore Singh	
4	Brochure	Dr. K. Santhi	Mrs. C. Sailaja
			Mr. Srinivas Nanda
5	Web site, easy chair/ e-mail creation	Prof. V. Bhagya Raju	
		Mr. B. Sridhar	
		Mr. Srinivas Nanda	
6	E-mail campaigning team	Dr. S. J. Sugumar	Mrs. M. Sirisha
			S. Aparna
			E. Vara lakshmi
			T. Ashwini
			L. Shiva

(continued)

(continued)

S.No.	Name of committee	Faculty in charge	Faculty
7	Physical campaigning team	Mr. A. Bhagya Raju	Mr. D. Surendra Rao
			Mr. R. Gopinath
			Mr. A. V. Rameswar Rao
			Mr. V. Sai Babu
			Mr. O. Ravinder
			Mr. K. Krishna Kumar
8	Applications for funding	Mr. K. Shashidhar	
9	Receiving papers and acknowledgment, attending queries of authors	Dr. K. Santhi	Mrs. C. Sailaja
			Mr. Srinivas Nanda
10	Review and sending report, acceptance letters to authors	Dr. S. J. Sugumar and Mr. B. Sridhar	Mrs. N. Ramyateja
			Mrs. K. Ramya Sree
			Ms. D. Sony
11	Conversion of papers	Dr. S. J. Sugumar	
12	List of guest	Dr. K. Santhi	
13	Invitation	Chief guest, participants (e-mail), departments	Mr. Sandeep Patil
			Mrs. M. Sirisha
			Mrs. N. Ramya Teja
			Mrs. C. Sailaja
			Mrs. K. Nadiya
14	Registration (ONLINE/SPOT) and kits and conference bags	Mr. Ch. Raja Rao	Mr. A. V. Rameswar Rao
			Ms. S. Swetha
			Mrs. K. Yashoda
15	Reception	Mrs. G. Kiranmaye	Mrs. K. Yashoda
16	Conference office	Prof. Anita Swamidas	
17	VC, MD, JNTUH messages	Mr. A. Mohan	
18	Pre-conference tutorials	Mr. R. P. Naraiah	
19	Program schedule	Dr. S. J. Sugumar	
20	Proceedings	Dr. K. Santhi	
		Prof. K. Nagaiah	
21	Travel arrangements for guests	Mr. D. Surendra Rao	
22	Program committee	Dr. S. J. Sugumar	Mrs. B. Anitha
			Ms. B. Aruna
			Mr. K. Sashidhar
			Mr. K. Krishna Kumar

(continued)

(continued)

S.No.	Name of committee	Faculty in charge	Faculty
23	Program arrangements/posters (technician requisition)/IT request	Dr. S. J. Sugumar	Mr. V. Saibabu
24	Purchase committee	Prof. S. Maheswara Reddy	Prof. P. C. Rao
			Mr. V. Saibabu
			Mr. A. V. Rameswar Rao
25	Food committee	Mr. R. Gopinath	
26	Accommodations	Mr. Chinna Narasimhulu	
27	Certificates	Mrs. C. Sailaja, Mrs. N. Ramyateja	
28	Banners	Mr. K. Krishna Kumar	
29	Inauguration and valedictory function	Prof. Ravi Kishore Singh	Mr. Sandeep Patil
30	Photographs and video	Mr. O. Ravinder	
31	Press release and media	Mr. B. Srinivas	
32	After conference attending queries of authors	Respective Conveners	
33	Journal contacts	Dr. K. Santhi	
		Dr. M. A. Khadar baba	Mr. B. Srinivas

Reviewer's List

Internal Reviewers

Prof. Ravi Kishore Singh, Associate Director
Dr. S. V. Ranganayakulu, Dean (R&D), GNI
Prof. M. A. Kadar Baba, HOD, ECE, GNITC
Dr. K. Santhi, Professor, ECE
Dr. S. Sugumar, Professor, ECE
Dr. Syed Jalal Ahmad, Professor, ECE
Prof. Anita Swamidas, Professor, ECE
Prof. CH. Hemasundara Rao, Professor, ECE
Prof. N. V. Purnachandar Rao, Professor, ECE
Prof. A. Mohan, Professor, ECE
Mr. V. Bhagya Raju, Associate Professor, ECE
Mr. K. Shashidhar, Associate Professor, ECE
Mr. B. Sridhar, Associate Professor, ECE
Mrs. G. Kiran Maye, Associate Professor, ECE
Mr. Bachu Srinivas, Associate Professor, ECE
Dr. R. Vinoth Kanna, HOD, EEE, GNIT

External Reviewers

Dr. Nazib Uddin, HOD, Professor, NIT Srinagar
Dr. Gulal Mohemmed Rather, Professor, NIT Srinagar
Challa S. Sastry, Department of Mathematics, IIIT Hyderabad
Dr. Suryakanth V. Gangashetty, Assistant Professor, IIIT Hyderabad
Dr. Somasundaram, PDF Scholar, IISc Bangalore
Dr. B. Thayaneswaran, Assistant Professor, Sona College of Technology, Salem, Tamil Nadu
Dr. C. Rajasekaran, Professor, ECE, KSRCT, Namakkal, Tamil Nadu
Arul Jyothi, Associate Professor, SREC, Coimbatore
M. Nirmala, Associate Professor, KSRCT
Dr. Shiva Subramanyam, KSRIT, Tamil Nadu

Dr. Supha Laxmi, Professor and Head, Paavai Institutions, Tamil Nadu
Dr. M. Maheswaran, Professor, Kongu Engineering College
Dr. Gunavathi, Associate Professor, VIT, Vellore
Dr. Maheshwar, Professor, Sri Krishna College of Engineering and Technology, Coimbatore
Dr. Malmurugan, Professor, PAL Institutions
Dr. M. V. Jithin Kumar, Research Coordinator, Heera College of Engineering and Technology, Kerala
Gnanou Florence Sudha, Pondicherry Engineering College, Pondicherry
Dr. J. Yogapriya, Dean (R&D), Kongunadu College of Engineering and Technology, Trichy, Tamil Nadu
Mrs. Rohini R. Mergu, Assistant Professor, Walchand Institute of Technology, Solapur
Dr. Jakulin Moni, Professor, Karunya University, Tamil Nadu
Dr. V. R. Vijay Kumar, Professor, Anna University, Coimbatore
Dr. Kanchana Bhaskar, Professor, Dean (Academics), VIT Chennai
Dr. S. P. Singh, MGIT, Hyderabad
Dr. K. Jayashangkar, Principal, Vasavi College of Engineering, Hyderabad
Dr. B. L. Raju, Principal, ACE College of Engineering, Hyderabad
Dr. P. G. Geetha, Professor, Sri Vidyaniketan, Tirupati
DR. R. P. Ramkumar, Professor, CSE, MREC
Dr. Pasha, HOD, Professor, BVRIT
Dr. B. Lokeswar Rao, Professor, CMRCET, Hyderabad
Dr. Nageswara Rao, Professor, TKRCE, Hyderabad
Dr. Karunakar, Associate Professor, GITAM, Visakhapatnam
Dr. M. Suresh, Professor, CMRCET, Hyderabad
Dr. C. V. Narasimhulu, Professor, GCET, Hyderabad
Dr. A. S. N. Murthy, Professor, BVRIT, Hyderabad
Dr. P. Narahari Shastry, Professor, CBIT
Dr. Mahesh, Associate Professor
Dr. Geetha, Professor, Sri Vidyaniketan, Tirupati
Dr. B. K. Madhavi, Professor
Dr. Keerti Kumar, Professor
Dr. D. Venkat Reddy, Professor, MGIT
Sanket Goel, Associate Professor
Dr. D. Jayanthi, Professor, GRIET
Dr. I. V. Subba Reddy, Professor, GITAM University
Dr. Gulam Rasol Bagh, NIT Srinagar
Dr. Ramprasad, KHIT, Guntur
Dr. Usha Sree, Professor, VJIET
Prof. P. V. Rao, Professor, VBIT
Dr. Prabha Selvaraj, Professor, CSE, MRIET
Dr. Brahma Reddy, Professor, VBIT
Dr. Rangaiah, Professor, RRCE
Dr. Pushamala, Professor, DSCE University

Dr. Humaira Nishat, Professor, CVR College of Engineering
Dr. Kanaka Durga, Professor and HOD, MVSR
Dr. Abbas Ahmed
Dr. Prakash Rao, Professor, St. Peters Engineering College
Dr. Keerthikumar, Professor, ECE Department
Dr. Shankar Babu, Professor, TKR Engineering College
Dr. I. A. Pasha, BVRIT
A. Raja Sekhar, Professor and HOD, Methodist College of Engineering and Technology
Dr. Sharma, Professor, Sri Indu College of Engineering and Technology
Dr. Kezia Joseph, Professor, Stanley College of Engineering and Technology for Women

National and International Advisory Board List

International Advisory Board for ICIECE2017

Dr. Xiao-Zhi Gao, Finland University
Prof. Libor Rufer, CIMA, Micro and Nano Systems Groups, France
Dr. Vishal M. Patel, State University of New Jersey, USA
Dr. Savatri Bevinakopp, MIT Australia
Dr. C. H. Suresh Babu, K.K. University, Abha KSA
Shri. Rajashekhar N., INPHI, UK
Dr. Surgey Mosin, Vladimir State University, Russia
Dr. Katina Michael, University of Wollongong, Australia
Dr. Ahmed Faheem Zobaa, BU, UK
Dr. Akhtar Kalam, VU, Australia
Dr. Alfredo Vaccaro, US, Italy
Dr. David Yu, UMW, USA
Dr. Dimitri Vinnikov, TUT, Estonia
Dr. Gorazad Stumberger, UM, Slovenia
Dr. Jagadish Nayak, BITS Pilani, Dubai Campus
Dr. Lausiong Hoe, Multimedia University, Malaysia
Dr. Hussian Shareef, UK, Malaysia
Dr. Murad Al-Shibli, Head, EMET, Abu Dhabi
Dr. Nesimi Ertugrul, UA, Australia
Dr. Richarad Lanchard, LBU, UK
Dr. Shashi Paul, DM, UK
Dr. Zhao Xu, HKPU, Hong Kong
Dr. Ahmed Zobaa, Brunel University London, UK
Dr. Adel Nasiri, UMW, USA
Dr. P. N. Sugunathan, NTU, Singapore
Dr. Hiroya Fuji Saki, University of Tokyo
Dr. Fawnizu Azmadi Hussin, Universiti Teknologi Petronas, Malaysia
Dimov Stojce Ilcev, DUT, Durban, South Africa

National Advisory Board for ICIECE2017

Dr. Mohammed Zafar Ali Khan, Associate Professor and HOD, EE Department, IIT Hyderabad
Dr. Gulam Mohammed Rather, Professor, ECE, NIT Srinagar
Dr. N. Bheem Rao, Associate Professor, NIT Warangal
Dr. P. Radha Krishna, Principal, Research Scientist, Infosys Labs, Hyderabad
Dr. M. Madhavi Latha, Professor, ECE, JNTU Hyderabad
Dr. V. Malleswara Rao, Professor and HOD, ECE, GITAM University, Visakhapatnam
Dr. T. Srinivasulu, Professor, Professor and Dean, Faculty of Engineering, KU, Warangal
Dr. S. Ramanarayana Reddy, HOD, CSE, IGDTUW, Delhi
Dr. N. V. L. Narasimha Murthy, IIT Bhubaneswar
Dr. P. V. Rao, Raja Rajeswari College of Engineering, Bengaluru
Dr. B. N. Bhandari, JNTUH, Hyderabad
Dr. P. Lakshmi Narayana, Osmania University, Hyderabad
Dr. Pamela Chawla, Director, Institute of Engineering, MAU, Himachal Pradesh
Dr. Novalina Jacob, Scientist, ADRIN, Hyderabad
Dr. M. Lakshminarayana, Scientist-H (Retd) and Former Associate Director, DLRL
Ms. Madhumita Chakravarti, Scientist-G

Contents

Part III VLSI

Part IV Communication

Editors and Contributors

About the Editors

Dr. H. S. Saini is a Managing Director of Guru Nanak Institutions and obtained his Ph.D. in the field of Computer Science. He has over 22 years of experience at university/college level in teaching UG/PG students and has guided several B.Tech., M.Tech., and Ph.D. projects. He has published/presented more than 30 high-quality research papers in international and national journals and proceedings of international conferences. He is the editor for *Journal of Innovations in Electronics and Communication Engineering (JIECE)* published by Guru Nanak Publishers. He has two books to his credit. He is a lover of innovation and is an advisor for NBA/NAAC accreditation process to many institutions in India and abroad.

Prof. Ravi Kishore Singh is an Associate Director of Guru Nanak Institutions Technical Campus and an alumina of REC (now MNIT Jaipur). He did his M. Tech. from IIT Bombay in the field of Communication Engineering. He has served Indian Army in the core of Electronics and Mechanical Engineering for 20 years before hanging his uniform as Lt Col. He has rich industrial experience as army officer managing workshops and has been teaching faculty for more than 6 years while in services. He started his career as Teaching Assistant at MNIT Jaipur for 1 year before joining army. As professor, he has served for more than 11 years after premature retirement from the army

services. He has served as HOD, Vice Principal, and Principal of engineering college before being approved as an Associate Director of this institute. He had hands-on experience in high-tech electronic equipments and has done many courses on radars and simulators. He has published many papers on microstrip antennas, VLSI, and radar signal processing in national and international conferences. He is presently pursuing his Ph.D. from GITAM University.

Dr. Vishal M. Patel is an Assistant Professor in Rutgers University, the State University of New Jersey, Piscataway, New Jersey, USA. He obtained his Ph.D. in the field of Electrical Engineering from University of Maryland. He is a member of the information forensics and security technical committee of IEEE Signal Processing Society. He is also an Associate Editor of IEEE Signal Processing Magazine and IEEE Biometrics Compendium. He has over 7 years of experience at university/college level in teaching.

Dr. K. Santhi completed her Ph.D. in Anna University, Chennai, in the year 2015; M.E. in Applied Electronics from Anna University, Chennai, in the year 2007; and B.E. in Electrical and Electronics Engineering from Madras University in the year 2000. She is working as a Professor in the Department of Electronics and Communication Engineering at Guru Nanak Institutions Technical Campus, Hyderabad. She has more than 25 publications in international and national journals and conferences which include IEEE, Springer, and Elsevier. She has organized many seminars, workshops, and international conferences. She is a Member of IEEE and Life Member of ISTE and IETE. Her research interest areas are digital image processing, electronics, control system, and image analysis for metallography. She has 19 years of teaching and 9 years of research experience.

Dr. S. V. Ranganayakulu is currently working as Dean (R&D) in Guru Nanak Institutions Technical Campus. He holds master's degree in Electronics, M.Phil. in the area of Liquid Crystal Display (LCD) from Andhra University, and Ph.D. in the area of Ultrasonic Engineering from Osmania University, Hyderabad. He also holds NDT Level II certification awarded by ASNDT. He has 25 years of teaching as well as administrative experience at postgraduate and undergraduate levels at various institutions. He guided 32 M.Phil. scholars and 8 PG projects and is presently guiding 6 Ph.D. scholars. He has to his credit 42 papers in international and national journals. He has also presented 46 research papers in national and international conferences. He is an editorial board member in various national and international journals. He is Fellow of Acoustical Society of India and Ultrasonics Society of India. He also severed as the Member of Board of Studies in Electronics and Instrumentation in Acharya Nagarjuna University for 8 years. He was awarded Research Excellence Award by Indus Foundation for extensive contribution in research and development. He has published four textbooks. Moreover, he filed one patent and industrial design as a part of Intellectual Property Rights (IPR).

Contributors

B. Abraham David R&D Division, DSP Engineer, Vision Krest Embedded Technologies, Hyderabad, India

Subrata Kumar Aditya Department of Electrical and Electronic Engineering, University of Dhaka, Dhaka, Bangladesh

Syed Jalal Ahmad MIET, Jammu, Jammu and Kashmir, India

Syed Awais Ahmed Department of ECE, Guru Nanak Institutions Technical Campus, Hyderabad, India

G. Akhil Department of E&C, Manipal Institute of Technology, Manipal, Karnataka, India

Md. Aleem Research scholar, SSSUTMS, Sehore, MP, India

Basavaraj Amrapur Department of Electrical & Electronics Engineering, PDA College of Engineering, Kalaburagi, Karnataka, India

Thota Anurag Department of ECE, Guru Nanak Institutions Technical Campus, Hyderabad, India

V. Aparna Manipal Institute of Technology, Manipal, India

Sushruth Badri Manipal Institute of Technology, Manipal, India

P. Balaji CSE Department, CBIT, Hyderabad, India

Ajinkya Bankar Electronics and Telecommunication Department, Vidya Pratishthan's Kamalnayan Bajaj Institute of Engineering and Technology, Baramati, India

Rajkumar D. Bhure GITAM, Hyderabad, Telangana, India

C. Bhuvaneswari Department of Electrical and Electronics Engineering, Sathyabama University, Chennai, India

S. M. K. Chaitanya Department of ECE, G. V. P. College of Engineering (Autonomous), Visakhapatnam, Andhra Pradesh, India

Debashis Chakraborty Department of CSE, St.Thomas' College of Engineering & Technology, Kolkata, India

M. Chandra Mohan JNTUHCEH, Hyderabad, India

P. Chandra Sekhar Reddy Department of ECE, JNT University, Hyderabad, Andhra Pradesh, India

P. Chenna Reddy Department of Computer Science and Engineering, JNTUA, Anantapuramu, Andhra Pradesh, India

Bandella Deepika Chowdary ECE, Guru Nanak Institutions Technical Campus, Hyderabad, India

Tejash G. Chowhan Department of ECE, Guru Nanak Institutions Technical Campus, Hyderabad, India

Somasundaram Devaraj Sri Shakthi Institute of Engineering & Technology, Coimbatore, Tamil Nadu, India

Abhijit Dey GNITC, Hyderabad, Telegana, India

Ravilla Dilli Department of ECE, Manipal Institute of Technology, Manipal, India

Mahendra M. Dixit Department of E&CE, SDMCET, Dharwad, Karnataka, India

M. Durga Rani PSCMRCET, Vijayawada, India

B. Ebenezer Abishek Vels University, Pallavaram, Chennai, Tamil Nadu, India

M. Elangovan Department of Electronics and Communication Engineering, Government College of Engineering, Bargur, Tamil Nadu, India

Umar Farooq Department of Electronics and Communication, National Institute of Technology Srinagar, Srinagar, India

Rajeswara Rao Gangula G.V.P. College of Engineering (Autonomous), Visakhapatnam, India

Jayanand P. Gawande Instrumentation and Control Department, MKSSS's Cummins College of Engineering for Women, Pune, India

Aaruni Goel Department of Computer Science and Engineering, Mewar University, Chittorgarh, Rajasthan, India

Sasibhushana Rao Gottapu Andhra University college of Engineering, Visakhapatnam, India

K. Gunavathi Department of Electronics and Communication Engineering, PSG College of Technology, Chennai, Tamil Nadu, India

Ayan Hore Department of CSE, St.Thomas' College of Engineering & Technology, Kolkata, India

Apurwa S. Jagtap MKSSS'S Cummins College of Engineering for Women, Pune, India

Pratik Jain Department of CSE, St.Thomas' College of Engineering & Technology, Kolkata, India

A. Jaya Lakshmi Vardhaman College of Engineering, Hyderabad, Telangana, India

S. Jerritta Vels University, Pallavaram, Chennai, Tamil Nadu, India

M. Naga Lakshmi Kalyani PSCMRCET, Vijayawada, India

K. Krishna Kumar GNITC, Hyderabad, Telangana, India

K. Santhi Guru Nanak Institutions Technical Campus, Hyderabad, Telangana, India

Y. Kumari Department of ECE, PSCMR College of Engineering and Technology, Vijayawada, Andhra Pradesh, India

J. Lakshmi Narayana PSCMRCET, Vijayawada, India

J. Lavanya Electronics and Communications Department, VJIT, Moinabad, India

K. Leelaram Vels University, Pallavaram, Chennai, Tamil Nadu, India

M. Lokesh Chowdary Gudlavalleru Engineering College, Gudlavalleru, Andhra Pradesh, India

Nirmala Madian K. S. Rangasamy College of Technology, Namakkal, Tamil Nadu, India

Sirisha Madiraju Department of ECE, Guru Nanak Institutions Technical Campus, Hyderabad, India

Ranjan Kumar Mahapatra Department of Electronics and Communication Engineering, NITK, Surathkal, India

R. Maheswar Department of ECE, Sri Krishna College of Technology, Coimbatore, Tamil Nadu, India

V. Mahima Department of ECE, Veltech Rangarajan Dr Sagunthala R&D Institute of Science and Technology, Chennai, India

Mihir Malladi Department of Electronics and Communication Engineering, CMR Institute of Technology, Bengaluru, India

A. Mallaiah Gudlavalleru Engineering College, Gudlavalleru, Andhra Pradesh, India

K. Manjunath Chari GITAM University, Hyderabad, Telangana, India

V. Mithun Department of Electronics and Communication Engineering, CMR Institute of Technology, Bengaluru, India

Shaik Noor Mohammad SSSUTMS, Sehore, Madhya Pradesh, India

Amruta V. More Instrumentation and Control Department, MKSSS's Cummins College of Engineering for Women, Pune, India

N. Mounika PSCMRCET, Vijayawada, India

Murthy K. R. Narasimha Department of Computer Science and Engineering, M. S. Ramaiah University of Applied Sciences, Bengaluru, India

Akshay Naregalkar VNR Vignana Jyothi Institute of Engineering and Technology, Hyderabad, India

K. B. N. Naveen Department of Electronics and Communication Engineering, CMR Institute of Technology, Bengaluru, India

R. Obul Kondareddy Department of CSE, Institute of Aeronautical Engineering, Hyderabad, India

Anjali S. Patil Instrumentation and Control Department, MKSSS's Cummins College of Engineering for Women, Pune, India

Sanjeeva Polepaka JNTUH, Hyderabad, India

S. Premkumar Pondicherry Engineering College, Pillaichavady, Puducherry, India

N. Punith Department of Electronics and Communication Engineering, CMR Institute of Technology, Bengaluru, India

Arun Raaza Vels University, Pallavaram, Chennai, Tamil Nadu, India

K. Ragini G. Narayanamma Institute of Technology & Science (for women), JNTUH, Hyderabad, India

Dhanasekaran Rajagopal Guru Nanak Institute of Technology, Hyderabad, Telangana, India

V. Rajendran Vels University, Pallavaram, Chennai, Tamil Nadu, India

P. Rajesh Kumar Department of ECE, Andhra University College of Engineering (Autonomous), Visakhapatnam, Andhra Pradesh, India

B. Rama Rao Department of ECE, Aitam, Tekkali, India

G. V. Ramanaiah Department of ECE, PSCMR College of Engineering and Technology, Vijayawada, Andhra Pradesh, India

A. Ramesh Department of ECE, PSCMR College of Engineering and Technology, Vijayawada, Andhra Pradesh, India

C. Ramesh CMR Institute of Technology, Bengaluru, India

Rangayya Department of Electronics & Communication Engineering, APPA Institute of Engineering and Technology, Kalaburagi, Karnataka, India

D. Elezebeth Rani GITAM University, Vizag, India

Kovvur Ram Mohan Rao IT Department, Vasavi College of Engineering, Hyderabad, India

Padmakar Rao Electronics and Communications Department, VJIT, Moinabad, India

Ghulam Mohammad Rather Department of Electronics and Communication, National Institute of Technology Srinagar, Srinagar, India

M. Ravinder KCEA, Nizamabad, Telangana, India

O. Ravinder GNITC, Hyderabad, Telangana, India

Jyoti M. Roogi Department of Electronics and Communication Engineering, CMR Institute of Technology, Bengaluru, India

Sudhir K. Routray Department of Telecommunication Engineering, CMR Institute of Technology, Bengaluru, India

Etee Kawna Roy Department of Electrical and Electronic Engineering, University of Dhaka, Dhaka, Bangladesh

D. Sagar Department of Computer Science and Engineering, M. S. Ramaiah University of Applied Sciences, Bengaluru, India

V. Saminadan Pondicherry Engineering College, Pillaichavady, Puducherry, India

P. Saravanan School of Computing, Sathyabama University, Chennai, India

Mrinal J. Sarma Department of Electronics and Communication Engineering, CMR Institute of Technology, Bengaluru, India

M. Satya Sai Ram Department of Electronics and Communication Engineering, Chalapathi Institute of Engineering and Technology, Guntur, Andhra Pradesh, India

Kakara Satyavathi Department of ECE, Malla Reddy Institute of Engineering & Technology, Hyderabad, India

B. Senthil Tn Govt, Chennai, India

N. V. Seshagiri Rao Department of ECE, PSCMR College of Engineering and Technology, Vijayawada, Andhra Pradesh, India

A. H. Sharief Gandhiji Institute of Science and Technology, Jaggayapeta, India

K. P. Sharmila CMR Institute of Technology, Bengaluru, India

N. S. V. Shet Department of Electronics and Communication Engineering, NITK, Surathkal, India

Revati Shriram MKSSS'S Cummins College of Engineering for Women, Pune, India

K. Shruthi Springer-Verlag, Computer Science Editorial, Heidelberg, Germany

S. M. Shyni Department of Electrical and Electronics Engineering, Sathyabama University, Chennai, India

R. P. Singh SSSUTMS, Sehore, Madhya Pradesh, India

Ravi Kishore Singh ECE, Guru Nanak Institutions Technical Campus, Hyderabad, India

M. Sirisha Department of ECE, GuruNanak Institutions Technical Campus, Hyderabad, India

Sri Soumya Somu Manipal Institute of Technology, Manipal, India

A. L. Sreenivasulu Department of Computer Science and Engineering, JNTUA, Anantapuramu, Andhra Pradesh, India

Ch. Srinivasa Rao JNTUKUCEV, Vizianagaram, India

M. Srivani Department of ECE, GuruNanak Institutions Technical Campus, Hyderabad, India

Chilakala Sudhamani Department of Electronics and Communication Engineering, CMR Technical Campus, Hyderabad, Telangana, India

S. J. Sugumar Department of ECE, Guru Nanak Institutions Technical Campus, Hyderabad, India

Sheereen Sulthana G. Narayanamma Institute of Technology & Science (for women), JNTUH, Hyderabad, India

M. Susithra Pondicherry Engineering College, Pillaichavady, Puducherry, India

N. Susmita Department of ECE, GuruNanak Institutions Technical Campus, Hyderabad, India

M. Swamy Das CSE Department, CBIT, Hyderabad, India

M. Krishna Teja Department of ECE, GuruNanak Institutions Technical Campus, Hyderabad, India

S. Thenmozhi Department of ECE, Sri Krishna College of Technology, Coimbatore, Tamil Nadu, India

Rusydi Umar Department of Informatics Engineering, Faculty of Industrial Technology, Ahmad Dahlan University, Yogyakarta, Indonesia

G. Vamsi Krishna VNR Vignana Jyothi Institute of Engineering and Technology, Hyderabad, India

K. Vamsi Meghana Manipal Institute of Technology, Manipal, India

B. Vanajakshi PSCMRCET, Vijayawada, India

K. Vasanth Sathyabama University, Chennai, Tamil Nadu, India; Department of Electronics and Communication Engineering, Vidya Jyothi Institute of Technology, Hyderabad, India

A. K. Vasistha Department of Computer Science and Engineering, Mewar University, Chittorgarh, Rajasthan, India

C. Vijaya Department of E&CE, SDMCET, Dharwad, Karnataka, India

Kalyani P. Wagh Sathyabama University, Chennai, Tamil Nadu, India

Asmita Wakankar Instrumentation and Control Department, MKSSS's Cummins College of Engineering for Women, Pune, India

Part I
Signal and Image Processing

Development and Simulation Analysis of a Robust Face Recognition Based Smart Locking System

D. Sagar and Murthy K. R. Narasimha

Abstract Face recognition based smart locking systems are susceptible to variation in ambient light conditions. This paper presents a robust face recognition based smart locking system. The novelty of our work is that the choice of the algorithm for face detection and recognition is based on the intensity of light at that time. This system uses basic principal component analysis, linear discriminant analysis, and its variants for face detection and recognition. Access is granted to the user if their image matches one in a predefined database. In case the light intensity is so low that no algorithm gives a satisfactory result, our system will authenticate via a Bluetooth-based one-time passcode. MATLAB/Simulink was used to simulate this system which was subsequently prototyped. The developed prototype had 90% accuracy in low light conditions when larger training databases are used and 90% accuracy in normal light conditions when smaller training databases are used.

Keywords Face Recognition · Principal component analysis (PCA) Linear discriminant analysis (LDA) · Histogram equalization (HE) MATLAB/Simulink

1 Introduction

Face recognition is one of the techniques used by smart locking systems to determine whether an individual should be granted access to a restricted resource. The basic principle of face recognition based smart locks is face detection followed by face recognition by comparing against a set of known images. There are quite a few smart locking systems that work on the principle of facial recognition.

D. Sagar (✉) · M. K. R. Narasimha
Department of Computer Science and Engineering,
M. S. Ramaiah University of Applied Sciences, Bengaluru, India
e-mail: sagar.cs.et@msruas.ac.in

M. K. R. Narasimha
e-mail: nmurthy.cs.et@msruas.ac.in

H. S. Saini et al. (eds.), *Innovations in Electronics and Communication Engineering*,
Lecture Notes in Networks and Systems 33,
https://doi.org/10.1007/978-981-10-8204-7_1

Android's trusted face feature [1] is one of the most well-known facial recognition based smart locks. It unlocks a smartphone by authenticating the user based on an image captured using its front camera.

This type of smart locking system opens up a plethora of possible applications in the automotive sector as well. Automobiles like Maybach Exelero, Lamborghini Veneno, Bugatti Veyron, etc. cost millions of dollars. Under these circumstances, the ownership rights of the individual are of utmost importance [2]. It is of utmost importance that access to vehicles is restricted to their owners only [3, 4].

Face recognition based smart locks generally suffer from one disadvantage. The intensity of light when the image is taken contributes significantly to the effectiveness of the face recognition algorithm, as evidenced in [5]. Attempts to invent robust face recognition algorithms that are resistant to lighting variations have been documented extensively, such as in [6–9]. While these algorithms fulfill the mandate of reducing the effect of improper illumination, their complexity makes it unlikely for them to be implementable and prototyped.

Our paper addresses this lacuna by developing a smart and robust face detection based locking system. This system utilizes three basic algorithms for face detection and recognition: Principal Component Analysis (PCA) [10], PCA with Histogram Equalization [11] and Linear Discriminant Analysis (LDA) [12]. The novelty of our system is that the decision of which algorithm to use for the face detection and recognition is based on the intensity of light at the moment the test image is captured. To handle the case where the intensity of light is lesser than the lowest threshold, our system incorporates a Bluetooth-based One-Time Passcode (OTP) module that authenticates the user by an OTP sent via a preconfigured Bluetooth device.

The rest of the paper is organized as follows. In Sect. 2, we have summarized some of the existing literature in the area of facial recognition based smart locking techniques. Section 3 deals with the design of our system followed by Sect. 4 that documents the hardware and software developments of the system. The developed system is analyzed for performance and other aspects in Sect. 5, while Sect. 6 concludes our paper and presents some directions for the enhancement of this system.

2 Related Work

The authors of [13] have developed an attendance system based on face recognition. The authors have considered a cohort of 100 students and hypothesized that the process of manual attendance marking is tedious and time-consuming. Using face recognition to mark attendance is also susceptible to drawbacks such as illuminating conditions, head pose, light intensity, etc. The objective of this project is to develop the face recognition system that can overcome abovementioned drawbacks and use it in the application for attendance registration for students.

The authors of [14] propose a web-based online embedded door access control and home security system using face recognition. Face recognition is done using PCA and the electromagnetic doors are controlled through active web pages enhanced with software like Javascript and HTML. Communication is handled using ZigBee and a GSM module is used to send notifications to the owner.

The authors of [15] propose an autonomous car system that uses facial recognition to restrict unauthorized use of the vehicle. This work also uses geolocation services to accurately pinpoint the location of vehicles. The authors also claim that geolocation is useful in detecting cases of over speeding.

The authors of [16] propose a mechanism to use facial analysis to identify and recognize human emotions. These parameters have subsequently been used in the implementation of a home automation system.

3 Design of the Proposed System

The high-level block diagram of our proposed system is shown in Fig. 1. Initially, the system is in idle state and the user engages the system by touching the impact sensor. This avoids the system from working unnecessarily. Once the system is engaged, the camera is activated which clicks a picture. Simultaneously, the intensity of light at that instant is captured using a Light-Dependent Resistor (LDR).

After this step, the face (if any) is detected in the image and then the face recognition algorithm takes over to recognize the face by comparing it against a set of predefined images. The process of face recognition is explained in greater detail subsequently. If the face in the image matches one in the database, the user is granted access. The system operates a DC motor to symbolize this phase.

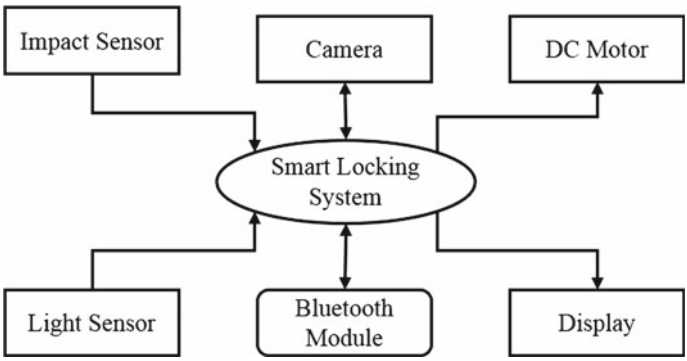

Fig. 1 Block diagram of the smart locking system

3.1 Design Specifications of the System

To achieve the functionality of the system as identified above, we arrived at the following set of design specifications for our system.

(1) Once threshold set for force sensor is crossed, the system should initiate the authentication process and read light sensor's values.
(2) Depending on the intensity of the light, the system should select method of authentication.
(3) If the recorded value from the light sensor is below-set threshold, the system should initiate the OTP authentication process.
(4) If OTP authentication process is initiated, the system should initiate the Bluetooth module.
(5) The system should allow only registered Bluetooth device to connect with Bluetooth module interfaced to the system.
(6) If Bluetooth pairing is successful, the system should send generated OTP to the paired device and wait for the response from the paired device.
(7) If system receives response in the form OTP from the paired device, the system should verify the received OTP with the sent OTP.
(8) If sent and received OTP matches, the system should turn the motor, allowing access to the user.
(9) If sent and received OTP do not match, the system should go back to idle state.
(10) If the value of the light sensor is above-set threshold, the system should activate the camera to take a picture.
(11) Based on the intensity of the light measured, an appropriate algorithm is chosen to perform face recognition.
(12) If the picture matches a face in the stored data, the system should turn the motor, allowing access to the user.
(13) If the picture does not match a face in the stored data, the system should go back to idle state.

3.2 Changing the Face Detection and Recognition Algorithms

From the existing literature in [17] and [18], we have observed that for images that have a high level of light intensity (images taken in bright light), the technique chosen for image detection and recognition is PCA combined with histogram equalization. For images where the ambient light is slightly lesser, just PCA gives accurate results. For images taken in low light intensity conditions, LDA combined with enhance technique gives the best results.

Table 1 Brightness levels and corresponding algorithms

Brightness range (%)	Method of authentication
≥ 70	PCA + histogram equalization
≥ 50 and <70	PCA
>20 and <50	LDA + enhance
<20	OTP using Bluetooth

In our system, we have defined three brightness levels and the corresponding face detection and recognition techniques. If the light intensity is lower than the lowest threshold, then the Bluetooth module takes over to authenticate the user. This is tabulated in Table 1.

3.3 Flowchart of the Proposed Smart Locking System

The flowchart of the system is presented in Fig. 2. This flowchart is developed considering that the restricted resource is a door and the user is trying to open it. Once the system is started, the force sensor is monitored to see whether the user wants to authenticate himself. This is necessary so that the system does not attempt to authenticate random faces.

Once the system confirms that the user has triggered the force sensor for authentication, the system initiates the light sensor (LDR) to evaluate the external environment in terms of the lighting condition. If the LDR detects enough light for

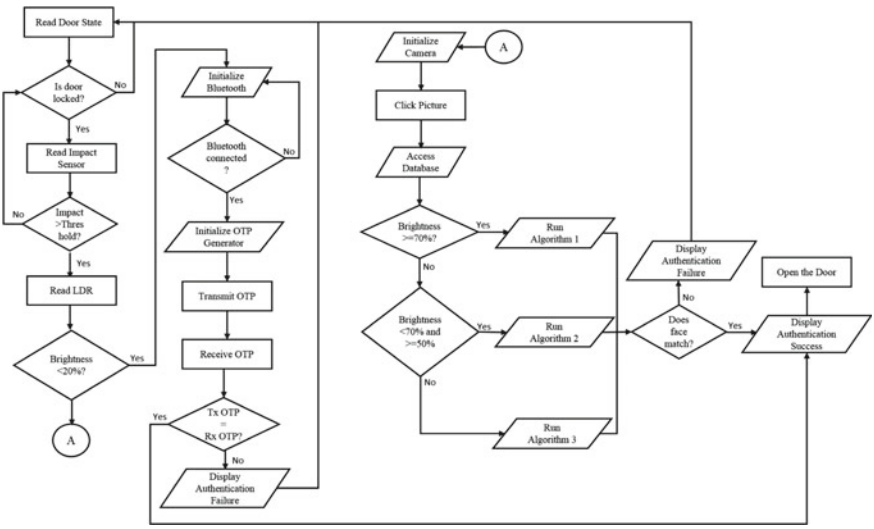

Fig. 2 Flowchart of the developed smart locking system

face recognition, the system initiates the face recognition process by activating the camera and taking a photo of the user.

This is followed by running algorithm 1 (PCA + Histogram Equalization), algorithm 2 (PCA), or algorithm 3 (LDA + Enhance) based on the intensity of the light measured. Once the face is detected, the system compares it against a database of images that are allowed to access the resource. The door is opened if the face is recognized as matching any face image in the database.

If the light intensity is lower than the lowest threshold, the system initiates the OTP-based authentication system by initiating the Bluetooth module. The user's smartphone and smart lock are paired. Once the system authenticates the paired device, the system initiates OTP generating algorithm and sends an OTP to the phone. After the response is received from the smartphone, the system verifies the received OTP with the sent OTP to authenticate the user and unlock the smart lock.

4 Implementation of the System

4.1 Software Implementation

The face recognition based smart locking system designed in the previous section is simulated using MATLAB/Simulink. Figure 3 shows part of the code written to simulate PCA and Fig. 4 shows how histogram equalization is performed on a given test image. The other algorithm used for face detection and classification is a combination of LDA and enhance shown in Figs. 5 and 6, respectively. In case the light intensity is too low for any algorithm to work, the user is authenticated via OTP. The code for this is shown in Fig. 7.

```
TestImage = imread('test.jpg');
TestImage=TestImage;
axes(handles.axes1);
pause(1);
imshow(TestImage);
similarity_score = pcaeigen(TestImage,images,num_images)
set(handles.text2,'string','Processing with Algorithm 2 (50-69) ')
```

Fig. 3 Code snippet of PCA of a test image

Fig. 4 Code snippet of histogram equalization

```
TestImage = imread('test.jpg');
TestImage=adapthisteq(TestImage);
axes(handles.axes1)
pause(1);
```

```
imshow(TestImage)
similarity_score = ldaeigen(TestImage)
set(handles.text2,'string','Processing with Algorithm 3 (21-49) ')
```

Fig. 5 Code snippet of LDA of a test image

```
TestImage = imread('test.jpg');
%TestImage=imgradient(TestImage,'prewitt');
TestImage=enhance(TestImage);
TestImage=rgb2gray(TestImage);
axes(handles.axes1)
pause(1);
```

Fig. 6 Code snippet to perform image enhancement

```
newotp=otp;
fopen(s);
    fwrite(s,strcat('O',num2str(newotp)));
    fclose(s);
    set(handles.text2,'string','Generating OTP ')
```

Fig. 7 Code snippet to initialize OTP

4.2 Hardware Prototype

The developed software was ported onto a hardware prototype created using a Renesas board (RL78 G13), LDR sensor, impact sensor, Bluetooth module, DC motor, and a motor driver module. We programmed the Renesas microcontroller using the Cubesuite+ IDE. The schematic diagram is shown in Fig. 8 and the prototype is shown in Fig. 9.

5 Testing and Analysis of the System

5.1 Simulation Analysis

1. Uniqueness of the OTP

Our system generates a 4-bit OTP to authenticate users. This OTP is transmitted via an onboard Bluetooth module to the user's smartphone. The user then re-enters the OTP which is verified by the system. We tested the OTP generation for its uniqueness and found that the OTP generated was unique for all set variables which we considered. This result is presented in Fig. 10.

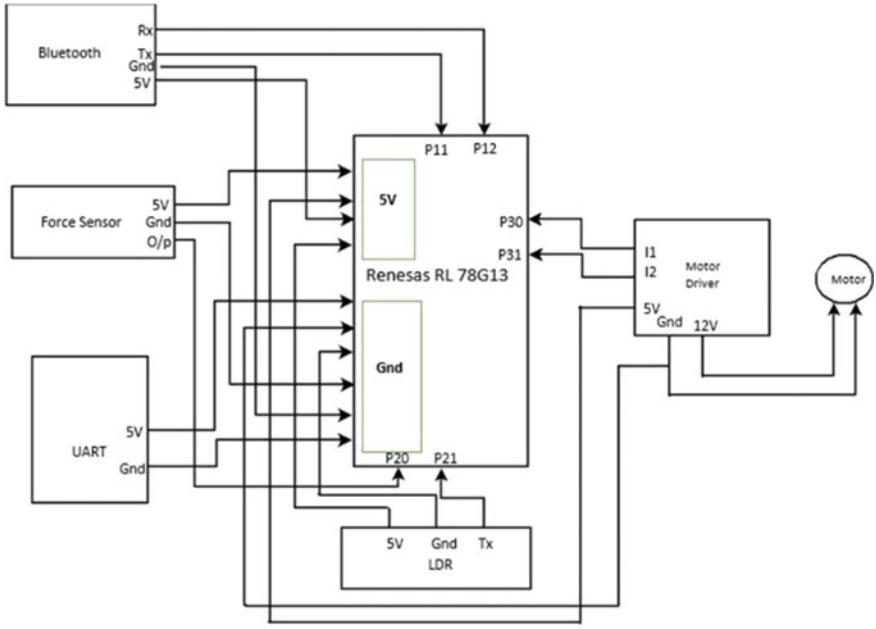

Fig. 8 Schematic diagram to develop hardware prototype

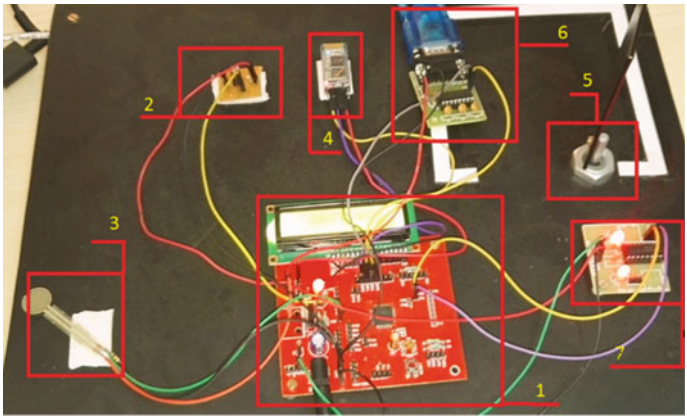

Fig. 9 Hardware prototype of the developed system

2. Time taken for user authentication

This analysis was performed to estimate the amount of time taken by the system to authenticate the user. This time is taken to be the time between the camera clicking the picture to the motor turning to signify granting access, or the notification

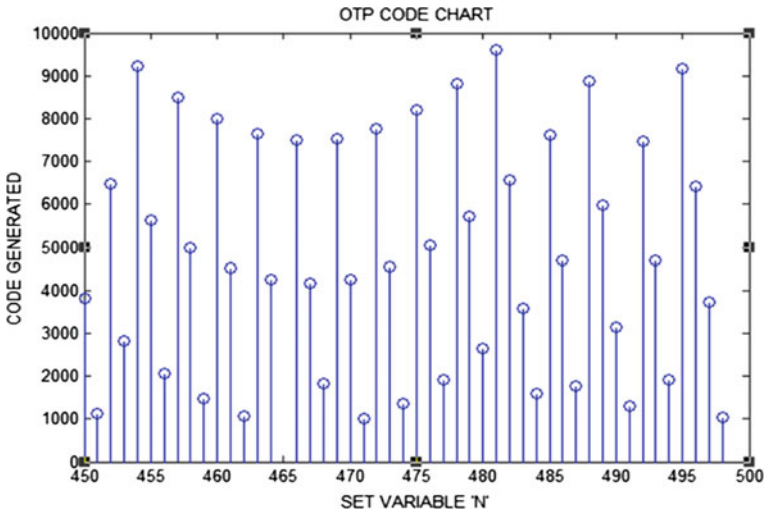

Fig. 10 OTP code chart

regarding authentication failure. It was found that PCA + Histogram Equalization (algorithm 1) took 15 s to complete, whereas PCA (algorithm 2) took 10 s. LDA + Enhance (algorithm 3) took about 12.5 s to complete.

5.2 Testing the Hardware Prototype

The developed hardware prototype was tested with a series of images with varying light intensities. Figures 11 and 12 show the subject under dark and bright light intensity, respectively.

Fig. 11 Testing under dim light condition

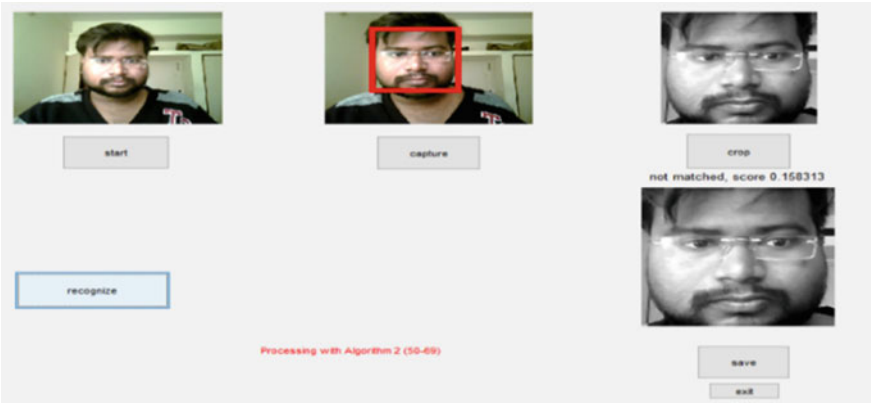

Fig. 12 Testing under bright light condition

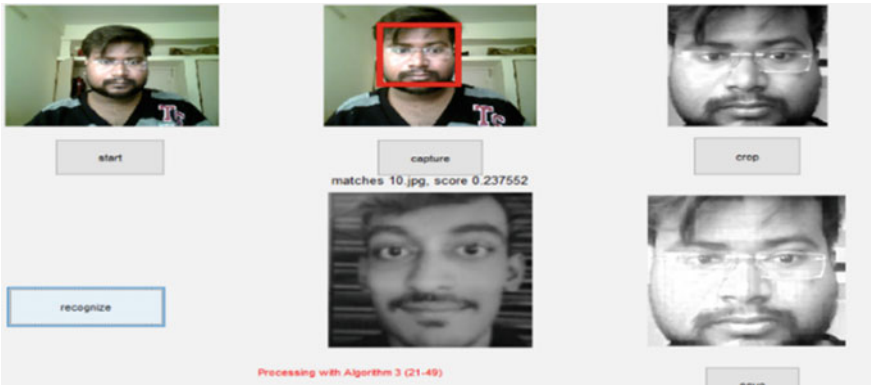

Fig. 13 Authentication failure

It is seen that the system is able to recognize the face in both cases. Figure 13 shows that the access is not granted if the test image does not match any image in the database.

6 Conclusion and Future Direction

From this work, we would like to conclude that it is possible to build a low-cost and easy to implement face recognition based locking system that can be used to control access to restricted resources such as automobiles, warehouses, etc.

Most of the work that we have surveyed involves the development of algorithms that are resilient to background intensity changes. We have addressed the same

issue successfully, albeit by a different approach; we have changed the algorithm used for face detection and recognition based on the intensity of the ambient lighting.

The system that we have developed is limited to 2D image processing which can be extended to 3D image processing for a more efficient authentication process.

We have also noted the fact that the OTP authentication process is vulnerable for false authentication due to the fact that OTP-based authentication is restricted to authentication of the registered Bluetooth device and not the user.

Informed consent: Additional informed consent was obtained from all individual participants for whom identifying information is included in this article.

References

1. Duino J (2015) Trusted face in lollipop, explained, In: Android central. Available via http://www.androidcentral.com/face-unlock-explained. Accessed 27 Jan 2017
2. Hard A (2016) The 10 most expensive cars in the world make Teslas look like toyotas. In: Digitaltrends. Available via http://The10MostExpensiveCarsintheWorldMakeTeslaslooklike Toyotas. Accessed 27 Mar 2017
3. National Crime Records Bureau, Crime in India: a compendium, Ministry of Home Affairs, Government of India, New Delhi, 2014
4. MSN (2016) 25 companies richer than countries. In: MSN. Available via http://www.msn.com/en-za/money/financephotos/25-companies-richer-than-countries/ss-BBrvrKF#image=4. Accessed 27 Mar 2017
5. Wang H, Li S, Wang Y (2017) Face recognition under varying lighting conditions using self-quotient image. In Proceedings of the sixth IEEE international conference on automatic face and gesture recognition, Seoul
6. Ding C, Choi J, Tao D, Davis L (2016) Multi-directional multi-level dual-cross patterns for robust face recognition. IEEE Trans Pattern Anal Mach Intell 38(3):518–531
7. Li B, Mian A, Liu W (2017) Using kinect for face recognition under varying poses, expressions, illumination and disguise. In: 2013 IEEE workshop on applications of computer vision (WACV), Tampa, pp 186–192
8. Lai Z, Dai D, Ren C, Huang K (2014) Multilayer surface Albedo for face recognition with reference images in bad lighting conditions. IEEE Trans Image Process 23(11):4709–4723
9. Liu H, Yang M, Gao Y, Cui C (2014) Local histogram specification for face recognition under varying lighting conditions. Image Vis Comput 32(5):335–347
10. Turk M, Pentland A (1997) Face recognition using eigenfaces. In: Proceedings of the 1991 IEEE computer society conference on computer vision and pattern recognition, Maui, pp 586–591
11. Sinha U, Kangarloo H (2002) Principal component analysis for content-based image retrieval. RadioGraphics 22(5):1271–1289
12. Izenman A (2013) Linear discriminant analysis. In: Modern multivariate statistical techniques, pp 237–280
13. Wagh P, Thakare R, Chaudhari J (2015) Attendance system based on face recognition using Eigen face and PCA algorithms. In: 2015 international conference on green computing and internet of things (ICGCIoT), Noida, pp 303–308
14. Sahani M, Nanda C, Sahu A (2015) Web-based online embedded door access control and home security system based on face recognition. In: 2015 international conference on circuit, power and computing technologies (ICCPCT), Nagercoil, pp 1–6

15. Faisal M, Thakur A (2017) Autonomous car system using facial recognition and geo location services. In: 2016 6th international conference on cloud system and big data engineering (confluence), IEEE, pp 417–420
16. Khowaja S, Dahri K, Khumbar M (2015) Facial expression recognition using two-tier classification and its application to smart home automation system. In 2015 international conference on emerging technologies (ICET), Peshawar, pp 1–6
17. Dhere P (2015) Review of PCA, LDA and LBP algorithms used for 3D Face Recognition. Int J Eng Sci Innovative Technol (IJESIT) 4(1):375–378
18. Singh A (2012) Comparison of face recognition algorithms on dummy faces. The Int J Multimedia its Appl 4(4):121–135

An Efficient Speech Compression Technique in Time Domain with Nearly Constant Compression

Ayan Hore, Pratik Jain and Debashis Chakraborty

Abstract Speech compression is a widely scoped field with multiple possibilities in the fields of digital communication and transmission of data. It is of particular importance in digital signal processing. There are many commercially available methods both in time and frequency domains to aid the same. Speech file has multiple frequent redundancies present in the raw data. Taking into account the possibility that the frequencies present can be effectively encoded without appreciable change in speech quality, this paper goes on to describe an efficient and new approach with a satisfactory compression ratio and PSNR value for a sampling rate.

Keywords Speech · Compression · ADPCM · ASCII · Huffman
Sample value · MSE · PSNR · CR

1 Introduction

Data compression is a domain that encompasses the field which finds out the redundancies in data which can be reduced and/or encoded without causing significant loss in the quality. This is the same for text, image, audio, and video as well. Conventional methods include run length encoding (RLE), statistical, and dictionary-based methods. Long runs of identical samples can be identified by RLE [1], whereas dictionary methods check for similar phrases in data. Depending on the approach and necessity, compression algorithms can be categorized as lossy or

A. Hore (✉) · P. Jain · D. Chakraborty
Department of CSE, St.Thomas' College of Engineering & Technology, Kolkata 700023, India
e-mail: ayanhore18@gmail.com

P. Jain
e-mail: coolpratik1995@gmail.com

D. Chakraborty
e-mail: sunnydeba@gmail.com

H. S. Saini et al. (eds.), *Innovations in Electronics and Communication Engineering*,
Lecture Notes in Networks and Systems 33,
https://doi.org/10.1007/978-981-10-8204-7_2

lossless. The biggest constraints for uncompressed data transmission are exorbitant bandwidth necessity and storage space [2–5]. The problems thus presented had been addressed throughout history which started with Morse code and proceeded forth to Huffman's algorithm [6] using binary coding. Morse code was invented in 1838 for its usage in telegraphy and one of the first and foremost examples of data compression. It represented the text by a series of dots and dashes, just 9 years prior to the introduction of Boolean algebra by George Boole. It took another half a century for Boolean logic to become fully functional in the domain of logic and computation and finally pave the way for binary representation and usage. Morse code initiated that way for compression by using smaller codewords for the more commonly used letters in English. Modern work started to seek its way in the 1940s when Claude Shannon and Robert Fano devised a systematic way to assign codewords depending on the probability of blocks, which was further optimized by David Huffman in the early 1950s. In the late 1970s, pointer-based encoding became the choice of fashion, as envisaged by its pioneers Abraham Lempel and Jacob Ziv. Images presented itself as the mighty contender in the 1980s, a challenge suitably responded by GIF, JPEG, TIFF, etc.

Now with the advent of telephony, speech compression gained its relevance and importance in the domain of audio compression and data compression as a whole. Thus, it has become a major field of digital signal processing [7]. While in audio compression the trade-off between transmission quality and storage space gained much attention, speech compression had its own nuances, thanks to the certain biological features of both the human vocal cord and auditory system. These factors are exploited along with the redundancies of existing data and its component frequencies in the input signal. For example, the human ear has a hearing threshold and possesses a certain frequency range from 20 Hz to 20 kHz. The human voice also has a similar limitation as it ranges from 500 Hz to 2 kHz [1]. In addition to this, frequency and temporal masking are two properties of the human auditory system which is further exploited for audio compression [1].

In our case of speech compression, the sample values for the input signal are stored in a format. WAV stores uncompressed raw audio data in 16-bit PCM format. The requirement of data compression is wide and varied depending on the requirement of acceptable loss in data quality and requisite compression ratio (CR). And as such the transmission and storage of such data present a considerable challenge. Hence, peak signal-to-noise ratio (PSNR) and CR are factors which help in determining the efficiency of the strategies in action. Communication with time evolved from scribbled text messages to telephony and speech transmission thus emerged as a major player. The challenges in speech have been taken up in earnest and form a domain of utmost importance in digital signal processing. These challenges are being met with a variety of techniques in frequency domain, which involves discrete wavelet transform or discrete Fourier transform [8, 15] and as in this paper, the techniques available in the time domain [9] have been chosen for implementation and further usage.

2 Proposed Method

First, the proposed strategy commences from the application of ADPCM (Adaptive differential pulse code modulation) [10, 11] on the raw speech file which is the requisite input. This is followed by the subsequent transformation of the output to its corresponding hexadecimal code. Then, Huffman's algorithm is performed on the same. The binary output is stored as ASCII.

2.1 Algorithm Strategy

Obtaining the sampling frequency and bits per sample value of input speech signal, the individual 16-bit frames are passed on for performing ADPCM encoding on each sample. The 16-bit ADPCM [12, 13] encoder generates an output within the range of 0–15 and thus suitably converted into corresponding hexadecimal form. Now, Huffman coding algorithm is performed, and thus the binary code generated is stored. Now every 8 bits are converted into its corresponding ASCII form which is stored as the final compressed output.

For decompression, the ASCII values are read from the final output file and it is converted to its corresponding 8-bit binary values. These values served are stored and used to perform decoding the Huffman tree. The hexadecimal values on re-obtaining are then decoded to its equivalent decimal values. These values are fed to the ADPCM decoder which generates the decompressed output speech file. And hence, the CR and PSNR are calculated.

Here, ADPCM expands as adaptive differential pulse coding algorithm. ASCII is the abbreviated form of American Standard Code for Information Interchange, which is a character encoding standard. MSE is the mean squared error and PSNR stands for peak signal-to-noise ratio. CR is used to represent compression ratio.

2.2 Algorithm for Compression

The algorithm for ADPCM encoder is stated in a stepwise manner:

1. ADPCM encoder accepts 16-bit signed integer input obtained from the speech sample and it returns an 8-bit output which contains the 4-bit code for ADPCM which ranges from 0 to 15.
2. Restore the previous values of the samples predicted and the step size index of the quantizer.
3. The step size of the quantizer is found from a table lookup using the step size index of the quantizer.

4. The difference between the actual and predicted sample is calculated.
5. The sign bit of the ADPCM code is set if needed and the absolute value of the difference is computed.
6. A temporary variable is used to save the quantizer step size.
7. The difference is quantized into ADPCM code using quantizer step size.
8. The ADPCM code is inversely quantized to predict the difference using the step size of the quantizer.
9. The new predicted sample value is calculated by the fixed predictor when the old predicted sample value is added to the predicted difference.
10. Check for possible overflow of new predicted sample, which itself is a signed 16-bit integer number.
11. The new quantizer step size index is obtained by the addition of previous index and the table lookup using the ADPCM code.
12. Again check for possible overflow of the new quantizer step size index.
13. The new predicted sample is saved and the step size of the quantizer for next iteration.
14. Return the obtained ADPCM code.

The ADPCM code is thus encoded to its equivalent hexadecimal code and stored. Huffman algorithm is applied to this character string stored. Huffman encoding is based on the number of occurrences of the data item. The basic principle involved requires the usage of lower number of bits for the most frequent data. The encoded data are transmitted to enable decoding.

The algorithm for Huffman encoding is listed as follows:

1. Initialization by putting all nodes in open list which is always kept sorted.
2. Repeat until the open list has only one node remaining.
   a. From the open list, pick two nodes with the lowest frequency probability and consecutively create a parent node.
   b. Assign the sum of the frequencies of the children nodes to the parent node and insert that to the open list.
   c. Assign the codes (0, 1) to the two branches of the tree thus obtained and delete the children from the open list.

The encoding of the hexadecimal code ends here. The resultant code thus obtained is converted to its corresponding 8-bit ASCII values and stored.

2.3 Algorithm for Decompression

To decode, the ASCII values are converted to its equivalent 8-bit binary values. This is the encoded Huffman value.

The encoded Huffman code is mapped from the dictionary which was assigned before and the decoded data is thus obtained. This data is thus fed to the ADPCM decoder.

The algorithm for ADPCM decoder is as follows:

1. ADPCM decoders accept an 8-bit number containing the 4-bit ADPCM code which ranges from 0 to 15 and returns a 16-bit signed integer number.
2. The previous values of predicted sample and quantizer step size index are restored.
3. The quantizer step size is obtained from a table lookup using the quantizer step size index.
4. The ADPCM code is inversely quantized into a predicted difference using the quantizer step.
5. Fixed predictor calculates the new predicted sample by the addition of old predicted sample to the predicted difference.
6. Check for possible overflow of the new predicted sample, a signed 16-bit sample.
7. The new quantizer step size is found by adding the previous index and a table lookup by the usage of the ADPCM code.
8. Again check for possible overflow of the new quantizer step size index.
9. The new predicted sample value and quantizer step size index for next iteration are saved.
10. Return the new sample values.

2.4 Performance Measures

The following equations are used here for calculation of compression results:

$$\text{CR} = \frac{\text{Size of Input Signal} - \text{Size of Output Signal}}{\text{Size of Output Signal}} \tag{1}$$

$$\text{MSE} = \frac{1}{n}\sum_{i=1}^{n}(P_i - Q_i)^2 \tag{2}$$

where

N the number of speech samples in the input signal,
P_i ith sample in the input signal, and
Q_i ith sample in the output signal.

$$\text{RMSE} = \sqrt{\text{MSE}} \tag{3}$$

$$\text{PSNR} = 20\log_{10}\frac{max_i|P_i|}{\text{RMSE}} \tag{4}$$

where $max_i\,|P_i|$ is the magnitude of the maximum possible sample value in the input signal.

2.5 *Experimental Results*

See Table 1.

2.5.1 Figures

See Fig. 1.

Table 1 Experimental results of proposed method (P.M.) and MP3 on test files

Sl. No.	Results			CR (MP3)	PSNR (MP3)
	Filename	CR (P.M)	PSNR (P.M)		
1.	fen4.wav	81.9	45.154	49.84	84.288
2.	fen5.wav	81.76	45.154	49.60	84.28
3.	fge1.wav	80.23	45.154	74.69	42.12
4.	fge2.wav	79.36	45.154	74.69	42.85
5.	men3.wav	84	45.154	49.39	83.28
6.	men6.wav	82.16	45.154	47.83	84.28
7.	mge1.wav	82.56	45.154	74.69	42.58
8.	mge2.wav	79.36	45.154	74.69	42.97

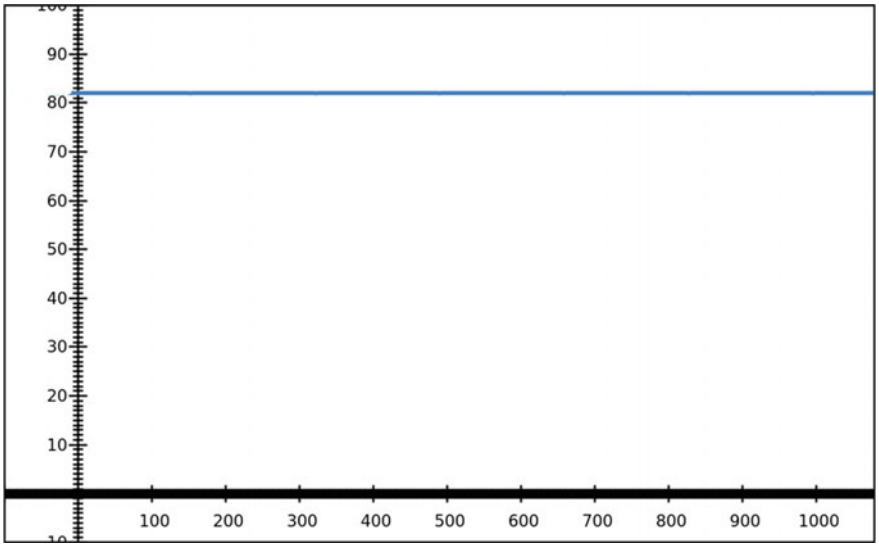

Fig. 1 Graph representing nearly constant compression ratio with respect to downloaded [14] input files of varying sizes

3 Conclusion

The requirement of speech compression in line with specific needs to be served in the various fields of communication that has led to the creation of algorithms that have tried to maximize its outreach on the field of efficient application be it in cellular networks, VoIP, or any modern communication system. Thus, the identification of redundancies remains the most important factor which when done in accordance with the desired trade-off, it is often found that the stakes are considerably high for either CR or PSNR. The method proposed in this paper promises a stable PSNR while performing with a CR better than that of MP3, which is a very popular standard for some time. In future, it may so happen that once the presence of similar samples is detected before initiation of compression, the various available techniques in a domain [8, 9] will be used to identify and separate the regions. Once this feat is attained, it will lead on ahead to applying the suitable algorithms followed by the proposed technique in this paper. It will possibly greatly reduce the size of the compressed file even further followed by consequent application of any preferable entropy coding, for instance, Huffman. Thus, with the possible future inclusion of identifying further redundancies, it might possibly attain even higher standards while keeping the stakes high for an acceptable quality along with storage space and bandwidth required for transmission on any network efficiently.

Acknowledgements We would like to thank Professor Subarna Bhattacharjee for her words of advice, supporting suggestions. Her criticisms, encouragement, and reviews presented to us gave better and more transparent approach and understanding. We owe a lot to the other faculty members of the department of computer science and information technology. It was in one such class of design and analysis of algorithms that we first envisioned the above algorithm. All reviews and comments paid us a dividend to ensure that the final work came into shape.

References

1. Salomon D (2007) Data compression the complete reference, 4th edn. Springer, London. ISBN 1846286026
2. Sun L et al (2013) Guide to voice and video over IP for fixed and mobile networks, computer communications and networks. Springer, London. https://doi.org/10.1007/978-1-4471-4905-7_2
3. ITU-T (1988) Pulse code modulation (PCM) of voice frequencies. ITU-T G.711
4. Forouzan BA (2007) Data communications and networking, 4th edn. McGraw-Hill, NewYork. ISBN 0072967757
5. Cormen TH, Leiserson CE, Rivest RL, Stein C (2001) Introduction to algorithms, 2nd edn. MIT Press and McGraw-Hill (ISBN: 0-262-03293-7)
6. Hemanthakumar MP, Swetha HN (2014) Design and implementation of ADPCM based audio compression 3(5):50–55
7. http://www.speech.cs.cmu.edu/databases/
8. Rajesh G, Kumar A, Ranjeet K (2011) Speech compression using different transform techniques. In: 2011 2nd international conference on computer and communication technology (ICCCT-2011), Allahabad, pp 146–151. https://doi.org/10.1109/iccct.2011.6075173

9. Wang Z (1984) Fast algorithms for the discrete W transform and for the discrete Fourier transform. IEEE Trans Acoust Speech Signal Process 32(4):803–816. https://doi.org/10.1109/tassp.1984.1164399
10. Vatsa S, Sahu OP (2012) Speech Compression using discrete wavelet transform and discrete cosine transform. Int J Eng Res Technol 1(5)
11. Cuperman V, Gersho A (1985) Vector predictive coding of speech at 16 kbits/s. IEEE Trans Commun 33(7):685–696
12. Cummiskey P, Jayant NS, Flanagan JL (1973) Adaptive quantization in differential PCM coding of speech. Bell Syst Tech J 52:1105–1118. https://doi.org/10.1002/j.1538-7305.1973.tb02007.x
13. Jayant NS (1974) Digital coding of speech waveforms: PCM, DPCM, and DM quantizers. Proc IEEE 62(5):611–632. https://doi.org/10.1109/PROC.1974.9484
14. Lilly BT, Paliwal KK (1996) Effect of speech coders on speech recognition performance Spoken Language, 1996. ICSLP 96. In: Proceedings., fourth international conference on, Philadelphia, vol 4, PA, USA, pp 2344–2347
15. Nelson M (1995) The data compression book, 2nd edn. IDG Books Worldwide, Inc. (ISBN: 1558514341)

Unsharp Masking-Based Image Enhancement of Nanodispersed 10O.O6 Liquid Crystal Compound

Y. Kumari, N. V. Seshagiri Rao, A. Ramesh and G. V. Ramanaiah

Abstract The main motto of the image enhancement in image processing is to process an image with suitable technique and to provide better visibility for a specific application. Novel image processing techniques are required to identify key features like transition temperatures, clear phase identification in the liquid crystalline images. Characterization and mesomorphic behavior in pure and 1% ZnO nanodispersed liquid crystalline N–(p–n–decyloxybenzylidene)–p–n–hexyloxy anilines, 10O.O6 compounds, are carried out using a polarizing microscope and images are preserved for enhancement. Both the compounds exhibit NACIG phases, and the transition temperatures of the 1% ZnO nanodispersed 10O.O6 are reduced compared with pure 10O.O6. Further, in this work, a novel image enhancement technique of combined unsharp masking is proposed on pure and 1% ZnO nanodispersed 10O.O6 liquid crystalline compounds for better visibility of phases at transition temperatures. The proposed method is used to identify the uniform regions and to detect the defects which may not be clearly observed from polarizing microscope.

Keywords Image enhancement · Nanodispersed LC (Liquid crystal) compound Phase transitions · Polarizing microscope · Unsharp masking

Y. Kumari (✉) · N. V. Seshagiri Rao · A. Ramesh · G. V. Ramanaiah
Department of ECE, PSCMR College of Engineering and Technology, Vijayawada, Andhra Pradesh, India
e-mail: kumarinvsr@gmail.com

N. V. Seshagiri Rao
e-mail: nvsrab@gmail.com

A. Ramesh
e-mail: rameshavula99@gmail.com

G. V. Ramanaiah
e-mail: gvr.m.tech@gmail.com

H. S. Saini et al. (eds.), *Innovations in Electronics and Communication Engineering*, Lecture Notes in Networks and Systems 33,
https://doi.org/10.1007/978-981-10-8204-7_3

1 Introduction

In the field of condensed matter physics, liquid crystals are mesophases with a degree of order in between that of solid and liquid. Liquid crystals (LC) are soft condensed matter and nowadays plays a wide role in various branches of technology such as optical switches, mobile phones, smart cards, information and integrated display devices, etc. The molecular structure of these materials is related to their mesophases [1]. So the identification and characterization of these mesophases will provide a very important information on the pattern and texture of different phases like nematic, smectic, and cholesteric. Suspensions of various nanoparticles to liquid crystals recently gained momentum because they combine the fluidity and anisotropy of liquid crystals with specific properties of particles strongly affects the dielectric properties of the system.

The liquid crystalline molecule is characterized by different LC phases due to the change in the local molecular order with the temperature giving rise to different phases. To identify the phase transitions in liquid crystalline materials, there are several techniques such as differential scanning calorimetry (DSC), polarizing optical microscope (POM), differential thermal analysis (DTA), etc. POM is the most widely used technique for identification of phase transition temperatures, whereas DSC and DTA give the presence of phase transitions in a material by detecting enthalpy and entropy changes.

Contrast enhancement is one of the requirements to visualize and understand the microscopic image content [2–8]. Generally, two types of algorithms are extensively developed for contrast enchantment of images. Type I deals with the process of enhancing the pixels in spatial domain and Type II concentrates by transformed pixels in frequency domain. Type I spatial domain enhancement is most widely used for contrast enhancement of digital images. The powerful technique used in many applications is global histogram equalization (GHE). GHE distributes the pixel intensities according to a uniform distributer taking in a nonuniform distribution of pixels. The technique uses full range of pixels and at times tends to produce noisy images. Hence, adaptive histogram equalization (AHE) is proposed to improve on the drawback of GHE. AHE uses a window of pixels on which the histogram equalization is applied. These adaptive algorithms do enhance the image progressively well compared to GHE, but the results need to be post-processed to remove blocking artifacts that are caused by inconsistent variations between blocks of enhanced pixels. Type II contrast enhancement operates on sub-bands of frequency coefficients of pixels to modify globally and locally the desired frequency components. These algorithms are complex to execute and require additional steps to reorganize the sub-bands for inverse transformation. The process of transformation degrades the image.

2 Methodology Based on Image Processing

Unsharp masking is a filter-based approach. From the image, an unsharp mask is constructed by subtracting the original image from the filtered image. The filter generates a low-pass image. The mask contains the local brightness variations of the image. The original image is contrast enhanced with adaptive histogram equalization. Using the weighted addition approach, a set of three images, i.e., the local brightness mask, the original image, and histogram equalized image, are added in proportions to create a high contrast color image. This method protects the edges, color, and texture information of the image for better image analysis.

Depending on the width of the filter kernels, different properties are induced. For small kernels, there is an increase in sharpness resulting in almost no contrast enhancement to the original image. Large kernels impose blur but alter the appearance of contrast to a large extent.

The weight of pixels used from histogram equalized image is around 0.2–0.4 depending on the distribution of darkness in the original image. If the distribution of darkness is more, the weight parameter is upscaled and vice versa. The darkness parameter is computed by summing the values of pixels in the original image and dividing it with maximum value of brightness in the original image.

3 Results and Discussion

The weight vector (α) for most of the liquid crystalline images is around 0.2–0.4. From the below results, it can be noticed that weighted histogram equalization combined unsharp masking produces high contrast images compared with AHE (adaptive histogram equalization). The images are also tested with unsharp masking-based contrast enhancement, which produced artifacts on color images in the darker portions of the image. By combining unsharp masking with histogram equalization, these artifacts are eliminated and clear colored texture preserving contrast enhancement is achieved.

Figures 1, 2, 3, 4, 5, and 6 show the resultant enhanced images of pure 10O.O6 compound with histogram equalization and using proposed combined unsharp masking technique at transition temperatures. Figures 7, 8, and 9 show the images of 1% ZnO nanodispersed 10O.O6 compound at transition temperatures.

3.1 Experimental Results

Figure 10 shows the DSC curve of proposed pure and 1% ZnO nanodispersed 10O.O6 compounds. The transition temperatures of the pure and nanodispersed compound can be observed from DSC curve, and Table 1 shows the enthalpy values for both the cases.

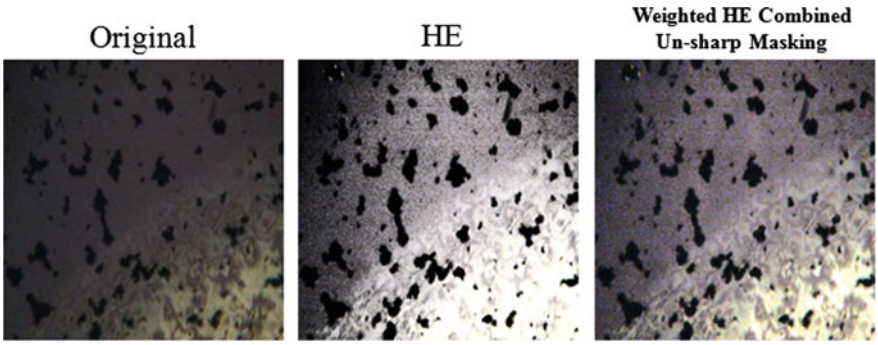

Fig. 1 Isotropic–nematic transition in 10O.O6 pure compound at 110.3 °C

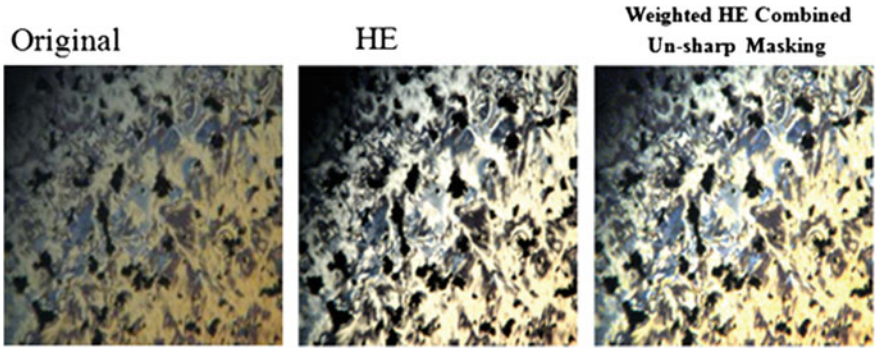

Fig. 2 Nematic–smectic-A transition in 10O.O6 pure compound at 105.6 °C

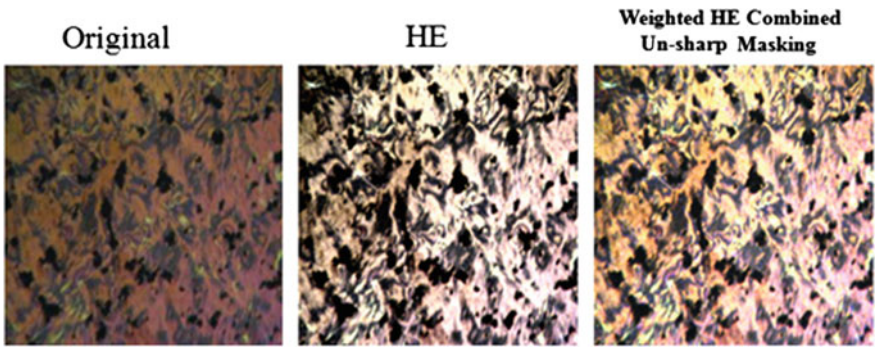

Fig. 3 SmA–SmC transition in 10O.O6 pure compound at 94 °C

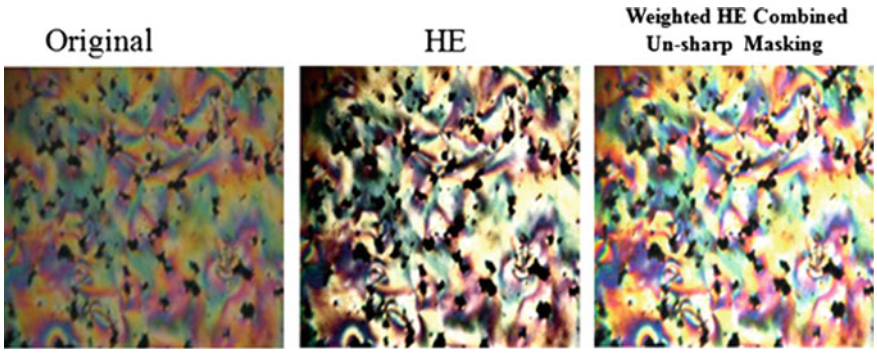

Fig. 4 SmC–SmI transition in 10O.O6 pure compound at 89 °C

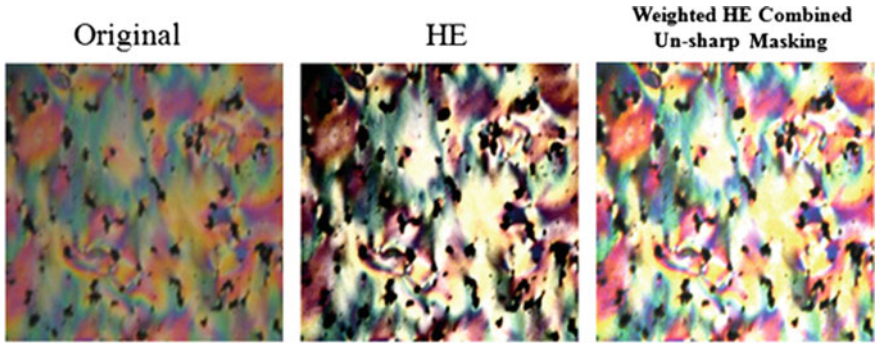

Fig. 5 SmI–SmG transition in 10O.O6 pure compound at 84.2 °C

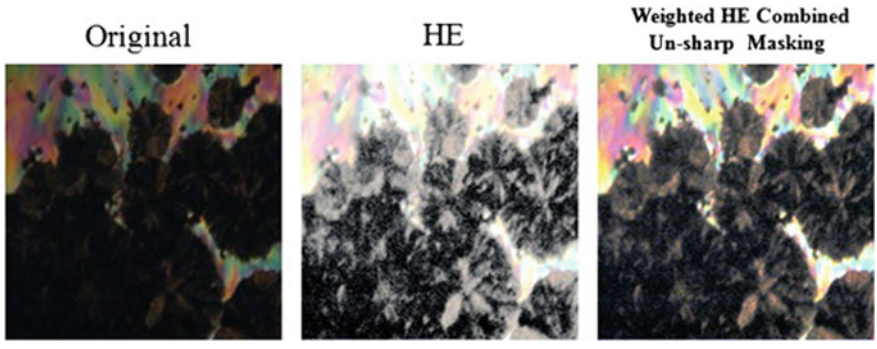

Fig. 6 SmG–solid transition in 10O.O6 pure compound at 74.1 °C

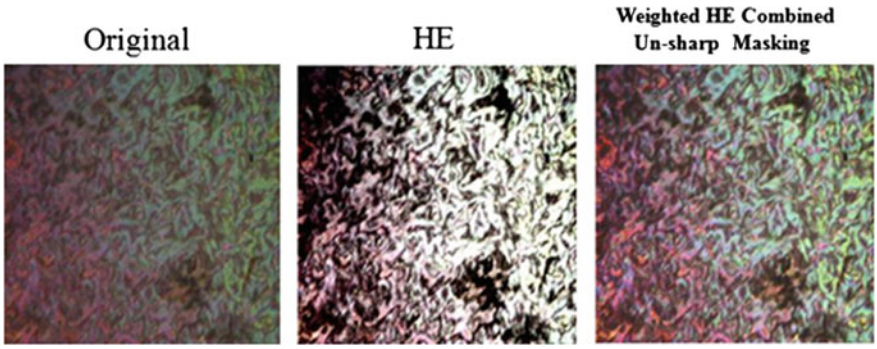

Fig. 7 Nematic transition in 1% ZnO nanodispersed 10O.O6 compound at 109.5 °C

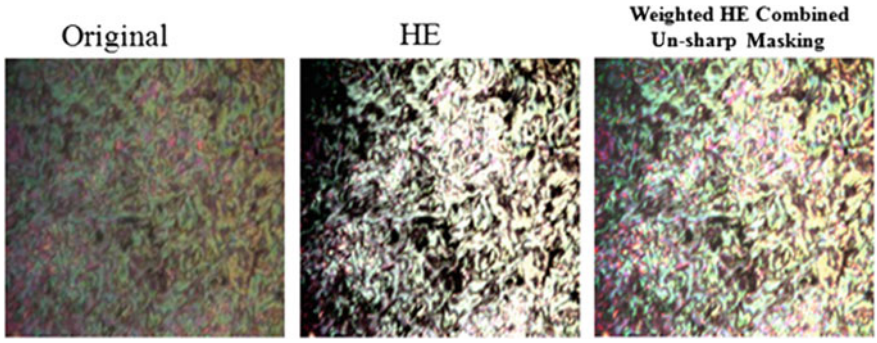

Fig. 8 Nematic–SmA in 1% ZnO nanodispersed 10O.O6 compound at 104.5 °C

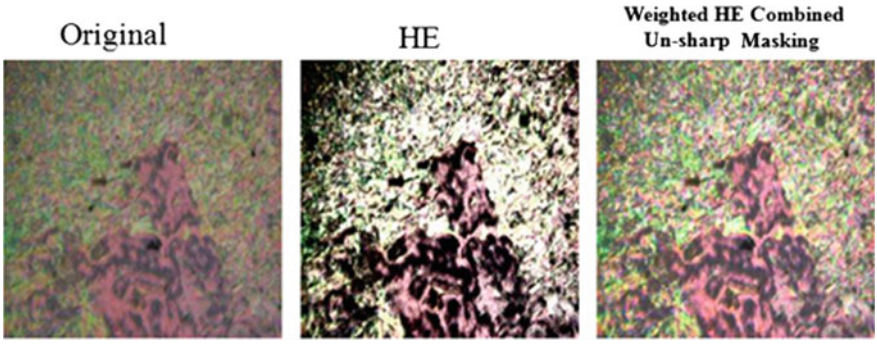

Fig. 9 SmA–SmC in 1% ZnO nanodispersed 10O.O6 compound at 93.3 °C

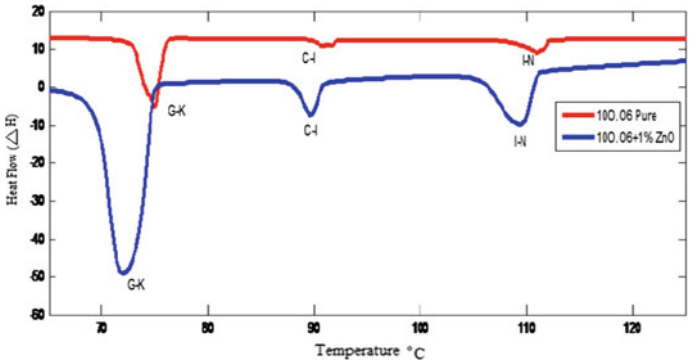

Fig. 10 DSC curve for 10O.O6 pure and 10O.O6 + 1% ZnO compounds

Table 1 Phase variants, transition temperatures, enthalpy values of 10O.O6 pure, and 1% ZnO nanodispersed compounds

Compound	Phase variants		Scan rate	G-K	I-G	C-I	A-C	N-A	I-N
10O.O6 pure	NACIG	Cooling	10 °C/min	75.02		91.65			111.07
			ΔH J/gm	69.98		0.17			14.67
		TM		73.90	83.80	88.80	94.0	105.80	110.20
10O. O6 + 1% ZnO $ZnOBaTiO_3$	NACIG	Cooling	20 °C/min	72.01		89.58			109.62
			ΔH J/gm	49.87		3.51			11.03
		TM	–	73.80	77.80	91.70	93.1	104.40	110.50

4 Conclusion

Unsharp masking technique is proposed in this paper to enhance the image quality of pure and 1% ZnO nanodispersed liquid crystalline compound 10O.O6. It is been noticed that weighted histogram equalization combined unsharp masking produces high contrast images compared with histogram equalization. The proposed method holds combination of the local brightness mask, original image, and histogram equalized image in proper proportions to create a high contrast color image.

Acknowledgements Authors like to express their gratitude toward the department of ECE and management of PSCMR College of Engineering for their support and encouragement.

References

1. Priestley EB, Wojtowicz PJ, Sheng P (1974) Introduction to liquid crystals. RCA Laboratories, Princeton, NJ
2. Madhav BTP, Pardhasaradhi P, Manepalli RKNR, Pisipati VGKM (2015) Homomorphic filtering textural analysis technique to reduce multiplicative noise in the 11Oba nano-doped liquid crystalline compounds. Phase Trans 88(7):735–744
3. Madhav BTP, Pardhasaradhi P, Manepalli RKNR, Pisipati VGKM (2015) Histogram equalisation technique to analyse induced cholesteric phase in nanodoped liquid crystalline compound. Liq Cryst 42(7):989–997
4. Madhav BTP, Pardhasaradhi P, Manepalli RKNR, Kishore PVV, Pisipati VGKM (2015) Image enhancement using virtual contrast image fusion on Fe_3O_4 and ZnO nanodispersed decyloxy benzoic acid. Liq Cryst. https://doi.org/10.1080/02678292.2015.1050704
5. Madhav BTP, Gopala rao MV, Pisipati VGKM (2015) Multispectral correlations technique for finding phase transition temperatures in 7O.Om series. Liq Cryst Today 24(2):38–46
6. Rambabu M, Prasad KRS, Venu Gopala Rao M, Madhav BTP, Pisipati VGKM (2015) Thermal and phase behavior studies of hydrogen-bonded compounds (SA:nOBA) using POM, DSC and image-processing techniques. Liq Cryst Today 24(3):81–92
7. Madhav BTP, Gopala rao MV, Pisipati VGKM (2015) Identification of liquid crystalline phases in 7O.O9 compound based on structural similarity index measure, Taylor & Francis. Liq Cryst 42(2):198–203
8. Pardhasaradhi P, Madhav BTP, Gopalarao MV, Manepalli RKNR, Pisipati VGKM (2015) Gradient measurement technique to identify phase transitions in nano dispersed liquid crystalline compounds. Phase Trans. https://doi.org/10.1080/01411594.2015.1091074

Active Contour Model Applied to Segmentation of Human Face

Rangayya and Basavaraj Amrapur

Abstract Active contours or snakes have been broadly used in image processing applications and computer vision system. Face contour represents relevant and useful information commonly implemented in biometric applications using human face information. For parametric deformable models, snakes are broadly applied in detection of boundary, modeling of shape, motion tracking, etc. In this paper, the segment of facial information using snake or active contour model has been applied. The import information is retrieved that is face image from given database image for identifying or verifying a human face purpose. The accurate snake contour of simulation results shows that it can be fitted for face detection.

Keywords Deformable model · External force · Internal force
Face image and simulation

1 Introduction

Face detection is a computer technology that finds the size and location of human faces in images. Face recognition is another technique for automatically identifying or verifying a human face from a given digital image or a video frame from a source by looking at selected facial features. The exactness of face detection increases the performance of face recognition.

Active contour plays important role in analysis of human face; It can be used for face segmentation in biometric application. It can be considered as an

Rangayya (✉)
Department of Electronics & Communication Engineering, APPA Institute of Engineering and Technology, Kalaburagi Karnataka, India
e-mail: Rangu2kiran@gmail.com

B. Amrapur
Department of Electrical & Electronics Engineering, PDA College of Engineering, Kalaburagi Karnataka, India
e-mail: bamarapur@yahoo.com

H. S. Saini et al. (eds.), *Innovations in Electronics and Communication Engineering*,
Lecture Notes in Networks and Systems 33,
https://doi.org/10.1007/978-981-10-8204-7_4

important process for face recognition system. The snake model was introduced by Kass et al. [1] as an elastic contour extraction technique for region of interest, boundary detection. In this system, the applicant boundary points are tested and moved in such a way that the total energy level of a snake will reach a minimum with respect to all the possible object contours.

Snake model [1], or deformable model [2], has been adopted broadly for image segmentation [1] and objects capture [3]. In spite of the fact that there are numerous active models [2], the most broadly used snake models are active contours also known as deformable contours [4] and active surfaces also known as deformable surfaces. The snake models deface over field of face image and acquire a essential quality information. The energy function is usually divided into two functions, first one is internal energy, which compels the smoothness and tautness of the model, and the other one is external energy that defines the flexible model to the region of interest. We focus on parametric active contours [1] and discrete active surfaces.

Snake or active contour is a shape which is defined within the image domain and it can be moved to the region of interest under the influence of internal force [5]. Snakes are widely used in many application, segmentation, shape modeling, detection of edge, etc.

If an expert locates the snake to desired contour, it does the best way to segment the face region. A snake is a flexible curve through which the minimization of an energy function deforms and adjusts its curve initially on the basis of additional image information to provide a boundary of a region of interest [6].

The energy function to be minimized is obtained from forces which are both internal and external to the snake [7–11]. Internal forces are responsible for the flexibility, whereas external forces that are derived from the image or from some higher level processes are responsible for moving the snake toward region of the interest in an image.

Sections 2, 3, and 4 explain about the proposed method on face images, results, and conclusion, respectively.

2 Proposed Method

A snake curve is characterized by equation $Y(S) = [Y(S), X(S)]$, $S \in [0, 1]$ that deforms over the region of interest that is face image to minimize the energy. By explanation, the total energy minimization up the total frame is given by the following equation:

$$E = 1/2 \int_0^1 \{\alpha Y'(s) + \beta Y''(s)\} + E_{\text{ext}}\{\text{Y(s)}\} \tag{1}$$

The first half of the integration is concerned with the internal energy of snake model, which forces restriction to its movement by controlling the flexibility and rigidity of the curve, which are controlled by α and *β,* respectively, where α and β are the first-order derivative and second-order derivative scaling parameters that define the accuracy and tightness of the shape, respectively. $Y'(S)$ and $Y''(S)$ are the first-order and second-order derivatives of $Y(S)$ with reference to S, whereas E_{ext} implies the external energy of the snake model [12]. To minimize Eq. (1), the contour needs to obey the following Euler equation:

$$\alpha y'(\mathrm{s}) + \beta Y''(s) - \nabla E_{\text{ext}} = 0 \tag{2}$$

where ∇ is the gradient operator. This can be treated as a force balance equation

$$E_{\text{int}} + E_{\text{ext}} = 0 \tag{3}$$

where $E_{\text{int}} = \alpha Y'(s) + \beta Y''(s)$ is the inner force to drive shape smoothness and $E_{\text{ext}} = \nabla E_{\text{ext}}$ is the outer force to bring the contour close to the region of interest.

The second half part of equation characterizes the external energy, and it causes the deformable model move the curve toward critical element in an image that is face image. The outer force for a gray level image $Y(m, n)$ can be written as

$$E_{\text{ext}}(m,n) = -\left|\nabla(Gs(m,n) * Y(m,n))\right|^2 \tag{4}$$

where $Gs(m, n)$ denotes Gaussian filter related to the region of interest that is face image, in order to enhance the face image's boundary, which leads sector nearer to boundaries of the gradient term that results in larger values and in consequence heavy potential.

3 Results and Discussion

The proposed method has been applied to standard Yale database face images. The experiments have been performed on a computer with the Pentium i3—1.7 GHz processor, Windows 7 operating system; the algorithms were realized as scripts for the MATLAB 7.6.0 interpretation. For experiments, we used images from Yale database. The original images obtained from Yale database are as shown in Fig. 1a. Then, the initialization of contour has been made manually and the curve moves toward face image when the internal energy and external energy becomes equal; then, curve fits the boundary of image as shown in Fig. 1b. The clarity of the image can be viewed by using blur images shown in Fig. 1c.

Once the face image is segmented, then from the segmented image the geometrical features are calculated whose values are tabulated in Table 1.

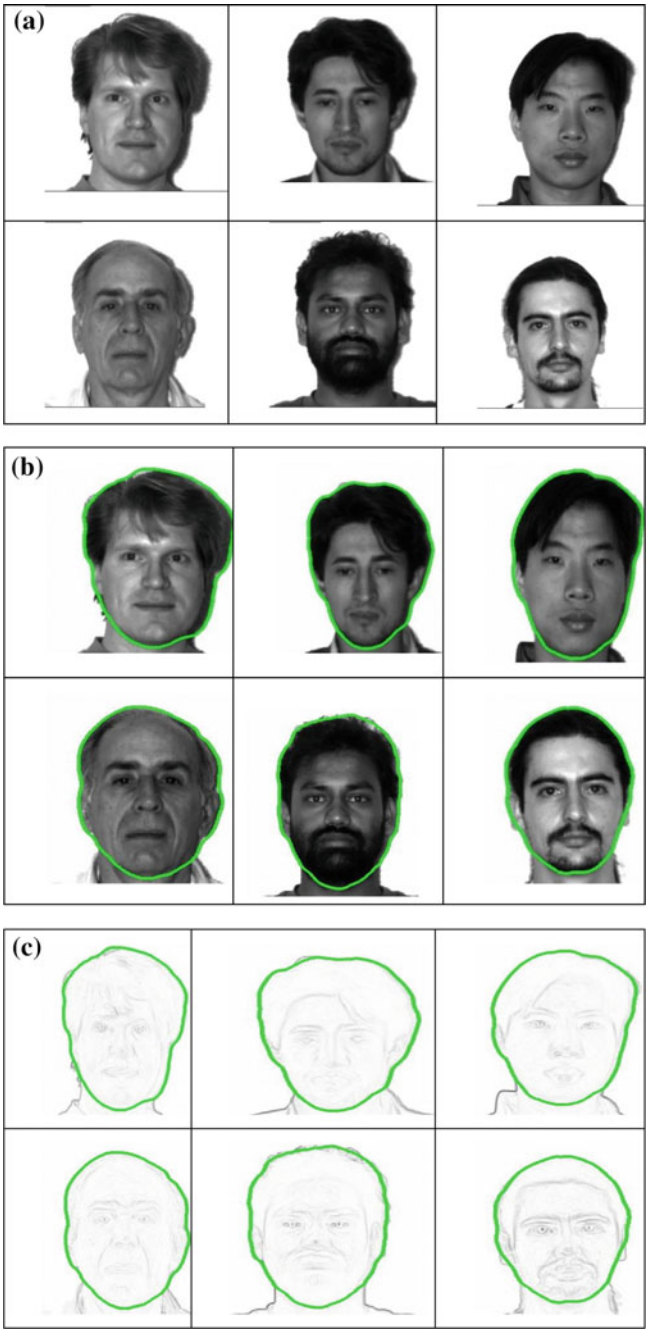

Fig. 1 **a** Face images 1, **b** Face images after applying snake, **c** Blurred face images after applying snake

Table 1 Results after segmentation of face images

Sl. no.	Area	Mean	Peri
1	24,887	0.267	646.5
2	23,621	0.365	593.3
3	23,670	0.309	586.1
4	21,838	0.277	579.3
5	26,045	0.448	591.6
6	22,152	0.315	536.9

The selected images measured the contour detection of faces. It is presented in figure which presents detection of faces, main reason for incorrectly detected chin, and a hairline near is that edge smoothness.

The results of the face detection are shown in below figures. Active contour performs well in controlled for face images taken from the Yale databases. Consider the images of face databases as shown in Fig. 1a, b show segmented images after applying snake, and Fig. 1c shows blurred image that shows clear segmentation of face images. In figure, first image is the original image containing face and second one gives the snake applied result.

4 Conclusion and Future Work

In this paper, snake is applied to face images for segmentation of face images. The database of face images is taken from Yale database. This algorithm produces good results for face image segmentation, and these results are used for face recognition for better results for further process. The improved results of segmentation may be obtainable by combining the increased framework with large data from face image. For instance, the active or snake contour technique includes both boundary and sector features that can get improved outcome than those situated on only boundary information.

Snake can also be freely tailored and increased for a variety of applications. One probable disadvantage of snake is that the faint boundaries might be affected by the strong boundaries along with the unwanted information.

References

1. Kass M, Witkin A, Terzopoulos D (1987) Snakes: active contour models. Int J Comput Vis 1:321–331
2. Yan H (2001) Human face image processing techniques. Int J Image Graphics I(2):197–215
3. Amarapur B, Kulkarni PK (2011) External force for deformable models in medical image segmentation: a survey. Signal Image Process: Int J (SIPIJ) 2(2)
4. Face database available from http://vision.ucsdedu/iskwak/ExtYaleDatabase/download.html

5. Xu C (1998) Student Member, IEEE, and Jerry L. Prince, Senior Member, IEEE. Snakes, shapes, and gradient vector flow. IEEE Trans Image Process 7(3)
6. Mahapatra D, Routray A, Mishra C (2006) An active snake model for classification of extreme emotions. 1-4244-0726-5/06/$20.OO 2006 IEEE
7. Kim S-K, Park YJ, Toh K-A, Lee S (2010) SVM-based feature extraction for face recognition. Pattern Recogn 43(2010):2871–2881 (ElsevierLtd)
8. Hsu C-Y, Wang H-F, Wang H-C, Tseng K-K, Tang Y-J (2010) Automatic extraction of face contours. 978-1-4244-8126-2/10/$26.00 ©2010 IEEE
9. Ramesh R, Kulkarni AC, Prasad NR, Manikantan K (2016) Face recognition using snakes algorithm and skin. In: Proceedings of international conference on signal, network, computing and systems, ICSNCS 2016, vol 1
10. Cohen LD (1991) An active contour models and balloons. CVGIP: Image Underst 53(2): 211–218
11. Chen C, Tamie L, Jason J, Steven H, Richard B, Bill H, Paul A, William J, Peter R (2004) Segmentation of arterial geometry from ultrasound images using balloon models. In: IEEE international conference proceedings, pp 1319–1322
12. Li B, Action ST (2007) Active contour external force using vector field convolution for image segmentation. IEEE Trans Image Process 16(8)2096–2105

Electroencephalograph (EEG) Based Emotion Recognition System: A Review

Kalyani P. Wagh and K. Vasanth

Abstract Brain–computer interfacing is recent technology through which we can communicate with the outside world using the brain signals. This technology plays an important role in the biomedical field. BCI can be used to identify various human emotions. These emotions play an important role in human psychology. Recognition of emotion is subject of interest for both psychologists and engineers. Many researchers are doing a lot of work in the same field. The objective of this paper is to present study of various stages involved in electroencephalography (EEG) signal analysis for human emotion detection. The review gives an explanation of each method like EEG signal acquisition, signal preprocessing, feature extraction, and signal classification.

Keywords Emotion detection · Electroencephalography · Signal preprocessing Feature extraction · Classification

1 Introduction

Human–computer interface (HCI) is the system which allows the user to understand brain signals as a command for computer to mentally control the computer [1]. These systems are also known as brain–computer interfaces (BCI).

Recent research shows that BCI is useful for physically challenged human being. Such persons who have lost all their controlled actions can only rely on their cognitive actions to interact with others; BCI is useful for them. Also, BCI will be helpful for persons having epilepsy problem. BCI can be helpful for paralyzed persons and persons having mental disorders.

K. P. Wagh · K. Vasanth (✉)
Sathyabama University, Chennai, Tamil Nadu, India
e-mail: vasanthecek@gmail.com

K. P. Wagh
e-mail: kalyaniwagh13@gmail.com

H. S. Saini et al. (eds.), *Innovations in Electronics and Communication Engineering*,
Lecture Notes in Networks and Systems 33,
https://doi.org/10.1007/978-981-10-8204-7_5

Likewise, human emotions play an important role in decision-making activities. Emotions are necessary for accurate translation of actions as well as communication. Emotion classification can be used in various medical applications like neurology and psychology. The neurological disorder diagnosis can be performed by using automatic emotion detection based system [2].

One can identify human emotions from speech, facial expression, or body gestures. But these methodologies do not provide an efficient and appropriate output, because facial expressions may be false and it can be easy to express false emotions by changing speech tone [3, 4]. Another way of recognizing emotions is through physiological signals. There are two different ways for detecting emotions physiologically; one is to collect signals from peripheral nervous system such as electrocardiogram signal (ECG) and electromyogram (EMG).

In case of ECG signal, emotions are associated with heart rate, blood volume pulse, stroke volume, cardiac output, peripheral vascular resistance, and myocardial contractility. The EMG signal measures muscular activity of body which corresponds to emotion. Galvanic skin response (GSR) is another signal associated with EMG. It gives skin conductance. This signal is also useful for detecting emotion. Another way of detecting emotion is through brain signal, i.e., electroencephalogram (EEG) signal [5]. EEG tells accurate feeling of any person, as these signals will generate in the brain, which is the heart of nervous system. The most advantage of EEG is that it is an instant and continuous signal of brain's activities. Also, recordings of EEG signal can be both cost-effective and with no risk of side effects.

2 Materials and Methods

2.1 What Is EEG Signal?

Brain is source of all emotions. Human brain is separated into three main parts: Cerebrum, cerebellum, and brain stem. Cerebrum is the largest segment of the brain. It is the outermost layer of gray matter making up the superficial aspect of cerebrum. Problem-solving, thinking, movements, and feeling these all are happening due to cerebrum. Cerebellum is responsible for control coordination and balance. There are four major lobes in the brain. They are frontal, parietal, occipital, and temporal lobe. The right hemisphere of brain is responsible for negative emotions (disgust, fear, stress, etc). The left hemisphere of brain is responsible for positive emotions (happiness, joy, etc.) (Fig. 1).

Brain waves generate electrical potential in the brain when neurons are active. This electrical potential can be measured outside the skull, which is nothing but EEG. There are mainly two methods for capturing EEG signal, invasive and noninvasive.

EEG signal undergoes changes in amplitude as well as in frequency for different emotions [6]. EEG-based BCI is useful for classification of various emotions in

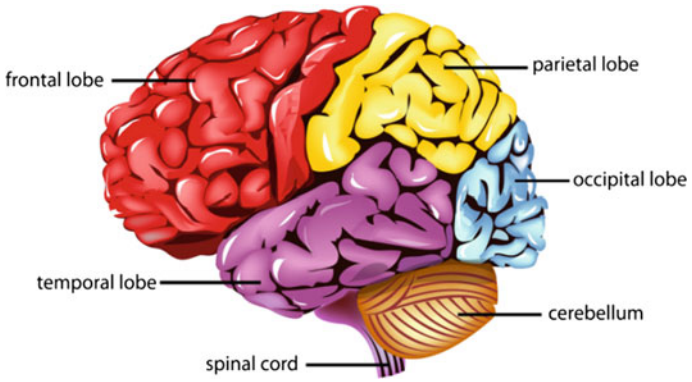

Fig. 1 Parts of human brain

which EEG signal related to different emotional activities are captured and different emotions are classified. The EEG signals are used to examine the following clinical problems:

- Examining alertness, coma;
- Locating damaged area due to head injury, stroke;
- Monitoring anesthesia depth;
- Examine epilepsy;
- Find out seizure origin;
- Used to monitor the brain development;
- Examine sleep disorders and physiology; and
- Examine mental disorders.

The EEG signal frequency ranges from 0.5 to 50 Hz. The basic frequency of EEG signal is classified into five frequency bands (Fig. 2).

2.2 EEG Electrode and 10–20 Electrode Placements System

Various types of electrodes are used to record EEG signals. These are disposable electrodes, reusable disk electrodes, electrode cap, saline-based electrodes, and needle electrodes [7].

Electrode setting position for recording EEG is standardized by International Federation of Societies for Electroencephalography and Clinical Neurophysiology. The method is called as 10–20 system. It contains 21 electrodes (excluding the earlobe electrodes), as shown in Fig. [8]. The electrodes placed at earlobe are called A1 and A2. They are connected to the left and right earlobes, respectively. These electrodes are used as the reference electrodes. The electrode interval is 10 or 20% of that specified distance. On the left side of brain, the odd electrodes are placed and

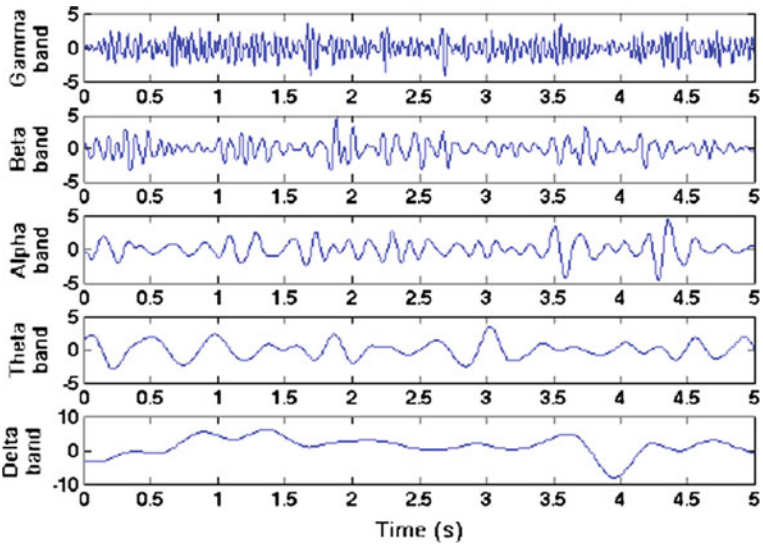

Fig. 2 EEG frequency bands

the even ones on the right side. Remaining electrodes are placed in between the above electrodes with the same distance between them [9, 10] (Fig. 3).

2.3 *EEG Correlates to Emotion*

Researchers have expressed human emotion on two-dimensional planes as valence and arousal (Fig. 4).

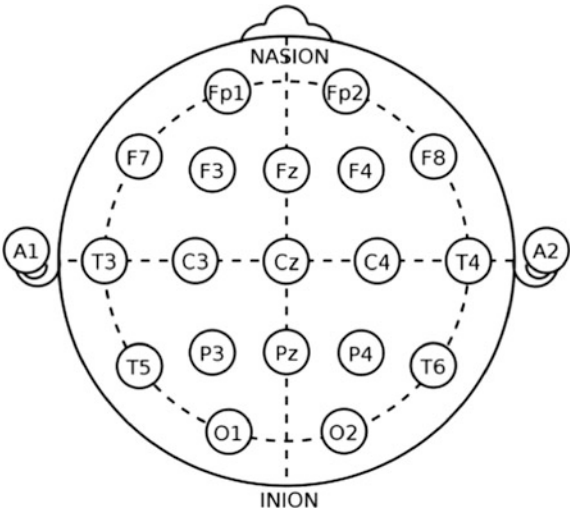

Fig. 3 Standard 10–20 EEG electrode positions for the placement of 21 electrodes

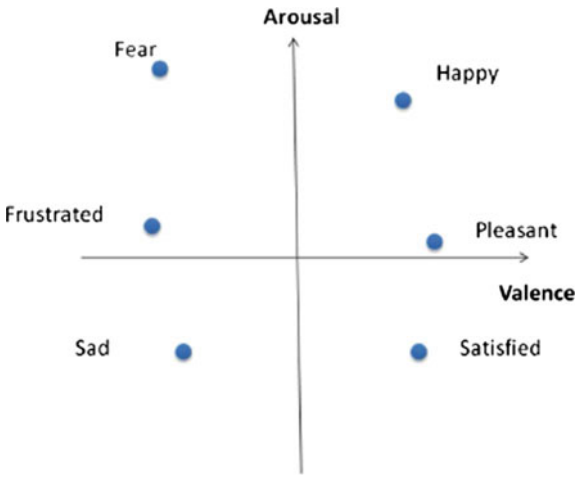

Fig. 4 The relationship of valence–arousal model

Observing large activity of beta-waves and low activity of alpha-waves is characteristics of high arousal emotional state. Beta-waves are observed when brain is busy in doing higher activity and alpha-waves with relaxation. Thus, arousal state can be identified by ratio beta/alpha-waves [11] (Table 1).

3 Proposed System

Figure 5 explains, in general, the processing steps to guess the emotional state from EEG signals. The recorded EEG signal goes through various preprocessing techniques. Here, we are using various noises reducing algorithms and filtering methods to improve the signal-to-noise ratio of an EEG signal [8, 12–14]. After that, the feature extraction step finds out various important features from EEG signal like band powers, ERP, Variance, Skewness, etc. to correlate it with different emotional states. Last step is the classification of emotional state by using various classifiers like SVM, PCA, etc.

3.1 Acquire EEG Signal

One can capture real-time EEG signal by using various headsets and devices like EMOTIV Epoc+ which consists 14 channels, EMOTIV insight which consists five channels, and electrode cap. Otherwise, analysis is possible by using various databases like DEAP database, interface dataset: Emotion detection in the loop from brain signals and facial images, SJTU emotion EEG dataset (SEED) [15].

Table 1 Location and state associated with EEG signal frequency bands

Rhythm	Frequency (Hz)	Location	Reason	Too much	Too little
Delta band	1–4	Frontal lobe	Drowsiness and sleep stages	Brain injuries, learning problems, inability to think	Inability to refresh body, inability to refresh the brain, poor sleep
Theta band	4–7	Midline, temporal	Drowsiness and sleep stages	hopelessness, hyperactivity, inattention	Poor emotional awareness, stress
Alpha band	8–12	Frontal, occipital	Person is awake and eyes are closed calmness	negligence, inattentive, too relaxed	Anxiety, high stress, sleeplessness
Beta band	13–30	Frontal, central	Alertness, eyes open active thinking, active attention high anxiety or excitement	Adrenaline, nervousness, inability to relax, stress	Daydreaming, depression, poor cognition
Gamma band	25–100	In the thalamus and moves from the back of the brain to the front and back	Consciousness state	Anxiety, high arousal, stress	Depression, learning disabilities

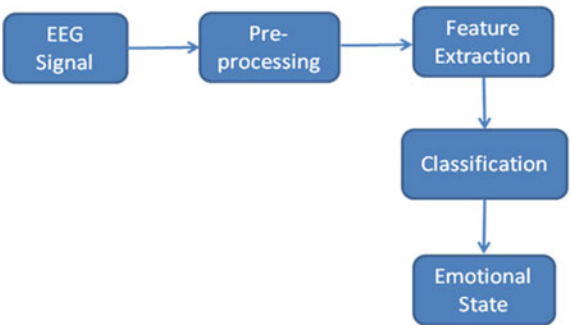

Fig. 5 System architecture

By self-exploiting of subjects or by using standard stimulus set provided by International Affective Picture System (IAPS) and International Affective Digitized Sound System (IADS), we can induce emotional state. The IAPS provides a set of normative emotional stimuli for experimental investigations of emotion and attention. The IADS provides a set of acoustic emotional stimuli for experimental investigations of emotion and attention [16, 17] (Fig. 6).

Fig. 6 EEG headsets with electrodes

3.2 EEG Signal Analysis Methods

Analysis of EEG signal consists of mainly three steps. These are EEG signal preprocessing, feature extraction, and classification of emotions [2].

3.2.1 EEG Preprocessing

Signal preprocessing is also called as signal enhancement. EEG signals are having very low amplitudes in the range of 1–2 mV. Thus, they can be easily infected by noise. The noise can be electrode noise or can be generated from the human body itself. These noises are called the artifacts. It is required to take away these artifacts from the original signal for the appropriate analysis of the EEG signals [6, 18]. During recording of EEG signal, various technical artifacts can occur like cable movement, electrode noise, baseline movement, and EMG disturbance [13]. Furthermore, some artifacts also get generated due to body muscle movement, eye blinking, sweating, body muscle movement, eyeball movement, etc. So, it is necessary to reduce these artifacts from the original EEG signal for proper processing and analysis of the diseases related to brain.

In order to minimize these artifacts from the captured EEG signals, a bandpass filter is used that will remove frequencies below 2 Hz and above 40 Hz [19].

EEG signal preprocessing can be done by using techniques like [1, 9, 12, 20, 21] (Table 2).

Table 2 EEG correlation with emotion (Literature Review)

Ref. no.	Year	Participant	Stimulus	Channel	Pre-processing	EE6 signal features	Feature extraction method	Classifier	Emotion	Accuracy (%)	Real time
1	2003		Visual audio	C3, C4, P3, P4, 01, 02			Genetic algorithm	SVM, NN, LDA			
2	2007	6	Visual audio	24 electrodes	Average mean reference	Delta, theta, alpha, beta, gamma frequency bands and statistical parameters	DWT	FCM, FKM	Happy, sad, fear, anger, disgust, surprise		No
3	2008		Visual audio	C3, Cz, C4		Power spectral entropy		SVM		90	
4	2008	6	Visual audio	63 electrodes	Average mean reference	Statistical parameters—energy, root mean square, reoccurring energy	WT	FCM	Happy, fear, disgust, surprise		No
5	2009		Visual audio	8 electrodes	Independent Component Analysis	Power spectral density	FFT	Bayesian network	Joy, neutral, anger, sad, surprise	70	No

(continued)

Table 2 (continued)

Ref. no.	Year	Participant	Stimulus	Channel	Pre-processing	EE6 signal features	Feature extraction method	Classifier	Emotion	Accuracy (%)	Real time
6	2009	20	Visual audio	62 electrodes	Surface Laplacian	Delta, theta, alpha, beta, gamma frequency bands and statistical parameters	WT	KNN, LDA	Happy, fear, disgust, surprise, neutral	83.04	No
7	2010		Visual audio	FP1, FP2, T3, T4, Pz	BPF	Higher order spectra	Genetic algorithm	SVM	Calm, excited	82	No
8	2010	25	Visual audio	Afz, AFl, AF2, 01, 02, Oz	Surface Laplacian	Delta, theta, alpha, beta, gamma frequency bands and statistical parameters	DWT	KNN, LDA	Happy, surprise, disgust, fear, neutral	83.26 75.21	No
9	2011	15	Visual audio	FPl, FP2, T3, T4, Pz	BPF	Approximate entropy, wavelet oentropy		SVM		73.25	No
10	2011	5	Visual audio			Mean, Std. Dev, power spectrum	FFT	SVM, k-NN, MLP	Happy, relax, fear, sad	66.51	No
11	2011	16	Visual audio	FP1, FP2, F3/ F4		Higher order crossing, cross correlation		SVM	Arousal, valence	63	No

(continued)

Table 2 (continued)

Ref. no.	Year	Participant	Stimulus	Channel	Pre-processing	EE6 signal features	Feature extraction method	Classifier	Emotion	Accuracy (%)	Real time
12	2011	6	Visual audio		BPF	Delta, theta, alpha, beta, gamma frequency bands	FFT	SVM	Arousal, valence	88	No
13	2012	10	Visual audio	FP1, FP2, F3, F4	BPF	Spectrum energy of delta, theta, alpha, beta, gamma frequency bands	Gabor function and WT	Probabilistic network	Happy, sad, fear, anger, disgust, surprise	64.78	No
15	2013		Visual audio	AF3, AF4, F3, F4, F7, F8, FC5, FC6, P7, P8, T7, T8, 01, 02	5th order sine filter	PSD	WT	SVM	Happy	70.55	Yes
16	2013	4	Visual audio	FP1, FP2, F3, F4	8th order Bans pass filter	Entropy	Multiwavelet transform	SVM	Happy, sad, fear, neutral	80.83	No
17	2013	14	Visual audio	FC5, F4, F7, AF3	BPF	FD, HOC, Statistical	Higuchi algorithm	SVM	Positive and negative	53.70	No
18	2013	6	Visual audio		Down sampling	Energy spectrum. differential entropy	Linear dynamic system	SVM, KNN			

(continued)

Table 2 (continued)

Ref. no.	Year	Participant	Stimulus	Channel	Pre-processing	EE6 signal features	Feature extraction method	Classifier	Emotion	Accuracy (%)	Real time
19	2013	30	Visual audio	Fz, Cz, Pz, C3, C4, T7, T8		Alpha wave reaction time		QDA	Happy		
20	2013	20	Visual audio	62 electrodes	3rd order Butterworth filter	Delta, theta, alpha, beta, gamma frequency bands and statistical parameters	DWT	KNN, LDA	Happy, sad, fear, disgust, neutral		
21	2014	32	Visual audio	FP1, FP2	BPF	Entropy and power	CWT		Valence and arousal		
22	2014	40	Visual audio	Fpl, Fp2, F7, F8, F3, F4, Fz, C3, C4, Cz, T7, T8, P7, P8, P3, P4, Pz, 01, 02	2nd order Butterworth filter, ICA	Correlation and coherence estimation, statistical properties	FFT				
23	2014	22	Visual audio	AF3, AF4, F3, F4, F7, F8, FC5, FC6, P7, P8, T7, T8, 01, 02	IIR filter	Absolute power density, relative power density, mean frequency	FFT	ANOVA	Happy, sad, fear, anger, disgust, surprise		

(continued)

Table 2 (continued)

Ref. no.	Year	Participant	Stimulus	Channel	Pre-processing	EE6 signal features	Feature extraction method	Classifier	Emotion	Accuracy (%)	Real time
24	2014	5	Visual audio			Common spatial pattern with delta, theta, alpha, beta, gamma frequency bands		SVM	Arousal, valence		
25	2015		Visual audio		BPF	Root mean square, variance, linear prediction coefficients		KNN			
26	2015	32	Visual audio	Fpl, Fp2, AF3, AF4, F3, F4, F7, F8, FC5, FC6, T7, T8, P7, P8, P3, P4, 01, and 02	Down sampling	Wavelet energy, wavelet entropy	DWT	SVM	Happy and sad		

- Common average referencing (CAR),
- Surface Laplacian (SL),
- Independent component analysis (ICA),
- Principal component analysis (PCA),
- Single-value decomposition (SVD),
- Common spatio-spatial patterns (CSSP),
- Frequency normalization,
- Local averaging technique (LAT), and
- Robust Kalman filtering.

3.3 *Feature Extraction Methods*

The core objective of feature extraction is to take out important features of EEG signal which contain all information needed to recognize emotion. Once we obtain the noise-free EEG signals from the signal enhancement stage, essential features were extracted from the EEG signal. Then, these features are given to classifier for emotion classification. The EEG signal contains frequency-domain features, time-domain features, and time–frequency-domain features [22, 23]. There are various methods for feature extraction like FFT, DWT, STFT, HOC, PCA, autoregression, ICA, etc.

3.3.1 Fast Fourier Transform

Measured EEG signals were transformed into power spectrum using FFT. Then, transformed EEG signals were divided into different frequency bands. FFT decomposes input signal to complex exponential functions of different frequencies [12, 24] (Table 3).

$$X(f) = \int_{-\infty}^{+\infty} x(t)\mathrm{e}^{-2\pi ft}\mathrm{d}t$$

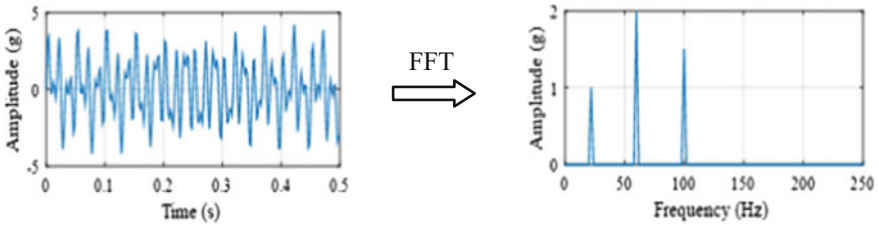

Table 3 Details of various features of EEG signal to classify emotion

Feature	Details
Time-domain features	
Power spectral entropy	It describes complexity of the system. It is information entropy that can quantify the spectral complexity of an uncertain system. The time series signal becomes power spectrum using Fast Fourier Transform. The information entropy of power spectrum is called power spectral entropy. It reflects spectra of EEG signal [34, 35]
Root mean square	It gives more information about variation in amplitude of the signal. It is the square root of arithmetic mean of squares of the original values. [34, 36]. If N is set of values $\{x1, x2, x3\ldots xn\}$, then RMS value is given by $X_{\mathrm{RMS}} = \sqrt{\frac{1}{N}(x1^2 + x2^2 + \cdots x3^2)}$
Mean	It is the sum of all numbers in dataset divided by size of dataset. Suppose sample dataset is $\{x1, x2, x3\ldots xn\}$, then arithmetic mean μ_x calculated as $\frac{1}{N}\sum_N^1 Xn$
Standard deviation	It shows variation exists from the mean. If this value is low then data points are very close to the mean and if this value is high then data points are spread out over large range [37] $\sigma = \frac{1}{N-1}\sum_{n-1}^{N}(Xn - \mu x)$
Variance	It gives information about data distribution from its mean value. It is nothing but square of standard deviation. It is the type of probability distribution. It measures how far a set of numbers get spread. It is average power of the time series signal. Large variance indicates high power [23, 34, 37] $V = \sigma^2$ If random variable is X, then its expected value is $E(X)$, then the variance of $X(1)$ is the covariance of X with itself is given as $\mathrm{Var}(X) = \mathrm{Cov}\ (X, X) = E\ [(X - \mu)^2]$
Power	Power is measure of the amplitude of EEG signal. It indicates the strength of signal. It gives information about basic rhythms present in EEG signal. Power can be calculated using FFT $\mathrm{Power} = \sum \frac{X^2}{L(x)}$
Skewness	It is measure of symmetry or lack of symmetry. A distribution, or dataset, is symmetric if it looks the same to the left and right of the center point $\mathrm{Skew}(X) = E\left[\left(\frac{x-\mu}{\sigma}\right)\right]$ Where X is real-valued random variable, μ and σ are mean and standard deviation, E is statistical expectation
Kurtosis	It is measure of whether the data are heavy tailed or light tailed relative to normal distribution. It is nothing but degree to which the distribution is peaked. Kurtosis is measured against the standard normal distribution $\mathrm{kurtosis} = \frac{m_4[x(n)]}{m_2 2[x(n)]}$
Linear prediction coefficients	It helps to remove redundant patterns of the signal. This method predicts the data using linear combination of previous values [34]

(continued)

Table 3 (continued)

Feature	Details
Time-domain features	
Entropy	It is measure of randomness of signal. Common approach uses histogram-based estimation $\partial = \sum_1^n x^2 - \log(x^2)$
Frequency-Domain Features are features derived from the EEG signal spectrum which contains various frequency bands like delta, theta, alpha, beta, and gamma [38]	
Time–Frequency Domain combines time-domain and frequency-domain analysis. They are joint functions of f and t. It gives energy representation of EEG signal in the time–frequency plane. Commonly used TFDs are wavelet transform and STFT, spectrogram. TFD analyses clean signal for good result. In this method, extracted features are dependent on each other [38]	

As EEG signals are nonstationary, and its spectrum changes with time. Also, Fourier transform does not represent nonstationary signals, so we will go for Wavelet transform, which works in time–frequency domain.

3.3.2 Autoregression

It works in time, frequency, and spatial domain. It is used to calculate power spectral density of EEG signal [5, 25]. It gives better frequency resolution. It is parametric type of feature extraction method. There are various methods to calculate autoregression like Yule–Walker method and Burg's method.

3.3.3 Discrete Cosine Transform

DCT is used to translate time-domain signal into frequency-domain. We can calculate the mean value of EEG signal by using DCT [26, 27]. This is nothing but a set of DCT coefficient signal. Here, input is a set of N EEG samples and

$$c(u,v) = \alpha(u)\alpha(v)\sum_{x-0}^{N-1}\sum_{y-0}^{N-1} f(x,y)\cos\left[\frac{\pi(2x+1)u}{2N}\right]\cos\left[\frac{\pi(2y+1)v}{2N}\right]$$

The first coefficient is DC coefficient which holds the average signal value. Remaining coefficients are AC coefficients. DCT is having two properties: one de-correlation and another energy compaction. So DCT energy is concentrated in few coefficients. Thus, these two properties will help to extract important features from image and leaving unwanted data from image.

3.3.4 Wavelet Transform

As EEG signal is nonstationary, time–frequency-domain method like wavelet transform is most suitable technique for feature extraction. At different frequency

bands, it successfully analyzes multi-resolution signal [10, 20, 24]. This can be achieved by decomposing signal at different approximations and detailed components by using low-pass and high-pass filter.

$$\mathrm{CWT}(a,b) = \int_{-\infty}^{\infty} x(t)\psi *_{ab} (t)\mathrm{d}t$$

where $x(t)$ is the unprocessed EEG signal, a is the dilation, and b is the translation factor. By using this method, we can split the original EEG signal into different frequency bands (Fig. 7).

At high frequencies, it gives good time resolution and poor frequency resolution. And at low frequencies, it gives good frequency and poor time resolution.

3.3.5 Short Time Fourier Transform

Brain signals are nonstationary signals. So, its spectrum changes with time. The Fourier transform is not the right choice for representing nonstationary signal [25, 28]. STFT is nothing but FT multiplied by window function. In STFT method, original signal is separated into small segments. These segments can be assumed as stationary. Then, window function "w" is chosen. For window function, width of window must be equal to the segment of the signal. Then, calculate FT. Now shift the window to new location, and calculate FT.

$$X_{\mathrm{STFT}}(t,f) = \int \left[x(t)w^*(t-f)\mathrm{e}^{-j2\pi ft}\mathrm{d}t\right.$$

Here, $x(t)$ is the original EEG signal, $w(t)$ is the window function, and * is the complex conjugate.

3.3.6 Higher Order Crossing

This technique gives us finite zero means series. Zero count is used to express level zero [6, 29]. So HOC is referred as zero crossing count. Spectral analysis and discriminate analysis combine with HOC and extract the relevant feature. By using

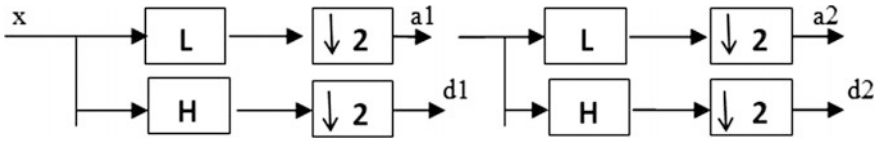

Fig. 7 DWT tree

signal segmentation, HOC emotions can be identified. Cross-correlation can be used to extract feature from EEG signal. This method provides optimum result.

3.3.7 Principal Component Analysis

One can fine pattern in the data by using this statistical method. The set of variables possibly is correlated with a set of uncorrelated variables using linear transformation and known as principal components [2]. The detailed algorithm is shown below:

a. Collect the input data.
b. Calculate covariance matrix from mean vector.
c. Find eigenvector and eigenvalue.
d. New feature vector is generated.
e. Transform the samples on the new vector.
f. New Data = Row feature vector * Row data adjust.

3.3.8 Independent Component Analysis

It transforms random multivariate signal into components which are independent of each other. This method is used to remove artifacts from EEG signal. It shows that information carried out by one component cannot be indirect from other. Thus, features can be extracted from mixed signals. The multivariate equation can be written as

$$p(x(t)) = \Pi_{i=1}^{c} p(xi(t))$$

3.4 Classifier

The classifier is used to draw a boundary between two or more classes. Based on their measured features, label the classes. This boundary will look like a separating hyperplane in multidimensional feature space. The best classifier will find the better hyperplane which has a maximum distance from all the classes [30].

3.4.1 Support Vector Machine

SVM is supervised classifier. It is used for pattern classification. SVM provides maximized margin in data. It always provides single solution [30]. It finds a separating hyperplane which separates data with large margin for linearly separable data.

$$x \in R^1 \Phi(x) R^H$$

where $\Phi(x)$ is the kernel function, used to find hyperplane. SVM does not require training data again and again. For two dimensions, data is separated into two groups as +1 or −1. For three-dimensional data, it requires two hyperplanes to separate data points in (Fig. 8).

To form hyperplane, two parallel lines H1 and H2 are drawn. Mark the distance between hyperplane and data points. Data points which are on planes H1 and H2 are known as SVM vectors. Overall accuracy of this classifier is good and also it carries low error rate. This classifier has some disadvantages like wastage of memory and little bit slow testing phase. Also, defining suitable kernel for relevant task is difficult.

3.4.2 Linear Discriminant Analysis

This method is used to recognize the pattern of given data. Combination of linear features is used to separate classes of objects. This method is like regression analysis. By calculating distance between the new sample data and training data, unknown inputs are calculated [5, 31, 32]. Thus, we can find the optimal hyperplane. This method is having complex structure. It is a very simple method to classify the different types of emotion. For classifying the discrete emotion, it does not require any external parameters. It makes use of hyperplanes to perform classification. Separating hyperplane is obtained by searching for the projection that maximizes the distance between the classes means and minimizes the interclass variance.

3.4.3 K-Means Algorithm

It is simple unsupervised learning algorithm for classification. It divides set of features into k clusters [2, 6, 33]. From numbers of clusters, define centroid for each cluster using formula

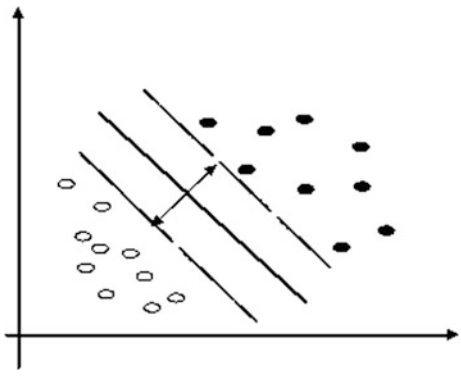

Fig. 8 Hyperplane using SVM

$$J = \sum_{j=1}^{K} \sum_{i=1}^{x} \left\| X_i^{(j)} - C_j \right\|^2$$

where C_j is the cluster center. Then, find out distance from object to centroid. Here, grouping is based on minimum distance. The algorithm for k-means is

a. Initialization

   Define the number of clusters (k).
   Designate a cluster center for each cluster.

b. Assign each remaining data point to the closest cluster center.
c. Calculate the new cluster center.
d. Calculate the sum of within-cluster sum of squares. If this value has not significantly changed over a certain number of iterations, stop the iterations else go to step 2.

3.4.4 K-Nearest Neighbor

This classifier decides by comparing testing data with training data. The detailed algorithm is explicated below (Fig. 9):

1. The classification is performed by considering training dataset.
2. Training dataset contains input and target variables.
3. Test data is compared with reference data.
4. This classifier works with "k" patterns. The distance of unknown pattern determines its class considering neighbor points.
5. Thus, given target is classified.

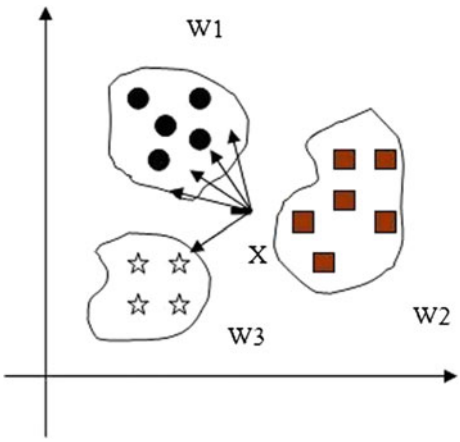

Fig. 9 Clusters using KNN

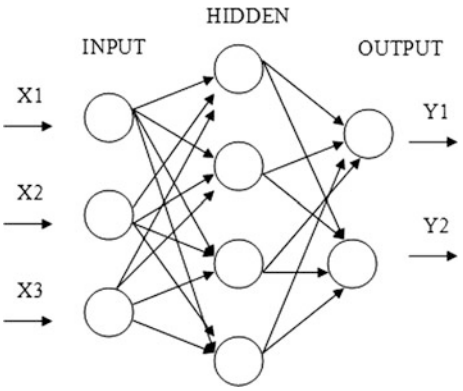

Fig. 10 Neural network classifier

3.4.5 Neural Network

Information is stored in the neurons. Information is passed from one node to another through neurons. NN consists of three layers: input layer, hidden layer, and output layer. This network has the ability to arrange nodes itself [2]. NN has the capacity to withstand failure. Thus, neural network used to find the specific emotion. Neural network can be divided into three, supervised training, unsupervised training, and reinforcement training. In supervised learning, the output which we exactly want can be found from target class. There is no target class in unsupervised training; we should find the output, which is related to the problem. Reinforcement is the combination of both. Using these NNs, we can find out specific emotion (Fig. 10).

4 Limitations in Current Systems

- Research in this field is still in primary stages.
- Very few electric signals from the brain will generate if electrodes are placed outside the skull.
- The skull will create scar tissue in the brain if electrodes placed inside.
- The current technology is unfinished.
- Reading people's inner thoughts comes with a massive amount of ethical issues.

5 Conclusion and Future Work

This paper gives a detailed survey on various techniques involved in the analysis of human emotions based on brain–computer interface and machine learning algorithms. From above observations, we can conclude that EEG signals give better

feature extraction results as compared to other signals. Objective is to work on the various drawbacks mentioned above. The proposed system will attempt to improve accuracy of various feature extraction and classification methods. Further, proposed framework will be developed in such a way that it will help medically disordered persons.

References

1. Murugappan M, Ramchandran N, Sazali Y, Hazry D, Zunaidi I (2008) Time frequency analysis of EEG signals for human emotion detection. Springer Proceeding 21:262–265
2. Sreeshakthy M, Preethi J, Dhilipan A (2016) A survey on emotion classification from EEG signal using various techniques and performance analysis. Int J Inf Technol Comput Sci
3. Hosseini SA, Sistani MBN (2011) Emotion recognition method using entropy analysis of EEG signal. IJ Image Graphics Signal Process 5:30–36
4. Liu Y (2011) Real-time EEG-based emotion recognition and its applications. Lecture Notes in Computer Science
5. Jatuaiboon N, Ngum SP, Israsena P (2013) Real time EEG based happiness detection system. Scientific World J, Article ID 618649
6. Wang XW, Nie D, Lu BL (2011) EEG based emotion recognition using frequency domain features and support vector machines
7. Sanei S, Chambers JA (2013) Introduction to EEG. In: EEG signal processing Sanei/EEG signal processing
8. Zang A, Yang B, Huang L (2008) Feature extraction of signals using power spectral entropy. In: IEEE international conference on biomedical engineering and informatics
9. Nie D, Wang XW, Shi LC, Lu BL (2011) EEG based emotion recognition during watching movies. IN: 5th international IEEE EMBS conference on neural engineering
10. Nie D, Wang XW, Shi LC, Lu BL (2011) EEG-based emotion recognition using frequency domain features and support vector machines. ICONIP Part I, LNCS 7062. Springer, Heidelberg, pp 734–743
11. Matlovic T, Gaspar P, Moro R, Simko J, Bielikova M (2016) Emotions detection using facial expressions recognition and EEG. In: 2016 11th international workshop on semantic and social media adaptation and personalization (SMAP)
12. Murugappan M, Ramchandran N, Sazali Y (2010) Classification of human emotion from EEG signal using discrete wavelet transform. J Biomedical science and engineering 3:390–396
13. Nasehi S, Pourghassem H (2012) An optimal EEG based emotion recognition algorithm using gabor features. In: WSEAS transactions on signal processing, vol 8, issue 3
14. Murugappan M, Yuvaraj R et al (2014) On the analysis of EEG power, frequency and asymmetry in Parkinson disease during emotion processing. In: Behavioral and brain functions
15. Liu Y, Sourina O (2013) EEG databases for emotion recognition. In: 2013 international conference on cyberworlds
16. Garrett D, Peterson D, Anderson CW, Thaut MH (2003) Comparison of linear, nonlinear and feature selection methods for EEG signal classification. IEEE Trans Neural Syst Rehabil Eng 11(2)
17. Liao LX, Corsi AM, Chrysochou P, Lockshin L (2015) Emotional responses towards food packaging: a joint application of self-report and physiological measures of emotion. In: Food quality and preference
18. Murugappan M, Murugappan S, Zheng BS (2013) Frequency band analysis of ECG signals for emotional state classification using discrete wavelet transform. J Phy Ther Sci 25:753–759

19. Bashashati A (2007) A survey of signal processing algorithms in brain-computer interfaces based on electrical brain signals. J Neural Eng
20. Ko KE, Yang HC, Sim KB (2009) Emotion recognition using EEG signals with relative power values and Bayesian network. Int J Control Autom Syst 7:865–870
21. Murugappan M, Ramchandran N, Sazali Y (2011) Combining spatial filtering and wavelet transform for classifying human emotions using EEG signals. J Med Biol Eng 31:45–51
22. Conneau AC, Essid S (2014) Assessment of new spectral features for EEG based emotion recognition. In: IEEE international conference on acoustic, speech and signal processing
23. Patil A, Panat A, Ragade SA (2015) Classification of human emotions from electroencephalogram using support vector machine. 2015 international conference on information processing (ICIP)
24. Zhang S (2009) A novel peak detection approach with chemical noise removal using short-time FFT for prOTOF MS data. In: PROTEOMICS
25. Lee YY, Hsieh S (2014) Classifying different emotional states by means EEG based functional connectivity patterns. PLOS ONE 9(4)
26. Vaid S, Singh P, Kaur C (2015) Classification of human emotions using multiwavelet transform based features and random forest technique. Indian J Sci Technol
27. Islam M, Ahmed T, Yusuf MSU, Ahmad M (2015) Cognitive state estimation by effective feature extraction and proper channel selection of EEG signal. J Circuits Syst Comput
28. Bajaj V, Pachori RB (2015) Detection of human emotions using features based on multiwavelet transform of EEG signal. In: Brain Computer Interface, Springer
29. Garrett D, Peterson DA, Anderson CW, Thaut MH (2003) Comparison of linear, nonlinear, and feature selection methods for EEG signal classification. IEEE Trans Neural Syst Rehabil Eng 11(2)
30. Ilyas MZ, Saad P, Ahmad MI (2015) A survey of analysis and classification of EEG signals for brain-computer interfaces. In: 2015 2nd International Conference on Biomedical Engineering (ICoBE)
31. Liu Y, Sourina O (2013) EEG databases for emotion detection. In: International conference on cyber worlds
32. Candra H et al (2015) Recognizing emotions from EEG subbands using wavelet analysis. IEEE
33. Petrantonakis PC, Haddjileontiadis LJ (2011) A novel emotion elicitation index using frontal brain asymmetry for enhanced EEG based emotion recognition. IEEE Trans Inform Technol Biomed 15(5)
34. Bhuvaneswari P, Satheesh Kumar J (2015) Influence of linear features in nonlinear electroencephalography (EEG) signals. In: Procedia Computer Science
35. Huang L (2008) Feature extraction of EEG signals using power spectral entropy. In: 2008 international conference on BioMedical engineering and informatics
36. Maksumov A (2004) Enhanced feature analysis using wavelets for scanning probe microscopy images of surfaces. J Colloid Interface Sci, 20040415
37. Panat A, Patil A, Galgatte G (2013) Comparison of statistical parameters of FMRI images of brain for the purpose of analysis of emotions. In: Fifth international conference on advances in recent technologies in communication and computing (ARTCom 2013)
38. Zheng W-L, Zhu J-Y, Lu B-L (2017) Identifying stable patterns over time for emotion recognition from EEG. IEEE Trans Affective Comput
39. Murugappan M, Ramchandran N, Sazali Y, Hazry D, Zunaidi I (2007) EEG feature extraction for classifying emotions using FCM and FKM. Int J Comput Commun 1(2)
40. Hosseini SA, Khalilzadeh MA, Niazmand V (2010) Higher order spectra analysis of EEG signals in emotional stress states. In: IEEE International conference on information technology and computer science
41. Kim MK, Kim M, Oh E, Kim SP (2013) A review on the computational methods for emotional state estimation from human EEG. In: Computational and mathematical methods on medicine, Hindawi Publishing Corporation, vol 2013, Article ID 573734

42. Bajaj V, Pachori RB (2012) Classification of human emotions based on multi-wavelet transform of EEG signal. ScienceDirect, AASRI Procedia 2012
43. Duan RN, Zhu JY, Lu BL (2013) Differential entropy feature for EEG based emotion classification. In: International IEEE EMBs conference on neural engineering, 6–8 Nov 2013
44. Sorkhabi MM (2014) Emotion detection from EEG signals with continuous wavelet analyzing. Am J Comput Res Repository 2(4):66–70
45. Bhuvaneswari P, Satheesh Kumar J (2015) Influence of linear features in nonlinear EEG signals. ScienceDirect Procedia Computer Science 47:229–236
46. Soleymani M, Esfeden SA, Pantic M, Fu Y (2014) Continuous emotion detection using EEG signals and facial expressions
47. Soleymani M, Esfeden SA, Fu Y, Pantic M (2016) Analysis of EEG signals and facial expressions for continuous emotion detection. IEEE Trans Affect Comput 7(1)
48. Puthankatti Subha D, Joseph PK, Acharya R (2010) EEG signal analysis: a survey. J Med Syst 34:195–212
49. Bos DO (2017) EEG based emotion recognition
50. Al Fahoum AS, Al Fraihat AA (2014) Methods of EEG signal feature extraction using linear analysis in frequency and time frequency domains. In: ISRN Neuroscience, Vol 2014, Article ID 730218, Hindawi Publication
51. Liu Y, Sourina O, Nguyen MK (2011) Real-time EEG-based emotion recognition and its applications
52. Liu Y, Sourina O, Nguyen MK (2010) Real time EEG based Human emotion recognition and visualization
53. Bos DO, EEG based emotion recognition, the influence of visual and auditory stimuli
54. Teplan M (2002) Fundamentals of EEG measurement. Meas Sci Rev 2, Section 2
55. Li M, Lu B-L (2009) Emotion classification based on gamma-band EEG
56. Yuen CT, San WS, Seong TC (2009) Classification of human emotions from EEG signals using statistical features and neural network. Int J Integr Eng
57. Conneau A-C, Essid S (2014) Assessment of new spectral features for EEG-based emotion recognition. In: IEEE International Conference on Acoustic, Speech and Signal Processing (ICASSP)
58. Wang Q, Sourina O (2013) Real-time mental arithmetic task recognition from EEG signals. IEEE Trans Neural Syst Rehabil Eng 21(2)
59. Lal TN, Schröder M, Hinterberger T, Weston J, Bogdan M, Birbaumer N (2004) Support vector channel selection in BCI. IEEE Trans Biomed Eng 51(6)
60. Panat A, Patil A (2012) Analysis of emotion disorders based on EEG signals of human brain. Int J Comput Sci Eng Appl 2(4)
61. Kaundanya VL, Patil A, Panat A (2015) Classification of emotions from EEG using K-Nn classifier. In: Proceedings of 11th IRF international conference, 15th February-2015, Bengaluru, India, ISBN: 978-93-84209-90-2
62. Puthankattil Subha D (2008) EEG signal analysis: a survey. J Med Syst
63. Alarcao SM, Fonseca MJ (2017) Emotions recognition using EEG signals: a survey. IEEE Trans Affective Comput

A Brain Tumor: Localization Using Bounding Box and Classification Using SVM

Sanjeeva Polepaka, Ch. Srinivasa Rao and M. Chandra Mohan

Abstract The brain tumor is defined as the abnormal growth of unhealthy and unnecessary cells in the brain. The objective of the proposed method is to identify and locate the presence of tumor in the Magnetic Resonance Imaging (MRI) of brain images. The proposed method incorporates three phases to determine the presence of brain tumor, namely, preprocessing, identifying/locating the tumor region, and classifying the tumor region. The input image is filtered to reduce the noise in the preprocessing phase. In the second phase, Bounding Box (BB) is used to identify/locate the tumor region in the filtered image. Subsequently, in the third phase, Support Vector Machine (SVM) is used to classify the exact tumor location. Finally, the brain tumor is localized absolutely by the proposed tumor detection method. Moreover, the proposed method is evaluated with the publicly available standard dataset and compared with a contemporary method. The experimental results concluded that the proposed method has higher tumor detection accuracy than the existing method.

Keywords Brain tumor · Tumor detection · Filtering · Bounding box SVM classifier

1 Introduction to Brain Tumor

A tumor also termed as lesion or neoplasm is defined as the abnormal tissue growth due to the uncontrolled division of cells. In other words, a tumor is developed, whenever a normal or abnormal cell divides into multiple numbers even when there

S. Polepaka (✉)
JNTUH, Hyderabad, India
e-mail: psanjesus@gmail.com

Ch. Srinivasa Rao
JNTUKUCEV, Vizianagaram, India

M. Chandra Mohan
JNTUHCEH, Hyderabad, India

H. S. Saini et al. (eds.), *Innovations in Electronics and Communication Engineering*,
Lecture Notes in Networks and Systems 33,
https://doi.org/10.1007/978-981-10-8204-7_6

is no necessity. Typical brain tumor types are primary and metastatic brain tumors. A primary brain tumor is defined as an abnormal growth of cells that begins in the brain and does not expand to other body regions. Two types of primary brain tumor are benign and malignant. Table 1 summarizes the salient features of primary brain tumor from [1] and [2]. Figure 1 shows the MRI scans of brain images with benign and malignant brain tumors [1].

The metastatic brain tumor or secondary brain tumor is defined as the tumor that grows in some other part of the body and later spreads to the brain. The secondary brain tumor is mainly caused due to carrying of bloodstream with cancer cells to the brain. In most of the cases, the type and size of the tumor determine the severity of the disease. In the medical field, MRI is the commonly used mechanism to visualize the internal structure of the human body. Similarly, the MRI of brain image shows the apparent distribution of the tissues and the presence of tumor region in the human brain. To identify/locate such tumor(s) in the human brain, the proposed method includes three phases, namely, preprocessing, identify/locate the tumor, and the classification phase.

The organization of the paper is as follows: Sect. 2 deals with the existing brain tumor detection methods. Sections 3 and 4 comprise the proposed method and experimental results, respectively. Finally, Sect. 5 draws the conclusion.

Table 1 Salient features of primary brain tumor

Symptoms	Benign tumor	Malignant tumor
Growth	Grows slowly	Grows rapidly
Borders	Distinct borders	Attach and encroach brain tissues
Spreading	Spreads rarely	Spreads to other parts of brain
Tumor status	Easy to remove	Hard to remove
Threatening level	Low risk	High risk

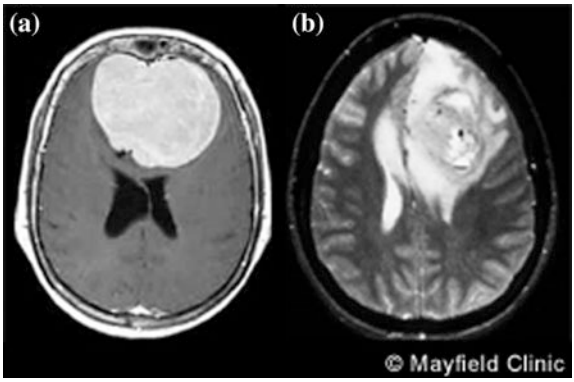

Fig. 1 MRI scans: **a** benign brain tumor and **b** malignant brain tumor. *Source* Brain tumor overview [1]

2 Existing Methods

This section deals with some of the existing methods of brain tumor segmentation techniques with their merits and demerits.

The Enhanced Darwinian Particle Swarm Optimization (EDPSO) method adopted in [3] overcomes the drawbacks of Particle Swarm Optimization (PSO) technique to segment and detect brain tumor from MRI images. In this method, tracking algorithm preprocessed the MRI images, and for the image enhancement Gaussian filter was applied. The EDPSO method segmented the brain image, and the classification process was carried out by Adaptive Neuro-Fuzzy Inference System (ANFIS). The study compared and evaluated the performance based on execution time and accuracy of proposed EDPSO with the existing PSO model. The model was tested on 101 brain images (87 images with tumor and 14 images without tumor) and found that the accuracy was 95% in 53.456 s in EDPSO, which is high when compared to the PSO model. The author claimed that the segmentation accuracy might be improved further by combining optimization techniques with EDPSO method.

Aslam, Khan, and Sufyan adopted an improved edge detection algorithm for brain tumor segmentation [4]. The proposed algorithm overcomes the drawback of edge detection algorithm (simple and sensitive to threshold) and watershed algorithm (which gives closed contours but too sensitive for composite images). The performance evaluation of the improved Sobel edge detection and watershed algorithm revealed that this improved model has superior result than the earlier methods. Though the study evaluated the proposed technique subjectively and objectively, the dataset used for testing is not available. The authors claimed that the efficiency might be enhanced by tuning the performance of Closed Contour Algorithm.

Eman et al. [5] integrated the benefits of K-means clustering and fuzzy C-means clustering to detect brain tumor from MRI images. Further, this integrated technique was compared with another segmentation algorithm regarding accuracy, processing time, and performance. The dataset taken for the study includes Digital Imaging and Communication in Medicine (DICOM), Brainweb, and BRATS database. The other segmentation techniques used for the study were K-means, expectation maximization mean shift, and fuzzy C-means. The proposed method undergoes four stages before the comparison. They were (a) preprocessing (for denoising and skull removal), (b) clustering (for integrating K-means and fuzzy C-means), (c) extraction and contouring (for thresholding and level set method), and (d) validation stage. As the accuracy was evaluated based on the ground truth of the processed image, the performance of the algorithm is evaluated approximately for the DICOM images. Otherwise, this integrated technique will be superior to the earlier methods.

Rajendran and Dhanasekaran [6] developed an improved method with the combination of Enhanced Possibilistic Fuzzy C-Means (EPFCM) and Parametric Deformable model with Gradient Vector Field (GVF) to detect and segment the

tumor from MRI brain images. The above two methods were combined as the demerit of one method acts as the merit of the other method. The first phase of the proposed method segments the image by the region-based method and the second phase of segmentation by the boundary-based method. The experimental results revealed an average similarity metrics and Jaccard index of 95.3 and 82.1%, respectively, which indicated the overlap degree between the automated segmentation result and manual segmentation was higher. Though the authors showed the liberal metric values, they failed to specify the dataset(s) used for evaluation.

Hota et al. [7] reviewed several papers based on intelligent techniques (like Artificial Neural Network (ANN) and fuzzy logic techniques) which are investigated to detect the tumor in the human brain image. The study revealed that irrespective of the model, it is necessary to preprocess the data due to high dimensionality and noise. The majority of the research work includes segmentation, feature extraction, and feature reduction to classify medical images. The results revealed that ANN classified the medical image data successfully and accurately than other techniques without any human inspection. ANN, when combined with fuzzy logic, developed a hybrid classification model for human brain's MRI data classification. Experimental results concluded that accuracy might be improved by integrating ANN with some other techniques.

Nidhi and Poonam [8] imposed a technique on the detection of a brain tumor and edema from MRI images. The method incorporates the regular operations on MRI images like filtering, enhancement, arithmetic operations, segmentation, and extracting Region of Interest (RoI). The Sobel segmentation method detected the tumor and edema regions, and then the final image was superimposed on the original MRI brain image to highlight the tumor and edema boundaries. Though the authors claimed to extend the method for other imaging modality for different human organs (like lung, liver, and breast), the results and the dataset used for the study are not specified explicitly.

Usually, the treatment and diagnosis of a brain tumor depend upon imaging. Shweta [9] preprocessed brain MRI images for noise removal. Using Sobel operator, the edges were detected, and the watershed algorithm was applied. The watershed segmented images of the tumor are superimposed to yield the resultant image. The results revealed that Marker-Controlled Watershed Segmentation (MCWS) method gave more accurate results when compared to other segmentation techniques. The proposed technique neither quantified the accuracy nor indicated the comparative accuracy values of the proposed method with other segmentation methods. Further, the major drawback of this method was that neither evaluated with standard datasets nor calculated the attributes of tumor region (like tumor area and tumor volume).

Segmenting RoI from MRI is a vital and fundamental approach in Digital Image Processing (DIP) based tumor identification process. Hemang [10] proposed a hybrid approach (a combination of watershed method and edge detection method) to detect the tumor boundaries in MRI brain images for various patients. Even though the superimposed picture highlights the tumor area clearly, the author failed

to specify the dataset(s) or the images used for evaluating this method and the segmentation accuracy/efficiency.

Simran and Gurjit surveyed the various methods used to detect and segment the brain tumor [11]. The survey revealed the limitations of each technique. In this survey, images with high noise or low brightness which were omitted or ignored by other researchers were considered for the study. Simran and Gurjit implemented a hybrid technique using fuzzy and region growing segmentation method to detect tumor by applying the trilateral filter. Authors failed to specify the information about the dataset considered for the evaluation and its corresponding segmentation accuracy. Even though the study covered the rare area of brain tumor detection methods, without the specification details of the dataset used and the accuracy level, the study remains incomplete.

Image processing applications play a vital role in medical fields to identify the diseases. Mahalakshmi and Velmurugan's method [12] detected and separated brain tumor using PSO with swarm intelligence. The four steps involved in the brain tumor extraction were as follows: (i) conversion of DICOM into image file format, (ii) implementation of PSO algorithm to detect the presence of tumor, (iii) selection of the best resultant image based on time, and (iv) extraction of tumor affected region by using appropriate filter techniques. The study concluded that during the segmentation phase, the PSO algorithm performed well. Though the experimental results were fair, there is no clear distinction in the dataset(s) used for evaluation.

By considering the benefits and barriers of the existing brain tumor detection methods, the proposed adopts BB method to locate the tumor region precisely and SVM classifier to classify the tumor meticulously from the brain tissues.

3 Proposed Work

Figure 2 shows the steps incurred in the proposed method of brain tumor segmentation. The three phases of the proposed method are (i) preprocessing, (ii) identifying/locating the tumor region, and (iii) classifying the tumor using SVM classifier. The following section deals with the description of three phases in the proposed method.

Preprocessing Phase: In the first phase, series of necessary processing procedures on the input brain MRI images is carried to reduce the noise and improve the image quantity. The size of the input MRI brain image is 256 × 256 pixels size. Initially,

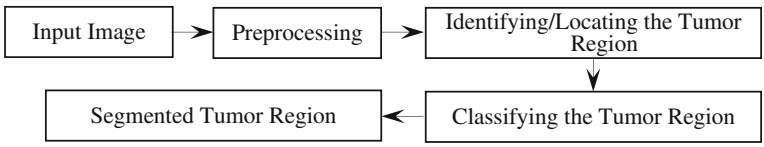

Fig. 2 Proposed method of brain tumor segmentation

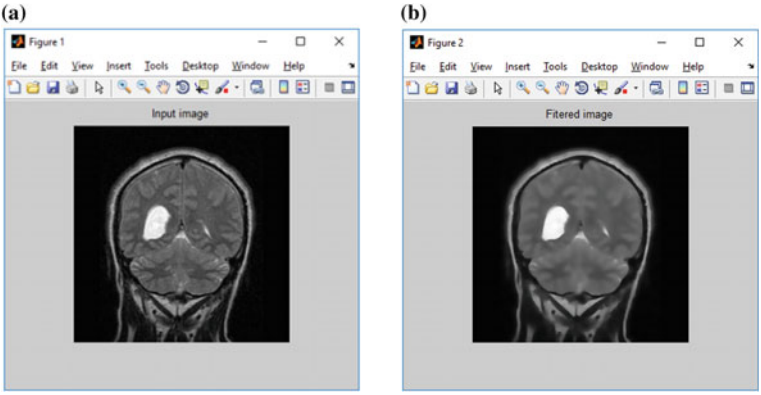

Fig. 3 Preprocessing phase: **a** input image and **b** filtered image

the denoising of input image takes place. According to Guan et al. [13], anisotropic diffusion filter outperformed the other filters, namely, moving average filter, median filter, and frequency domain low-pass filter in reducing the noise by preserving the object boundaries. Henceforth, the proposed method adopts anisotropic diffusion filter for diminishing the noise present in the input image. Further, the resultant image after the filtering process preserves the object boundaries even without the enhancement process. Figure 3a shows the input image, and Fig. 3b shows the resultant filtered image after the preprocessing phase.

Identifying/locating the Tumor Region Phase: The second phase of the proposed method deals with identifying/locating the tumor region using Bounding Box (BB) method. Experimental results concluded that some of the earlier algorithms [14–16] have an efficient performance in determining the RoI by using BB method. Henceforth, the proposed method adopts BB method to identify the location of the tumor region in the input brain image. Table 2 shows the pseudocode for detecting/locating the tumor in the MRI of brain images. The BB algorithm's implementation is based on the symmetrical property of the brain structure [17]. The right and left lobes of the brain are almost identical in nature until the occurrences of any abnormalities (like a tumor). The BB algorithm is initiated with an assumption that the tumor is located on any one-half of the brain images. Figure 4 shows the detection of tumor region using the BB method from the filtered image during the second phase.

Tumor Region Classification Phase using SVM Classifier: The third phase of the proposed method deals with the classification of tumor region using SVM classifier. Earlier algorithms [18–20] concluded that SVM plays a vital role in both the linear and nonlinear classification scenarios. The objective of SVM is to determine the optimum hyperplane which separates the classes with the maximum margins among the training data. The major advantage of SVM classifier lies in quick learning even with the large datasets [18]. In SVM classification process, nearly one-third of images from the dataset are considered as training data while the other part is used

Table 2 Pseudocode for localizing the tumor region

Steps	Processing
Input image	Filtered image
Step 1	Symmetry line [12] is drawn over the filtered image
Step 2	Due to the bisection of filtered image using the symmetrical line, one-half is considered as the reference image and while the other half is considered as the test image for evaluation
Step 3	The abnormalities in both the regions are identified by performing the horizontal and vertical scanning process
Step 4	During the scanning process, average intensity determines the abnormal regions in the image
Step 5	Based on the average intensity, the score plot function (E) is determined
Step 6	Minimum and maximum values are determined using the graph
Step 7	From the determined maximum and minimum values, a pair of points (i, j) is identified which satisfies the criteria that difference between them $[E(i) - E(j)]$ is maximum
Step 8	These coordinates form the BB boundary
Output image	Localized tumor region

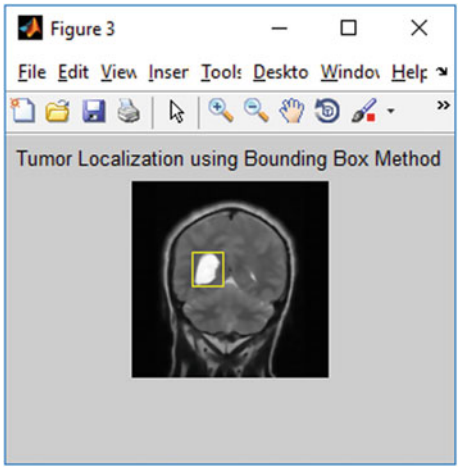

Fig. 4 Localizing the tumor region using bounding box method

for testing purpose. With the completion of the training phase, the SVM completely identifies the tumor(s) present in the input image. As the classification efficiency of SVM depends on the number of training datasets, classification accuracy can be improved by training more datasets. Figure 5a shows the classification of tumor region by the SVM classifier whereas Fig. 5b shows the segmented tumor region from the input image using the proposed method. The classification of tumor region's boundary in the proposed method by the SVM classifier is shown in Fig. 5a using the green color notation.

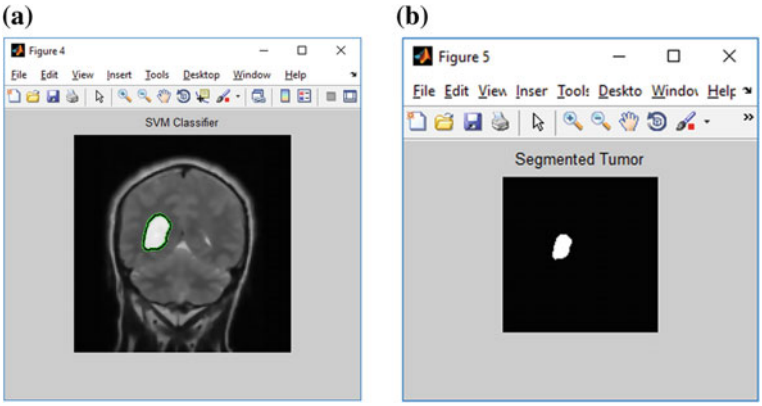

Fig. 5 **a** Tumor classification using the SVM classifier and **b** segmented tumor

4 Experimental Results

The proposed method of brain tumor identification, classification, and segmentation is implemented in MATLAB version 8.3.0.532 (R2014a) installed on Intel I3 3.10 GHz processor machine with 3 GB RAM. The proposed method is evaluated on the publicly available datasets from World Wide Web. Out of 101 MRI brain images initially, 50 images are considered for evaluating the proposed method, including 35 brain images with tumor and rest of (15) images without tumor.

Figure 6 shows the steps in identifying the tumor region in the three brain MRI samples using the proposed method. Figure 6a–e shows the input MRI brain image, filtered image, tumor localization using BB method, tumor classification using SVM classifier, and the segmented tumor region, respectively.

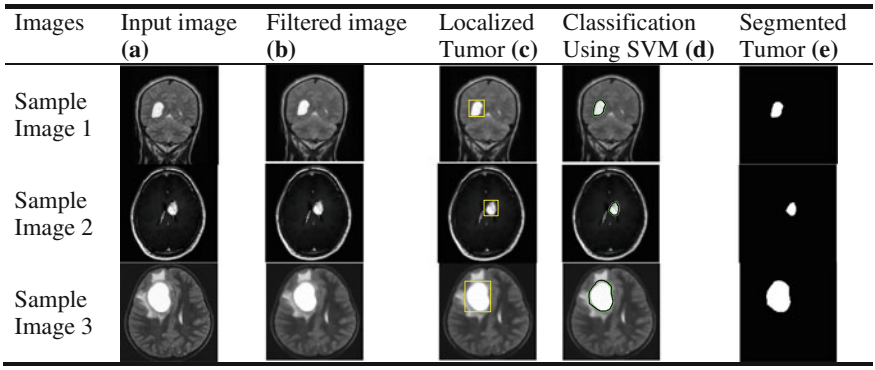

Fig. 6 **a** Input image, **b** filtered image, **c** localizing the tumor region using BB method, **d** classification of tumor region using SVM classifier, and **e** segmented tumor region using the proposed method

When the segmentation accuracy is compared with the existing method [3], the proposed method resulted in the absolute segmentation of tumor in all the images. Thereby yielding 100% segmentation accuracy, whereas the existing method resulted in 92% and 95% accuracies for PSO- and EDPSO-based segmentations.

5 Conclusion

Image diagnosis plays a vital role in the medical field. Even though there are some imaging techniques, Computed Tomography (CT) scan and MRI play a major role in analyzing and diagnosing the brain tumor. When compared to CT scan, brain MRI reveals the tissue structure clearly which in turn helps in detecting the presence of tumor region. Therefore, the proposed method put forth brain MRI for diagnosis using three phases. In the preprocessing phase (first phase), the input image was filtered to remove the excessive noise, and also, the boundaries were refined. In the second phase, the localization of tumor region took place using the BB method. Finally, the absolute classification of the brain tumor from the normal brain tissues using the SVM classifier was carried out in the third phase.

Experimental results concluded that the proposed method has higher tumor segmentation accuracy than the existing method. Further, the author would like to extend their work by evaluating the proposed method with more number of images from standard datasets and live images.

References

1. Brain tumor overview. http://www.mayfieldclinic.com/PE-BrainTumor.htm
2. Brain tumors-A handbook for the newly diagnosed, American Brain Tumor Association, http://www.abta.org/secure/newly-diagnosed-1.pdf
3. Vasupradha V, Kavitha AR, Roselene RS (2016) Automated brain tumor segmentation and detection in MRI using enhanced Darwinian particle swarm optimization (EDPSO). Procedia Comput Sci 92:475–480
4. Aslam A, Khan E, Sufyan B (2015) Improved edge detection algorithm for brain tumor segmentation. Procedia Comput Sci 58:430–437
5. Eman AM, Mohammed E, Rashid AA (2015) Brain tumor segmentation based on a hybrid clustering technique. Egypt Inform J 16:71–81
6. Rajendran A, Dhanasekaran R (2011) Fuzzy clustering and deformable model for tumor segmentation on MRI brain image: a combined approach. Procedia Eng 30:327–333
7. Hota HS, Shukla SP, Gulhare KK (2013) Review of intelligent techniques applied for classification and preprocessing of medical image data. Int J Comput Sci Issues 10:267–272
8. Nidhi P, Tumor PB (2014) Brain tumor and edema detection using Matlab 7.6.0.324. Int J Comput Eng & Technol 5:122–131
9. Shweta P (2014) Brain tumor extraction using marker-controlled watershed segmentation. Int J Eng Res Technol 3:2020–2022
10. Hemang JS (2014) Detection of tumor in MRI images using image segmentation. Int J Adv Res Comput Sci Manag Stud 2:53–56

11. Simran A, Gurjit S (2015) A study of brain tumor detection techniques. Int J Adv Res Comput Sci Softw Eng 5:1272–1278
12. Mahalakshmi S, Velmurugan T (2015) Detection of brain tumor by particle swarm optimization using image segmentation. Indian J Sci Technol 8:13–19
13. Guan F, Ton P, Ge S, Zhao L (2014) Anisotropic diffusion filtering for ultrasound speckle reduction. Science China, Technological Sciences 57:607–614
14. Priyanka BS (2013) An improvement in brain tumor detection using segmentation and bounding box. Int J Comput Sci Mob Comput 2:239–246
15. Jayalaxmi SG, Vinayadatt VK (2013) Automatic detection and segmentation of brain tumors using binary morphological level sets with bounding box. In: Proceedings of 3rd international conference on computer engineering and bioinformatics, pp 37–43
16. Baidya NS, Nilanjan R, Russell G, Albert M, Hong Z (2012) Quick detection of brain tumors and edemas: a bounding box method using symmetry. Comput Med Imaging Graph 36:95–107
17. Ray N, Saha BN, Brown MRG (2007) Locating brain tumors from MR imagery using symmetry. In: 41st Asilomar conference on signals, systems and computers, pp 224–228
18. Dipali BB, Patil SN (2016) Brain tumor MRI image segmentation using FCM and SVM techniques. Int J Eng Sci Comput 6:3939–3942
19. Parveen S, Amritpal S (2015) Detection of brain tumor in MRI images, using combination of fuzzy C-means and SVM. In: 2nd international conference on signal processing and integrated networks, pp 98–102
20. Nithyapriya G, Sasikumar C (2014) Detection and segmentation of brain tumors using AdaBoost SVM. Int J Innovative Res Comput Commun Eng 2:2323–2328

Improved Normalization Approach for Iris Image Classification Using SVM

R. Obul Kondareddy and B. Abraham David

Abstract With the rapid improvement of information technology, security and authentication of individuals have become a greater significance. Iris recognition is one of the best solutions in providing unique authentication for individuals based on their IRIS structure. Iris normalization is meant to extract the iris region and represent it in the spatial domain, Daugman's rubber sheet model is so far a standard and efficient method of implementing this process. In this paper, a low complex, simpler and improved version of rubber sheet model is proposed. The main aim of this method is to minimize the complex computations that were involved in the conventional rubber sheet model and to provide an equivalent performing approach with very less computations. Classification performance is evaluated with CASIA and IIT Delhi IRIS databases using SVM classifier.

Keywords IRIS · Normalization · Rubber sheet model

1 Introduction

In the present scenario, keeping the data secured and authenticated is most difficult and very important to any organization or individual. Most of the researchers are focusing and developing different new applications on biometrics. Among all the biometrics, iris recognition is playing a vital and unique role. This works according to the visual features of a person like freckles, rings, furrows, and corona. Due to the high variation of randomness in abovementioned features, iris recognition is found to be highly tricky process [1].

R. Obul Kondareddy
Department of CSE, Institute of Aeronautical Engineering, Hyderabad, India

B. Abraham David (✉)
R&D Division, DSP Engineer, Vision Krest Embedded Technologies, Hyderabad, India
e-mail: David-bagadam.abrahamdavid@gmail.com

H. S. Saini et al. (eds.), *Innovations in Electronics and Communication Engineering*,
Lecture Notes in Networks and Systems 33,
https://doi.org/10.1007/978-981-10-8204-7_7

Iris is a thin, circular structure in the eye responsible for controlling the diameter and size of the pupil and thus the amount of light reaching the retina. Iris lies between the lens of the human eye and cornea. The normal width or diameter of the iris is 12 mm and the pupil size may vary between 10 and 80% of the iris diameter. Eye color is defined by that of the iris. For more information, please refer [2]. This organ is externally visible; it has the unique quality of epigenetic pattern which stables throughout the adult life. This versatile character makes it very attractive to use as an identifying individual biometric application. By using different image processing techniques, we can extract the unique iris pattern from a digitalized eye image, encode them into a biometric template and store in the database.

John Daugman implemented a working model for automated iris recognition system [2], though the model is the most successful and well-known system so far that has been developed. Most of the popular recognition models include the one proposed by Wilde et al. [3, 4], Boles and Boashash [5], Lim et al. [6], and Noh et al. [7].

The Daugman's system was tested under several studies, the result rate always leads to zero failure rate. By doing experiments on millions of irises, Daugman's system always gives perfect identification of individuals. By doing experiment on 520 iris images, Wildes et al., who established the prototype system, also gave flawless performance reports. By taking the database of 6000 eye images, another researcher, Lim.et al. proposed a system which attains recognition of 98.4%.

The main objective of this paper is to present low complexity based IRIS normalization method to minimize the complex computations that were involved in the conventional rubber sheet model and to provide an equivalent performing approach with very less computations. Here, we use Log Gabor filters for extracting the features from normalized images. Feature extraction of this IRIS images was implemented using Log Gabor filters. A performance comparison is presented with CASIA [8] and IIT Delhi [9] IRIS databases using SVM classifier.

This paper is organized as follows, Sect. 1 gives a brief introduction about the physical dimensions and the importance of IRIS recognition system continuing with Sect. 2 which clearly depicts the implementation of Daugman's rubber sheet model. Section 3 explains neatly about the proposed approach of minimizing the complexity involved in the Daugman's model, Sect. 4 shows the performance analysis of the proposed approach with different classifiers and databases.

2 Daugman's Rubber Sheet Model

In this particular model, we use Daugman's integro-differential operator to find the coordinates of iris boundary. First

- $r_{\min}$ is the possible minimum,
- $r_{\max}$ is maximum radius

And the λ value for iris will be set to establish a searching parameter. For the nonideal database of WVU, 50% of the image size will be set for $r_{\max}$, and 33% of

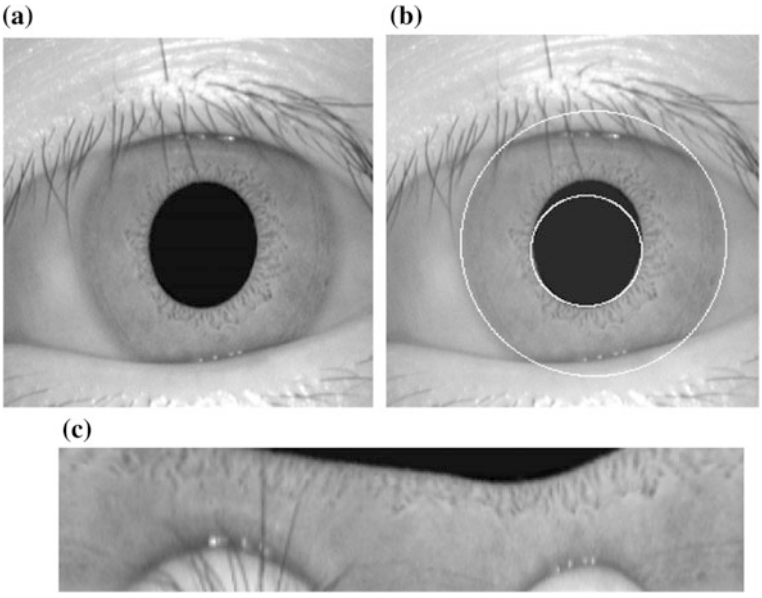

Fig. 1 **a** Input iris Image **b** Localized Image **c** Normalized Image

$r_{\min}$ will be set for $r_{\max.}$ Using λ, the operator will find the maximum pixel intensity value change (J) in the image which lies in the defined radius parameters with a circular integral centered which lies on the points of ($x0$, $y0$), with radius r of the radial derivate of the original image blurred with a Gaussian kernel G (Fig. 1).

$$J(r, x_0, y_0) = G_\sigma(r) * \left(\frac{d}{dr}\right) \int \frac{I(x,y)}{2\pi r} ds \tag{1}$$

$$G_\sigma(r) = \frac{1}{\sigma\sqrt{2\pi}} \text{ep}\left(\frac{-r^2}{2\sigma^2}\right) \tag{2}$$

In this rubber sheet model, we can remap each point within the iris region by taking a pair of polar coordinates. This model will be accountable or responsible for imaging distance, pupil dilation, and nonconcentric pupil misplacement. It is not responsible for rotational inconsistencies.

3 Proposed Iris Recognition System

The proposed approach involves the following steps: (a) Iris segmentation (b) Iris normalization (c) Feature extraction (d) Classification

(a) **Iris Segmentation**

In iris recognition system, segmentation is the basic step. Here, from the captured eye image, we will isolate the iris region. Canny method finds edges by looking for maxima of the gradient in iris image. By using derivative of Gaussian filter, we can calculate the gradient. In this, we use two thresholds to detect the weak and strong edges. This approach is tougher to detect the true weak edges. In canny edge detector, the output will be edge strength image and the orientation image. The intensity value of the image will be increased by adjusting the gamma correction factor.

(b) **Iris normalization**

The proposed improved normalization approach involves partitioning the circular region obtained through Daugman's Model. The approach divides the 360° circular region into a trapezoidal portion as shown in Fig. 2. This approach mainly considers the mapping area between 202.5° and 337.5° in the circular region. This region when segmented look like a trapezoid which is shown in Fig. 3c.

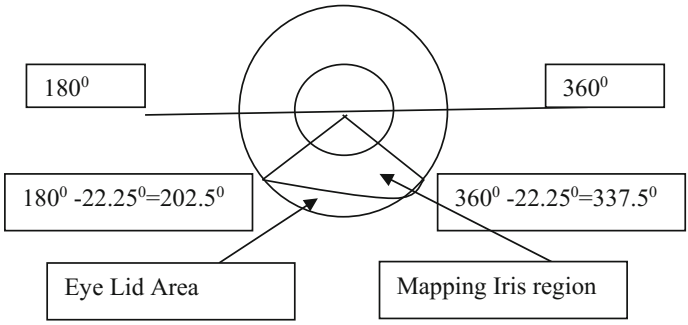

Fig. 2 Mapping area for the proposed approach

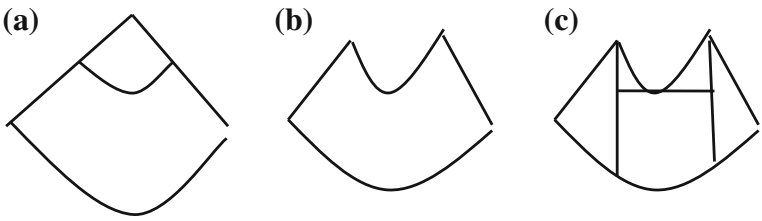

Fig. 3 **a** Cropped region from Fig. 2 **b** after removal of upper part **c** Trapezoidal portion

The proposed approach is as follows:

Step 1: *considering lower half iris, i.e., lower half circle: Starting from angle* 180–360. *(Lower circular portion)*
Step 2: *Consider only* 75% *of the lower half circle, eliminating* 25%, *i.e.,* 22.5% *from left and* 22.5% *from right, means from left* 180–202.5 = 22.5%, *and from right, i.e., from* 360–22.5 = 337.5, *i.e.,* 22.5% *deducted from right.*
Step 3: *Now get the shape of trapezoid, and convert that trapezoid to rectangle by removing the Triangular shapes from both the sides of Trapezoid.*
Step 4: *Finally get a small rectangular normalized iris image for which the features are calculated.*

(c) **Feature Extraction**

In feature extraction, the fundamental information in iris pattern will generate a binary template which is used for classification and recognition. By combing or grouping, the iris pattern and 1D Log Gabor filter generate an iris feature set. This is a logarithmic approach which is used to produce 0 DC components for any bandwidth. This will be represented in mathematical terms as

$$G(f) = \exp\left(\frac{-\log\left(\frac{f}{f_o}\right)^2}{2\log\left(\frac{\sigma}{f_o}\right)}\right. \tag{3}$$

where f_0 represents the center frequency and σ gives the bandwidth of the filter.

When this filter is applied, the 2D normalized pattern will be divided into a number of 1D signals. These will be convolved with 1D Gabor wavelets. Here, we take 1D signal as equal to all the rows of 2D normalized patterns. Each row corresponds to a circular ring of the iris region. The angular direction will be taken with respect to the column of the normalized pattern since maximum independence occurs only in angular direction. The filter is constructed by calculating the radial filter component such as center frequency of filter and normalized radius of the center frequency plane [10].

(d) **SVM Classifier**

Support vector machine is wide-ranging classification tool which is used in many successful applications. SVM performs pattern recognition between two classes by finding a perfect surface which has the maximum distance to the closest point in training set. Assuming linearly separable data, the goal of maximum margin classification is to separate the two classes by a hyper-plane such that the distance to the support vectors is maximized. This hyper-plane is called the optimal separating hyper-plane (OSH) which has the form

$$f(x) = \sum_{i=1}^{l} \alpha_i y_i x_i . x + b \tag{10}$$

The coefficients in the above equation are the solutions of a quadratic problem. Classification of the new data point x is performed by computing the sigh of the right side of the Eq. 10. So this will allow applying multi-class classification

$$d(x) = \frac{\sum_{i=1}^{l} \alpha_i y_i x_i . x + b}{\left|\left|\sum_{i=1}^{l} \alpha_i y_i x_i . x + b\right|\right|} \tag{11}$$

The sign of d is the classification result for x and $|d|$ is the distance from x to the hyper-plane [11–13].

Different types of kernels are used like

(i) Linear: $K(x, y) = x.y$
(ii) Polynomial $K(x, y) = (\gamma x.y + c)^{\circ}$
(iii) Radial basis function $K(x, y) = \mathrm{e}^{-\gamma|x-y|^2}$
(iv) Sigmoid $K(x, y) = \tanh(\gamma x.y + c)$.

4 Performance Analysis

For the performance evaluation of the proposed approach, the image is taken from CASIA iris image database version 1 available at [8]. In which for the experiment, 20 users of each three images are considered for training and two for testing, similarly the IIT Delhi database in which, 20 users three images of each are considered for training and the two for testing. Feature vector of each image was generated using the concept explained in Sect. 3. When classified with conventional rubber sheet model, the proposed approach shows an improvement of 7% decrement in processing time with almost same recognition rate (Figs. 4, 5, and 6).

For the evaluation, two parameters are considered, first the classification rate and second average processing time for normalization. In the earlier analysis, it was found that classification is decreased from 89 to 86% with the proposed approach which is not a significant loss as per our knowledge. However, the average processing is decreased by 30% using on 70% of the CPU processing time, this is a significant improvement.

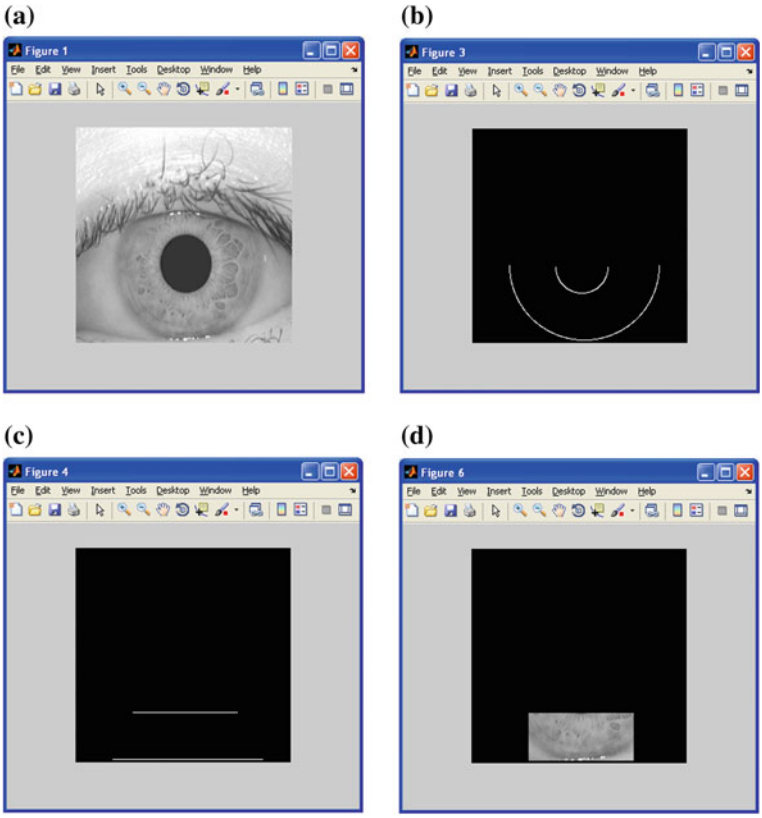

Fig. 4 **a** Eye Image **b** Extraction of Half circular region **c** Conversion into trapezoidal region **d** Extraction of iris in rectangular form

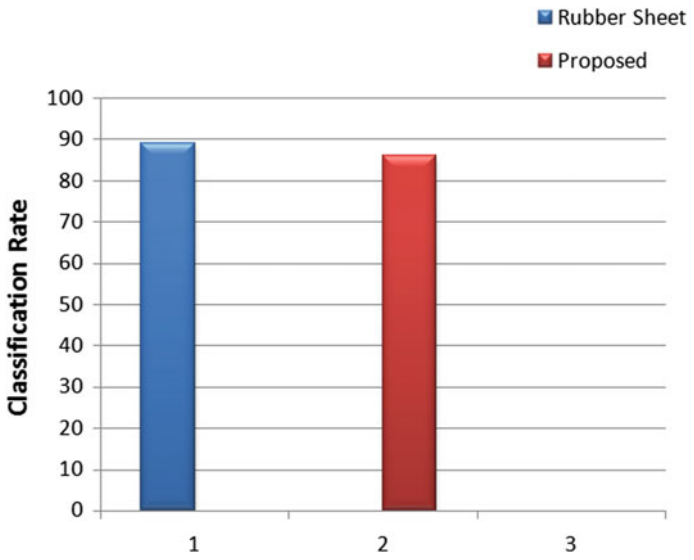

Fig. 5 Classification rate analysis for proposed normalization approach using SVM

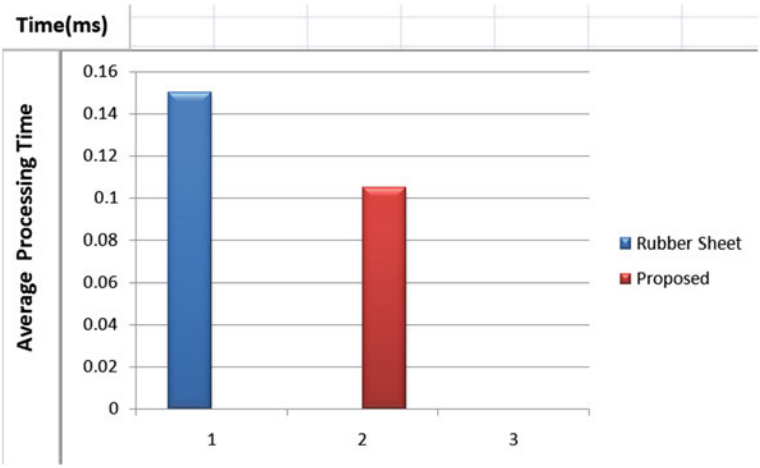

Fig. 6 Average processing time for normalization

5 Conclusion

A new improved method of iris normalization is proposed in this method and the performance evaluation in terms of classification rate and average processing time is evaluated with different dataset of iris images. The experimental findings prove that the proposed approach is consuming 70% of the processing when compared to

the conventional rubber sheet model which makes it significant for further research analysis. The proposed approach can be further extended by analyzing this with different multi-class classifiers.

References

1. Seetharaman K, Ragupathy R (2012) Iris recognition based image authentication. Int J Comput Appl 44(7)
2. Daugman J (2002) How iris recognition works. In: Proceedings of 2002 international conference on image processing, vol 1
3. Wildes R (1997) Iris recognition: an emerging biometric technology. In: Proceedings of the IEEE, vol 85, no 9
4. Wildes R, Asmuth J, Green G, Hsu S, Kolczynski R, Matey J, McBride S (1994) A system for automated iris recognition. Proceedings IEEE Workshop on Applications of Computer Vision, Sarasota, FL, pp 121–128
5. Boles W, Boashash B (1998) A human identification technique using images of the iris and wavelet transform. IEEE Trans Signal Process 46(4)
6. Lim S, Lee K, Byeon O, Kim T (2001) Efficient iris recognition through improvement of feature vector and classifier. ETRI J 23(2)
7. Noh S, Pae K, Lee C, Kim J (2002) Multi-resolution independent component analysis for iris identification. In: The 2002 international technical conference on circuits/systems, computers
8. http://www.cbsr.ia.ac.cn/english/IrisDatabase.asp
9. http://www4.comp.polyu.edu.hk/∼csajaykr/IITD/Database_Iris.htm
10. Amir AH, Reza P (2009) Efficient iris recognition through improvement of feature extraction and subset selection. Int J Comput Sci Inform Sec 2(1)
11. Vapnik VN (2000) The nature of statistical learning theory, 2nd edn. Springer-Verlag, New York
12. Cortes C, Vapnik V (1995) Support-vector networks. Mach Learn 20(3):273–297
13. Vapnik V (1998) Statistical Learning Theory. Wiley, New York

Performance Parameter Based Comparison of the Slantlet Transform and Discrete Cosine Transform (DCT) for Steganography in Biomedical Signals

Apurwa S. Jagtap and Revati Shriram

Abstract In this paper, we present patient's information hiding using the Slantlet Transform and Discrete Cosine Transform (DCT). DCT transforms the signal from spatial domain to frequency domain. It can separate the image into high-, middle- and low-frequency components. In DCT-based technique, insertion of secret information in carrier depends on the DCT coefficients. The Slantlet Transform is known as Orthogonal Discrete Wavelet Transform (ODWT). It separates 1-D signal in two sub-bands, LL and HH. It divides 2-D signal into four sub-bands, HH, HL, LH and LL and the secret information is embedded in these sub-bands. At first, DCT is used for data hiding. For that, 1-D ECG signal and some biomedical images (2-D) are used as cover signal. The secret information is embedded in lower DCT coefficients. Similarly, Slantlet transform is used for hiding patient's data in same biomedical signals ECG and biomedical images, respectively. Original signals and embedded signals are compared. To analyse the performance of the transforms used for data hiding, Mean Squared Error (MSE), Normalised Root Mean Squared Error (NRMSE) and Peak Signal to Noise Ratio (PSNR) are calculated. MSE between original and embedded signals is less.

Keywords Discrete Cosine Transform (DCT) · The Slantlet Transform
Mean Squared Error (MSE) · Normalised Root Mean Squared Error (NRMSE)
Peak Signal to Noise Ratio (PSNR)

A. S. Jagtap (✉) · R. Shriram
MKSSS'S Cummins College of Engineering for Women, Pune, India
e-mail: apurwa.jagtap@cumminscollege.in

R. Shriram
e-mail: revati.shriram@cumminscollege.in

H. S. Saini et al. (eds.), *Innovations in Electronics and Communication Engineering*,
Lecture Notes in Networks and Systems 33,
https://doi.org/10.1007/978-981-10-8204-7_8

1 Introduction

To represent signals in many different ways and to extract information that is not readily available in the signal, mathematical transformations are applied to the signal. Mathematical transformations are applied to the signal to extract additional or hidden information about the original signal, which may not be available obvious otherwise [1]. Mathematical transformations are applied to the signals or images for data compression, security and various analysis. For that purpose, various transformations are used depending upon the suitability of that particular transform for specific application such as Discrete Cosine Transform (DCT), Discrete Fourier Transform (DFT), Discrete Wavelet Transform (DWT) and Slantlet Transform. DCT can be used for steganography applications to protect signals and data while storing and transmission of records from hackers [2]. Slantlet transform is wavelet-like transform known as Orthogonal Discrete Wavelet Transform (ODWT) discovered by Dr. Ivan Selesnick in 1999. DWT is used for a variety of applications. Slantlet Transform provides better time localisation and smoothness than DWT and it provides better signal compression than DCT [3, 4].

In this paper, we compare data hiding algorithm by using DCT and Slantlet transform. We have taken five 1-D ECG signal samples from MIT-BIH database and five biomedical images as a covered signal and secret information including patients name, blood group and disease and the treatment is hidden in cover signal. To analyse which transform proves better for data hiding, performance parameter analysis is performed by calculating Mean Squared Error (MSE) and Peak Signal to Noise Ratio (PSNR).

This paper is divided into following sections: Sect. 2 explains DCT and Slantlet Transform. Section 3 explains data hiding using DCT and Slantlet Transform. Section 4 describes the results and Sect. 5 explains the conclusion and future work.

2 Signal Transforms

In this section, DCT and Slantlet Transform are explained.

2.1 Discrete Cosine Transform

DCT is variant of Discrete Fourier Transform. It is known as real-valued transform. DCT converts intensity function into weighted sum of periodic basic cosine functions. DCT transforms the signal from spatial domain to frequency domain. It separates the signal in high-, middle- and low-frequency components. For a 1-D signal and image of two-dimensional DCT can be given as [5]:

$$c(u) = a(u)\sum_{x=0}^{N-1} f(x)\cos\left[\frac{(2x+1)u\pi}{2N}\right], \quad \text{for } u = 0, 1, 2, \ldots N-1 \tag{1}$$

$$\begin{aligned} f(x) &= \sum_{u=0}^{N-1} a(u)c(u)\cos\left[\frac{(2x+1)u\pi}{2N}\right], \quad \text{for } x = 0, 1, 2, \ldots N-1 \\ a &= \begin{cases} \sqrt{\frac{1}{N}} & \text{for } u = 0 \\ \sqrt{\frac{2}{N}} & \text{for } u = 1, 2, \ldots, n-1. \end{cases} \end{aligned} \tag{2}$$

$$\begin{aligned} c(u,v) &= a(u)a(v)\sum_{x=0}^{N-1}\sum_{y=0}^{N-1} f(x,y)\cos\left[\frac{(2x+1)u\pi}{2N}\right]\cos\left[\frac{(2x+1)v\pi}{2N}\right], \\ &\text{for } u = v = 0, 1, 2, \ldots N-1 \end{aligned} \tag{3}$$

$$\begin{aligned} f(x,y) &= \sum_{u=0}^{N-1}\sum_{v=0}^{N-1} a(u)a(v)c(u,v)\cos\left[\frac{(2x+1)u\pi}{2N}\right]\cos\left[\frac{(2x+1)v\pi}{2N}\right], \\ &\text{for } x = y = 0, 1, 2, \ldots N-1 \\ a &= \begin{cases} \sqrt{\frac{1}{N}} & \text{for } u = v = 0 \\ \sqrt{\frac{2}{N}} & \text{for } u = v = 1, 2, \ldots n-1. \end{cases} \end{aligned} \tag{4}$$

2.2 The Slantlet Transform

Dr. Ivan Selesnick [3] proposed Slantlet Transform in 1999. DWT can be used for various applications but there exists trade-off between time localisation and smoothness. For this reason, Slantlet transform is proposed. Filter bank implementation of Slantlet transform is similar to DWT filter bank. Slantlet provides short windows at highest frequencies and long windows at low frequencies. Slantlet retains higher percentage of energy after compression as compared to DWT. It provides better embedding capacity and good imperceptibility. The runtime of Slantlet transform is better than DWT. It provides efficient representation of piecewise linear signals and multiresolution analysis are:

$$\begin{aligned} G0(z) = &\left(-\sqrt{10/20} - \sqrt{2/4}\right) + \left(3\sqrt{10/20} + \sqrt{2/4}\right)z^{-1} \\ &+ \left(-3\sqrt{10/20} - \sqrt{2/4}\right)z^{-2} + \left(\sqrt{10/20} + \sqrt{2/4}\right)z^{-3} \end{aligned} \tag{5}$$

$$\begin{aligned} G1(z) = &\left(7\sqrt{5/80} - 3\sqrt{55/80}\right) + \left(-\sqrt{5/80} - \sqrt{55/80}\right)z^{-1} \\ &+ \left(-9\sqrt{5/80} + \sqrt{55/80}\right)z^{-2} + \left(-17\sqrt{5/80} + 3\sqrt{55/80}\right)z^{-3} \\ &+ \left(-17\sqrt{5/80} - 3\sqrt{55/80}\right)z^{-4} + \left(9\sqrt{5/80} + \sqrt{55/80}\right)z^{-5} \\ &+ \left(-\sqrt{5/80} - \sqrt{55/80}\right)z^{-6} + \left(-7\sqrt{5/80} - 3\sqrt{55/80}\right)z^{-7} \end{aligned} \tag{6}$$

$$\begin{aligned} G2(z) = &\left(\sqrt{1/16} + \sqrt{11/16}\right) + \left(\sqrt{3/6} + \sqrt{11/16}\right)z^{-1} \\ &+ \left(\sqrt{5/6} + \sqrt{11/16}\right)z^{-2} + \left(\sqrt{7/16} + \sqrt{11/16}\right)z^{-3} \\ &+ \left(\sqrt{7/16} - \sqrt{11/16}\right)z^{-4} + \left(\sqrt{5/16} - \sqrt{11/16}\right)z^{-5} \\ &+ \left(\sqrt{3/16} - \sqrt{11/16}\right)z^{-6} + \left(\sqrt{1/16} - \sqrt{11/16}\right)z^{-7} \end{aligned} \tag{7}$$

$$G3(z) = Z^{-3}G2(1/z) \tag{8}$$

3 Proposed System

In this paper, we have proposed algorithm to hide a secret information in biomedical signals. The biomedical signals include 1-D ECG database from MIT-BIH database and few 2-D biomedical images including 'mri.tif', 'spinal.tif', 'dental.tif', 'foot.tif' and 'lung.tif'. All the images are of the same size. These signals are used as cover signals to hide secret information. Secret information hidden in all the signals (1-D and 2-D) is same. At first, data hiding is hidden using DCT and then Slantlet Transform is applied. The main objective behind this is to analyse which algorithm proves to be better in hiding information in biomedical signals. Figure 1 shows the block diagram of the proposed system. DCT and Slantlet Transform are applied to the cover signals simultaneously, then secrete information is embedded in lower DCT and lower slantlet coefficients and after that signal is again Reconstructed by inverse DCT and inverse Slantlet Transform. Then MSE, NRMSE, and PSNR are calculated between the original signal and reconstructed signal after embedding secret information.

4 Results and Discussion

The algorithm is implemented in MATLAB 2013. It is observed that Slantlet transform is complex to implement than DCT. We have compared the performance of both transform using DCT and Slantlet transform for data hiding by calculating Mean Squared Error (MSE), Normalised Root Mean Squared Error (NRMSE) and Peak Signal-to-Noise Ratio (PSNR) (Fig. 2).

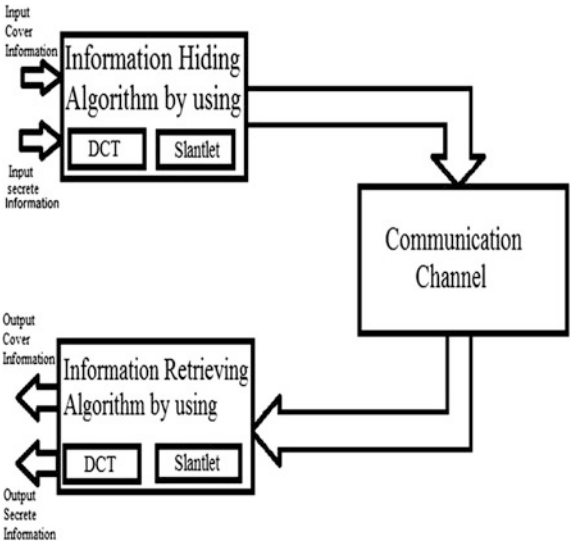

Fig. 1 Block diagram of the proposed system

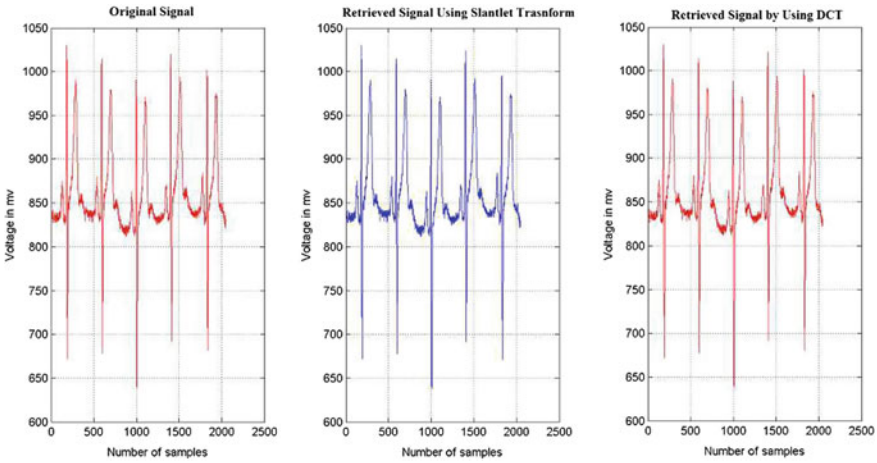

Fig. 2 Results obtained for data hiding using Slantlet Transform and DCT in 1-D signal

4.1 Performance Parameter Analysis

We have measured Mean Squared Error (MSE), Normalised Root Mean Squared Error (NRMSE), and Peak Signal-to-Noise Ratio (PSNR) to compare the original input signal and reconstructed signal after hiding information by using DCT and

Slantlet Transform. The parameters measured to analyse performance of the transform are defined as follows (Fig. 3).

Mean Square Error (MSE) measures the average of squares of errors or deviations that is difference between estimator expected value and estimated value.

$$\mathrm{MSE}(x, y) = \frac{1}{N}\sum_{i=1}^{N}(x_i - y_i)^2 \tag{9}$$

where x_i denotes the length of 1-D input signal and pixel values of 2-D input signals, and y_i denotes the length of reconstructed 1-D signal and pixel values of 2-D reconstructed signal after data hiding by using DCT and Slantlet transform N denotes the dimension of signals.

Normalised Root Mean Squared Error (NRMSE) measures normalised root mean squared value of error between the two signals.

$$\mathrm{NRMSE}(x, y) = \left\| \sqrt{\frac{1}{N}\sum_{i=1}^{N}(x_i - y_i)^2} \right\|^2 \tag{10}$$

Peak signal-to-noise ratio gives the ratio between the maximum possible power of a signal and the power of corrupting noise that affects the quality of the signal. PSNR is usually expressed in terms of the logarithmic decibel scale.

$$\mathrm{PSNR}(x, y) = 10\log_{10}\left((\mathrm{Peakval})^2/\mathrm{MSE}\right) \tag{11}$$

These parameters are calculated between the original input signal and the reconstructed signal after embedding secret information in it by using DCT and Slantlet Transform. These performance parameters measure the amount of distortion and analyse quality of original and reconstructed signal after embedding information in it.

Fig. 3 Results obtained for data hiding using Slantlet Transform and DCT in 2-D signal

4.2 Discussions

We have implemented data hiding algorithm on five biomedical images including 'mri.tif', 'dental.tif', 'spinal.tif', 'foot.tif' and 'lung.tif' and five subjects of ECG samples from MIT-BIH database by using DCT and Slantlet transform.

Observations in Tables 1 and 2 show MSE and NRMSE between original signal and signal after embedding information by using DCT and Slantlet transform. From observations, it can be seen that MSE and NRMSE are more for implementation by using Slantlet transform than DCT for both 1-D ECG signal and 2-D biomedical images.

Observations in Table 3 show PSNR between original signal and signal after embedding information by using DCT and Slantlet transform. From observations, it can be seen that PSNR values are similar for both signal and images by using DCT and Slantlet Transform.

Table 1 MSE by using DCT and Slantlet Transform for 1-D and 2-D signals

File no.	Gender	MSE by using DCT	MSE by using Slantlet Transform	Image	MSE by using DCT	MSE by using Slantlet Transform
100	Male	1.5537×10^{-6}	2.2544	mri.tif	8.5454×10^{-4}	9.5214×10^{-3}
101	Female	2.5532×10^{-5}	1.7155	dental.tif	4.1729×10^{-4}	6.3156×10^{-1}
105	Female	1.6906×10^{-5}	8.6167×10^{-1}	mri.tif	8.5454×10^{-4}	9.5214×10^{-3}
107	Male	1.8182×10^{-6}	1.1591	mri.tif	8.5454×10^{-4}	9.5214×10^{-3}
117	Male	1.6167×10^{-6}	1.1132	lungs.tif	2.5025×10^{-3}	1.1132

Table 2 NRMSE by using DCT and Slantlet Transform for 1-D and 2-D signals

File no.	Gender	NRMSE by using DCT	NRMSE by using Slantlet Transform	Image	NRMSE by using DCT	NRMSE by using Slantlet Transform
100	Male	1.2464×10^{-3}	1.5014	mri.tif	2.9232×10^{-2}	9.7578×10^{-2}
101	Female	5.0525×10^{-3}	1.3097	dental.tif	8.4145×10^{-2}	7.9471×10^{-1}
105	Female	4.1117×10^{-3}	9.2826×10^{-1}	spinal.tif	6.3950×10^{-2}	1.2020×10^{-1}
107	Male	1.3484×10^{-3}	1.2426	foot.tif	7.8125×10^{-2}	9.8183×10^{-2}
117	Male	1.2715×10^{-3}	1.5051	lungs.tif	5.0025×10^{-2}	1.81222

Table 3 PSNR by using DCT and Slantlet Transform for 1-D and 2-D signals

File no.	Gender	PSNR by using DCT	PSNR by using Slantlet Transform	Image	PSNR by using DCT	PSNR by using Slantlet Transform
100	Male	$1.1850 \times 10^{+2}$	$5.6839 \times 10^{+1}$	mri.tif	$9.6909 \times 10^{+1}$	$6.8343 \times 10^{+1}$
101	Female	$1.0635 \times 10^{+2}$	$5.8079 \times 10^{+1}$	dental.tif	$1.0002 \times 10^{+2}$	$5.0126 \times 10^{+1}$
105	Female	$1.0814 \times 10^{+2}$	$6.1070 \times 10^{+1}$	spinal.tif	$9.0109 \times 10^{+1}$	$6.6532 \times 10^{+1}$
107	Male	$1.1782 \times 10^{+2}$	$5.8522 \times 10^{+1}$	foot.tif	$8.8370 \times 10^{+1}$	$6.8294 \times 10^{+1}$
117	Male	$1.1833 \times 10^{+2}$	$5.9957 \times 10^{+1}$	lungs.tif	$9.2242 \times 10^{+1}$	$4.2966 \times 10^{+1}$

5 Conclusion

In this paper, we present data hiding algorithm by using DCT and Slantlet transform and performance parameter analysis is done to analyse accuracy and suitability of transform for data hiding. The algorithm is implemented on 1-D biomedical signals and 2-D biomedical images using DCT and Slantlet transform. We have tested quality of reconstructed signals (1-D and 2-D) after data hiding using DCT and Slantlet transform. We have calculated MSE, PSNR and BER between the input signal and reconstructed signal after embedding data in it by using DCT and Slantlet transform. MSE and BER between the input signal (1-D and 2-D) and the reconstructed signal before embedding information by using DCT are less than MSE and BER between the input signal (1-D and 2-D) and the reconstructed signal after embedding information by using the Slantlet transform. It is found that DCT is better for data hiding in 1-D and 2-D signals than Slantlet Transform.

Acknowledgements We would like to acknowledge Dr. Ivan W. Selesnick for their efforts for helping us in the implementation and study of Slantlet Transform. The support of The Instrumentation and Control Department, the Management and the Principal Dr. M. B. Khambete of MKSSS's Cummins College of Engineering for Women Karvenagar, Pune is gratefully acknowledged.

References

1. Abduljabbar RB (2016, Feb) Steganography system by using Slantlet Transform. J Info Comm Intell Syst (JICIS) 2(1)
2. Isa MRM, Aljareh S (2012, Oct) Biometric image protection based on discrete cosine transform watermarking technique. Int Conf Eng Technol (ICET)
3. Selesnick IW (1999, May) The Slantlet Transform. IEEE Trans Signal Process 47(5)
4. Kumar S, Muttoo SK (2009, Nov) Distortionless data hiding based on Slantlet Transform. Int Conf Multimedia Info Networking Secur 1:48–52

5. Shuwang C, Tao A, Litao H (2009, Dec) Discrete cosine transform image compression based on genetic algorithm. Int Conf Info Eng Comput Sci
6. Mutt SK, Kumar S (2009) Secure image steganography based on Slantlet Transform. Int Conf Methods Models Comput Sci
7. Mohammed RT, Khoo BE (2012, Sep) Image watermarking using Slantlet Transform. IEEE Symp Ind Electron Appl. Indonesia
8. Lafta MM, Alwan IM (2011) Watermarking in image using Slantlet Transform. Iraqi J Sci 52 (2):225–230

Q-Factor Based Modified Adaptable Vector Quantization Techniques for DCT-Based Image Compression and DSP Implementation

Mahendra M. Dixit and C. Vijaya

Abstract In the context of multimedia application, image compression is an integral part of image processing, which is a significant constituent in the present world of computation and communication. The work presented here focusses on the design and the selection of modified adaptive vector quantization techniques used in the image compression and its influence on the quality (Q-factor) of the reconstructed image. The proposal also considers and suggests the modifications to two existing methods by providing comparative evaluation. Both experiments have been tested on MATLAB framework and DSP TMS320C6713. The performance metrics used in the proposed designs are MSE, PSNR, CR, bpp, and percentage space saving with respect to variations in quantization levels, starting from 10 to 90. Such suggested implementations prove to provide better off-the-shelf solutions.

Keywords Image compression · DCT · *Q*-factor · Quantization
DSP

1 Introduction

With the advent of digital cameras and fast growing multimedia applications, the most commonly faced difficulties are the storage, manipulation, and transfer of the digital images. The necessity to reduce the extent of digital data stored, time for processing and transmission is of great concern in the modern world. Image compression research targets at decreasing the number of bits are required to denote an image. Image compression systems take into consideration the psycho-visual features together in spatial and frequency domains and exploit the spatial correlation along with the statistical redundancy. However, usages of the algorithms are

M. M. Dixit (✉) · C. Vijaya
Department of E&CE, SDMCET, Dharwad, Karnataka, India
e-mail: mmdixitmm@yahoo.co.in

C. Vijaya
e-mail: vijayac26@yahoo.com

H. S Saini et al. (eds.), *Innovations in Electronics and Communication Engineering*,
Lecture Notes in Networks and Systems 33,
https://doi.org/10.1007/978-981-10-8204-7_9

dependent typically on the information contained in images. A compression system is often named as compressor and the decompression system is termed as decompressor [1].

2 Related Work and Background

Joint Photographic Experts Group (JPEG) [2] and Moving Picture Experts Group (MPEG) [3] are newly the most widely used image and video compression standards. In literature, Kornblum has discussed the generation of quantization matrix, which provides fundamental incite for the conduction of this research effort [4]. In addition, the article presented by Fu et al. speaks about new de-blocking quantization table for luminance part in baseline JPEG [5]. Adel et al. have experimented the JPEG steganography to measure the performance of quantization tables [6]. Jog et al. have worked on Embedded Zero-tree Wavelet (EZW) image Coder Decoder (CODEC) in image compression and its DSP implementation of [7].

The vision research and image sciences laboratory has published DCT-based image compression [8]. Distinguishing and approximating chunk DCT image compression quantization factors [9] is done by Ramin Samadani. Wu and Tsang worked on calculating the efficiency of color image compression built on changing decimation and implementation on VLSI [10]. The work by Dixit et al. focused on the comparison of DCT-based image compression and SVD techniques [11].

3 DCT-Based Image Compression Technique

The proposed research work deals with DCT-based image compression. The block diagram is shown in Fig. 1.

The fundamental approach of this system development is to use the DCT-based compression of image data, along with the usage of variable vector quantization. The image is grouped into 8×8 macro blocks and type-2 2D-DCT is further applied. The coefficients of DCT are then quantized with the help of 2D vector quantization. Here, two different modified vector quantization techniques have been experimented and discussed in Sects. 4.1 and 4.2, respectively.

3.1 Applying DCT Algorithm to Image with Quantization and Decompression Process

This section deals with the algorithm used in image compression using DCT. The steps are as mentioned below.

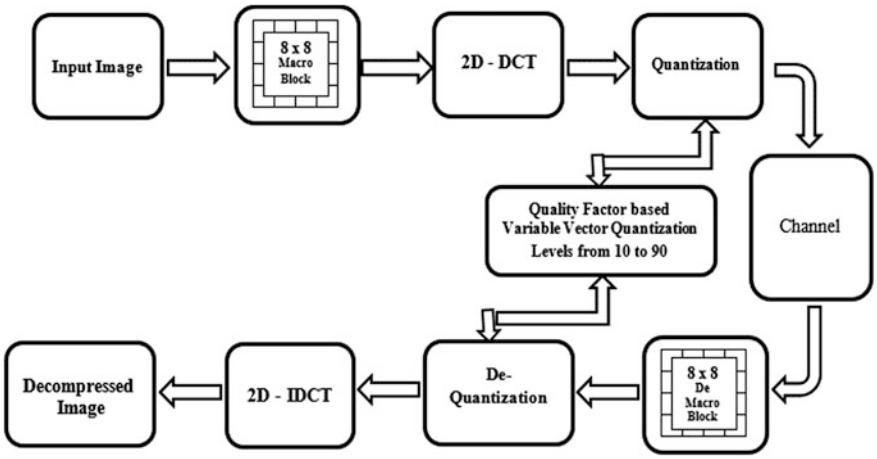

Fig. 1 DCT-based image compression with variable Q-factor

- DCT equation shown in (1) computes the DCT coefficient of an image. Here N being the block size that the DCT is applied.

$$T = \left\{ \frac{1}{\sqrt{N}} \text{ if } i = 0 \quad \text{and} \quad \sqrt{\frac{2}{N}} \cos\left[\frac{(2j+1)i\pi}{2N}\right] \text{ if } 1 \le i \le (N-1), 0 \le j \le (N-1) \right\} \tag{1}$$

- As DCT is intended for pixel standards alternating from −128 to 127, the original chunk is clipped off by deducting 128 from each entry.
- After obtaining the leveled off matrix M, perform DCT, which is obtained by multiplication of matrices.

$$D = T \times M \times T' \tag{2}$$

- The following matrix Q_{50} has been referred from [2, 4], which is used in JPEG. This quantization matrix enables to use it as Q-factor in the proposal.

$$Q_{50} = \begin{bmatrix} 16 & 11 & 10 & 16 & 24 & 40 & 51 & 61 \\ 12 & 12 & 14 & 19 & 26 & 58 & 60 & 55 \\ 14 & 13 & 16 & 24 & 40 & 57 & 69 & 56 \\ 14 & 17 & 22 & 29 & 51 & 87 & 80 & 62 \\ 18 & 22 & 37 & 56 & 68 & 109 & 103 & 77 \\ 24 & 35 & 55 & 64 & 81 & 104 & 113 & 92 \\ 49 & 64 & 78 & 87 & 103 & 121 & 120 & 101 \\ 72 & 92 & 95 & 98 & 112 & 100 & 103 & 99 \end{bmatrix} \tag{3}$$

A notable and extremely valuable highlight of the JPEG is that variable levels of image compression and Q-factors are attainable through particular quantization matrices.

- For the following step, quantization level 50 is used in JPEG compression.

$$C = \text{round}\left(\frac{D}{Q}\right) \tag{4}$$

- During the reconstruction of the image, every component of C is multiplied by the corresponding component of the quantization table initially used.

$$R = Q \times C \tag{5}$$

- Inverse DCT is then calculated in Eq. (5).

$$O = \text{round}\left(T' \times R \times T\right) + 128 \tag{6}$$

4 Design of Quality Factor Based Modified Adaptable Vector Quantization

This part of the discussion is distributed into two subparts. First and foremost part pacts with the Jesse's [4] procedure for generating quantization matrix, which nearly matches the JPEG standard quantization matrix elements for level 50. In Sect. 4.1, incremental modifications are suggested to such a model. Second, the use of APBT-JPEG [5] based quantization table with incremental modifications, which replaces the quantization level 50 of JPEG standard is found in Sect. 4.2.

4.1 Generation of Quantization Matrix Based on Jesse's Analysis and Suggesting Incremental Modification (Proposed Technique—1)

The vector quantization matrix design has been analyzed with the help of the Independent JPEG Group (IJG). It is learnt that Jesse [4] projected a formula of quality factor based quantization, which is given in Eq. (9), and utilizes (7) and (8) correspondingly, where Q is the quantization level varying from 1 to 99 and i is an index for quantization elements in one dimension.

$$S = (Q < 50)? \frac{5000}{Q} : 200 - 2Q \tag{7}$$

$$Ts[i] = \left\lfloor \left[\frac{S * Tb[i] + 50}{100} \right] \right\rfloor \tag{8}$$

It is seen that $Ts[i]$ value is floored. Its modified version is as given below.

$$Ts[i] = \left[\frac{S * Tb[i] + 50}{100} \right] \tag{9}$$

Using Eq. (9), a base matrix of quantization level 50 is modified as shown in (10). Using (10) other levels are generated.

$$\text{Proposed } Q_{50} = \begin{bmatrix} 16.50 & 11.50 & 10.50 & 16.50 & 24.50 & 40.50 & 51.50 & 61.50 \\ 12.50 & 12.50 & 14.50 & 19.50 & 26.50 & 58.50 & 60.50 & 55.50 \\ 14.50 & 13.50 & 16.50 & 24.50 & 40.50 & 57.50 & 69.50 & 56.50 \\ 14.50 & 17.50 & 22.50 & 29.50 & 51.50 & 87.50 & 80.50 & 62.50 \\ 18.50 & 22.50 & 37.50 & 56.50 & 68.50 & 109.5 & 103.5 & 77.50 \\ 24.50 & 35.50 & 55.50 & 64.50 & 81.50 & 104.5 & 113.5 & 92.50 \\ 49.50 & 64.50 & 78.50 & 87.50 & 103.5 & 121.5 & 120.5 & 101.5 \\ 72.50 & 92.50 & 95.50 & 98.50 & 112.5 & 100.5 & 103.5 & 99.50 \end{bmatrix} \tag{10}$$

4.2 Generation of Quantization Matrix Based on Qiming Fu's Proposal and Suggesting Incremental Modifications (Proposed Technique—2)

This portion of the description deals with the generation of quantization matrix, which is designated as Q^* in the literature [5]. The author [5] designs a quantization table for the level of 50, which contains incongruity in comparison with (10).

$$Q^* = \begin{bmatrix} 8.00 & 12.0 & 14.1 & 16.7 & 20.5 & 26.5 & 37.4 & 64.0 \\ 12.2 & 18.6 & 21.5 & 25.5 & 31.2 & 40.4 & 57.2 & 97.6 \\ 14.1 & 21.5 & 24.8 & 29.4 & 36.1 & 46.7 & 66.1 & 112 \\ 16.7 & 25.5 & 29.4 & 34.9 & 48.8 & 55.3 & 78.3 & 133 \\ 20.5 & 31.2 & 36.1 & 42.8 & 52.5 & 67.9 & 96.0 & 164 \\ 26.5 & 40.4 & 46.7 & 55.3 & 67.9 & 87.8 & 124 & 212 \\ 37.4 & 57.2 & 66.1 & 78.3 & 96.0 & 124 & 175 & 299 \\ 64.0 & 97.6 & 112 & 133 & 164 & 212 & 299 & 512 \end{bmatrix} \tag{11}$$

Referring to (11), few elements of the matrix have greater values than 255, which in turn indicate more amount of bits are essential to denote the pixel values and less amount of bits to denote coefficient of DCT in that position. Modifications that are suggested to this section to consider the maximum pixel value to be 255 and any value beyond 255 is to be represented as only 255. Second, using Q^* and the formula given in Eq. (9), quantization level 50 is generated, which is represented in matrix (12). The new matrix obtained after incremental modifications is termed as Q^*_{50}. This base matrix is then utilized for the generation of quantization matrices from level 10 to 90 and experimented.

$$Q^*_{50} = \begin{bmatrix} 8.50 & 12.70 & 14.61 & 17.21 & 21.00 & 27.00 & 37.99 & 64.50 \\ 12.77 & 19.12 & 22.03 & 26.00 & 31.78 & 40.95 & 57.70 & 98.16 \\ 14.60 & 22.032 & 25.38 & 29.98 & 36.66 & 47.25 & 66.62 & 113.3 \\ 17.21 & 26.00 & 29.98 & 35.43 & 49.34 & 55.89 & 78.84 & 134.2 \\ 21.00 & 31.78 & 36.66 & 43.34 & 53.05 & 68.44 & 96.58 & 164.5 \\ 27.00 & 40.95 & 47.25 & 55.89 & 68.44 & 88.34 & 124.7 & 212.5 \\ 37.99 & 57.70 & 66.62 & 78.84 & 96.58 & 124.7 & 176.1 & 255.0 \\ 64.50 & 98.16 & 113.3 & 134.2 & 164.5 & 212.5 & 255.0 & 255.0 \end{bmatrix} \quad (12)$$

5 Experimental Results and Discussion

The performance measures used in this proposal are enlisted in Eqs. (13), (14), (15), (16), and (17), respectively.

$$\text{MSE} = \frac{1}{m \times n} \sum_{i=0}^{m-1} \sum_{j=0}^{n-1} I(i,j) - K(i,j)^2 \quad (13)$$

$$\text{PSNR} = 20 \log_{10} \left(\frac{\text{MAX}_I}{\sqrt{\text{MSE}}} \right) \quad (14)$$

$$\text{CR} = \frac{\text{Size of Uncompressed Image}}{\text{Size of Compressed Image}} \quad (15)$$

$$\text{bpp} = \frac{\text{Size of Uncompressed Image}}{m \times n} \quad (16)$$

$$\% \text{ Space Saving} = \left[1 - \frac{\text{Size of Compressed Image}}{\text{Size of Uncompressed Image}} \right] \times 100 \quad (17)$$

5.1 Result Analysis for Proposed Technique—1

The modified technique related to Jesse's representation, as discussed in Sect. 4.1, is on quality based quantization table and this modified scheme is applied to standard test images. It is observed from the experimentation that the functions floor, ceil, and round are avoidable. Using this technique, for Lenna.png, the quality of the processed image, during reconstruction, will have variable PSNR ranging from 27.85 to 40.46 dB, with MSE being very small ranging from 0.0015 to 8.29×10^{-05}. In addition, it measures CR of 20.99–5.64, percentage space saving of 95.24–82.26 with the maximum bpp of 0.84. Figure 2 shows variability in image quality based on quantization matrices. The dual *Y*-axis graphs of variable quantization levels versus MSE and PSNR, percentage space saving, and bpp are shown in Fig. 3a, b, respectively.

5.2 Result Analysis for (Proposed Technique—2)

As mentioned in Sect. 4.2, in continuation, Qiming Fu's scheme with incremental modification has been successfully incorporated as a basic quantization table for level 50 in the generation of variable quantization matrix from level 10 to 90. Figure 4 shows variability in image quality based on quantization matrix. The dual *Y*-axis graphs of variable quantization levels versus MSE and PSNR, percentage space saving and bpp are shown in Fig. 5a, b, respectively. This experiment when applied to Lenna.png provides the PSNR values ranging from 27.35 to 40.30 dB

Fig. 2 Reconstructed image quality for proposed technique—1

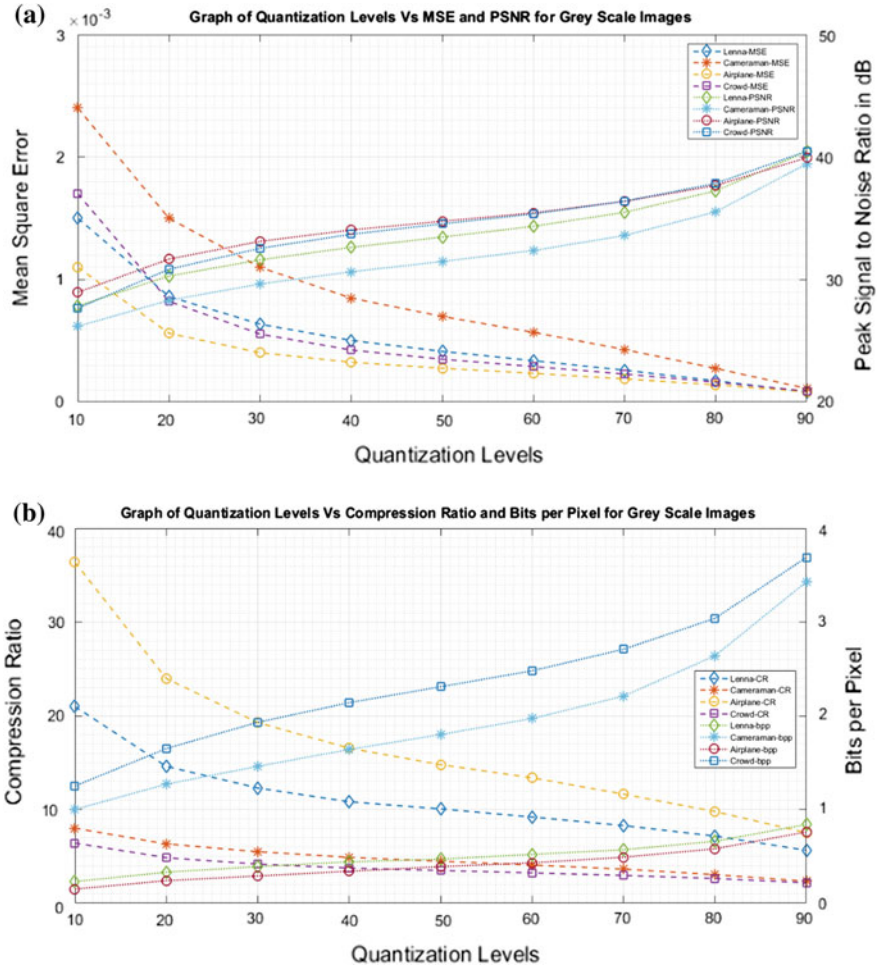

Fig. 3 **a** Quantization levels versus MSE and PSNR, **b** quantization levels versus CR and bpp

Fig. 4 Reconstructed image quality for proposed technique—2

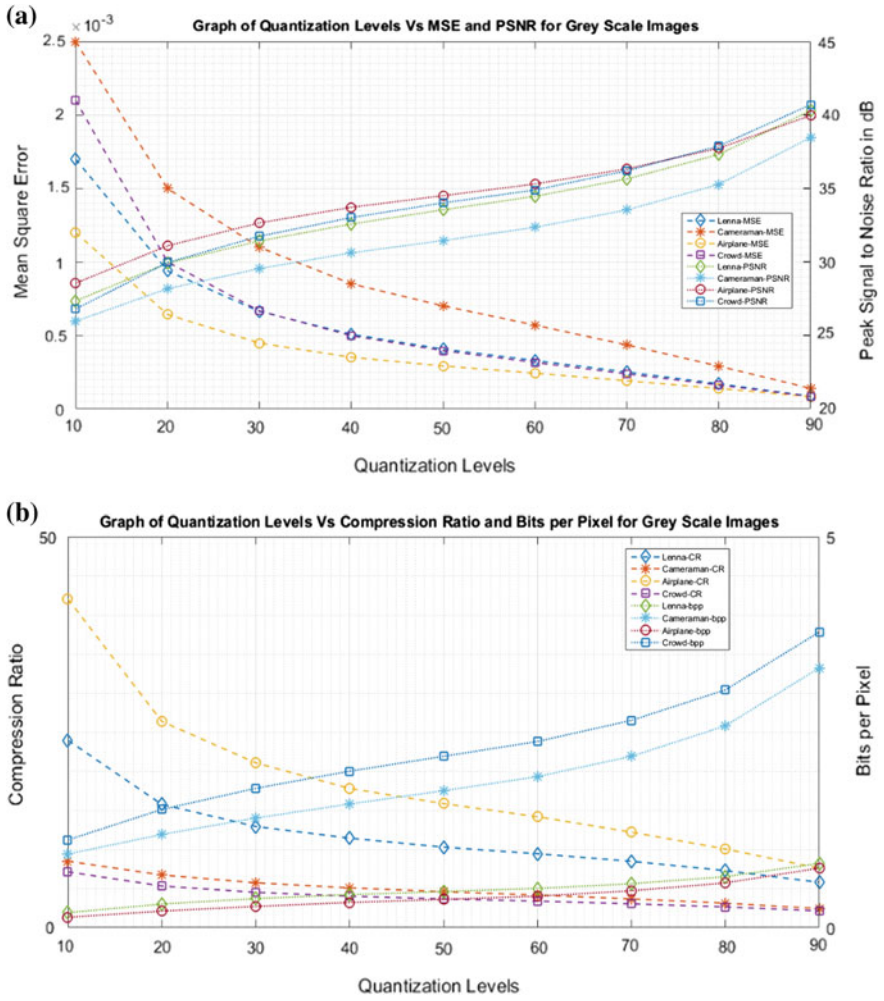

Fig. 5 **a** Quantization levels versus MSE and PSNR, **b** quantization levels versus CR and bpp

with MSE being 0.0017 to 8.61 $\times$ 10^{-05}, CR varying from 23.96 to 5.78, with percentage space saving of about 95.83 to 82.71, having maximum bpp of 0.82, in accordance with the quantization levels varying from 10 to 90.

5.3 Implementation on DSP TMS320C6713

The experimentations performed and mentioned in Sects. 5.1 and 5.2 are further extended and implemented onto a low-cost hardware platform TMS320C6713. The algorithms revealed in Sects. 4.1 and 4.2 are used once again and applied to the

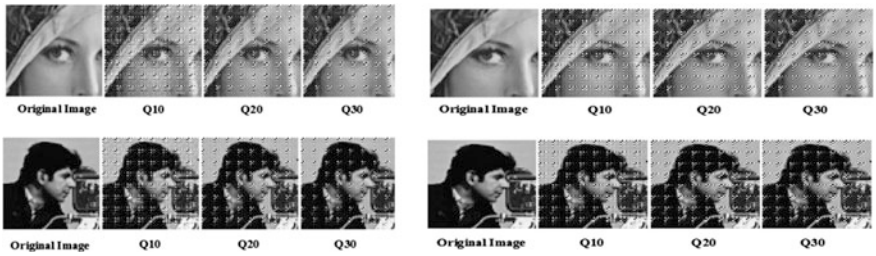

Fig. 6 Reconstructed image quality of proposed technique—1 and technique—2

same test images. The algorithm is developed using C-language utilizing CCS studio, which is interfaced to DSP board. Figure 6 shows reconstructed image quality of proposed techniques prototyped on DSP.

5.4 Comparative Evaluation

The comparison between the proposed techniques of Sects. 4.1 and 4.2 and existed techniques [4, 5] is carried out with all the performance parameters. For the quantization level of 30, it is observed that the proposed and existed techniques mentioned have meager differences in terms of quantitative parameters (Table 1). Referring to Table 1, it is seen that the proposed technique of suggesting incremental modifications to [4] (proposed technique—1) for the quantization level of 30 provides greater performance with respect to PSNR and quality of the reconstructed image to a certain extent.

Table 1 Comparative evaluation at quality level of 30

Existed and proposed techniques	Image name	Computation of performance parameters for quality factor based quantization level of 30				
		MSE	PSNR in dB	CR	bpp	% space saving
JPEG standard Jesse's scheme [4]	Lenna.png	6.30×10^{-04}	31.65	12.18	0.39	91.79
	Cameraman.tif	0.0011	29.67	5.45	1.47	81.65
	Airplane.png	3.99×10^{-04}	33.16	18.99	0.30	94.73
	Crowd.tif	5.46×10^{-04}	32.62	4.138	1.93	75.83
Qiming Fu. et al. scheme [5]	Lenna.png	6.63×10^{-04}	31.43	12.92	0.36	92.26
	Cameraman.tif	0.0011	29.56	5.721	1.40	82.52
	Airplane.png	4.48×10^{-04}	32.67	21.07	0.27	95.25
	Crowd.tif	$6.67 \times 10-^{04}$	31.75	4.502	1.77	77.79

(continued)

Table 1 (continued)

Existed and proposed techniques	Image name	Computation of performance parameters for quality factor based quantization level of 30				
		MSE	PSNR in dB	CR	bpp	% space saving
Proposed technique—1 suggesting incremental modifications to [4]	Lenna.png	6.36×10^{-04}	31.61	12.29	0.39	91.87
	Cameraman.tif	0.0011	29.65	5.49	1.46	81.78
	Airplane.png	4.03×10^{-04}	33.12	19.27	0.30	94.81
	Crowd.tif	5.55×10^{-04}	32.56	4.16	1.93	75.97
Proposed technique—2 suggesting incremental modifications to [5]	Lenna.pns	6.63×10^{-04}	31.43	12.92	0.37	92.26
	Cameraman.tif	0.0011	29.56	5.72	1.40	82.52
	Airplane.png	4.48×10^{-04}	32.66	21.07	0.27	95.25
	Crowrd.tif	6.67×10^{-04}	31.75	4.50	1.78	77.79

6 Conclusions

This research experiment is a straightforward and upright proposition to the work emphasized and represented in [4, 5] respectively. As per the comparative evaluation, for the quantization level of 30, it is witnessed that the proposed techniques reproduce better reconstructed image quality in comparison with other existing techniques, in turn facilitating improved PSNR. In continuance, at the quantization level of 30, the reconstructed images do not undergo significant artifacts. However, for the quantization level of 50, the performance of both the proposed techniques closely matches with the existing techniques of [4, 5] in spite of the reduction in flooring function, thereby reducing the computational overheads. Such proposals discussed in this article find applications in internet technology, where variable *Q*-factor based image compression and decompression is required. These proposed techniques may find abundant usage in digital cameras and mobile applications.

Acknowledgements The authors would like to thank the AICTE-RPS Grants (Ref. No.: 8023/RID/RPS-115(Pvt.)/2011–12) for providing financial assistance towards this research work.

References

1. Pu IM (2006) Fundamental data compression. ISBN-13:978–0-7506-6310-6, ISBN-10: 0-7506-6310-3. British Library Cataloguing in Publication Data and Library of Congress Cataloguing in Publication Data, Butterworth-Heinemann Publications Copyright © 2006

2. Skodras A, Christopoulos C, Ebrahimi T (2001) The JPEG 2000 still image compression standard. IEEE Signal Process Mag 36–58, Sept 2001
3. Martínez JM (ed) (2002) The MPEG standard, ISO/MPEG N4674, Overview of the MPEG-7, Standard, Version 6.0, MPEG Requirements Group, Jeju, Mar 2002
4. Kornblum JD (2008) Defense Cyber Crime Institute, United States, Using JPEG quantization tables to identify imagery processed by software, Digital Investigation S21–S25, 2008 Digital Forensic Research Workshop. Published by Elsevier Ltd. https://doi.org/10.1016/j.diin.2008.05.004
5. Fu Q, Jiang B, Wang C, Zhou X (2015) A novel deblocking quantization table for luminance component in baseline JPEG. J Comm 10(8):629–637, Aug 2015. https://doi.org/10.12720/jcm.10.8.629-637
6. Almohammad A, Ghinea G, Hierons RM (2009) JPEG steganography: a performance evaluation of quantization tables, 2009. In: International Conference on Advanced Information Networking and Applications. IEEE Computer Society, pp 471–478, 1550–445X/09, 2009 IEEE. https://doi.org/10.1109/aina.2009.67
7. Jog SM, Lokhande SD (2009) A DSP implementation of embedded zero tree wavelet (EZW) image CODEC in image compression system. Rev Paper Int J Recent Trends Eng ACEEE 2(4):162–164
8. DCT based Image Compression, Vision Research and Image Science Laboratory. http://visl.technion.ac.il
9. Samadani R (2005) Characterizing and estimating block DCT image compression quantization parameters. In: Asilomar Conference on Signals, Systems and Computers, Nov 2005, Pacific Grove, CA, USA ©IEEE
10. Wu A, Tsang PW (2010) VLSI implementation of computation efficient color image compression scheme based on adaptive decimation for portable device application. J Signal Process Syst 59(3):267–279, June 2010. Kluwer Academic Publishers Hingham, USA
11. Dixit MM, Kumar P (2010) Comparative analysis of variable quantization DCT and variable rank matrix SVD algorithms for image compression applications. In: IEEE-ICCIC-2010, IEEE-Xplore, pp 908–912, Dec 2010. https://doi.org/10.1109/iccic.2010.5705879

Bio-Signal System Design for Real-Time Ambulatory Patient Monitoring and Abnormalities Detection System

Akshay Naregalkar and G. Vamsi Krishna

Abstract This paper aims to design and implement low-cost real-time patient vital sign monitoring in moving ambulance that provides patient's clinical data to doctors well in advance so the doctors are well prepared on the arrival of patient and also do further research to protection of human life and to implement technology for social cause. The system is developed such that it will transmit the essential details of a person to the hospital personnel. Also, camera-aided interaction between the doctor and the patient provided by this system also provides important information about patient condition in ambulance; the doctor can also interact with the patient attendant in ambulance and other hospital staff, surgeons, and doctors in case of emergency and give them instructions on the required immediate treatment for the patient on his/her arrival at hospital. In addition to this, the algorithms are designed to detect abnormalities in patient conditions and to create alerts. This work is implemented at VNR VJIET, Hyderabad as a part of UGC funded Research project.

Keywords Real time · Ambulance · Hospital · Patient monitoring
Algorithm · Vital parameter · Biosensors

1 Introduction

Patients from remote places can greatly benefit from technologies that continuously monitor their vital parameter status until they are admitted to the hospital [1]. This paper explains the designed and developed system for real-time patient monitoring in ambulance while in transit. This system is an integration of vital signs biosensors, electronic patient recorder, and web technology to allow remote monitoring of patient vital sign status. This system shall facilitate coordination between patient

A. Naregalkar (✉) · G. Vamsi Krishna
VNR Vignana Jyothi Institute of Engineering and Technology, Hyderabad, India
e-mail: akshay.naregalkar@gmail.com

G. Vamsi Krishna
e-mail: vamsikrishna_g@vnrvjiet.in

H. S. Saini et al. (eds.), *Innovations in Electronics and Communication Engineering*,
Lecture Notes in Networks and Systems 33,
https://doi.org/10.1007/978-981-10-8204-7_10

attendant from the ambulance and medical professionals at hospitals and specialists who can provide consultation from another location. The information about the patient can be stored in a database as a cloud and can be shared by different doctors simultaneously [1, 2]. Web Publishing Tool in LabVIEW software can be used to monitor the patient and assist the ambulatory staff [3–6].

In this paper, a real-time patient monitoring system in ambulance while in transit is designed to transmit patient's health conditions such as heart rate, body temperature, blood pressure, ECG signal, fatigue, air lung volume, and vital signs like patient physical appearance are acquired using Data Acquisition board [7] and are sent to the hospital and doctor. The algorithms are also implemented to detect the abnormalities in these parameters using LabVIEW and biosensors are interfaced through signal conditioning circuit to NI USB—6281. This research work is carried out by keeping the following objectives in mind to provide a real-time solution.

i. To design a system and to do further research to protect human life and to implement technology for social cause.
ii. To design and implement low-cost and cost-effective real-time vital sign monitoring of patient in ambulance.
iii. To provide patient's clinical data to doctors well in advance so the doctors are well prepared on the arrival of patient.

The system implemented can be placed on board in an ambulance to measure and transmit real-time patient information continuously and also the patient visuals to the hospital using mobile network or telephony [8, 9]. This information can be received at the hospital by doctors for initial patient health assessment and preparation by discussing with other experts before the patient reaches the hospital. The doctors can also suggest first aid treatment to patient by ambulatory staff in case of accidental and snake poisoning cases [5].

2 Proposed Methodology

The real-time patient monitoring system implemented is shown in Fig. 1. The vital patient parameters are measured using biosensors and then converted into electrical signals to interface with a computer using Data Acquisition board. The signal processing is done using LabVIEW software. This data is then transferred to hospital using Internet Toolkit and Web Publishing Toolkit of LabVIEW.

Also, the bio-signals are monitored to check any abnormalities using designed algorithms.

To check the ECG abnormalities, algorithm is implemented such that it will measure P–R, QRS, and Q–T intervals and will compare with normal values [6]. Also, it will display the alarm in case of abnormalities found. The blood pressure is monitored and using algorithm, hypotension or hypertension condition can be detected. The heart rate is measured to detect life-threatening disease like

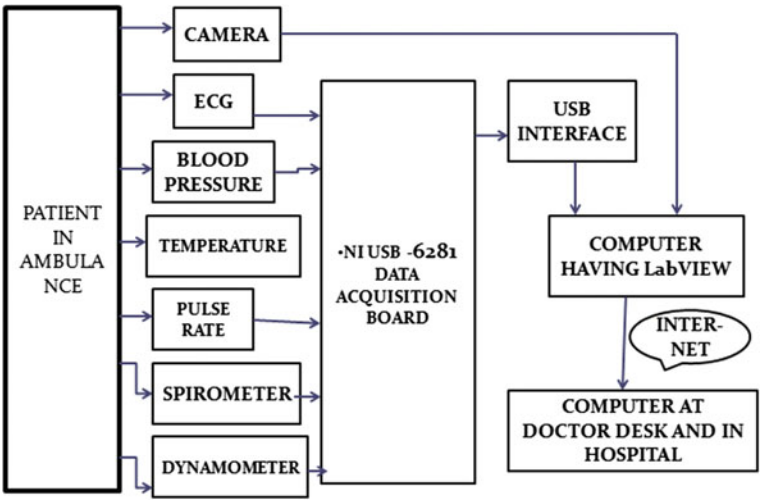

Fig. 1 Block diagram of the proposed system

arrhythmias which may affect pumping functionality of the heart. The arrhythmias may be either tachycardia (for faster heartbeat, i.e., more than 100 beats per minute or bradycardia (for very slower heartbeat, i.e., less than 60 beats per minute). The patient body temperature measurement is measured to determine fever, hypothermia, and hyperthermia [10–12].

The dynamometer is used to access muscular fatigability. The spirometer is used to in pulmonary function assessment where the air volume exhaled from the lungs after the maximal expiration is monitored. For video conferencing purpose among doctor, ambulatory staff, and hospital staff, the vital parameters monitored are transferred using Web Publishing Tool through Internet.

3 Design Implementation

System design and implementation are done using Real-Time Monitoring and Control using Virtual Instrumentation Technology with LabVIEW software and associated hardware like biological sensors, camera, and other medical equipments.

Figure 2 shows steps those are implemented to meet project objectives.

3.1 ECG Module

The electrocardiogram (ECG) Sensor is a standard 3-lead that measures electrical signals produced during muscle contractions [13, 14]. Each of the three leads on the sensor connects to disposable electrodes. The ECG graph as shown in Fig. 3 gives

Fig. 2 Project design flow

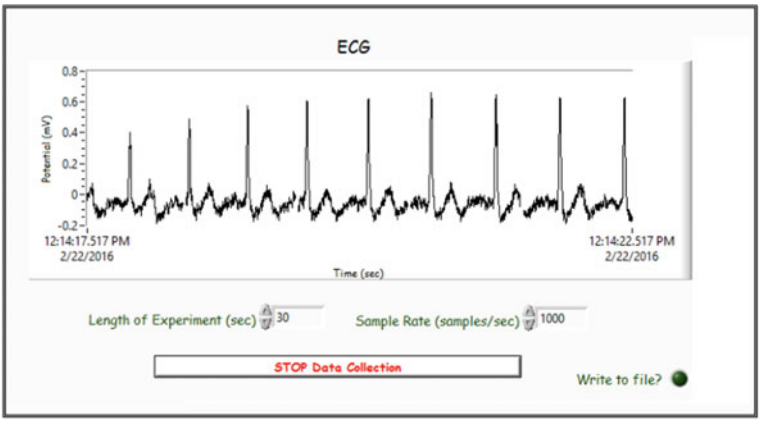

Fig. 3 ECG measurement

the contraction and repolarization of the heart's chambers. The ECG electrodes placed on the surface of the skin record a summation of action potentials and give rise to resultant voltage [5, 15].

Table 1 gives the typical time spans for each deflection.

The abnormalities in ECG can be detected using LabVIEW. These signals can also be useful to determine cardiogenic shocks [9]. The implemented algorithm in LabVIEW is shown in Fig. 4.

Table 1 Duration ECG waves

Type of interval	Duration (seconds)
P–R interval	0.12–0.20
QRS interval	<0.1
Q–T interval	<0.38

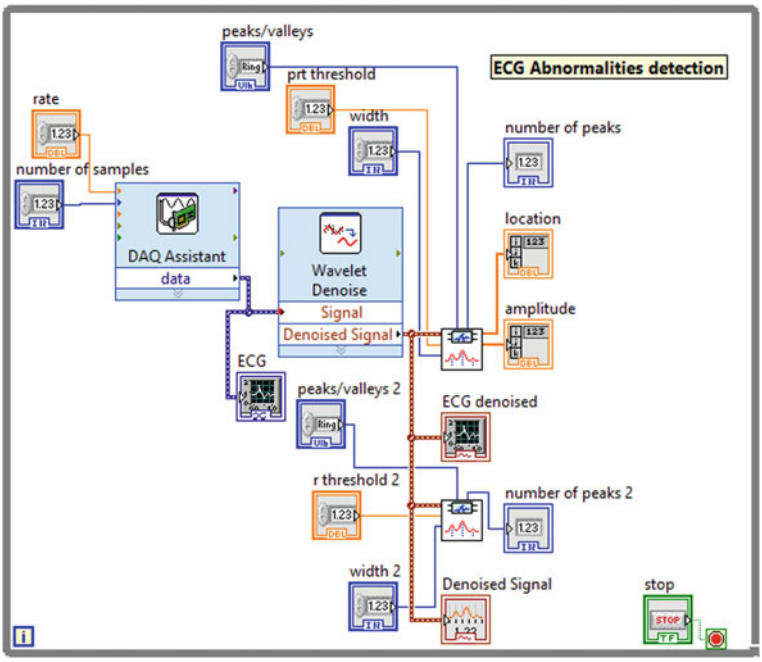

Fig. 4 ECG abnormalities detection

3.2 Blood Pressure Module

Blood pressure is one of the important signs showing the health conditions of a person. High blood pressure is termed as hypertension. Long-term hypertension can lead to heart attacks, chokes, and organ failure such as chronic renal failure. Hypotension occurs when blood pressure drops suddenly and supply of blood to the brain deprives suddenly which can lead to dizziness or lightheadedness. This inadequate blood flow can cause strokes, heart attacks, and even kidney failures.

The blood pressure sensor as shown in Fig. 5 uses oscillometric method to measure the systemic arterial blood pressure in human in a noninvasively way. This device converts pressure into voltage. The cuff pressure related to the maximum amplitude can calculate mean arterial pressure (MAP). That can be used to calculate minimum and maximum blood pressures. The cuff pressure is measured and interfaced to PC using USB 6281 where it is processed using LabVIEW software.

Table 2 shows the normal and abnormal blood pressure ranges [15].

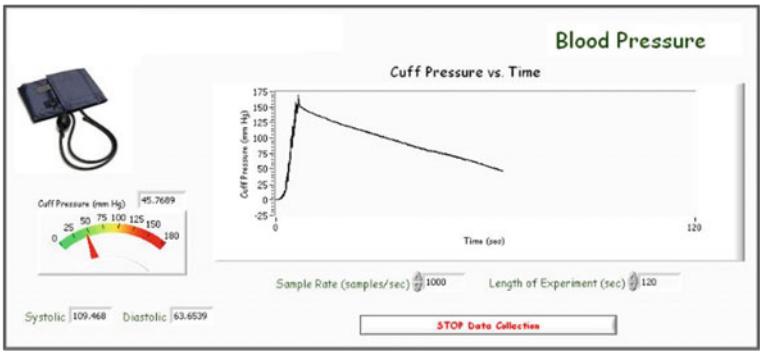

Fig. 5 Blood pressure measurement

Table 2 Blood pressure ranges

Category	Systolic (mmHg)	Diastolic (mmHg)
Normal	90–119	60–79
Hypotension	<90	<60
Prehypertension	120–139	80–89
Stage 1 hypertension	140–159	90–99
Stage 2 hypertension	≥ 160	≥ 100

3.3 Heart Rate Module

The heart rate sensor measures heart rate by registering the small electrical signals carried across the surface of a person's skin each time heart contracts [10]. By graphing this signal, the heart rate can be determined using Hand-Grip Heart Rate sensor. With this, one can plot a pulse for each heartbeat and analyze the time between the peaks to determine the heart rate using LabVIEW as shown in Fig. 6.

3.4 Temperature Module

The body temperature measurement is useful to determine fever, hypothermia, and hyperthermia [10]. A thermistor is used to determine body temperature of the patient. The LabVIEW front panel for temperature measurement is as shown in Fig. 7.

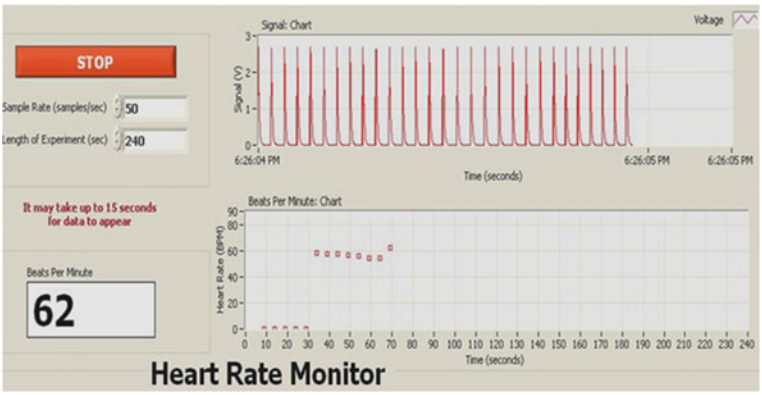

Fig. 6 Heart rate monitoring

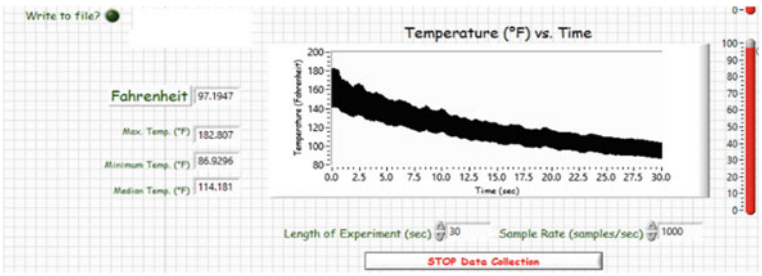

Fig. 7 Temperature monitoring

3.5 *Fatigue Measuring Module*

Fatigue measurement is done by using dynamometer which consists of strain-gauge that can be used to measure grip strength and muscle fatigue studies in Newton's or kilograms force. The fatigue measurement is shown in Fig. 8.

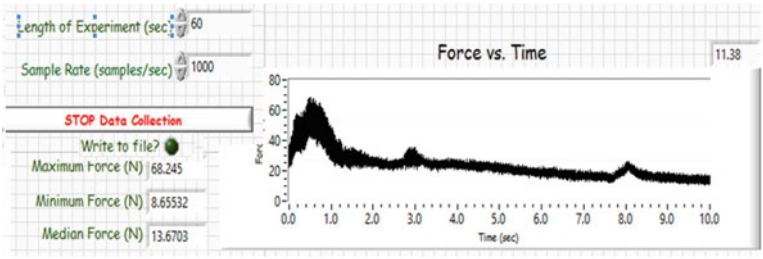

Fig. 8 Fatigue monitoring

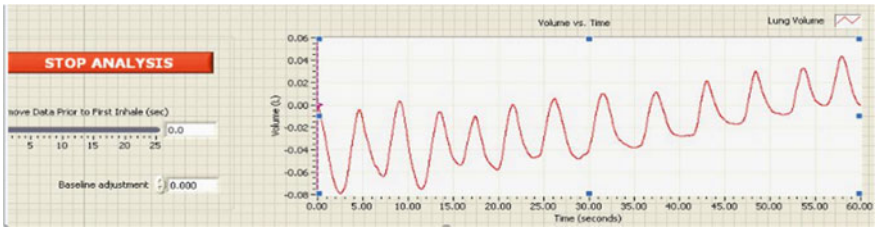

Fig. 9 Spirometer measurements

3.6 Lung Functioning Analysis Module

Spirometric measurement of air volume in lung provides information about normal function of the lungs and related respiratory diseases. Spirometry measures the amount (volume) and/or speed (flow) of air that can be inhaled and exhaled. The spirometry measurement is as shown in Fig. 9.

3.7 Telemetry Module with LabVIEW Web Publishing Tool

The patient information from ambulance can be transmitted to hospital using LabVIEW Web Publishing Tool, Web Server. The 3G Internet facility can be used for data transfer purpose. The front panel of the VIs will be shared with the doctors. Thus, the patient vital parameters are measured in ambulance and monitored in the hospital and also can be accessed by doctors at anywhere as it gives real-time overview of patient's condition prior to their arrival at the hospital. This will help them to be prepared in advance to treat the patients once they arrive.

4 Results and Discussions

The ECG readings obtained from the patient reveal good health of the patient by detecting time interval readings from an ECG wave. By measuring blood pressure, detection of hypotension and hypertension is done with LabVIEW code. Also, temperature, air lung volume, and patient fatigue are also detected. These parameters are monitored on front panel designed in LabVIEW. The parameters are transferred to hospital and doctor by creating URL web page with LabVIEW Web Publishing Tool and transferred with 3G Internet. Thus, a real-time patient monitoring system in ambulance while in transit is designed to transmit all the patient vital parameters to the hospital and doctor.

The algorithms are also implemented to detect the abnormalities in these parameters. The system is implemented using LabVIEW real-time environment and biosensors are interfaced through signal conditioning circuit to NI USB—6281.

5 Conclusion

Thus, the system implemented will monitor and transfer patient vital parameters continuously to hospital from ambulance from remote location using created URL web page that can be shared at the same time by different Doctors. Also, the system will provide alerts for abnormalities in measured parameters. This will allow emergency room doctors to get a real-time overview of patient's condition prior to their arrival at the hospital and in advance preparations to treat the patients once arrive. By using Camera Acquisition System in ambulance and hospital, a video conferencing facility can be provided and this can be used in first aid treatment.

References

1. Mehta B, Rengarajan D, Prasad A (2012) Real time patient tele-monitoring system using LabVIEW. Int J Sci Eng Res 3(4):1–11
2. Muthaiyan M, Goel N, Prakash DS (2012) Virtual e-medic: a cloud based medical aid. Int J Comput Electr Autom Control Inf Eng 6(11):1–4
3. Natarajan N, Aparna S, Sam Jeba Kumar J (2012) Robot aided remote medical assistance system using LabVIEW. Int J Comput Appl 38(2):0975–8887
4. Ganser M, Dhar S, Kurup U, Cunha C (2015) A data-driven approach towards patient identification for telehealth programs. In: Big Data (Big Data), 2015 IEEE international conference, pp 2551–2559
5. Akshay N, Vamsi Krishna G (2016) Design & implementation of real time bio-signal acquisition system for quality health care services for the population of rural India. In: IEEE international conference on recent trends in electronics information communication technology, pp 1315–1399
6. Akshay N, Jonnabhotla NAV, Sadam N, Yeddanapudi ND (2010) ECG noise removal and QRS complex detection using UWT. In: 2010 international conference on electronics and information engineering (ICEIE), vol 2, pp 438–442
7. Lascu M, Lascu D (2007) LabVIEW based biomedical signal acquisition and processing. In: Proceedings of the 7th WSEAS international conference on signal processing, computational geometry & artificial vision, Athens, Greece
8. Figueredo MVM, Dias JS (2004) Mobile telemedicine system for home care and patient monitoring. In: Proceedings of the 26th annual international conference of the IEEE EMBS San Francisco, CA, USA
9. Suma KV, Sandeep S, Vikram S, Hanjar K (2015) Cardiogenic shock monitoring system for ambulance. In: 2015 international conference on advances in computing, communications and informatics (ICACCI), pp 1357–1360
10. Yan W, Zhigang M, Sihai Q (2010) System of medical emergency ambulance for community based on Zigbee. In: 2010, 2nd international conference on information science and engineering (ICISE) date of conference, pp 6983–6985

11. Almadani B, Bin-Yahya M, Shakshuki EM (2015) E AMBULANCE: real-time integration platform for heterogeneous medical telemetry system. Procedia Comput Sci 63:400–407
12. Bellos CC, Rosso R (2014) Identification of COPD patients' health status using an intelligent system in the CHRONIOUS wearable platform. IEEE J Biomed Health Inf 18(3):731–738
13. Julio YER (2015) Development of a prototype arduino-mobile in area of telemedicine for remote monitoring diabetic people. In: Asia-Pacific conference on IEEE conference computer aided system engineering (APCASE), pp 36–40
14. Sarmiento CA, Castano FA, Hernandez AM, Lemos JD (2015) Device for integration of clinical information of biomedical equipments. Health care exchanges (PAHCE), 2015 Pan American, pp 1–11
15. Lascu M, Lascu D (2014) Smart multi-level tool for remote patient monitoring based on a wireless sensor network and mobile augmented reality. Sensors 14:17212–17234

Automated Heart Rate Measurement Using Wavelet Analysis of Face Video Sequences

Amruta V. More, Asmita Wakankar and Jayanand P. Gawande

Abstract To overcome the drawbacks of the conventional heart rate measurement method, a new approach is developed to measure cardiac pulse automatically using video imaging technique and wavelet analysis. In this paper, the color video images of the human face are used for detection of cardiac pulses. The specific region of interest (ROI) in face image is detected to obtain red, green, and blue intensity signals. Next normalized red, green, and blue intensity signals are decomposed using discrete wavelet transform (DWT) to obtain approximate and detail coefficients. Then, the specific frequency band from decomposed signal is obtained with the help of bandpass filter using Hamming window function. The cardiac pulse is measured with the help of pulse frequency in power density spectrum of filtered signal. The cardiac pulse measured with help of this system is compared with heart rate measured from reference ECG signal of the same object. This technique improves the accuracy from 73.14 to 89.86% if forehead of the subject is considered instead of face.

Keywords Cardiac pulse · Discrete wavelet transform (DWT)
Face detection · Power spectrum density (PSD)

A. V. More (✉) · A. Wakankar · J. P. Gawande
Instrumentation and Control Department, MKSSS's Cummins College of Engineering for Women, Pune 411052, India
e-mail: amruta.more@cumminscollege.in

A. Wakankar
e-mail: asmita.wakankar@cumminscollege.in

J. P. Gawande
e-mail: jayanand.gawande@cumminscollege.in

H. S. Saini et al. (eds.), *Innovations in Electronics and Communication Engineering*,
Lecture Notes in Networks and Systems 33,
https://doi.org/10.1007/978-981-10-8204-7_11

1 Introduction

The continuous assessment of cardiovascular function in human being is necessary for the diagnosis of chronic diseases. The measurement of heart rate is one of the simplest methods to identify the risk factor in cardiovascular diseases. The electrocardiogram (ECG) is the conventional technique to measure the cardiac pulse. In ECG, the electrodes are attached to the arms, legs, and chest of the patient with the help of adhesive gel which is not comfortable and can cause skin irritation. So, it has become a need to measure the cardiovascular pulse of patient so that the system will provide suitable comfort level to patient and system will give more accurate heart rate. So new system is proposed which is a noncontact type automated system and it accurately measures the heart rate of patient [1, 2].

Poh et al. [3] have developed a new methodology that overcomes problems of motion artifacts by applying independent component analysis on recorded video signals and a finger blood volume pulse (BVP) sensor is used to correlate the cardiac pulse signals from the face video. Lewandowska et al. [4] explained algorithm which measures pulse rate directly from face image captured from webcam by using principal component analysis. After some enhancement, the proposed technique helps in monitoring person at home. Gault and Farag [5] explained the noninvasive and measurement methods for cardiac pulse measurement from human face using thermal IR camera. Heart rate is calculated from 512 video frames with the help of wavelet analysis, vascular mapping, and blood perfusion modeling.

In this paper, we present automated and noncontact type method which measures cardiac pulse from video images based on wavelet analysis. Face video is recorded to capture subsequent changes in the amount of reflected light for cardiovascular pulse measurement. When ambient light is incident on face, some amount of light is absorbed and some amount of light is reflected. Subsequent changes in amount of reflected light related to every cardiac cycle can be used for cardiovascular pulse measurement. The rest of the paper is organized as follows: Sect. 2 describes automatic cardiovascular pulse detection algorithm is explained in detail. The flow diagram represents the step of the algorithm. Experimental setup, which is followed during experimentation and experimental results showing results of face detection and different RGB traces, is given in Sect. 3. Finally, Sect. 4 presents the conclusion.

2 Wavelet-Based Cardiac Pulse Detection

For every cardiac cycle, blood volume changes in the facial blood vessels. Cardiovascular pulses are measured with the help of reflected light when ambient light is incident on face [3]. Based on this principle, new system is developed for the cardiovascular pulse measurement which is noncontact type automated system.

Figure 1 shows the flow diagram of cardiovascular pulse measurement algorithm. The system consists of basic webcam (Built-in camera on HP 15 ab-032tx) to record the video for analysis. All videos are recorded at 30 frames per second (fps) with pixel resolution of 640 × 480. Video is captured in color format for 60 s and saved in WMV format.

Voila and Jones algorithm is used for face detection which detects faces within the video frames and highlights the face region for each video frame. For each detected face, the algorithm gives x and y coordinates of the highlighted region

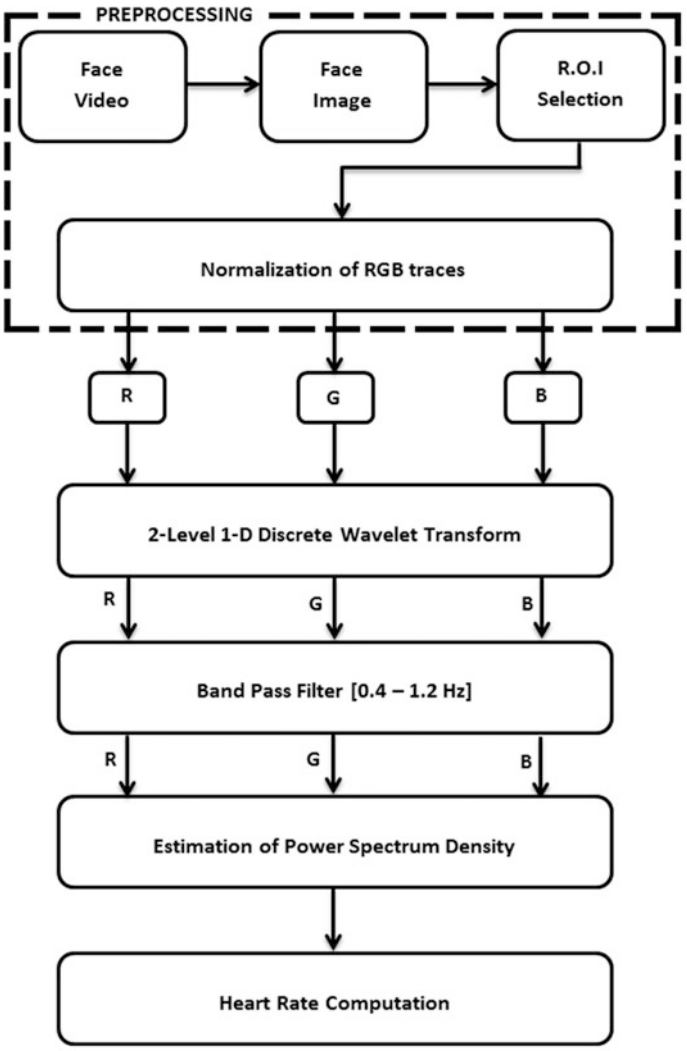

Fig. 1 Flow diagram of cardiovascular pulse measurement algorithm

along with its height and width which defines box and considers it as a region of interest (ROI) for the subsequent calculation.

The RGB channels are obtained from the region of interest. Spatial average of all pixels present in the ROI of RGB channels is obtained to get raw RGB traces which are denoted by $X_1(t)$, $X_2(t)$, and $X_3(t)$.

The normalization is the transformation of X_i (t) to $X_i'(t)$ to obtain normalized RGB signal having zero mean and unit variance.

$$X'(t) = \frac{1}{\sigma_i}[X_i(t) - \mu_i] \tag{1}$$

for each i = 1,2,3 where σ_i and μ_i are the standard deviation and mean of $X_i(t)$, respectively. The normalized RGB signals are analyzed using two-channel wavelet filter bank consist of low pass filter (H_0) and high pass filter (H_1) of analysis filter bank. The analysis scaling and wavelet function are given by the two-channel filter bank [6, 7] as follows:

$$\emptyset(t) = \frac{2}{H_0(\omega)|_{\omega=0}} \sum_n h_0(n)\emptyset(2t - n) \tag{2}$$

$$\varphi(t) = \frac{2}{H_1(\omega)|_{\omega=0}} \sum_n h_1(n)\emptyset(2t - n) \tag{3}$$

where h_0(n) and h_1(n) are the analysis low pass filter (LPF) and high pass filter (HPF) coefficients, respectively [6, 7].

Bandpass filter is used to pass certain ranges of frequencies and rejects frequencies outside that ranges. In this system, the performance limits is [0.75, 4] Hz which corresponds to [45, 240] bpm to provide a wide range of heart rate. Hence, BPF with hamming window function is used to provide all frequencies present in the range of 0.75–4 Hz [8]. The power density spectrum (PDS) of decomposed signal is used to obtain all contained peaks around that frequency to calculate normalized pulse frequency (fp). Hence, periodogram is calculated to obtain normalized pulse frequency (fp) [8]. While capturing video, ECG signal of the same person is also obtained from the PowerLab software. PDS of obtained ECG signal is calculated to obtain reference pulse frequency for heart rate calculation from reference ECG signal. This reference heart rate is used to calculate proposed system's accuracy.

3 Experimental Results

The experimentation is performed inside a room with changing amount of sunlight as the only illumination source. Ten volunteers are participated in the experimentation as per ethical standards. Subject is seated in a chair in front of a laptop,

approximately 0.5 m away from the webcam. Video of one minute is recorded for all subjects. From each frame of recorded face video, center 60% width and full height of box is considered to obtain region of interest (ROI). The RGB channels are obtained from the region of interest. Spatial average of all pixels present in the ROI of RGB channels are obtained to get raw RGB Trace. These raw RGB traces are normalized by following Normalized Equation, i.e., Eq. (1). Normalized RGB signal is decomposed using the Daubechies (db1) wavelets into different levels by following traditional convolution method of 1D DWT decomposition. Approximate coefficient of second level decomposed signals is as shown in Fig. 2, which are considered for bandpass filtering. Figure 3 shows filtered decomposed signal.

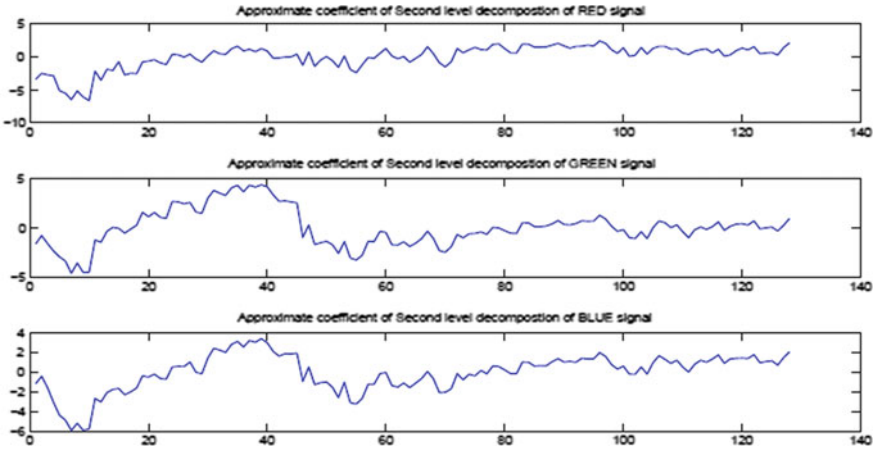

Fig. 2 Second level decomposition of normalized RGB trace of forehead

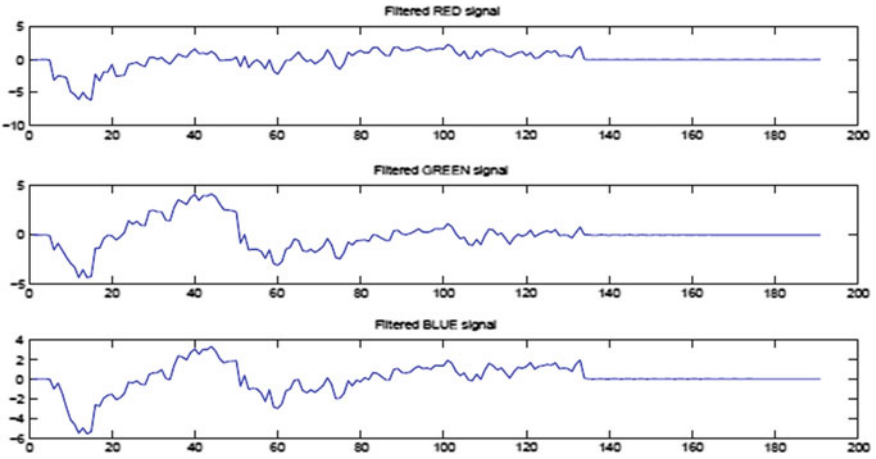

Fig. 3 Filtered RGB signal of forehead

Normalized pulse frequency is obtained from the power density spectrum as shown in Fig. 4. Heart rate is obtained from reference ECG Signal as well as video signal. Both answers are compared to calculate the absolute error of this system. Heart rates of different subjects by considering face as well as forehead are calculated and compared to reference heart rate to calculate accuracy as shown in Table 1.

Hence from Table 1, we can observe that the error is 26.86% which can be reduced if we consider the forehead of person instead of face. Hence after face detection, center 60% width and full height of box are considered to obtain the new region of interest (ROI). Only forehead is obtained from calculated region of interest.

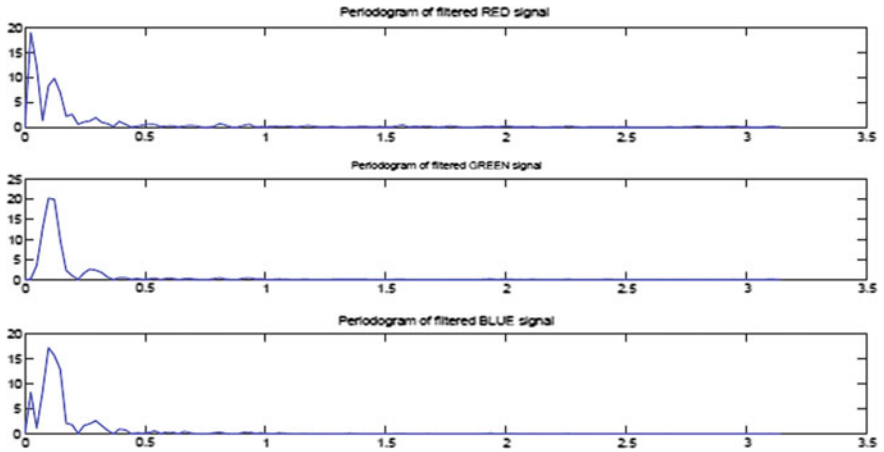

Fig. 4 PSD of filtered RGB signal of forehead

Table 1 Heart rate calculation from subject's face and forehead

	Heart rate (bpm)			MAE (%)	
Subject	Face image	ROI forehead	Reference ECG	Face	Forehead
Subject 1	63	91	87	27.59	4.59
Subject 2	63	70	84	25.00	16.66
Subject 3	120	77	93	29.03	17.20
Subject 4	84	84	102	17.64	17.64
Subject 5	70	84	84	16.67	00.00
Subject 6	98	70	82	16.32	14.63
Subject 7	54	70	72	25.00	2.77
Subject 8	77	77	92	16.31	16.30
Subject 9	105	63	60	75.00	5.00
Subject 10	90	70	75	20.00	6.67
Mean absolute percentage error				26.86	10.14

4 Conclusion

After face video recording, face and forehead are detected from each frame of video. After separation of ROI of detected face into RGB channels, raw RGB trace is obtained which shows spatial average over of all pixels in the ROI and they are normalized. Wavelet decomposition is done up to second level to obtain approximate coefficient. Bandpass filter using hamming window helps to pass frequencies present in operational range and reject all out of the range frequencies. Power density spectrum gives pulse frequency which is useful in the calculation of heart rate. As compared to heart rate obtained from the reference signal, this system improves accuracy from 73.14 to 89.86% if forehead is considered instead of face to calculate heart rate. In order to improve the accuracy of this system, the various orthogonal and biorthogonal wavelets can be tested to estimate the heart rate from face video.

Acknowledgements All authors are thankful to all the participants and the Principal Dr. M. B. Khambete of MKSSS Cummins College of Engineering for Women Karvenagar, Pune for the support.

Compliance with Ethical Standard All procedures performed in this study involving human participants were in accordance with ethical standards as laid down in the 1964 Declaration of Helsinki and its later amendments or comparable ethical standards. Informed consent was obtained from all individual participants involved in the study.

References

1. Cromwell L, Weibell FJ, Pfeiffer EA (2017) Biomedical instrumentation and measurements, 2nd edn. PHI Learning Private Limited, Delhi
2. Carr JJ, Brown JM (2015) Introduction to biomedical equipment technology, 4th edn. Pearson Publication
3. Poh MZ, McDuff DJ, Picard RW (2010) Noncontact, automated cardiac pulse measurements using video imaging and blind source separation. Opt Expr 18:10762–10774
4. Lewandowska M, Ruminski J, Kocejko T (2011) Measuring pulse rate with a webcam—a non-contact method for evaluating cardiac activity. In: Proceedings of the federated conference on computer science and information systems, pp 405–410
5. Gault TR, Farag AA (2013) Fully automatic method to extract the heart rate from thermal video. In: Computer vision and pattern recognition workshops (CVPRW), IEEE conference, pp 2160–7516, Sept 2013
6. Gawande JP, Rahulkar AD, Holambe RS (2016) A new approach to design triplet halfband filter banks based on balanced-uncertainty optimization. Digit Signal Process Elsevier 56:123–133

7. Gawande JP, Rahulkar AD, Holambe RS (2015) Design of new class of regular biorthogonal wavelet filter banks using generalized and hybrid lifting structures. Signal Image Video Process Springer 9:265–273
8. Proakis JG, Manolakis DG (2012) Digital signal processing: principles, algorithms and applications, 4th edn. Pearsons Publication, 2012

Enhancing the Quality of Failed Planetary Gear Regions Using Intensity Transformation

K. Santhi, Dhanasekaran Rajagopal, Somasundaram Devaraj and Nirmala Madian

Abstract Component failure analysis is a challenging task in any industry, in particular; gears are complicated parts and are failed frequently. This is one of the important tasks analyzed to improve the reliability and life of the gear component. As per the failure analysis procedure, for evidence purpose, gears are carried out visual examination, photo documentation, and metallographic examination. With help of a still camera, the failure zone of gear is studied that is cut for further investigation like optical and scanning electron microscope. Unfortunately, the still images are not clear and identification of gear component are challenging issues. So, image processing techniques are employed to enhance the quality of image for its further analysis. The input image is subjected to sharpening which helps in obtaining the high-frequency component in the image. After sharpening the image, the intensity is distributed over the span of 0–255 pixels. The gamma correction is performed on the sharpened image before contrast adjustment. The intermediate intensity values of the histogram are selected for enhancing the quality of the images. The results prove that the Proposed techniques is identified the failed regions of planetary gear box.

Keywords Planetary gear · Still images · Contrast enhancement
Modified histogram equalization · Gamma correction

K. Santhi (✉)
Guru Nanak Institutions Technical Campus, Hyderabad, Telangana, India
e-mail: drsanthignitc@gmail.com

D. Rajagopal
Guru Nanak Institute of Technology, Hyderabad, Telangana, India

S. Devaraj
Sri Shakthi Institute of Engineering & Technology, Coimbatore,
Tamil Nadu, India

N. Madian
K. S. Rangasamy College of Technology, Namakkal, Tamil Nadu, India

H. S. Saini et al. (eds.), *Innovations in Electronics and Communication Engineering*,
Lecture Notes in Networks and Systems 33,
https://doi.org/10.1007/978-981-10-8204-7_12

1 Introduction

The process of failure analysis is an important task for maintenance team in every organization. The maintenance team is responsible to find out the cause of the failures and also the organization is responsible to monitor the issue. Surely failure analysis will improve the reliability and enhance the quality of the product. Failure analysis is the route of gathering and investigating statistics to conclude the cause of a failure and how to avoid it from recurring. It is a significant control in manufacturing industry, where it is a very important tool used in the development of new products and for the upgradation for the existing products [1].

Most of the failures occur in the mating parts like gears, piston, etc., due to overload, poor alignment, mismatched parts, and improper maintenance. Our mechanical department research team has a big task to identify the cause of the failure in the planetary gearbox [2]. A proper sample piece was cut from the planet gear close to the failure origin and the pictorial view was taken with high quality commercial camera for purpose of evidence but the images do not hold good clarity and visibility, meanwhile sample piece was destroyed for further test. Images are identified with low resolution. It is not supported to analyze to find the causes of failure. That is the reason, the research team delays to recognize the cause of failure. In general, cracks may be formed due to fatigue, as a significance of manufacturing processes and metallurgical discontinuities.

The image processing algorithm performed is explained below.

2 Methodology

The input images taken require processing to enhance the quality of the image. The quality enhancement is performed using intensity transformation which is also an equalization procedure. The quality of an image is identified by its histogram. Based on the histogram, a conclusion is derived whether the image requires image enhancement. The enhancement of the image is based on two parameters (i) contrast and (ii) brightness. Adjusting the contrast and brightness helps in better enhancement. The input image is a low-resolution image but image resolution depends on the physical characteristics of the sensor [3]. The quality of the image can be improved by processing the image [4]. Optimum green plane masking [5] using enhanced genetic algorithm is used for contrast enhancement for retinal images. The enhancement is done based on modified conventional unsharp masking. Saliency-aided visual enhancement [6] is a screening tool to find neoplasm in medical application. Unsharp masking is used to enhance the contrast of the white light endoscopic (WLE) images.

The algorithm for the enhancement of the proposed work is given in Fig. 1.

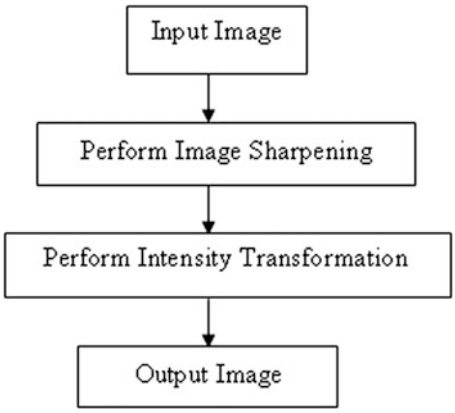

Fig. 1 Algorithm flow

2.1 *Sharpening of the Input Image*

The visual quality of the image gets degraded when the high-frequency components in the images are attenuated. These frequencies are important as they are responsible to give the edge and fine details in an image. When enhancing these frequencies, the quality of the image is improved. The edge and fine details can be enhanced by image sharpening process. The image sharpening is performed on the image using unsharp masking. The high-frequency component is obtained as shown in Fig. 2. Let the red line be the input signal and the black line be the low-frequency components. Subtracting the two signal helps in preserving the high frequency.

The unsharp masking performed on the image is given as

$$I_{\text{Sharp}}(x, y) = I(x, y) + \lambda * H(I(x, y)) \tag{1}$$

where $I(x, y)$ is the input image, λ is the tuning parameter, as λ increases, the sharpening is better $H(.)$ is the high-pass filter.

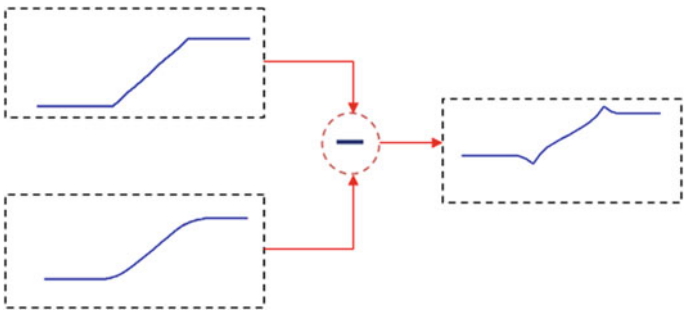

Fig. 2 High frequency components

2.2 Intensity Transformation

The sharpened image is now subjected to intensity transformation. Image transformation is performed by gamma correction operation. Gamma defines the relation between the pixel intensity value and its luminance. Gamma correction is a nonlinear function that impacts on the luminance value to improve the image quality. The general representation of gamma transformation is given as

$$I_{\text{Transformed}}(x, y) = C * I(x, y)^{\gamma} \tag{2}$$

where C and γ are constants.

The output of the gamma corrected image is considered and the contrast and the brightness values are adjusted. A nonlinear histogram adjustment is done using Gamma so the histogram of the output image is scaled. The minimum value of the histogram represents the dark region of the image and the maximum value of the histogram is the bright region. The adjustment is done considering the intermediate shades of the gray value of the histogram. The obtained output is the enhanced image.

3 Results and Discussion

The proposed image processing helps to enhance the quality of the image which helps in failure analysis. The input images considered for the analysis are shown in Fig. 3. The histogram of the input images is plotted in Fig. 4.

Fig. 3 Input images

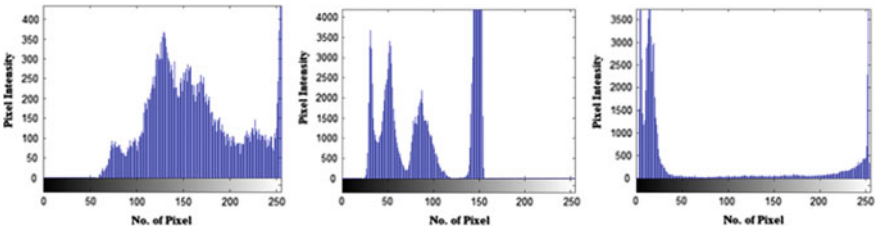

Fig. 4 Histogram of the input image

From the histogram of the image, it is clear that the intensity value is not distributed equally so the quality of the image is poor. The images considered are blurred in nature. The blurring effect can be reduced by sharpening using unsharp mask. The sharpen image along its histogram is shown in Fig. 5.

After sharpening the image, the intensity is distributed over the span of 0–255 pixels. The sharpening helps in getting the edges better. The sharpened image is further subjected to contrast and brightness adjustment. The gamma correction is performed on the sharpened image before contrast adjustment. The intermediate intensity values of the histogram are selected for enhancing the quality of the image further. The quality improvement of the image with the selected intensity value of input image is shown in Fig. 6.

The quality metrics peak signal-to-noise ratio is considered for analyzing the image quality improvement as shown in Table 1.

From the above table, it is clear that the image quality is improved better by intensity transformation compared to basic histogram equalization.

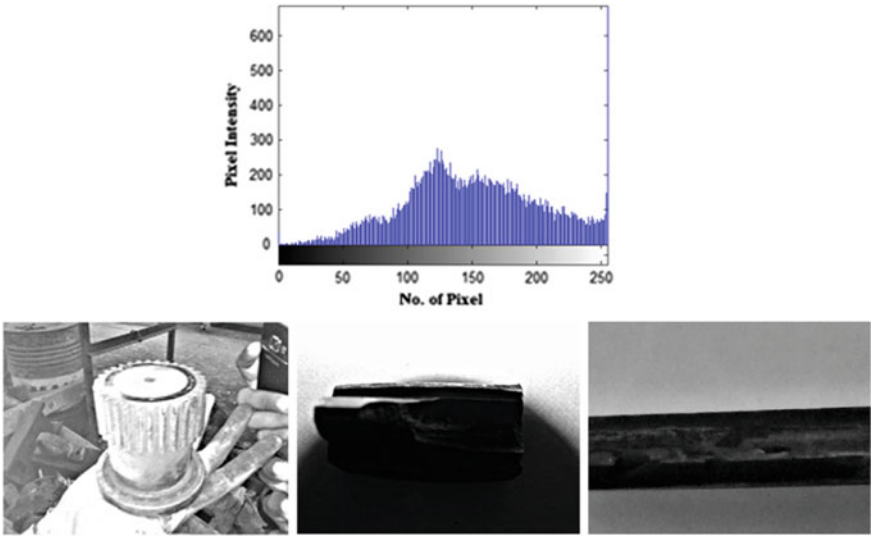

Fig. 5 Sharpen image along its histogram

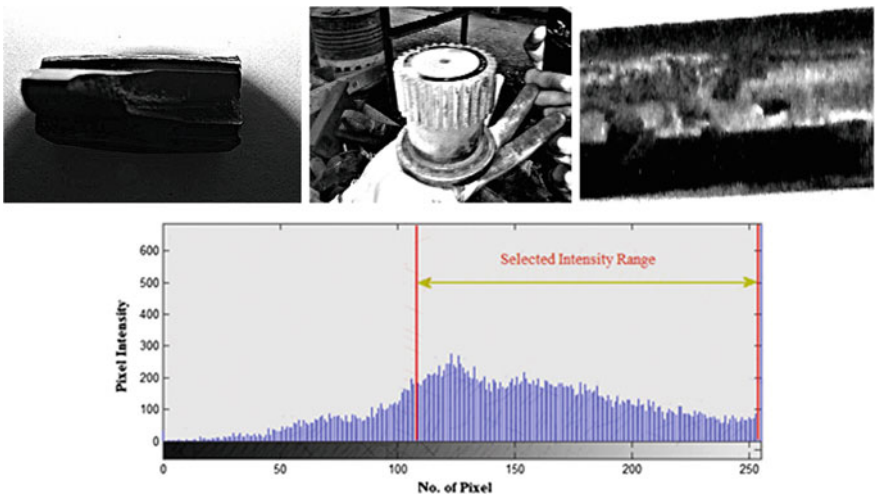

Fig. 6 Quality improvement of the image with the selected intensity value of input image

Table 1 Quality metrics analysis using PSNR

Type of image	Basic histogram equalization (HE)	Intensity transformation
Second stage sun gear	14.9312	40.5970
First stage sun gear	10.8151	52.8847
First stage planet gear	12.5792	41.0997

4 Conclusion

The proposed method is well suitable for low-resolution images. Experimental results show that intensity transformation along intensity selection helps in enhancing the quality of images. The quality enhancement is further analyzed using the quality metric which shows that the proposed method is suitable for improving the image quality.

References

1. Dhanasekaran R, Senthil Kumar P, Baskaran S, Santhi K Failure analysis of first stage planet gear. Int J Emerg Technol Appl Eng Technol Sci 3(2):476–478
2. Dhanasekaran R, Senthil Kumar P, Santhi K (2012) Microstructure and wear behavior of planetary gear material and metal carbide coating. Int Rev Mech Eng 6(6):1321–1325

3. Irani M, Peleg S (1991) Improving resolution by image registration. CVGIP Graph Models Image Process 53(3):231–239
4. Santhi K, Wahida Banu RSD, Dhanasekaran R (2014) Contrast enhanced for microstructure of steel materials and engine components. Adv Mater Res 984–985:1375–1379
5. Daniel E, Anitha J (2015) Optimum green plane masking for the contrast enhancement of retinal images using enhanced genetic algorithm. Optik 126:1726–1730
6. Deeba F, Mohammed SK, Bui FM, Wahid KA (2017) Efficacy evaluation of save for the diagnosis of superficial neoplastic lesion. Med Imaging Diagn Radiol 5

Part II
Embedded Systems

Arduino-Based Smart Street Lamp Control System to Save Energy and Improve Lamp Life

K. Shruthi and G. Akhil

Abstract Population growth and industrial development have led to increase in demand for energy in recent times. Because of which we can no longer afford to waste resources. Using resources effectively and efficiently has become a prime concern for us. In this paper, an intelligent street lamp controlling system is proposed. The proposed system helps to save huge amounts of energy and also helps increase lamp life. The design of the prototype of the proposed system is discussed in the paper.

Keywords Arduino · Lamp life · LDR · LED · Normal operation
PIR · RTC · Season-based operation

1 Introduction

Currently, street lamps are switched on throughout the night at full power. In most cities after certain time, most roads are empty and the street lamps glow wasting electricity.

Street lighting is an important component of power consumption throughout the world. India is no different. In the fiscal year 2013, street lighting consumed about 8478 GWh of electricity, and that figure can be reduced by 25–60% through the use of energy-efficient LED technologies. Furthermore, using intelligent street lamp controlling systems leads to additional energy savings of 15–20%. Just by installing

K. Shruthi (✉)
Springer-Verlag, Computer Science Editorial,
Tiergartenstr. 17, 69121 Heidelberg, Germany
e-mail: Shruthi.K@manipal.edu

G. Akhil
Department of E&C,
Manipal Institute of Technology, Manipal, Karnataka, India
e-mail: gummadiakhil71@gmail.com; LNNS@Springer.com

H. S. Saini et al. (eds.), *Innovations in Electronics and Communication Engineering*,
Lecture Notes in Networks and Systems 33,
https://doi.org/10.1007/978-981-10-8204-7_13

such systems, nearly 700 million KWh of energy can be saved per year, which amounts to about INR 350 crores every year. Using led lights total energy savings of 5000 million KWh can be done. This translates to about INR 2500 crores every year. The above statistics are true if assumed that 1KWh costs about INR 5. In some states of India, it is even higher up to INR 7 which would lead to much more savings [1].

Also, it is the light output that decides the lifespan of an LED street light, rather than the design specification. An LED street light is considered to be at the end of its life, when its brightness decreases by 30%. From the graph shown in Fig. 1, it can be observed that continuous usage of the lamp for long hours brings down the brightness which in turn reduces the lamp life.

From the above statistics, it can be observed that energy has to be saved and lamp life have to be improved. The proposed system targets at energy saving as it is operated in two different modes and also helps to increase lamp life. The proposed system comprises of LDR, PIR and temperature sensors, an RTC, and a microcontroller. LED is used to represent street lamp.

The proposed system has two modes of operation. One of the modes is dependent on LDR whereas the other mode depends purely on RTC. Temperature and PIR sensors are used in both modes. The working of the proposed system is described in Sect. 2 and the implementation of the system is described in Sect. 3. The results are presented in Sect. 4.

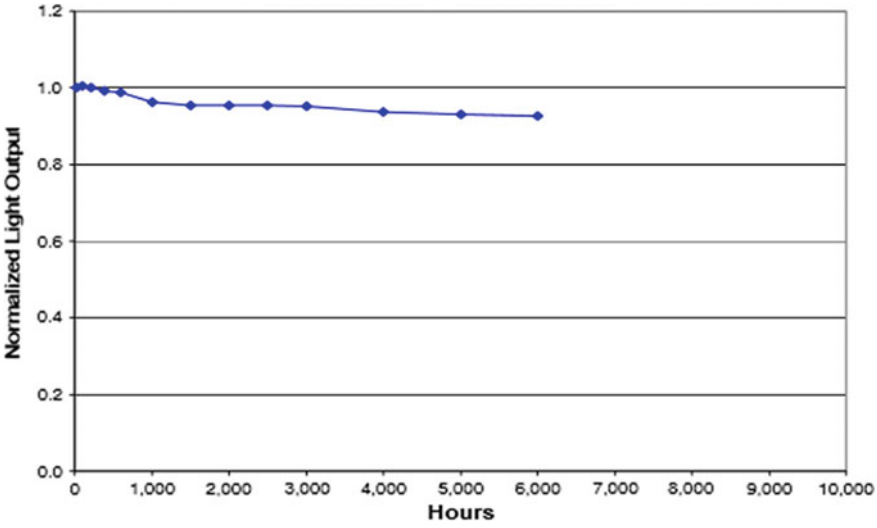

Fig. 1 Graph showing the light output of a Philips Lumileds K2 LED declines over time [2]

2 Proposed System Functionality

In the proposed system, the microcontroller (Arduino) takes input from motion (PIR) sensor, RTC, LDR, and temperature sensors. Depending on the status of these inputs, the Arduino decides the output. In addition to these sensor inputs, there are two push buttons which decide the mode of operation. The Arduino gives output to three devices that is the LCD, RTC (only once), and street light (LED). The RTC has to be initially programmed by the Arduino. After programming, it then reads the RTC for time information regularly. The time is displayed on the LCD and when the system is powered up or reset "select mode" message is displayed (Figs. 2 and 3).

Modes of Operation
In the system, there are two modes of operation.

MODE 1 (Normal Operation)—the Arduino takes input from LDR, to differentiate between night and day. As soon as it is night the Arduino switches ON the LED. Simultaneously, it reads input from RTC and if the time crosses a certain value which is preset then it will put the system in low power mode by controlling the LED using 70% duty cycle PWM wave. The duty cycle can be further lowered to increase energy savings. If during this time PIR sensor ever detects any vehicle then PWM wave goes back to 100% duty cycle for 3 s so that the vehicle can pass by. This duration can be adjusted to get a balance between safety and energy savings. The temperature sensor also keeps sensing the temperature of the street lamp and if the value crosses 70 °C, the LED (lamp) will receive a PWM wave of 60% duty cycle till the temperature drops back again. The LCD is used to display time and mode in which the system is operating in.

MODE 2 (Season-based Operation)—the switching ON of the street lamps depends on time not on LDR. Generally, LDRs have to be used in highly controlled environment but streets are not controlled environments so if LDRs get spoilt, the mode of operation can be switched and the system becomes independent of LDR. In this mode for each month from January to December, there is a time set for the lights to turn ON and turn OFF. This is the only difference in the mode 2 operation when compared to mode 1 and everything else functions similarly to Mode 1.

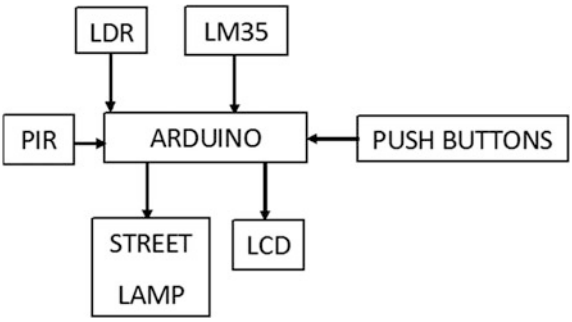

Fig. 2 Block diagram of the proposed system

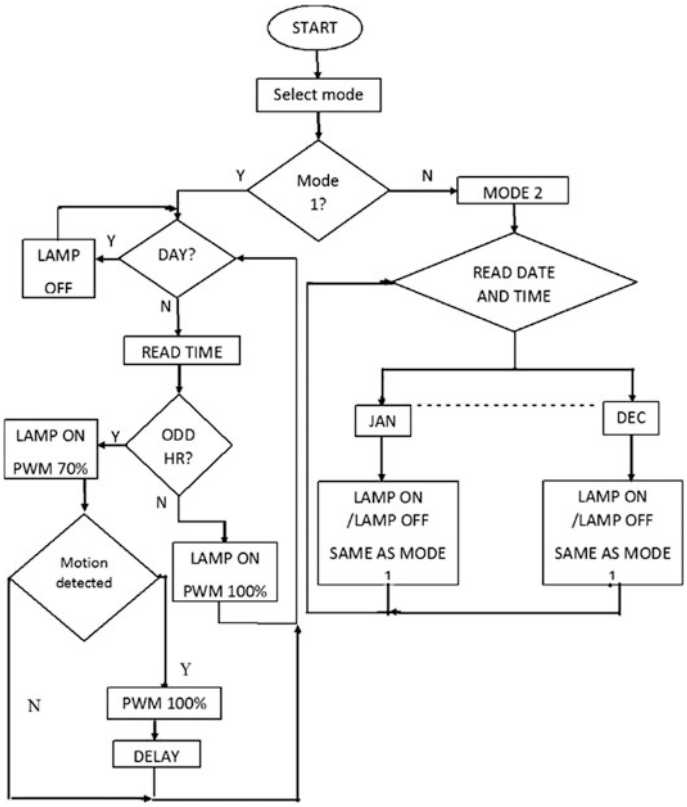

Fig. 3 Flowchart depicting system operation

3 System Implementation

A. Arduino [3]

Arduino/Genuino Uno is a microcontroller board based on the ATmega328P. It contains the features required to support the microcontroller and it just needs to be connected to a computer using a USB cable. Arduino IDE 1.6.12 is the firmware used for programming. Each time a new code is written, it is automatically compiled and the controller in the board gets programmed.

B. RTC [4]

The DS1307 serial real-time clock (RTC) is a low power, full binary-coded decimal (BCD) clock/calendar plus 56 bytes of NVSRAM. Address and data are transferred serially through an I2C, bidirectional bus. The clock/calendar provides seconds, minutes, hours, day, date, month, and year information. It operates in either the 24-h or 12-h format with AM/PM indicator.

C. LDR [5]

Photoconductivity is an optical phenomenon in which the materials' conductivity is increased when the light is absorbed by the material. A Light Dependent Resistor (LDR) or a photo-resistor is a device whose resistivity is a function of the incident electromagnetic radiation. Hence, they are light sensitive devices.

D. PIR [6]

PIR sensors or "Passive Infrared", "Pyroelectric", or "IR motion sensors" senses motion, and are always used to detect whether a human has moved in or out of the sensors range. They are small, inexpensive, low power, easy to use, and don't wear out.

E. LCD [7]

A 16 × 2 LCD (Liquid Crystal Display) screen is an electronic display module and finds a wide range of applications. LCDs are economical, easily programmable, have no limitation of displaying special and even custom characters. A 16 × 2 LCD means it can display 16 characters per line and there are 2 such lines.

F. Proposed System Circuit Diagram

The circuit diagram for designing the prototype of the proposed system is shown in Fig. 4.

4 Results

The results obtained for different cases are presented in this section. The experimental setup of the proposed system is shown in Fig. 5.

It can be seen in Fig. 5 that "select mode" has been displayed on the LCD as soon as the system is powered ON.

When mode 1 is selected and it is day time, then time and mode 1 gets displayed on the LCD. The lamp (LED) remains OFF. This is shown in Fig. 6.

When mode 1 is selected and it is night, then lamp (LED) is turned off depending on whether it is odd hour or not. If it is not an odd hour, i.e., street is busy, then LED glows with full brightness. This is shown in Fig. 7.

When mode 1 is selected, it is night and it is an odd hour, then the LED brightness is controlled using PWM. Figure 8 shows the Arduino Serial window displaying the PWM value when the condition is satisfied

When mode 1 is selected, it is night and it is an odd hour, then the LED brightness is controlled using PWM. During this condition, if any vehicular

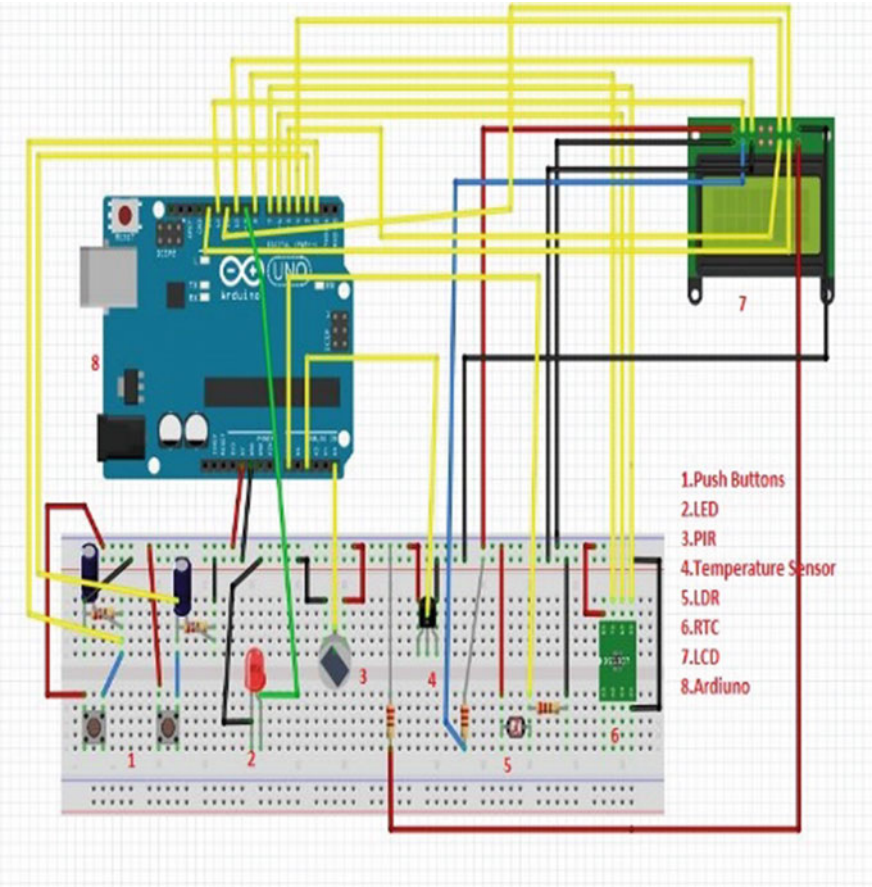

Fig. 4 Circuit diagram of the prototype of the proposed system

movements are sensed by PIR sensor, then the LED brightness is increased momentarily. Figure 9 shows the PIR sensor values received on the Arduino Serial window.

When mode 2 is chosen then based on the month and time set, the LED turns ON and OFF. In Fig. 10, the LED is OFF at evening 6.33 PM. When the time crosses 6.35 PM, the lamp (LED) turns ON automatically as shown in Fig. 11. Note that date is also displayed.

The lamp temperature is sensed by a temperature sensor. When the temperature goes beyond certain limits, the lamp (LED) is made to glow at less brightness till the temperature comes down. Figure 12 shows the temperature sensor values displayed on the Arduino Serial window.

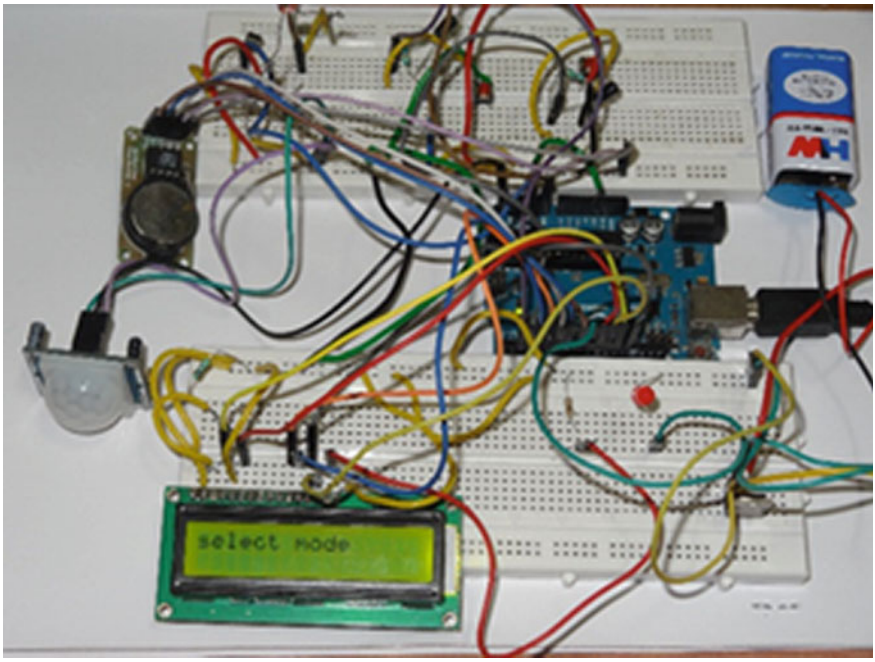

Fig. 5 Experimental set up of the proposed system when powered ON

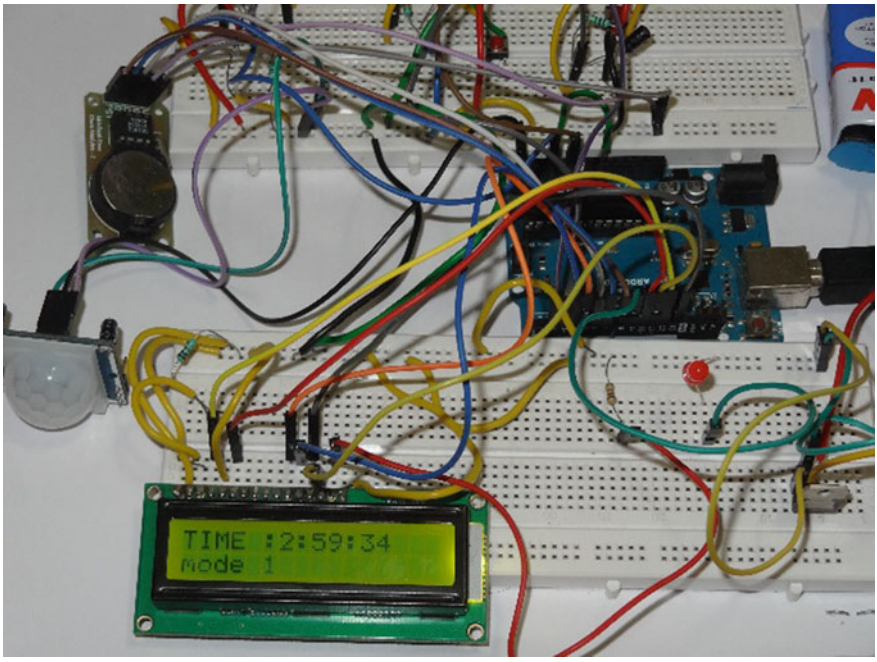

Fig. 6 Mode 1 operation and LED OFF as it is day

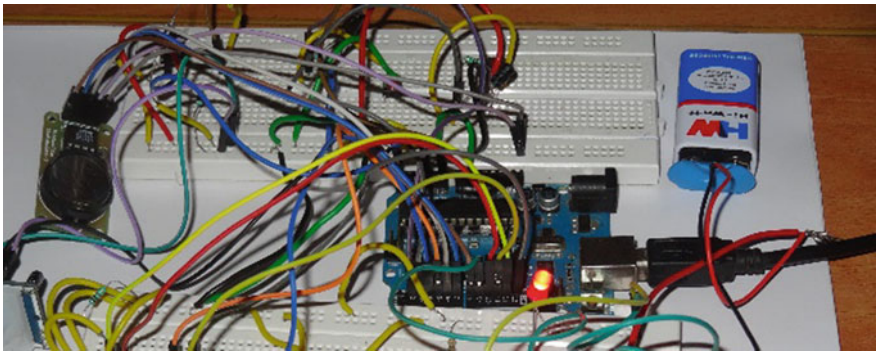

Fig. 7 LED glowing on the night and not an odd hour

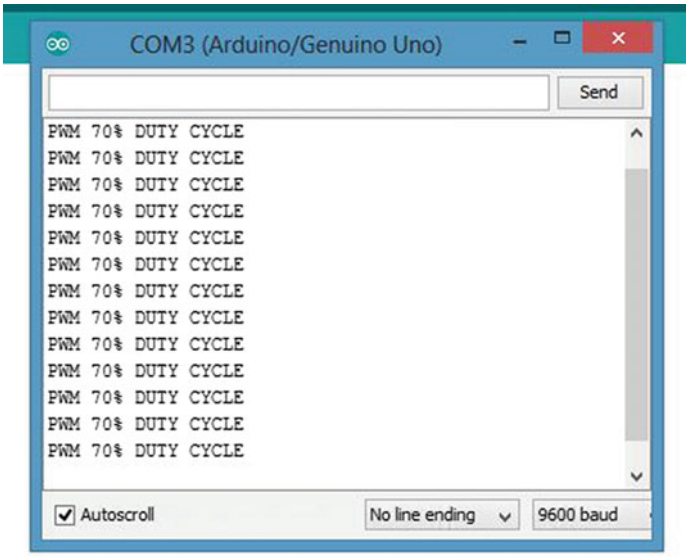

Fig. 8 PWM output displayed in Arduino serial monitor

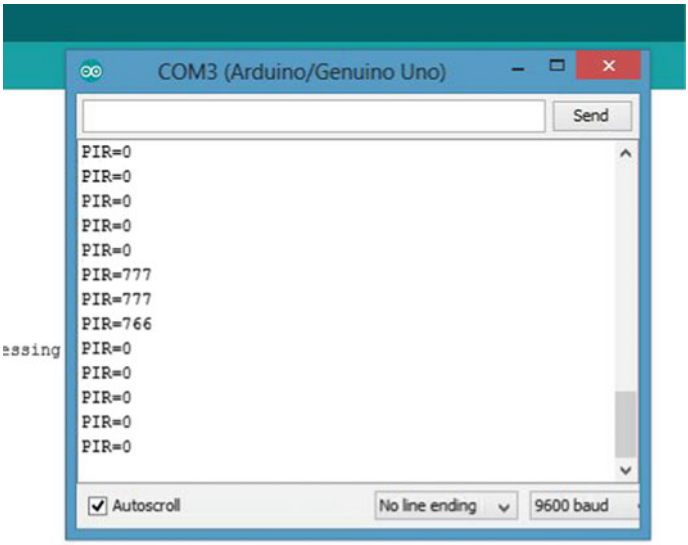

Fig. 9 PIR sensor values

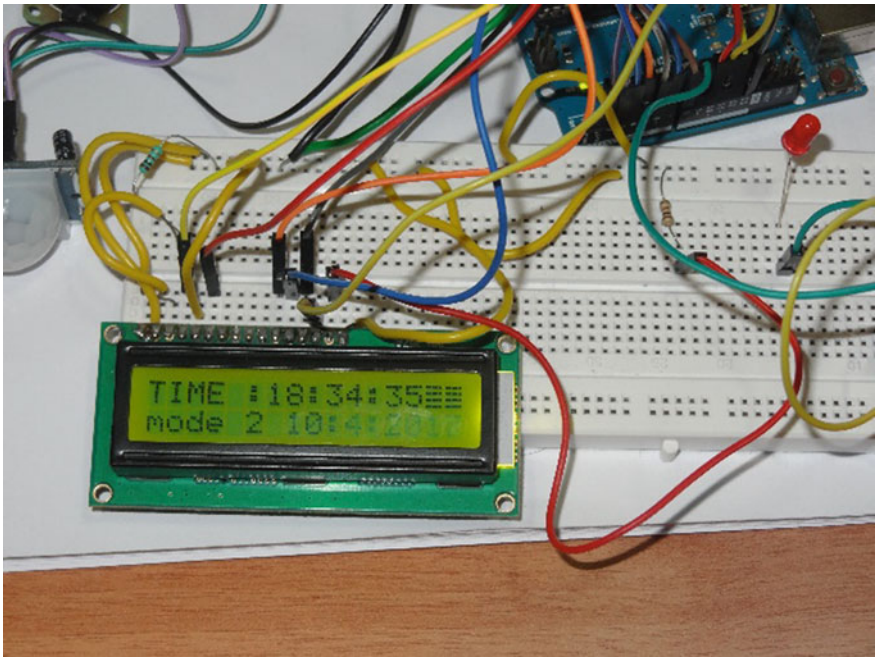

Fig. 10 LED OFF as it is evening and the specified time is not met

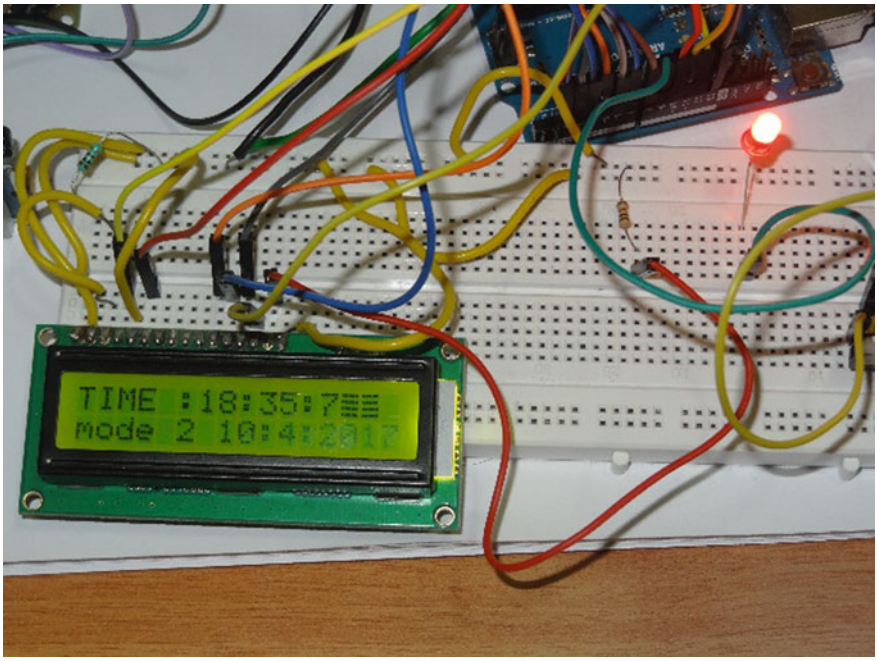

Fig. 11 LED ON as it is evening and the specified time is met

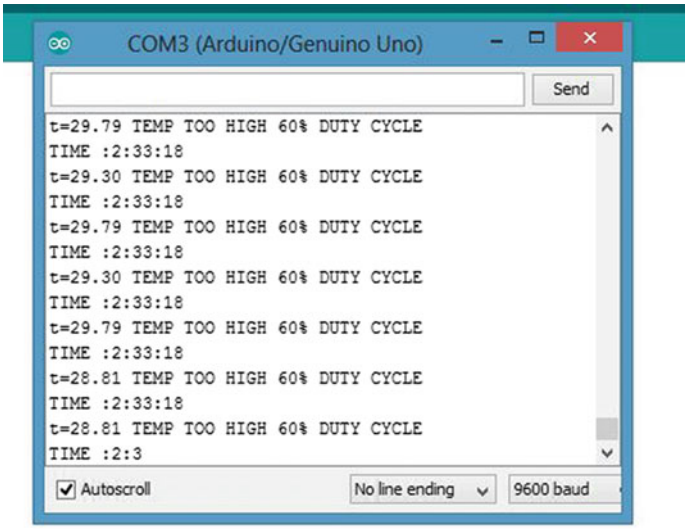

Fig. 12 Temperature sensor output

5 Conclusion

The prototype for the proposed system was thus designed and tested for the different cases. Since there are two different modes of operation of the system and the lamp is turned ON and OFF based on different conditions, rather than keeping it ON continuously, energy is saved at least to an acceptable extent. Also, the temperature sensing of the lamp will help to decide the duration of the lamp to be ON at full brightness. Since it glows at lesser brightness, the lifespan of the lamp is also improved.

References

1. India: Energy-Efficient Street Lighting—Implementation and Financing Solutions. By The World Bank, June 2015
2. Philips, Technology white paper "Understanding power LED Lifetime Analysis"
3. https://www.arduino.cc/en/Main/arduinoBoardUno
4. https://www.elprocus.com/rtc-ds1307/
5. https://www.electrical4u.com/light-dependent-resistor-ldr-working-principle-of-ldr/
6. https://learn.adafruit.com/pir-passive-infrared-proximity-motion-sensor/overview
7. https://www.engineersgarage.com/electronic-components/16x2-lcd-module-datasheet

GPS Based Autonomous Ground Vehicle for Agricultural Utility

S. Thenmozhi, V. Mahima and R. Maheswar

Abstract Farming is a tedious job when carried out manually. With the advent of technology, various researches are done in this field. The innovative idea is to automate the process of seed sowing, to reduce the human labour and to increase the speed with consistent quality. The unmanned mobile robots are employed to serve this purpose. The location of the Autonomous Ground Vehicle in a vast area can be tracked with the help of GPS, and its position can be monitored through a remote device. A prototype has been designed for precise seed sowing process. The inter-seed distance is maintained by the use of servomotor. The vehicle is controlled by ATMEGA328 microcontroller. The direction of the path to be followed is deduced by using a compass module. Speed and accuracy have been the areas of concern while designing the system.

Keywords GPS · Autonomous Ground Vehicle · Compass module

1 Introduction

Agriculture is considered to be the backbone of Indian economy. In the earlier days, the seeds were broadcasted by hand which was a difficult job as only the trained person can disperse the seeds in a way that the inter-seed distance and row to row distance between the crops were maintained. Later, sowing is done by dropping the

S. Thenmozhi (✉) · R. Maheswar
Department of ECE, Sri Krishna College of Technology,
Coimbatore, Tamil Nadu, India
e-mail: s.thenmozhi@skct.edu.in

R. Maheswar
e-mail: r.maheswar@skct.edu.in

V. Mahima
Department of ECE, Veltech Rangarajan Dr Sagunthala R&D Institute
of Science and Technology, Avadi, Chennai, India
e-mail: mahi.90may@gmail.com

H. S. Saini et al. (eds.), *Innovations in Electronics and Communication Engineering*,
Lecture Notes in Networks and Systems 33,
https://doi.org/10.1007/978-981-10-8204-7_14

seeds behind the country plough manually which is followed by farmers owing tractors. Both these methods are inefficient since there was a wide variation in seed distribution leading to low productivity. Hence, precision in seed sowing is necessary for producing maximum yield.

This can be achieved by using modern agricultural techniques which in turn reduced human intervention through automation. The Autonomous Mobile Robots (AMRs) are becoming increasingly popular because of its wide range of applications. AMR is usually fitted with the sensors and computation units which aid in identifying the nature of soil, crop and their requirements. Based on the information from the sensors, seed sowing, the water supply, fertilizer spraying, etc. can be done accurately as per the necessity so that the complete process in agriculture from sowing to yielding can be fully automated.

2 Related Works

The path planning discussed in [1] concentrates on unknown terrain applications. Pre-planning of path is done for applications involving safety issues. In [2], a low cost autonomous unmanned aerial vehicle is described for analysing the crop. The NDVI (Normalized Difference Vegetation Index) technique discussed measures the photosynthetic activity of a plant, to obtain information about crop's health and parameters that affect them such as watering, fertilizer or pests. The analysis of crop's health would increase the yield through reduced fertilizer use and it also avoids diseases at the earlier stages. The work considered in [3] concentrates on designing and developing the prototype of mobile robot for pesticide spraying application. It is done through three stages: learning, implementation and training stage. This is to achieve maximum crop yield with minimum human intervention. A work similar to the proposed work is discussed in [4]. A prototype of autonomous Agricultural Robot is designed for seed sowing applications. A four-wheeled vehicle controlled by microcontroller is employed for sowing seed at optimal depth and also at optimal distances in order to achieve maximum yield.

3 Proposed Model

In India, the existing system is mechanically operated which has so many drawbacks. The proposed system (Fig. 1) consists of GPS for tracking the path in the field for the purpose of seed sowing. The compass module aids in keeping the robot on track. The speed of the servomotor is made proportional to the inter-seed distance, which can be varied depending upon the nature of the seed.

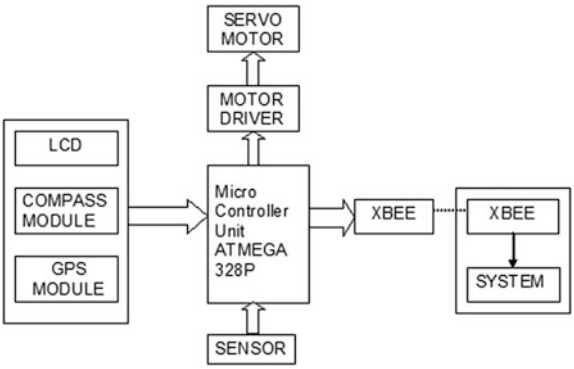

Fig. 1 Components of the autonomous ground vehicle

3.1 GPS Module

The position of the vehicle is tracked with the help of GPS module. When the system is powered, the GPS starts to receive signals from the satellites [5]. The GPS is said to get a fix on the location, usually when the GPS is able to sense the signal from a minimum of four different satellites. This can be viewed with the help of Mini GPS Software (Fig. 2). Required port and baud rate are set for synchronizing

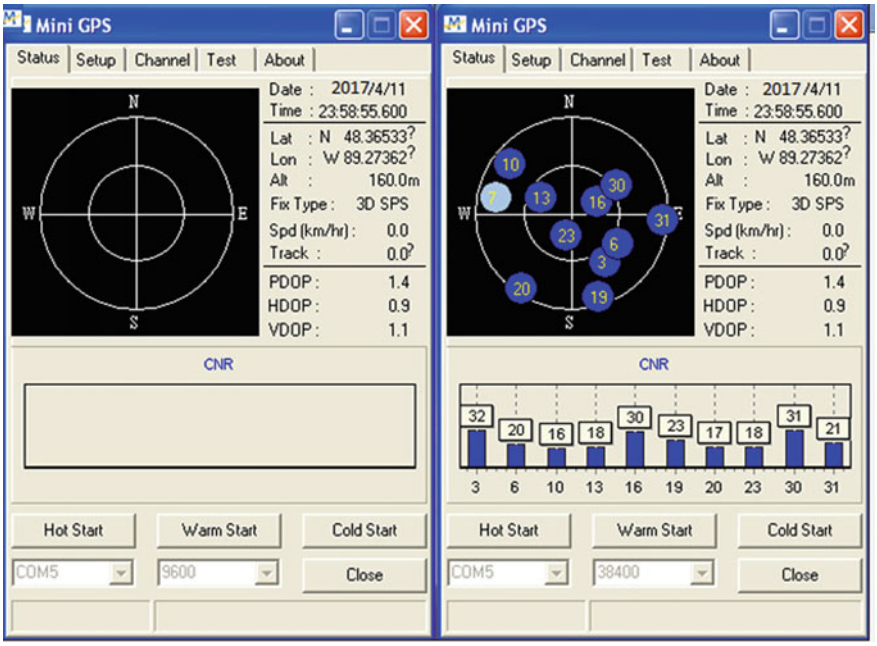

Fig. 2 Mini GPS tool showing sky chart, status and signal level

the GPS with the microcontroller. The GPS produces a set of data continuously regarding the position of the earth which includes the current position w.r.t the earth in terms of latitude and longitude. These location details are fed as inputs to the microcontroller. Four (A, B, C, D) such waypoints which are positions of four corners of the field are fed as input.

3.2 Compass Module

This module is added in order to increase the accuracy and precision of the system. The direction to be moved from one waypoint to another point is determined by the compass module. It determines the degree or angle of the current location with the help of a magnetic compass which is fed as input to the microcontroller. Based on this input, the path to be followed is maintained.

3.3 Function of Microcontroller

The path to be tracked in the field is fed in the form of waypoints (A, B, C, D) through GPS to the microcontroller (Fig. 3). The microcontroller compares the current location with the initial point (A). It then calculates the distance to be travelled and the vehicle moves with enough drive from the dc motors. According to the inputs from the compass module, the vehicle turns either to the right, left or straight. It then travels to the next waypoint (B). Once point B is reached, the servomotor stops such that the seeds are not dropped until it reaches the point (B1). The servomotor starts when the vehicle starts moving from the point (B1) to the point (A1) and so on. When it reaches the last point (D), the vehicle stops sowing automatically and reaches the point (A).

Figure 4 depicts the internal wiring connections involved in interfacing the microcontroller with dc motors, compass module, GPS and Xbee modules.

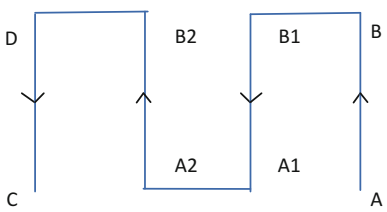

Fig. 3 A typical path to be tracked by the vehicle

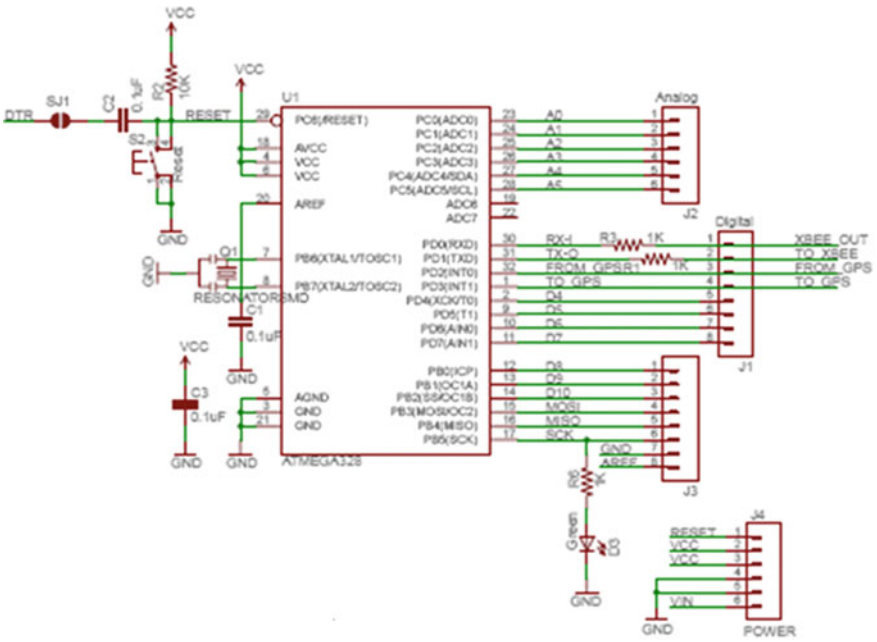

Fig. 4 Schematic diagram

3.4 DC Motors

The vehicle is fitted with two dc motors. One motor is used for turning the vehicle left and right. Another motor is used for moving the vehicle forward. When the supply is given, a torque is produced by the motor. This torque will help in moving the vehicle.

3.5 Driver Circuit

The microcontroller cannot provide enough power to drive the dc motors. Hence, driver circuit is used (Fig. 5). The driver circuit consists of L293 IC which gives enough power to drive the wheels of the robot. Now, the robot moves and tracks all the waypoints.

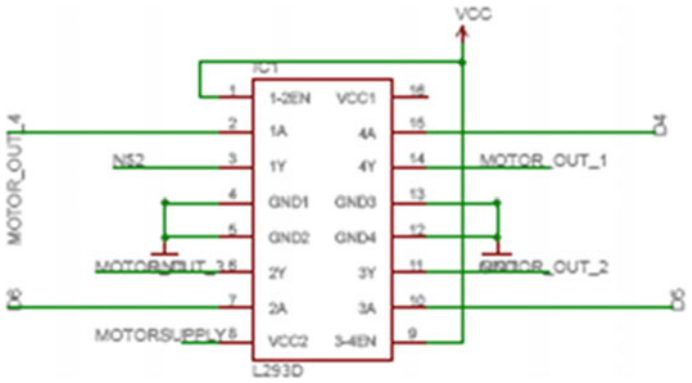

Fig. 5 Driver circuit

3.6 Servomotor

The seed tank consists of a servomotor. As the supply is given to the servomotor, the shaft rotates. The speed of the shaft can be controlled by the potentiometer (0–10 kΩ). The tank is fitted with seed pipe. A planar sheet is fitted to the shaft with a hole in it. As the hole comes in contact with seed pipe each time as the shaft rotates, the seeds are dropped one by one. The distance between the seeds is controlled by varying the speed of the shaft.

3.7 Xbee Module

As the vehicle moves in the field especially of very large area, it is not possible for us to locate the current status [5] of the vehicle. Hence, an Xbee module (transmitter) is fitted to the truck which transmits the current status of the truck. The details monitored are latitudinal and longitudinal points which can be decoded to determine the location.

4 Results and Discussion

Figure 6 and 7 show the four-wheeled autonomous vehicle that is designed [6, 7]. The prototype was tested in various fields. The inter-seed distance and row to row distance between the crops are the parameters that have been considered. In most of the cases, it was observed that both the practical and theoretical values did not differ much, achieving accuracy in seed sowing. This would further simplify and automate the process of fertilizer spraying, weeding, etc. to a great extent.

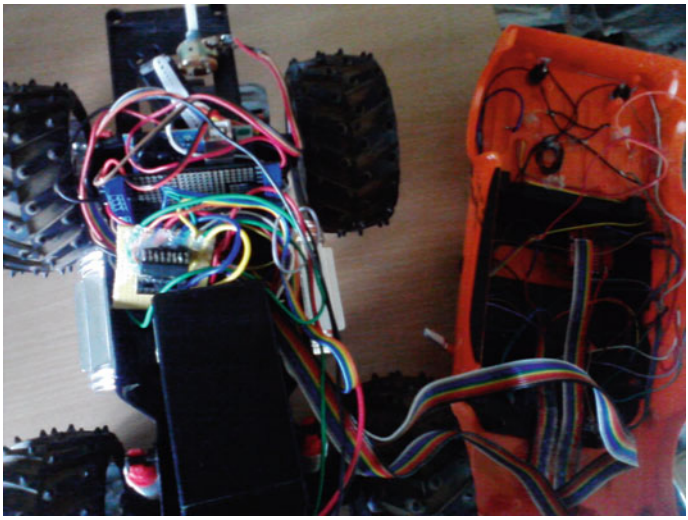

Fig. 6 Prototype with internal connections

Fig. 7 Prototype fitted with GPS, Xbee and compass module

Table 1 shows the comparison of the theoretical values with that of the practical values obtained during the process of sowing different seeds maintaining the inter-seed distance and row to row spacing.

Table 1 Seeding distance of various crops

Crop type	Inter-seed distance			Row-row spacing		
	Theoretical*		Practical	Theoretical*		Practical
	Range	Chosen value	Obtained value	Range	Chosen value	Obtained value
Corn	(4–6)″	5″	4.9″	(30–36)″	33″	32″
Wheat	(6–10)″	8″	8.1″	(7.5–15)″	10″	11.1″
Soybean	(2–4)″	3″	2.6″	(24–30)″	31″	29″
Peanut	(6–8)″	7″	6.6″	(12–24)′	19″	20″
Chickpea	(3–6)″	4.5″	4.4″	(18–24)″	22″	21″

*Theoretical values differ from region to region. The prototype can be programmed for any region by modifying the code

5 Conclusion and Further Approach

This paper has presented design and development of an autonomous seed sowing machine. The main advantage of the vehicle is the maintenance of inter-seed distance. The vehicle has been tested in various fields which are regular in shape. Further research has been concentrated on extending the work for irregular fields. When the vehicle is moving in an irregular field, there may be obstacles adjacent to it resulting in damage to the vehicle or any other destruction. To avoid this, the vehicle may be fitted with proximity sensor that radiates the IR rays, which when strikes the obstacle is reflected back, so that the direction can be changed.

Acknowledgements This work was supported by Electronics Sector Skills Council of India sponsored Centre of Excellence in VLSI and Embedded System Design, Sri Krishna College of Technology, Coimbatore, India.

References

1. Delmerico J, Mueggler E, Nitsch J, Scaramuzza D (2017) Active autonomous aerial exploration for ground robot path planning. IEEE Rob Autom Lett 2(2), April 2017
2. Velasquez LC, Argueta J, Mazariegos K (2016) Implementation of a low cost aerial vehicle for crop analysis in emerging countries. IEEE Glob Humanitarian Technol Conf
3. Ko MH, Ryuh BS, Kim KC, Suprem A, Mahalik NP (2015) Autonomous greenhouse mobile robot driving strategies from system integration perspective: review and application. IEEE/ASME Transac Mechatron 20(4), Aug 2015
4. Naik NS, Shete VV, Danve SR (2017) Precision agriculture robot for seeding function. In: IEEE International conference on inventive computation technologies (ICICT), Vol 3, Jan 2017
5. Anupama J, Kavitha A, Harsha S, Karthick M (2014) Design and development of autonomous ground vehicle for wild life monitoring 2(5), May 2014
6. Sezer V, Dikilita C, Ercan Z, Heceoglu H, Bner A, Apak A, Gokasan M, Mugan A (2012) Conversion of a conventional electric automobile into an unmanned ground vehicle (UGV). In: Proceedings of the IEEE international conference on mechatronics, 13–15 April
7. Lim JH, Song SH, Son JR, Kuc TY, Park HS, Kim HS (2010) An automated test method for robot platform and its components. Int J Softw Eng Appl 4(3)

Systematic Method for Detection and Prevention of Fire Accidents in Rail Transport

B. Vanajakshi and N. Mounika

Abstract Exemplary embodiment of the present disclosure is directed toward a systematic method for preventing fire in a rail transport. The system includes a flame detector which detects fire at a critical fire point in compartments of a rail transport, a control unit which receives the detected fire information from the flame detector for transmitting digital signals, an alarm unit which notifies the detected fire information to the passengers through an alarm, a liquid-crystal display unit which displays a fire presence compartment number of the rail transport, a power activation and deactivation unit which deactivates a power of the rail transport and activates battery bulbs in the compartments of the rail transport, water sprinkling pipes which split the water in the fire presence compartments, a power relay unit which controls the speed of the rail transport, and emergency services alerting unit which transmits an information of detected fire information to the emergency services through a communication network [1].

Keywords Rail transport · Flame detector · Alarm · Liquid-crystal display unit Power activation and deactivation unit · Water sprinkling pipes

1 Introduction

Trains are moderate vehicles which are used for transporting people and goods. Mostly, people prefer train journey for long distance as it is cheaper. But nowadays, fire accidents occur in many trains. The main purpose of a systematic method for preventing fire in rail transport is to rescue the people's life and save the government property [2]. This project will focus on the system that will detect and control the fire accidents in running trains (Fig. 1).

B. Vanajakshi (✉) · N. Mounika
PSCMRCET, Vijayawada, India
e-mail: vanaja2birudu@gmail.com

N. Mounika
e-mail: mounikaneelam.15@gmail.com

H. S. Saini et al. (eds.), *Innovations in Electronics and Communication Engineering*,
Lecture Notes in Networks and Systems 33,
https://doi.org/10.1007/978-981-10-8204-7_15

Fig. 1 Firing train

2 Background

In railway vehicles, low-error smoke gas detection is of utmost interest. In particular, the fire load introduced by the passengers cannot be controlled, which is why fires that break out can spread quickly and countermeasures must be taken very quickly. For example, a fire-fighting system must be able to tackle very quickly a fire that has broken out. If the fire spreads and the fire-fighting system fails, serious damage must be anticipated in most cases, which is why it is imperative that smoke detection must be designed with redundancy.

There has been an alarming increase in railway fires in recent years. Fire on a running train is more catastrophic than on a stationary one, since fanning by winds helps to spread the fire to other coaches. Moreover, passengers sometimes jump out of a running train on fire, resulting in increased casualties. In the light of the aforementioned discussion, there is a need for a system and method for preventing fire in rail transport.

3 Proposed System

In this system, when the fire occurred in any coach, that fire can be monitored and controlled totally in six stages:

Stage1: *Alarm* will be activated and *LCD* unit displays the fire presence compartment number.
Stage2: *Power supply* should be turned off.

Stage3: *Battery bulbs* will glow with the help of inverter.
Stage4: *Doors* and *windows* should be opened automatically.
Stage5: *Water* is sprinkled through water pipes.
Stage6: Automatically, the train should be slowed down and then stopped depending upon the speed.
Stage7*: Emergency services alerting unit* transmits the detected fire information to the emergency services through a communication network.

4 System Model

The system includes a flame detector configured to detect the fire at a critical fire point in one or more compartments of a rail transport. The system includes a control unit configured to receive the detected fire information from the flame detector for transmitting one or more digital signals [3]. One or more digital signals are received by the control unit for activating one or more water sprinkling pipes. A direct current motor configured to operate the one or more water sprinkling pipes. The power relay unit decreases the speed of the rail transport and also we use GPS (Global positioning system) to track the place where the fire accident occurred.

5 Brief Description of Drawings

Other objects and advantages of the present invention will become apparent to those skilled in the art upon reading the following detailed description of the preferred embodiments, in conjunction with the accompanying drawings.

Figure 3 illustrates a diagram of a fire prevention system in multiple compartments of the rail transport. As shown in the figure, a flame detector is configured to detect fire at a critical fire point in one or more compartments of a rail transport; a control unit is configured to receive the detected fire information from the flame detector for transmitting one or more digital signals;

6 Detailed Description of Drawings

It is to be understood that the present disclosure is not limited in its application to the details of construction and the arrangement of components set forth in the following description or illustrated in the drawings. The present disclosure is capable of other embodiments and of being practiced or of being carried out in various ways. Also, it is to be understood that the phraseology and terminology used herein is for the purpose of description and should not be regarded as limiting.

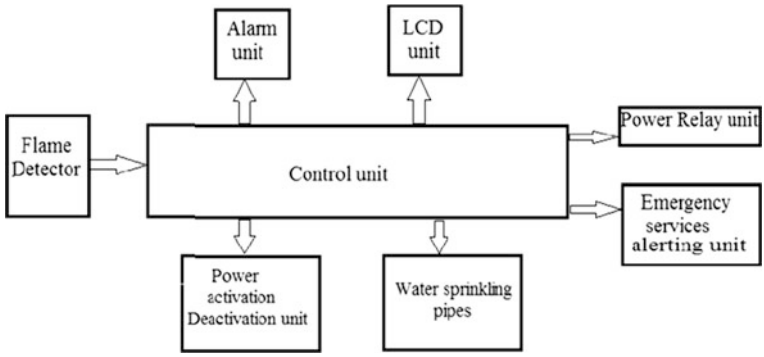

Fig. 2 Fire prevention system in the rail transport

Referring to Fig. 2 is a block diagram depicting a fire prevention system in rail transport. It depicts a flame detector which may configure to detect fire in compartments of a rail transport. The flame sensor may detect the fire at a critical point. The critical point may be referred as a predetermined value or preset value for detecting the fire. The flame detector transmits detected fire information to a control unit [4]. The system may include a power activation and deactivation unit which may be configured to deactivate a power in the rail transport for preventing of spread the fire into other compartments due to the power supply. Then, doors and windows may be opened automatically in the compartments of the rail transport. The communication network may include but not limited to global system for mobile communication, Zigbee, other wireless communications, and the like.

Referring to Fig. 3 is a diagram depicting a fire prevention system in multiple compartments of the rail transport. The diagram depicts an engine compartment of the rail transport which may be include a flame detector, an alarm unit, a liquid-crystal display unit, and power activation and deactivation unit. The flame detector may be configured to detect fire in the engine compartment of the rail transport. The control unit activates the alarm unit, the liquid-crystal display unit, and the power activation and deactivation unit. The alarm unit provides an alarm in the rail transport. At the same time, the liquid-crystal display unit may configure to display a fire presence compartment number in the rail transport. Then, the rail transport doors and windows are opened automatically due to the occurrence of the fire in any compartment.

Referring to Fig. 4a is a flow diagram depicting a method for preventing fire in the rail transport. The first step in this method starts with a flame detector that detects the fire in the compartments of the rail transport. The detected fire information is transmitted to a control unit at the next step. At next step, the control unit activates an alarm unit, a liquid-crystal display unit.

Referring to Fig. 4b is a flow diagram depicting fire preventing steps in the rail transport. The first step in this method is that, the control unit receives the detected fire information in the rail transport from the flame detectors which are used to

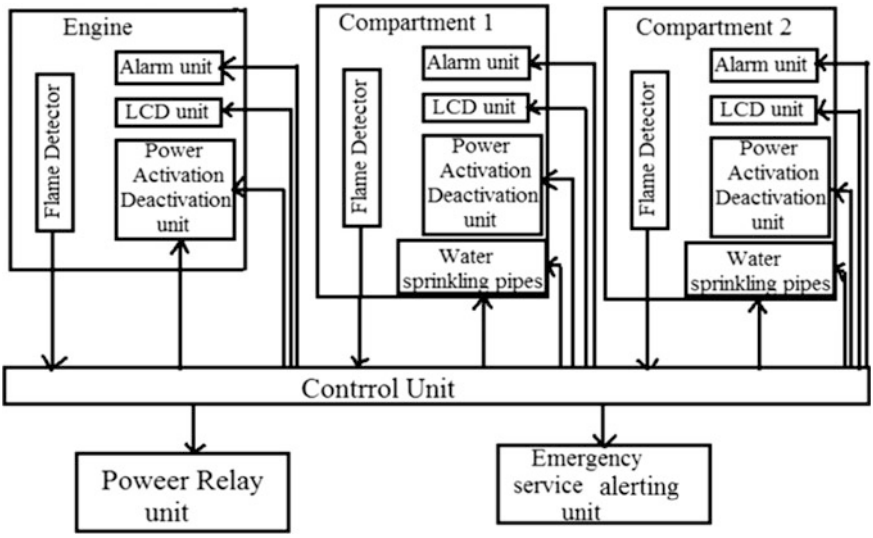

Fig. 3 Fire prevention system in multiple compartments of the rail transport

detect the fire in the rail transport at the critical fire point. At next step, an alarm unit alerts the passengers in the rail transport by providing a buzzer, bell, and voice announcement.

7 Experimental Results

Firing Train Figure 5 indicates the firing train and the fire is detected by the sensor and this is the first stage of this project. This is a black color device and it has a lm-35 fire sensor. When the fire is detected in any coach, this fire sensor will detect the fire (Figs. 6 and 7).

Figure 8 shows the glowing of battery bulbs. This action can be performed automatically when the power supply is turned off. Figure 9 shows the water sprinkling to reduce fire. The water can be sprinkled through water pipes.

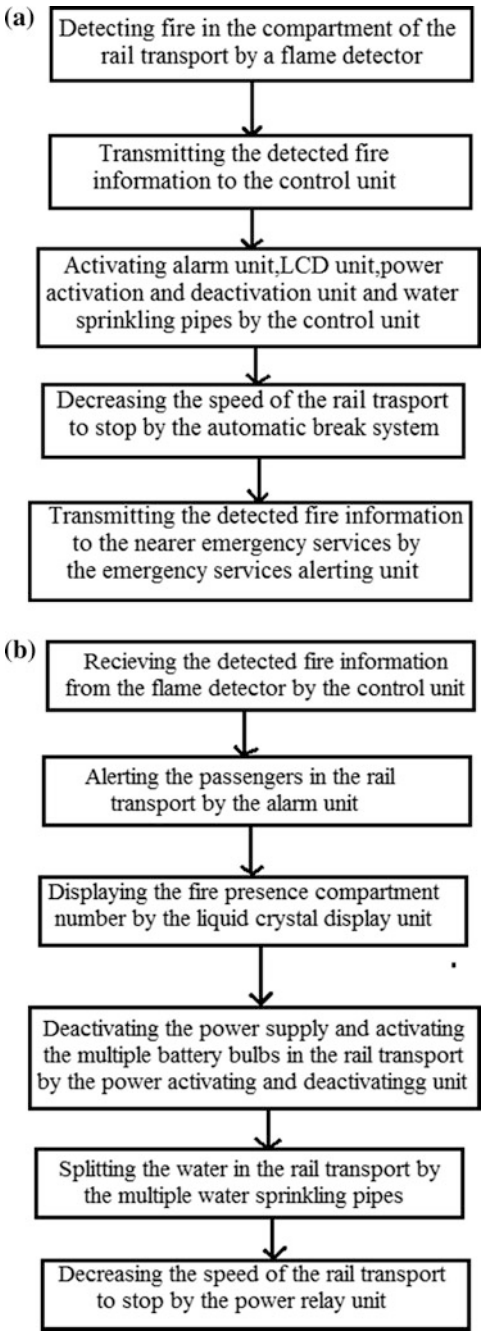

Fig. 4 **a** Method for preventing fire in the rail transport **b** Fire preventing steps in the rail transport

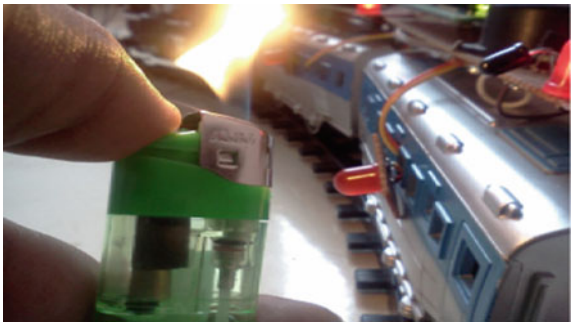

Fig. 5 Firing sensor

Fig. 6 Display

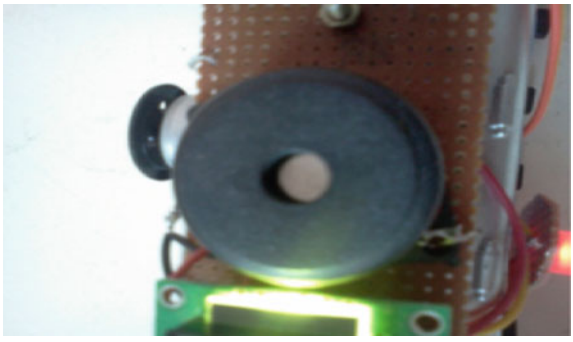

Fig. 7 Buzzer

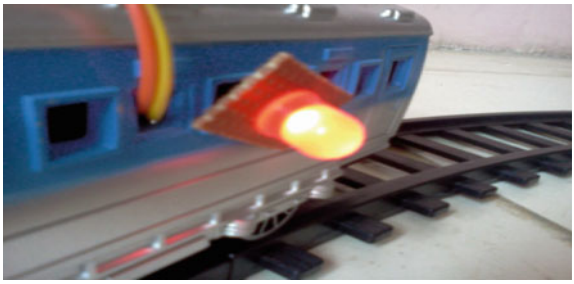

Fig. 8 Glowing of battery bulbs

Fig. 9 Water sprinkler

8 Conclusion

With the help of wireless sensor network prototype module, the microcontroller can sense the data from different sensors like fire sensor and smoke sensor which are used for taking necessary actions using communication network. Fire accidents are to be controlled and reduced with the concept of this "systematic method for preventing fire in rail transport" and rescue the lives of many people and save government property.

References

1. Stankovic JA, Abdelzaher TF, Lu C, Sha L, Hou JC Realtime communication and coordination in embedded sensor networks
2. NASA National Eronauticsand Space Administration
3. Bai X, Kumar S, Yun Z, Xuan D Lai T-H Deploying wireless sensors to achieve both coverage and connectivity
4. Craig WC (2003) ZigBee: wireless control that simply works. ZigBee Alliance

A Virtual Instrumentation-Based Data Acquisition System for Vibration Monitoring and Analysis

S. M. Shyni, K. Vasanth and C. Bhuvaneswari

Abstract The proposed work aims at monitoring the vibration of the bridge in virtual instrumentation namely LabVIEW for finding the age of the bridge ensuring the safety. The vibration is measured by the vibration sensor and the output is monitored through the PC by virtual instrumentation method. Embedded Controller is programmed to read the sensor value. The vibration sensor is connected to the Analog-to-Digital Converter of the controller through the signal conditioning. Then, the output is transmitted to the PC through the wireless technology. The firmware for the microcontroller is done by embedded 'C' program. The LabVIEW software processes the data from serial port of the PC and takes the appropriate precautions and actions to prevent the bridge from further damage.

Keywords Data acquisition · Monitoring · Vibration · Sensors
LabVIEW

1 Introduction

Structurally, concrete bridges became unstable because of material ageing, improper usage disruption, cracks, deterioration and damages due to strong vibrations like earthquakes. Hence, it is necessary to monitor the bridges often ensuring the safety. Various types of sensors are available for monitoring the bridge

S. M. Shyni (✉) · C. Bhuvaneswari
Department of Electrical and Electronics Engineering,
Sathyabama University, Chennai, India
e-mail: shynima@gmail.com

C. Bhuvaneswari
e-mail: bhuns_sekar@yahoo.co.in

K. Vasanth
Department of Electronics and Communication Engineering,
Vidya Jyothi Institute of Technology, Hyderabad, India
e-mail: vkbece@vjit.ac.in

H. S. Saini et al. (eds.), *Innovations in Electronics and Communication Engineering*,
Lecture Notes in Networks and Systems 33,
https://doi.org/10.1007/978-981-10-8204-7_16

vibration. In [1] Microfibre-based sensors are used for the simultaneous measurement of vibration and temperature. Wireless sensor network is employed for testing the bridge vibration [2, 3].

The virtual instrumentation system is introduced to measure vibration signals. The system includes a vibration sensor, a signal conditioning circuit, a data acquisition device and a PC [4]. Describes LabVIEW based data acquisition and analysis for vibration monitoring and vibration fault simulation systems (VFSS). The design of data acquisition and signal processing system of mechanical vibration signal was described in [5] based on LabVIEW software. In our paper, the vibration of the bridge is monitored and analyzed by virtual instrumentation method.

A data acquisition board is designed and constructed [6] for vibration monitoring using the ADXL202 acceleration sensor which can be connected to the computer through the microcontroller. The microcontroller plays an important role in the data acquisition and the communication with the computer. Wavelet technique is adapted to process the vibration signals acquired from the bridge monitoring in [7]. The vibration response of bridge is collected by a set of commercially available Mica2 Motes equipped with accelerometer [8]. The fuzzy logic decision system is used to collect vibration data with the help of fuzzy clustering ensuring safety [9]. Here, back propagation algorithm is used to predict the amount of damage in the bridge [10]. Vibration monitoring of bridges in one city or specific area using industrial soft middleware is presented in [11]. The comparison of bridge vibration analysis using accelerometers and piezoelectric cable sensor is presented. It has been concluded that piezoelectric cable vibration sensor is widely used for monitoring systems effectively.

2 Vibration Monitoring Data Acquisition System

The vibration of the bridge is monitored and is processed in virtual instrumentation namely LabVIEW. The entire process consists of three stages; namely sensing stage, signal conditioning stage and a processing stage. The sensing stage comprises a vibration sensor which measures the vibration of the bridge. These signals are amplified in the signal conditioning stage. Operational amplifiers (op-amps) are

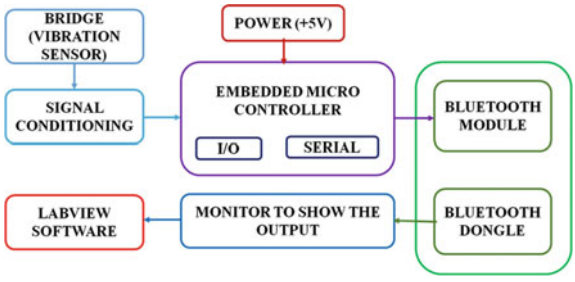

Fig. 1 Vibration monitoring data acquisition system

Table 1 Comparison of different types of sensors

Parameters	Piezoelectric sensor	Accelerometer	Electromagnet Velocity Sensor
Temperature range	−40–150 °C	−40–105 °C	−40–130 °C
Sensitivity	26 ± 8mv/g at 5 kHz	800mv/g at 1.5 g	26 ± 8mv/g at 5 kHz
Frequency range	Up to 20 kHz	Up to 11 kHz	Up to 15 kHz
Operation up to 120 °C	Yes	No	Yes
Mechanical durability	Excellent	Poor	Fair
Linearity	Good	Poor	Good

employed to carry out the amplification of the signal in the signal conditioning stage. These amplified signals are further processed in the processing stage. An Analog-to-Digital Converter (ADC) and a microcontroller are used in the processing stage. Figure 1 represents the vibration monitoring data acquisition system for the bridge.

2.1 Sensing Stage

In sensing stage, vibration sensors are used for measuring the oscillations of the bridge. Vibration sensors can be selected considering five main features: measuring range, frequency range, accuracy, transverse sensitivity and ambient conditions. Table 1 focuses on the various factors for choosing vibration sensor. The piezoelectric sensor is identified as the best vibration sensor because of its reliability, high degree of sensitivity and compact design. These sensors give a better performance over a wide temperature range and resist damage due to severe shocks and vibrations. Virtual instrumentation method is used to monitor the output of the vibration sensor through PC. Embedded Controller is programmed to read the sensor value. The vibration sensor is connected to the signal conditioning for further amplification.

2.2 Signal Conditioning Stage

Signal conditioning stage includes amplification, filtering, converting, range matching, isolation and any other processes required to make sensor output suitable for processing after conditioning. Figure 2 represents the block diagram of signal conditioning stage. The amplification of vibrated signals is carried out by operational amplifiers. The two main function of signal amplification is it increases the resolution and signal-to-noise ratio of the input signal. Low pass filters are employed to remove the unwanted signals. The signal conditioning connects the

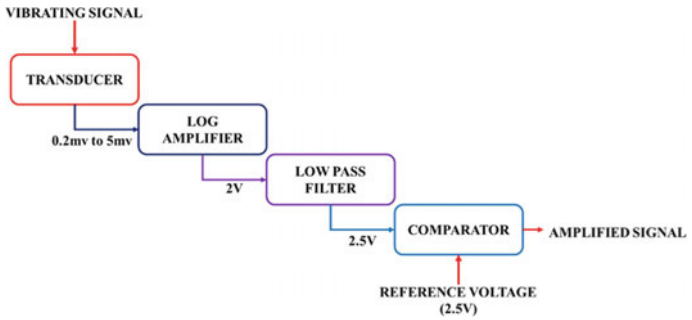

Fig. 2 Signal conditioning

vibration sensor to the embedded microcontroller. A transducer is a device capable of converting energy from one form into another. Transducers is connected at both the input and output stage of the measuring system. The input transducer converts the desired physical quantity into another energy form. The output transducer, called the actuator converts the energy into a form on which another independent system can react.

2.3 Processing Stage

The amplified signal from the signal conditioning is directed to processing stage, which consists of an Analog-to-Digital Converter (ADC) and an embedded microcontroller. The ADC used in the interfacing kit is PCF8591. The PCF8591 is a single-chip, single-supply low power 8-bit CMOS data acquisition device with four analog inputs, one analog output and a serial I^2C-bus interface. Various types of microcontrollers are compared in Table 2. The microcontroller of MCS51 series is selected as it is flexible and works better in the communication field.

Figure 3 shows the interconnection of embedded microcontroller between signal conditioning and Bluetooth module. The processed output of the microcontroller is transmitted to PC through Bluetooth.

Table 2 Comparison between various types of microcontrollers

Microcontroller	No of bits	Processor (MHz)	Flexibility (ISP)	Power consumption	Cost
MCS 51 series	8 bit	16–300	Easy	54 mW	300
PIC	16 bit	4–33	Complex	10 mW	400
ARM	32 bit	33	Complex	100 mW	900

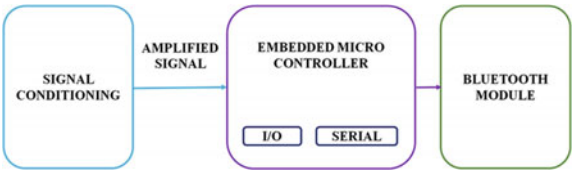

Fig. 3 Embedded microcontroller

2.4 Bluetooth Module

Bluetooth aims at allowing short-range communications between several devices. It is an industrial specification for wireless personal area network. Bluetooth is a radio standard and communications protocol primarily designed for low power consumption, based on low-cost transceiver microchips in each device. Table 3 shows the Comparison of Bluetooth over other wireless communication devices.

In our system, the Bluetooth device transmits the obtained input data whereas the PC receives the data through the Bluetooth dongle device. This acquired data is monitored and analyzed by the LabVIEW software in order to take the appropriate precautions and actions to prevent the bridge from further damage.

3 Virtual Instrumentation with LabVIEW

A bridge has been selected for monitoring the vibration levels and its safety factor. It is constructed with fastening screw Grey cast iron M 8 × 25 of quality 8.8 cm. The screw is made of aluminum M 8 × 30 with quality 8.8 cm. Its tightening torque is 20 ± 5 Nm. Its position is arbitrary mounted. It is resistant to saline fog and industrial climate. The entire setup is connected to the bridge to monitor the

Table 3 Comparison of Bluetooth over other wireless communication devices

Technology	Operating frequency	Data transfer rate	Cost	Range	Current required	Connection type
Bluetooth	2.4 GHz	720 kbps	Low	10 m	Medium	FHSS
Radio frequency	915 MHz	Slow	High	30 m	High	FHSS
Wi-Fi	2.4 GHz	11 Mbps	High	300–1400 ft	High	DSSS
ZigBee	2.4 GHz	20–200 kbps	Low	1000 m	Medium	–

vibration. If the vibration is below 80 m/s^2, it will not be detected. Figure 4a shows the analysis of a bridge when vibration is not detected. This analysis shows that the vibration level is normal.

If the vibration is above 80 m/s^2, the vibration will be detected. Figure 4b shows the analysis of a bridge when vibration is detected. It is indicated by the glowing of light. This points out that the vibration level is high.

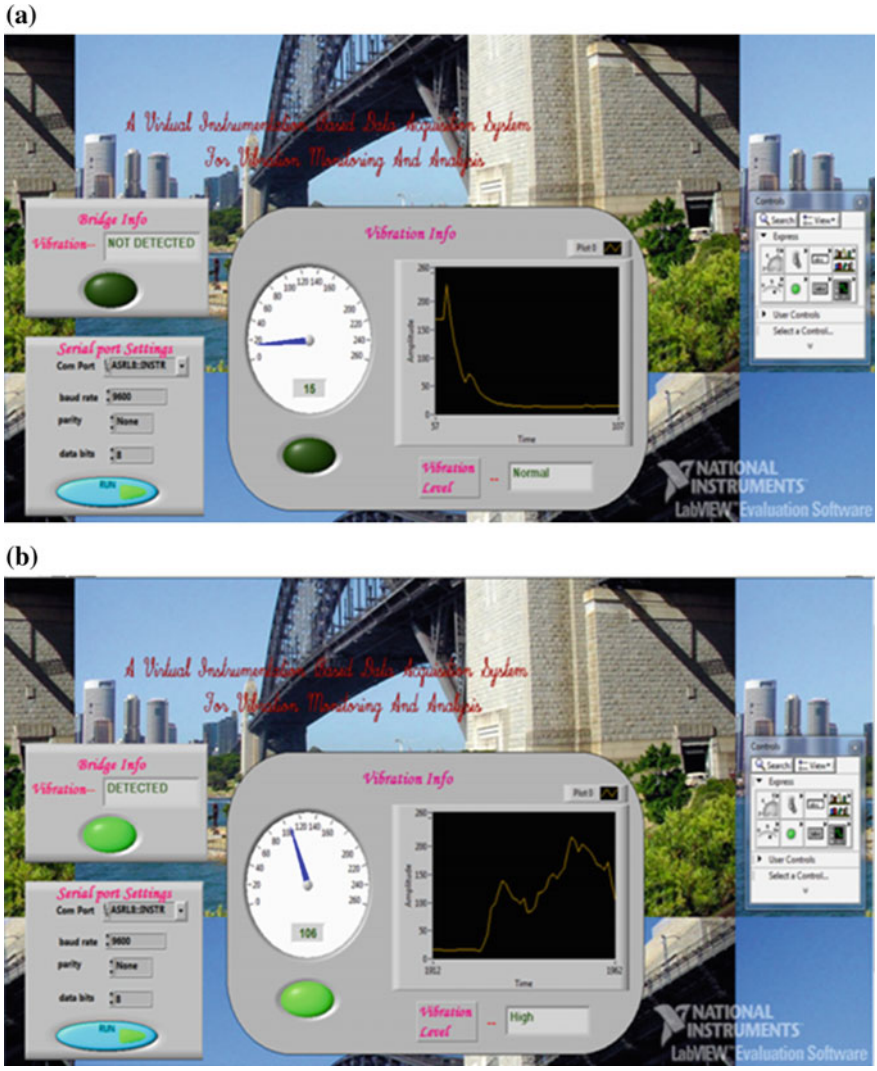

Fig. 4 **a** Simulation analysis when vibration is not detected. **b** Simulation analysis when vibration is detected

4 Conclusion

A virtual instrumentation based data acquisition system for vibration monitoring and analysis has been implemented. This project will help to a great extent to monitor the vibration occurred on the bridge and to prevent the bridge from further happening damages. The vibration monitoring can be done thoroughly without any disturbance. Acquiring the data from microcontroller to the PC through Bluetooth automatically by wireless communication is implemented. Experimental results indicate that LabVIEW is more simple, visual and reliable for monitoring and analyzing the vibration with high-speed performance.

References

1. Zhang Q, Zhu T, Zhang J, Chiang KS (2013) Micro-fiber-based FBG sensor for simultaneous measurement of vibration and temperature. IEEE Photonics Technol Lett 25(18):1751–1753
2. Whelan MJ, Gangone MV et al (2009) Real-time wireless vibration monitoring for operational modal analysis of an integral abutment highway bridge. Eng Struct:2224–2235
3. Whelan MJ, Gangone MV, Janoyan KD (2009) Highway bridge assessment using an adaptive real-time wireless sensor network. IEEE Sens J 9(11):1405–1413
4. Gani A, Salami MJE (2002) A LabVIEW based data acquisition system for vibration monitoring and analysis. In: Student conference on research and development, pp 62–65
5. Zhao H (2011) Application of LabVIEW in the design of data acquisition and signal processing system of mechanical vibration. In: International conference on mechatronic science, electric engineering and computer, pp 2551–2554
6. Katalin A (2008) Microcontroller based system for vibration analysis. In: IEEE international conference on automation. Quality and testing. Robotics, vol 2, pp 171–174
7. Chen X, Gao Z et al (2010) Application of wavelet analysis in vibration signal processing of bridge structure. In: International conference on measuring technology and mechatronics automation, vol 1, pp 671–674
8. Ali S, Shaikh FK et al (2014) Smart structural monitoring—a case of bridge damage detection. In: International conference on wireless communications, vehicular technology. Information theory and aerospace & electronic systems, pp 1–5
9. Meyyappan L, Jose M et al (2003) Fuzzy-neuro system for bridge health monitoring. In: International conference of the North American fuzzy information processing society, pp 8–13
10. Shao P, Zhang X, Ge Y (2010) An approach to distributed remote bridges monitoring based on soft middleware. In: International conference on signal acquisition and processing, pp. 172–176
11. Shimoi FN, Cuadra C (2015) Comparison of vibration analysis for a bridge using accelerometers and a piezoelectric cable sensor. In: IEEE multi-conference on systems and control, pp 595–600

Nighttime Vehicle Detection Using Computer Vision

Sushruth Badri, Sri Soumya Somu, K. Vamsi Meghana and V. Aparna

Abstract Many accidents occur during the night due to the improper visibility of the road ahead. One of the main reasons is of the discomfort posed by the high beam light of the oncoming vehicle, glares our eyes while driving. This discomfort might result in a lapse of concentration thereby resulting in an accident. Our primary aim is to automatically detect the head light using tracking and segmenting the frames extracted from the video signals that are fed by a camera and automatically switch the lighting condition of our vehicle from low beam to high beam or vice versa to avoid discomfort to the driver of the oncoming vehicle. We use MATLAB to simulate the results of our algorithm. In MATLAB, we mainly use computer vision and image processing to make necessary alterations to the input to get the necessary output.

Keywords Segmentation · Tracking · Blob analysis · Headlight detection Computer vision

1 Introduction

90% of a driver's reaction depends on his visibility of the oncoming road condition and vehicles, and visibility of the same is severely limited during the night, making it dangerous to drive at night. Currently while driving the car headlight of the vehicle is switched on throughout the night at full power. The number of vehicles on road is increasing drastically making it even more difficult to drive at night. During the night, most of the accidents occur due to dazzling of the headlight. The headlight beam of the oncoming vehicle directly affects the driver's eyes and results in blurred vision or glare. It takes around 3–8 s for the driver to come back to the normal vision. This nighttime vehicle detection system can switch the headlights from high beam to low beam or vice versa without the intervention of the

S. Badri · S. S. Somu · K. Vamsi Meghana · V. Aparna (✉)
Manipal Institute of Technology, Manipal, India
e-mail: aparna.sreejith@manipal.edu

H. S. Saini et al. (eds.), *Innovations in Electronics and Communication Engineering*,
Lecture Notes in Networks and Systems 33,
https://doi.org/10.1007/978-981-10-8204-7_17

driver by processing some road and light conditions fed by the camera. Our main objective is to reduce the brightness on the eyes of the oncoming observer while making sure that the user will not be caused discomfort. It is important for the auto dipper to differentiate between headlight and taillight and then dim the light accordingly. Our primary goal is also to run the system of switching from low beam to high beam and vice versa without any manual effort. Low beams ensure less illumination whereas high beams provide clear visibility of the road ahead when vehicles are absent. Safety is always important while travelling at nighttime. A black and white camera is also sufficient to detect the cars and identify whether it is a headlight or a taillight depending on the brightness (Headlights provides high illumination and taillights provide low illumination). Segmentation, tracking and detection are the three main steps of our project.

The proposed system can be implemented in MATLAB. Then it can further be implemented in hardware.

2 Methodology

Our proposed method consists of the following four steps:

Pre-processing:

At first in MATLAB, the video sample is imported using VideoFileReader. The number of training frames is set and the input is taken from the camera and demarcated into corresponding frames. Then each frame is cropped to get only the area of interest. The frame is cropped and then evaluated to eliminate the street lights since these lights might also be detected as oncoming vehicular lights in later steps. Hence, we crop and remove the above part which contains street lights. Each input frame from the camera undergoes this process and all the further steps are done on these cropped frames.

Segmentation:

Segmentation is used to make the identification of the headlight in a much easier way. Image segmentation is the process of dividing the image into different parts which can be further processed separately.

1. Background Subtraction

Background subtraction method is used to partition the frames to foreground (white) and background (black). The frames with RGB values are converted into greyscale images which will greatly simplify the further processing of the input frames. Greyscaling discards the color values of an image and simplifies the process of differentiating the headlights from the background greatly compared to its RGB counterpart. In MATLAB, the Foreground Detector System object draws similarities between a video frame and a background model, and determines which areas of the frame lie in the foreground and which ones lie in the background. It then

masks the foreground to show only the background of the present frame. After grey-scaling the images will have to go through the filtering process. This process filters out any noise in the image. The next step is to remove other unwanted objects and noises. We can do that using clean foreground detector. We then remove the noises from the foreground to obtain only the headlights, street lights and other significant and few unwanted lights.

2. Identifying Round Objects

Using thresholding, we convert the RGB frame into a greyscale image. Then prepare for boundary tracing. By using morphological functions, we remove all objects containing fewer than 20 pixels. This will eliminate any pertaining noise in the frame giving us a clearer frame to process further. For the next step we are required to compute the area enclosed by different light blobs to eliminate the unwanted blobs. Incomplete blobs result in faulty area computations. Hence, we fill any holes and use regionprops to estimate the area bounded by each of the boundaries that are traced. Option 'noholes' speed up the processing by stopping bwboundaries from searching for inner contours. We then compute the circularity of the blobs using the following formula.

$$\text{circularity} = (\text{Perimeter}.\hat{}2)./(4 * \text{pi} * \text{area})$$

After finding the circularity of each blob, we eliminate the ones which have a circularity of less than 0.94. This will help any irregular or non-circular reflections on the roads. By this process, we finally identify the round shape objects and remove the vehicle headlight reflections identified on the road. We now have only the required lights that we need to track to decide whether to dip the light or not.

Tracking:

Detected lights in the frame are tracked using Blob Analysis technique indicating a green box around the lights detected. In MATLAB, we use vision. Blob Analysis returns a blob analysis object, H, with each stated property set to the stated value. We use BoundingBoxOutputPort to find coordinates of bounding boxes. We set this property to true. This gives us coordinates of the bounding boxes. We then set the minimum and maximum blob area to 50 and 500 or may vary according to the surrounding conditions. The step of blob analysis computes and returns the statistics of input image. We then insert a rectangular green box to track the vehicle headlights. In this way, we take every frame and try to detect the vehicle headlights. Even if one light is detected, the light can be switched from high beam to low beam. When no oncoming lights are detected, the lights will be in high beam. In this way, we can successfully detect the lights and provide a better way of switching the lights automatically to avoid any discomfort experienced by the driver in switching the lights and the oncoming vehicle driver. This is a simple yet very effective way for the above purpose as can be seen in the results of simulations that have been shown in the result analysis section.

3 Result Analysis

Segmented Result:

1. *Foreground* Segmentation:

   The lights are shown in white and the background in black (Fig. 1).

2. Clean Foreground Result:

   The noise is eliminated from the segmented frame (Fig. 2).

3. Detecting Round Objects:

   The boundaries are added to round objects and circularity is calculated. The objects with circularity less than 0.94 are neglected (Fig. 3).

Tracking:

The detected lights are tracked as follows (Fig. 4).

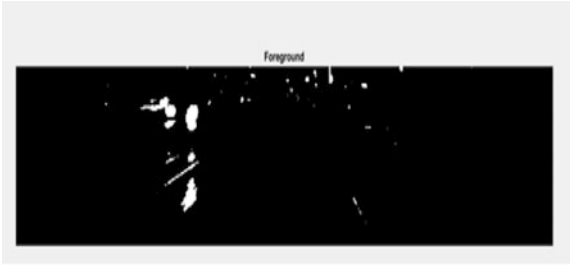

Fig. 1 Foreground segmentation result

Fig. 2 Clean foreground result

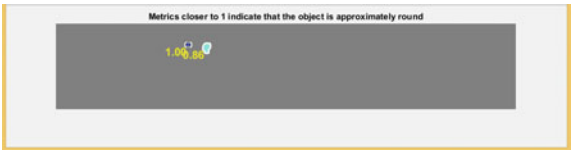

Fig. 3 Detecting round objects

Fig. 4 Lights are tracked and green boxes are inserted around them

4 Future Scope

We presented a software for detecting and tracking the oncoming vehicles for driving safely during the night. The system performance is satisfactory for real-time conditions. One of the many advantages of this system is that it is a simple algorithm and works well in real-time conditions. The classification mistakes between vehicles, road signs and other features of the frame are very low and can be improved using distinctive invariant features and by increasing the size of the testing and training data. The results are encouraging and several improvements will be included to the current implementation in the future. Further improvements can be done in the classification phase to increase the accuracy of the classification of various features of the frame. To attain a more consistent tracking of the oncoming headlights, some parameters such as the blob area and shape of the blob can be experimented. Hardware implementation can also be sought after, owing to the projects simple hardware demands.

References

1. Jakub Sochor B (2014) Fully automated real-time vehicles detection and tracking with lanes analysis
2. Alcantarilla PF, Bergasa LM, Jiménez P, Parra I, Llorca DF (2011) Automatic lightbeam controller for driver assistance. Mach Vis Appl. https://doi.org/10.1007/s00138-011-0327-y
3. Jurić D On-road night-time vehicle light detection and tracking methods overview
4. Nemade B (2016) Automatic traffic surveillance using video tracking. Procedia Comput Sci 79:402–409

Detection of Inadequate Growth of Early Childhood and Development of Adult Disease Alert via Embedded IoT Systems Using Cognitive Computing

S. J. Sugumar, Sirisha Madiraju, Tejash G. Chowhan, Thota Anurag and Syed Awais Ahmed

Abstract The objective of the work is to bring the awareness of the childhood growth problems and the corresponding developmental adult diseases like CVD and Type 2 diabetes using IoT-embedded systems. Nowadays, there are a wide range of abnormalities found in the early growth of the child due to malnutrition and enteric infections which increase the risk for the metabolic syndrome. This leads to stunting (poor height growth) and obesity in the young generation. The medical record of the child from the infant stage to the age of 18 years is stored in the cloud database and is compared with the reference records and provides information about growth syndromes and guides to appropriate doctor and the hospital. Cognitive computing approach using support vector data description algorithm is applied in the outlier detection. The odd data which are likely to have stunting is marked using the outlier detection in the cloud dataset and an alert is sent to the parents about the stunting effect on the child. The proposed idea helps in building a young and energetic healthy nation.

Keywords Child growth · Stunting · BMI · Z-score · IoT

1 Introduction

Providing a healthy generation to the nation has been a long-term goal of Indian Government through Pediatric Healthcare centers. However, these centers are not successful because of many reasons like lack of better hospitality, good laboratory test equipment and people to maintain data are not specialized doctors. The result of these issues in pediatric healthcare centers has been that early diagnosis or treatment

S. J. Sugumar (✉) · S. Madiraju · T. G. Chowhan · T. Anurag · S. A. Ahmed
Department of ECE, Guru Nanak Institutions Technical Campus, Hyderabad, India
e-mail: sjsgnitc@gmail.com

S. Madiraju
e-mail: madiraju.sirisha@gmail.com

H. S. Saini et al. (eds.), *Innovations in Electronics and Communication Engineering*,
Lecture Notes in Networks and Systems 33,
https://doi.org/10.1007/978-981-10-8204-7_18

of diseases is not done [1]. At the fundamental level, PHCs does two vital jobs: First, the study of diseases based on symptoms and their therapy either at the centers or through recommendation. Second, health culture leading to improved sanitation and hindrance of childhood diseases in particular stunting that leads to effects of diabetes and cardiovascular diseases [2]. The proposed idea, therefore, is to increase the effectiveness of health care in rural via IoT-enabled medical devices. The Internet of Things allows people and things to get connected Anytime, Anyplace, with Anything, and/or Anyone. Smartphones and the tablets are the main contributors for IoT. Mobile devices are like windows to IoT and are capable of performing a wide range of tasks for both patients and doctors. Huge volume of data exchange is also performed by mobile devices in addition to providing mobility and connectivity [3].

2 Related Work

Lei and Yu proposed an idea of smart hospital access based on Internet of Things in order to overcome the defects of the present hospital information access system, such as the rigid information point, firm networking mode and so on. Investigations says that the solution to the existing problem of early and better diagnosis and cure of children is the design of smart hospital [4]. Soumya Kanti Datta advocates for applying IoT for custom-made smart homes with healthcare. The main assistance of the paper is giving a combined approach for detection, execution, and communication with physical devices, producing high-level abstraction from wearable sensors using Machine-to-Machine Measurement (M3) framework, getting cross-domain sensor data together by utilizing M3 and home automation control devices using data from health sensor [5]. Moeen Hassanalieragh emphasizes on the analysis and challenges for IoT in realizing this idea for the health care in future. The accessibility of information at previously unimagined and time-based longitudes attached with a novel creation of smart handling algorithms can: (a) simplify a development in the exercise of medicine, from the recent post factor diagnose-and-treat combative standard, to a practical framework for prediction of diseases at an emerging period, joined with avoidance, nurse back to health, and on the whole management of health as a substitute of disease, (b) permit personalized treatment and supervision options targeted mainly to the precise situations and requests of the individual, and (c) helps in reducing health care cost while spontaneously improving results [6].

India carries the largest burden of developmental adult disease and deaths in the world in the last two decades. ordinary heights of Indian men and women are 5 ft 5 in (165 cm) and 5 ft (152 cm) correspondingly which is based on a 2006 study by National Institute of Nutrition (Indian Council of Medical Research). The average American height for men is 5 ft 10 in. (177 cm) tall. The average height of China people is 5 ft 6 in. (167.1 cm). “Stunting” refers to the abnormality in the growth of height (less height growth) because of less nutritional eating habits. The height-for-age

z-scores considered in this case is greater than two standard deviations less than the threshold value. The worst metabolism during fetal leads to low weight accrues in the initial stages of life followed by poor height gain in children and adults. It is evident that cardiovascular disease (CVD) and type-2 diabetes (T2DM) are the major concerns of stunting.

3 Proposed Methodology

The idea is to connect the people in rural and weaker urban areas to the doctor in a child specialty hospital through the IoT system developed. The growth rate and the disease symptoms of a child obtained from various medical data such as current, standard and the physiological biomarkers measured using wearable sensors outfitted in a small range radio signal as ZigBee or low power Bluetooth, used to move data to the concentrator. Then the concentrator relays the aggregated data to a cloud system for a long-term storage using the Internet. The stored data as well as data incurred by the medical record from the respective health center is taken into consideration and a reference is set using the following algorithms and processes which are compared with the patient child's data. Storage, analytics, and visualization are the major parts of the Cloud processing. *Analytics* involves diagnoses and prognoses of child growth conditions and diseases using sensor data along with e-Health records or reference data. *Visualization* is a pictorial representation of data and analyses in a readily visible format which has a vital role in any such systems, which are shown in Fig. 1.

Cognitive computing is an extremely powerful tool that helps medical researchers in performing analytics to determine solutions to life-threatening diseases. Sensor data analysis can theoretically utilize a wide range of pattern

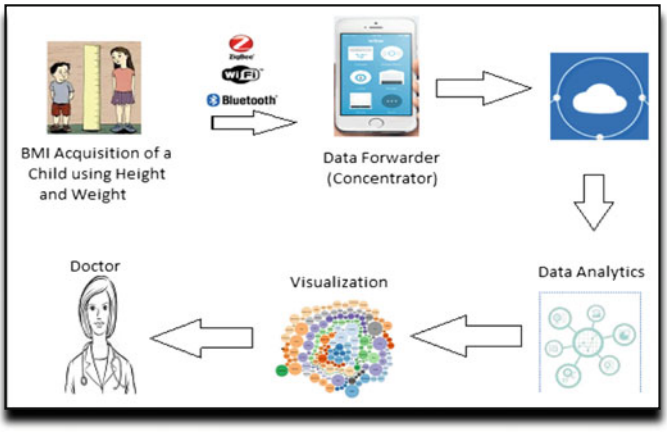

Fig. 1 IoT-based communication architecture of the proposed system

recognition amongst the stored medical reference records and patient child's data and machine learning technique [7]. The healthcare centers and hospital-based medical readings that are taken which represents a massive opportunity for data analytics and machine learning algorithms which can potentially identify correlations between sensor observations and pre-stored medical records and reference data. The use of analytics with the reference data and the patient child's measured data together can improve accuracy, allows detection of inadequate growth of the child and enable personalization. The **Predictive analytics** used in the descriptive data to forecast likely outcomes in the detection of early childhood growth failure in future.

Outlier detection is a predictive analytics approach which is aimed at finding irregular samples, i.e., medical data of child who does not match the reference values in a given data set $\{x_i\}$ [8]. In the same way as clustering, the definition of similarity between samples plays a central role in outlier detection, because samples that are dissimilar from reference medical records are usually regarded as outliers. The objective of outlier detection is to judge whether a newly given data set $\{x_i'\}n'$ $i' = 1$ has the same property as the original data set $\{x_i'\}n$ $i = 1$. The similarity between samples is utilized in outlier detection, while similarity between data sets is needed in change detection. If $n' = 1$, i.e., only a single point is provided for detecting change, the problem of change detection may be reduced to an outlier problem [9]. If the labels of inliers and outliers are available for $\{x_i\}_{i=1}^{n}$, outlier detection can be formulated as supervised classification. Learning a stable decision boundary between inliers and outliers is often difficult as a parameter for outliers may change over time. However, there are robust methods against outliers. The proposed method here is Support vector data description, used to detect outliers. This is an unsupervised outlier detection algorithm that does not involve explicit density estimation. More specifically, for kernel function *K(x, x'),* Lagrange dual optimization [8] is used in this analytics which is given by

$$\max_{\alpha}\left[\sum_{i=1}^{n}\alpha_i K(X_i,X_i)-\sum_{i,j=1}^{n}\alpha_i\alpha_j\left(X_i,X_j\right)\right] \tag{1}$$

subject to $0 \le \alpha_i \le C$ for $i = 1, \ldots, n$.

$$\sum_{i=1}^{n}\alpha_i = \sum_{i=1}^{n}\alpha_i = 1 \tag{2}$$

and outlier criterion becomes

$$K(x,x) - 2\sum_{j=1}^{n}\alpha^{\wedge}{}_j K(x_i,x_i) - a_i > 0 \tag{3}$$

where, for i such that $0 < \alpha^{\wedge}{}_i < C$,

$$\alpha_i = k(x_i, x_i) - 2\sum_{j=1}^{n} \alpha^{\wedge}{}_j K\left(x_i, x_j\right) \tag{4}$$

When $K(x_i, x_i)$ is constant for all $i = 1,\ldots, n$, which is satisfied e.g., by the Gaussian kernel.

$$K\left(x, x^{'}\right) = \exp\left(-\frac{\left\|x - x^{'}\right\|^2}{2h^2}\right) \tag{5}$$

The above optimization problem is simplified as

$$\min_{\alpha} \sum_{i,j=1}^{n} \alpha_i \alpha_j K\left(x_i, x_j\right) \tag{6}$$

subject to $0 \leq \alpha_i \leq C$ for $i = 1,\ldots, n$.

$$\sum_{i=1}^{n} \alpha_i = 1 \tag{7}$$

Outlier detection results are dependable on the choice of the trade-off parameter C (Gaussian bandwidth) and the appropriate tuning parameters.

4 Results and Discussion

The experimental setup consists of health monitoring technology made of Raspberry Pi 3 (Home Health Hub reference platform), contains ARM Cortex-A53 with abilities such as Wi-Fi connectivity and power optimization shown in the Fig. 2 and the Things Speak readings are shown in Fig. 3. The hub measures patient via different sensors and stores it in the cloud securely. These stored data can be accessed by those who are there for patient's care. The proposed idea is first developed as a prototype and tested verified in in-house lab testing. The model is implemented with selected primary health centers and hospitals. As this model is focused on rural usage, we will provide the model to rural people and test its user-friendly nature.

The proposed algorithm uses inlier and outlier models to extract data from the cloud. The proposed method here is Support vector data description, used to detect outliers. In Fig. 3 the circled samples are the results of support vector data description for Gaussian Kernel and are regarded as outliers for the effect of stunting at age 12. Out of 10 samples given as input, it has detected 5 samples as

Fig. 2 Experimental setup

outliers, i.e., 5 children's in the group of data has been affected by stunting effect and those children need to be taken care for further medical care otherwise they will end up with CVD or Type 2 diabetes.

The results show that the children with moderate height, weight, and BMI during the initial stage of life and increased weight in a later stage, develop CVD in adult age.

Markers of risk

The mechanism used as an ideal marker of threat for evaluating the effects of nutrition on upcoming stunting risk. Potential markers of risk incorporate the following:

1. *Height-for-age Z-score*: This Z-score less than 2 standard deviations less than the mean is recognized as a factor stunting and the markers of nutritional deficiency. However, in many cases where genetics is considered, the height Z-scores will not be the best analyst of threat [10].

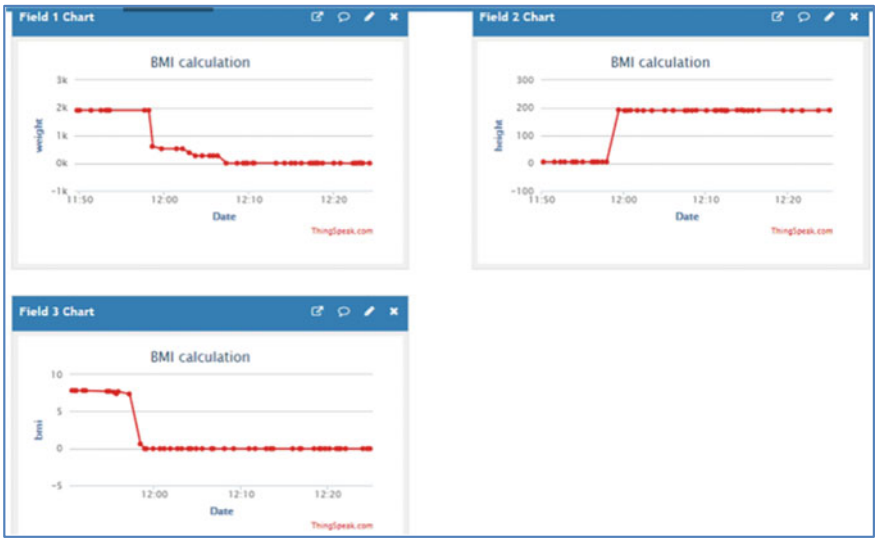

Fig. 3 Thing speak output

2. *BMI-for-age Z-score*: It renders the benefit as it takes into consideration both height and weight. Children with inadequate growth due to undernourishment or abdominal infections are likely to be lean and low fat mass and thus have a less weight for height. Thus, as a marker of risk, BMI-for-age is more likely to affect children with tall physique genes who are relatively undernourished but not technically stunted.

Figures 4 and 5 show the stunting effect of an individual with height, weight and BMI z-score. Figure 4 shows the stunting effect where the child with poor BMI and height in the early childhood gains weight in the adult age and also it shows that increase in the height is less. In Fig. 5, healthy childhood growth is referred which

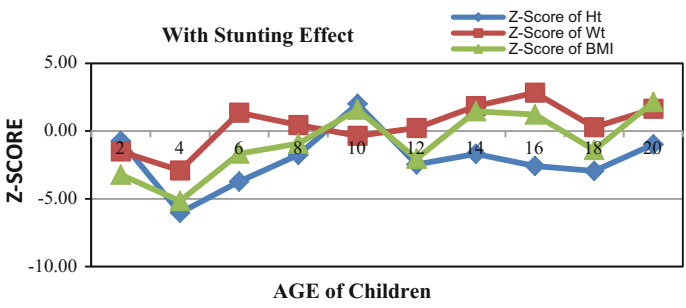

Fig. 4 With stunting effect

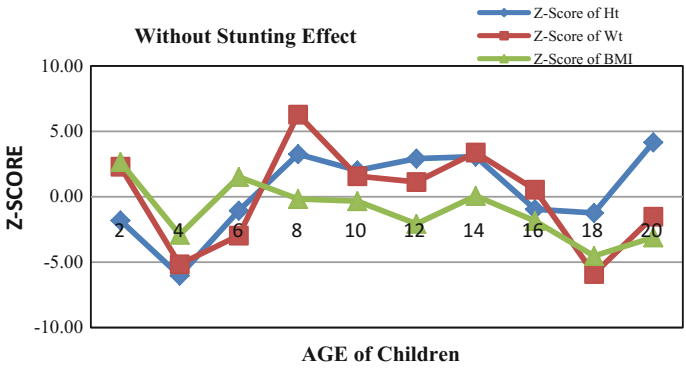

Fig. 5 Without stunting effect

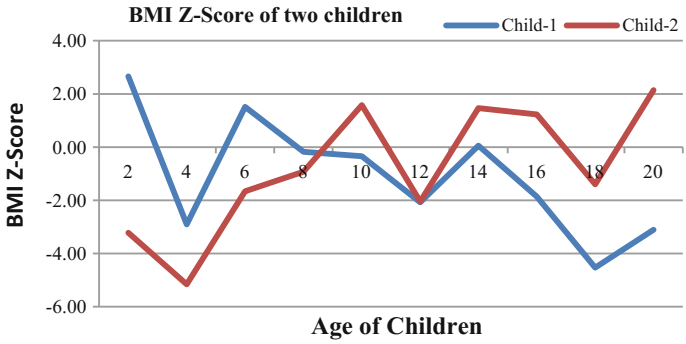

Fig. 6 BMI Z-score of two children

leads to a good height growth in the adult age. In overages the individual with low BMI in childhood may suffer from obesity. BMI Z-score of individuals is compared in the Fig. 6. It shows that child with poor childhood growth has large BMI in the adult age leading to more weight and less height. The child with healthy growth in childhood has good height in adult age. There is a rapid weight gain in the child with low BMI in childhood, this may also lead to Type-2 diabetes, glucose intolerance.

5 Conclusion

The proposed methodology helps in detecting stunted child by comparing the child's medical record with the reference (previously stored medical record) and notifies the parents to make necessary steps in improving the health of the child.

Steps are taken in reduction of weaker children in the country. The stored medical data of child can be accessed anywhere any time. The mother will be educated on medical care for child health via smart devices. Locally endemic diseases and its identification will be prevented and controlled. Collection and reporting of vital statistics about child specialty doctors and hospital services will be done via IoT system. The early adult death rate due to lack of knowledge of medical information with the people is improved. Better and proper medical services will be offered to the people. The algorithm developed extracts the odd data from the cloud in the detection of inadequate childhood growth and alerts for development of adult disease which helps in reduction of number of stunted children in the country.

References

1. Levey AS et al (2003) National Kidney Foundation practice guidelines for chronic kidney disease: evaluation, classification, and stratification. Ann Intern Med 139(2):137–147
2. DeBoer MD et al (2012) "Early childhood growth failure and the developmental origins of adult disease: do enteric infections and malnutrition increase risk for the metabolic syndrome? Nutr Rev 70(11):642–653
3. Gubbi J et al (2013) Internet of things (IoT): a vision, architectural elements, and future directions. Future Gener Comput Syst 29(7):1645–1660
4. Yu L, Yang L, Zhu X (2012) Smart hospital based on internet of things. JNW 7(10): 1654–1661
5. Datta SK et al (2015) Applying internet of things for personalized healthcare in smart homes. In: 24th Wireless and optical communication conference (WOCC), 2015. IEEE
6. Hassanalieragh M et al (2015) Health monitoring and management using internet-of-things (iot) sensing with cloud-based processing: opportunities and challenges. In: IEEE international conference on services computing (SCC), 2015. IEEE
7. Hossain MS, Muhammad G (2016) Cloud-assisted industrial internet of things (iiot)–enabled framework for health monitoring. Comput Netw 101:192–202
8. Sugiyama M (2015) Introduction to statistical machine learning. Morgan Kaufmann
9. Zhang Y, Duffield N (2001) On the constancy of internet path properties. In: Proceedings of the 1st ACM SIGCOMM workshop on internet measurement, ACM
10. Saunders SR, Hoppa RD (1993) Growth deficit in survivors and non-survivors: biological mortality bias in subadult skeletal samples. Am J Phys Anthropol 36(S17):127–151

Design and Implementation of IoT-Based Monitoring and Control of a Strategic Telerobot

S. J. Sugumar, M. Sirisha, M. Srivani, N. Susmita and M. Krishna Teja

Abstract Strategic design and implementation of IoT-based monitoring and controlling of a telerobot using Raspberry Pi is presented. To control the telerobot a set of commands from cloud computing system (ThingSpeak) is communicated via Wi-Fi system. The cloud computing is a type of internet-based computing that provides shared computer processing resources and data to computers and other devices on demand. Raspberry Pi owes its advances in integrated with ARM and Wi-Fi with less power consumption. The cloud-based control, which helps the operator at remote to maintain a frequent communication with the telerobot, and execute prognostic control actions. The accurate motion of the telerobot is guaranteed by the instantaneous control that runs perpetually. The telerobotics is tested in-house using the proposed strategic design with a different task, and its performance is verified with the benchmark test.

Keywords IoT · Telerobotics · Raspberry Pi · ThingSpeak

1 Introduction

Telerobotics is the area of robotics concerned with the control of semi-autonomous robots from the distance using IoT-based wireless network (like Wi-Fi, Bluetooth, and similar). The applications of telerobotics reside in places where human utilization is less possible due to riskiness of life [1]. Self-governing robot systems are still not viable due to lack of artificial intelligence. The rapid development of the Internet on Things networks provide various Internet-based telerobotics

S. J. Sugumar (✉) · M. Sirisha · M. Srivani · N. Susmita · M. K. Teja
Department of ECE, GuruNanak Institutions Technical Campus, Hyderabad, India
e-mail: sjsgnitc@gmail.com

M. Sirisha
e-mail: madiraju.sirisha@gmail.com

H. S. Saini et al. (eds.), *Innovations in Electronics and Communication Engineering*,
Lecture Notes in Networks and Systems 33,
https://doi.org/10.1007/978-981-10-8204-7_19

applications such as telesurgery, tele-training, planetary exploration, fire-fighting, war-front operations, search/rescue operations, landmine detection and clearance, and entertainment.

The telerobot can be build using embedded IoT devices like Arduino, Raspberry Pi can be connected to the Internet. Fetching or uploading data to ThingSpeak storage which is an IoT cloud service provider using APIs is done by these boards. This stored data can be accessed by other clients like Mobile, Tablet, laptop connected to Internet using ThingSpeak APIs.

In this design, we incorporate telerobot control to complete the task given by the remote operator sporadically, for which the robot trajectories are planned and executed by the onboard controller. At times the operator can adjust the length of these path segments to maintain frequent interactions with the telerobot. Only when the task to be carried out is well defined in advance this can happen. The proposed design is used to build the telerobotics testbed and its capabilities whose performance were demonstrated by benchmark experiments.

2 Related Works

Some of the recent research methods on IoT-based telerobot is discussed here. In previous robots, the navigation of robot is controlled through GSM or either through Bluetooth/XBEE. Robots were navigated through a simple SMS, but you can't see visually what's there in front of the robot. The status of the sensor is feedbacked to the system through an SMS. In the same way with Bluetooth/XBEE. James Kuffner coined the term Cloud Robotics to explain a new approach to robotics that takes the benefit of the Internet as a resource for massively parallel computation and real-time sharing of vast data resources. A. John Paul Antony and Dr. S. Rajpandian [2] presented "Web-Based Control and Monitoring Of Telepresence Robot" in which each Telerobotic control operations performed from Techbot Web User Interface by using JS and PHP. As the Techbot Web User Interface can be accessible to anyone with Internet connection, it renders local installation unnecessary. Thus, users can easily control from anywhere over Internet, the TechRobot in anytime. Many telepresence robots are created in this world. The work we propose uses a strategic approach to resolve the on path challenges and travel to the targeted position with given delay response time.

3 Proposed System Model

The proposed IoT-based Raspberry Pi Robot is performed in such a way the movement directions are written in python script controlled through ThingSpeak for the real-time remote control and monitor of the telerobot. Figure 1 illustrates the communication architecture of the strategic telerobot.

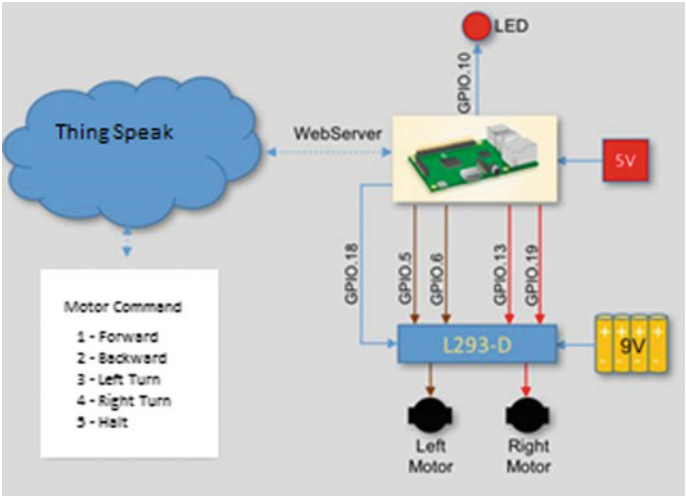

Fig. 1 Communication architecture for telerobotics

The change in the direction of the robot is informed via a user command that are transferred to a Thing Speak cloud which is usually done from a web interface through a web browser. The cloud system processes the user commands using scripts written in python and sends to the Wi-Fi module connected to the telerobot. The Thing Speak commands are used to control the robot movements like forward, backward, left, right and stop. The ThingSpeak framework software runs on Raspberry Pi which runs with Raspibian Jessie operating software. The python file includes the library files of GPIO library and is used to change the IO pins mode and the data of the IO pins. HTTP, URL, json and web browser libraries are used to interface the pi with the ThingSpeak cloud. The python file first sets all the GPIO pins as output pins which are given to the motor driver module. The motor driver module runs the two DC motors in the required direction. The direction controls are read from the ThingSpeak cloud channel field through an url command using channel read API key. The control command is given in the ThingSpeak channel field using MATLAB Analysis window, which is available in the ThingSpeak environment.

The hardware components include Raspberry Pi, motor driver (L293D), Wi-Fi transmitter, 60 rpm dc motors and a 12 V battery to run motors. The Wi-Fi transmitter is used to activate the receiver Wi-Fi inbuilt in Raspberry Pi module. The ThingSpeak cloud is opened on any mobile or desktop or laptop provided with username and secured password. The controls to the robot can be varied through channel fields of the ThingSpeak and the same is updated in graphical form in MATLAB visualization. This can be made public or private view using an option at the time of creation of the channel. Commands can be updated for every 15 s. The Raspberry PI along with ThingSpeak cloud acts as Internet of Things (IoT) to control the telerobot remotely. This can be accessed from anywhere provided with Internet.

4 Differential Drive Model

The strategic telerobot works with two control variables called rotation speeds of wheels φ_1 & φ_2 and three output variables $\dot{x}$, $\dot{y}$ and $\dot{\theta}$, differential drive (a non-holonomic) [3] system with less control variables than output variables. The arrangement of two wheels of telerobot in the same axis makes them the wheels to rotate independently. The robot takes a straight path with same rotation speed in two wheels, whereas a curved path with difference in the rotation speed and a point turn when same speed but opposite in direction with middle of the two wheels as center of turning. The forward kinematics equations [4] of elementary model, which neglects all the physical issues such as fiction, inertia and mechanical structure inaccuracy, is used in differential drive model. The translational speed $(\dot{x}_R)$, instantaneous rotation (ω_1) and total rotation $\left(\dot{\theta}\right)$ are given by

$$\dot{x}_R = r\frac{\dot{\varphi}1 + \dot{\varphi}2}{2} \tag{1}$$

$$\omega_1 = r\frac{\varphi_1}{2l} \tag{2}$$

$$\dot{\theta} = \frac{r(\dot{\varphi}_1 - \dot{\varphi}_2)}{2l} \tag{3}$$

The robot references frame (R) with refer to the general inertial reference frame (I) is to be known to define the robot motion and the robot motion is given as:

$$\dot{\xi}_I = \begin{bmatrix} \dot{x} \\ \dot{y} \\ \dot{\theta} \end{bmatrix} = f(l, r, \theta, \varphi_1; \dot{\varphi}_2) \tag{4}$$

The standard orthogonal rotation transformation gives the relation between references frame as follows:

$$R(\theta)^{-1} = \begin{bmatrix} \text{cosine}(\theta) & \text{sine}(\theta) & 0 \\ -\text{sine}(\theta) & \text{cosine}(\theta) & 0 \\ 0 & 0 & 1 \end{bmatrix} \tag{5}$$

The between frames motion of a robot:

$$\dot{\xi}_R = R(\theta)\dot{\xi}_I \tag{6}$$

$$\dot{\xi}_R = R(\theta)^{-1}\xi_R \tag{7}$$

Substituting 90° point turn where $\theta = \frac{\pi}{2}$ into Eq. (5):

$$\dot{\xi}_{\mathrm{R}} = R\left(\frac{\pi}{2}\right)\dot{\xi}_1 = \begin{bmatrix} 0 & 1 & 0 \\ -1 & 0 & 0 \\ 0 & 0 & 1 \end{bmatrix} \begin{bmatrix} \dot{x} \\ \dot{y} \\ \dot{\theta} \end{bmatrix} = \begin{bmatrix} \dot{y} \\ -\dot{x} \\ \dot{\theta} \end{bmatrix} \tag{8}$$

Inverse of Eq. (5):

$$R(\theta)^{-1} \begin{bmatrix} \mathrm{cosine}(\theta) & -\mathrm{sine}(\theta) & 0 \\ \mathrm{sine}(\theta) & \mathrm{cosine}(\theta) & 0 \\ 0 & 0 & 1 \end{bmatrix} \tag{9}$$

Thus the differential derive model is obtained by substituting Eqs. (1), (3), (8) and (9) into (7):

$$\dot{\xi}_I = \begin{bmatrix} \mathrm{cosine}(\theta) & -\mathrm{sine}(\theta) & 0 \\ \mathrm{sine}(\theta) & \mathrm{cosine}(\theta) & 0 \\ 0 & 0 & 1 \end{bmatrix} \frac{r}{2} \begin{bmatrix} \dot{\varphi}_1 + \dot{\varphi}_2 \\ 0 \\ \frac{\dot{\varphi}_1 - \dot{\varphi}_2}{l} \end{bmatrix} = \begin{bmatrix} \dot{x} \\ \dot{y} \\ \dot{\theta} \end{bmatrix} \tag{10}$$

The mathematical model is transferred into Matlab coding model with the forward standard orthogonal rotation transformation into a Matlab function block. The robot motion is obtained by solving the function and verified with random input simulation.

Robot Dynamics and Estimation [5]. The dynamics of a three-wheel design in which the front wheel pivots for steering, the distance between the rear wheels *a* and the distance between the rear axle and pivot point of the front wheel *b*. The robot's *x-y* position on the course $p = (px, py)$ as the position of the center of the back axle. The configuration of this robot is shown in Fig. 2. The robot platform is made stable using left and right wheel actuators as two independent DC motors and a free wheel caster. The linear velocities v_L and v_R are used for the left and right wheel to move to a desired point *(x, y)* and desired orientation *q*.

$$v_L = r_w.\omega_L \tag{11}$$

$$v_R = r_w.\omega_R \tag{12}$$

The linear velocities of right and left wheels gives the relation between the linear *v(t)* and angular w*(t)* speeds of the platform (2) where r_c is the radius of robot chassis. It is assumed as the movement of the wheels on the plane is slip free.

$$v(t) = \frac{v_L(t) + v_R(t)}{2}, \quad \omega(t) = \frac{v_R(t) - v_L(t)}{r_c} \tag{13}$$

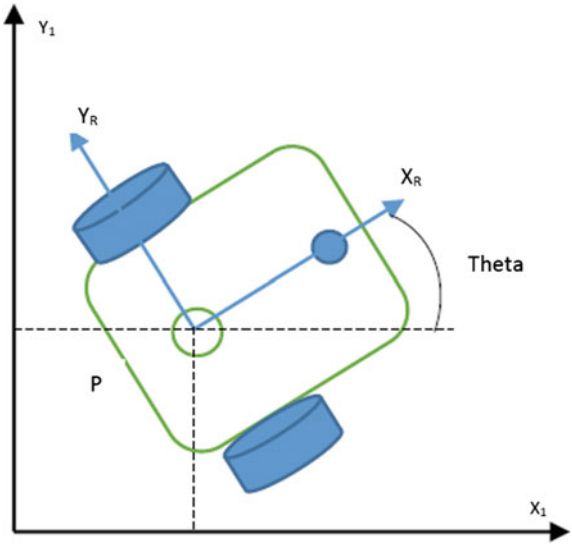

Fig. 2 Communication architecture for telerobotics

The kinematic model is simulated using the following:

- $v_L = v_R$—robot moves forward,
- $v_L < v_R$—robot turns left,
- $v_R < v_L$—robot turns right.

Initially, parameters are assumed as: rc = 0.15 m, (*xini, yini*) = (−0.5[m], −0.5 [m]) and θ = 0°rad. The simulated robot behavior is shown in the result section.

5 Telerobot Subsystem

Subsystem: *Actuators and Sensors*. The prototype described in this work uses DC motors as actuators [6]. In order to estimate the mechanical capacity of these actuators, it is proposed to use the maximum velocity, acceleration, and weight of the system as

$$\upsilon = 1\,\mathrm{m/s},\ a = 1\,\mathrm{m/s^2},\ m = 1.74\,\mathrm{kg}. \tag{14}$$

Based on the mass m and acceleration a, force F is calculated as

$$F = ma = (1.74\,\mathrm{kg})\left(1\,\mathrm{m/s^2}\right) = 1.74\,\mathrm{N}. \tag{15}$$

Force, F_{rm} for the right wheel motor and F_{lm} for the left wheel motor. One motor provides half of the total force required, that is,

$$F_{\mathrm{rm}} = F_{\mathrm{lm}} = F/2 = 1.74N/2 = = 0.87\ \mathrm{N} \tag{16}$$

The wheel diameter is 0.07 m (r = 0.035 m), the required torque for each motor is

$$\tau_{\mathrm{rm}} = F_{\mathrm{rm}} r = \tau_{\mathrm{lm}} = F_{\mathrm{lm}} r = (0.87\,\mathrm{N})\,(0.035\,\mathrm{m}) = 0.03045\,\mathrm{Nm}, \tag{17}$$

Since $v = \omega_{\mathrm{w}} r$, the angular velocity is related to each wheel and it is determined by

$$\omega_{\mathrm{w}} = \upsilon/r = 1\mathrm{m/s}/0.035\,\mathrm{m} \approx 28.5714\,\mathrm{rad/s} \approx 272.8282\,\mathrm{rpm}. \tag{18}$$

Hence, the power required, P_{w}, is calculated as follows:

$$P_{\mathrm{w}} = \tau_{\mathrm{rm}} \omega_{\mathrm{w}} = (0.03045\,\mathrm{Nm})\,(28.5714\,\mathrm{rad/s}) \approx 0.869\,\mathrm{W}. \tag{19}$$

So that the motors selected are *GNM3150* (24 V, 55 W) and the desired velocity ωd between 65 and 90% of the no-load motor velocity (i.e., 3526 rpm), and thus

$$2291.9\ \mathrm{rpm} < \omega_d < 3173.4\ \mathrm{rpm}. \tag{20}$$

The power for the motors is supplied with two YUASA batteries 12 V@12 Ah.

6 Results and Discussion

The hardware and software components used to develop the telerobot are L293D motor drive, ultrasonic sensor, Raspberry Pi, DC motor, 12 V battery, ThingSpeak and python. The description of the telerobot and the kinematic control and the operations performed ThingSpeak Interface over an internet is explained in this section. Telerobot interfaced with ThingSpeak is shown in Fig. 3. In-house-fabricated robot with differential drive mechanism along with two DC motors controlled by a controller is used for the experiment. The motors are powered using two 12 VDC batteries, Raspberry Pi board with 3.3 V and driver with 9–24 V, 15 A to drive DC motor.

The strategic movements the telerobot needs to follow which includes tasks such as 'travel to a point', 'travel to a position', 'track a path', 'travel in a loop' and 'sidestep hurdles'. The strategic tasks are defined to make the telerobot to track, monitor and transfer the information about the environment.

To make the robot to travel to a point and position the initial angular movement and velocity is verified with the control algorithm developed wherein distance of robot from instantaneous position to the goal (target) position are measured and robot control vectors viz. linear velocity v and angular velocity w are obtained for

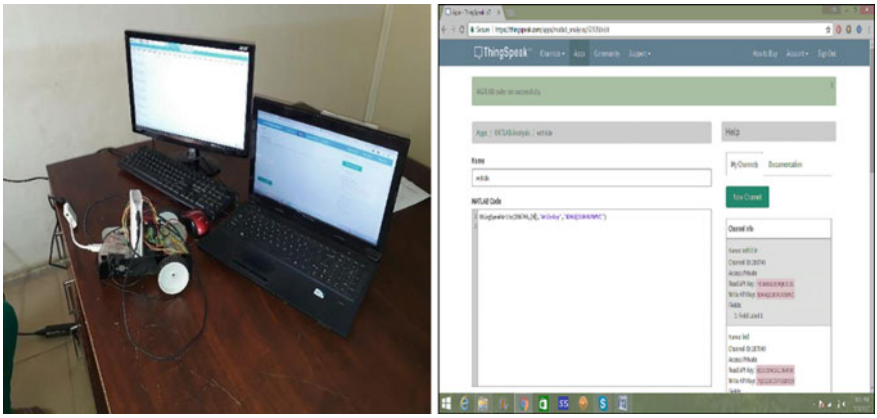

Fig. 3 Telerobotic interface with ThingSpeak

the robot and is made to run the distance to reach the target. The simulation results to verify the angular velocity and angular displacement is shown in Fig. 4. Both the velocity and displacement makes the robot to make initial movement after 30 milliseconds of time as depicted in the results. Both the parameters have been verified for left and right wheel.

To make the telerobot to track a path and loop the Kinematics motion model is applied to the robot and are transformed to right and left wheel speeds to control the robot. The maximum speed of robot motors is set to 60 RPM. The two wheels of differential drive robot considered here are driven independently. All the three wheels of the robot contribute to the robot motion individually and assumed to be slip free. When both the wheels are at same speed, the robot moves forward. Right movement is achieved when left wheel is more speed than the right wheel and vice

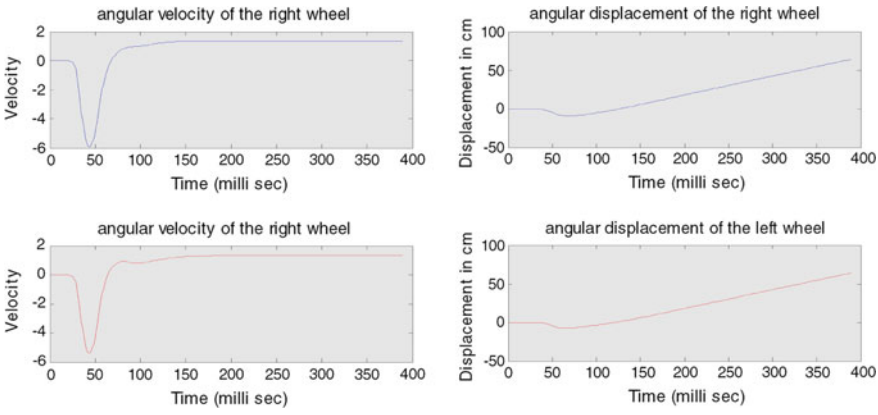

Fig. 4 Simulation results for angular velocity and displacement

versa for left movement. Sharp turns are achieved by driving both the wheels in opposite direction with same speed. The third castor wheel is used for stability in the motion of robot.

In the simulation, when $v_L < v_R$, there is a linear increase in orientation θ which turns the robot left in accordance with the coordinate system. When $v_R < v_L$, there is a linear decrease in orientation θ which turns the robot right in accordance with the coordinate system. When orientation θ is zero the robot moves forward and the x coordinate varies linearly and y coordinate remains unchanged. The results for direction of movement to track the robot is shown in Figs. 5 and 6.

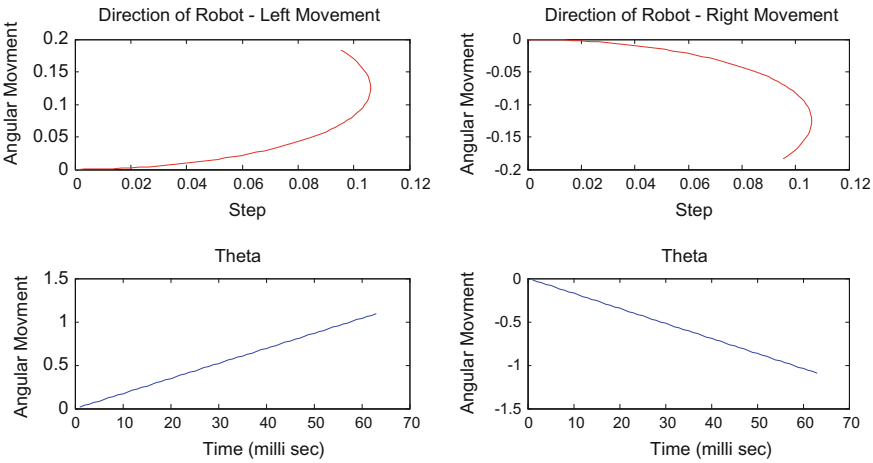

Fig. 5 Direction of telerobot left and right movement

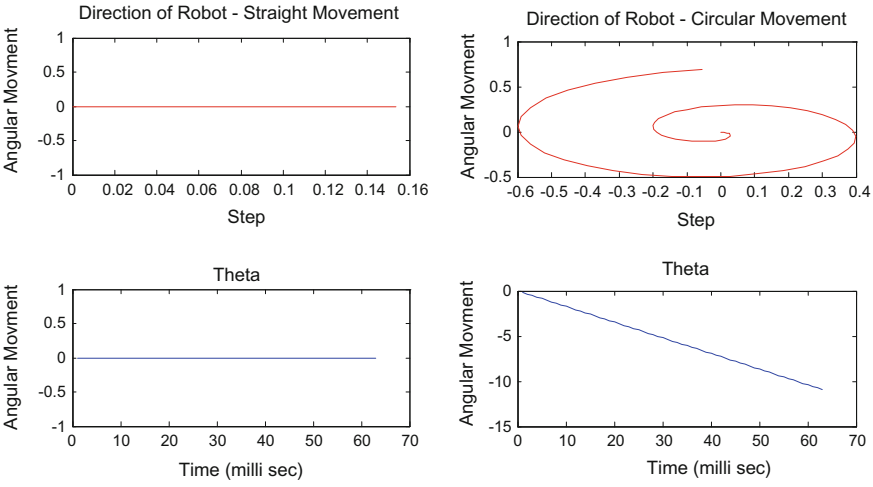

Fig. 6 Direction of telerobot in straight and circular movement

The hurdles which are in the path are solved by using an ultrasonic sensor. The sensor data is fed to the Raspberry Pi which compares with the heading angle of the robot and determines the direction of movement on right or left unit the obstacle is resolved on the path.

7 Conclusion

In this work, a telerobot system for monitoring and tracking applications using a strategic control algorithm is developed and simulated using MATLAB programming. The telerobot is being controlled using IoT wireless network with internet to make the robot travel to a position and overcoming the hurdles on the path. In this work the telerobot is validated with the kinematic model developed to implement the strategic movements. The telerobot provides a 4 s delay response to follow the commands which are given through the cloud system developed. This delay in response is based on communication architecture which is via the Wi-Fi wireless network and the response provided by electromechanical arrangement of the strategic telerobot. Future it is planned to integrate real-time voice-based GPS monitoring and tracking applications with delay response time optimized will be deliberated.

References

1. Jhansi Rani K, Niranjan Reddy K (2015) IOT based secure system for monitoring and control of coal mine environment of robotics. Int J Recent Adv Eng Technol (IJRAET), ISSN (Online) 3(9):2347–2812
2. Antony AJP, Rajpandian S (2014) Web-based control and monitoring of telepresence robot. Int J Innovative Res Sci Eng Technol 3(3) (Mar 2014)
3. Myint C, Win NN (2016) Position and velocity control for two-wheel differential drive mobile robot. Int J Sci Eng Technol Res (IJSETR) 5(9) (Sept 2016)
4. Malu SK, Majumdar J (2014) Kinematics, localization and control of differential drive mobile robot. Glob J Res Eng: Robot Nano-Tech 14(1) (Version 1.0 Year 2014)
5. Armah S, Yi S, Abu-Lebdeh T (2014) Implementation of autonomous navigation algorithms on two-wheeled ground mobile robot. Am J Eng Appl Sci 7(1):149–164
6. Aung WP (2007) Analysis on modeling and simulink of DC motor and its driving system used for wheeled mobile robot. In: Proceedings of world academy of science, engineering and technology, vol 26, pp 299–306 (December 2007)

Part III
VLSI

Design of Wallace Tree Multiplier Using Sparse Kogge-Stone and Brent–Kung Adders

M. Lokesh Chowdary, A. Mallaiah and A. Jaya Lakshmi

Abstract In many digital signal processors and different applications, the massive role is played by the multiplier. In any VLSI design mainly power, area and speed play a massive role, by improving any of these parameters the overall performance will be improved. Array multipliers and Tree multipliers are various types of multipliers, among those Wallace tree multiplier belongs to Tree multiplier which is better than booth multiplier in terms of speed, area, design complexity. Different existing approaches had been developed for the reduction of partial products. One of the existing approaches uses full adders and half adders in Wallace tree multiplier, but by using this approach number of stages would be increased when higher order multiplication is considered. To overcome this, an approach is proposed which includes 4:2 compressors & parallel prefix adders in Wallace tree multiplier design.

Keywords Wallace tree multiplier · 4:2 compressors · Brent–Kung adder Sparse Kogge-Stone adder

1 Introduction

Multiplier plays a massive role in most of the applications like ALU, DSP & other PROCESSORS. Multiplication process must run faster in order to decide the fast response of the overall system design. The fast response of multiplication will be decided on the selected multipliers like Array multiplier, booth multiplier, Braun multiplier, etc., and also on the various multiplication techniques. Fast response of the multiplier is also based on the adders, there are different types of adders like CSA, RCA, CLA adder, etc. In general Wallace tree multiplication [1], if two *N*-bit

M. Lokesh Chowdary (✉) · A. Mallaiah
Gudlavalleru Engineering College, Gudlavalleru, Andhra Pradesh, India
e-mail: lokesh.maddipati@gmail.com

A. Jaya Lakshmi
Vardhaman College of Engineering, Hyderabad, Telangana, India

H. S. Saini et al. (eds.), *Innovations in Electronics and Communication Engineering*,
Lecture Notes in Networks and Systems 33,
https://doi.org/10.1007/978-981-10-8204-7_20

numbers are multiplied then N^2 partial product terms would be generated and the overall result would contain 2 N terms. In the existing approach to the Wallace tree multiplier [2] the partial products formed in the various stages are reduced with the help of Full adders [2] and Half adders. Further, the delay in the overall design can be reduced by using modified full adder [2] in the Wallace tree multiplier which in turn reduces the partial product terms. In order to improve the overall performance, a method is proposed to reduce partial products [3] in which the Wallace tree multiplier is designed by using a 4:2 compressor [3]. Parallel prefix adders [4] like Sparse Kogge-stone adder and Brent–Kung adder are used for the final addition of partial product terms in the multiplier. Further reduction of a number of cells used in the multiplier an extension for Kogge-Stone adder is designed which is Sparse Kogge-Stone adder [5]. Brent–Kung adder is high speed and area efficient adder.

2 Wallace Tree Multiplier

Two positive integers can be multiplied by using Wallace tree multiplier, and partial product terms that are reduced can be added up to two final intermediate results. As the number of gates increases for higher order multiplication, the complexity will be high so to reduce this the partial product reduction phase is used. This utilizes the combination of 4:2 compressors, full adder, and half adders. And also the final addition of last two rows is done by using sparse Kogge-Stone adder and Brent–Kung adders to achieve more speed. Wallace tree multiplication processing stages divided into three: Generation of partial products, Reduction of partial products, Addition of partial products (Fig. 1).

In $N * N$ multiplication, the partial product could be generated by performing AND operation between two operands, which involves N^2 AND gates.

Partial product terms can be reduced by different approaches like half adders, 3:2 compressors [3] and 4:2 compressors [6]. Depend upon this various ways are used to reduce the partial product term 3:2 or 4:2 compressors are used. A 3:2 compressor generates outputs as the sum and carry, out of three inputs is available if one input is carry then it will be considered as full adder (Fig. 2).

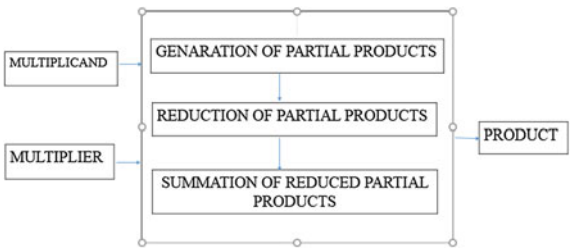

Fig. 1 Wallace tree multiplier block diagram

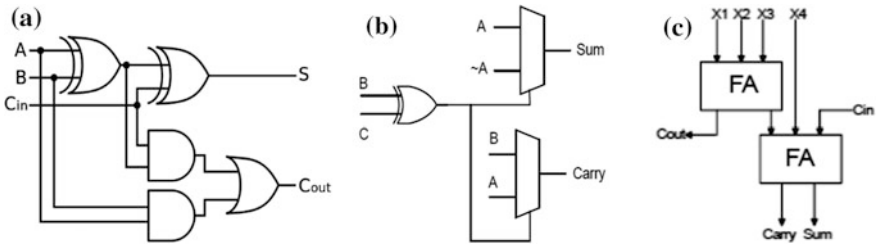

Fig. 2 **a** Conventional 3:2 compressor **b** Modified full adder **c** 4:2 compressor block

In 3:2 compressor, for generation of sum it requires two XOR gates, and for carry it requires one XOR, two AND, one OR gate delays. So, for the reduction of delay, these are replaced by one XOR and two MUX.

The 4:2 compressor [6] has 4 inputs A, B, C, D along with this there will be one more input which is obtained from the previous block carry output and 2 outputs, sum bit S and carry it C are produced, along with this a carry out bit Cout is produced which will be given as input to next compressor block.

As the number of full adders increases, the XOR gates required for the generation of the sum will be increased due to which the delay will be increased so to improve the speed the XOR gates are replaced by MUX's. The carry out bit Cout is propagated to the next compressor block as input, i.e. carry in bit Cin block. The delay and the logic complexity will be reduced by using parallel prefix adders [7]. The partial products reduction in Wallace tree multiplier using full adders and half adders is shown in Fig. 6 and further reduction of partial products using 4:2 compressors is shown in Fig. 7 (Figs. 3 and 4).

3 Parallel Prefix Adders

Three major steps involved are (1) By using no. of input bits, the carry generation and carry propagation signals will be evaluated. (2) Prefix computation: In this, the carry signal will be calculated in parallel. (3) Finally, the sum bits are generated for the given inputs.

4 Brent–Kung Adder

Kogge-stone adder occupies a larger area, and its performance is high. Brent–Kung adder occupies less area when compared to Kogge-Stone Adder and it has less wiring complexity and its operation starts with the generation and propagation signals from the input. This Brent–Kung adder mainly contains black and grey cells which use the generation and propagation signals to generate the output (Fig. 5).

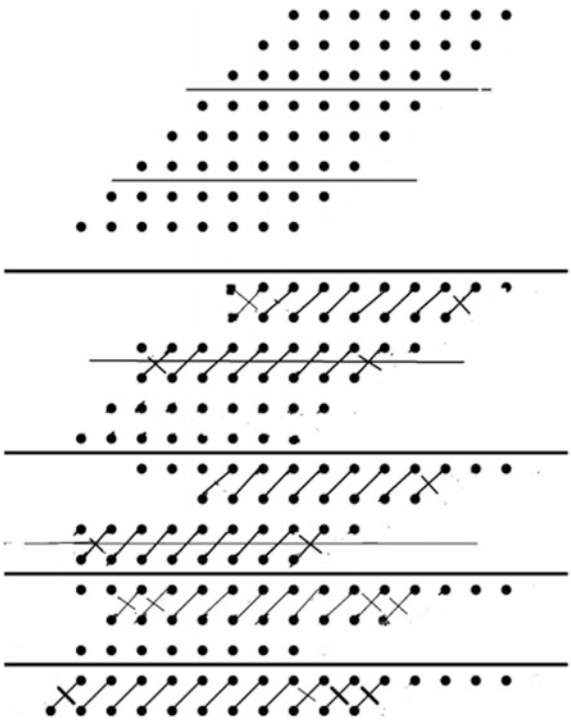

Fig. 3 Wallace tree multiplier partial product reduction using full adder

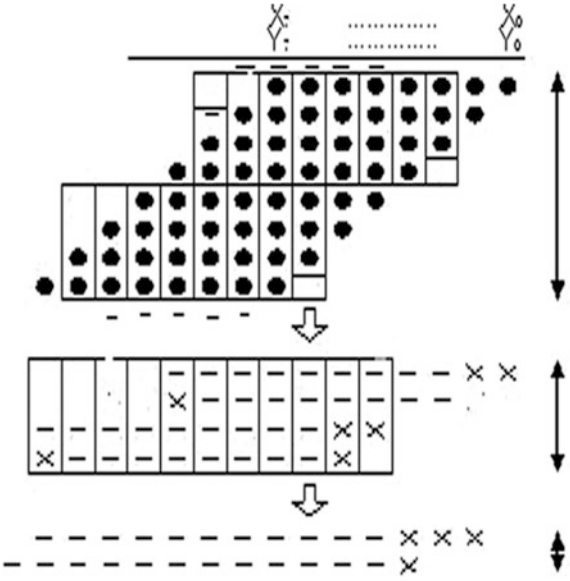

Fig. 4 Wallace tree multiplier partial product reduction using 4:2 compressor

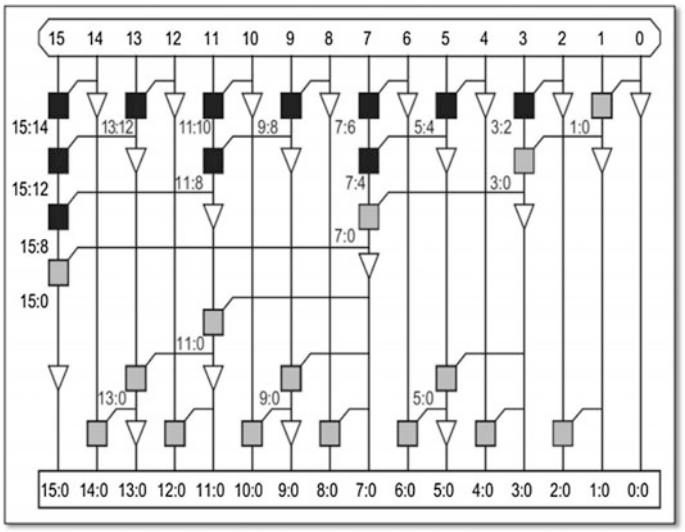

Fig. 5 Brent–Kung adder

Brent–Kung adder tree has (2 $\log_2$ N − 1)stages. The maximum fanout for each bit stage is limited to 2. The logic level of Brent–Kung adder [8] is low. The wiring tracks allowed is 1. The total cells used to construct Brent–Kung adder tree is 2*N*.

5 Sparse Kogge-Stone Adder

The Sparse Kogge-Stone adder [5] is divided into two halves out of those two halves the lower half is occupied with a large number of smaller Ripple Carry adder and the upper half is filled with Carry tree. This means as the lower half is filled with Ripple Carry adder is says that the Sparse Kogge adder [5] ends up with Ripple Carry adder. This adder is used in order to improve the speed of the block further (Fig. 6).

6 Results

The simulation results and comparison tables of Wallace tree multiplier using different compression techniques with parallel prefix adders, i.e. sparse Kogge-Stone adder and Brent–Kung adder is as follows (Figs. 7, 8, 9, 10, 11 and Tables 1, 2):

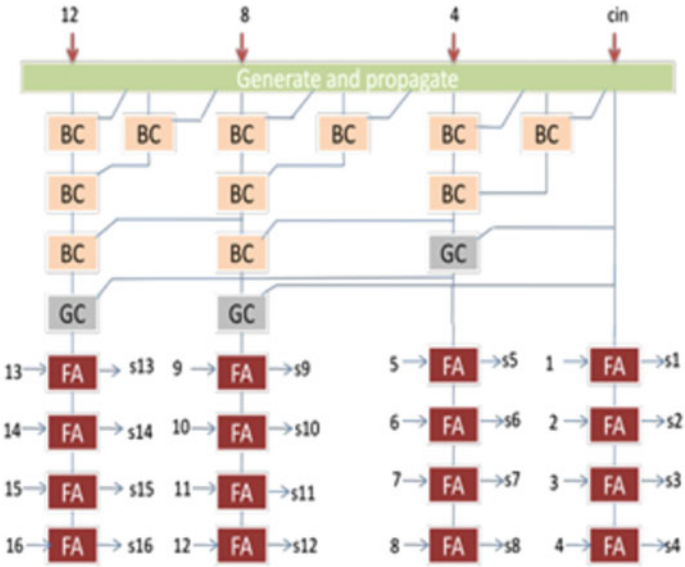

Fig. 6 Sparse Kogge adder [5]

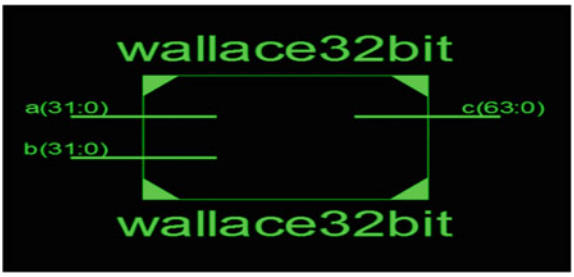

Fig. 7 RTL schematic diagram for 32 bit Wallace tree multiplier

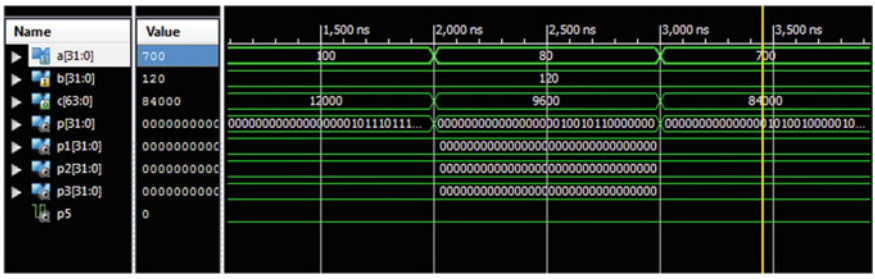

Fig. 8 Bit Wallace tree multiplier using 4:2 compressor and Kogge-Stone adder

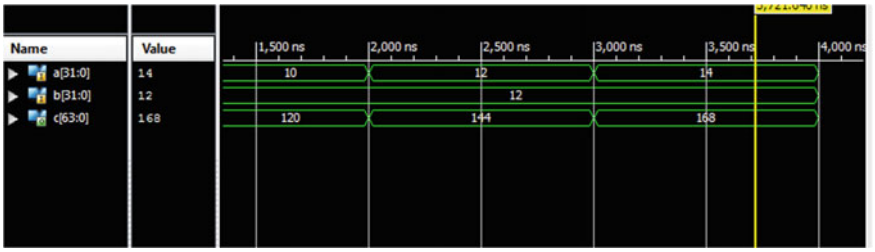

Fig. 9 Bit Wallace tree multiplier using 4:2 compressor and Brent–Kung adder

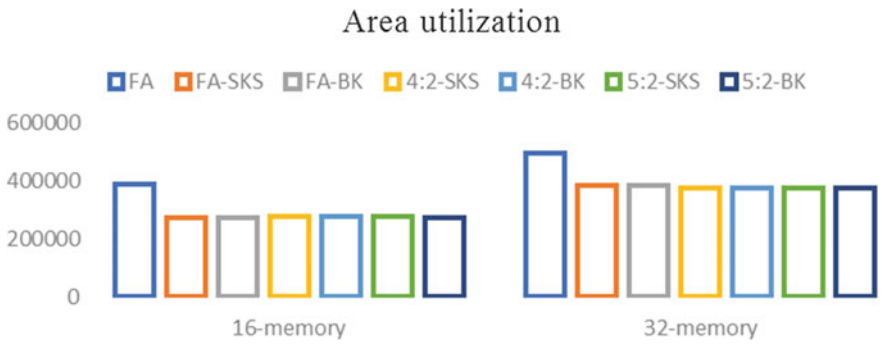

Fig. 10 Area comparison between 16-bit and 32-bit Wallace tree multiplier

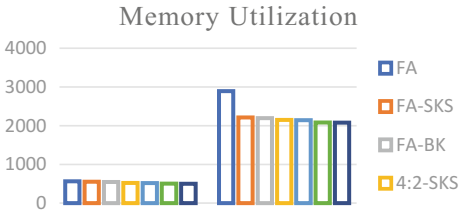

Fig. 11 Memory comparison between 16-bit and 32-bit Wallace tree multiplier

Table 1 Comparison table for full adders and parallel prefix adders

Compression technique	Full adder		Full adder			
Adder used	FA		SKS		BK	
Bits	16	32	16	32	16	32
Slices LUT	564	2353	552	2212	544	2196
Iob	64	128	64	128	64	128
Delay(ns)	12.918	15.89	10.95	13.12	9.703	12.043
Memory (Kb)	387,460	494,052	272,916	384,124	272,124	383,989

Table 2 Comparison table for 4:2 compressor and parallel prefix adders

Comp. Techn.	4:2 Compressor				5:2 Compressor			
Adder used	Sks		Bk		Sks		Bk	
Bits	16	32	16	32	16	32	16	32
Slices LUT	520	2150	516	2142	503	2082	500	1978
Iob	64	128	64	128	64	128	64	128
Delay (ns)	8.385	10.754	9.199	11.369	8.993	11.329	8.993	11.329
Memory (Kb)	275,264	373,564	275,235	373,472	274,220	372,476	273,916	373,372

7 Conclusion

In this paper, an improved Wallace tree multiplier is designed by using 4:2 and 5:2 compressors along with parallel prefix adders like Sparse Kogge-Stone adder and Brent–Kung adder. The multiplier is implemented using Xilinx 14.7 ISE version and simulation is done by ISim simulator. By the proposed method, the area is reduced up to 84% when compared to Wallace tree multiplier design by using a modified version of full adders and delay is also reduced to 11.3 ns.

References

1. Bais K, Ali Z (2016) Design of a high-speed Wallace tree multiplier. Int J Eng Sci Res Technol 5(6) (June 2016)
2. Jaiswal KB, Nithish Kumar V, Seshadri P, Lakshminarayanan G (2015) Low power Wallace tree multiplier using modified full adder. In: 2015 3rd international conference on signal processing, communication and networking (ICSCN)
3. George JP, Ramesh P (2015) Wallace tree multiplier using compressor. Int J Curr Eng Technol 5(3) (June 2015)
4. Padmajarani SV, Muralidhar M (2012) A new approach to implement parallel prefix adders in an FPGA. Int J Eng Res Appl (IJERA) 2(4):1524–1528 (July–August 2012)
5. Sreenivasa Goud E, Praveen Kumar PC (2013) Design and characterization of Sparse Kogge stone parallel prefix adder using FPGA. Int J Sci Eng Technol Res 02(06):467–479 (July 2013)
6. Dhivya C, Thiruppathi M, Sowmiya R (2015) Design of 8x8 Wallace multiplier using mux based full adder with compressor. Int Res J Eng Technol (Irjet) 02 (08 Nov 2015)
7. Kumar P, Kaur J (2014) Design of modified parallel prefix knowles adder. Int J Sci Res (IJSR) 3(7) (July 2014)
8. Potdukhe PP, Jaiswal VD (2016) Design of high speed carry select adder using Brent Kung adder. In: International conference on electrical, electronics, and optimization techniques (ICEEOT)—2016
9. Nair S, Khade RH, Saraf A (2015) Design and analysis of various 32 bit multipliers in an approach towards a fast multiplier. Int J Adv Res Electr Electron Instrum Eng 4(7) (July 2015)

10. Swathi AC, Yuvraj T, Praveen J, Raghavendra Rao A (2016) A novel modified low power Wallace tree multiplier using full and half adder. Int J Innov Res Electr Electron Instrum Control Eng 4(5) (May 2016)
11. Kaur JK (2013) Structural VHDL implementation of Wallace multiplier. Int J Sci Eng Res 4 (4) (April 2013)
12. Bansal H, Sharma KG, Sharma T (2014) Wallace tree multiplier designs: a performance comparison. Innov Syst Des Eng 5(5)
13. Rani G, Kumar S (2014) Delay analysis of parallel-prefix adders. Int J Sci Res (IJSR) 3(6) (June 2014)
14. Rani G, Kumar S (2014) Delay analysis of parallel-prefix adders. Int J Sci Res (IJSR) 3(6) (June 2014)

High Stability and Low-Power Dual Supply-Stacked CNTFET SRAM Cell

M. Elangovan and K. Gunavathi

Abstract MOSFET is replaced by the best adaptable nanodevice, Carbon Nanotubes Field-Effect Transistor (CNTFET) for low-power, small area and delay-optimized VLSI circuit design [1, 2]. In this paper, a dual supply-stacked CNTFET SRAM cell is designed. The performance of 6T CNTFET SRAM cell, stack CNTFET SRAM cell and dual supply-stacked CNTFET SRAM cell is observed by calculating performance metrics of the memory cell such as static power and Static Noise Margin (SNM). From the simulation, it is observed that dual supply stack CNTFET SRAM cell static power is 15.8% lesser, SNM is 1.8% higher than stacked CNTFET SRAM. SNM improvement of 9.62% and static power reduction of 46.92% is obtained in dual supply-stacked CNTFET SRAM cell than 6T CNTFET SRAM cell. *Simulation is carried out using Stanford University 32 nm CNTFET model invoked in CADENCE EDA tool.*

Keywords CNTFET · SRAM · SNM · Static power

1 Introduction

Memory plays a vital role in VLSI digital systems, embedded and most of the portable devices. The on-chip caches are reducing the access time between main memory and processor. Caches are realized using SRAM. It consumes more power for data write operation than a read operation. This is due to driving the bit lines into full swing. The CNTFET-based SRAM cells offer the best performance such as

M. Elangovan (✉)
Department of Electronics and Communication Engineering,
Government College of Engineering, Bargur, Tamil Nadu, India
e-mail: m.elangovan@gcebargur.ac.in

K. Gunavathi
Department of Electronics and Communication Engineering,
PSG College of Technology, Chennai, Tamil Nadu, India
e-mail: kgunavathi@2010.gmail.com

H. S. Saini et al. (eds.), *Innovations in Electronics and Communication Engineering*,
Lecture Notes in Networks and Systems 33,
https://doi.org/10.1007/978-981-10-8204-7_21

high stability, low power, less read and write time than CMOS-based SRAM cells [3]. Stacked CNTFET SRAM design reduces the leakage power, provides high stability than conventional 6T CNTFET SRAM cell [4]. In this work, a dual supply is implemented in stacked CNTFET SRAM cell. The stability and power performance of stacked dual supply CNTFET SRAM cell is observed. The results are compared with 6T CNTFET SRAM and stack CNTFET SRAM cells. The rest of the paper is organized as follows. Section 2 describes the operations of 6T CNTFET SRAM cell. In Sect. 3, SRAM performance parameters are defined. Section 4 provides the details of simulation and results of proposed work. Conclusions of this work are summarized in Sect. 5.

2 SRAM Cell Structures and Operations

2.1 Stacked CNTFET SRAM

SRAM is a volatile memory. It retains stored data until the power is available. The data is lost when the power is switched off. The Transistors T1-T10 form a stacked CNTFET SRAM cell. It is used to store a single bit. Transistors T1-T8 are makes storage cell and T9-T10 are acts as access transistors for write and read operations. Access transistors are controlled by word line (WL). Q and QB are storage nodes of the storage cell. The data is transferred from outside world to the storage cell for a write operation or storage cell to sense amplifier for read operation through bit lines BL and BLB. Stacked CNTFET SRAM Cell is shown in Fig. 1.

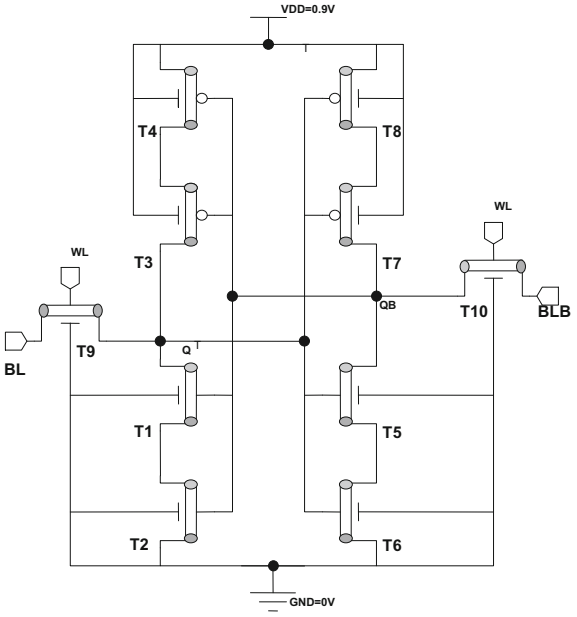

Fig. 1 Stacked CNTFET SRAM cell

Consider a data 1 to be written in the storage node Q of a storage cell. Set BL = 1, BLB = 0 and WL = 1. Transistors T3, T4, T5, T6, T9 and T10 are turned on. Transistors T1, T2, T7 and T8 are turned off. Therefore, VDD is connected with storage node Q, appearing as bit 1 is stored in node Q and Ground is connected with QB, appearing as bit 0 is stored in QB node. During hold mode, WL is set to low. So, the access transistors are turned off.

Thus, in turn, storage cell cannot be accessed. The stored data is held in the storage cell. Before read operation, both BL and BLB should be precharged to VDD by keeping WL = 0. After a while, by applying WL = 1 the access transistors are turned on. Therefore, the storage nodes Q and QB are connected to the BL and BLB respectively. Now, the BL value is pulling towards VDD through T9, T3 and T4 transistors to logic 1 and BLB value is discharging through T10, T5 and T6 transistors to logic 0. Sense amplifier detects the potential difference between BL and BLB to find out the stored bit is either 1 or 0. Here stacked transistor pairs (T1, T2) or (T3, T4) or (T5, T6) or (T7, T8) are simultaneously switched (ON or OFF). This is due to the transistor pair gates are tied together. The OFF condition of stacked transistors improves their own threshold voltage. This, in turn, reduces the leakage current of the memory cell [4].

2.2 Dual Supply-Stacked CNTFET SRAM

The Read, Write and Hold operations of dual supply-stacked CNTFET SRAM cell is similar to that of stacked CNTFET SRAM cell, but in dual supply-stacked CNTFET SRAM cell the substrate of all P-CNTFETs are connected to the potential (VDD^{+}) higher than the supply voltage (VDD) and N-CNTFETs are connected to potential (VSS_{-}) lower than the ground potential (GND) as shown in Fig. 2. It provides strong reverse biasing to the junction between the substrate to drain and substrate to the source. These high reverse biasing decreases the leakage current of the reverse biased junction and reduce the standby power of the entire circuit. The additional of VDD^{+} and VSS_{-} changes the body potential of the device. This increases the threshold voltage of the transistors; in turn, SNM of the memory is improved (Fig. 2).

3 SRAM Performance Parameters

3.1 Static Power or Standby Power

The leakage currents due to reverse biased parasitic diodes between well and substrate, subthreshold conduction and other currents drawn during ‘OFF’ condition of transistors leads to static power or standby power dissipation [5, 6].

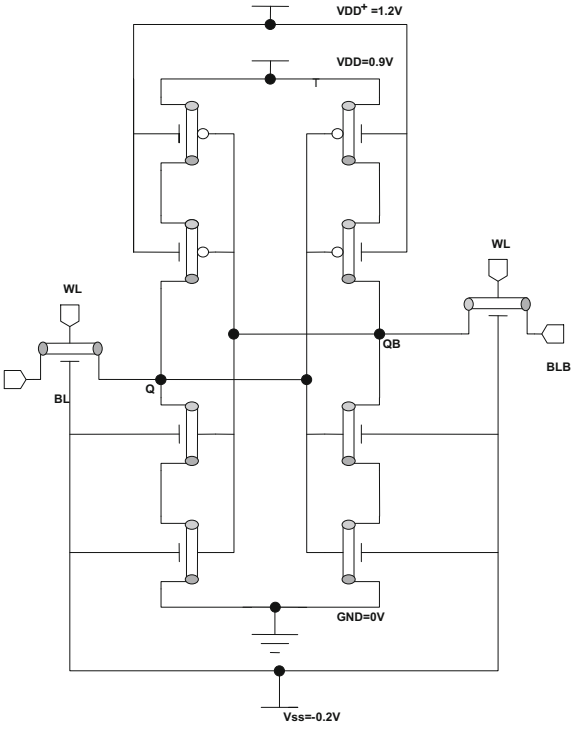

Fig. 2 Dual supply CNTFET SRAM cell

3.2 Static Noise Margin

The stability of memory cell is determined by static noise margin. The maximum amount of noise voltage can be tolerated by the memory cell without changing its state is called static noise margin (SNM) [7, 8]. Storage nodes isolated from the bit lines improves the stability of the SRAM cell [9]. SNM is proportional to the transistors threshold voltage and power supply [10, 11].

4 Simulation and Results

The simulation results show that the stability of proposed dual supply CNTFET SRAM cell offers low static power than CNTFET 6T-SRAM cell and stack CNTFET SRAM cell. The static power decreased to 126 pW from 149.7 pW for Stack CNTFET SRAM and from 273.42 pW for CNTFET 6T-SRAM. In dual supply-stacked CNTFET SRAM the substrates of NCNTFET and PCNTFET are connected with negative supply and higher than VDD respectively, in turn, improves the threshold voltage of the storage cell transistors which improve the

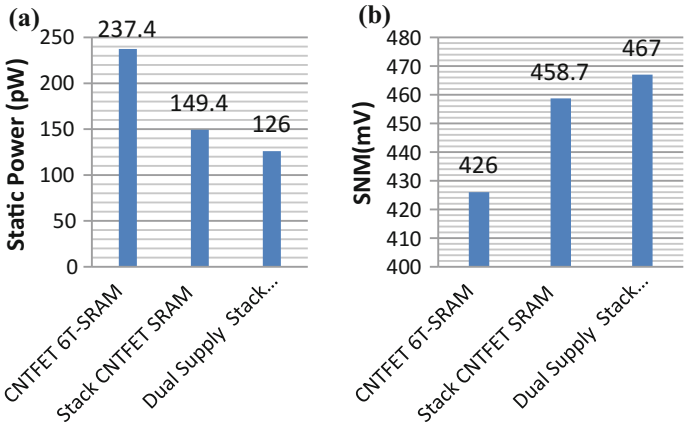

Fig. 3 **a** Static power comparison of different types of SRAM cells **b** SNM comparison of different types of SRAM cells

Table 1 SNM and static power comparison of different types of SRAM cells

SRAM cell	SNM (mV)	Static power (pW)
CNTFET 6T-SRAM	426	237.42
Stack CNTFET SRAM	458.7	149.4
Dual supply stack CNTFET SRAM	467	126

stability of the circuit. The stability of dual supply CNTFET SRAM is improved to 467 mV from 458.7 mV for Stack CNTFET SRAM and from 426 mV for CNTFET 6T-SRAM. Continuous increasing of substrate voltage of PCNTFET higher than source voltage and decreasing of NCNTFET substrate voltage lower than source voltage still improves the power and stability performance of the cell (Fig. 3 and Table 1).

5 Conclusion

Dual supply-stacked CNTFET SRAM cell is designed and its functionality is verified by writing and reading logic "1" as well as logic "0". Performance analysis of 6T CNTFET SRAM cell, stack forced CNTFET SRAM cell and Dual supply CNTFET SRAM cell is carried out by calculating static power and SNM from the simulation it is observed dual supply-stacked CNTFET SRAM cell are consuming least static power and high stability than 6T CNTFET SRAM cell, stack forced CNTFET SRAM but stacked CNTFET increases the threshold voltage which in turn increase the delay of the circuit.

References

1. Deng J (2007) Device modeling and circuit performance evaluation for nanoscale devices: silicon technology beyond 45 nm node and carbon nanotube field effect transistors. Ph.D. thesis, Stanford University
2. Dai H (2002) Carbon nanotubes: synthesis, integration, and properties. Acc Chem Res 35(12)
3. Zhang Z, Delgado-Frias JG (2014) Near-threshold CNTFET SRAM cell design with-line boosting and removed metallic CNT tolerance. IEEE Trans Nano Tech 13(2) (March 2014)
4. Rajendra Prasad S, Madhavi BK, Lal Kishore K (2012) Design of 32 nm forced stack CNTFET SRAM cell for leakage power reduction. In: International conference on computing, electronics and electrical technologies [ICCEET]
5. Birla S, Shukla NK, Pattanaik M, Singh RK (2010) Device and circuit design challenges for low leakage SRAM for ultra low power applications. Can J Electr Electron Eng 1(7):157–167
6. Zhang Z, Delgado-Frias JG (2011) Low power and metallic CNT tolerant CNTFET SRAM design. In: 11th IEEE international conference on nanotechnology. Portland Marriott, 15–18 August 2011
7. Mukherjee D, Mondal HK, Reddy BVR (2010) Static noise margin analysis of SRAM cell for high speed application. IJCSI Int J Comput Sci 7(5) (Sept 2010)
8. Birla S, Pattanaik M, Singh RK (2011) Static noise margin analysis of various SRAM topologies. IACSIT Int J Eng Technol 3(3):304–309
9. Sivamangai NM, Gunavathi K (2011) A low power SRAM cell with high read stability. ECTI Trans on Electr Eng Electron Commun 9(1) (Feb 2011)
10. Rahman N, Singh BP (2013) Static-noise-margin analysis of conventional 6T SRAM CELL at 45 nm technology. Int J Comput Appl 66(20):0975–8887 (March 2013)
11. Tiwari M, Sharma KK, Rawat LS, Kohli VC (2015) Impact of oxide thickness on gate capacitance, drain current and transconductance—a comprehensive analysis on MOSFET, nano wire FET and CNTFET devices. Int J Res Emerg Sci Technol 2(6) (June 2015)

Design of a New Subthreshold-Level Shifter Using Self-controlled Current Limiter

Sheereen Sulthana and K. Ragini

Abstract This brief presents new design of subthreshold-level shifter capable of converting an input signal from subthreshold voltage of 0.1 V to above threshold voltage of 1.2 V. Level shifter (LS) circuit makes use of a self-controlled current limiter (feedback loop) for shifting the signal by detecting the output error. In addition, the proposed design has ample process-voltage-temperature (PVT) variation tolerance. Simulation results of subthreshold LS design in 65-nm CMOS technology, shows that the circuit can shift the signal with limited delay, static power and energy consumption. Modified Wilson current mirror (MWCM) LS design (extension) is also implemented in 65-nm technology, which shows much improvement in terms of delay, power, and energy consumption compared to subthreshold LS design.

Keywords Level shifter · Low leakage (static) power · Current mirrors
Subthreshold voltage · Wilson current mirror

1 Introduction

Due to the intense growth of battery-operated portable devices, the demand for low-power circuit design has increased significantly. One of the most effective ways to reduce both dynamic and static power dissipation of digital circuits is achieved by lowering the supply voltage below the threshold voltage of transistor [1]. But as the supply voltage is reduced, delay of the circuit increases. Hence, an alternate method is to divide the entire circuit into two parts (high- and low-voltage domain) where each part operates at proper supply voltage [2]. However, high-voltage

S. Sulthana (✉) · K. Ragini
G. Narayanamma Institute of Technology & Science (for women),
JNTUH, Hyderabad, India
e-mail: sheereensultana@gmail.com

K. Ragini
e-mail: K.Ragini@gmail.com

H. S. Saini et al. (eds.), *Innovations in Electronics and Communication Engineering*,
Lecture Notes in Networks and Systems 33,
https://doi.org/10.1007/978-981-10-8204-7_22

domain of the circuit will not be able to identify changes in signals from low-voltage domain, especially subthreshold voltages. To overcome this problem, level shifters (LS) are necessary to convert the signals from subthreshold voltage levels to high-voltage levels. The LS circuit should be designed to achieve minimum propagation delay and power consumption [2–5].

Numerous LSs are developed starting from basic standard LS like differential cascode voltage switch (DCVS) LS and current mirrors. These LSs [6] suffer from contention between pull-up and pull-down devices. Also, wide NMOS devices should be chosen for conversion, which is not acceptable as it increases the area on chip. Several other solutions are proposed to overcome these problems.

In [3], LS is proposed for logic voltage shifting and can operate correctly with an input at as low as 127 mV and an output voltage at 1.8 V. Even though the circuit is working well at 127 mV input signal, the delay of the circuit observed was much more which is not acceptable. Hasanbegovic et al. in [4] presented diode-connected and off-biased PMOS transistors which are used to reduce drive capability of pull-up logic. This design achieves a trade-off between speed of the device and power consumption.

Osaki et al. described a current generation scheme with the help of logic error correction circuit which works by detecting the input and output logic levels [5]. This circuit's speed performance is degraded and area is more since more number of transistors is used.

This paper is organized as follows: Sect. 1 includes introduction about the subthreshold LS design, Sect. 2 explains the subthreshold LS design, Sect. 3 includes the results of subthreshold LS with a comparison to existing level shifter designs and MWCM LS.

2 Subthreshold-Level Shifter

In this paper, a new subthreshold LS on the basis of the current mirror is presented. This design is capable of self-controlling the current limiter by detecting the output voltage error, exhibiting superior static power and energy consumption [6]. The schematic of the proposed design is shown in Fig. 1.

2.1 Operational Principles of Subthreshold-Level Shifter

The essential operational principles of subthreshold LS circuit are introduced in detail in this section. Simulated waveforms with respect to voltage are shown in Fig. 2. Input signal voltage and frequency are set to 0.2 V and 1 MHz, output voltage is converted to 1.2 V respectively. When the input signal INL is at its high state, transistor MN1 is switched ON and starts conducting, whereas signal INLN is at "0". Transistor MN2 is switched OFF, leading to current flowing through devices

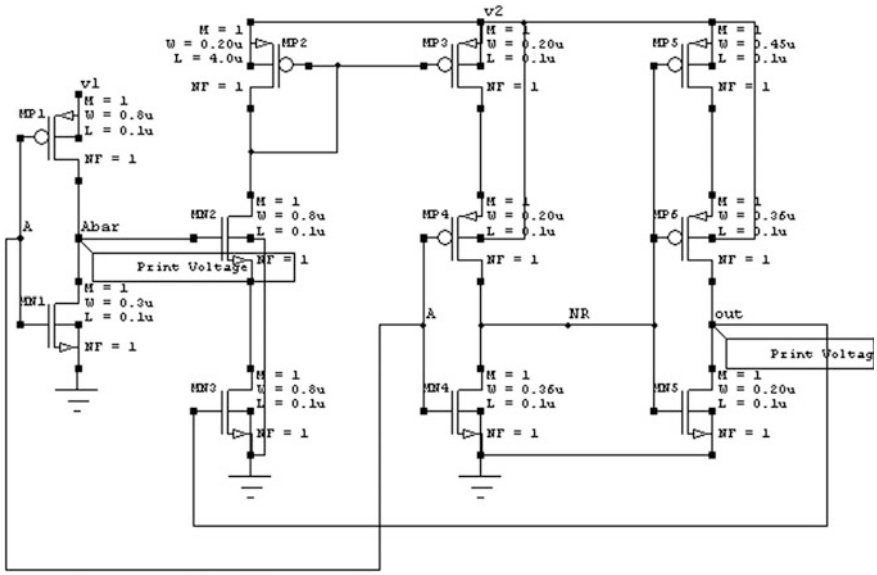

Fig. 1 Schematic of subthreshold-level shifter

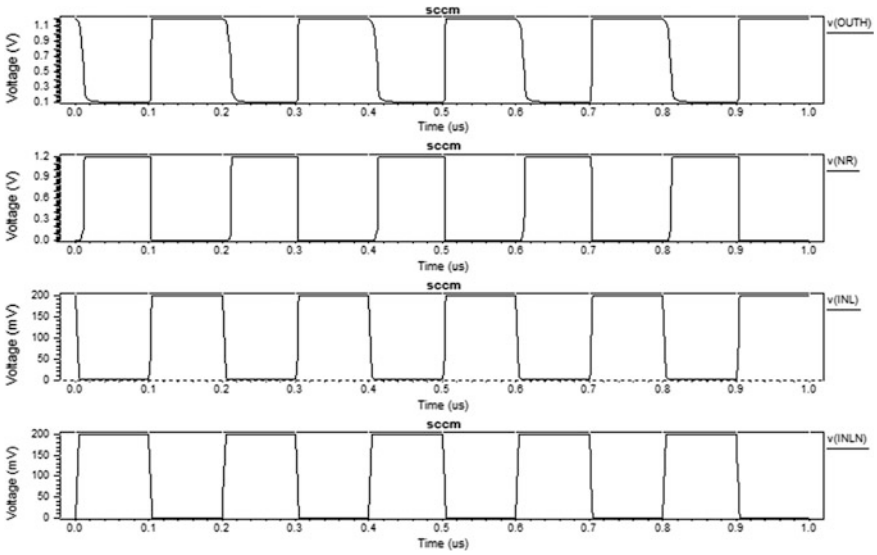

Fig. 2 Transient waveforms of subthreshold LS

MP2 and MP3 to be cut off. As the input signal INL is at its high state, transistor MN4 in the second part of circuit starts conducting. The node NR is at its "low" state, and the output OUTH is charged to high voltage of 1.2 V [6].

The high voltage of output signal is fed to input of transistor MN3. A high-to-low transition at input INL initiates voltage conversion. By the time output is fed to MN3, a very little delay is observed during which the input signal is now at "0". Inverted output INLN is provided to MN2 transistor. Transistors MN2 and MN3 can be termed as the referenced current path, as current mirror is switched off even if one of the transistors is switched OFF. Although the device MN3 is switched ON by output signal, current mirror is switched OFF by transistor MN2 all the time. Thus, conversion is performed and circuit exerts considerable amount of reduction in energy and power consumption [6]. During the entire process, the current through current mirror is determined by the output. If the output signal is at "1" state (wrong state), current mirror is always ON, which continues to provide current to node NR until the output achieves correct value i.e., "0" state. Therefore, the subthreshold LS circuit is capable of self-controlling current limiter by detecting output voltage error [6].

3 Results and Discussion

The performance of new subthreshold LS design is evaluated using T-SPICE with a set of 65-nm process technology in this section. Furthermore, three PVT corners, including typical, worst and best corners are illustrated; TT with a temperature of 25 °C, and 1.2 V V_{DDH} represent the typical corner. SF is chosen for worst-case corner which signifies that the pull-down devices have to overpower the corresponding pull-up devices to make the LS switch (convert). Best corner involves FS, a 10% V_{DDH} reduction, and a temperature of 125 °C, which facilitates the correct voltage conversion of subthreshold LS.

Figure 3 describes the propagation delay against V_{DDL} across PVT corners. It is observed that the delay grows exponentially with V_{DDL} scaled into the deep subthreshold regions, because the drive current of the pull-down transistors decreases drastically as V_{DDL} is scaled to subthreshold voltages. In addition, the delay of the worst-case corner is approximately 100 times more than that of the best-case corner at 0.2 V. Still, the LS operate correctly across PVT corners. At V_{DDL} = 0.2 V, subthreshold LS circuit has a delay of 13.92 ns by a 10000-sample Monte Carlo (MC) simulation with local variations. Indeed, the delay value obtained is faster than the delay of 18.4 ns from [7] and 43.2 ns from [8], where they have also used a current limiter to realize the voltage conversion.

Energy, dynamic and static power consumption against V_{DDL} are illustrated in Figs. 4 and 5, respectively. The energy consumption is reduced by scaling the voltage in the above threshold, but as the V_{DDL} continues to be lowered to deep subthreshold region, the energy starts to rise. For a voltage conversion stage from 0.2 to 1.2 V, it dissipates 90.4 fJ per transition, while the LSs from [7] and [8] consume 93.9 fJ and 182.7 fJ at this point, exhibiting an improvement. The dynamic power consumption is reduced as the voltage is scaled down but starts to

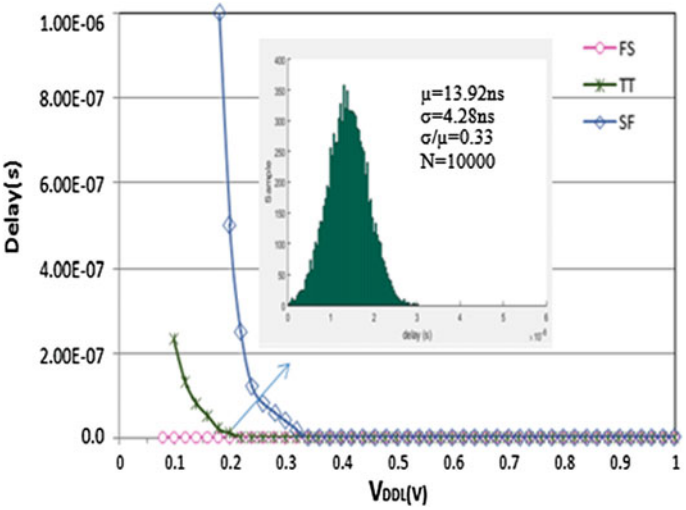

Fig. 3 Propagation delay against V_{DDL}

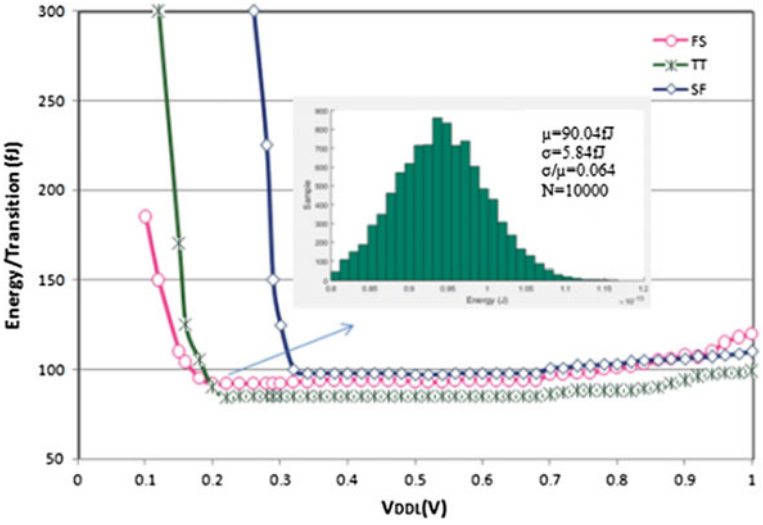

Fig. 4 Energy dissipation against V_{DDL}

increase below 0.3 V. The static power consumption of 1.96 nW is obtained, whereas the LSs from [7] and [8] consume 6.6 nW and 8.6, comparing with subthreshold LS design.

To understand how low the minimum V_{DDL} of this circuit is, a 10000-sample MC simulation is performed, with a minimum allowable input signal of 0.1 V for

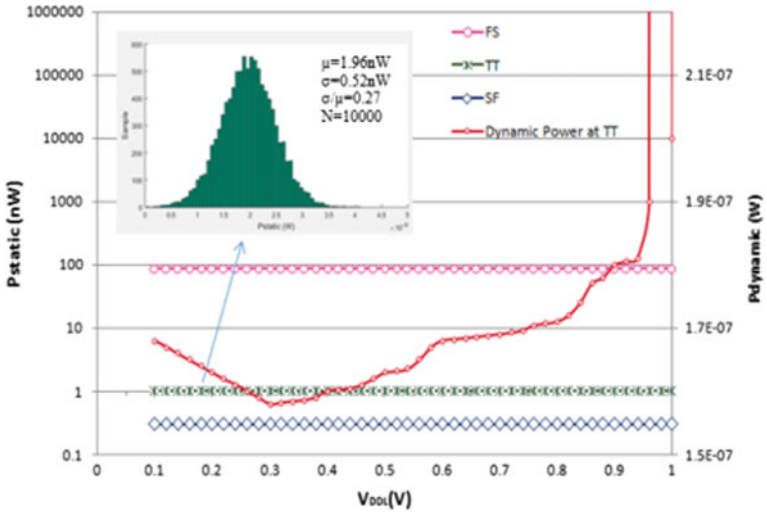

Fig. 5 Dynamic and Static power consumption as a function of V_{DDL}

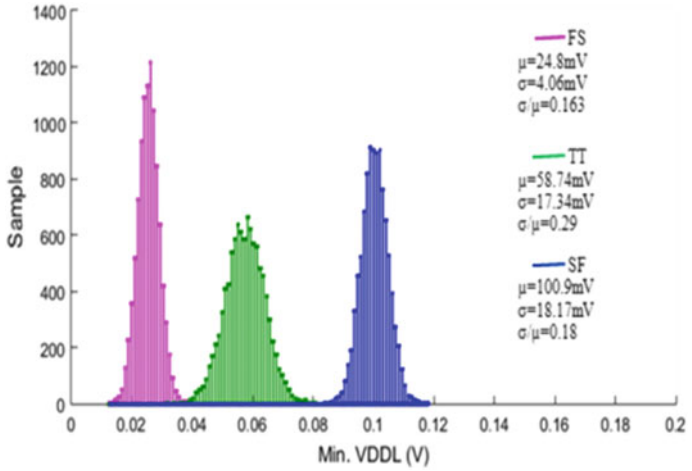

Fig. 6 Statistical distribution of minimum V_{DDL}

converting to 1.2 V. Subthreshold LS design is able to operate at a minimum V_{DDL} of 100.9 mV under extreme PVT variations which can be seen in Fig. 6. The new subthreshold LS design has a small normalized coefficient of variation (σ/μ) across parameter variations compared with other existing LSs, indicating more flexibility to process variations.

The experimental results demonstrate that the minimum V_{DDL} can be achieved as low as 0.1 V. In addition, for a V_{DDL} = 0.2 V, the marginal input frequency can be

up to 265 kHz as shown in Fig. 7. Subthreshold LS design achieves a considerable improvement in terms of speed, energy, and static power dissipation. The layout of the subthreshold LS is shown in Fig. 8.

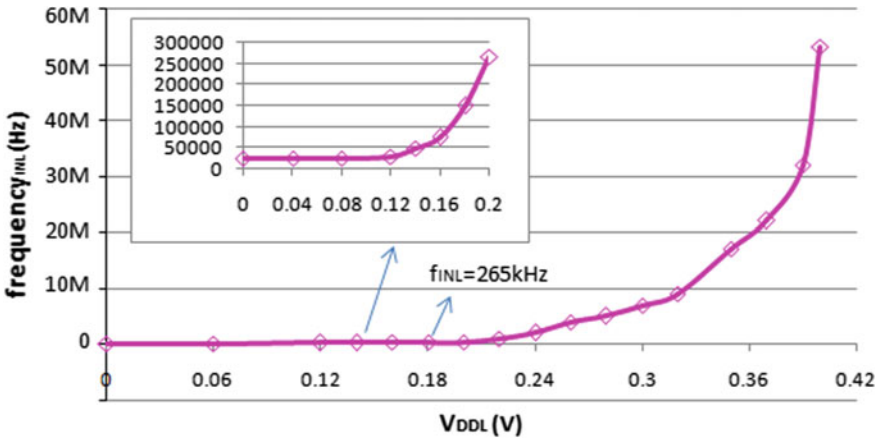

Fig. 7 Measured max input frequency

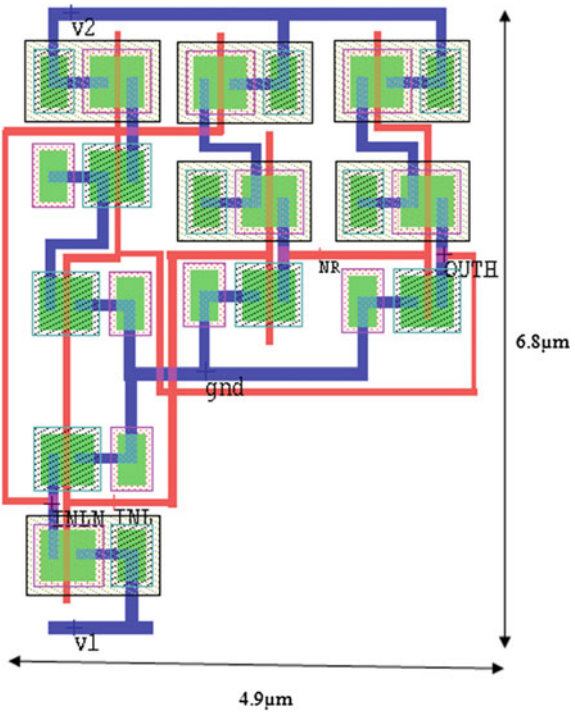

Fig. 8 Layout of subthreshold LS

The characteristics of the subthreshold LS are compared with the existing LSs and MWCM LS, in Table 1. All these level shifters are compared in terms of area, delay, energy and power consumption. DCVS and Current Mirror LS presented by Chavan et al. [1] are implemented in 65-nm technology. Voltage conversion from 0.25 to 1.0 V is achieved by DCVS LS. There is a contention noticed between pull-up and pull-down devices, which imply pull-up and pull-down strengths should be properly balanced to make sure correct functionality of LS. Current mirror circuit [1] is capable of converting an input signal of 0.2–1.0 V, but it introduces a large amount of static current and energy waste with high input "ON". Two-stage LS design presented by Wooters et al. [9] is also implemented in 65-nm technology for better comparison with subthreshold LS and MWCM LS. In this, both stages adopt conventional DCVS circuit and it is able to convert an input signal of 188 mV to 1.2 V, but at the expense of speed performance.

When compared to subthreshold LS design, MWCM LS achieves considerable improvement in speed, energy and static power consumption. For a voltage conversion stage from 0.1 to 1.2 V, modified Wilson current mirror LS dissipates 88.4 fJ, while the subthreshold LS design consumes 90.04 fJ exhibiting an improvement. Also for static power dissipation, a value of 1.16 nW is achieved which is less, compared to the value of 1.96 nW obtained from new subthreshold LS. Modified Wilson Current Mirror (MWCM) LS is a more sophisticated and superior design compared to subthreshold LS and it achieves considerable improvement in terms of speed, energy and static power consumption. This circuit utilizes two current mirrors in its design by which static power is reduced [2]. This circuit is able to convert an input signal of 0.1–1.2 V output signal.

Table 1 Comparison of level shifters in terms of delay, energy, static power and area

Tech (nm)	Level shifters	Delay (ns)	Energy (fJ)	P_{static} (nW)	Area (μm^2)	Min. V_{DDL}	V_{DDH} (V)
65 nm	DCVS LS	7.4	2.7 × 10^3	4700	39.7	0.25 V	1.0
65 nm	Current mirror LS	12.8	1.2 × 10^3	3420	39.2	0.2 V	1.0
65 nm	Two-stage LS	34.9	96.3	9.8	N/A	185 mV	1.2
65 nm	Current mirror	13.92	90.04	1.96	33.32	100 mV	1.2
65 nm	Modified WCM	12.24	88.4	1.16	31.6	100 mV	1.0

4 Conclusion

A new design of subthreshold-level shifter is presented in this paper, which can convert an input signal from minimum voltage of 0.1–1.2 V. The circuit explores a self-controlled current limiter scheme by detecting the output voltage error. Results obtained demonstrate that subthreshold LS circuit can convert signal with a significant improvement in terms of delay, energy and static power consumption compared to existing LS designs. Subthreshold LS circuit is flexible over a range of voltage and temperature variations. MWCMLS design is also implemented in 65-nm technology and is able to convert an input signal from 0.1 to 1.0 V. Simulation results of this LS show much improvement in terms of delay, power and energy consumption compared to subthreshold LS. Subthreshold circuits are suitable for specific applications which require extremely low power consumptions, such as pacemaker, hearing aids, cochlear implants, wireless sensors (Sensaris) and environmental monitors.

References

1. Chavan A, Macdonald E (2008) Ultra low voltage level shifter to interface sub and super threshold reconfigurable logic cells. In: Proceedings of IEEE Aerospace Conference, Big Sky, MT, USA, 2008, pp. 1–6
2. Talebzadeh A, Saberi M (2016) A low-power wide range voltage level shifter using a modified Wilson current mirror. In: Proceedings of ICEE conference, Mashhad, Iran, 2016, pp. 1363–1366
3. Shao H, Tsui C (2007) A robust, input voltage adaptive and low energy consumption level converter for sub-threshold logic. In: Proceedings of 33rd ESSCIRC, 2007, pp. 312–315
4. Hasanbegovic A, Aunet S (2009) Low-power sub threshold to above threshold level shifter in 90 nm process. In: Proceedings of NORCHIP conference, Trondheim, Norway, 2009, pp. 1–4
5. Osaki Y, Hirose T, Kuroki N, Numa M (2012) A low-power level shifter with logic error correction for extremely low-voltage digital CMOS LSIs. J Solid-State Circ 47(7):1776–1783
6. Wen L, Cheng X, Tian S, Wen H, Zeng X (2016) Sub threshold level shifter with self-controlled current limiter by detecting output error. IEEE Trans Circuits Syst II, Exp Briefs 63(4):346–350
7. Lukemeier S, Ruckert U (2010) A sub-threshold to above-threshold level shifter comprising a Wilson current mirror. IEEE Trans Circuits Syst II, Exp Briefs 57(9):721–724
8. Chen TH, Chen J, Clark LT (2006) Subthreshold to above threshold level shifter design. J Low Power Electron 2(2):251–258
9. Wooters SN, Calhoun BH, Blalcok TH (2010) An energy-efficient sub-threshold level converter in 130-nm CMOS. IEEE Trans Circuits Syst II, Exp Briefs 57(4):290–294

Heart Sound Signal Analysis and Its Implementation in VHDL

Anjali S. Patil, Jayanand P. Gawande and Ajinkya Bankar

Abstract Cardiac auscultation is a primary diagnostic tool in the detection and management of cardiac disease. It is a noninvasive technique of listening to sounds produced by heart. In order to make the system reliable and proceed to make real-time operation, a new method is developed and evaluated. A novel framework for heart sound analysis based on discrete wavelet transform (DWT) decomposition and its implementation in VHDL is presented in this paper. Autocorrelation of the average Shannon energy envelope is extracted as feature from the sub-band coefficients of the heart signal with the DWT. Simulation is done in both MATLAB and Xilinx ISE 12.1 with the help of ModelSim simulator. The proposed method is evaluated on publically available datasets published in the PASCAL Classifying Heart Sounds Challenge.

Keywords Discrete wavelet transform (DWT) · Heart sound · Very high-speed integrated circuit hardware description language (VHDL)

1 Introduction

The heart sounds are mainly classified as first, second, third, fourth, and finally murmurs. The first heart sound also called as lub is produced due to the closing of mitral and tricuspid valves which allow the flow of blood from atria into the

A. S. Patil (✉) · J. P. Gawande
Instrumentation and Control Department, MKSSS's Cummins College of Engineering for Women, Pune 411052, India
e-mail: anjali.patil@cumminscollege.in

J. P. Gawande
e-mail: jayanand.gawande@cumminscollege.in

A. Bankar
Electronics and Telecommunication Department, Vidya Pratishthan's Kamalnayan Bajaj Institute of Engineering and Technology, Baramati 413102, India
e-mail: ajinkya_003@yahoo.com

H. S. Saini et al. (eds.), *Innovations in Electronics and Communication Engineering*, Lecture Notes in Networks and Systems 33,
https://doi.org/10.1007/978-981-10-8204-7_23

ventricles for 0.1–0.12 s duration having 30–50 Hz frequency. The second heart sound also called as dub produced when ventricular systole ends due to the closing of semilunar valves. The frequency range of second heart sound is 50–70 Hz, and its duration is 2550 ms. The third heart sounds are produced due to the stoppage of ventricular filling. The frequency range is below 30 Hz and its duration is 0.1–0.2 s. The fourth heart sounds also called atrial heart sounds are produced due to the contraction of the atria. The duration of fourth heart sound is 0.03–0.06 s and its frequency is 10–50 Hz. Murmurs occur in abnormal hearts between normal heart sounds. They are high pitch sounds having range 100–600 Hz and are longer in duration compared to normal heart sounds [1].

The existing monitor heart sound detection method such as electrocardiogram (ECG) requires to wear adhesive gel patches or chest traps which causes skin irradiation and discomfort. Low-cost and noninvasive method photoplethysmography (PPG) is used to detect volumetric changes in blood in peripheral circulation that makes Improper pulse sensing error. Traditional phonocardiogram which records sounds and murmurs made by heart with help of machine called phonocardiography (PCG) has limitations of heart sound storage and processing for lack of quantitative analysis function [1, 3].

This work is divided into two parts. In the first part, wavelet analysis of heart sound signal is obtained in MATLAB. In the second part, wavelet decomposition is implemented in the VHDL by using Xilinx ISE 12.1 and program is simulated in ModelSim simulator.

The paper is organized as follows: Database information and the wavelet analysis of heart sound signal in MATLAB are described in Sect. 2. Section 3 describes VHDL implementation of wavelet analyzed part. Section 4 represents simulation results of both MATLAB and VHDL. Finally, Sect. 5 presents the conclusion.

2 Analysis of Heart Sound Signals

2.1 Database Information

Heart sound datasets collected by the Real Hospital Portugues de Beneficencia, Brazil are used [4]. It consists of two public heart sound datasets. Dataset A contains signals that have a sampling frequency of 4410 Hz. Dataset B contains signals with a sampling frequency of 4000 Hz. Different lengths of audio files are present, i.e., between 1 s and 30 s. Database is present in three categories; Normal, murmur, and extra systole category. 200 normal, healthy heart sounds samples present in Normal category. As the device is removed from the body, these samples contain noise in the final second of the recording. Murmur category contains 66 samples. The noise in form of a whooshing, roaring, rumbling, or turbulent fluid is present (1) between lub and dub and (2) between dub and lub. Extra systole category

contains 46 samples and they are occasional and difficult to identify. As heart sounds are out of rhythm having extra or skipped heartbeats such as a lublub dub or a lub dub-dub [4, 5, 6].

2.2 *Estimation of Heart Rate from Heart Sound Signals*

The block diagram of the detailed steps is summarized in Fig. 1.

Heart sound signal block acquires database signal from its location, i.e., read the signals MATLAB. In the preprocessing step of wavelet analysis signals are downsampled by 2 and after downsampling signals are normalized with their maximum absolute value. Next step is the 1-D decomposition using discrete wavelet transform (DWT). DWT is a multiresolution decomposition of a signal. It decomposes a signal into its components in different frequency bands. Convolution method involves decomposition of signals into approximate and detail coefficients. The decimated and normalized heart sound signal is decomposed into four levels by using the Order Six Daubechies (db6) wavelet, due to its morphological similarities to heart sound components. The approximation wavelet coefficients at the fourth level are selected for feature extraction using normalized average Shannon energy envelopes (ASEs) [2]. ASE is calculated using Eq. 1.

$$\mathrm{Es}(n) = -\left(\sum_{i=1}^{N} \Phi a, 4(i)^2 \log \Phi a, 4((i))^2\right) \tag{1}$$

where, Φa, 4(i) is normalized approximate coefficients.

Autocorrelation of ASE provides an automatic and shift invariant accumulation of the periodicity over multiple cardiac cycles. Autocorrelation function can be viewed as the feature representation of the heart sound [2]. It is defined by Eq. 2.

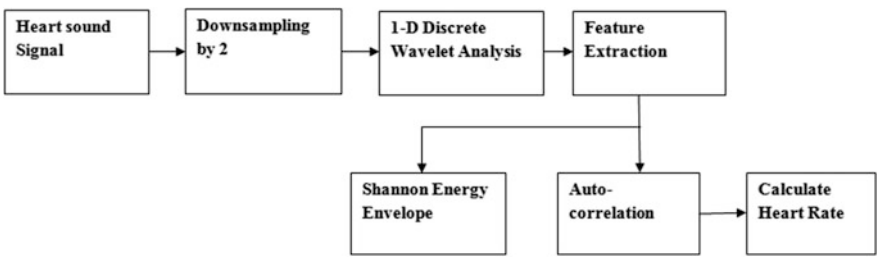

Fig. 1 Block diagram of detailed heart rate calculation

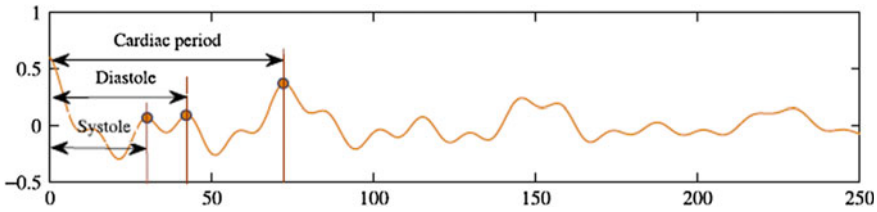

Fig. 2 Heart rate calculation using autocorrelation

$$r(m) \sum_{i=0}^{N-m-1} e(n)e(n+m) \tag{2}$$

where $e(n + m)$ is the time-shifted version of the ASE signal $e(n)$ with a time lag of m for $m = 0, 1, \ldots, M$.

Finally, from autocorrelation function, heart rate is calculated as shown in the Fig. 2.

3 VHDL Implementation of Heart Sound Signals

Field programmable gate array (FPGA) is used to implement the Verilog or VHDL. VHDL stands for very high-speed integrated circuit hardware description language. VHDL is used to describe the structure and behavior of electronic circuits and digital logic circuits [3]. VHDL uses a general purpose parallel programming language. Xilinx ISE 12.1 is used for VHDL coding, i.e., for FPGA implementation. Simulation results are verified in ModelSim 5.7 g simulator. Flowchart for the detailed VHDL implementation is shown in Fig. 3.

4 Experimental Results

In the wavelet analysis of heart sound signals, autocorrelation results are obtained using all three databases, i.e., normal, murmur, and extrasystole. Preprocessing results, DWT decomposition results, and ASE, autocorrelation results are shown in Fig. 4.

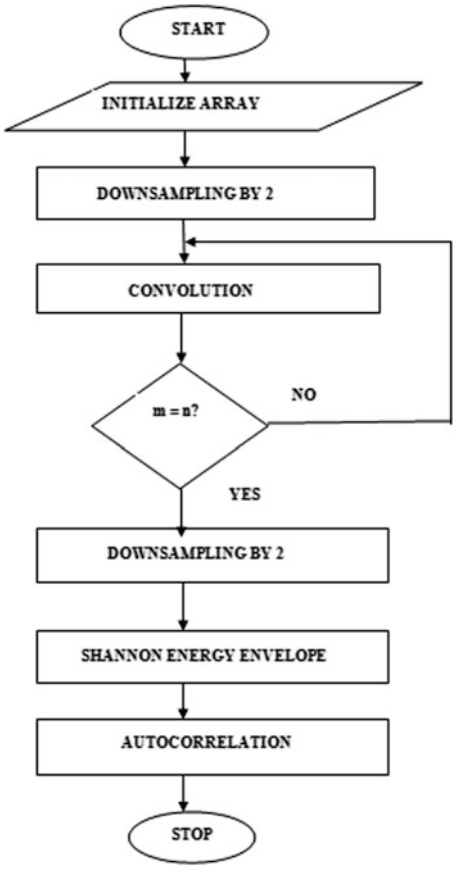

Fig. 3 Flowchart of implementation in VHDL

From these outputs, first highest peak within range 30–120 is considered as suitable peak for the calculation of the heart rate of the heart sound signals. Table 1 shows the heart rates of different category signals.

VHDL implementation results from the simulation in ModelSim are obtained. Dataflow results from the simulation and its corresponding autocorrelation result output plot in MATLAB are shown in Fig. 5.

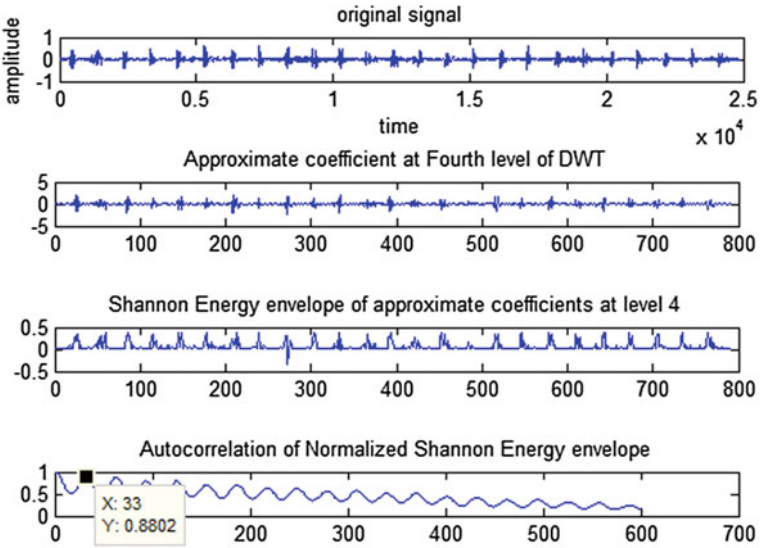

Fig. 4 MATLAB results

Table 1 Heart rate calculation using different samples

Sr No.	Category	Samples	Cardiac period	Heart rate
1	Normal	113_B1	43	83.72
2	Normal	103_D1	32	112.5
3	Normal	103_D2	31	116.12
4	Murmur	112_A	41	87.80
5	Murmur	112_B	42	85.71
6	Murmur	112_D	43	83.72
7	Extrasystole	127_C2	38	94.73
8	Extrasystole	128_A	40	90
9	Extrasystole	130_D	33	109.09

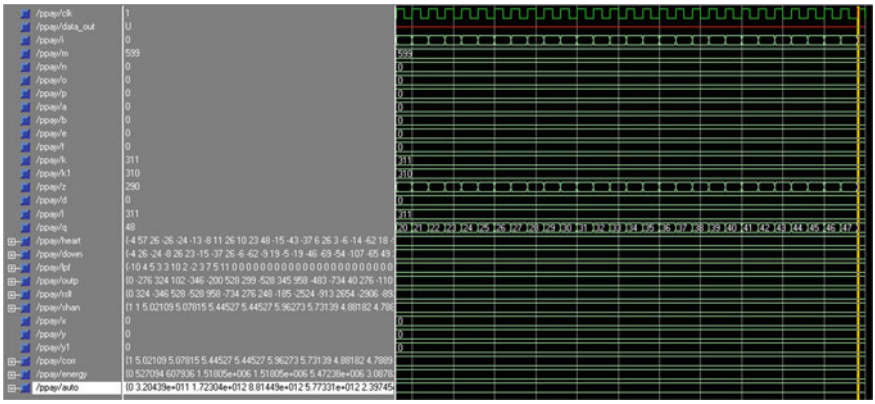

Fig. 5 ModelSim simulation results of VHDL implementation

5 Conclusion

Heart sound signals from the dataset are analyzed using DWT. Feature extraction of the decomposed signal is obtained using average Shannon energy envelope and autocorrelation. According to autocorrelation reference Fig. 2. Cardiac period of each sample from normal, murmur, and extrasystole category is obtained. Heart rate is calculated by using the obtained cardiac period. The exact algorithm is implemented in VHDL for the real-time analysis of heart sound signals. Heart rate shows best varying results for extrasystole category signals of dataset.

References

1. Cromwell L, Weibell FJ, Pfeiffer EA (2014) Biomedical Instrumentation and measurements. PHI Learning Private Limited, Second Edition, Delhi
2. Deng S-W, Han J (2016) Towards heart sound classification without segmentation via autocorrelation feature and diffusion maps. Elsevier, Future Generation Computer Systems 60, 13â˜A, S21
3. Wei M, Sun K, Wang C, Cheng X (2015) A Design and Implementation for Heart Sound Detection Instrument based on FPGA. In: 3rd international conference on machinery, materials and information technology applications (ICMMITA 2015)
4. Ana C, Tiago TV, Vinhoza SSM, Miguel T (2012) Coimbra, Heart sound segmentation of pediatric auscultations using wavelet analysis. In: Proceedings of I2 MTC, May 2012, pp 1722–1725
5. Cao Z, Zhou S, Li F (1998) The quantitative analysis approach for a heart sound information system. In: Proceedings of the 20th annual international conference of the IEEE engineering in medicine and biology society
6. Senthil Kumar TK, Arun A, Jagannathan PV (2014) Diagnosing Heart Abnormality from PCG Signals using K-Means Clustering. Int J Sci Technol

7. Shovan B, Bo-Wei C, Wen J, Seungmin R, Chih-Hung C, Jhing-Fa W (2016) Detection of the third heart sound based on nonlinear signal decomposition and time-frequency localization based on FPGA. IEEE Trans Biomed Eng 63(8)
8. Mohamed GE, El-Moursy MA, El-Hennawy AE El-Simary MA, Amal Z (2016) FPGA-based electrocardiography(ECG) signal analysis system using least-square linear phase finite impulse response(FIR) filter. J Elect Syst Inform Technol 3:513–526
9. James N, Nikolay A,Taikang N (2009) Quantitative analysis of heart sounds and systolic heart murmurs using wavelet transform and AR modeling. In: 31st annual international conference of the IEEE EMBS Minneapolis, Minnesota, USA, September 2–6
10. Taegeun P, Juyoung K, Junrye R (2007) Low-complexity bit-serial VLSI architecture for 1D discrete wavelet transform. Circ Syst Signal Process 26(5):619–634

Part IV
Communication

Cooperative Spectrum Sensing Over Rayleigh Fading Channel

Chilakala Sudhamani and M. Satya Sai Ram

Abstract Cooperation among secondary users improves the spectrum sensing performance by allowing local decisions measured over independent sensing channels. This reduces the miss detection and false alarm probabilities. Most of the works in cooperative spectrum sensing techniques assume perfect channels between the cooperating secondary users. In this paper, we considered the effect of imperfect channels. Total error rate and success probabilities are calculated for an additive white Gaussian noise channel and a Rayleigh fading channel. The optimal number of cooperative secondary users is estimated over nonfading and fading channels. Simulation results show the variation of success probability with respect to channel imperfection for different number of secondary users. This is useful for identifying the unutilized spectrum.

Keywords Cognitive radio · Cooperative spectrum sensing · Rayleigh fading channel · Channel imperfection

1 Introduction

Cognitive radio concept was first presented by Mitola [1] to solve the problem of spectrum scarcity identified by the Federal Communication Commission [2]. Cognitive radio scans the available spectrum bands, seizes their information, and identifies the spectrum holes. All secondary users (SU) sense the spectrum and send

C. Sudhamani (✉)
Department of Electronics and Communication Engineering,
CMR Technical Campus, Hyderabad 50140, Telangana, India
e-mail: sudhamanich@gmail.com

M. Satya Sai Ram
Department of Electronics and Communication Engineering,
Chalapathi Institute of Engineering and Technology, LAM,
Guntur 522034, Andhra Pradesh, India
e-mail: msatyasairam1981@gmail.com

H. S. Saini et al. (eds.), *Innovations in Electronics and Communication Engineering*,
Lecture Notes in Networks and Systems 33,
https://doi.org/10.1007/978-981-10-8204-7_24

their observations to the base station that takes the final decision about the incumbent's signal presence or absence. The main principle of this concept is to access the PU spectrum by the SU when it is free without causing any harmful interference to the PU. Therefore, spectrum sensing techniques are used to identify the spectrum holes. Different spectrum sensing techniques and their set of advantages and disadvantages are discussed in [3, 4]. With single SU, the false alarm probability increases. So, to improve the probability of detection and reduce the probability of false alarm, cooperative spectrum sensing (CSS) has been used. CSS utilizes the cooperation among SUs for spectrum sensing and then improves the probability of successful detections of PUs by taking advantage of the spatial diversity obtained from the users' channel conditions each having independent shadowing and multipath fading effects. In addition, cooperation reduces the possibility of the hidden node problem also.

CSS has been studied in the literature [5]. In [6, 7], the detailed review of most of the works done in CSS is provided and the main advantages and the limits are highlighted. The performance of single SU-based spectrum sensing in fading channels such as Rayleigh and Nakagami has been studied in [8]. In CSS, all SUs sense the PU individually and send their sensing information in the form of 1-bit binary decisions, i.e., 1 or 0 to the fusion center (FC). To improve the spectrum sensing performance over fading channel, collaborative sensing technique was implemented in [9]. The authors considered a collaborative sensing method with more secondary users to overcome the receiver uncertainty problem. The authors in [10] explained the concept of user collaboration to improve the spectrum access over imperfect channels. The performance of CSS over fading channels was compared for all fusion rules in [11]. The authors in [12] showed that the cooperative technique has better performance than noncooperative. The existing works explained about the collaborative spectrum sensing over nonfading additive whitegaussian noise (AWGN) channel. In this paper, we considered CSS over Rayleigh fading channel.

The rest of this paper is summarized as follows: In Sect. 2, the system model is introduced. In Sect. 3, detection and false alarm probabilities of nonfading AWGN and Rayleigh fading channel are described. The simulation results and discussion are presented in Sect. 4. Finally, we draw our conclusion in Sect. 5.

2 System Model

Consider a CSS with K number of secondary users, one primary user and one fusion center which are shown in Fig. 1.

In CSS, each secondary user senses the local spectrum independently and then forwards their binary local decisions (1 or 0) to the fusion center. The fusion center combines all the local decisions and makes a final decision to identify the presence or absence of the PU. In a CR network, hypothesis testing is used to identify the

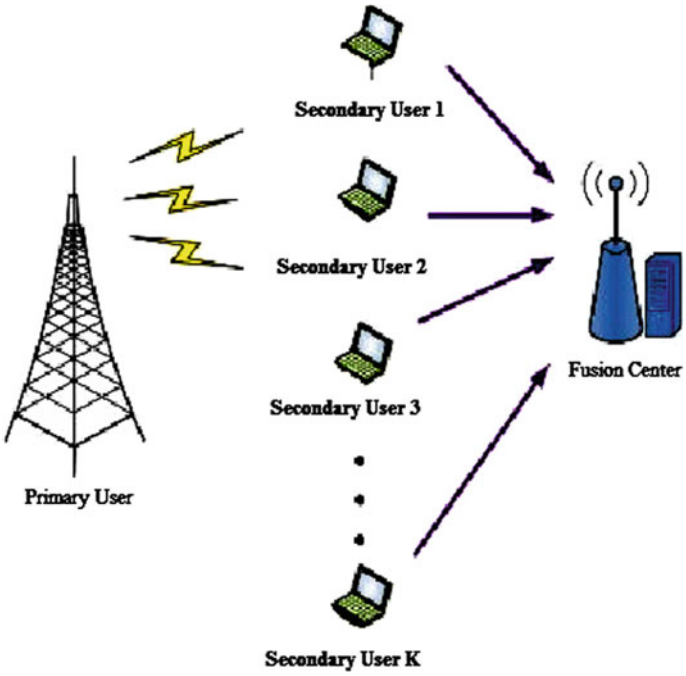

Fig. 1 Cooperative spectrum sensing with K secondary users, one primary user, and one fusion center

presence (H_0) or absence (H_1) of the PU. Under these two hypotheses, the received signal strength of the SU is given by [13]

$$Y_j(t) = n_j(t) \quad : H_0 \tag{1}$$

$$Y_j(t) = h_j s(t) + n_j(t) \quad : H_1 \tag{2}$$

where $n_j(t)$ is the AWGN of the j-th SU, h_j is the channel gain of the sensing channel between the PU and the j-th SU, and $s(t)$ is the transmitted signal of the PU.

3 Probability of False Alarm and Probability of Detection

For a nonfading channel, the probability of detection and the probability of false alarm of j-th secondary user are given as [14]

$$P_{d,j} = Q\left(\sqrt{2\gamma}, \sqrt{\lambda}\right) \tag{3}$$

$$P_{f,j} = \frac{\Gamma(U, \lambda/2)}{\Gamma(U)} \tag{4}$$

where U is the time bandwidth product, λ is the detection threshold, γ is the signal-to-noise ratio, $Q(.,.)$ is the Marcum Q-function, $\Gamma(.,.)$ is the incomplete gamma function, and $\Gamma(.)$ is the gamma function.

In this paper, we assumed a fading channel as Rayleigh fading channel instead of AWGN nonfading channel because the received signal is the combination of multipath fading signals. If the signal amplitude follows a Rayleigh distribution, then the signal-to-noise ratio (γ) follows an exponential probability density function and the probability of detection for a Rayleigh fading channel is given as [15]

$$f(\gamma) = \frac{1}{\bar{\gamma}} \exp\left(\frac{-\gamma}{\bar{\gamma}}\right), \gamma \geq 0 \tag{5}$$

$$\text{avg}P_d = \int_x Q\left(\sqrt{2\gamma}, \sqrt{\lambda}\right) f_{\bar{\gamma}}(x) \mathrm{d}x \tag{6}$$

Average probability of detection is obtained by substituting Eq. (5) in Eq. (6) as follows:

$$\text{avg}P_{d,\text{Ray}} = \mathrm{e}^{\lambda/2} \sum_{K=0}^{U-2} \frac{1}{K!} \left(\frac{\lambda}{2}\right)^K + \left(\frac{1+\gamma}{\bar{\gamma}}\right)^{U-1} \cdot \left(\mathrm{e}^{\frac{\lambda}{2(1+\bar{\gamma})}} - \mathrm{e}^{\frac{\lambda}{2}\frac{1}{K!}} \sum_{k=0}^{U-2} \left(\frac{\lambda\bar{\gamma}}{2(1+\bar{\gamma})}\right) \right) \tag{7}$$

In CSS, K secondary users sense the PU channel and forward their local decisions to the fusion center. The fusion center will combine all the local decisions according to soft, quantized soft, and hard fusion rules. In the soft combination, all the CRs will send their total sensing information to the FC. In the quantized soft method, CR users quantize the sensed data and then forward that quantized samples for the soft combination. In the hard combining method, each CR user makes a one-bit local decision and forwards that local decision to the fusion center for hard combining [10]. In all these three methods, we are using hard combining method for reducing the channel overhead.

By using majority fusion rule, the probability of detection and the probability of false alarm at the fusion center are given respectively as [10]

$$P_{d,\text{Maj}} = \sum_{l=\lfloor K/2 \rfloor}^{K} \begin{bmatrix} K \\ l \end{bmatrix} P_{d,j}^{l} \left(1 - P_{d,i}\right)^{K-l} \tag{8}$$

$$P_{f,\mathrm{Maj}} = \sum_{l=\lfloor K/2 \rfloor}^{K} \left[\begin{matrix} K \\ l \end{matrix} \right] P_{f,j}^{l} \left(1 - P_{f,i}\right)^{K-l} \tag{9}$$

$$P_{m,\mathrm{Maj}} = 1 - P_{d,\mathrm{Maj}} \tag{10}$$

These equations are used to calculate the total error rate in nonfading channel and the success probability of fading channel.

4 Simulation Results

In this paper, we considered a CSS with K number of secondary users, one primary user, and one fusion center. Let us consider a time bandwidth product of 240, channel imperfection as 15–25%, signal-to-noise ratio of 10 dB, and path loss exponent of 2. Figure 2 shows the variation of total error rate with respect to the detection threshold as the number of SUs is changing from 1 to 10. We observe that as the detection threshold increases, the error rates decrease till threshold and the number of secondary users is constant and then increases continuously. This conveys that the error rate decreases to an optimal value, i.e., for 5 numbers of SUs then subsequently increases for higher number of SUs. We say that the optimal number of SUs for minimum error rate is 5 which are also depicted in Table 1.

Table 1 shows the minimum error rate for different numbers of cooperative SUs. As the number of SUs increases, the error rate decreases up to $K = 5$ and then increases. Therefore, the optimal number of cooperative SUs for a nonfading channel is identified as $K = 5$.

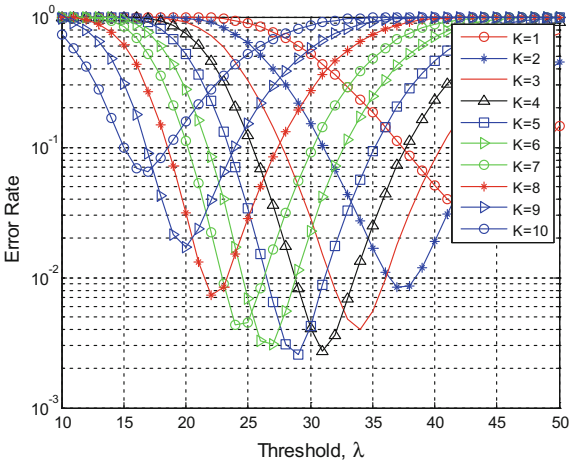

Fig. 2 Total error rate for different number of secondary users

Table 1 Minimum error rate for $K = 1$ to $K = 10$

No. of SUs	Minimum error rate	No. of SUs	Minimum error rate
01	0.03	06	0.003
02	0.009	07	0.005
03	0.005	08	0.008
04	0.003	09	0.018
05	0.002	10	0.065

In CSS, most of the work is done by assuming perfect channels between cooperative SUs. We here considered imperfect channels between the cooperative secondary users for reporting their sensed information to the fusion center. The graphs are plotted for different secondary users 1, 5, 10, 15, 20, and 25 by varying the channel imperfection between the cooperative secondary users from 15 to 25%. For $k = 1$, as the channel imperfection increases from 15 to 25%, there is no much variation in the success probability along with the detection threshold. The minimum probability of detection is 0.9 and maximum is 1.

As the number of cooperative SUs increases from $K = 1$ to $K = 5$ then the minimum success probability decreases from 0.9 to 0.6 for the same detection threshold. The variation in the success probability with the channel imperfection is shown in Figs. 1, 2, and 3. By this, we observe that the number of cooperative SUs increases the success probability increases but in this case, it decreases because of the channel imperfection.

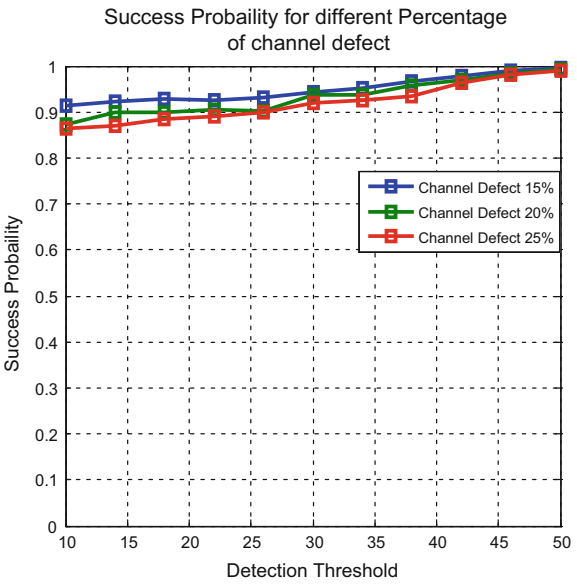

Fig. 3 Success probability with respect to detection threshold for $K = 1$

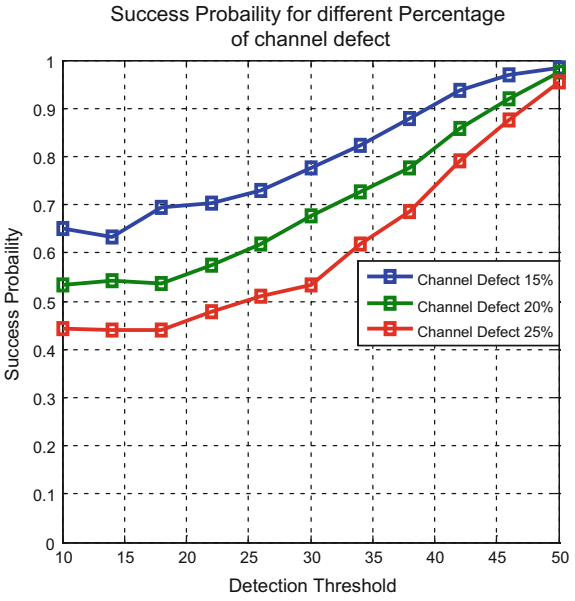

Fig. 4 Success probability with respect to detection threshold for $K = 5$

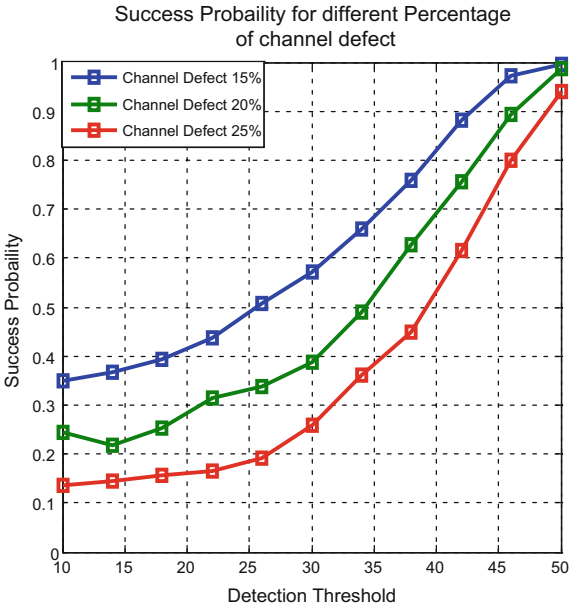

Fig. 5 Success probability with respect to detection threshold for $K = 10$

As the number of users goes on increasing from $K = 5$ to $K = 10$ and $K = 15$, the minimum success probability decreases from 0.6 to 0.35, 0.2 and 0.1 which is shown in Figs. 4, 5, and 6. Further, the number of users goes on increasing the

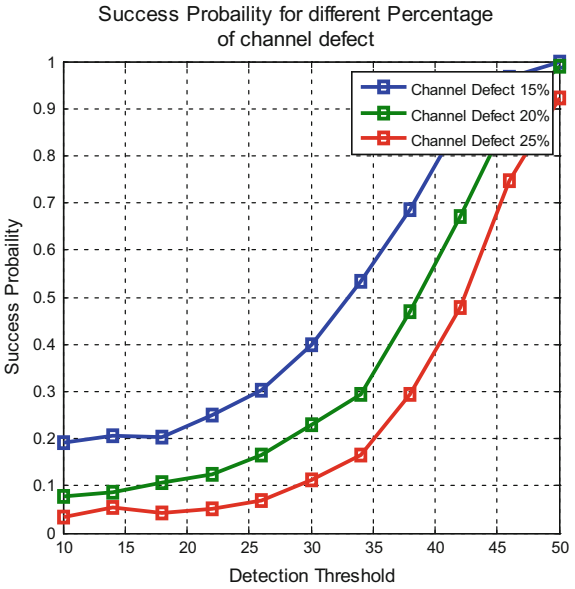

Fig. 6 Success probability with respect to detection threshold for $K = 15$

success probability decreases to zero for small detection thresholds and then increases as the detection threshold increases. From this, it is observed that the optimal number of cooperative secondary users for a Rayleigh fading channel is $K = 5$.

As the number of cooperative secondary users increases, the energy consumption increases and the energy efficiency decreases. But, our main aim is to improve the energy efficiency by decreasing the energy consumption and by increasing the channel throughput. To improve the energy efficiency, the optimization technique is used. So, in this paper, we calculated the optimal number of cooperative secondary users for both nonfading and fading channels.

5 Conclusion

In this paper, we studied CSS over AWGN nonfading channel and Rayleigh fading channel. The performance of CSS has been investigated via the total error rate versus detection threshold for a nonfading channel and the performance of CSS over Rayleigh fading is presented and the success probabilities for different channel defects are compared. In this paper, we observed the optimal number of cooperative secondary users as 5 for nonfading and fading channels. The optimal number of cooperative secondary users is used to reduce the energy consumption and improve the energy efficiency. In future, we want to implement the CSS over Ricean and Nakagami fading channels.

References

1. Mitola J, Macguire GQ (1999) Cognitive radio: making software radios more personal. IEEE Pers Commun Mag 6(4):13–18
2. Spectrum Policy Task Force (2002) Rep. ET Docket, Washington, D.C., USA
3. Yucek T, Arslan H (2009) A survey of spectrum sensing algorithms for cognitive radio applications. IEEE Commun Surv Tuts 11(1):116–130
4. Zeng Y, Liang Y-C, Hoang AT, Zhang R (2010) A review on spectrum sensing for cognitive radio: challenges and solutions. EURASIP J Adv Signal Process
5. Quan Z, Cui S, Sayed A, Poor H (2009) Optimal multiband joint detection for spectrum sensing in cognitive radio networks. IEEE Trans Signal Process 57(3):1128–1140
6. Rif-Pous H, Blasco M, Garrigues C (2012) Review of robust cooperative spectrum sensing techniques for cognitive radio networks. Wireless Pers Commun 67(2):175–198
7. Akyildiz IF, Lo BF, Balakrishnan R (2011) Cooperative spectrum sensing in cognitive radio networks: a survey. Elsevier Phys Commun 4(1):40–62
8. Nallagonda S, Suraparaju S, Roy SD, Kundu S (2011) Performance of energy detection based spectrum sensing in fading channels. In: Proceedings of IEEE International Conference on Computer and Communication Technology (ICCCT'11), pp 575–580
9. Ghasemi A, Sousa ES (2007) Opportunistic spectrum access in fading channels through collaborative sensing. IEEE J Sel Areas Commun 2(2):71–82
10. Ghasemi A, Sousa ES (2006) Impact of user collaboration on the performance of opportunistic spectrum access. In: Proceedings of the IEEE Vehicular Technology Conference (VTC Fall'06), Montreal
11. Lee SH, Lee YH (2009) Hard decision combining-based cooperative spectrum sensing in cognitive radio systems. In: proceedings of the international conference on wireless communication and mobile computing, 21–24 June, ISBN: 978-1-60558-569-7, pp 906–910
12. Armi N, Saad NM, Arshad M (2009) Hard decision fusion based cooperative spectrum sensing in cognitive radio system. ITB 3(2):109–122
13. Singh A, Bhatnagar MR, Mallik RK (2016) Performance of an improved energy detector in multi hop cognitive radio networks. IEEE Trans Veh Technol 65:732–743
14. SethiR, Bala I (2013) Performance evaluation of energy detector for cognitive radio networks. In: IOSR J Electron Commun Eng 8:46–51
15. Stuber GL (2002) Principles of mobile communications, 2nd edn. Kluwer Academic Publishers, Norwell, MA

ICI Cancellation in OFDM Systems Under Stanford University Interim Channel Model

N. Mounika, M. Durga Rani, J. Lakshmi Narayana and M. Naga Lakshmi Kalyani

Abstract In orthogonal frequency division multiplexing (OFDM) systems, it is observed that intercarrier interference (ICI) is the most pervasive effect. Due to the Doppler shift or phase noise, the intercarrier interference effect will occur. In this paper, to alleviate the ICI, a parallel cancellation algorithm and space frequency techniques are combined to form a new technique called space frequency parallel cancellation scheme. The performance of this space frequency parallel cancellation approach is evaluated under SUI (Stanford University Interim) channeling environment.

Keywords SUI · SF · SFPC · ICI · BER

1 Introduction

With OFDM, it is possible to have an overlapping of subchannels in the frequency domain, unlike FDM in which several low-rate user signals are modulated with a separate carrier and transmitted in parallel. Compared to conventional communication techniques like TDMA (time division multiple access), FDMA (frequency division multiple access), and CDMA (code division multiple access), orthogonal frequency division multiplexing communication system has a number of advantages. OFDM is a key scheme for bandwidth-efficient modulation technology and high data rate wireless applications (Figs. 1 and 2).

N. Mounika (✉) · M. Durga Rani · J. Lakshmi Narayana · M. N. L. Kalyani
PSCMRCET, Vijayawada, India
e-mail: mounikaneelam.15@gmail.com

M. Durga Rani
e-mail: mullapudi.durga@gmail.com

J. Lakshmi Narayana
e-mail: jln_9976@yahoo.com

M. N. L. Kalyani
e-mail: mlakshmikalyani@gmail.com

H. S. Saini et al. (eds.), *Innovations in Electronics and Communication Engineering*,
Lecture Notes in Networks and Systems 33,
https://doi.org/10.1007/978-981-10-8204-7_25

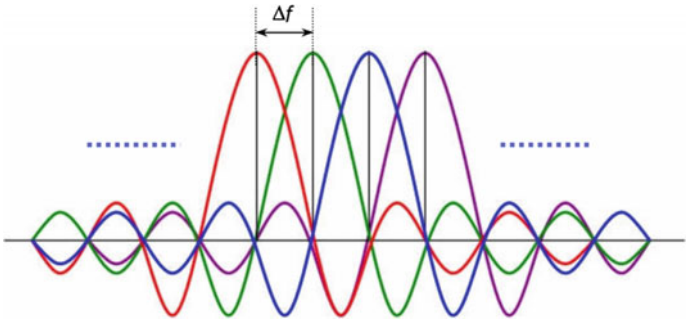

Fig. 1 Orthogonality in orthogonal frequency division multiplexing (OFDM)

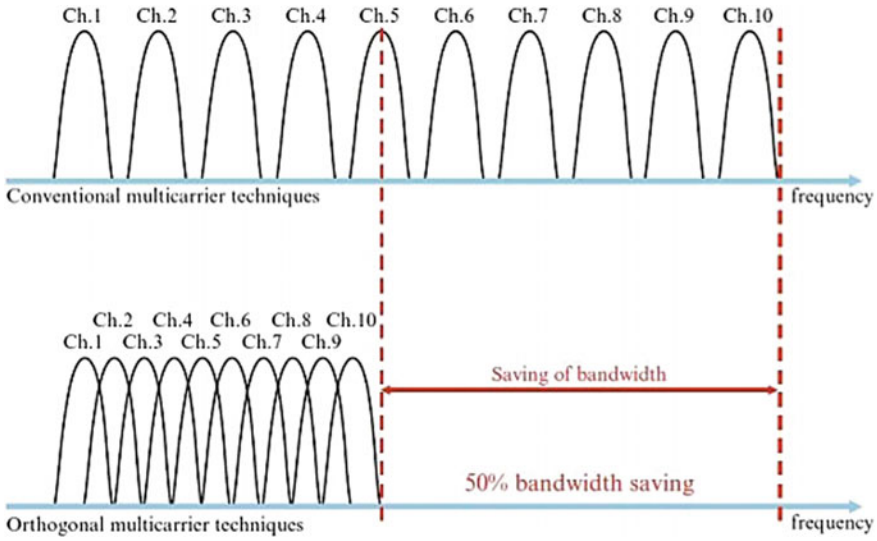

Fig. 2 Conventional and orthogonal multi-carrier techniques

OFDM system has better spectral efficiency as well as high data rate. Because of some special characteristics like flexible and reliable high-speed data rates, and robustness against narrowband interference and frequency selective fading, OFDM is also termed as a future generation communication system.

2 Literature Survey

The subcarriers (multiple frequency channels) are orthogonal to each other in OFDM. Due to the difference between the transmitter and receiver local oscillator frequencies or due to Doppler shift of the channel, the frequency offset sensitivity is existing between the transmitted and received signals, which lead to intercarrier interference [1]. Various techniques are proposed to combat the ICI in OFDM systems [2].

3 OFDM System Model

Openness to the small differences in frequency at the transmitter and the receiver called frequency offset which is the main disadvantage of the OFDM [3] system. The baseband transmitted signal after applying IFFT is

$$y_k = \sum_{n=0}^{N-1} i_n e^{j\frac{2\pi}{N}kn} \qquad \mathrm{k} = 0, 1 \ldots \mathrm{N} - 1 \tag{1}$$

where 'i_n' is the data symbol. Add a cyclic prefix to the signal and then apply parallel to serial conversion then the signal is transmitted [4] (Fig. 3).

$$\hat{i}_n = \frac{1}{N} \sum_{K=0}^{N-1} t_k \, \mathrm{e}^{-j\frac{2\pi nk}{N}} = \frac{1}{N} \sum_{n=0}^{N-1} \sum_{k=0}^{N-1} H_n \, i_n \, \mathrm{e}^{j\frac{2\pi(n+\epsilon)k}{N}} \, \mathrm{e}^{-j\frac{2\pi mk}{N}} \tag{2}$$

4 Parallel Cancellation Approach

The PC-OFDM approach has two branch operations as shown in Fig. 4.

The upper branch is a regular OFDM system in which IFFT is calculated at the transmitter and FFT is calculated at the receiver as shown in Fig. 3. In the lower branch, FFT operation is performed at the transmitter which is given below.

$$y'_k = \sum_{n=0}^{N-1} i_n \mathrm{e}^{-j\frac{2\pi}{N}kn} \qquad \mathrm{k} = 0, 1 \ldots \mathrm{N} - 1 \tag{5}$$

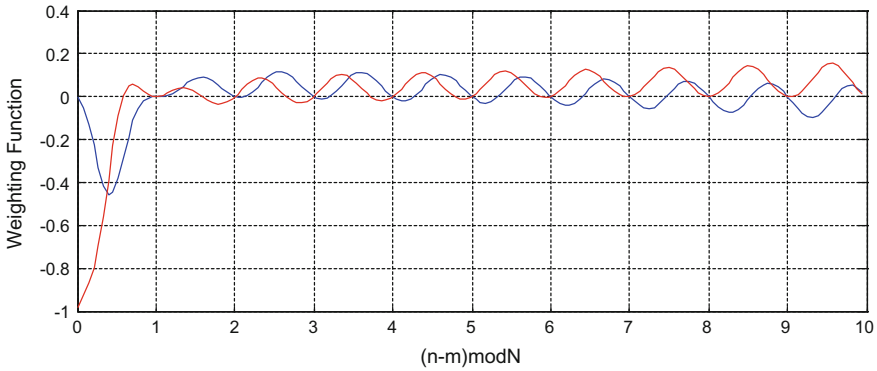

Fig. 3 Weighting function of in regular OFDM systems

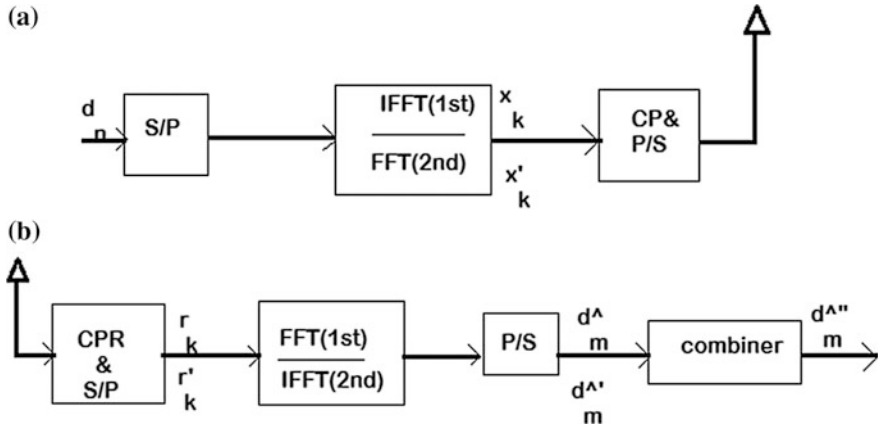

Fig. 4 **a** PC-OFDM Transmitter **b** PC-OFDM Receiver

IFFT operation is performed in the lower branch as shown below.

$$\underset{m}{\overset{\wedge}{i'}} = \frac{1}{N}\sum_{k=0}^{N-1} i'_k e^{j\frac{2\pi mk}{N}} = \frac{1}{N}\sum_{n=0}^{N-1}\sum_{k=0}^{N-1} i_n H'_n e^{j\frac{2\pi(-n+\varepsilon)k}{N}} e^{j\frac{2\pi mk}{N}} \tag{6}$$

$$= H'_m i_m q_0 + \sum_{n=0, n\neq m}^{N-1} H'_n i_n q_{n-m} \tag{7}$$

5 SF-OFDM Systems

Figure 5 shows the block diagram for the space frequency orthogonal frequency division multiplexing system. At the transmitter, the input vector is given by $i = [i_0 i_1 \ldots i_{N-1}]^T$. In this system, two N length blocks are formed through space frequency coding for two branches (upper and lower) as two parallel input data vectors as given below.

$$i_2 = \left[i_1 - i_0^* \ldots i_{N-1} - i_{N-2}^*\right]^T \quad i_1 = \left[i_0 - i_1^* \ldots i_{N-2} - i_{N-1}^*\right]^T,$$

The two input data vectors i_1 and i_2 are sent to two parallel IFFT blocks and transmitted with cyclic prefix through two transmit antennas $T1$ and $T2$. At the receiving side, it performs the operations like de-multiplexing to separate the two branch signals.

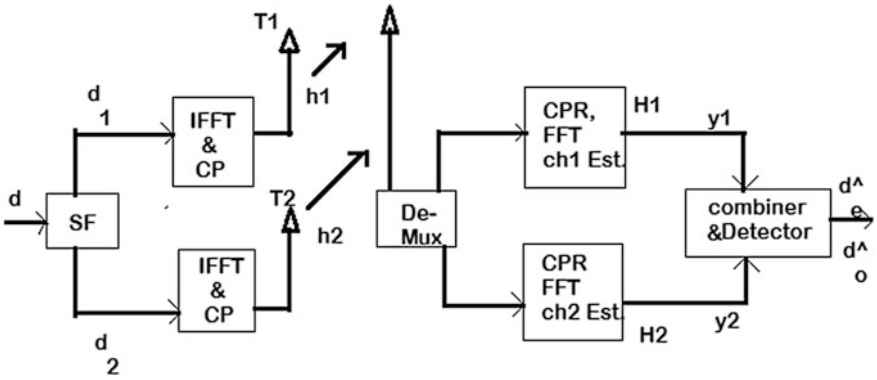

Fig. 5 Block diagram of SF-OFDM transceiver

6 Proposed Approach

The parallel cancellation and space frequency-OFDM techniques are combined naturally as both the techniques PC-OFDM and SF-OFDM are per OFDM symbol basis. The Fig. 6 shows that two vectors of length N are formed as input data vectors i_1 and i_2 at the transmitter.

After removing the cyclic prefix using CPR, FFT is calculated in the upper branch and IFFT is calculated in the lower branch.

7 SUI (Stanford University Interim) Channel Model

The SUI (Stanford University Interim) is one of the channel model used to estimate the bit error rate performance of the system. This SUI channel response depends upon the components like shadowing, path loss, Doppler spread, multipath fading,

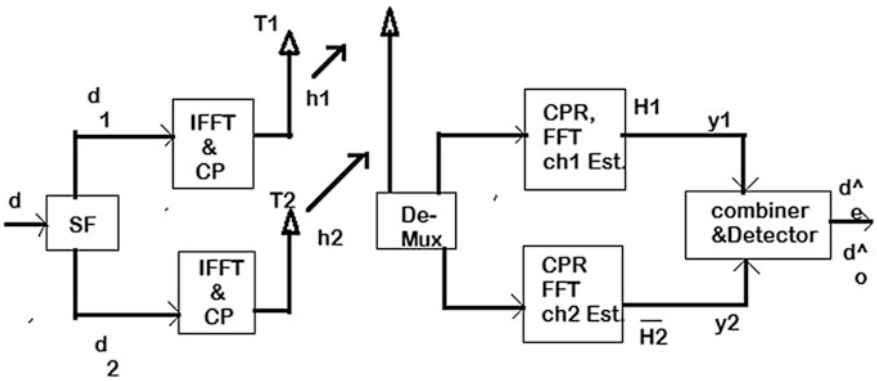

Fig. 6 Proposed approach's block diagram (SFPC)

Table 1 Classification of SUI Channels

			Terrain	Tree density
Terrain type	A	SUI-5, SUI-6	Hilly terrain	Moderate to heavy tree density
	B	SUI-3, SUI-4	Hilly terrain with	Light tree density
			Flat terrain	Moderate to heavy tree density
	C	SUI-1, SUI-2	Mostly flat terrain	Light tree densities

co-channel interference and adjacent channel interference. These parameters are changed according to the atmospheric conditions like tree density, terrain and beam width and antenna height. These parameters are random in nature Based on these above Stanford University channels are proposed (Table 1).

7.1 SUI Channel Model Parameters

BTS antenna height	30 m
Cell Size	7 km
BTS antenna beam width	120
Receive antenna height	6 m
Polarization	Vertical only
Receive antenna beam width	Omnidirectional

8 Simulation Results

The bit error rate performance of the Parallel Cancellation-OFDM, Space Frequency-OFDM and Space Frequency Parallel Cancellation-OFDM schemes has been assessed by simulations. The BER performance of the existing and proposed approaches are shown below.

The Space Frequency Parallel Cancellation scheme is compared with the existing Space Frequency scheme in Fig. 7 with different $N = 256$, $N = 512$ and $N = 1024$ subcarriers (Figs. 8 and 9).

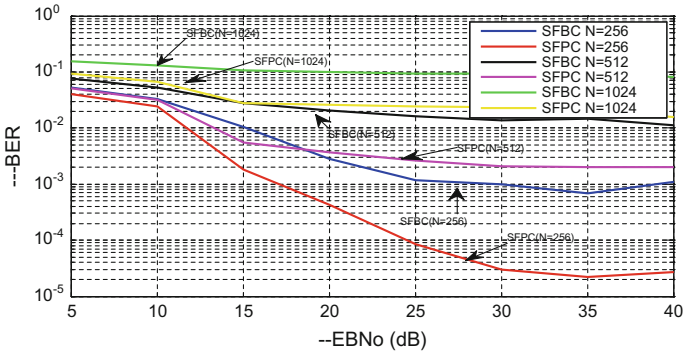

Fig. 7 BER performance for the proposed and existing SFBC schemes with $N = 256, 512, 1024$

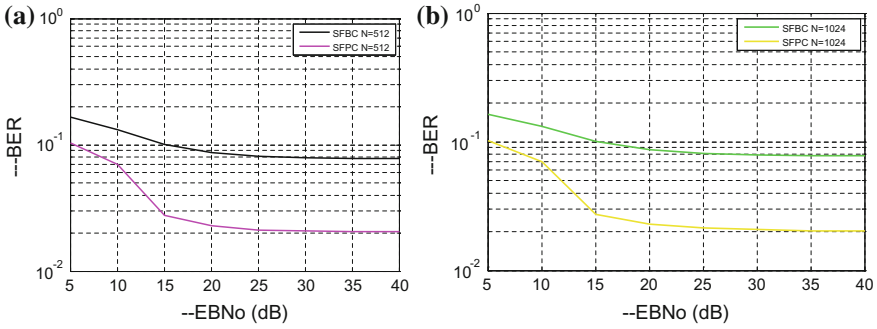

Fig. 8 **a** SFBC & SFPC with $N = 256$ **b** SFBC & SFPC with $N = 512$ **c** SFBC & SFPC with $N = 1024$

Fig. 9 BER performance for the proposed and SFBC under SUI channel with different subcarriers

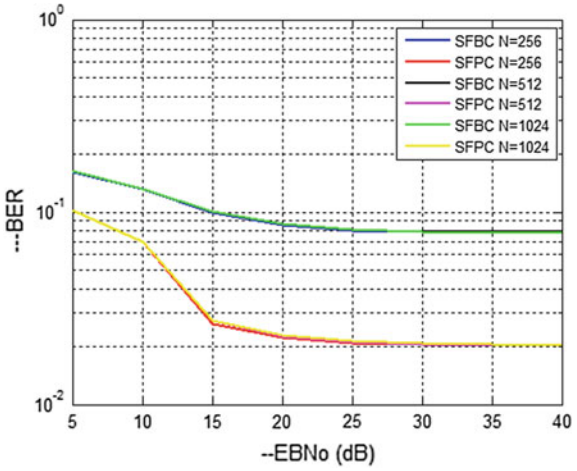

9 Conclusion

The proposed space frequency parallel cancellation-OFDM approach is tested with existing parallel cancellation scheme and space frequency approach under different Stanford University Interim (SUI) channel models. The simulation results show that for the OFDM block size of 256 numbers of subcarriers, the SFPC-OFDM approach is showing better results even at 1024 subcarriers also, when compared against the existing PC-OFDM and SF-OFDM approaches. It is shown that the SFPC-OFDM approach is performing well under different Stanford University Interim channeling environments when compared against the existing parallel cancellation approaches.

References

1. Seyedi A, Saulnier GJ (2005) General ICI self-cancellation scheme for OFDM systems. IEEE Trans Vehicular Technol 54(1):198–210
2. Yeh HG,Yao K (2012) A Parallel ICI Cancellation Technique for OFDM Systems. In: Proceedings of 2012 IEEE GlobeCom, Anaheim, CA, Dec. 2012 pp 3703–3708
3. Yeh HG, Wang CC (2004) New parallel algorithm for mitigating the frequency offset of OFDM systems. In: Proceedings of IEEE VTC Fall 2004, Sept. L.A., pp 2087–2091
4. Alamouti SM (1998) A simple transmit diversity technique for wireless communications. IEEE J Select Areas Commun 16(8):1451–1458
5. Zhao Y, Haggman S-G (2001) Inter carrier interference self-cancellation scheme for OFDM mobile communication systems. IEEE Trans Commun 49(7):1185–1191
6. Armstrong J (1999) Analysis of new and existing methods of reducing inter-carrier interference due to carrier frequency offset in OFDM. Commun IEEE Trans 47(3):365–369

Analyzing Performance and QoS Parameter Estimation for VANET Using D2D

K. P. Sharmila and C. Ramesh

Abstract Intelligent transport systems (ITSs) are becoming an important part of our society, a wide variety of ITS applications need vehicle-to-vehicle (V2V) and vehicle-to-infrastructure (V2I) communication. LTE-assisted device-to-device communication (D2D) is considered for V2V communication. D2D communication overcomes the traditional routing techniques used for V2V communication and also provides a solution for dead ends (failure recovery) in V2V communication. In this paper, we analyze various quality of services (QoS) parameters such as throughput, packet delivery rate, bit error rate, delay, and packet loss rate. We also analyze the performance through D2D framework. The simulation results are presented to illustrate the QoS and performances for VANET through D2D communication.

Keywords ITS · VANET · D2D · Performance parameters · QoS

1 Introduction

Cellular networks are experiencing exponential growth in traffic and this has made industry look for new channel access methods in addition to the conventional methods and infrastructure-based methods that use cellular nodes as access point. 3GPP (Third-generation partnership project) LTE (long-term evolution) aims to provide higher network capacity, high data rates, and public safety services.

WiMAX [1] and LTE-A 4G cellular technologies have tremendously efficient physical and MAC layer. Their performances are still chasing behind mobile users growing data, and therefore there is a need to modernize conventional communication method. D2D (Device-to-device) communication is one of the methods that has gained a lot of attention and acts as a means to offload cellular traffic.

K. P. Sharmila (✉) · C. Ramesh
CMR Institute of Technology, Bengaluru, India
e-mail: hod.tce@cmrit.ac.in

H. S. Saini et al. (eds.), *Innovations in Electronics and Communication Engineering*,
Lecture Notes in Networks and Systems 33,
https://doi.org/10.1007/978-981-10-8204-7_26

LTE devices having D2D capability have potential to become competitor of fall-back public safety network and will function when eNodeB is not functional [2].

Using D2D communication, the spectrum utilization, energy efficiency, and throughput are improved. Cellular network integrates D2D by providing in-band communication or out-band communication. Licensed spectrum is used to have D2D communication in in-band communication. In-band communication also known as underlay approach use dedicated pool of resources where as in out-band communication also known as overlay approach use dedicated pool of resources subtracted from cellular users [3].

The works in the [4–9] investigated the D2D communication for improving efficiency of cellular network. The potential D2D use cases were also introduced such as multicasting, peer-to-peer communication, and video distribution.

Qualcomm's FlashLinq first attempted to implement D2D communication in cellular network [10] which is PHY/MAC network architecture for D2D communication underlaying cellular networks. FlashLinq took advantage of OFDM/OFDMA technologies and distributed scheduling, using which an efficient method for timing synchronization, peer discovery, and link management in D2D-enabled cellular networks created. Proximity services (ProSe) as D2D communication is investigated by 3GPP along with academia and telecommunication companies.

D2D communication is termed as proximity service by 3GPP. It has two main components:

i. Direct discovery (Proximity Detection): D2D-enabled terminals monitor their vicinity continuously to discover proximate devices to establish D2D link for communication. D2D direct discovery is done by a predefined channel which as compared to wireless IEEE 802.11xx gives a short latency time. Once the device discovery is completed, the user equipment (D2D-enabled device) can use the underlay network or the ad hoc network to communicate between them.
ii. Direct communication: Direct communication lets the D2D-enabled equipment to communicate with each other through LTE network or unlicensed band interface.

As D2D is altogether a novel component being added, it brings up many design challenges such as a choice between uplink and downlink for D2D communications, multiple access technology, resource allocation schemes, D2D functions when UE is in different coverage scenarios, etc.

Figure 1 shows both the method: direct discovery and direct communication.

2 D2D Communication

D2D communication involves two main steps: Direct discovery and direct communication. Various scenarios are considered for the direct discovery; they are as follows:

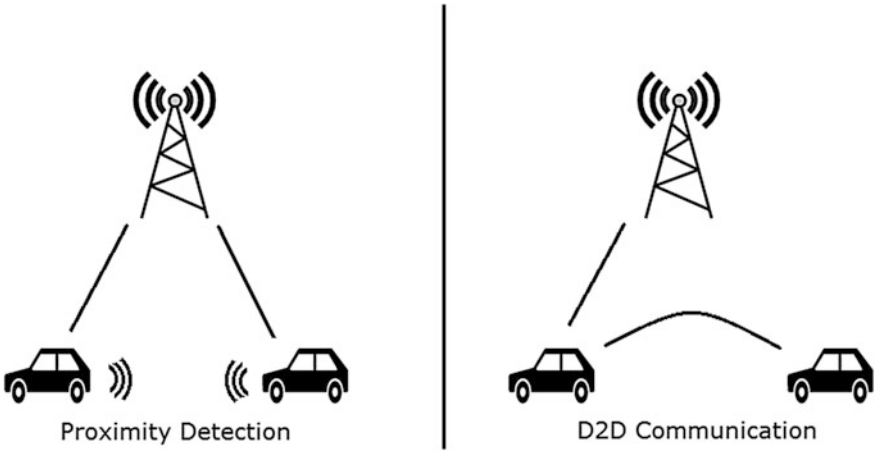

Fig. 1 Both the direct discovery and direct communication

i. Vehicles enabled with D2D communication are in coverage;
ii. Vehicles enabled with D2D communication are in partial coverage; and
iii. Vehicles enabled with D2D communication are out of coverage.

In the first two scenarios, vehicles in partial coverage and vehicle in full coverage network provide the information about the resources to be used in V2V communication between vehicles

In the out-of-coverage scenario, radio resources are preconfigured in the device for a specific geographical area. Figure 2 shows both the method: direct discovery and direct communication. Pure vehicle-to-vehicle communication (V2V) can suffer failure or blocking and it is known as dead end. By D2D communication along with ITS architecture, we can avoid dead ends that occur in the communication system. The idea here is to take advantage of the ITS network management feature and allow vertical handover between access media to recover dead ends.

Figure 3 shows both the method: Direct discovery and direct communication

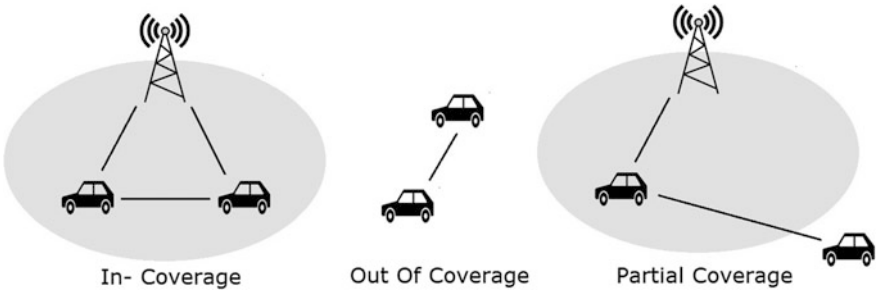

Fig. 2 Different coverage scenarios

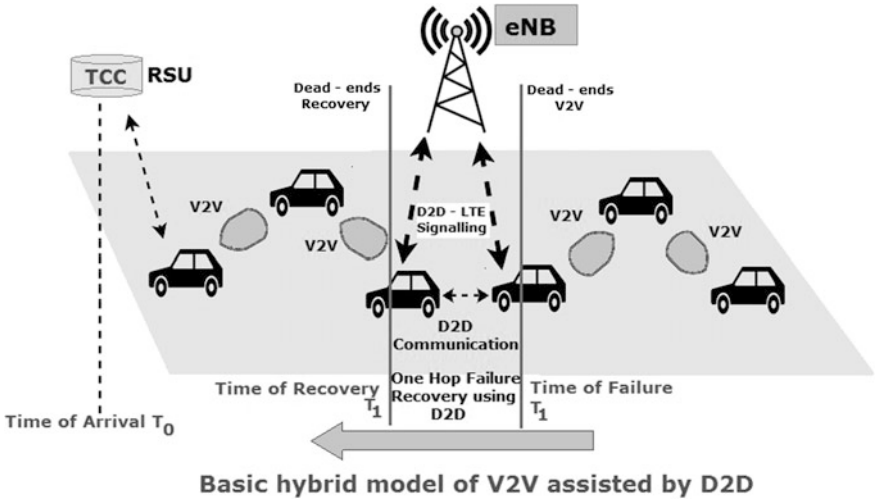

Fig. 3 Model showing V2V and V2I communication [4]

3 Protocol Stack

Physical layer performs the functions like error detection, forward error correction, mapping of transport channels to physical channels, multiple input multiple output (MIMO) antenna processing, beamforming, transmit diversity, RF processing, etc. These functions are performed in order to provide data transport services.

Protocol stack for the D2D communication is as shown in Fig. 4. MAC layer provides radio resource allocation services, data transfer services to the upper layers and also support different functions like scheduling, mapping between logical channels and transport channels, radio resource section for sidelink, etc. Functions such as broadcast of system information, paging, and establishment/modification are done by RRC layer.

3.1 Functional Entities

ProSe Function: A logical entity that runs on the network side and is responsible for all control-related PC3 messages between UE and ProSe server is a ProSe function. Proximity services (ProSe) protocol is responsible for functions such as direct provisioning for direct discovery and direct communication, direct discovery name management, storage of ProSe-related subscriber data, and acting as location services client to enable EPC level ProSe discovery.

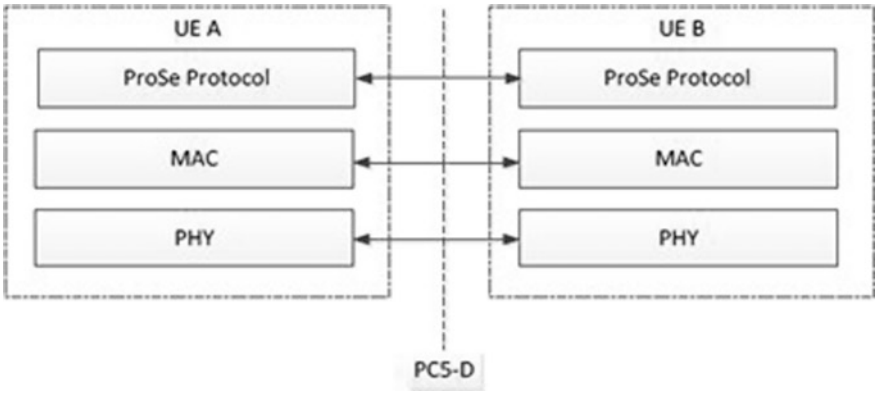

Fig. 4 Protocol stack

i. ProSe Management: D2D communication between the user equipment occurs in the case when the UEs are in coverage. When the UEs enter out-of-coverage ad hoc and cluster head topologies are used for communication, ProSe services should be in network management and control.
ii. Synchronization: When D2D-enabled user equipment is in coverage, they are synchronized to their corresponding eNBs. When user equipments are out of coverage, in such case periodic transmission of the synchronization signal is needed.
iii. Device Discovery: User equipments that are nearby are to be detected for both commercial and public safety user equipments. In direct discovery, UEs search for nearby user equipments that are participating in D2D communication and periodically transmit and receive discovery signals.
iv. Direct Communication: Different transmission formats are defined like unicast, relay, groupcast, and broadcast. For supporting user-to-user communication, many changes are required like physical layer change and new standards like modulation format, power control, channel measurements, and HARQ operations.

ProSe App Server: ProSe application server hosts the ProSe-based application; the applications are not part of 3GPP. These application servers can communicate with the UE which are enabled by ProSe application. **UE enabled with ProSe (ProSe-based application in UE)**: ProSe-enabled UE can be used to contact a friend who is nearby or in close vicinity. They can also be used to get service alerts like availability of taxi or bus or alerting the presence of emergency vehicle in the absence of network.

4 Simulation Results

The simulation for LTE-A is performed using NS3 tool. The VANET code is written in C++ and necessary modified files are called in the code. The LTE eNodeB is placed between the roads. The V2I non-safety application traffic is

flowing downlink from eNodeB to random number of sink nodes (usually half the number of total vehicles) and V2V safety application traffic is exchanged using LTE D2D.

The various parameters considered for simulation are shown in Table 1.

Scenario 1: Typical VANET scenario with fixed nodes and speed.
Tables 2 and 3 show the results of the QoS parameters obtained by simulating the VANET scenario for 20 vehicles moving at an average speed of 20 m/s with below traffic:

i. V2I Traffic: Downlink traffic of 1000 B sent to 10 random vehicles.
ii. V2V Traffic: BSM traffic of 200 B exchanged between all vehicles using D2D at a frequency of 10 Hz.

The simulation parameters are obtained based on the safety transmission distance for both V2I and V2V traffics. Both the results of V2V and V2I depict that throughput is good; the delay increases with distance but is consistent and PDR decreases with increasing distance.
Scenario 2: V2V PDR for increasing number of vehicles
Table 4 shows the results of the QoS parameters obtained by simulating the VANET scenario for increasing vehicles moving at an average speed of 20 m/s with below traffic:

Table 1 Simulation parameters for LTE-A

Simulation parameters	
No. of vehicles	120
Speed of vehicles	20 m/s
Simulation area	1500*300 m Road
Simulation duration	20 s
Number of vehicles for application traffic	Half the total number of vehicles
Traffic types	V2I: Application Traffic of 1000B being sent at an interval of 0.1 s to 10 random Nodes as downlink traffic from eNodeB V2V: BSM (Basic Safety Messages) of 200 bytes being sent as a broadcast at a frequency of 10 Hz by all nodes as LTE D2D
	For LTE-A
Channel bandwidth	10 MHz
Transmission power	eNB (40DBm)/UE(20DBm)
Propagation loss model	Friis
Data rate/RB allocation	DL(50)/UL(50)
Mac scheduler	PfFfMacScheduler
LTE Frequency band used	DlEarfcn (100)/UlEarfcn (18100)
LTE eNodeB RRC—SRS periodicity	160

Table 2 Results for V2I traffic for LTE-A for number of nodes 20 and sink nodes 10

Distance	Throughput (kbps)	Average delay (ms)	Bit error rate	Average PDR	Average PLR
50	228.5611	127.0195	0.2559	0.9559	0.0441
100	196.2467	144.9812	0.3554	0.8399	0.1601
150	204.3528	146.296	0.3695	0.8524	0.1476
200	200.1726	145.618	0.3622	0.8459	0.1541
250	155.513	162.4246	0.4373	0.7295	0.2705
300	159.0438	166.8721	0.4543	0.7461	0.2539
350	157.0695	164.3853	0.4448	0.7368	0.2632
400	145.7358	172.7871	0.4784	0.6805	0.3195
450	147.683	175.6473	0.4878	0.6897	0.3103
500	147.4492	175.3039	0.4866	0.6886	0.3114

Table 3 Results for V2V traffic for LTE-D2D for number of nodes 20

Distance	Throughput (kbps)	Average delay (ms)	Average PLR	Average PDR	Bit error rate
50	227.296	130.1607	0.0648	0.9352	0.2758
100	186.6805	152.501	0.1619	0.8381	0.3643
150	194.6629	156.4329	0.1511	0.8489	0.3773
200	190.5465	154.4053	0.1567	0.8433	0.3706
250	151.0999	168.3895	0.2961	0.7039	0.4575
300	159.0438	166.8721	0.2539	0.7461	0.4543
350	152.5332	160.0244	0.2896	0.7104	0.4639
400	141.2233	176.5417	0.3444	0.6556	0.4984
450	142.6089	178.1795	0.3322	0.6678	0.5064
500	142.4425	177.9828	0.3336	0.6664	0.5055

i. V2I traffic: Downlink traffic of 64 B sent to half the number of total number of vehicles.
ii. V2V traffic: BSM traffic of 200 B exchanged between all vehicles using D2D at a frequency of 10 Hz.

From Table 4, it can be easily inferred that for a given transmission distance the PDR of V2V traffic is approximately consistent which indicates reliability of D2D technology. However, for distances of 250 and 350 m, the PDR is observed to be only 70% which is poorer compared to 802.11p and LTE interworking. But for distances greater than 450 m, the PDR remains at 60% and is much better than existing technologies where PDR deteriorates to less than 50% for distances above 450 m.

Table 4 V2V PDR for increasing nodes

Increasing nodes/safety distance	V2V PDR % (50 m)	V2V PDR % (150 m)	V2V PDR % (250 m)	V2V PDR % (350 m)	V2V PDR % (450 m)
20	93.52	84.89	73.22	71.04	66.78
30	91.47	82.86	70.51	71.77	64.27
40	89.79	82.69	71.96	71.78	63.06
50	88.34	82.52	70.38	72.18	62.76

Scenario 3: V2V PDR for increasing mobility

Table 5 shows the results of the QoS parameters obtained by simulating the VANET scenario for increasing vehicle speed with fixed vehicles as 20 with below traffic:

a. V2I traffic: Downlink traffic of 64 B sent to 10 random vehicles.
b. V2V traffic: BSM traffic of 200 B exchanged between all vehicles using D2D at a frequency of 10 Hz.

Similar to high-dense scenarios, here in high-mobility scenarios, the PDR is better at larger distances of 450 m and above compared to existing technologies of 802.11p and LTE interworking.

4.1 Performance Analysis of a Typical VANET Scenario With V2I as LTE Downlink and V2V as LTE D2D

From Fig. 5a, b, it can be inferred that for increasing distance, the throughput, bit error rate, and PDR decrease, while the average delay increases. Unlike the conventional technologies like 802.11p where there are a sharp increase and decrease in safety transmission distance, here the variation is constant indicating robustness of LTE-A technology for V2I applications. The same results are obtained for V2V traffic.

Table 5 V2V PDR for increasing speed

Increasing speed	V2V PDR % (50 m)	V2V PDR % (250 m)	V2V PDR % (450 m)
5	93.29	71.17	65.47
10	93.06	71.75	66.4
15	93.29	70.68	66.23
20	92.63	71.21	66.67
30	92.77	71.9	66.25
40	92.4	72.04	66.62

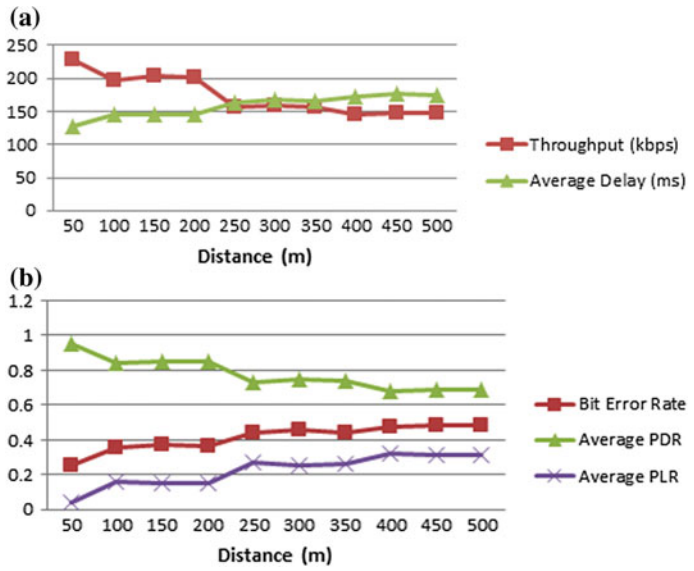

Fig. 5 V2I QoS parameters graph for different safety transmission distances

4.2 Performance Analysis for V2V Traffic for Increasing Node Size

From Fig. 6, it can be inferred that the PDR remains approximately constant for a particular transmission distance. It is of interest that for 450 meters the PDR is approximately 60% which indicates that LTE-D2D is a better solution for larger distances compared to existing technologies where the PDR is below 50% as the safety transmission distance increases.

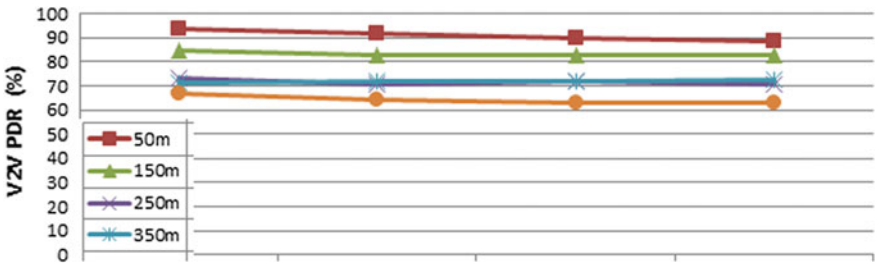

Fig. 6 V2V PDR for increasing node size

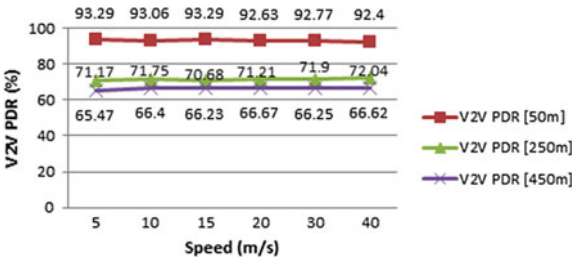

Fig. 7 V2V PDR for increasing speed for transmission distance

4.3 Performance Analysis for V2V Traffic for Increasing Speed

Figure 7 displays the performance graph for V2V traffic for increasing speed indicating mobility environment keeping node size fixed at 20. The graph below clearly indicates that for a given transmission distance and increasing speed, the PDR is not affected making it suitable for V2V communication.

5 Conclusion

In high-mobility and high-dense scenarios for larger distances, LTE D2D performance is consistent and better than its predecessor technologies such as 802.11p and LTE interworking. For a given transmission distance, the QoS parameters for V2V traffic remain constant indicating reliability which is a requirement for mission-critical applications. The average E2E latency is comparable and tolerable for V2V communication as with other technologies as 802.11p and LTE interworking. As already concluded in previous chapters that V2I traffic QoS is best suitable when implemented in LTE, the same also affirms here. With the introduction of D2D technology in cellular systems, LTE-A provides a novel solution to be implemented in VANETs. The need to install RSUs and OBUs is done away with this infrastructure, thereby making it cost effective for operators and consumers. As LTE-A is being fast deployed across the globe and constant innovation and enhancements are underway, the need to maintain and upgrade the vehicular systems based on LTE-A is minimal, thereby making LTE-A a good choice for vehicular networking.

References

1. IEEE Standard for Local and Metropolitan Area Networks Part 16: Air Interface for Fixed and Mobile Broadband Wireless Access Systems (2006) IEEE Std 802.16-2004/Cor 1-2005 (Amendment and Corrigendum to IEEE Std 802.16-20044), p 0 1-822

2. Hakola S, Chen T, Lehtomaki J, Koskela T (2010) Device-To-device 40; D2D 41; Communication in cellular network—performance analysis of optimum and practical communication mode selection. In 2010 IEEE wireless communication and networking conference, pp 1–6
3. Cheng X, Yang L, Shen X (2015) D2D for intelligent transportation systems: a feasibility study. IEEE Trans Intel Transp Syst 16(4):1784–1793
4. Lin Y-D, Hsu Y-C (2000) Multihop cellular: a new architecture for wireless communications. Proceedings IEEE INFOCOM 3:1273–1282
5. Kaufman B, Aazhang B (2008) Cellular networks with an overlaid device to device network. In: Proceedings of Asilomar conference on signals, systems and computers, pp 1537–1541
6. Doppler K, Rinne M, Wijting C, Ribeiro C, Hugl K (2009) Deviceto-device communication as an underlay to LTE-advanced networks. IEEE Commun Mag 47(12):42–49
7. Doppler K, Rinne MP, Janis P, Ribeiro C, Hugl K (2009) Device-to-device communications; functional prospects for LTE-Advanced networks. In: Proceedings of IEEE ICC workshops, pp 1–6
8. Osseiran A, Doppler K, Ribeiro C, Xiao M, Skoglund M, Manssour J (2009) Advances in device-to-device communications and network coding for IMT-Advanced. In: ICT mobile summit
9. Peng T, Lu Q, Wang H, Xu S, Wang W (2009) Interference avoidance mechanisms in the hybrid cellular and device-to-device systems. In: Proceedings of IEEE PIMRC, pp 617–621
10. Wu X, Tavildar S, Shakkottai S, Richardson T, Li J, Laroia R, Jovicic A (2010) FlashLinQ: a synchronous distributed scheduler for peer-to-peer ad hoc networks. In: Proceedings of IEEE Allerton conference on communication, control, and computing, pp 514–521

DDTRCSTCT: Design of Doppler Tolerant Radar Code to Increase SNR Using Trellis Code Technique

Rajkumar D. Bhure, K. Manjunath Chari and Syed Jalal Ahmad

Abstract In todays world the defense security system facing most important interesting issue for the doppler radar is the detection of multiple moving targets attacks. But the process of detection and ranging target fails because the shadow of fast-moving targets (noise) may hide the slow-moving targets, which may lead a serious damage in the battlefield environment. Hence, measurement of these parameters (i.e., range and resolution) of target is a challenging issue. Considering these challenges, current research trend concentrates on enhancement of Merit Factor (MF) as well as Signal-to-Noise Ratio (SNR) of the radar system. In this paper, a novel approach has been proposed, namely, trellis code generation using quad code sequence. This method improves the Merit Factor (MF) of the main lobe; on the other hand, it reduces the side spikes of the noise amplitude below 80 dB caused by fast-moving attacks during target detection process. Thus enhanced SNR acheived by creating multiple clear windows at different Doppler's (frequency shift) with respect to target range. We have validated our approach using Matlab.

Keywords Quad code · Trellis coding technique · Doppler · Matlab
Side spikes · SNR

R. D. Bhure (✉)
GITAM, Hyderabad, Telangana, India
e-mail: bhure.rajkumar@gmail.com

K. Manjunath Chari
GITAM University, Hyderabad, Telangana, India
e-mail: hodece_hydcampus@gitam.in

S. J. Ahmad
MIET, Jammu, Jammu and Kashmir, India
e-mail: Jalal0000@yahoo.com

H. S. Saini et al. (eds.), *Innovations in Electronics and Communication Engineering*,
Lecture Notes in Networks and Systems 33,
https://doi.org/10.1007/978-981-10-8204-7_27

1 Introduction

In present scenario, speedy and consistent identification of MMTs in the battle space are quite hard for military personals. Radar stands for Radio Detection and Ranging, which detects the presence of a physically remote target through the receiver and processing of backscattered electromagnetic waves.

Radar system used the various coding technique to find the present position of the target by taking the autocorrelation of the transmitted pulse with the received reflection from the target. The received reflection conveys the information about the velocity and range of the target in terms of Doppler shift and delay. These received reflections are further managed by filtering and coding techniques. Such radars are used in aviation, sounding satellites, meteorology, radar guns, slow-moving targets (helicopters, fighter aircraft), and fast Inter-Continental Ballistic Missile (ICBM) and bistatic radar (air-to-surface missile), etc.

Radar, which can effectively sense the target and exactly determine its range and speed in a multi-target environment, capable of being considered as high-resolution radar. The decision about range (R) of the pulse radar can be measured in terms of the senders pulse width, i.e., "$R = (C\ \mathrm{Tp})/2$" Where "C" is the speed of light and "Tp" is the pulse width and dividing factor "2" represents the back and forth distance of radar. But, this type of explanation about range performance is mostly valid for fundamental (basic) pulse radars, which transmit unmodulated (static frequency) pulses to increase resolution. However, all the proposed approaches fail to get a clear window at desired Doppler. In this paper, we present an approach to enhance Signal-to-Noise Ratio (SNR) with respect to desired Doppler. In this approach, we use equal weighted hex codes to generate trellis code Sequence for increased SNR in Doppler tolerant Radar. The rest of the paper is organized as follows: in Sect. 2, we present the related work, and in Sect. 3, we presented our proposed approach, and we conclude our paper in Sect. 4.

2 Related Work

Faulconbridge and Barton [1, 2] presented an approach in which the reverberation of signal after passing the Doppler filter bank results in impulses having narrow width with large peak values. Hence, the relative velocity of the radar and the target itself is large compared to the signal transmission, which cannot be ignored, as the acknowledged signal is inaccurate and does not match with the Doppler filter. This misalliance results in the loss of the signal as well as increases the amplitude of the side spikes in the compacted pulse. But under different Doppler conditions, the Doppler tolerant waveform with minimum signal loss is always desired.

Lewis and Kretschmer [3] presented a novel approach called polyphase pulse compression codes. The authors implemented this approach using phase-coded waveform and digital correlator, which is used as a matched filter in the proposed

approach. However, the proposed approaches have no restriction on code elements and are normally derived from the phase history of the frequency-modulated pulse.

Binary phase codes [4] were originally developed by Golay and Barker in which the phase feature is restricted to 0 or π. The main weakness of these codes is sensitivity to Doppler shift. However, the Golay complementary codes generate high amplitude noise spectrum, in which sidelobe leads hide all multiple moving targets under the main lobe. Hence this does not allow the doppler radar to find the definite range of the target, at the desired Doppler's shift, several Complementary codes and polyphase codes knowledge same problems of side lobe hiding at Doppler shift. Due to which side lobes mask secondary moving and multiple targets. Hence, it fails to improve the SNR to the expected level.

The Costas signals [5] was anticipated, with the intention of improving auto-correlation. In the same manner, an overlaying of orthogonal codes [6] were proposed and also in pulse modulation [7, 8] of Costas frequency hops were introduced using phase codes and complementary sequences. However, rare approaches presented Costas signals outside the orthogonality condition, which requires frequency separation "*f*" that should be equal to the inverse of pulse duration Tp. So it fails to improve the resolution and SNR for moving targets of radar.

Borwein et al. [9] proposed binary phase codes, in which the phase elements are restricted to 0 or π. Lewis and Kretschmer [10] presented a polyphase codes which are derived from the phase history of Linear Frequency Modulation (LFM) pulses examples of such codes are Frank codes, *P*1 and *P*2 codes, which are only available when $L = k2$ which leads increase in Doppler frequency, but fails presented approach to minimize the side spikes (noise).

Reddy and Anuradha [11] proposed a model in which the authors improved the SNR of Mesosphere–Stratosphere–Troposphere (MST) by the use of Kaiser hamming and cosh hamming window function. In this approach, merit factor is improved by enhancing the power of the main lobe. But it fails to eliminate the dominating noise peaks due to side lobes. Hence, application of such an approach will be limited to stationary targets.

Singh et al. [12] proposed an approach to detect multiple moving targets by windowing technique. This method can overcome oversampled PTM code by generating multiple windows with respect to desired Doppler. In comparison with the main window, there are multiple windows in succession but on some specific Doppler frequencies, and the side lobe is above 0.2 dB. However, it increases the merit factor but range resolution degraded because most of the multiple moving targets are appearing below 0.2 dB. Hence, SNR may be affected.

3 Proposed Approach

The presented approach has been generated from convolutional codes, and the sequence of the code can be represented as (n, k, s). Where number of outputs signifies "n" and "k" are the number of inputs bits and "s" shows the number of

shift registers. Actually, the convolution codes are produced by passing the information successively through a series of shift registers. The current n-bit output is subjected not only on the value of the current block of "k" input bits but also on earlier "$s-1$" blocks of "k" input bits. So, the current output of "n" bits is a function of the last "$s \times k$" bits. Figure 1 reflects the generation of convolution codes of (n, k, s). Here, the Fig. 1 presents the convolution encoder for (n, k, s) in which the quad code sequential bits $M(x)$ is given as an input sequence. After each input bit, the Mi changes, which changes the shift register "Mi-1, Mi-2" bits. Initially, Mi-1 and Mi-2 are set in 00 states. The corresponding output $X1$ and $X2$ are generated by the use of exclusive OR combination of state of the shift registers. The complete output of Fig. 1 is represented in Fig. 2.

Figure 2 represents the state transition diagram in which the left side nodes are current states and the nodes on the right are the resulting next state. A black solid line represents the state transition for M0 = 0 and a solid red line represents for M0 = 1 here the initial state of the shift registers are at 00 states.

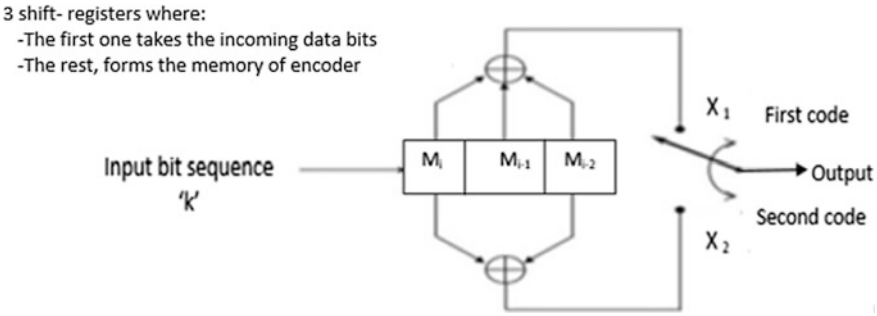

Fig. 1 Convolution encoder

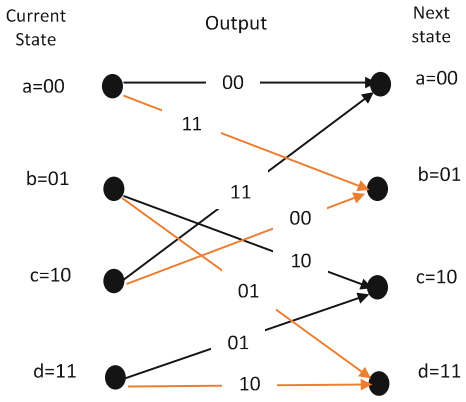

Fig. 2 State transition diagram

For a successful trellis code generation, the input bit sequence must satisfy the following algorithm:

i. It will have $L + s$ Levels, where L = length of message bits and s = length of a shift register.
ii. The first $(s-1)$ levels are for the departure of the encoder for its initial state.
iii. The last $(s-1)$ levels are for returning to the initial state.
iv. The levels $s-1 < P < L$ the structure is periodic or repeated.

In this paper, we primarily produce the radar target detection bits by the use of Trellis Coding Technique (TCT). The Trellis Coding (TC) is a method which generates the code word from a given data (i.e., user-defined code), here it is called transmitting polynomial represented by $M(x)$. The user-defined code considered as transmitting polynomial $M(x)$ is to be generated by considering the equal weighted binary hex code sequence of decimal numbers from 0 to 15 which is divisible by three can be represented as

$$B(x) = \prod_{i=1}^{q} c_i \quad \text{Where } C = 3,\ q = 4 \tag{1}$$

However, Eq. (1) does not able to calculate all the equal weighted numbers from 0 to 15, so the missing numbers in the series can be computed by the use of Eqs. (2) and (3).

$$G(x) = \frac{I_N + E_N}{I_N} = 05 \qquad (\text{i.e. in binary hex coding } '0101') \tag{2}$$

where "I_N" is the first decimal number obtained from Eq. (1), and the last decimal number "E_N" is obtained from Eq. (1), and the continual decimal number is designed as

$$R = 2 * G(x) = 2 * 05 = 10 \qquad (\text{i.e. in binary hex coding } '1010') \tag{3}$$

As these two combined terms (i.e., 0101, 1010) and $B(x)$ together considered as input quad code input sequence $M(x)$ for trellis code generation and can be represented as

$$M(x) = 001101010110100110101100$$

Therefore, according to the designed algorithm, the number of levels required = $L + K-1 = 24 + 3-1 = 26$

First and last $K-1$ levels are = $2-1 = 2$.

Periodic levels lies between = $K-1 < P < L = 2 < P\ (26) > 24$.

Figure 3 represents the resultant code word generation with the help of trellis code tree of length 48 bits and is given by

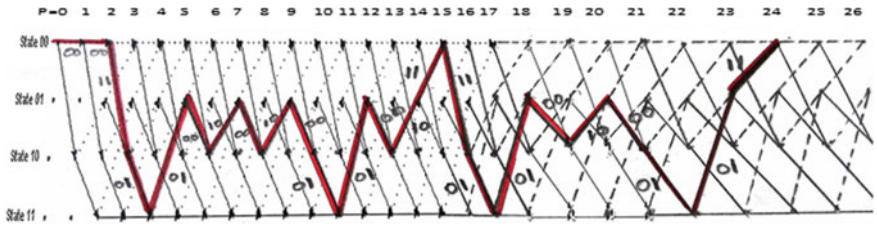

Fig. 3 Trellis code tree

$$T_R = 0\,0\,0\,0\,1\,1\,0\,1\,0\,1\,0\,0\,1\,0\,0\,0\,1\,0\,1\,0\,1\,0\,0\,1\,1\,1\,1\,0\,1\,0\,1\,0\,0\,0\,1\,0\,1\,1\,1$$

To increase the SNR and merit factor of the received signal the code length is further increased by the use of EX-OR operation of "T_R" sequence (see Fig. 4). The resultant code word can be represented as

$$Tc_W = T_R E_R = 0\,0\,0\,0\,1\,1\,0\,1\,0\,1\,0\,0\,1\,0\,0\,0\,1\,0\,1\,0\,1\,0\,0\,1\,1\,1\,1\,0\,1\,0\,1\,0\,0\,1\,0\,0\,0$$
$$0\,1\,0\,1\,1\,1\,0\,0\,1\,1\,1\,1\,0\,0\,1\,0\,0\,0\,1\,0\,1\,1$$

where E_R = 0 0 1 1 1 1 0 0 1 0 0 0 1 0 1 1 (EX-OR Operation of T_R, refer Fig. 4).

Furthermore we are again increasing the length of the code word simply by appending the complementary bits of "Tc_W" to the right of the code to increase further merit factor as well as the SNR of the received pulse, this process of taking complementary bits with "Tc_W" will continue till the length of the code word reaches 256 bits, which is the nominal length considered for current literature. The presented approach is called as Trellis Code Generation using Quad Code Sequence (TCGQCS). The required code word length is defined as

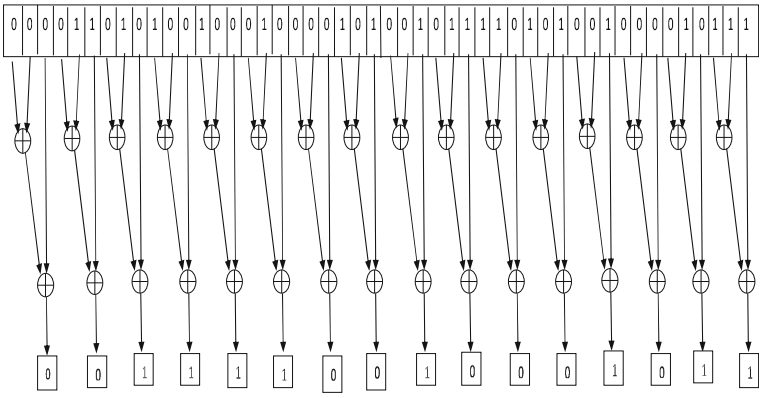

Fig. 4 Ex-OR operation of T_R

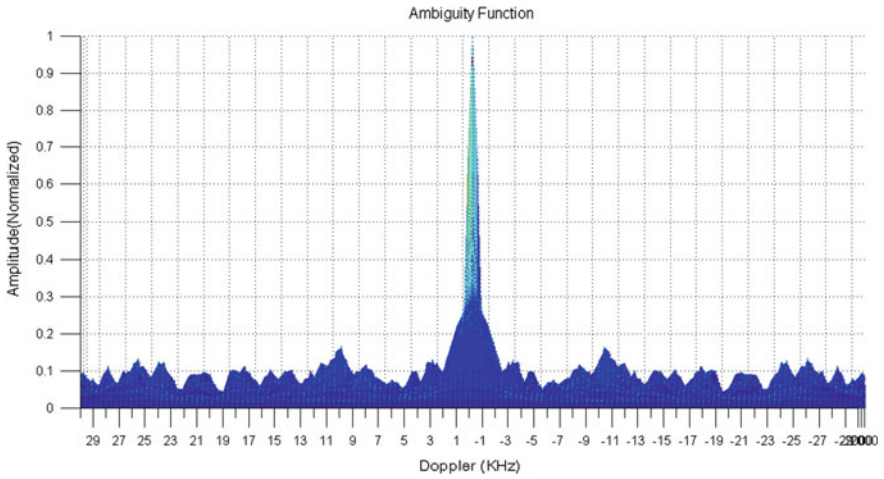

Fig. 5 Doppler versus amplitude variation

$$T_{\mathrm{RTDI}} = T_{CW} \tag{4}$$

where T_{RTDI} will be the initial radar target detection code, and the next code can be embodied as

$$(T_{\mathrm{RTDI}})_1 = T_{CW}\overline{T_{CW}} \tag{5}$$

$$(\mathbf{T_{RTDI}})_{\mathbf{n}} = (\boldsymbol{T}_{\mathbf{RTDI}})_{\mathbf{n-1}}\left(\overline{\boldsymbol{T}_{\boldsymbol{RTDCI}}}\right)_{\mathbf{n-1}} \tag{6}$$

Equations 4, 5 and 6 are adapted to obtain final code word of length 256 bits long and can be tested for the detection process of multiple moving targets.

Figure 5 represents the variation of Doppler versus amplitude. From the figure, we observe that a clear window from 0 to 30 kHz, if we consider 0.2 (normalized amplitude) as a threshold value of target detection as per the current literature. Also from the figure, it is observed that three clear windows have been created (i.e., 3–9; 12–23; 27–30) if we considered 0.1 (normalized amplitude); this shows further improvement of target detection with respect to the latest art of work (i.e., Sing et al. 2017). This huge number of windows enhances the probability of target detection at desired Doppler.

4 Conclusion

By the use trellis coding technique, one can achieve the high range resolution in Doppler tolerant radar system by improving the detection probability of multiple moving targets with higher Signal-to-Noise Ratio (SNR). The presented approach is

very simple but very much effective to minimize the noise introduced by side spikes. Hence, the masked secondary multiple and moving target can detect their present position with respect to range and Doppler frequency. Here, we also conclude that the presented approach will give the clear information about the moving targets from 0 to 35 kHz Doppler frequency which is the practical frequency of detection process. The presented approach reduces the amplitude peaks of almost all side spikes (noise) below 0.1. This is very faithful and effective development of increasing signal-to-noise ratio in radar engineering.

References

1. Faulconbridge I (2002) Radar Fundamentals. Argos Press, Australia
2. Barton DK (1975) Pulse Compression. Artech House, Norwood, MA
3. Lewis BL, Kretschmer FF (1981) A new class of polyphase pulse compression codes and techniques. IEEE Trans Aerospace Electron Syst 17:364–371
4. Pace PE, Ng CY (2010) Costas CW frequency hopping radar waveform: peak side lobe Improvement using Golay complementary sequences. Electron Lett 46(2):169–170
5. Freedman A, Levanon N (1986) Staggered costas signals. In: IEEE transactions on aerospace and electronic systems, vol AES-22, no. 6, pp 695–702
6. Levanon N, Mozeson E (2004) Orthogonal train of modified Costas pulses. In: Proceedings of the IEEE radar conference, April 2004, pp 255–259
7. Yang H, Zhou J, Wang F, Zhang Z (2011) Design and analysis of Costas/PSK RF stealth Signal waveform. In: IEEE CIE international conference on radar
8. Lemieux J, Ingels F Analysis of FSK/PSK modulated radar signals using Costas arrays and complementary Welti codes. In: Record of the IEEE international radar conference, 990, pp 589–594
9. Borwein P, Kaltofen E, Mossinghoff M (2007) Irreducible polynomials and Barker Sequences. ACM Commun Comput Algebra 41(4)
10. Lewis BL, Kretschmer F (1981) A new class of polyphase pulse compression codes and Techniques. IEEE Trans Aerospace Electr Syst 17(3):364–372
11. Ravi Krishna Reddy D, Anuradha BJ (2015) Improved SNR of MST Radar Signals By Kaiser-Hamming and Cosh-Hamming Window Functions. Int J Eng Res Appl 5(3):32–38
12. Singh K, Elizabath Rani D Syed Jalal Ahmad (2016) Re-sampling binary hex code windowing technique to enhance target detection. Indian J Sci Technol, 9(47). https://doi.org/10.17485/ijst/2016/v9i47/105952

Automated Security Intrusion Alert System for Wide Range of Applications

J. Lavanya and Padmakar Rao

Abstract This work focuses on a novel system that actively detects motion and notifies the administrator with the GSM. This work aims at to create a responsive and affordable security system which can be installed at any place. The functions and processing is will be done using a simple prototyping board KL25Z provide by ARM and powered by the Cortex M0+ processor. The hardware is installed at college premises for testing and found working.

Keywords KL25Z · ARM cortex · FRDM · Motion · Security System · SIM800 · SMS · Ultrasonic · HCSR-04

1 Introduction

Having safety in one's home is a very important matter to consider for every homeowner, either in an individual house or an apartment. In today's world where safety is the prime concern for any establishment, a proper cost-effective and efficient solution is required. Having a system that is completely automated makes the life simpler and far more reliable compared to having depend on manpower constantly. The main inspiration behind the creation of this project is that there is a severe need for a cost-effective and modifiable security system [1].

Being modifiable means that one can always tweak the prototype to serve a better function. Using a prototyping board makes the designing simpler as well as more adaptable. Not to forget that this project bridges the gap between the security device and the administrator, when the latter is away [2].

This proposed paper is prepared in the conventional Springer format with as much accuracy as possible.

J. Lavanya (✉) · P. Rao
Electronics and Communications Department, VJIT, Aziz Nagar, Moinabad, India
e-mail: lavanyaj@vjit.ac.in

H. S. Saini et al. (eds.), *Innovations in Electronics and Communication Engineering*,
Lecture Notes in Networks and Systems 33,
https://doi.org/10.1007/978-981-10-8204-7_28

1.1 Existing Methods

There have been many algorithms and systems proposed which in many cases are in effect. Some of them have a major advantage while others have sharper drawbacks. Two of these most widely used systems are

A. *Circuit Breaker System*: The circuit breaker system is one of the most primitive systems that we know when it comes to any type of security. We can see that the concept is in effect in many DIY projects [3] where a simple open circuit or a closed circuit is designed to respond when the circuit breaks. Conceptually speaking, it is considered very simple to design and implement, but one that is riddled with holes and drawbacks.
B. *RFID*: Over the past few years, we have seen a steep rise in the radio frequency-based technologies. This led to the introduction of a new identification method, called the RFID. It stands for Radio Frequency Identification which has a large amount of application in the present world. We see this technology being actively used in commercial markets, airports, and various other places. The basic concept of this technology is that it uses a specific tag as a mode of identification. This tag is attached to the required item in order to keep track of it. Today, we see the best RFID security systems in effect. Eventually, they have also seen their application in the home security domain. The simplest design application includes tagging the people who are accessing a place and keeping track of this information. RFID needs to go a long way to perfect and improve on its present situation. Other working specifications include that it uses upper layer and middle layer ID to detect any anomalies in the system.

1.2 Advantaged

The existing systems have a myriad of advantages. These advantages stem from various designs and implementation. Advantages of the above conventional systems are as follows: circuit breaker system is simple and easy to implement design. It uses a very common set of components and does not make the maintenance complex. Circuit breaker is more of a concept, when in reality it is a method which can be implanted in more than imaginable systems. Examples are window circuit breaker, door circuit breaker, wire circuit breaker, etc. Web security systems are more helpful than one can normally consider. They function using a stand-alone power supply [4] and operate in an automated loop. The data is constantly updated online for the administrator to keep an eye on. Faster response and simpler interface are one of the given pluses of this system. Additionally, it is widely compatible and adjustable [5].

1.3 Disadvantages

These mentioned systems have drawbacks as any other device in the world. We look at these to avoid future errors or to rectify them in a better design [6]. The disadvantages of these systems are that they have a tough time during maintenance.

Responses of these systems are sometimes may be unreliable, though unlikely.

Cost to function ratio is too large. Upgradability is less along with the functionality. In most cases, these systems [7] are managed by a central [8] Institution/Company. The failsafe methods known are very few. This paper is organized into following Sects. 2, 3 and 4.

Section 2 gives a look into the proposed system with the relevant block diagram and its brief.

Section 3 includes the synthesis of the system. It gives a detailed information about the components used as well as their working conditions.

Section 4 shows the testing method in real time and the outputs observed in various situations.

2 Proposed Methodologies

The main objective of this design was to integrate long distance communication with home security [9] in reporting possible incidents of intrusion and robbery to the security administrator when he/she is away from home, through the use of GSM technology. Specifically, this included:

Creating a device that is triggered when there is motion detected near the doors or windows [10]. Administrator can get the alert while intruder entered in to the home by using GSM technology [11] in sending notifications to the security administrator's mobile number notifying him of a possible intruder to home. Measuring the time, it takes before the intrusion notification is received by the security administrator relative to the regular time taken in sending an SMS message using a mobile phone [12].

2.1 Block Diagram

The system's block diagram is given in Fig. 1. It has all the major components and including the sensors. Functionally, this diagram gives a simple understanding of the individual block and how they are connected to each other.

It also outlines the simple connections and the pins that each and every wire/jumper is connected to. The board used has multiple ports, but for simplicity, only the ones used are shown.

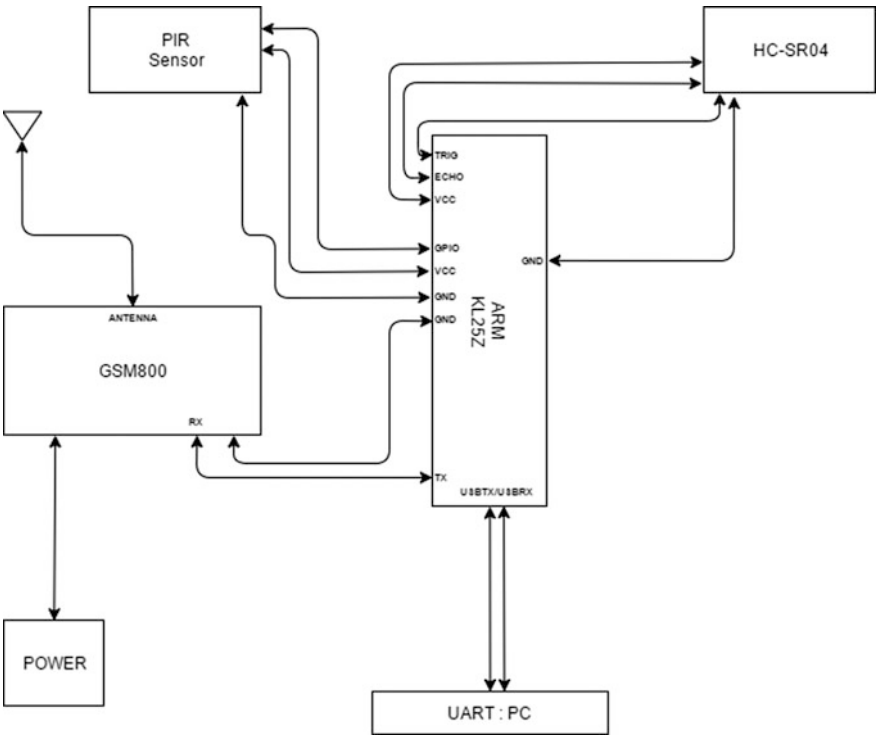

Fig. 1 Block diagram showing the component

2.2 Functionality

The devised system is completely controlled and operated using the onboard microcontroller. This ARM controller will continuously monitor the sensors, detector, and GSM modem [13].

If the voltage level of sensor input pins goes to 0 or ZERO, then it will send the "AT + CMGS ="USER MOBILE NUMBER" to GSM modem through serial port. The GSM modem will respond with the character ">".

After receiving ">" character microcontroller again send the type of security problem SMS + CTRL Z to GSM Modem. GSM modem now sends the type of problem to user.

ARM controller senses the change and immediately feeds an AT + CMGS = +9192856379 command to the GSM modem. GSM modem appends a ">" character to microcontroller feed.

After receiving ">" character microcontroller again sends the "MOMENT DETECTED" SMS to GSM Modem. GSM modem sends the SMS to user.

As soon as the device is powered on, it turns the GSM module ON [6]. The GSM module has a PWON pin. It must be connected to the microcontroller. Any input/output bit in the microcontroller configured as OUTPUT should work except the USART port which is needed for the GSM module connection. In this design, the author used bit 5 of Port C.

2.3 Flowchart

The flowchart of the algorithm is given in Fig. 2. It mainly highlights the running of the main loop and the method used to verify if the break-in detected is a valid detection or not. The other elements used in the blocks are mainly responsible for the sensing of output from the sensors and then sending the notification SMS to the administrator.

The flowchart as a whole is a single parent loop, which consists of more inner loops. These are designed to carry out the functions of checking the sensor values as well as performing calculations with as less delay as possible.

To give a simple brief, the flowchart has a main loop that runs the system, one motion check loop, one counter loop, and finally a loop that sends the SMS when initiated.

3 Synthesis

3.1 Hardware Implementation

Hardware Implementation talks about the components and other physical aspects of the proposed design. The system we implement uses a PIR sensor, GSM800 Module, Ultrasonic Sensor, Power Unit, and a KL25Z FRDM prototyping board. Each and every element used has its own function and data sheet. The sensors have been pre-calibrated to operate in the desired range and with the necessary accuracy.

A. *KL25Z FRDM Board*: FRDM stands for the Freescale Freedom Development board. The one used in this project is the KL25Z kit which has an ARM microcontroller embedded as the core. It is an L series controller which is built on the Cortex M0+ core. There are various reasons for selecting this specific board as the primary test device. It comes with a maximum operating clock frequency of 48 MHz, a 128 kB of flash memory. Along with these, we have a full USB controller and many analog/digital peripherals. The KL25Z hardware placement is similar to that of an ARDUINO UNO, which makes it compatible for use with all the available shields. It also has many interfaces like the RGB LEG, a single tough capacitive slider, and a 3-axis accelerometer. We can

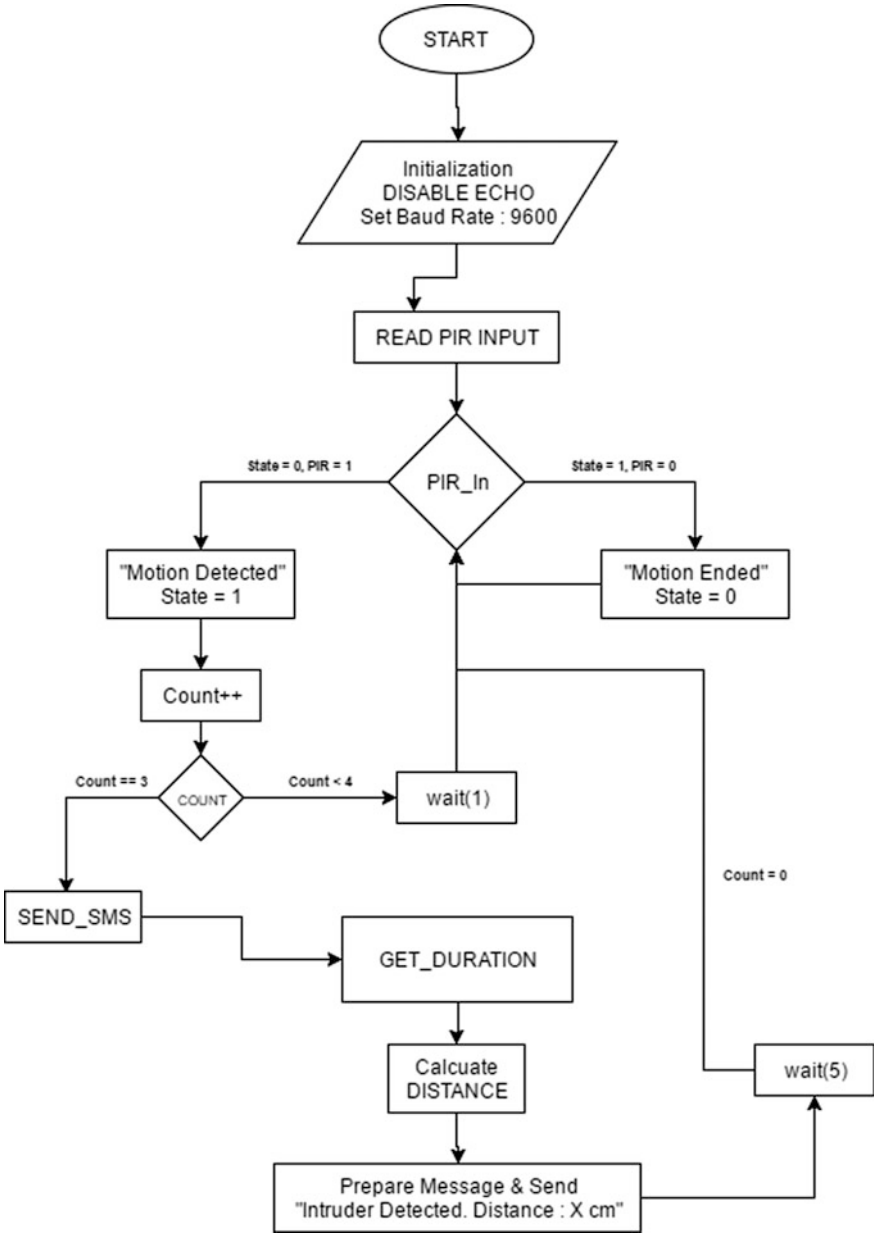

Fig. 2 Flowchart of the algorithm

connect this board to the system for development or debugging using the two ports, through the OpenSDA port. Other features include serial communication, debugging, flashing, etc.

B. *SIM800 Module:* Global system for mobile is a special device which uses a SIM card as its ID and communicates to other SIM through a subscription via a mobile operator. Spec: SIM800 is a quad-band GSM/GPRS module designed for the global market. The operation takes place in the frequency ranges of 850, 900, 1800 and 1900 MHz. This specific modem boasts a GPRS option which is of a multi-slot class 10 or class 12. It also supports multiple coding methods. The dimensions of this device make it economical, with a size of only 24 × 24 × 3 mm. This makes it easier to use in all products like mobiles, PDAs, automobiles, etc. SIM800 has a power saving design which uses only 1.2 mA in sleep mode. It also supports TCP/IP "ATTENTION" commands.

C. *PIR Sensor*: Motion sensors allow you to sense motion, almost always used to detect whether a human has moved in or out of the sensors line of sight. They are often referred to as "Passive Infrared", "Pyroelectric", or "IR motion" sensors. They are small, inexpensive, low power, easy to use, and do not wear out. For these reasons, they are commonly found in appliances and gadgets used in homes or businesses.

D. *Ultrasonic Sensor*: Ultrasonic module HCSR04 is a free hand obstacle-sensing device which has a range of 2 cm to a maximum of 400 cm. It also surpasses in terms of accuracy, with a maximum deflection of 3 mm. In this sensor, a stream of pulses is aimed at the target. This pulse train gets reflected by the target and comes back to the sensor, where they are detected as echoes. Receiver side sensors detect the time delay between each emitted and reflected echo pulse to accurately determine the sensor-to-target distance.

3.2 Operation of Proposed Technique

The system works in a very methodic manner. Initially, it takes around 15 s for the primary startup which mostly runs the setup code. It also does some AT functions like turning off the ECHO in the serial line.

Once the setup is done, the control of the system moves into the while loop of the main program. Inside this while loop, the PIR sensor output is measured as frequently as possible at a constant baud rate. This sensor gives its response to motion in the form of constant 1's and 0's. FRDM board picks up on these bits through a GPIO pin and determines if any motion is present or not.

If the motion is detected, the timer cycle of the loop is activated, which checks every second for 3 s for any motion. As soon as it verifies that there has been motion for three solid seconds, it is known that there is an intruder in the vicinity. After this, the control moves onto the SMS cycle.

The SMS cycle is the external function that is present outside the main loop. Initially, the function calls another function called *getDist()* to access the HC SR-04 in order to get the distance of the intruder from the sensor. *After getting the distance, the SMS function is resumed, and the SMS with an alert along with the distance details is sent to the administrator.*

$$\textbf{Distance} = \textbf{time}/\textbf{2}*\textbf{sonic\_speed} \quad (\text{sonic\_speed} = 34359.5\,\text{cm/s})$$

4 Results

The results are recorded in three stages. One stage is when the system is just starting up and initializing. The second stage is when the motion is detected but it is a faulty response. Finally, the last stage verifies the detection and initiates the SMS to be sent.

Case (i): Initializing: As shown in Fig. 3, the initial setup where the baud rates are set along with running some pre-AT commands through the GSM module.

Case (ii): Invalid Motion Detected: As shown in Fig. 4, the second case where the motion is detected but immediately after, we see that there is a motion stop bit passed. These are the residual bits that pass through sometimes and need to be avoided. Hence, we opt for a 3 s' motion check loop.

The motion check that is set up for 3 s makes sure that we receive a valid motion detected response throughout the time. This time duration can be extended to more than 3 s, but with problems of its own.

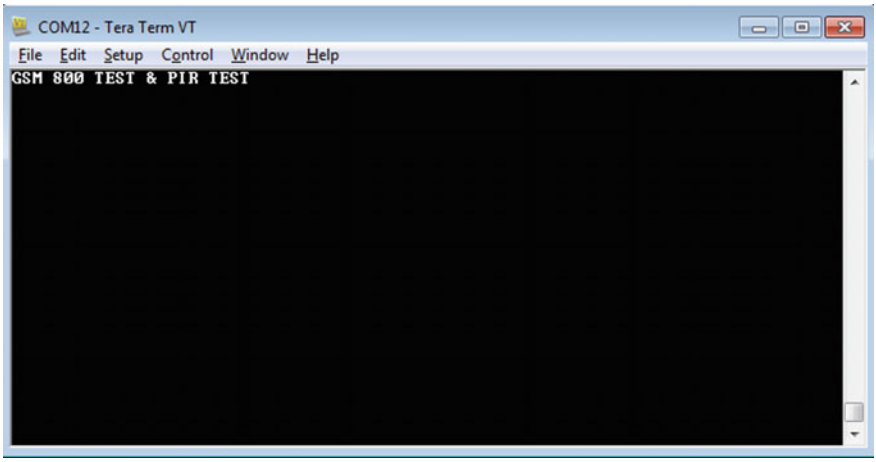

Fig. 3 Before initialization

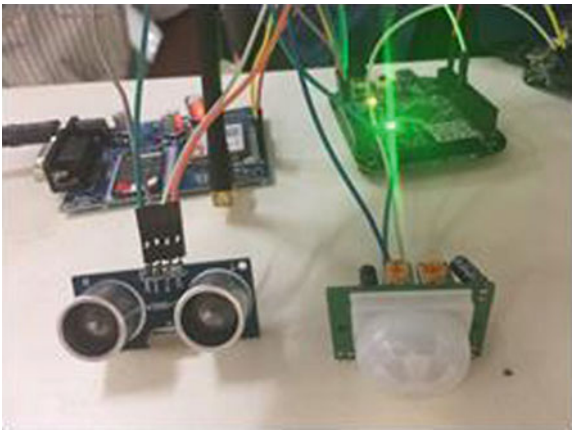

Fig. 4 Result when there is no motion

Fig. 5 Result when motion is detected and notification is sent

Once it has been decided that the motion is due to a moving entity in the field, the program loop moves onto the next set of instructions which deal with the as shown in Fig. 5.

This event of detection can be seen in real time using a terminal during debugging.

On the other hand, the terminal output can be seen in the presence of motion without response time. The output response is shown in Fig. 6.

Case (iii): Motion Detected: This is the last case, where the motion is detected and verified after the 3 s' response check. In this instance, the SMS function is called

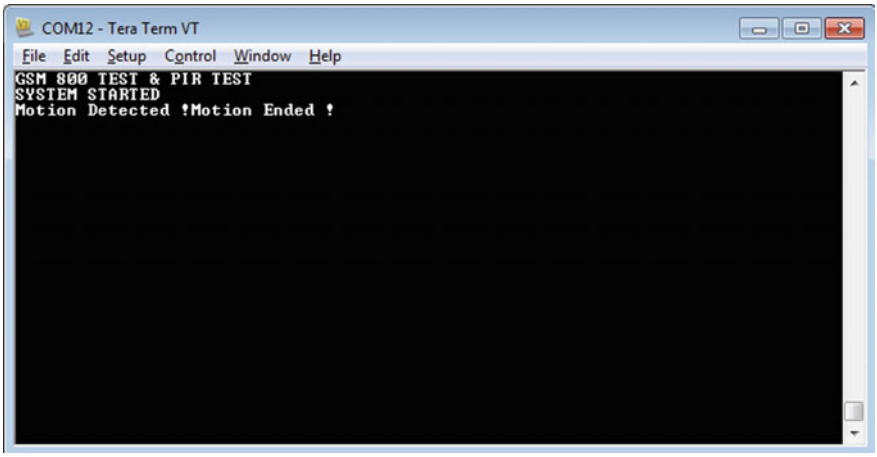

Fig. 6 Terminal output in the presence of motion

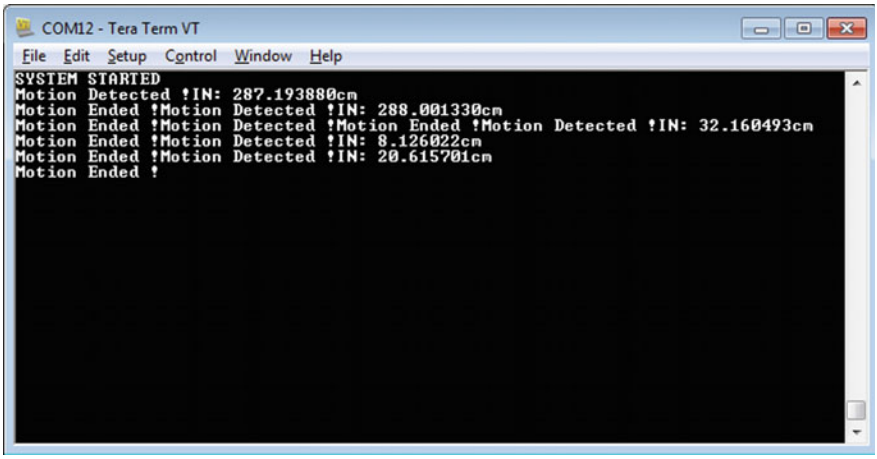

Fig. 7 Terminal output in the presence of motion with response time

along with the Get Distance function. On successfully getting HC SR-4 distance, the SMS is sent and the administrator is notified. The notification response is depicted in Fig. 7.

5 Conclusion

The paper which is based on designing a novel system could successfully overcome few drawbacks and is practically tested. We have designed a proper cost-effective system to perform the very basic function of the more advanced security systems.

Today, security systems cost a huge sum of money but do very little in terms of future upgrades or compatibility. This is successfully solved in our project which makes having a security system affordable to all.

Future scope for this field is that the administrator himself can make changes to the existing system with added functionalities and more operations. The main intent of this experiment is not to create a full proof system, but to highlight the growing ways in which security can be embraced and how easily available the means are.

Acknowledgements We are thankful to the VJIT management for giving us encouragement and support to finish our proposed work successfully.

References

1. Boob S, Jadhav P (2010) Wireless intrusion detection system. Int J Comput Appl (0975-8887) 5(8):1–5
2. Lange PM, Nielsen KLG (2014) Phase recognition in an operating room using sensor technology. IT University of Copenhagen
3. Winkler F (2007) Arduino workshop. http://www.arduino.cc (spring)
4. Hareendran TK (2014) GSM home security alarm system with Arduino. Library Security System
5. Eslaminejad MR, Sookhak M, Razak SA (2015) A review of routing mechanisms in wireless sensor networks. Int J Comput Sci Telecommun 2(7)
6. Indian Institute of Science (2013) Wireless sensor networks for human intruder detection. J Indian Inst Sci 90(3) (Jul–Sep)
7. Ramadan MN, Al-Khedhar MD (2015) Intelligent anti-theft and tracking system for automobiles. Int J Mach Learn Comput 2(1)
8. Axelsson S (2000) The base-rate fallacy and the difficulty of intrusion detection. ACM Trans Inf Syst Secur 3(3):186–205
9. Garri K, Sailhan F, Bouzefrane S, Uy M (2011) Anomaly detection in RFID system. Int J Radio Freq Ident Technol Appl 3:1–13
10. The Smart Detect Project Team (2014) Wireless sensor networks for human intruder detection. Indian Institute of Science, Bangalore, India
11. Yanbo Z, Zhaohui Y (2008) A low cost GSM/GPRS based wireless home security system. IEEE Trans Consum Electron 54(2):567–572
12. Pandey JK, Das Choudhary RN (2011) Embedded automobile engine locking system, using GSM technology. ITER. SOA University Odisha, India
13. Wan L, Chen T (2009) Automobile antitheft system design based on GSM. In: International conference on advanced computer control, pp 551–554

An Iterative ICI Compensation-Based MIMO-OFDM Signal Detection

B. Senthil

Abstract In this paper, an iterative intercarrier interference (ICI) cancellation-based MIMO-OFDM detection in the presence of frequency offset is proposed. This technique uses banded approximation of ICI terms in the channel matrix and achieves suboptimal performance with low complexity. We have considered the adjacent dominant ICI terms in the detection process which leads to improvement in BER performance of MIMO-OFDM.

1 Introduction

MIMO system is used with OFDM modulation for increasing the spatial diversity in addition to frequency diversity achieved by the multicarrier systems [1]. The MIMO-OFDM system is vulnerable to synchronization error, which occurs due to frequency offset and phase noise, and this leads loss of orthogonality between the carriers [2–5]. This results in intercarrier interference leading to reduction in the system performance. In order to overcome this problem, different techniques are available to estimate and compensate the frequency offset either blindly [6] or by using training symbols at the receiver [7, 8]. Detection methods discussed in the literature [1, 9–11] usually neglect the ICI term for symbol detection. In [12], an iterative signal detection is proposed for time-varying channel which also introduces the ICI in the receiver [13–16].

Here, we propose a detection technique based on [12] for MIMO-OFDM system which is independent of frequency offset compensation. This detection method achieves suboptimal performance in the presence of ICI due to frequency offset.

This paper is organized as follows: Sect. 2 presents the system model for frequency offset in MIMO-OFDM system. Section 3 explains the detection algorithm for ICI compensation. Section 4 discusses the simulation results, and Sect. 5 concludes the paper.

B. Senthil (✉)
Tn Govt, Chennai, India
e-mail: senthilbv@gmail.com

H. S. Saini et al. (eds.), *Innovations in Electronics and Communication Engineering*,
Lecture Notes in Networks and Systems 33,
https://doi.org/10.1007/978-981-10-8204-7_29

2 Paper Preparation

Here, we consider an MIMO-OFDM system with N_t transmit antennas, N_r receive antennas and N subcarriers. The input symbols $\tilde{\mathrm{x}}^{(v)}$ at the v^{th} transmit antenna and output symbols vector $\tilde{y}^{(v)}$ at the rth receive antenna are denoted by $\tilde{\mathrm{x}}^{(v)} = \left[x_0^v, x_1^v, \ldots, x_{N-1}^v,\right]^T$ and $\tilde{y}^{(r)} = \left[y_0^r, y_1^r, \ldots, y_{N-1}^r,\right]^T$, respectively. The output at the r^{th} receive antenna for the input at the v^{th} transmit antenna after performing the DFT is expressed as [17].

$$\tilde{y}^{(r)} = \sum_{v=1}^{N_t} \mathbf{F}\mathbf{E}^{(r)}\mathbf{H}^{(rv)}\mathbf{F}^H\tilde{\mathbf{x}}^{(v)} + \tilde{\mathbf{n}}^{(r)}, \tag{1}$$

where $\mathbf{F}$ is the N × N DFT matrix, $\mathbf{H}^{(rv)}$ is N × N circulant channel matrix representing v^{th} transmit antenna to r^{th} receive antenna and $\tilde{\mathbf{n}}^{(r)}$ is N × 1 Gaussian noise for r^{th} receive antenna.

The offset matrix is defined by $\mathbf{E}^{(r)} = diag\left\{1, e^{j2\pi\epsilon^{(r)}n/N}, \ldots, e^{j2\pi\epsilon^{(r)}n(N-1)/N}\right\}$ where n is the OFDM time index and $\epsilon^{(r)}$ is the normalized offset parameter for the r^{th} receive antenna.

Using the system model defined in [18], the received model based in carrier index can be written as

$$y_k = \mathbf{G}_{kk}\mathbf{x}_k + \underbrace{\sum_{\substack{p=0 \\ p \neq k}}^{N-1} \mathbf{G}_{kp}\mathbf{x}_p}_{ICI} + \mathbf{n}_k, \qquad k = 0, 1 \ldots, N-1, \tag{2}$$

where $\mathbf{x}_k = \left[x_k^1, x_k^2, \ldots, x_k^{N_t},\right]^T, \mathbf{y}_k = \left[y_k^1, y_k^2, \ldots, x_k^{N_r},\right]^T$ and $\mathbf{n}_k = \left[n_k^1, n_k^2, \ldots, n_k^{N_t},\right]^T$. The term $\mathbf{G}_{kp}$ in Eq. (2) defines the channel frequency response matrix as follows:

$$\mathbf{G}_{kp} = \begin{bmatrix} g_{kp}^{(11)} & g_{kp}^{(12)} \cdots & g_{kp}^{(1N_t)} \\ \vdots & \ddots & \vdots \\ g_{kp}^{(N_r1)} & g_{kp}^{(N_r2)} \cdots & g_{kp}^{(N_rN_t)} \end{bmatrix}, \tag{3}$$

where k, $p = 0,\ldots,N-1$. The channel frequency response matrix in the above equation is defined by [12].

$$g_{kp}^{(rv)} = \frac{1}{N}\sum_{n=0}^{N-1} e^{-j2\pi n(k-p-\epsilon^{(r)})/N} \sum_{l=0}^{L-1} h^{(rv)}(l)e^{-j2\pi lk/N} \tag{4}$$

where $\mathrm{h}^{(rv)}(l)$ is the channel impulse response for the r^{th} receive antenna from the v^{th} transmit antenna for the l^{th} tap and L is the length of the channel tap.

When the system has perfect synchronization, the channel frequency response is given by

$$g_{kk}^{(rv)} = \sum_{l=0}^{L-1} h^{(rv)}(l)\mathrm{e}^{-j2\pi lk/N}. \tag{5}$$

So the entries of $\mathbf{G}_{kk}$ consist of $N_r \times N_t$ channel frequency response matrices between transmitter and receiver. Let $\mathbf{X} = [\mathrm{x}_1, \mathrm{x}_2, \ldots, \mathrm{x}_{\mathrm{N}-1}]$, $\mathbf{Y} = [y_1, y_2, \ldots, y_{N-1}]$ and $\mathbf{N} = [\mathrm{n}_1, \mathrm{n}_2, \ldots, \mathrm{n}_{\mathrm{N}-1}]$ Using the notation defined above, the receiver output in Eq. (2) can be written as

$$\mathrm{Y} \;=\; \mathrm{GX} \;+\; \mathrm{N}, \tag{6}$$

where the channel matrix is defined as

$$G = \begin{bmatrix} G_{00} & G_{01} & \cdots & G_{(0)(N-1)} \\ G_{10} & G_{11} & G_{12} & \cdots \\ \vdots & \cdots & \ddots & \ddots \\ G_{(N-1)(0)} & \cdots & G_{(N-1)(N-2)} & G_{(N-1)(N-1)} \end{bmatrix}.$$

When the frequency offset is zero, the matrix G consists of diagonal block matrices $\mathbf{G}_{kp}$. For this systems, the MIMO detection can be done with ML or V-Blast techniques [0]. Usually, this detection algorithm neglect the ICI terms and this will increase the error in the symbol detection. Here, we have developed a detection for MIMO-OFDM in the presence of ICI which reduces the ICI effect in the detection process.

3 Detection Algorithm

In an iterative detection method, described in the steps that follow, the receiver considers a small number of adjacent ICI terms for cancelling ICI effect. The resulting channel matrix consists of diagonal elements with adjacent elements defined by the C. This matrix is called banded structure of channel frequency matrix expressed as follows:

$$G = \begin{bmatrix} G_{00} & G_{01} & \cdots & G_{(0)(N-1)} \\ G_{10} & G_{11} & G_{12} & 0 \\ \vdots & \cdots & \ddots & \ddots \\ G_{(N-1)(0)} & \cdots & G_{(N-1)(N-2)} & G_{(N-1)(N-1)} \end{bmatrix}.$$

In addition to the block diagonal matrix at the k^{th} carrier in the matrix, adjacent ICI terms are included in the G matrix for cancelling the ICI effect. Using this approximation model, we propose an iterative ICI cancellation detection scheme for MIMO-OFDM detection [0] as follows:

Step 0. Initialize the vector $X = 0$. For example, $x_k(1) = 0$, where $\mathbf{x}_k = \left[x_k^1, x_k^2, \ldots, x_k^{N_t},\right]^T$ for $k = 0, 1, \ldots, N-1$.

In the i^{th} iteration ($i = 1, 2, \ldots, M$), the following steps are carried out and the parameter M is set by the user for better detection performance.

Step 1. Compensate the dominant ICI term defined by the integer C

$$z_k = y_k - \sum_{\substack{p = k-C \\ p \neq k}}^{k+C} G_{kp} X_p(i) \qquad k = 0, 1, \ldots..., N-1. \tag{7}$$

An initial ICI compensation is done at this stage of detection.

Step 2. Based on the compensated ICI output $z_k(i)$, the detection can be done using ML metric defined as follows: $\hat{s}_k = \arg\min_{s_k} \epsilon \boldsymbol{A} |z_k(i) - \mathbf{G}_{kk}\mathbf{s}_k|$, $k = 0, 1, \ldots, N-1$, where $\mathbf{A}$ is the set of Q^{N_t} possible transmitted input symbols. The transmitted symbols is drawn from the symbol set Q.

Step 3. Update the symbols $\mathbf{x}_k(i+1) = \hat{s}_k$ Now, this estimated symbol sk is assigned for next iteration to reduce the ICI effect further.

After M iterations, the detected symbols are assigned to $\hat{\mathbf{x}}_k = \mathbf{x}_k\ (M)$, $k = 0, 1, \ldots, N-1$ and X is also updated.

4 Simulation

A 2 × 2 MIMO-OFDM system employing binary phase-shift keying (BPSK) is considered. A three-tap ($L = 3$) Rayleigh fading channel with exponential power delay profile is assumed. A different channel realization is assumed for an OFDM frame. The channel coefficients are assumed to be known at the receiver. The number of carriers is set to 8 and 16. The iteration parameter M is set at 10.

In Fig. 1, we show the bit-error-rate (BER) performance of iteration-based MIMO-OFDM detection. Two different values of the normalized offset parameter (ϵ) are taken which are chosen as 0.2 and 0.4. The number of dominant ICI terms for cancellation is considered as 1 and 3. The BER performance of the system is improved in the presence of the frequency offset when the number of dominant ICI terms is varied with 1 and 3.

The BER performance of the system is improved in the presence of the frequency offset when the number of dominant ICI terms is varied with 1 and 3. This

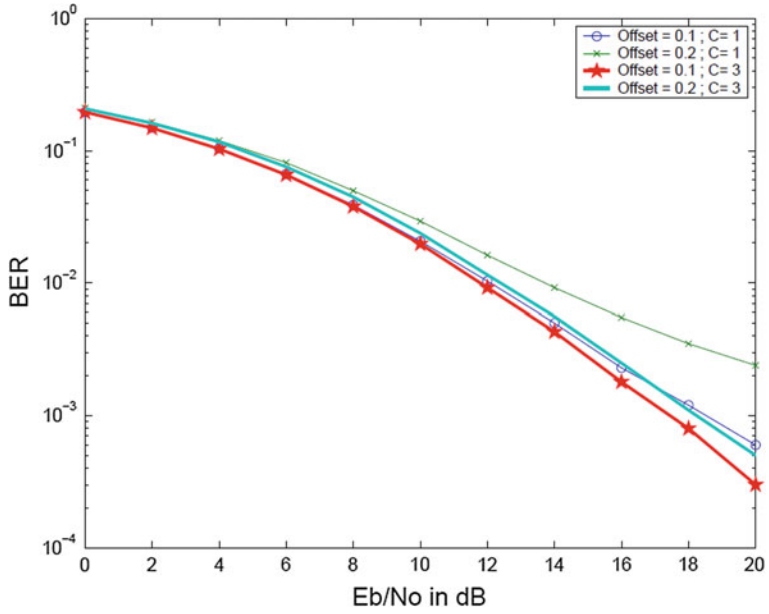

Fig. 1 MIMO-OFDM signal detection for different values offset and ICI term for $N = 8$

is due to the receiver compensating for the dominant ICI terms in the detection, and hence, the amount of ICI is reduced. The performance of this detection scheme is also improved as N increased.

5 Conclusion

The proposed iterative ICI cancellation-based detection for MIMO-OFDM system provides better performance in the high frequency offset without the need for any frequency offset compensation at the receiver. The complexity of the receiver depends on the number of adjacent dominant ICI terms selected for compensation. This detection technique achieves good BER performance over the existing system in the presence of ICI due to frequency offset when a higher number of ICI term cancellation is considered in the detection. By compromising on the receiver complexity, the BER performance of MIMO-OFDM detection is also improved in the varying offset.

References

1. Stuber GJJR, Barry SWMYMAI, Pratt TG (2004) Broadband MIMO-OFDM wireless communications. IEEE Proc 92(4):271–294
2. Senthil B, Aravind R, Prabhu KMM (2013) An enhanced intercarrier interference reduction scheme for OFDM system with phase noise. Circu Syst Signal Process 32:931. https://doi.org/10.1007/s00034-012-9477-
3. Molisch AF, Toeltsch M, Vermani S (2007) Iterative methods for cancellation of intercarrier interference in OFDM systems. IEEE Trans Veh Technol 56(4):2158–2167
4. Senthil B (2011) An ICI reduction scheme with enhanced frequency diversity for OFDM systems. In: 2011 National conference on communications (NCC). pp 1–4
5. Vlachos E, Lalos AS, Berberidis K (2017) Low-complexity OSIC equalization for ofdm-based vehicular communications. IEEE Trans Veh Technol 66(5):3765–3776
6. Yao Y, Giannakis GB (2005) blind carrier frequency offset estimation in siso, mimo, and multiuser OFDM systems. IEEE Trans Commu 53(1):173–183
7. Cheema M, Kulkarni SA (2015) Iterative ICI cancellation in MIMO OFDM WiMAX system with LDPC channel coding. In: 2015 international conference on computational intelligence and communication networks (CICN), pp 532–536
8. Minn H, Al-Dhahir N (2005) MIMO-OFDM training signal design in the presence of frequency offset and phase noise. IEEE ICSS 2005:263–267
9. Deng JH, Liao SM, Kuo YW, Hwang JK, Chiu YL (2009) An iterative receiver with intercarrier interference cancellation for OFDM communication systems with carrier-frequency and timing offsets over multipath fading channels. In: 2009 ieee 13th international symposium on consumer electronics, pp 346–350
10. Harbi YJ, Burr AG (2016) On ISI and ICI cancellation for FBMC/OQAM system using iterative decoding and ML detection. In: 2016 IEEE wireless communications and networking conference. pp 1–6
11. Kou YJ, Lu WS, Antoniou A (2005) An iterative intercarrier-interference reduction algorithm for OFDM systems. In: PACRIM. 2005 IEEE pacific rim conference on communications, computers and signal Processing, 2005, pp 538–541
12. Song WG, Lim JT (2006) Channel estimation and signal detection for MIMO-OFDM with time-varying channels. IEEE Commun Lett 19(7):540–542
13. Aboutorab N, Hardjawana W, Vucetic B (2012) A new iterative doppler-assisted channel estimation joint with parallel ICI cancellation for high-mobility MIMO-OFDM systems. IEEE Trans Veh Technol 61(4):1577–1589
14. Groh I, Gentner CS (2012) Iterative intercarrier interference mitigation for pilot-aided OFDM channel estimation based on channel linearizations. In: 2012 IEEE vehicular technology conference (VTC Fall). pp 1–5
15. Hwang SU, Lee JH, Seo J (2009) Low complexity iterative ICI cancellation and equalization for OFDM systems over doubly selective channels. IEEE Trans Broadcast 55(1):132–139
16. Zhang Y, Li J, Pang L, Ding Z (2001) Iterative intercarrier interference mitigation for mobile MIMO-OFDM systems. In: 2011 IEEE 22nd international symposium on personal, indoor and mobile radio communications. pp 959–963
17. Kim KJ, Iltis RA (2005) blind carrier frequency offset estimation in SISO, MIMO, and multiuser OFDM systems. IEEE Trans Commun 53(1):173–183
18. Zhang Y, Liu H (2006) Frequency-domain correlative coding forMIMO-OFDMsystems over fast fading channel. IEEE Trans Commun 10(5):347–349

An Improved Frequency Diversity Scheme for OFDM Systems with Frequency Offset

B. Senthil

Abstract In this paper, a modified symmetric symbol repetition (MSSR) scheme is presented for reducing the effect of intercarrier interference (ICI) due to the frequency offset. The proposed scheme improves the carrier-to-interference ratio (CIR) by reducing the ICI in the presence of frequency offset. The proposed MSSR exploits the frequency diversity over the frequency-fading channel and thereby achieves better BER performance compared with that of conventional intercarrier interference reduction techniques such as adjacent symbol repetition (ASR) and symmetric symbol repetition (SSR).

Keywords Intercarrier interference (ICI) · Symmetric symbol repetition (SSR) Adjacent symbol repetition (ASR) · Frequency offset

1 Introduction

Orthogonal frequency division multiplexing (OFDM) exploits the frequency diversity over multipath fading channels [1]. Although OFDM has advantages when used over frequency-selective fading channels, it is highly sensitive to synchronization errors such as frequency offset and phase noise [2, 3]. Frequency offset occurs due to mismatch of the carrier frequencies at the transmitter and receiver [4]. Phase noise is due to random fluctuation of the phase in the receiver oscillator [5]. In OFDM, intercarrier interference (ICI) due to synchronization errors destroys the orthogonality of the carriers [6–8]. In [9–12], ICI self-cancellation techniques have been discussed for reducing the effect of ICI due to synchronization errors.

In adjacent symbol repetition (ASR) [9], the performance of carrier-to-interference ratio (CIR) is improved by mapping the same data symbol on adjacent

B. Senthil (✉)
Tn Govt, Chennai, India
e-mail: senthilbv@gmail.com

H. S. Saini et al. (eds.), *Innovations in Electronics and Communication Engineering*,
Lecture Notes in Networks and Systems 33,
https://doi.org/10.1007/978-981-10-8204-7_30

OFDM subcarriers. However, ASR does not achieve frequency diversity as the channel frequency response (CFR) is the same on both the carriers. To overcome this drawback, symmetric symbol repetition (SSR) scheme [10] has been proposed to exploit the frequency diversity by placing the symbols which are symmetrical to total number of subcarriers. However, the SSR scheme fails to exploit the frequency diversity completely nearer to the center of OFDM block.

In this paper, we propose a modified symmetric symbol repetition (MSSR) scheme to exploit frequency diversity completely over a multipath fading channel. We evaluate the performance of the proposed MSSR in terms of CIR and BER, and compared with that of ASR and SSR in the presence of frequency offset over multipath fading channels.

2 Synchronization Error in OFDM

Although OFDM achieves good performance over frequency-selective fading channels, it is sensitive to narrowband interference caused in the subchannels [8, 11, 14]. In this section, we provide the OFDM system model in the presence of frequency offset. Let $\{S_k;\ k = 0 \ \ldots \ N - 1\}$ denote OFDM symbol block with N OFDM subcarriers.

Figure 1 shows the block diagram of OFDM in the presence of synchronization errors over frequency-selective fading channels.

The transmitted OFDM symbol S_k after taking IDFT is written as

$$s_n = \frac{1}{N}\sum_{k=0}^{N-1} S_k e^{j2\pi k/N}, \quad n = 0, 1, \ldots, N-1, \tag{1}$$

The received signal due to synchronization error is expressed as [13]

$$y_n = (s_n \otimes h_n)\exp(j\theta_n) + \omega_n, \quad n = 0, \ldots, N-1, \tag{2}$$

where θ_n is the phase offset due to frequency offset or phase noise.

After taking DFT [13], the received signal Y_k is written as

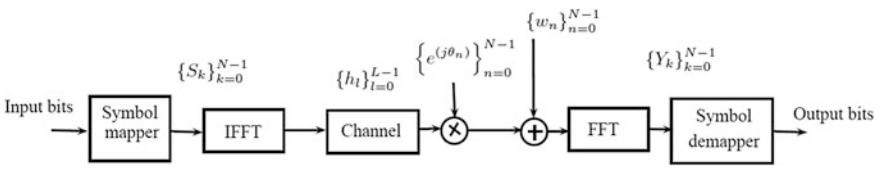

Fig. 1 Synchronization errors in OFDM systems

$$\begin{aligned} Y_k &= \sum_{n=0}^{N-1} y_n \exp\left(-j\frac{2\pi kn}{N}\right) \\ &= \sum_{n=0}^{N-1}\sum_{l=0}^{L-1} s_{((n-1)\bmod N)} h_l \exp\left(-j\frac{2\pi kn}{N}\right)\exp(j\theta_n) + W_k, \end{aligned} \tag{3}$$

where $s_{((n-1)\bmod N)} = \frac{1}{N}\sum_{k=0}^{N-1} S_k e^{j2\pi(n-l)k/N}$.

Using Eq. (1), the received signal Y_k is expressed as

$$\begin{aligned} Y_k &= \sum_{n=0}^{N-1}\sum_{l=0}^{L-1}\frac{1}{N}\sum_{m=0}^{N-1} S_m \exp\left(\frac{j2\pi(n-l)m}{N}\right) h_l \exp\left(\frac{-j2\pi kn}{N}\right)\exp(j\theta_n) + W_k \\ &= \frac{1}{N}\sum_{m=0}^{N-1} S_m \sum_{n=0}^{N-1} \underbrace{\sum_{l=0}^{L-1} h_l \exp\left(\frac{-j2\pi kn}{N}\right)}_{H_m} \exp\left(\frac{-j2\pi(m-k)n}{N}\right)\exp(j\theta_n) + W_k \\ &= \frac{1}{N}\sum_{m=0}^{N-1} S_m H_m \sum_{n=0}^{N-1} \exp\left(\frac{-j2\pi(m-k)n}{N}\right)\exp(j\theta_n) + W_k, \quad k = 0,\ldots,N-1 \end{aligned} \tag{4}$$

This phase offset, θ_n, limits the detection S_k by introducing ICI due to loss of orthogonality between the OFDM subcarriers. This reduces the BER performance of OFDM systems. In the following subsection, we discuss the effect of phase offset on the frequency offset in OFDM systems.

2.1 Frequency Offset in OFDM

Frequency offset occurs due to a mismatch between the carrier frequencies of the transmitter and receiver [13, 14]. The impact of frequency offset is to produce phase offset and ICI in the received signal. The phase offset, θ_n, is due to frequency offset, ε and is given by [13]

$$\theta_n = \frac{2\pi\varepsilon n}{N}, \quad n - 0,\ldots,N-1, \tag{5}$$

where ε is frequency offset normalized to sampling frequency [6]. Using Eq. (5), the received signal $Y_k\psi$ in the presence of frequency offset is given by

$$Y_k = \frac{1}{N}\sum_{m=0}^{N-1} S_m H_m \sum_{n=0}^{N-1} \exp\left(\frac{-j2\pi(m-k-\varepsilon)n}{N}\right)\exp(j\theta_n) + W_k, \quad k = 0,\ldots,N-1$$
$$= S_k H_k Q_0 + \sum_{\substack{m=0 \\ m\neq k}}^{N-1} S_m H_m Q_{m-k} W_k, \quad k = 0,\ldots,N-1 \tag{6}$$

The ICI component $Q_r\psi$ in Eq. (6) is expressed as

$$Q_r = \frac{1}{N}\sum_{n=0}^{N-1} \exp\left(\frac{-j2\pi n(r-\varepsilon)}{N}\right),$$
$$= \frac{1}{N}\frac{\sin(\pi(r-\varepsilon))}{\sin\left(\frac{\pi(r-\varepsilon)}{N}\right)}\exp\left(-j\pi(r-\varepsilon)\left(1-\frac{1}{N}\right)\right), \quad -(N-1) \le r \le (N-1) \tag{7}$$

As seen in Eq. (6), the ICI terms due to $Q_k\psi$ in Eq. (7), add the desired OFDM signal S_k. Hence, frequency offset in OFDM produces an error floor in BER performance by reducing effective SNR at the receiver.

3 Existing Symbol Repetition Methods

In this section, we discuss existing symbol repetition schemes such as ASR and SSR for OFDM system in the presence of frequency offset. Figure 2 shows OFDM system with Interference Cancellation reduction coding block at the transmitter and Interference Cancellation reduction decoding block at the receiver.

Let $\{D_k.; k = 0,\ldots,N/2-1\}$ express the data symbols at the input of the Interference Cancellation reduction coding block in Fig. 2.

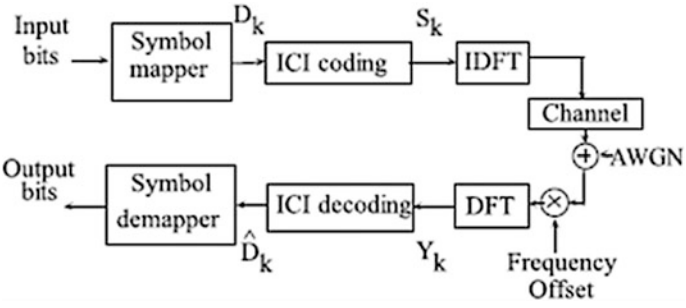

Fig. 2 OFDM systems with ICI reduction scheme

3.1 Adjacent Symbol Repetition

In ASR [9], the symbols are placed at the Interference Cancellation reduction coding block as follows:

$$S_{2k} = D_k, S_{2k+1} = -D_k, \text{ for } k = 0, \ldots, N/2 - 1.$$

The signal Y_k after passing through frequency-selective fading channels at the receiver is given by

$$Y_{2k} = \sum_{m=0}^{N/2-1} S_{2m} H_{2m} Q_{2m-2k} + S_{2m} + H_{2m} + Q_{2m+1-2k} + W_{2k} \tag{8}$$

The estimated subcarrier, $\hat{D}_{k,}$ is obtained by combining the Y_{2k} and Y_{2k+1} is defined as

$$\hat{D}_k = \frac{1}{2}(H^*_{2k} Y_{2k} - H^*_{2k+1} Y_{2k+1}), \quad k = 0, \ldots, N/2 - 1. \tag{9}$$

As discussed in [1], ASR scheme does not improve the BER performance of the OFDM system because the adjacent subcarriers see the same CFR at the kth and k + 1th subcarriers.

3.2 Symmetric Symbol Repetition

The drawbacks of ASR scheme is improved with SSR in which the mapping of transmitted symbols is done as follows: $S_k = D_k$, $S_{N-1-k} = -D_k$, for $k = 0,\ldots,$ $N/2 - 1$. For SSR, the received signal Y_k after taking DFT is expressed as

$$Y_k = \sum_{m=0}^{N/2-1} S_m H_m Q_{m-k} + S_{N-1-m} H_{N-1-m} + Q_{N-1-m-k} + W_k \tag{10}$$

The estimated subcarrier, $\hat{D}_k$, at the kth subcarrier is defined as

$$\hat{D}_k = \frac{1}{2}\left(H^*_k Y_k - H^*_{N-1-k} Y_{N-1-k}\right), \quad k = 0, \ldots, \frac{N}{2} - 1. \tag{11}$$

Even though the performance of SSR is better than ASR; the CFR is the same for a range of k close to $N/2$ and thereby reduces the frequency diversity performance of SSR.

3.3 Proposed Modified Symmetric Symbol Repetition

In order to overcome the drawbacks of SSR, We propose a MSSR to enhance the frequency diversity due to the frequency offset. In MSSR, the mapping of the symbol is done as follows: $S_k = D_k$, $S_{k+N/2} = -D_k$, for $k = 0,\ldots,N/2 - 1$.

After taking DFT, the received signal Y_k is expressed as

$$Y_k = \sum_{m=0}^{N/2-1} S_m H_m Q_{m-k} + S_{m+N/2} H_{m+N/2} + Q_{m-k+N/2} + W_k \tag{12}$$

The estimated subcarrier, $\hat{D}_k$, at the kth carrier using maximal ratio combining (MRC) is defined as

$$\begin{aligned} \hat{D}_k &= \frac{1}{2}\left(H_k^* Y_k - H_{k+\frac{N}{2}}^* Y_{k+\frac{N}{2}}\right), \quad k = 0,\ldots,\frac{N}{2} - 1. \\ &= \frac{1}{2} D_k \left(|H_k|^2 + \left|H_{k+N/2}\right|^2\right) Q_0 + \mathrm{ICI}_k + \bar{W}_k, \end{aligned} \tag{13}$$

where ICI_k is the ICI component,

$$\begin{aligned} \mathrm{ICI}_k = \frac{1}{2} \sum_{\substack{m=0 \\ m \neq k}}^{N/2-1} & H_k^* D_m H_m Q_{m-k} - H_k^* D_m H_{m+N/2} Q_{m-k+N/2} \\ & + H_{k+N/2}^* D_{N/2+m} H_m Q_{-(m-k+N/2)} - H_{k+N/2}^* D_m H_m Q_{-(m-k+N/2)} \\ \bar{W}_k = \frac{1}{2} & \left(H_k^* W_k - H_{k+N/2}^* W_{k+N/2}\right). \end{aligned}$$

As seen in Eq. (13), the CFRs H_k and $H_{(k+N/2)}$ see different values for all k. The proposed MSSR scheme improves the BER performance by having different CFRs at the kth and k + N/2th subcarriers. The ICI cancellation performance of MSSR scheme is improved with CIR of system in the presence of frequency offset. The CIR of MSSR at the kth subcarrier ($H_k = 1$ for all k) as

$$\mathrm{CIR}_k = \frac{\left|Q_k + Q_{-k} + Q_{(k+N/2)} + Q_{-(k+N/2)}\right|^2}{\mathrm{CIR1} + \mathrm{CIR2}} \tag{14}$$

where

$$\mathrm{CIR1} = \sum_{p=1}^{N/2-1} \left|Q_{k+p} + Q_{k-p}\right|^2$$

$$\text{CIR2} = \sum_{p=0}^{N/2-1} \left| Q_{-(k+p)} + Q_{-(N-1+k-p)} \right|^2$$

From Eq. (14), the proposed scheme reduces the ICI in the presence of frequency offset and also exploits the frequency diversity over frequency-selective fading channel.

4 Performance Analysis of Proposed Scheme

We analyse the performance of ASR, SSR and MSSR in the presence of frequency offset. In the following, we consider $H_k = 1$ for all ICI reduction scheme.

4.1 ICI Analysis of Adjacent Symbol Repetition (ASR)

The estimated subcarrier, $\hat{D}_k$, in Eq. (9) after combining of received signals Y_{2k} and Y_{2k+1} is defined as

$$\begin{aligned} \hat{D}_k &= \frac{1}{2}(Y_{2k} - Y_{2k+1}), \quad k = 0, \ldots, \frac{N}{2} - 1 \\ &= S_k(2Q_0 - Q_1 - Q_{-1}) + \sum_{\substack{m=0 \\ m \neq k}}^{N/2-1} S_m F_{m-k} + W_{2k} - W_{2k+1} \end{aligned} \tag{15}$$

where

$$F_r = 2Q_r - Q_{2r-1} - Q_{2r+1}, \quad 0 \leq r \leq N/2, \quad r \neq k \tag{16}$$

From the Eq. (16), we can see that there is ICI reduction in the presence of frequency offset.

4.2 ICI Analysis of Symmetric Symbol Repetition (SSR)

The estimated subcarrier $\hat{D}_k$ in Eq. (11) is expressed as

$$\hat{D}_k = \frac{1}{2}(Y_k - Y_{N-1-k}), \quad k = 0, \ldots, \frac{N}{2} - 1$$

$$\hat{D}_k = S_k\left(2Q_0 - Q_{N-1} - Q_{-(N-1)}\right) + \sum_{\substack{m=0 \\ m \neq k}}^{N/2-1} S_m F_{m-k} + W_k - W_{N-1-k}$$

where

$$F_r = Q_r + Q_{-r} - Q_{N-1-r} - Q_{-(N-1-r)}, \quad 0 \leq r \leq N/2, \quad r \neq k \tag{18}$$

Therefore, the ICI reduction in SSR scheme is governed by the terms Q_{N-1-r} and $Q_{-(N-1-r)}$ as presented in Eq. (16).

4.3 ICI Analysis of Modified Symmetric Symbol Repetition (SSR)

The estimated subcarrier $\hat{D}_k$ in Eq. (13) is expressed as

$$\hat{D}_k = \frac{1}{2}\left(Y_k - Y_{k+N/2}\right), \quad k = 0, \ldots, \frac{N}{2} - 1$$

$$\hat{D}_k = S_k\left(2Q_0 - Q_{N/2} - Q_{-(N/2)}\right) + \sum_{\substack{m=0 \\ m \neq k}}^{N/2-1} S_m F_{m-k} + W_k - W_{k+N/2} \tag{19}$$

where

$$F_r = Q_r + Q_{-r} - Q_{-(r+N/2)} - Q_{r+N/2}, \quad 0 \leq r \leq N/2, \quad r \neq k \tag{20}$$

Equation (20) shows that the proposed scheme produces reduction in ICI due to frequency offset. Hence, the proposed scheme reduces ICI in the presence of frequency offset.

4.4 BER Analysis

In general, the diversity performance of OFDM is mainly due to multipath fading channel. In ICI reduction scheme, the same symbol is placed in two different positions for reducing the ICI due to the frequency offset. Therefore, the proposed MSSR scheme achieves strong frequency diversity over frequency-selective fading channel. This improved diversity performance is equivalent to the performance of maximum ratio combing (MRC) over flat fading channel by considering two

independent signals available at the receiver. Therefore, we compare the performance of OFDM with symbol repetition scheme over multipath fading channel to MRC system having 2 × 1 antenna in flat fading ($L = 1$). Thus, the BER of MRC system for BPSK gives the upper bound for diversity performance of the proposed system for a given signal power γ_0 and is given by [7]

$$P_b = \frac{1}{2}\left[1 - \mu \sum_{r=0}^{M-1} \binom{2r}{r} \left(\frac{1-\mu^2}{4}\right)^r\right] \tag{21}$$

where M is the total number of transmit antenna and $\mu = \sqrt{\frac{\gamma_0}{1+\gamma_0}}$. For two branches MRC $(M = 2)$, Eq. (19) reduces to

$$P_b = \frac{1}{4}\left(2 - 3\mu + \mu^3\right) \tag{22}$$

5 Simulation Results

We perform OFDM system simulations of ASR, SSR and the proposed MSSR in the presence of frequency offset. QPSK modulation is assumed. The number of OFDM subcarriers is 64. In the signal-to-noise ratio (SNR) calculations, the transmitted symbol power is normalized to unity. In Figs. 3 and 4, the diversity performance of the proposed method is compared with ASR and SSR over a two-path ($L = 2$) and six-path ($L = 6$) Rayleigh fading channel.

As seen in Fig. 3, the proposed MSSR improves the BER performance about 2 dB over SSR and 8 dB over ASR, with frequency offset ($\varepsilon = 0.1$) at BER of 10^{-3} for channel length $L = 2$. In Fig. 4, the proposed MSSR scheme provides about

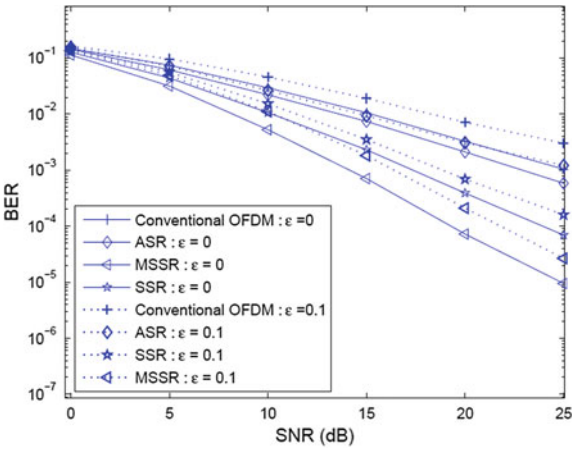

Fig. 3 BER performance of MSSR scheme over multipath fading channel for $L = 2$

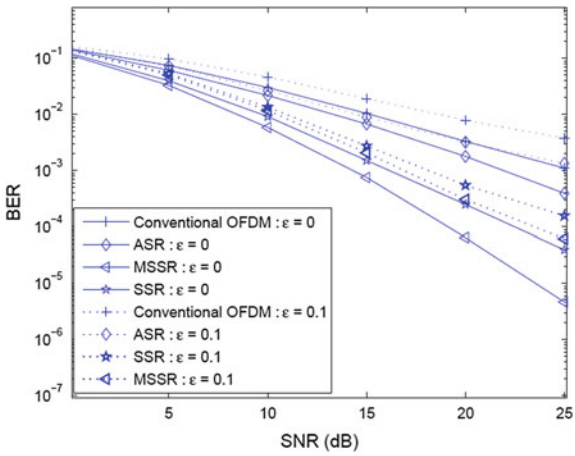

Fig. 4 BER performance of MSSR scheme over multipath fading channel for $L = 6$

4 dB over SSR at BER of 10^{-4} when $L = 6$. For both values of channel length L, MSSR always provides better performance than ASR and SSR as shown in Figs. 3 and 4.

This is because MSSR reduces ICI due to frequency offset and thereby improves the BER performance in the presence of frequency offset. Hence, the frequency diversity in MSSR is enhanced by exploiting the CFRs at the kth and $k + N/2$-th subcarriers.

6 Conclusion

In this paper, we have investigated ICI reduction performance of symbol repetition schemes in OFDM system due to the frequency offset. A MSSR scheme has been proposed to exploit the frequency diversity by placing the symbols with a spacing of half the OFDM symbol block. The OFDM system with MSSR (with and without frequency offset) provides better performance compared to OFDM with ASR and SSR over frequency-selective fading channels.

References

1. Senthil B, Aravind R, Prabhu KMM (2013) An enhanced intercarrier interference reduction scheme for OFDM system with phase noise. Circuits Syst Signal Process 32(2):931–943
2. Lee J, Lee J, Kim J, Kim Y (2015) Low-complexity ICI reduction method for OFDM systems with large subcarrier numbers. IEEE Trans Veh Technol 64(8):3505–3512
3. Ma TM (2017) A novel PRCC scheme for OFDM systems over frequency-selective fading channels. IEEE Signal Process Lett 24(5):634–637

4. Munier F, Eriksson T, Svensson A (2008) An ICI reduction scheme for OFDM system with phase noise over fading channels. IEEE Trans Commun 56(7):1119–1126
5. Perez-Calderon D, Lecuyer VB, Oria AC, Doblado JG (2016) Diversity technique for OFDM systems: enhanced time-frequency multiplexing (eTFM). IEEE Trans Broadcast 62 (3):505–511
6. Prasad R (2004) OFDM for wireless communication systems. Artech House
7. Rugini L, Banelli P (2005) BER of OFDM systems impaired by carrier frequency offset in multipath fading channels. IEEE Trans Wireless Commun 4(5):2279–2288
8. Ryu HG, Li Y, Park JS (2005) An improved ICI reduction method in OFDM communication system. IEEE Trans Broadcast 51(3):395–400
9. Sathananthan K, Rajatheva R, Slimane SB (2000) Cancellation technique to reduce intercarrier interference in OFDM. IEE Electron Lett 36(25):2078–2079
10. Senthil B (2011) An ICI reduction scheme with enhanced frequency diversity for OFDM systems. In: 2011 National Conference on Communications (NCC), pp 1–4
11. Tang S, Gong K, Song J, Pan C, Yang Z (2007) Intercarrier interference cancellation with frequency diversity for OFDM systems. IEEE Trans Broadcast 53(1):132–137
12. Tao L, Yu J, Zhang J, Shao Y, Chi N (2013) Reduction of intercarrier interference based on window shaping in OFDM RoF systems. IEEE Photonics Technol Lett 25(9):851–854
13. Wang CL, Huang YC (2010) Intercarrier interference cancellation using general phase rotated conjugate transmission for OFDM systems. IEEE Trans Commun 58(3):1122–1127
14. Zhao Y, Haggman SG (2001) Intercarrier interference self-cancellation scheme for OFDM mobile communication systems. IEEE Trans Commun 49(7):1185–1191

Reducing Intercarrier Interference in High-Speed OFDM Systems in Presence of Jitter Noise

A. H. Sharief and M. Satya Sai Ram

Abstract Carrier-to-interference ratio (CIR) plays a vital role in the uplink/downlink process of OFDM. Due to frequency offset (FO) there might be loss of orthogonality in OFDM modulated symbol there by signal-to-noise ratio will be reduced, it also introduce a timing jitter which can be defined as the deviation of timing edges from its expected areas. Jitter causes serious hardware impairments due to the synchronization imbalance. Hence, we have implemented a typical jitter noise reduction method which also improves the CIR performance there by degrades the intercarrier interference (ICI). We execute ultra-sampling criteria in the OFDM correspondence framework, by adjusting over examining in the framework we get lessened jitter power which enhances CIR performance which results in mitigation of ICI factor.

Keywords OFDM · Frequency offset · ICI · C/I ratio and timing jitter

1 Introduction

Now a day, Orthogonal Frequency Division Multiplexing (OFDM) is a proficient procedure for broadband remote correspondence framework, since it is a basic answer for multi-way blurring [1]. It is computerized multi-bearer regulation plan. OFDM can give extensive information rates and it is anything but difficult to execute with the assistance of Fast Fourier Transform and Inverse Fast Fourier Transform for demodulation and tweak separately. As information rates increment Inter Symbol Interference (ISI) is turning into a restricting variable in numerous

A. H. Sharief (✉)
Gandhiji Institute of Science and Technology, Jaggayapeta, India
e-mail: shariefah@gmail.com

M. Satya Sai Ram
Department of ECE, Chalapathi Institute of Engineering
and Technology, Guntur, India
e-mail: msatyasairam1981@gmail.com

H. S. Saini et al. (eds.), *Innovations in Electronics and Communication Engineering*,
Lecture Notes in Networks and Systems 33,
https://doi.org/10.1007/978-981-10-8204-7_31

optical fiber and optical remote frameworks and new types of OFDM which are appropriate for optical frameworks have been produced. Transmission at these high information rates requires rapid simple to computerized converters utilizing a precise testing clock. Timing jitter is the deviation of clock sign. In OFDM extensive number of restricted band sub-bearer is orthogonal, covering to each other, transmitted in parallel, isolate the accessible transmission transfer speed [1]. These sub-bearers have diverse frequencies. Since the data transfer capacity is smaller, every sub-channel requires a more extended image period. The utilization of OFDM in optical frameworks has expanding because of its high information rates, information rates in optical filaments are normally higher than in RF remote frameworks. Be that as it may, the real issue in OFDM is the impact of timing jitter [2, 3]. Its powerlessness to recurrence counterbalance mistakes between the transmitted and got signals, which may bring about by Doppler shift in the channel or by the contrast amongst transmitter and collector nearby oscillator frequencies. In these circumstances, the orthogonality of sub-transporters is lost, which brings about Intercarrier Interference (ICI).

2 Problem Outline

In the high information rate orthogonal recurrence division multiplexing (OFDM) frameworks has the issue of intercarrier interference (ICI) because of Timing jitter, this will lead the framework execution as high piece blunder rate. We propose another calculation to break down the connection between timing jitter which drives the additional ICI expressions in their association. The investigation demonstrates that bury transporter obstruction (ICI) has measure up to genuine and nonexistent parts and is autonomous of got subcarrier file. Moreover it is demonstrated that the parameters values impact the intercarrier interference (ICI) from the relative commitment on timing jitter, timing jitter assuming control for bigger jitter qualities overwhelming when timing jitter is moderately little. The planning jitter causes recognizable execution corruption in high recurrence band pass examining collectors and alleviation strategies are proposed in [4]. In [5], an upper headed for the impedance brought about by timing jitter is determined and the impacts of whole number oversampling are concentrated on. In [6], a more broad examination of timing jitter is introduced including the impact of both white and shaded planning jitter. In [6], we acquainted a planning jitter framework with depict the rotational and bury transporter impedance (ICI) impact of timing jitter in OFDM frameworks and in [7] we connected this grid to demonstrate that both fragmentary oversampling and whole number oversampling can be utilized to decrease the ICI power because of timing jitter [8]. I/Q awkwardness happens when a front-end segment doesn't regard the force parity or the orthogonality between the I and Q branch [9]. While having the capacity to effectively adapt to the recurrence particular nature of a multi-way spread channel, multi-bearer frameworks are extremely delicate to I/Q lopsidedness [10]. In request to adapt to these weaknesses, various methodologies

for a computerized pay of the I/Q irregularity have been proposed in the writing, see for instance [11]. In this paper, we acquaint another procedure which examines in point of interest the impact of timing jitter in OFDM frameworks. We present an inventive planning jitter network. This planning jitter grid can be de-made into a rotational lattice and an ICI network. This rearranges the investigation of the planning jitter issues in fast OFDM frameworks. After that oversampling strategy is utilized to alleviate the impact of timing jitter. We broaden the planning jitter lattice proposed into investigate the subtle element of the (ICI) in an oversampled framework, and watched the hypothetical and reenactment aftereffects of normal planning jitter commotion power.

2.1 Jitter

In any framework that utilizations voltage moves to speak to timing data, jitter is a deplorable part of the condition. Basically, jitter is the deviation of timing edges from their expected areas. Truly, jitter was kept under control by framework creators by utilizing moderately low flagging rates. Be that as it may, the planning edges connected with cutting edge fast serial correspondence transports render such techniques debatable. As flagging rates move above 2 GHz and comparing voltage swings keep on shrinking, a given framework's planning jitter turns into a noteworthy bit of the flagging interim and, subsequently, a pattern execution limiter.

A straightforward and instinctive definition for jitter is a piece of the SONET detail: "Jitter is characterized as the transient varieties of a computerized sign's noteworthy moments from their optimal position in time." This definition requires thumbnail portrayals of its parts. Exactly what is implied by "short-term?" Timing varieties are, by tradition, split into two classifications: jitter and meander. Timing varieties that happen gradually are known as meander; jitter alludes to varieties that happen all the more quickly. The edge amongst meander and jitter is characterized by the International Telecommunication Union (ITU) as 10 Hz. Meander is for the most part not an issue in serial correspondence joins, where a clock-recuperation circuit dispenses with it. What's more, that odd term "noteworthy moments" alludes to the moves, or edges, between rationale states in the advanced sign. Noteworthy moments are the accurate minutes when the transitioning signal crosses a picked abundancy edge, referred to differently as the reference level or choice limit. At long last, the expression "perfect position" can be considered along these lines.

3 Related Work

Orthogonal Frequency Division Multiplexing (OFDM) is being utilized for high information rate remote applications [12]. It is a multicarrier balance method which fuses orthogonal subcarriers. High Peak to Average Power proportion and

Interbearer Interference (ICI) are two primary drawbacks of the OFDM frameworks. In OFDM frameworks ICI happens because of recurrence counterbalance in the middle of the transmitter and beneficiary bearer frequencies or Doppler Effect [13]. Numerous systems have been produced to decrease the impact of ICI; ICI self-cancelation is a straightforward and advantageous strategy. ICI self-cancelation plan proposed by Zhao [3] uses information allotment and joining of $(1, -1)$ on two adjoining subcarriers i.e. same information is tweaked at kth and $(k+1)$th sub-transporters utilizing $(1, -1)$ as information designation and are joined at the recipient with weights 1 and -1. It is a standout among the most encouraging procedures to lessen ICI; notwithstanding, its execution corrupts at higher recurrence balances. Yeh et al. had proposed conjugate cancelation plan in [14]. In this plan, OFDM image and its conjugate are multiplexed, transmitted and consolidated at the recipient to decrease the impact of ICI. In any case, this plan demonstrates a critical change in CIR at low recurrence balances and its execution corrupts as transporter recurrence counterbalance increments. At higher recurrence counterbalance >0.25 its CIR execution is more awful than standard OFDM framework. In [15] the creator has proposed Phase Rotated Conjugate Cancelation (PRCC), which is an expansion to the plan proposed in [14]. In this an ideal estimation of stage is increased with the OFDM image and its conjugate sign to be transmitted on various way.

The ideal estimation of the stage relies on upon the recurrence balance and thus requires consistent bearer recurrence counterbalance (CFO) estimation and criticism hardware, which expands the equipment unpredictability [16, 17]. Another ICI self-cancelation plan [18] taking into account summed up information allotment $(1, \mu e^{j\theta})$ has been proposed in the writing to enhance CIR execution of ICI self-cancelation framework, where ξ is the ideal worth, which relies on upon recurrence balance. Along these lines for each standardized recurrence balance, an extraordinary estimation of ξ is to be increased with the information which again requires CFO estimation and criticism hardware [16, 17]. A symmetric symbol repeat ICI self-cancelation plan, which uses information portion and joining of $(1, -1)$ at kth and $N-1-k$th subcarrier. This plan demonstrates preferred CIR execution over ICI self-cancelation plan. One of the significant focal points of this plan is to accomplish the recurrence assorted qualities and consequently its execution in recurrence particular blurring channel observed to be superior to anything ICI self-cancelation plan. In this paper, we have proposed an ideal and problematic plan for SSR ICI cancelation plan to enhance the CIR execution.

The design depends on SSR ICI self-cancelation plan, in which an information is balanced at two symmetrically set subcarriers, i.e., kth and $N-1-k$th and uses an information assignment of $(1, -\lambda)$ to enhance CIR execution. To advance decrease the impact of ICI, got regulated information signal at k^{th} and $N-1-k$th subcarriers are joined with weights 1 and $-\xi$. The λ and ξ are the ideal qualities bringing about most extreme CIR. The ideal estimations of λ and ξ are the capacity of standardized recurrence balance, i.e., for each standardized recurrence counterbalance; there exist an interesting estimation of λ and ξ. This procedure requires

constant CFO estimation. To defeat this issue, author in [19] have proposed an imperfect way to deal with find problematic qualities. The got imperfect qualities λ_{so}, ξ_{so} are autonomous of standardized recurrence balance. Therefore, the proposed plan does not require any CFO estimation or criticism hardware and thus wipes out the necessity of complex equipment hardware. This approach has been tested with various channels such as additive white gaussian noise (AWGN), Rayleigh distribution (RD) and Rician distribution (RcD).

4 ICI Due to Frequency Offset

4.1 OFDM Transmission

For sending an OFDM tweaked image, we utilize numerous sinusoidal with recurrence detachment $\frac{1}{T}$ is utilized, where T is the image time frame. The data $a_{\mathbb{K}}$ to be send on each subcarrier k is duplicated by the comparing carrier $g_k(t) = e^{\frac{j2\pi kt}{T}}$ and the total of such tweaked sinusoidal structure the transmit signal. Numerically, the transmit sign is,

$$\begin{aligned} s(t) &= a_0 g_0(t) + a_1 g_1(t) + \cdots + a_{\mathbb{K}-1} g_{\mathbb{K}-1}(t) \\ &= \sum_{0}^{\mathbb{K}-1} a_{\mathbb{K}} g_{\mathbb{K}}(t) \\ &= \frac{1}{\sqrt{T}} \sum_{0}^{\mathbb{K}-1} a_{\mathbb{K}} e^{\frac{j2\pi kt}{T}} w(t) \end{aligned}$$

The elucidation of the above condition is as per the following:

(a) Every data signal $a_{\mathbb{K}}$ increases the sinusoidal having recurrence of k/T.
(b) Whole of all such regulated sinusoidal are included and the resultant sign is conveyed as $s(t)$.

4.2 OFDM Reception

In an OFDM recipient, we will duplicate the got signal with a bank of correlators and coordinate over the period. The correlator to concentrate data sends on subcarrier k.

The integral, $\frac{1}{\sqrt{T}} \int s(t) e^{-\frac{j2\pi mt}{T}} = a_{\mathbb{K}}, m = \mathbb{K}$

$$= 0, m \neq \mathbb{K}$$

where m takes values from 0 till $\mathbb{K} - 1$

4.3 Frequency Offset

In a run of the mill remote correspondence framework, the sign to be transmitted is up changed over to a transporter recurrence before transmission. The beneficiary is required to tune to the same bearer recurrence for down-changing over the sign to baseband, preceding demodulation as in Fig. 1. Be that as it may, because of gadget hindrances the bearer recurrence of the collector need not be same as the transporter recurrence of the transmitter. When this happens, the got baseband signal, rather than being focused at DC (0 MHz), will be focused at a recurrence f_δ, where $f_\delta = f_{T_x} - f_{R_x}$

The baseband representation is (overlooking clamor), $y(t) = s(t)e^{j2\pi f_\delta t}$,

Where $y(t)$ is the received signal

$s(t)$ = the transmitted signal and
f_δ = the frequency offset.

4.4 Impact of Frequency Offset in OFDM Receiver

Let us assume that the frequency offset f_δ is a fraction of subcarrier spacing $1/T$ i.e. $f_\delta = \frac{\delta}{T}$. Also, for simplifying the equations, lets us assume that the transmitted symbols on all subcarriers, $\alpha_{\mathbb{K}} = 1$

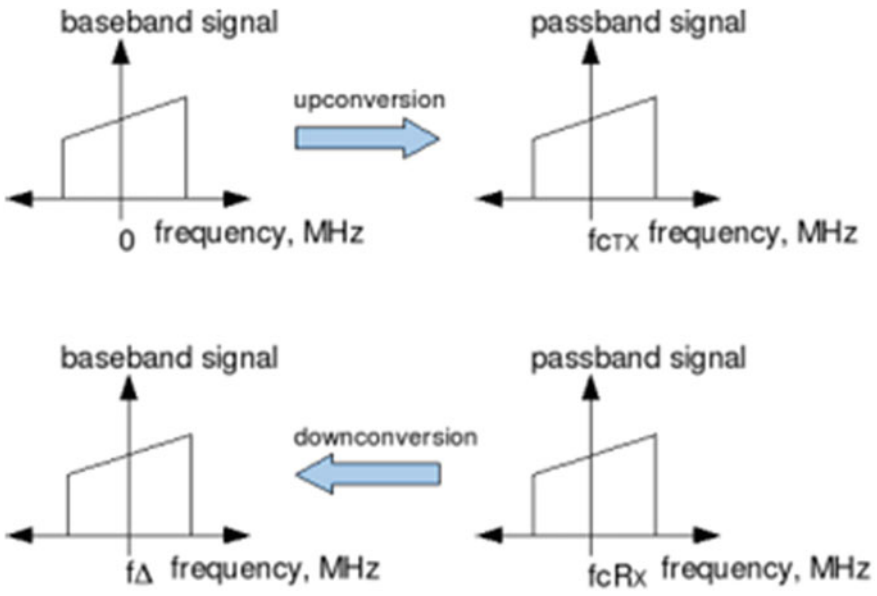

Fig. 1 Up/down transformation

The received signal is, $y(t) = s(t)\mathrm{e}^{\frac{j2\pi\delta}{T}t}$

The output of the correlator for subcarrier m is,

$$\frac{1}{\sqrt{T}}\int y(t)\mathrm{e}^{-\frac{j2\pi mt}{T}} = \frac{1}{T}\int \mathrm{e}^{\frac{j2\pi(k+\delta-m)t}{T}}, m = \in \{0,\ldots,\mathbb{K}-1\}$$

$$= \frac{1}{j2\pi(k+\delta-m)}\left(\mathrm{e}^{j2\pi(k+\delta-m)}-1\right)$$

For $\delta = 0$,

$$\frac{1}{j2\pi(k+\delta-m)}\left(\mathrm{e}^{j2\pi(k+\delta-m)}-1\right) = 1, \quad m = \mathbb{K}$$

$$\frac{1}{j2\pi(k+\delta-m)}\left(\mathrm{e}^{j2\pi(k+\delta-m)}-1\right) = 0, \quad m \neq \mathbb{K}$$

The necessary lessens to the OFDM beneficiary without any debilitations case.

However for non-zero estimations of, we can see that the abundancy of the connection with subcarrier incorporates m contortion because of

- Recurrence counterbalance between real recurrence $\frac{m+\delta}{T}$ and the sought recurrence $\frac{m}{T}$
- Bending obstruction with different subcarriers with wanted recurrence. This term is otherwise called Intercarrier Interference (ICI).

Carrier-to-Interference Ratio. The signal-to-interference ratio (*S*/*I* or SIR), otherwise called the carrier-to-interference ratio (*C*/*I*, CIR), is the remainder between the normal got adjusted transporter power *S* or *C* and the normal got co-channel impedance power *I*, i.e., cross-talk, from different transmitters than the valuable sign. The CIR looks like the bearer to-clamor proportion (CNR or *C*/*N*), which is the sign to-commotion proportion (SNR or *S*/*N*) of an adjusted sign before demodulation. A refinement is that meddling radio transmitters adding to *I* might be controlled by radio asset administration, while *N* includes clamor power from different sources, commonly added substance white Gaussian commotion (AWGN). The CIR proportion is contemplated in obstruction constrained frameworks, i.e., where *I* overwhelm over *N*, ordinarily in cell radio frameworks and broadcasting frameworks where recurrence directs are reused in perspective to accomplish abnormal state of region scope. The *C*/*N* is considered in clamor restricted frameworks. In the event that both circumstances can happen, the carrier-to-noise-and-interference ratio, *C*/(*N* + *I*) or CNIR might be considered. In radio building, a frequency offset is a purposeful slight movement of communicate radio recurrence (RF), to diminish obstruction with different transmitters.

Interference. The most imperative issue experienced in communicating through earthly transmitters is the impedance from different supporters. On a fundamental level, every supporter has an alternate radio recurrence (arranged by people in general power) in a typical gathering range to evade impedance from each other.

However still there are two issues: spurious radiation of contiguous channels and periphery gathering. Periphery gathering is unintended gathering under certain climate conditions. The astoundingly long-go gathering implies that the collector might be tuned to more than one transmitter (transmitting at same recurrence) in the meantime. These transmitters may transmit projects of various supporters and additionally the projects of the same telecaster. In simple transmission, even the transmitters transmitting the exceptionally same project meddle each other on account of stage contrasts of the approaching sign, yet in advanced transmission the transmitters transmitting the same system in the same channel may strengthen each other.

The Shift in RF. Keeping in mind the end goal to diminish the impedance from the periphery territory transmitters transmitting in the same channels, a strategy named recurrence balance is regularly utilized. By this strategy, a somewhat moved RF is doled out for a transmitter which might be meddled by different transmitters. In TV transmission, the moved RF is computed by the equation;

$$f_{\text{os}} = f_{\text{ch}} + \frac{f_L \cdot p}{12}, \tag{1}$$

where,

f_{os} = RF offset,
f_{ch} = Standard channel frequency,
p is an integer such that $-12 < p < 12$

f_L is the line frequency. (Note: 15,625 Hz for 625-line systems, 15,750 Hz for System *M* and System *J* and 20,475 Hz for *E*) Precision offset is the same as frequency offset, with the exception of that for this situation; the balance recurrence is created by a cesium controlled oscillator.

5 Proposed System Model

Figure 2 demonstrates how the jitter is characterized. The main hub demonstrates an OFDM signal tested at general planning interims of *T*/*N*. This is the perfect case. The lines in second pivot speak to uniform inspecting interims. The strong bolts speak to the real examining times. The impact of timing jitter causes deviation t between genuine inspecting times and uniform examining interims. In OFDM frameworks while timing jitter debases framework execution, a steady time balance from the perfect testing moments in naturally revised without punishment by the equalizer in the collector.

The piece chart of standard rapid OFDM framework is given in Fig. 2. In this paper we consider an OFDM framework where testing happens at baseband after the sign has been down changed over from RF or optical frequencies. The

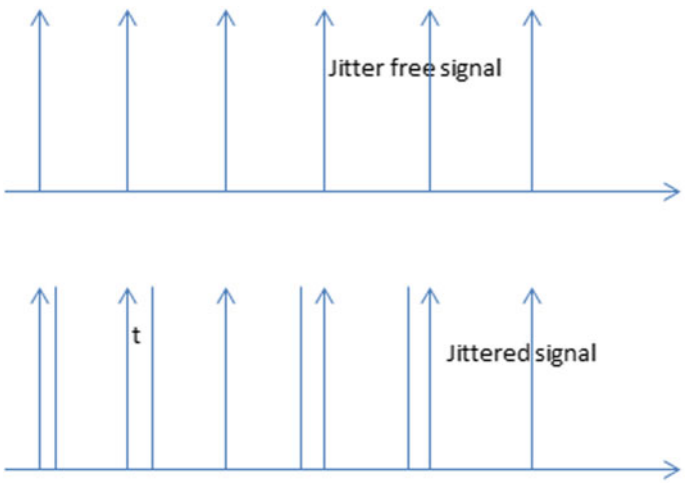

Fig. 2 Definition of timing Jitter

information to be transmitted in each OFDM The transporter sign is balanced with info sign, and serial information is changed over into parallel information. At the point when the parallel image streams are produced, every stream would be regulated and continued at various frequencies. At that point, the *N* images mapped to canisters of a converse quick Fourier change (IFFT). These containers relate to orthogonal sub-bearers in the OFDM images. Hence, the OFDM image can be communicated as takes after.

The block diagram of standard high-speed OFDM system is given in Fig. 3. In this paper we consider OFDM system where sampling occurs at baseband after the signal has been down converted from RF or optical frequencies.

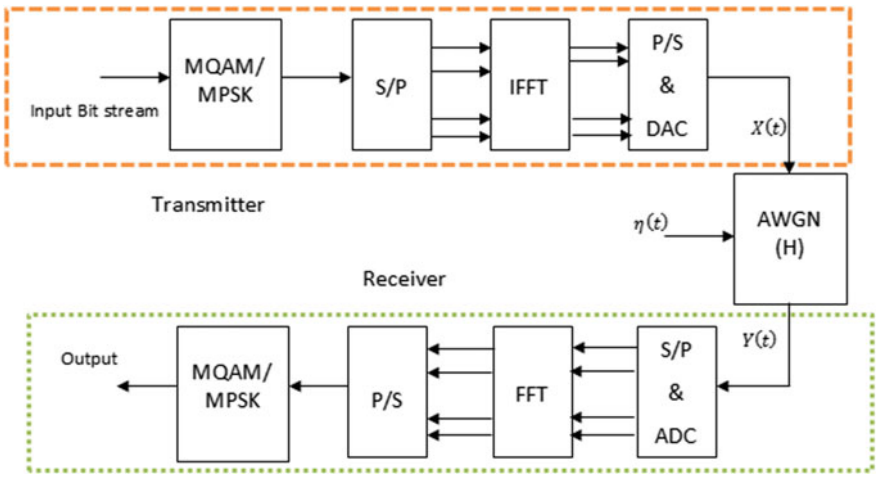

Fig. 3 Standard high-speed OFDM block diagram

$$Y = \left[Y_{-N/2+1} \ldots Y_0 \ldots Y_{N/2}\right]^T$$
$$X^T = \left[X_{-N/2+1} \ldots X_0 \ldots X_{N/2}\right]^T$$
$$H = \text{diag}\left(H_{-N/2+1} \ldots H_0 \ldots H_{N/2}\right)$$

And

$$\mathrm{W} = \begin{bmatrix} w-\frac{N}{2}+1,-\frac{N}{2}+1 & \cdots & w-\frac{N}{2}+1,0 & \cdots & w-\frac{N}{2}+1,-\frac{N}{2} \\ \vdots & \ddots & \vdots & \iddots & \vdots \\ w_0,-\frac{N}{2}+1 & \cdots & w_{0,0} & \cdots & w_{0,N/2} \\ \vdots & \ddots & \vdots & \iddots & \vdots \\ w\frac{N}{2},-\frac{N}{2}+1 & \cdots & w\frac{N}{2},0 & \cdots & w\frac{N}{2},\frac{N}{2} \end{bmatrix} \quad (2)$$

Timing jitter causes an added noise like component in the received signal.

$$Y = HX^T + (W - I)HX^T + N, \quad (3)$$

where I is the N × N identity matrix. In Eq. (3), the first term represents wanted term while the second term indicates jitter noise. In it was shown that the elements of the timing jitter matrix W are given by

$$w_{l,k} = \frac{1}{N} \sum_{n=-N/2+1}^{N/2} e^{j2\pi k\frac{\tau_n}{T}} e^{j\frac{2\pi}{N}(k-l)n}, \quad (4)$$

where n is the time index, k is the transmitted subcarrier index and l is the received subcarrier index.

5.1 System Description

The data to be transmitted in each OFDM, the carrier signal is modulated with input signal, and serial data is converted into parallel data. When the parallel symbol streams are generated, each stream would be modulated and carried over at different frequencies. Then, the N symbols mapped to bins of an inverse fast Fourier transform (IFFT). These bins correspond to orthogonal subcarriers in the OFDM symbols. Therefore, the OFDM symbol can be expressed as follows:

$$x_n = \frac{1}{\sqrt{N}} \sum_{k=-N/2+1}^{N/2} X_k e^{j\frac{2\pi}{N}kn} \quad (5)$$

Above condition gives the specimens at the yield of inverse fast Fourier transform (IFFT). The advanced to simple (D/A) converter then makes a simple time area signal which is transmitted through the channel. The simple sign at the yield of the advanced to simple converter (DAC), is given by

$$x(t) = \frac{1}{\sqrt{N}} \sum_{k=-N/2+1}^{N/2} X_k e^{j2\pi f_k t}, \tag{6}$$

where $f_k = K/T$. At the beneficiary, the got signal () is influenced by the sign. At the beneficiary, the sign is changed over back to a discrete *N*-point succession, relating to sub-transporters. The discrete sign is demodulated utilizing *N*-point Fast Fourier Transform (FFT) operation at the collector. So $Y(t)$ is given by

$$Y(t) = \frac{1}{\sqrt{N}} \sum_{k=-N/2+1}^{N/2} H_k X_k e^{j2\pi f_k t} + \eta(t), \tag{7}$$

where **η(t)** is additive Gaussian white noise.

After passing it through ADC block, the digitized signal is given by,

$$y_n = y\left(n\left(\frac{T}{N}\right) + t_n\right) + \eta_n \tag{8}$$

We now break down the impact of timing jitter in OFDM frameworks and impact of both basic and fragmentary oversampling in OFDM and demonstrate that either or both can be utilized to decrease the corruption brought on by the planning impact. To accomplish basic oversampling, the got sign is tested at the rate of MN/T, where is a number. For fragmentary oversampling some band-edge subcarriers are unused in the transmitted sign. When all *N* sub-bearers are adjusted, the transmission capacity of the baseband OFDM signal*N*/2T, so inspecting interims of *T*/*N*. In the general case, where both basic and partial oversampling is connected, the sign specimens after the ADC in the beneficiary are given by

$$y_{n_M} = y\left(\frac{n_M T}{NM}\right) = \frac{1}{\sqrt{N}} \sum_{k=-N_L}^{N_U} H_k X_k e^{\left(\frac{j2\pi k}{T} \times \frac{n_M T}{NM}\right)} + \eta\left(\frac{n_M T}{NM}\right), \tag{9}$$

where n_M = the oversampled discrete time list and η is the AWGN. With fundamental oversampling, the—point FFT in the collector is supplanted by an "oversized" NM point FFT. The yield of this FFT is a vector of length with components.

$$Y_{l_M} = \frac{1}{\sqrt{N}} \frac{1}{\sqrt{NM}} \sum_{n_M=-\frac{NM}{2}+1}^{NM/2} y_{n_M} \mathrm{e}^{\left(\frac{-j2\pi n_M l_M}{NM}\right)}, \tag{10}$$

where l_M is the index at the output of the point FFT. Then combining (4), (9), (10), we obtain the modified weighting coefficients for the oversampling case,

$$w_{\mathrm{l_M}} = \frac{1}{NM} \sum_{n_M=-NM/2+1}^{NM/2} \mathrm{e}^{j2\pi k \frac{\tau_{n_M}}{T}} \mathrm{e}^{j\frac{2\pi}{NM}(k-l_M)n_M} \tag{11}$$

In this area, we utilize the planning jitter framework to determine the impedance brought on by timing jitter. By utilizing the estimate $e = 1 + j\theta$ for little θ, as in (11) gets to be

$$w_{\mathrm{l_M},k} \cong \frac{1}{NM} \sum_{n_M=-NM/2+1}^{NM/2} \left(1 + \frac{j\pi k \tau_{n_M}}{T}\right) \mathrm{e}^{j\frac{2\pi}{NM}(k-l_M)n_M} \tag{12}$$

So for $k = l_M$ the variance of the weighting coefficients are given by

$$E\left\{\left|w_{l_M,k}\right|^2\right\} \approx \left(\frac{2\pi k}{MNT}\right)^2 \sum_{n_m} \sum_{d_m} E\left\{t_{n_M} t_{p_M}\right\} \mathrm{e}^{j\frac{2\pi}{MN}(k-l)d_M}, \tag{13}$$

where $E\{\cdot\}$ denotes the expectation operator. Where $n_M - p_M = d_M$

When the timing jitter is white, then

$$E\left\{\left|w_{l_M,k}\right|^2\right\} \approx \left(\frac{1}{NM}\right)\left(\frac{2\pi k}{T}\right)^2 E\left\{t_{n_M}^2\right\} k \neq l_M \tag{14}$$

From the above condition it can be demonstrated that white planning jitter is conversely corresponding to so expanding the number oversampling component diminishes the impact of timing jitter, i.e., entomb bearer obstruction (ICI). Where white planning jitter framework is $E\left\{\left|w_{l_M,k}\right|^2\right\}$ and it relies on upon k^2 yet not on l_m, so higher recurrence sub-transporters cause more ICI, however ICI causes all sub-bearers similarly. We now compute the normal jitter clamor power for every sub-bearer for the instance of white planning jitter, from (3) and (10),

$$Y_{l_M} = H_{l_M} X_{l_M} + \sum_{k=-N_L}^{N_U} \left(w_{l_M,k} - I_{l_M,k}\right) H_k X_k + \mathbb{N}(l), \tag{15}$$

where the second term speaks to the jitter noise. We consider a level channel with, $Hk = 1$, and accept that the transmitted sign force is appropriated similarly over the

utilized subcarriers so that for each utilized subcarrier $E\{X_k^2\} = \sigma_s^2$. At that point the normal jitter noise power, $P_j(l)$ to get signal force of *lth* subcarrier is given by

$$\frac{P_j(l)}{\sigma_s^2} = \frac{E\left\{\left|\sum_{k=-N_l}^{N_u}(w_{l,k} - I_{l,k})X_k\right|^2\right\}}{\sigma_s^2} = \sum_{k=-N_L}^{N_U} E\left\{\left|w_{l,k} - I_{l,k}\right|^2\right\} \tag{16}$$

For a system in which there are equal numbers of unused subcarriers at each band-edge so, where is number of used subcarriers. Then Eq. (16) becomes

$$\frac{P_j(l)}{\sigma_s^2} = \sum_{k=-N_v/2+1}^{N_v/2} E\left\{\left|w_{l,k} - I_{l,k}\right|^2\right\} \tag{17}$$

On the off chance that the image period is unaltered, lessening the quantity of subcarriers will decrease the general information rate, the transmit power and the transfer speed. To make a reasonable examination the image time frame is likewise decreased so that $Tv = vT/N$ where Tv is the image time frame for Nv utilized subcarriers and TN for N used subcarriers. At that point condition (18) given as

$$\frac{P_j(l)}{\sigma_s^2} = \sum_{k=-N_v/2+1}^{N_v/2} \frac{1}{NM}\left(\frac{2\pi k}{T_v}\right)^2 E\{\tau_n^2\} \tag{18}$$

Using $\sum_{k=-N_v/2+1}^{N_v/2} k^2 = \frac{1}{12}N_v(2+N_v^2)$, we obtain

$$\frac{P_j(l)}{\sigma_s^2} = \frac{2}{3M}E\{\tau_n^2\}\left(\frac{N_v}{N}\right)\left(\frac{\pi}{T_v}\right)^2 + \frac{1}{3M}E\{\tau_n^2\}\left(\frac{N_v^3}{N}\right)\left(\frac{\pi}{T_v}\right)^2 \tag{19}$$

Since the first term in Eq. (12) is very small, so it can be ignored. Then the equation will be rewritten as

$$\frac{P_j(l)}{\sigma_s^2} = \frac{\pi^2}{3M}E\{\tau_n^2\}\left(\frac{N_v N}{T_N^2}\right) \tag{20}$$

On the off chance that there is no indispensable oversampling or partial oversampling, $M = 1$ and $Nv = N$, therefore

$$\frac{P_j(l)}{\sigma_s^2} = \frac{\pi^2}{3}E\{\tau_n^2\}\left(\frac{N^2}{T_N^2}\right) \tag{21}$$

Contrasting 20 and 21, it can be seen that the mix of fundamental oversampling and fragmentary oversampling lessens the jitter clamor power by an element of ***Nv/NM***.

5.2 C/I Model

The discrete time OFDM image at the transmitter can be communicated as

$$x[n] = \frac{1}{\sqrt{N}} \sum_{k=0}^{N-1} X(k) \mathrm{e}^{\frac{j2\pi nk}{N}}, \quad n = 0, 1, 2, \ldots, N-1, \tag{22}$$

where N is all out quantities of subcarriers and $X(k)$ signifies the regulated information image transmitted on kth subcarrier. Because of AWGN channel and recurrence balance, the got OFDM sign can be composed as

$$y[n] = x[n] \mathrm{e}^{\frac{j2\pi \varepsilon n}{N}} + w[n] n = 0, 1, 2, \ldots, N-1, \tag{23}$$

where ε is the standardized recurrence counterbalance and $w[n]$ is the specimen of added substance white Gaussian clamor. The got information signal on kth subcarrier can be composed as

$$Y(k) = X(k)\mathbb{S}(0) + \sum_{l=0, l\neq k}^{N-1} X(l)\mathbb{S}(i-k) + W(k)$$

$$k = 0, 1, \ldots, N-1, \tag{24}$$

where $W(k)$ is kth the specimen of DFT of added substance noise. The grouping $\mathbb{S}(i-k)$ is characterized as the ICI coefficient amongst kth and ith subcarriers, which can be communicated as

$$\mathbb{S}(i-k) = \mathrm{e}^{\left(j\pi(i+\varepsilon-k)\left(1-\frac{1}{N}\right)\right)} \frac{\sin(\pi(i+\varepsilon-k))}{N sin\left(\frac{\pi}{N}(i+\varepsilon-k)\right)} \tag{25}$$

The ratio of CI at the kth subcarrier can be composed as

$$C/I = \frac{|\mathbb{S}(k)|^2}{\sum_{l=0, l\neq k}^{N-1} |\mathbb{S}(i-k)|^2} \tag{26}$$

6 Experimental Results

This section presents the simulation outputs of proposed model, experiments have been done in MATLAB 2015 version. We had considered 2000 symbols and 512 subcarriers to generate a transmitted source signal which will be sent through the OFDM transmitter section as given in Table 1.

Table 1 Simulation parameters

Parameters	Specifications
FFT & IFFT size	8
No. of Subcarriers	512
Epsilon	0.15 and 0.25
Channel model	AWGN
Modulation scheme	QPSK
Constellation points	4, 8, 16, and so on

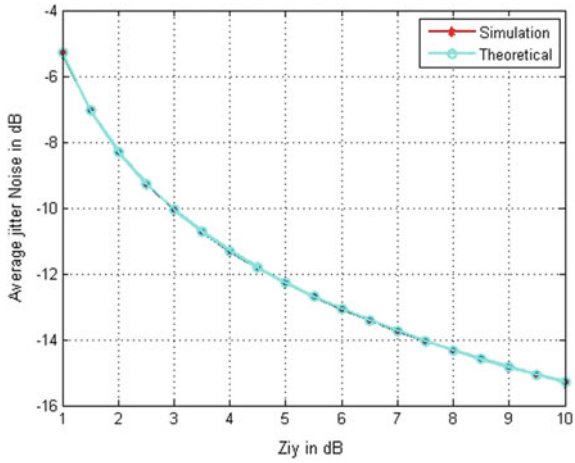

Fig. 4 Average jitter noise with variable ξ

Here we assumed that the ultra-sampling factor as ξ, the performance of average jitter noise power in dB to the variable sampling values have been given in Fig. 4, which concludes that the increasing in the value of ξ then the jitter noise power will gets reduced. It has also compared with the theoretical analysis and we got the approximated simulated curve.

Figure 5 has shown the performance of C/I ratio with the effect of normalized frequency offset, it has given that the C/I ratio will get reduced with the improvement in frequency offset as we discussed theoretically in the above sections. Section 2 has given that the jitter noise power is directly proportional to the ICI factor which means that the C/I ratio is indirectly proportional to the jitter noise power. It has shown in Fig. 6 that if average jitter noise power reduces then C/I ratio will be improved. For the value of −14 dB jitter noise power we got a C/I ratio of approximately 36 dB. We also compared the simulation results with the theoretical analysis. Figure 7 shown that the analysis of C/I ratio with the improvement in ξ, while increasing the ξ values the ratio of C/I has been stable in the original OFDM system, optimal and sub-optimal (SO) schemes proposed in [19].

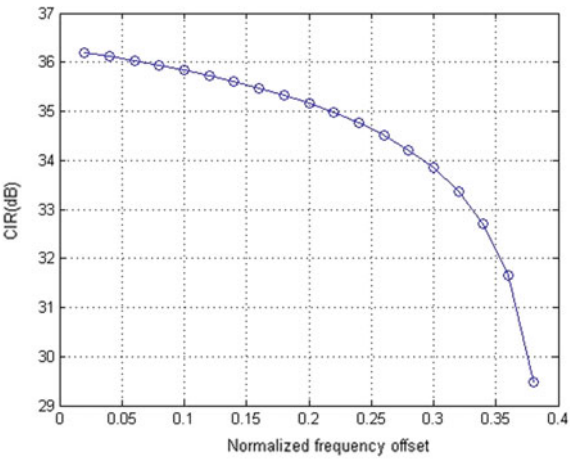

Fig. 5 Frequency offset effect on C/I ratio

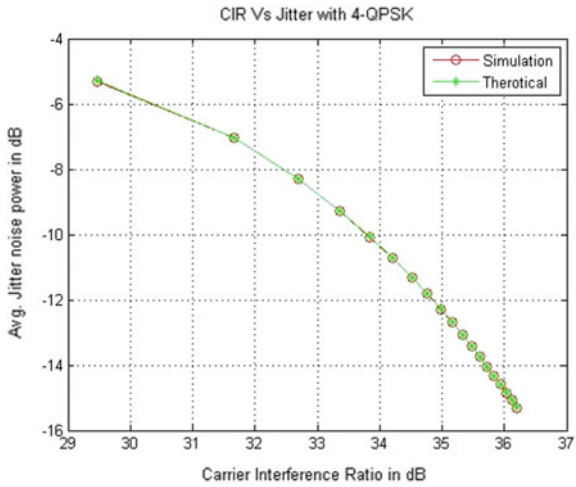

Fig. 6 Effect of average jitter noise power on C/I ratio

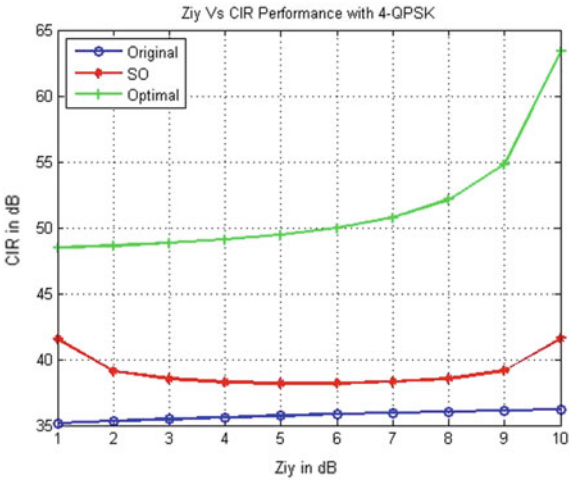

Fig. 7 C/I ratio in [19] with variable sampling values ξ

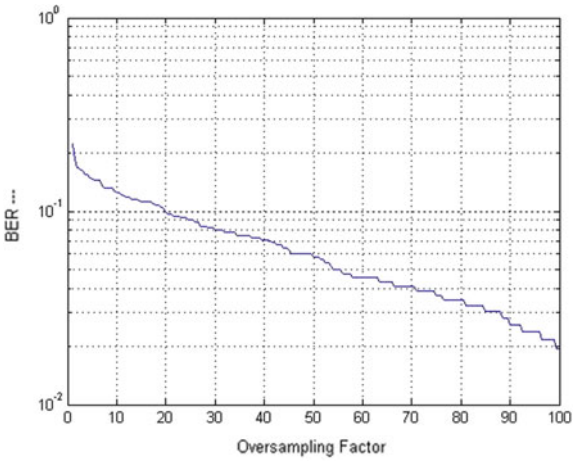

Fig. 8 Performance of BER with increasing values of sampling factor

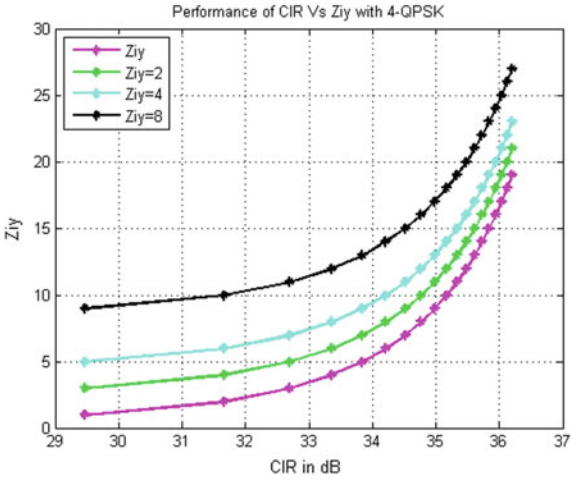

Fig. 9 Performance of C/I ratio with variable $\xi = 2, 4$ and 8

We considered the ICI cancelation schemes that have been proposed in [19] and produced an interaction between C/I ratio of those algorithms with our proposed model. It has shown that the C/I ratio has been improved dramatically for the higher values of ξ. Performance of BER with ultra-sampling have given in Fig. 8. Finally, we had analyzed the effect of variable ξ with the C/I ratio over AWGN channel with 4-QPSK modulation scheme. We can see the Fig. 9, it has shown that the ICI will get reduced with mitigation of ultra-sampling factor ξ.

7 Conclusion

In this article, a typical jitter noise reduction method has been implemented which also improves the CIR performance there by reduces the inter carrier interference (ICI). We had executed an ultra-sampling criteria in the OFDM correspondence framework for improving the C/I ratio, by adjusting over examining in the framework we have got inferior jitter power that enhances CIR performance which results in mitigation of ICI factor.

References

1. Armstrong J OFDM for optical communications. J. Light Wave Technol 27(1):189–204
2. Manoj KN, Thiagarajan G (2003) The effect of sampling jitter in OFDM systems. Proc IEEE Int Conf Commun 3:2061–2065
3. Onunkwo U, Li Y, Swami A (2006) Effect of timing jitter on OFDM based UWB systems. IEEE J Sel Areas Commun 24:787–793
4. Syrjala V, Valkama M (2009) Jitter mitigation in high-frequency band pass-sampling OFDM radios. WCNC pp 1–6
5. Manoj KN, Thiagarajan G (1990) The effect Wakimoto Jitter analysis of high speed sampling systems. IEEE J Solid-State Circuits 25:220–224
6. Onunkwo U, Li Y, Swami A (2006) Effect of timing jitter on OFDM based UWB systems. IEEE J Sel Areas Commun 24:787–793
7. Yang L, Fitzpatrick P, Armstrong J (2009) The effect of timing jitter on high-speed OFDM systems. Proc AusCTW 12–16
8. Tubbax J, Côme B, Liesbet Van der Perre L, Deneire L, Donnay S, Engels M (2003) IMEC - Kapeldreef 75, 3001 Heverlee, Belgium Compensation of IQ imbalance in OFDM systems
9. Windisch M, Fettweis G Dresden University of Technology, Vodafone Chair Mobile Communications Systems, D-01062 Dresden, Germany 'On the Impact of I/Q Imbalance in Multi-Carrier Systems for Different Channel Scenarios'
10. Windisch M, Fettweis G (2004) (Standard Independent I/Q Imbalance Compensation in OFDM Direct-Conversion Receivers. In: Proceedings of 9th International. OFDM Workshop (InOWo'04), Dresden, Germany, pp 15–16 (2004)
11. Yang L (2011) Timing jitter in high speed OFDM systems. Ph.D. dissertation, Electrical and Computer Systems Engineering. Monash University, Melbourne, Victoria
12. Wu Y, Zou WY (1995) Orthogonal frequency division multiplexing: a multicarrier modulation scheme. IEEE Trans Consumer Electron 41(3):392–399
13. Zhao Y, Haggman SG (2001) Intercarrier interference self-cancellation scheme for ofdm mobile communication systems. IEEE Trans Commun 49(7):1185–1191
14. Yeh H-G, Chang Y-K, Hassibi B (2007) A scheme for cancelling inter carrier interference using conjugate transmission in multicarrier communication systems. IEEE Trans Wireless Commun 6(1):3–7
15. Wang C-L, Huang Y-C (2010) Inter carrier interference cancellation using general phase rotated conjugate transmission for OFDM Systems. IEEE Trans Commun 58(3):812–819
16. Sathanantham K, Rajatheva RMAP, Ben Slimane S (2000) Analysis of OFDM in the presence of frequency offset and a method to reduce performance degradation. Global Telecommun Conf IEEE 1:72–76

17. Fu Y, Ko C (2002) A new ICI self–cancellation scheme for OFDM systems based on a generalized signal mapper. Int Sym Wireless Personal Multimedia Commun 3:995–999
18. Mathews JH, Fink KK (2004) Numerical Methods using Matlab, 4th edn. Prentice-Hall Inc
19. Sharief AH, SatyaSai Ram M (2016) An improved ICI self cancellation scheme for OFDM systems under various channels. In: Int J Electr Comput Eng (IJECE), 6(2):690–699

ESMBCRT: Enhance Security to MANETs Against Black Hole Attack Using MCR Technique

Shaik Noor Mohammad, R. P. Singh, Abhijit Dey and Syed Jalal Ahmad

Abstract Ad-hoc network also called MANET refers to a self-motivated, structure less temporary network that can be developed by the group of moving nodes. In this type of network nodes can leave or enter at any instant of time within the network. Therefore prone to the security threat, a major and well-known security attack that occurs in MANETs is a black hole attack. Almost all existing approaches are securing this nature of attack either based on the energy of a node or by providing a key. However as the network is mobile, so key distribution is a challenging task. So simply we can assume that distribution of keys is not possible in this network. The presented approach is a novel security method which doesn't require any key distribution called ***ESMBMCRT: Enhance Security to MANETs against Black hole Attack using modified CR Technique*** to provide the security. The presenting security method not only enhances the security to the network but also minimizes the energy consumed which is also the important concern of such networks. We authenticate our approach by using NS_2.

Keywords Security · MANET · CRT · Black hole · Hex codes

S. N. Mohammad (✉) · R. P. Singh
SSSUTMS, Sehore, Madhya Pradesh, India
e-mail: noor.468@gmail.com

R. P. Singh
e-mail: vc@sssutms.co.in

A. Dey
GNITC, Hyderabad, Telegana, India
e-mail: abhijitdey89@gmail.com

S. J. Ahmad
MIET, Jammu, Jammu and Kashmir, India
e-mail: jalal0000@yahoo.com

H. S. Saini et al. (eds.), *Innovations in Electronics and Communication Engineering*,
Lecture Notes in Networks and Systems 33,
https://doi.org/10.1007/978-981-10-8204-7_32

1 Introduction

Due to dynamic frequency reuse shared radio channel and no predefined infrastructure. MANETs divert the research community to focus on this era. As the nodes are mobile any node can proceed as a host or a router within the network. So MANET's are more subjected to security attacks such as active attacks (ex., network, MAC, and Transport layer and application layer attacks) and passive attacks (ex., snooping attack) in the network. However the nodes in MANET's are mobile, each node should prove its secrecy, authenticity, and integrity. Security threats like malicious node attack encounter in MANET's due to the decentralized Coordination. In the art of work, these security issues are addressed by key distribution among nodes. However, in MANET's any node can join the network and leave the network at any instant of time, so the distribution of keys is not possible. The term Security is referred as "the protection of confidential Information against malicious threats". In MANETs data transmission between any two nodes mainly depends on intermediate nodes. There are various secure routing protocols [1–3] which establish risk-less and protected route between end nodes. Such proposals attain safe and secure routing protocols by identifying the intermediate nodes and authenticating them by verifying the integrity of the nodes. However, cryptography-based Proposals believe that the authentication will be given by the main authority, but it may not be true because nodes in MANET's are mobile and here there is no main system which can provide the authentication. In the presented approach we are providing security against black hole attack using ***ESMBMCRT*** without distribution of key. We validate our approach with the help of NS2.

The remaining part of the presented paper is ordered as follows. Section 2 presents the art of work, Sect. 3 presents the proposed approach, and Sect. 4 presents node matching process. In Sect. 5 we present simulation results. In Sect. 6 we conclude our paper.

2 Art of Work

Wireless networks mainly MANETs are more prone to security threats, due to different parameters such as bandwidth, delay, mobility, and communication. Trust and Reputation are necessary for the development of security methods to the wireless networks. However, the availability of network cannot be guaranteed by secure routing protocols. They are very weak to security attacks, such as flooding and packet drop attacks. In [4, 5], the authors proposed ideas that encourage cooperation among the nodes between source and destination. However, such models fail to nullify security attacks like flooding attacks. In [6, 7] Trust and reputation approaches, which estimate integrity of the intermediate nodes between source and destination, are proposed. However, these models need more modification in the secure routing protocol operations to assemble confirmation of

integrity of the nodes. Therefore, trust models are more prone to challenges such as Trustful-elicitation. These models use trust decisions just for the reason of adopting secure routes, rather than expanding the trust decisions to enhance the security management algorithms [8–11]. Aarti and Tayagi [12] presented a survey that mainly focuses on issues, characteristics, and application, of various types of security attacks at different layers of network and security goals.

Wadbude and Richariya [13] described a security approach that uses a key allocation method. Here it is believed that the key will be available with the authorized central (authority) node. However, this model may not work if the authority node that possesses key moves away from the network. Sun and Yu [14] presented a model which uses key distribution at three layers for MANETs. It also analyzed key distribution format along with data transmission effectiveness between the source node and destination node. Mamatha and Sharma [15] presented a security model that identifies and prevents the compromised nodes in the network. This model is also based on key distribution, so it not only fails when the central coordinating node moves away from the network but also increases the complexity because of key allocation between the nodes. Elizabeth et al. [16] presented an improved security model by utilizing Elliptic Curve Cryptography (ECC), which will increase the difficulty due to an extra amount of numerical computations between the source and destination nodes. Mirchiardi et al. [17] described a model for MANETs that sense the mischief and response of a malicious node. But, here the work fails to give security to compromised nodes in MANETs when collision or incompatibility occurs in the route. This method is unsatisfactory due to less amount of transmission power.

Rana and Singh [18] described a model that provides a better and secure data transmission between the source-destination pairs by using a two-hop verification model. However, in this model more amount of processing power is required, which not only decreases the throughput but also increases the delay. Hu et al. [19] described a secured protocol that increases the lifespan of packets and guides the information packets towards the destination. But, this model fails to provide the security to midway nodes. Here any attacker can join the network and corrupt information. Chandrakant [20] described a security approach for MANETs which considers the energy of each node. This model cannot work always as compromised nodes may enter the network at different energies. Singh and Sharma [21] described how the malicious node (Black Hole) attack takes place in the wireless network system. They measured the initial time and set the same time as a waiting time for the source node to get the replicate request from further adjacent nodes. The authors presumed that here the wait time of data packet up to source is same as half of the route reply (RREP). So, this security method cannot support for multi-hop wireless network if the two different routes from source to the destination have a large amount of time difference to accept a request (this is because of variation in queuing delay and transmission time of one route when compared with another route).

Deshmukh et al. [22] presented an approach in which the authors try to remove the black hole attack using AODV approach. However, this particular approach is based on the time to live (TTL) which may not always true if the intermediate node

is far from the anchoring node, particularly when two routes exist between source and destination. While designing any secure wireless network, it is necessary to take close consideration of the bandwidth, delay, and overhead. This paper presents a very effective security method called ***ESMBMCRT*** for MANETs that do not require any key distribution and energy considerations. For providing complete security, reputation and trust, our model reduces the overhead and power consumption, which also increases the lifespan of the network.

3 Proposed Approach

Cyclic Redundancy (CR) is a well-known technique of digital communication used to control the errors encountered during transmission. Almost all communicative devices are designed to meet the requirement of hardware to satisfy CR to make the communication error-free. As a result, such type of coding techniques can secure the network to make the system intelligent and can save energy. In this paper, we are using a modified model of CR technique using modulo 2 operations (i.e. Ex-OR operation) to provide the security against Black hole attack in MANETs called "**ESMBMCRT**". An IPV4 packet header is used to store the security information. Also in presented approach, we use equal weighted Hex codes from 0 to 15 which are divisible by 3 to represent the initial concatenation series for the design of a code vector (i.e. 3, 6, 9, 12 and 15). After that we take the hex codes of this concatenation series (i.e. 0011, 0110, 1001, 1100, 1111), However hex code of '15' is not having equal weight of zeros and ones, so can be ignored. Thus the final concatenation series can be represented as '0011, 0110, 1001, and 1100'. This series can be mathematically represented as

$$\prod_{p=1}^{M} yp \tag{1}$$

where $M = 4$, $y = 3$ & $p = 1, 2, 3, 4$ and $y_1, y_2, y_3 \ldots . y_M$ represent the elements of the concatenation series. Among this series we initially choose first four bits as Divisor 'D_R' and remaining bits as Dividend 'D_D' (user defined) and can be represented as $D_R = 0011$ & $D_D = 011010011100$.

Initially, the source node will send this concatenation series to hop 1 and the security code word generated at hop 1 can be given as

$$H_1 = \frac{D_D}{D_R} \oplus R \tag{2}$$

where 'R' is the remainder of $\frac{D_D}{D_R}$ and H_1 is the security code word at hop1.

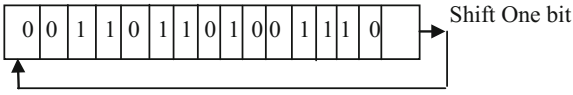

Fig. 1 One-bit shift towards left

However, Ex-OR operation of $\frac{D_D}{D_R}$ and R_1 at hop 1 is done manually, as no one should use software programme to break the code word. At the next stage (i.e. at hop 2), the concatenation series is shifted one bit from right to left as represented in Fig. 1.

The new code word generated at hop 2 can be represented as

$$0001101101001110$$

Here $D_{R1} = 0001$ & $D_{D1} = 1011010\ 01110$

Where D_{R1} is the Divisor at hop 2 & D_{D1} is the Dividend at hop 2.

Therefore $\frac{D_{D1}}{D_{R1}}$ will change the remainder, so the new security code word generated at hop 2 can be represented as

$$H_2 = \frac{D_{D1}}{D_{R1}} \oplus R_1 \tag{3}$$

This shifting of one-bit operation continues till destination node, so the security code word at nth hop can be represented as

$$H_n = \frac{D_D(n-1)}{D_R(n-1)} \oplus R_{n-1} \tag{4}$$

This changing of bit shifting will enhance the security of the network, as at every hop it will alter the designed code word. So is difficult to break the security, hence cannot allow the malicious node to enter the set-up of the designed system.

4 Node Matching Process

Consider a Fig. 2, in which black hole wants to enter and take part with the active nodes. Initially, the source node transmits towards its neighboring nodes. However, a neighboring node can also be a black hole attacker node. But during the matching process, only active nodes can access the data. This is because black hole attack cannot be able to synchronize with the source node in a given amount of time (i.e. TTL: time to live), due to the unavailability of resulted security code of hop 1 to match with the source node. This cannot take part within the network. This node matching process will continue at each and every intermediately node till destination node. In this way, black hole (compromised node) can be easily judged and eliminated from the network.

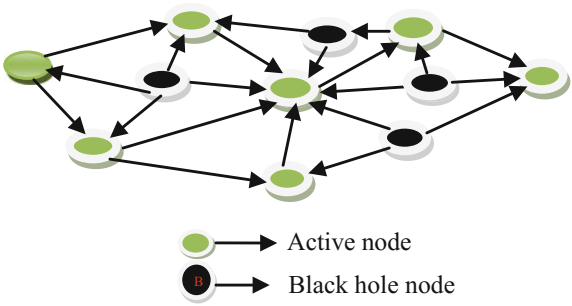

Fig. 2 4 hop MANET with Black hole attacker nodes

5 Simulation Results

In this section, we are representing simulated results using NS2, and compare with the art of work. Figure 3 represents the deviation of packet delivery ratio versus simulation time (ST) of the end pair. From the figure, it has been noticed that if end

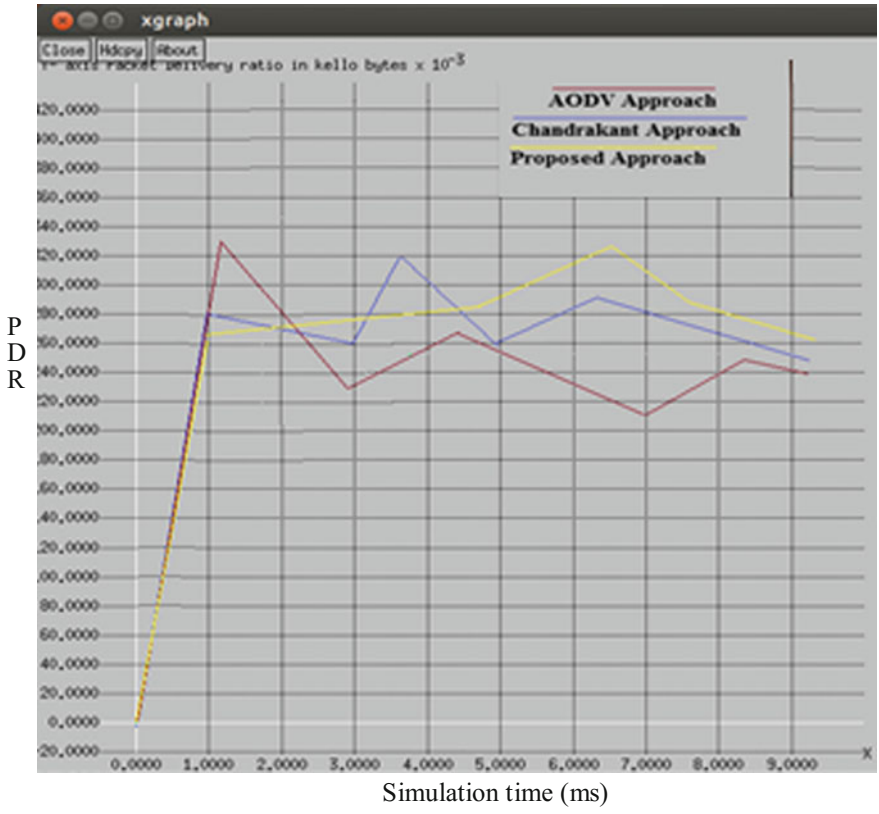

Fig. 3 Packet delivery ratio versus simulation time

pairs are far from each other, there will be more chances that maximum black holes can enter the network. However, the presented approach generates more packet delivery ratio when compared with the other two methods. This indicates that our approach does not allow black hole into the network.

Initially, the PDR of Chandrakant approach is higher than our approach, the reason behind this is that initially less number of black holes will interact within the network with the same energy, so cannot be allowed to take part in the network. Thus have more packet delivery ratio (PDR) in comparison with our approach. However during elapse of time more number of black holes will come with different energies and interact within the network, so black hole cannot be judged by Chandrakant approach, so black holes can easily enter within the network and disgrace the routine and change the behavior of the network. However, the presented method still shows higher packet delivery ratio than other two approaches, so energy may not always be a constraint to identify the black hole.

6 Conclusion

In this paper, we describe a novel approach called *Enhance Security to MANETs against Black hole Attack using modified CR Technique.* We also create different security code word at every intermediate node till destination node using bit shifting technique. This bit change gives more authentications to the node, so black hole can be easily detected at each and every hop. We compare our approach with AODV and Chanderkanth approach using network simulator (NS2) to validate our approach.

References

1. Jøsang A, Ismail R, Boyd C (2007) A survey of trust and reputation systems for online service provision. Decis Support Syst 43(2):618–644
2. Hu Y-C, Perrig A, Johnson DB (2002) Ariadne: a secure on demand routing protocol for ad hoc networks. In: Proceedings of international conference on mobile computing and networking. Atlanta, USA, pp 12–23
3. Papadimitratos P, Haas ZJ (2002) Secure routing for mobile ad hoc networks. In: Proceedings of SCS communication networks and distributed systems modeling and simulation conference. USA
4. Buttyan L, Hubaux J (2001) Nuglets: a virtual currency to stimulate cooperation in self-organized ad hoc networks. Swiss Federal Institute of Technology, Lausanne DSC/2001/001
5. Zhong S, Chen J, Yang YR (2003) Sprite: a simple, cheat-proof, credit-based system for mobile ad-hoc networks. INFOCOM 2003:1987–1997
6. Liu Y, Yang YR (2003) Reputation propagation and agreement in mobile ad-hoc networks. In: Proceedings of IEEE wireless communications and networking (WCNC 2003). New Orleans, USA, pp 1510–1515

7. Lindsay SY, Wei Y, Zhu H, Liu KJR (2006) Information theoretic framework of trust modeling and evaluation for ad hoc networks. IEEE J Sel Areas Commun 24(2):305–317
8. Zhou L, Haas ZJ (1999) Securing Ad hoc networks. IEEE Network 13(6):24–30
9. Luo H, Zerfos P, Kong J, Lu S, Zhang L (2002) Self-securing ad hoc wireless networks. IEEE ISCC 2002, IEEE Computer Society Washington, DC, USA ©2002, Jul 01 2002, p. 567. ISBN: 0-7695-1671-8
10. Chan AC-E (2004) Distributed symmetric key management for mobile ad hoc networks. INFOCOM 2004, China, pp 2414–2424
11. Balakrishnan V, Varadharajan V, Tupakula UK, Lucs P (2007) Trust integrated cooperation architecture for mobile ad-hoc networks. In: Proceedings of 4th IEEE international symposium on wireless communication systems (ISWCS 2007). Trondheim, Norway
12. Aarti, Dr Tyagi SS (2013) A Study of MANET: characteristics, challenges, application and security attacks. Int J advance Res Comput Sci Software Eng 3(5). May 2013
13. Wadbude D, Richariya V (2012) An efficient secure AODV routing protocol in MANET. Int J Eng Innovative Technol (IJEIT) 1(4):274–279
14. Sun B, Yu B (2009) The three-layered group key management architecture for MANET. In: Proceedings of 11th international conference advanced communication technology, vol 2. pp, 1378–1381
15. Mamatha GS, Sharma SC (2010) A highly secured approach against attacks in MANETS. Int J Comput Theory Eng 2:815–819
16. Elizabeth NE, Subsree S, Radha S (2014) Enhanced security key management scheme for MANETS. WSEAS Trans on Commun 13:15–25
17. Michiardi P, Molva R (2002) Core: A collaborative reputation mechanism to enforce node cooperation in mobile Adhoc networks. In: Proceedings of 6th IFIP communications and multimedia security conference. Portorosz, Slovenia, pp 107–121
18. Rana S, Sing M (2011) Performance analysis of malicious node aware routing for MANET using two hop authentication. Int J Comput Appl 25(3):17–24
19. Hu Y-C, Perrig A, Johnson DB (2005) Ariadne: a secure on-demand routing protocol for ad hoc networks. Wireless Netw 11(1):21–38
20. Chandrakant N (2013) Self-protecting nodes for secured data transmission in energy efficient MANETs. Int J Adv Res Comput Sci Softw Eng (3)6:673–675
21. Singh M, Sharma A (2015) Security issues in MANET. Int J Adv Res Comput Sci Softw Eng 5(8):471–473
22. Deshmukh sagar R, PN Chatur, Nikhil B Bhople (2016) AODV based secure routing against black hole in MANETs. In: IEEE International conference on recent trends in electronics information communication technology, May 2016, pp 1960–1964

Modified Phase Sequence in Hybrid Pts Scheme for PAPR Reduction in OFDM Systems

Kakara Satyavathi and B. Rama Rao

Abstract It is well known fact that high PAPR value degrades the performance of OFDM system. In this paper, PTS (Partial transmit sequence) based approach is opted for the reduction of PAPR and three major contributions are made to the traditional PTS scheme. First, the phase sequence that is to be multiplied is changed, second the system is extended with hybrid mechanism of SLM (selective mapping) and PTS scheme in which additional hybrid scheme is opted. Third the benefits of DHT (Discrete Hartley transform) are incorporated with this system. It is found from the experimental results that the proposed MSD (modified sequence DHT) based system able to decreases the PAPR at a considerate factor and also able to preserve the OBI (out of band interference).

Keywords OFDM · PAPR · Hybrid scheme · DHT

1 Introduction

OFDM scheme is very popular for high data rate transmission as it can cope with frequency selective channels [1, 2]. But is suffers from a large PAPR value due to the superposition of subcarriers in time domain. It mainly arises due to the inequalities of peak power in each sub carrier for few it very low and for few it many very high, this substantially increases the average power. This high PAPR value reduces the OFDM system efficiency and thereby increasing the cost of installing high RF amplifiers which in turn again leads to nonlinear characteristics.

To overcome this issue many researchers have proposed different algorithms to reduce the PAPR, few of them which related to our research work are stated in this

K. Satyavathi
Department of ECE, Malla Reddy Institute of Engineering & Technology, Hyderabad, India

B. Rama Rao (✉)
Department of ECE, Aitam, Tekkali, India
e-mail: Rao-bagadam.abrahamdavid@gmail.com

H. S. Saini et al. (eds.), *Innovations in Electronics and Communication Engineering*, Lecture Notes in Networks and Systems 33,
https://doi.org/10.1007/978-981-10-8204-7_33

paper. Selective mapping technique which is frequency domain [3], Partial transmit sequence which is in time domain [4] are the most prominent methods to achieve low PAPR. The conventional PTS scheme could reduce the PAPR to a larger extent but the complexity of it increases with the increase in sub-blocks, so in [5] a dummy signal insertion (DSI) concept was introduced to reduce the complexity while retaining the lower PAPR; however this concept degraded the spectrum efficiency. In [6] a hybrid scheme was introduced in which the side information is the sum of SLM and PTS parts and the computational complexity also less than the conventional PTS scheme. In [7], proposed a hybrid scheme integrating it with dummy signal insertion and achieved a considerable decrease in PAPR with low complexity.

This work focus on hybrid scheme of PAPR reduction with a new set of phase sequences and DHT coding, the new sequence reduces the complexity by decreasing the number of IFFTs this may result in slight degradation of PAPR which is further achieved with the use of DHT coding. This paper is organized as follows; section explains the need and necessity of the work. Section 2, presents all the related previous work done so far and the methods that were included with the current work. Section 3 presents the proposed methodology and its results are presented in Sect. 4.

2 Related Work

2.1 Papr

In OFDM the information carriers are divided into N sub carriers which are sent through L-sub channels with lower data rates. These sub channels are orthogonal to each other allowing them to overlap without interference however reducing the data rate at these sub-channels retains a lower ISI with in the occupied bandwidth fulfilling the objective of the system. But when these sub-channels are added together in time domain high PAPR occurs due to the inequalities in the amplitude of sub carriers. Mathematically it can be represented as

PAPR = Peak power/Average Power

$$x(t) = \frac{1}{\sqrt{N}} \sum_{n=0}^{N-1} X_n e^{j2\pi n \Delta f t} \quad 0 \le t \le NT, \tag{1}$$

where 'N' the no. of sub carriers and Δf is sub carrier spacing, then

$$\text{PAPR} = \frac{\max(|x(t)|^2)}{\frac{1}{NT} \int_0^{NT} |x(t)|^2 \mathrm{d}t} \tag{2}$$

To evaluate the reduction in PAPR value the complementary cumulative distributive function (CCDF) is used which shows the probability that the system exceeds than a certain PAPR value [8]. The CCDF is calculated using the following formula [9]:

$$P(\text{PAPR} > Z) = 1 - (1 - \exp(z))^N, \tag{3}$$

where N = no. of sub carriers

2.2 Hybrid Scheme

This scheme uses the advantages of both SLM and PTS schemes, this was initially proposed Pushkarev et al. in [6]. The scheme is illustrated in Fig. 1, in this the original OFDM symbols are multiplied with 'U' phase rotation sequences and then each of the OFDM symbols is partitioned into V disjoint sub-blocks. These sub-blocks are selected based on optimization with PTS scheme. This can be written as

$$\left\{ b_1^{\widehat{(u)}}, b_2^{(u)} \right\} = \text{argmin} \left\{ \sum_{v=1}^{2} b_v^{(u)} X_v^{(u)}, \right. \tag{4}$$

where $1 \leq u \leq U$ and $V = 2$

Obtain the block which has retained a lower PAPR by using PTS optimization. Lower PAPR from PTS block is statistically independent with each other.

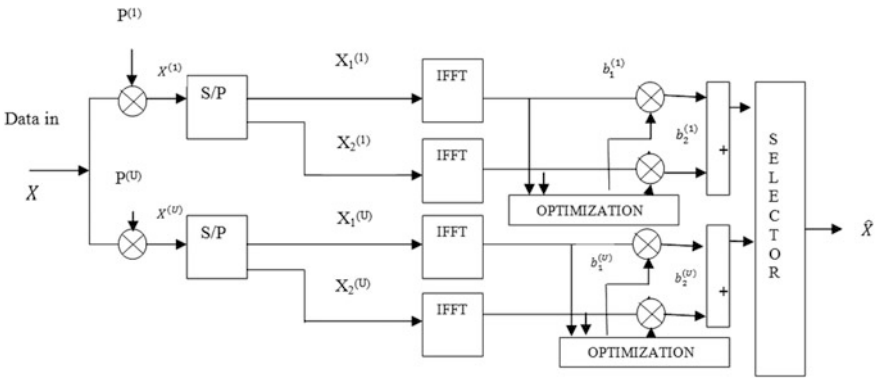

Fig. 1 Conventional hybrid scheme

2.3 New Phase Sequence

This concept is introduced here to reduce the complexity of the system, the new phase sequence is based on generation of '*N*' random values from the phase factors of {1, −1} when $W = 2$. So the total phase sequences will be *NV* where '*N*' is number of subcarriers and *V* disjoint sub blocks. In conventional PTS we require eight iterations to find the optimal phase sequence when $W = 2$ and $V = 4$ but in this case it may be N^8 which is practically impossible. So the same numbers of iterations were applied as it is in the case of C-PTS but with new phase sequences [10].

2.4 DHT Coding

This work is hybrid as it not only involves SLM and PTS but also incorporates the Discrete Hartley transform (DHT) which has the asymmetrical clipping property [11]. The N-point inverse DHT and DHT are represented as

$$X_n = \frac{1}{\sqrt{N}} \sum_{k=0}^{N-1} X_k \mathrm{cas}\left(\frac{2\pi kn}{N}\right) \tag{5}$$

$$X_k = \frac{1}{\sqrt{N}} \sum_{n=0}^{N-1} X_n \mathrm{cas}\left(\frac{2\pi kn}{N}\right), \tag{6}$$

where cas = cos(:) + sin(:) and n & k from 0 to N − 1.

From [11] it can concluded that the output of N-point DHT can be written as

$$Y_i = \begin{cases} \frac{1}{\sqrt{2}}\left[X_i \cos\left(\frac{\pi i}{L}\right) + X_{L-i} \sin\left(\frac{\pi i}{L}\right)\right] & 0 \le i \le L-1 \\ \frac{1}{\sqrt{2}}\left[X_{i-L} \cos\left(\frac{\pi i}{L}\right) + X_{2L-i} \sin\left(\frac{\pi i}{L}\right)\right] & L \le i \le 2L-1 \end{cases} \tag{7}$$

Here *Y* has anti symmetrical property so that the negative samples of '*Y*' can be treated as zeros without loss of information [12].

3 Proposed Work

The proposed approach is depicted in Fig. 2,

The data symbols are divided into disjoint blocks, each block symbols are applied with inverse DHT. And thus obtained symbols are multiplied with new phase sequences. An optimal block is selected based on PTS minimal PAPR scheme and thus forms an optimal candidate signal.

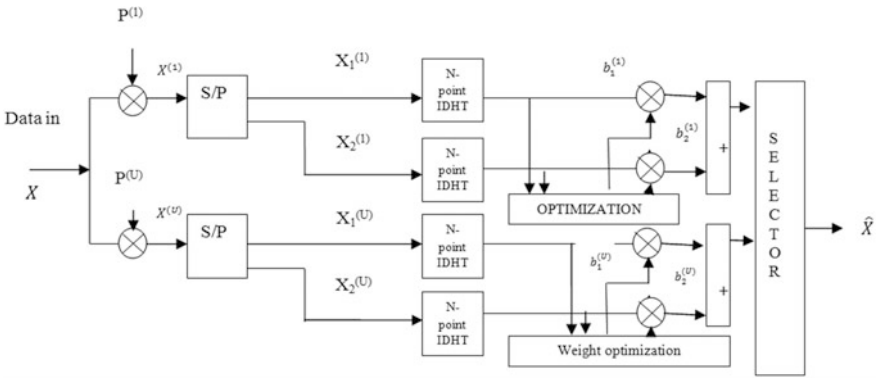

Fig. 2 Proposed approach block diagram

4 Experimental Results

In order to evaluate the performance of the system the proposed approach is implemented and compared against conventional Hybrid scheme and with DHT based clipping scheme. The result of PAPR analysis is shown in Fig. 3. It can be observed from the graph that the proposed approach is achieving low PAPR of 8 dB at 0.001 units of CCDF which 0.8–1 dB improvement with respect the traditional approaches. Figure 4 shows the power spectral density response of the

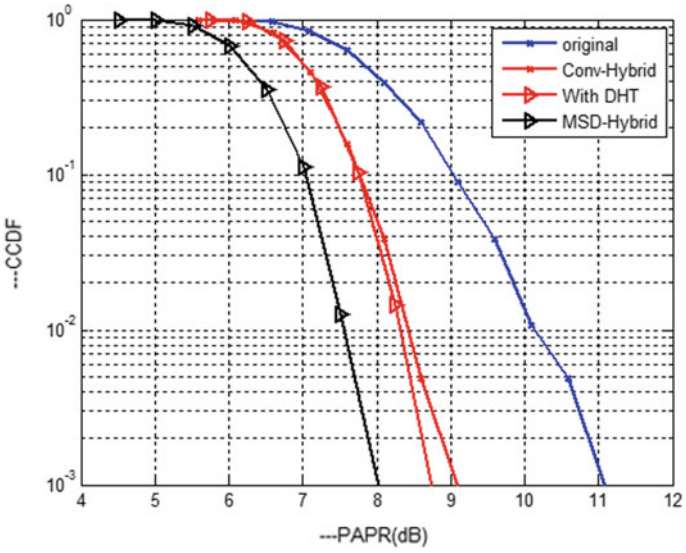

Fig. 3 PAPR analysis with $U = 6$, no. of symbols = 1024, no. of subcarriers = 128

proposed approach, it is clearly observed that the bandwidth can be used efficiently and reduces the OBI by 6–8 dB. This plays a important role when the data is of higher rate and more number of sub carriers (Fig. 5).

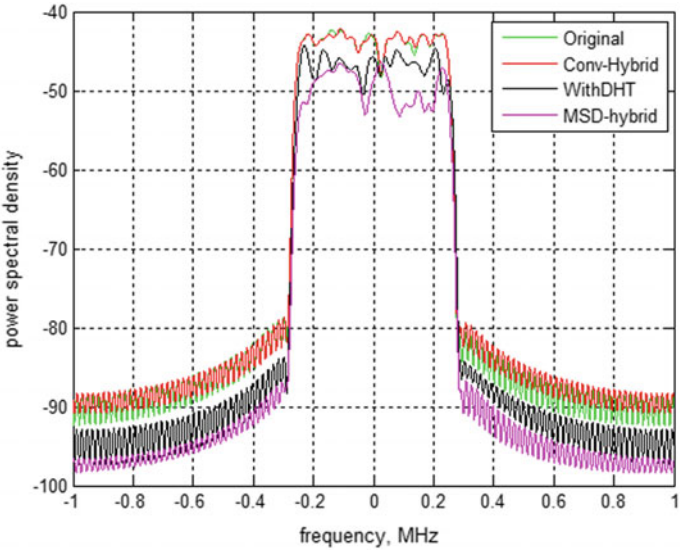

Fig. 4 PSD analysis with $U = 6$, no. of Symbols = 1024, no. of subcarriers = 128

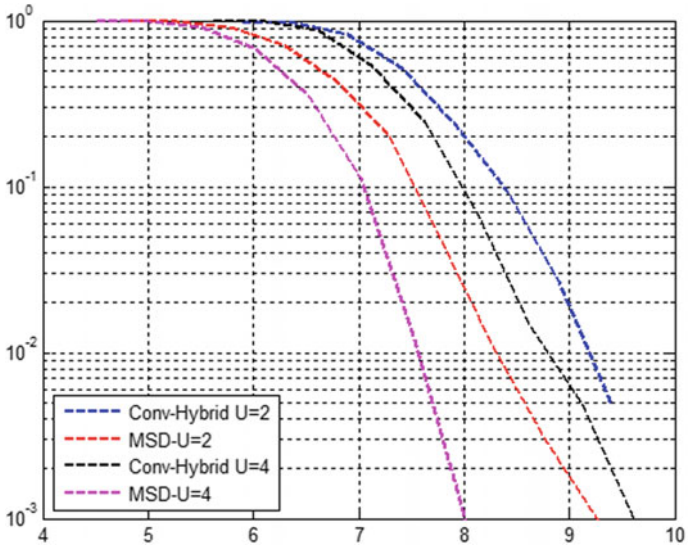

Fig. 5 PAPR analysis with $U = 2, 4$ for proposed and conventional hybrid approaches

5 Conclusion

A modified hybrid with DHT is proposed in this paper aims to attain a lower PAPR while preserving the concept of hybrid scheme. The proposed approach has gained a lower PAPR of 0.8–1 dB and it shows appropriate response at $U = 4$. Though the complexity issue is discussed in this paper it preserves the complexity issue and attains very good response at the same iterations of C-PTS. This work can be further extended by incorporating this scheme at both transmitter and receiver and evaluate the performance of the proposed approach under different channeling environments.

References

1. Hwang T, Yang C, Wu G, Li S, Li GY (2009) OFDM and its wireless applications: a survey. IEEE Trans Veh Technol 58(4):1673–1694
2. Chou HJ, Lin PY, Lin JS (2012) PAPR reduction techniques with hybrid SLM-PTS schemes for OFDM systems. In: 2012 IEEE 75th vehicular technology conference (VTC Spring). Yokohama, pp 1–5
3. Buml R, Fischer R, Huber J (1996) Reducing the peak to average power ratio of multicarrier modulation by selected mapping. Elect Lett 32(22):2056–2057
4. Yang L, Chen RS, Siu YM, Soo KK (2006) PAPR reduction of an OFDM signal by use of PTS with low computational complexity. IEEE Trans Broadcast 52(1):83–86
5. Varahram P, Azzo WA, Ali BM (2010) A low complexity partial transmit sequence scheme by use of dummy signals for PAPR reduction in OFDM systems. IEEE Trans Consumer Electron 56(4):2416–2420
6. Pushkarev PA, Ryu K-W, Yoo K-Y, Park Y-W (2003) A study on the PAR reduction by hybrid algorithm based on the PTS and SLM techniques. In: Proceedings of the 57th IEEE vehicular technology conference, vol 2. pp 1263–1267
7. Sravanti T, Vasantha N (2014) A combined PTS & SLM approach with dummy signal insertion for PAPR reduction in OFDM systems. In: International conference on computing and communication technologies. Hyderabad, pp 1–5
8. Han SH, Lee JH (2005) An overview of peak-to-average power ratio reduction techniques for multicarrier transmission. Wireless Commun IEEE 12(2):56–65
9. Müller SH, Huber JB (1997) A comparison of peak power reduction schemes for OFDM. In: Proceedings of IEEE GLOBECOM '97. Phoenix, AZ, pp 1–5
10. Varahram P, Ali BM (2011) Partial transmit sequence scheme with new phase sequence for PAPR reduction in OFDM systems. IEEE Trans Consum Electron 57(2):366–371
11. Zhou J, Qiao Y (2015) Low-PAPR asymmetrically clipped optical OFDM for intensity-modulation/direct-detection systems. IEEE Photonics J 7(3):1–8
12. Armstrong J, Lowery AJ (2006) Power efficient optical OFDM. Electron Letters 42(6): 370–372

Topology Control in Wireless Sensor Networks: A Survey

Ranjan Kumar Mahapatra and N. S. V. Shet

Abstract Topology control is found to be a prominent strategy, to prolong the lifetime of WSNs. It helps to control the power consumption of the sensor nodes. In this paper, topology construction and topology maintenance are taken into account as a part of review of topology control. Topology construction algorithms encompass to frame the reduced form of topology. Topology maintenance helps in providing a reduced topology intermittently, as soon as the current topology becomes no longer optimum. Simulation results demonstrate that sensor node battery lifetime can be prolonged by the appropriate use of topology control.

Keywords Wireless sensor networks (WSNs) · Topology control
Topology construction (TC) · Topology maintenance (TM) · Energy
Lifetime

1 Introduction

Wireless Sensor Networks [1] is now of intensive interest in several applications due to lightweight, cheap and can be communicated via wireless technologies. At the same time, among so many existing constraints (computational limitation, energy resources, etc.), limitation in battery lifetime of the sensor is one of them. Here ultimate goal for topology control is, to have reduced number of active nodes as well as active links so as to preserve those resources for future use. Topology control [2, 3] is generally defined as the technique of controlling the transmission power of the sensor nodes, without altering the network characteristics such as connectivity as well as coverage. Here maintenance [4] of the network topology

R. K. Mahapatra (✉) · N. S. V. Shet
Department of Electronics and Communication Engineering,
NITK, Surathkal 575025, India
e-mail: mahapatra.ranjankumar@gmail.com

N. S. V. Shet
e-mail: shet@nitk.ac.in

H. S. Saini et al. (eds.), *Innovations in Electronics and Communication Engineering*,
Lecture Notes in Networks and Systems 33,
https://doi.org/10.1007/978-981-10-8204-7_34

should be included so as to conserve energy even after a long time of network deployment. Hence basic operation in wireless sensor network is topology control which describes how efficiently wireless sensing field is monitored. It also explains about the mutual connection that exists between two sensing nodes. The remainder of the paper is arranged as follows: Sect. 2 explains about the taxonomy of topology control in brief. Section 3 explains the simulation work and results obtained and finally conclusions were drawn in Sect. 4.

2 Taxonomy of Topology Control

Figure 1 shows the general taxonomy of topology control.

2.1 Topology construction (TC)

It is the technique to build the reduced topology, i.e. the initial reduction of the sensor network topology. Once the initial topology is carried out and the nodes are located at random places, the administrator normally does not possess any control over the design of the deployed network. In general, the number of redundant nodes is more over a dense area:

- Which in turn increases the number of message collisions.
- Multiple copies of the required information are generated.

Modifying the above parameters, topology of the network can be controlled. In this paper, we have put emphasis on one of the transmission range based algorithm (i.e. KNeigh algorithm for simulation purpose) and one hierarchical-based protocol (cluster based LEACH). Simulation work shows that reduction in no of active nodes helps in preserving battery life.

2.1.1 LEACH protocol

Clustering is a process, where one node is chosen to act as a cluster for several neighbour sensor nodes. Maximum lifetime can be attained by the introduction of level of hierarchy based on the application requirement. LEACH protocol [5, 6] is

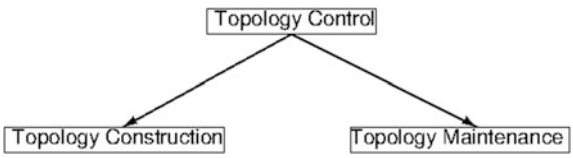

Fig. 1 Taxonomy of topology

one of them to solve the issues of limited lifetime and energy of the sensor nodes efficiently. LEACH protocol was presented by Heinzelman [7] in 2000. Here threshold distance of transmission be

$p_0 = \sqrt{\frac{E_{fs}}{E_{amp}}}$ is considered.

The energy consumption model for the radio transmitter is shown in Fig. 2.

$(E_{Tx}(L,p))$ and $(E_{Rx}(L))$ separated by the distance p to send L bit message is given by;

$$(E_{Tx}(L,p)) = \begin{cases} LE_{\text{elec}} + LE_{\text{fs}}p^2, & \text{if } p \le p_0 \\ LE_{\text{elec}} + LE_{\text{amp}}p^4, & \text{if } p \ge p_0 \end{cases} \quad (1)$$

$$(E_{Rx}(L)) = LE_{\text{elec}}, \quad (2)$$

where $E_{\text{elec}} \rightarrow$ Consumption of energy per bit, $E_{fs} \rightarrow$ the free space power loss, $E_{\text{amp}} \rightarrow$ the multipath power loss with acceptable bit error rate.

Idea: Sensor nodes can take the decision independently in the deployed sensor field whether to become a cluster head with a certain probabilities. Also it can elect cluster head periodically, which will lead to the prolonged network lifetime with reduced amount of spent energy.

Threshold value is given as:

$$T(n) = \begin{cases} \dfrac{n}{1 - s \times \left[r \times \text{mod}\,\frac{1}{s}\right]} & \text{if n } \epsilon \text{ H,} \\ =0; \text{ otherwise} \end{cases} \quad (3)$$

where s $\rightarrow$ desired percentage of the Cluster Head (CH), r $\rightarrow$ current round, H $\rightarrow$ set of nodes that have not become CH in the previous round.

LEACH operation comprise of rounds and each round starts with a set-up phase (organization of clusters) followed by a steady-state phase (data-transfer). Here overhead is minimized.

- Advertisement Phase [8, 7].
- Cluster Set-up Phase.
- Steady-state Phase.

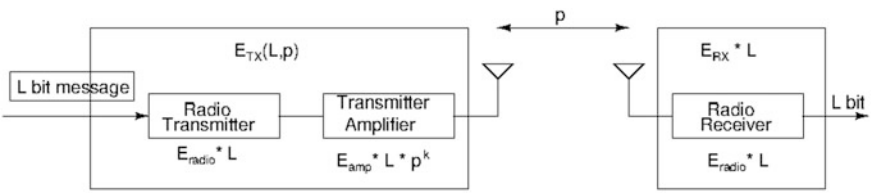

Fig. 2 Radio energy dissipation model

Performance evaluation of LEACH

Evaluation of routing protocols can be done in several ways. There is no such specific standard which exists. Numbers of rounds became the key parameter of the network lifetime when the first dead node appears. The time at which sensor nodes activity starts until the first dead sensor node appears, is generally termed as working time of the network. Here in this model, random distribution of 100 nodes in the area 200 $\times$ 200 m^2 has been deployed. Figure 3 shows the network lifetime for leach protocol after 3500 rounds. Simulation was performed using MATLAB R2012a.

Until the first dead sensor nodes appears in the network, no of rounds were counted. So the number of rounds becomes the key parameter for the sensor node network lifetime.

2.1.2 KNeigh Protocol

Here in our study, we assume that every node is associated with its K closest neighbours in the network.

In the paper [9], the KNeigh protocol [10, 11] was a distributed implementation for the computation of symmetric K-neighbour subgraph GK—based on the technique of distance estimation (RSSI [12], ToA [13]).

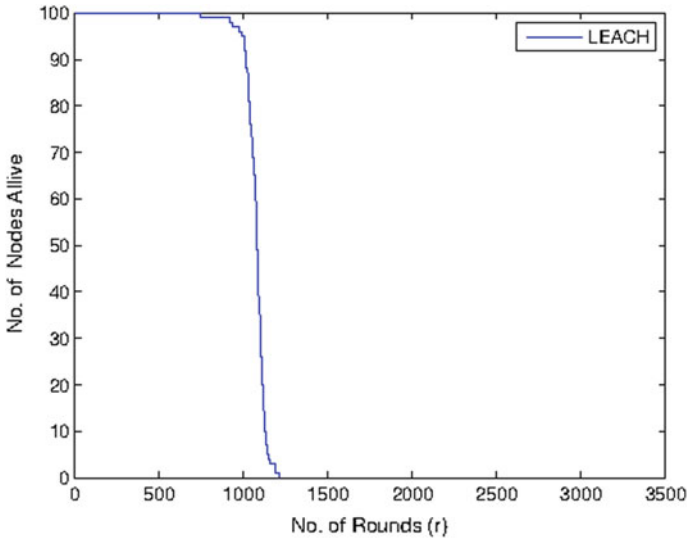

Fig. 3 Lifetime

Following are some of the features of KNeigh protocol

- Static nodes were used.
- All the nodes possess same maximum Tx power.
- It is simple and distance information between nodes are used.
- Network connectivity for the worst case is not guaranteed.

2.2 *Topology Maintenance (TM):*

From time to time, TM switches the reduced topology, when the existing current topology is not the optimum one. It is normally the iterative procedure of constructing, restoring and switching to new reduced topology until there is no more reduced topology. Sub-division of topology maintenance is shown in Fig. 4.

Static TM: This technique is normally pre-planned. Calculation of all the different topologies are done during the 1st topology is constructed. After all the topologies are built, they are stored in the memory for the future switching purpose as and when necessary. Some of the drawback of static TM is listed below

- Static TM takes additional time during the topology construction phase.
- It is very difficult to know a priori that, how much energy will be consumed by the topologies and their sensor nodes.

Dynamic Topology: This maintenance calculates a new reduced topology on demand, i.e. generates the TC mechanism as and when necessary.

- To trigger a reduced topology, dynamic TM mostly have, more as well as better information regarding the network (advantage).
- This technique consumes additional resources as many times they run (disadvantage). Hence both TC and TM must be energy efficient.

Hybrid TM: It utilizes static TM approach first by calculating all different reduced topologies at TC phase.

- If the sink possesses no connectivity, then hybrid TM utilizes dynamic TM by triggering new reduced topology on demand.

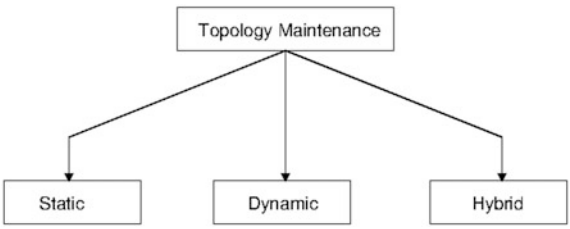

Fig. 4 Sub-division of TM

2.2.1 Topology Maintenance Algorithm

Classification of TM algorithm is shown in Fig. 5.

- DGTRec: This algorithm wakes up all the nodes which are inactive. Here existing reduced topology will be reset. Then a TC protocol is applied.
- Hence dynamically topology is reset. As shown in Fig. 6, consider that node P sends a packet to node R, which is at distance d. Here we have assumed that node R falls within the transmission range of node P at maximum power. Hence direct radio communication between nodes P and R is feasible. There is another node Q within the region K circumscribed by the circle having diameter d which intersects both P and R.

Here $d1 < d$ and $d2 < d$, so it is possible to send a packet from node P to node R via node Q as a relay

If we consider the signal is propagating from node P to node R in accordance with the free space model. Here $P_{PRdirect} \propto d^2$ and $P_{PQR} \propto \{d_1^2 + d_2^2\}$.

From the triangle PQR, Φ is the angle opposite to PR. So by the geometry we derive

$$d^2 = d_1^2 + d_2^2 + 2d_1 d_2 \cos \Phi \tag{4}$$

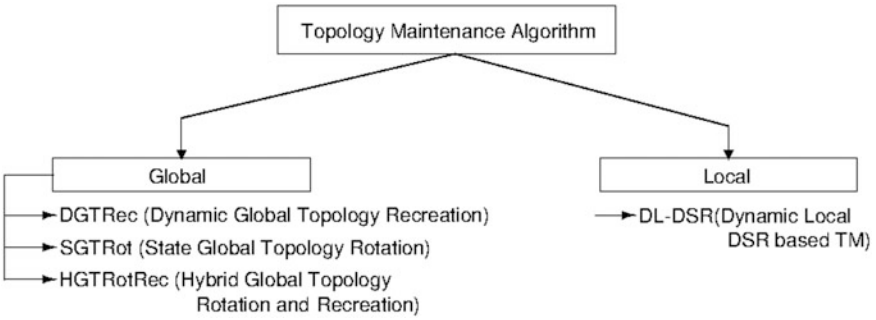

Fig. 5 Classification of TM algorithm

Fig. 6 Multihop communication for reduced energy

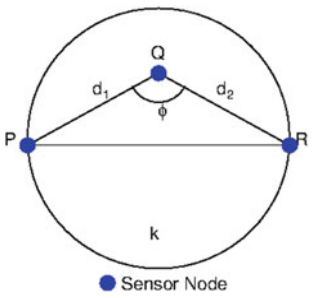

$$\text{As Q } \varepsilon \text{ K } \Rightarrow \cos \Phi < 0$$

$$\Rightarrow d^2 = d_1^2 + d_2^2 \tag{5}$$

Hence short, multi-hop path between sender and receiver is always desirable for radio communication, instead of long, energy-inefficient edges in regard with energy point of view.

3 Simulation and Results

The purpose of this experiment is to obtain the benefit of topology control by the implementation of topology control as well as topology maintenance. Here simulation is performed by the help of I.H.U. VLabs. While evaluating the performance, we had the assumption

- Architecture for sensor network used was 2D.
- Deployed sensor nodes have no information about their own location as well as about neighbours and there is no packet loss.

Parameters used for our simulations purpose is shown in Table 1.
Figure 7 shows the deployment of the 100 nodes.
Area of communication/sensing can be found in Fig. 8.
While simulating, link connectivity between nodes is shown in Fig. 9.
After simulation is over, the reduced topology with less number of active nodes is shown in Fig. 10.

Table 1 Parameter details

Parameters	Values
Deployment area	600 × 600 m
No of nodes	100
No of sinks	1
Sensing radius	20 m
Bit error rate	0
Node energy distribution	Constant and 100 mJ max
TC protocol	kNeigh Tree
K	6
TM protocol	DGETRec
Sensing and data protocols	Simple S and D
Data forwarding protocol	Simple forwarding
Node mobility	Simple random walk

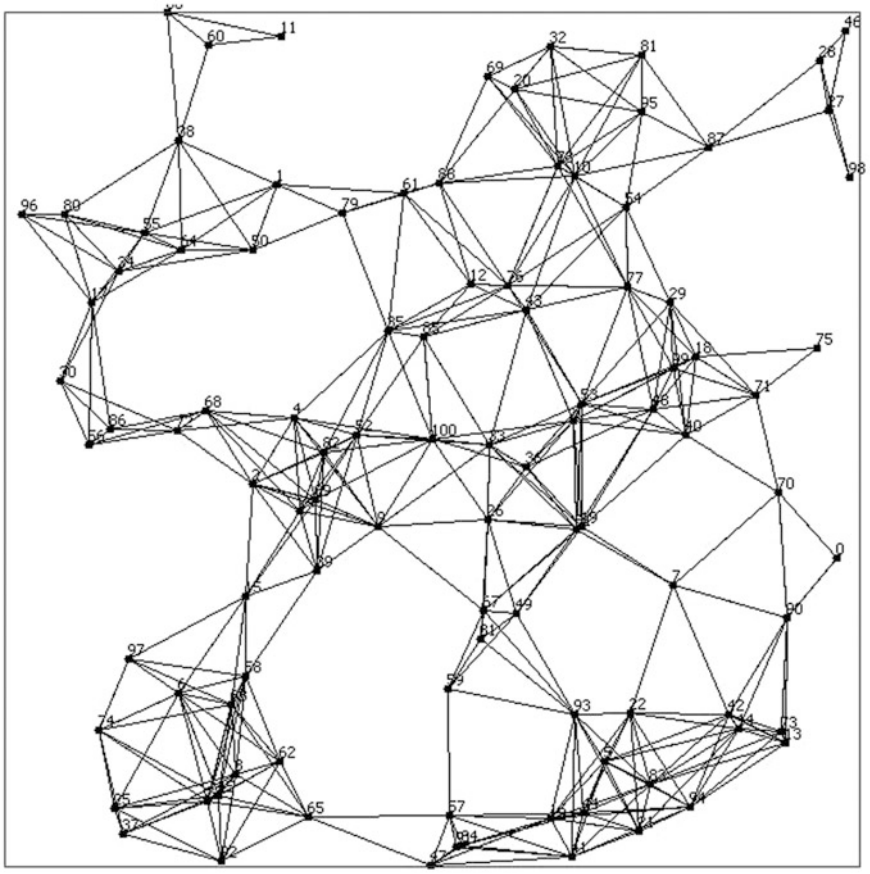

Fig. 7 Node deployment

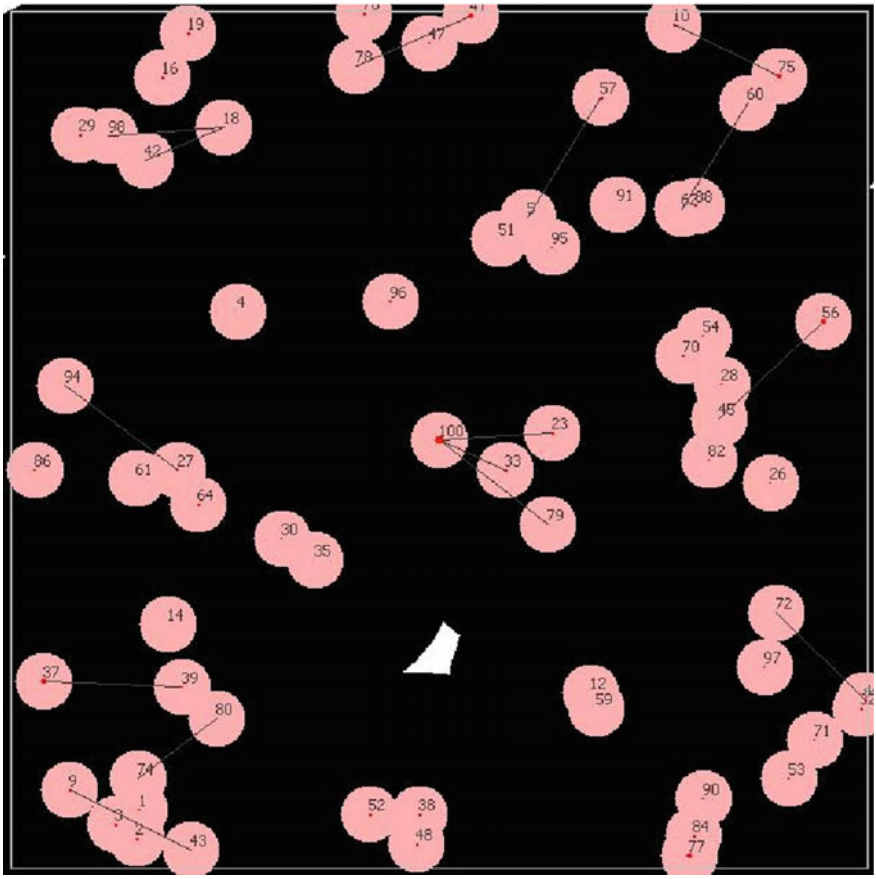

Fig. 8 Node topology with filled area

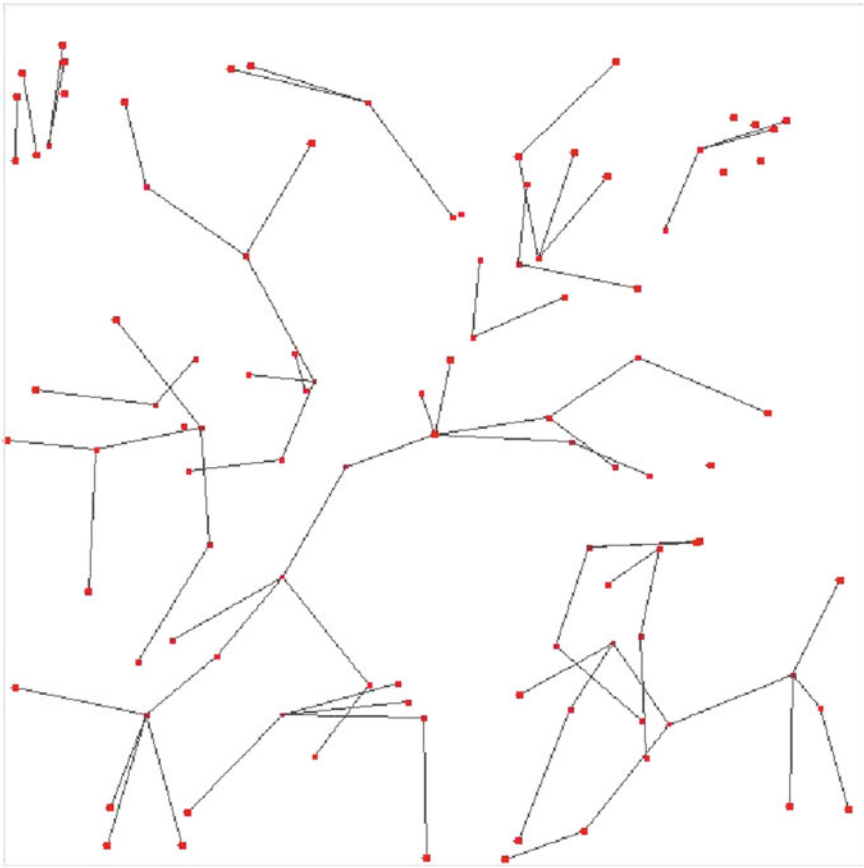

Fig. 9 Node topology with connectivity

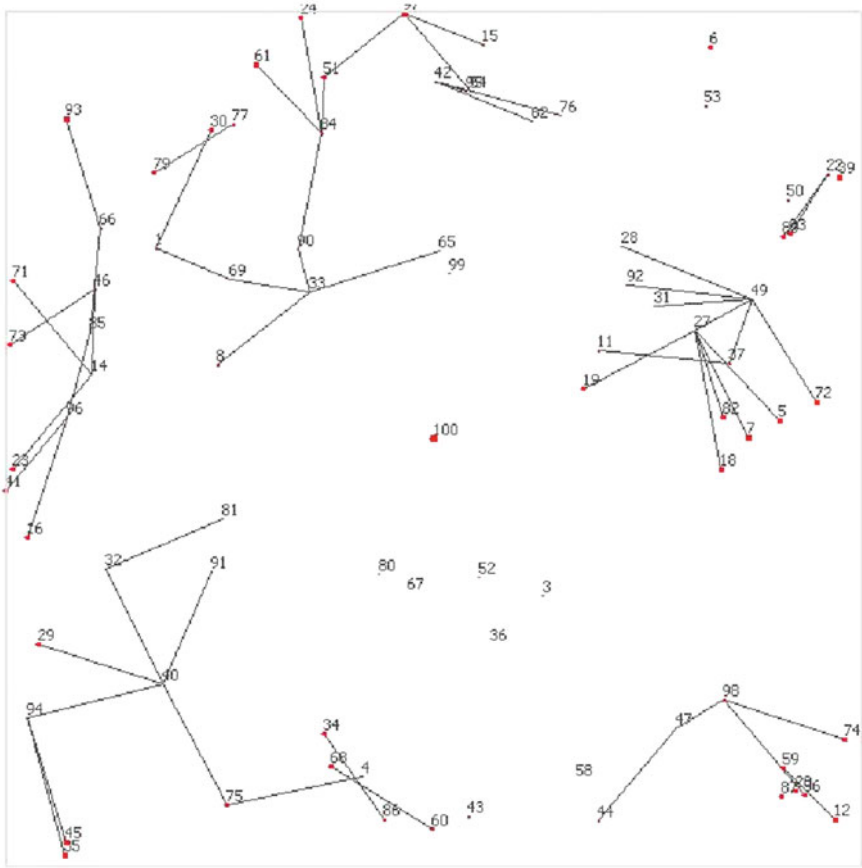

Fig. 10 Reduced node topology with less active node

4 Conclusion

In this paper, a brief survey was conducted on topology control in wireless sensor networks. Detailed taxonomy of topology control is studied and some of the protocols were used for simulation works. This survey allowed us to understand the need for topology control, to have a better network lifetime with conservation of energy. An important conclusion is that, we can achieve better network lifetime if we reduce network topology.

References

1. Dargie W, Poellabauer C (2010) Fundamentals of wireless sensor networks: theory and Practice. John Wiley & Sons, Hoboken
2. Santi P (2005) Topology control in wireless ad hoc and sensor networks. John Wiley & Sons, Hoboken
3. Santi P (2005) Topology control in wireless ad hoc and sensor networks. ACM computing surveys (CSUR) 37(2):164–194
4. Chen B, Jamieson K, Balakrishnan H, Morris R (2002) Span: an energy-efficient coordination algorithm for topology maintenance in ad hoc wireless networks. Wireless Netw 8(5): 481–494
5. Cui X (2007) Research and improvement of leach protocol in wireless sensor networks. In Microwave, antenna, propagation and EMC technologies for wireless communications, 2007 international symposium on. IEEE, pp 16–17
6. Heinzelman WB, Chandrakasan AP, Balakrishnan H (2002) An application-specific protocol architecture for wireless microsensor networks. IEEE Trans Wireless Commun 1(4):660–670
7. Heinzelman WR, Chandrakasan A, Balakrishnan H (2000) Energy-efficient communication protocol for wireless microsensor networks. In: System Sciences, 2000. Proceedings of the 33rd Annual Hawaii international conference on. IEEE, p 10
8. Murthy CSR, Manoj B (2004) Ad hoc wireless networks: architectures and protocols. Pearson education, London
9. Blough DM, Leoncini M, Resta G, Santi P (2003) The k-neigh protocol for symmetric topology control in ad hoc networks. In: Proceedings of the 4th ACM international symposium on Mobile ad hoc networking & computing. ACM, pp 141–152
10. Huang Z, Shen C-C, Srisathapornphat C, Jaikaeo C (2002) Topology control for ad hoc networks with directional antennas. In: Computer communications and networks, 2002. Proceedings eleventh international conference on. IEEE, pp 16–21
11. Borbash SA, Jennings EH (2002) Distributed topology control algorithm for multihop wireless networks. In Proc. 2002 World Congress on Computational Intelligence (WCCI 2002). Citeseer, pp 355–360
12. Savvides A, Han C-C, Strivastava MB (2001) Dynamic finegrained localization in ad-hoc networks of sensors. In: Proceedings of the 7th annual international conference on Mobile computing and networking. ACM, pp 166–179
13. Caffery JJ Jr (2000) A new approach to the geometry of toa location. In: Vehicular technology conference, 2000. IEEE-VTS Fall VTC 2000. 52nd, vol 4. IEEE, pp 1943–1949

Performance Analysis of Smart Grid Communication Network Architecture for WAMS

S. Premkumar, M. Susithra and V. Saminadan

Abstract In recent years, wide area monitoring systems' (WAMS) communication infrastructure plays a crucial role in the transformation to smart grid for real-time delivery of data with low latency. The advancement of WAMS has to be meticulously designed by optimizing the power systems and communication infrastructure. The performance of the communication infrastructure relies on the optimal placement of phasor measurement units (PMUs) in the power system. In the modified IEEE 14 bus system the optimal PMU placement and its backbone communication network has been designed and analyzed. With optimum number of PMUs for complete observability and minimal distance between PMUs and control centers effective monitoring is achieved for the stable operation of the grid. The minimal path between the PMUs to the control centers were obtained by Dijkstra algorithm. Finally using opnet the communication network has been analyzed using different routing protocols. The simulation results are analyzed and it shows that Multiprotocol Label Switching (MPLS) based PMU data transfer provides better performance.

Keywords Wide area monitoring system · Phasor measurement unit
Control center bus · Multiprotocol label switching

S. Premkumar (✉) · M. Susithra · V. Saminadan
Pondicherry Engineering College, Pillaichavady, Puducherry, India
e-mail: erprems@gmail.com

M. Susithra
e-mail: ersusithra@gmail.com

V. Saminadan
e-mail: saminadan@pec.edu

H. S. Saini et al. (eds.), *Innovations in Electronics and Communication Engineering*,
Lecture Notes in Networks and Systems 33,
https://doi.org/10.1007/978-981-10-8204-7_35

1 Introduction

Power failures are very frequent in most of the countries due to the dynamic behavior of electricity consumption and maintenance. To prevent blackouts, implementation of intelligent devices such as PMUs are very essential in the transmission network for reliable power delivery. Through current transformers and power transformers the PMU receives the voltage and current waveforms respectively and the signals are isolated, filtered, and sampled. Using these phasor data, real time and postmortem analysis can be performed to analyze abnormal events. The WAMS communication infrastructure provides dynamic stability of the overhead transmission networks with the placement of PMUs.

WAMS have several technical advantages compare to the Traditional Supervisory Control And Data Acquisition (SCADA) for steady state observation. The communication architecture for the collection of data from the PMUS requires a hierarchical architecture. All the PMUs manufactured by different vendors use C37.118 as a standard format for the communication of PMU data. C37.118 defines four types of packets for the communication of PMU data to the control centers.

1. Data frame: It consist of measured real time phasor data in binary format.
2. Configuration frame: It is a subset of the data available in the data frame which indicates the current real time data of the PMU.
3. Header frame: It contains information about the PMUs, the data sources and other information about the PMUS in human-readable form.

GPS paved the way for synchronized phasor measurement using PMUs which are placed in some or all branches in a bus to have complete observability of the grid. A PMU is a device which measures voltage and current of the branches synchronized with GPS clock at the rate of 25–30 sample per second. Due to high cost of PMUs only limited number of PMUS are installed at optimal locations in the transmission lines. Nowadays power systems are being operated close to the margins due to increase in demand for electricity. Due to dynamic behavior of the grid necessary steps has to be taken to prevent blackouts by implementing state-of-the-art technologies for better controllability, reliability, and stability of the grid. The vision of smart grid is to integrate communication technologies in the transmission and distribution networks for the delivery of electricity. The measurements obtained from the PMUs which are disposed in a wide geographical area must reach control centers with very low latency.

Bhonsle et al. proposed PMU-PDC placement formulation in two stages for the efficient functioning of wide area monitoring system [1], using binary integer programming technique to minimize the distance between PMU and PDC in cost point of view. However they had not analyzed about the delay performances and other critical factors. The authors in [2] developed an optimal placement method for the PMU-PDC to provide complete system observability for reliable communication network. They had developed only the methods by partitioning the WAMS

with hierarchical structure for the simultaneous placement of PMUs and PDCs. Kiran et al. analyzed the performance of WAMS communication infrastructure for different routing protocols in the presence of background traffic and link failure [3]. Their work does not focus on the optimal communication infrastructure for the optimal PMU placement in power system. Ivanov and Dimova provided the analysis of real time into a data delivery in wide area monitoring system [4]. The authors in [5] proposed an optimal placement of PMUs and the communication backbone network using multiobjective shortest path routing algorithm for reducing the cost of installation of optical, fibre ground wire without any delay analysis.

In this proposed work the communication backbone network for the modified IEEE 14 bus system is studied after obtaining the optimal buses and the shortest communication path by which the PMUs can be connected to CCB. The performance of the communication network is further evaluated in OPNET with IP and MPLS protocols.

2 PMU Placement Problem

Since PMUS are costly devices, placing PMUs on all the buses is an uneconomical and expensive. The objective of PMU placement problem deals with finding the optimal number of PMUs and its location considering the observability. The number of PMUs and its location must be sufficient to make the power system completely observable by obtaining the voltages of all the buses in a given system [6].

For an n-bus system, the PMU placement problem can be formulated as follows:

$$\min \sum_{i=1}^{n} \mathrm{w}_i \cdot \mathrm{x}_i \tag{1}$$

$$s.t \quad f(X) \geq 1_i$$

where,

X is a binary decision variable vector, whose entries are defined as:

$$x_i = \begin{cases} 1 & \text{if a PMU is installed at bus } i \\ 0 & \text{otherwise} \end{cases}$$

w_i is the cost of the PMU installed at bus 'i'.

$f(X)$ is a vector function, whose entries are non-zero if the corresponding bus voltage is solvable using the given measurement set and zero otherwise.

3 Simulation Analysis

The study has been conducted using modified IEEE 14 bus system which consists of two generators, 14 loads and 20 transmission lines [7]. The line parameters for the modified IEEE 14 bus system are shown in Table 1.

3.1 Communication System Design

The optimal placement problem formulation as stated in Eq. (1) is applied on test system. For complete observability the results obtained for the placement of PMUs are at buses 2, 7, 10, and 13 as shown in Fig. 1. While designing a communication path in a power system two types of communication control strategies are there. They are centralized communication strategy and decentralized communication strategy. If the communication directly takes place between the PMUs and control centers it is said to be centralized communication strategy. If the communication takes place not directly but through an intermediate hub then it is said to be decentralized communication strategy.

MOSP algorithm finds out the subordinate control centers referred as control center bus (CCB) [6].

To find an optimal location for the CCB using MOSP algorithm are as follows.

Step 1: Determine shortest path from a selective PMU bus to all the other buses in the system using Dijkstra algorithm.
Step 2: To find the distance of total coverage for each bus.
Step 3: To find the minimum distance in matrix K
Step 4: If two or more number of buses have the same minimum coverage distance then it is necessary to find minimum number of hops required for any bus to reach CCB.

Table 1 Modified IEEE 14 bus system line parameters

Lines	Length in kms	Lines	Length in kms
1–2	209.2	6–11	233.4
1–5	120.7	6–12	88.5
2–3	185	6–13	48.3
2–4	136.8	7–8	201.2
2–5	233.3	7–9	72.4
3–4	144.8	9–10	265.5
4–5	177	9–14	241.4
4–7	450.6	10–11	152.9
4–9	273.6	12–13	128.8
5–6	104.6	13–14	281.6

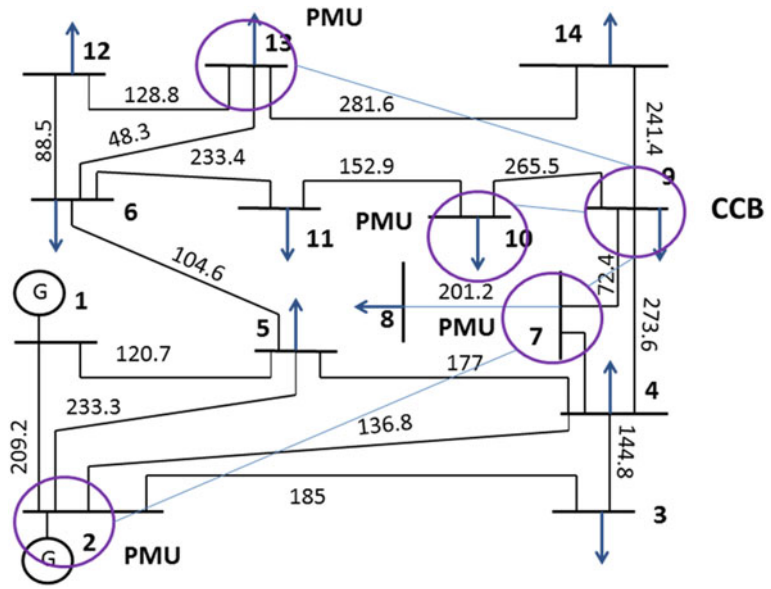

Fig. 1 Optimal communication architecture design for modified IEEE 14 bus system

On buses 2,7,10, and 13 the Dijkstra algorithm is applied to obtain the matrix K.

$$K = \begin{array}{c} \begin{matrix} bus2 & bus7 & bus10 & bus13 \end{matrix} \\ \begin{bmatrix} 209.2 & 748.3 & 611.6 & 273.6 \\ 0 & 587.4 & 724.2 & 386.2 \\ 185 & 595.4 & 683.9 & 941.4 \\ 136.8 & 450.6 & 539.1 & 796.6 \\ 233.4 & 627.6 & 490.9 & 152.9 \\ 337.9 & 724.2 & 386.3 & 48.3 \\ 587.4 & 0 & 337.9 & 595.4 \\ 788.6 & 201.2 & 539 & 796.6 \\ 458.6 & 72.4 & 265.5 & 523 \\ 724.2 & 337.9 & 0 & 434.6 \\ 571.3 & 490.8 & 152.9 & 281.7 \\ 426.4 & 724.2 & 474.8 & 128.7 \\ 386.2 & 595.4 & 434.6 & 0 \\ 651.8 & 313.8 & 506.9 & 281.7 \end{bmatrix} \end{array} \begin{matrix} bus1 \\ bus2 \\ bus3 \\ bus4 \\ bus5 \\ bus6 \\ bus7 \\ bus8 \\ bus9 \\ bus10 \\ bus11 \\ bus12 \\ bus13 \\ bus14 \end{matrix}$$

For each bus the total coverage is calculated by multiplying matrix E by a column vector of elements equal to the total number of PMUs of the considered system.

$$E = K[1 \quad 1 \quad 1 \quad 1]^T$$

The resultant matrix contains the bus with minimum distance for the placement of control center bus.

$$E = \begin{bmatrix} 1842.7 \\ 1697.8 \\ 2405.7 \\ 1923.1 \\ 1504.8 \\ 1496.7 \\ 1520.7 \\ 2325.4 \\ 1319.6 \\ 1496.7 \\ 1496.7 \\ 1754.1 \\ 1416.2 \\ 1754.2 \end{bmatrix} \begin{matrix} bus1 \\ bus2 \\ bus3 \\ bus4 \\ bus5 \\ bus6 \\ bus7 \\ bus8 \\ bus9 \\ bus10 \\ bus11 \\ bus12 \\ bus13 \\ bus14 \end{matrix}$$

From matrix E it is clear bus 9 have the least coverage distance from any PMUs. Hence, bus 9 is selected as CCB.

After finding out the CCB using MOSP with OPNET, the network performance of communication backbone network shown in Fig. 2 for the modified IEEE 14 bus system is analyzed [8]. The proposed architecture connects the substation routers with optical fibers to communicate different substation automation data. The following figure shows the overview of modified IEEE 14 bus system communication network topology. It consists of 14 nodes considered as substation connected to each other through PPP_SONET_OC3 cables. Each substation has a router and the automation devices are connected to this router. The differential service code point for the PMU traffic is considered as 64EF. The proposed network is investigated based on two different protocols namely IP and MPLS.

The comparative analysis of the communication network between IP and MPLS shows reduced end to end delay based on MPLS as shown in Fig. 3. The MPLS protocol takes an average of 0.06 ms for the PMU data to reach the control center.

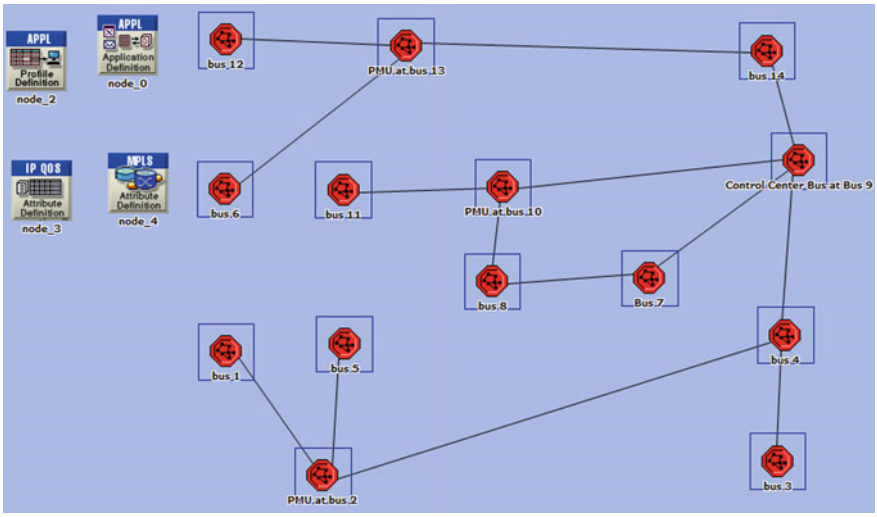

Fig. 2 Network model of modified IEEE 14 bus system

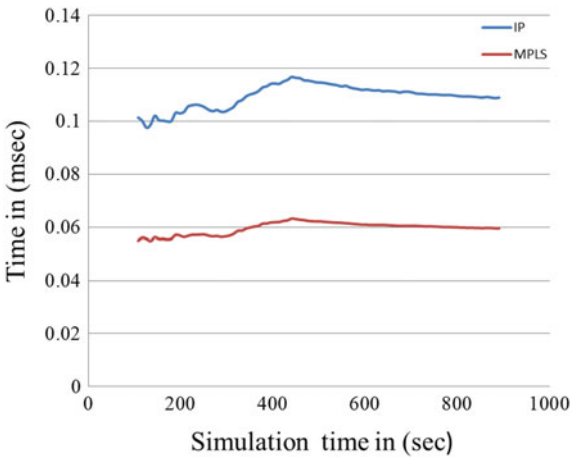

Fig. 3 End-to-end delay analysis between PMUs and CCB

4 Conclusion

This work deals with three different issues regarding planning of PMU installation in the modified IEEE 14 bus system. The optimal placement of PMUs was identified using linear programming method. Second, the CCB location is identified using MOSP algorithm to have the shortest path from the different buses. Third the OPNET analysis shows the PMU data reaches the CCB within the specified limit using MPLS protocol even in case of link failures.

References

1. Bhonsle JS, Junghare AS (2015) An optimal PMU-PDC placement technique in wide area measurement system. In: Smart technologies and management for computing, communication, controls, energy and materials (ICSTM), International conference on energy and materials. pp 401–405
2. Fesharaki FH, Hooshmand RA, Khodabakhshian A (2013) A new method for simultaneous optimal placement of PMUs and PDCs for maximizing data transmission reliability along with providing the power system observability. Electr Power Syst Res 100:43–54
3. Gajrani K, Sharma KG, Bhargava A (2012) Performance assessment of communication network in WAMS. Int J Distrib Parallel Syst 3(6):127–137
4. Ivanov M, Dimova R (2014) PMU traffic evaluation in wide area monitoring and control systems. Comput Syst Commun 3(1):3–11
5. Ghasemkhani A, Monsef H, Rahimi-Kian A, Anvari-Moghaddam A (2015) Optimal design of a wide area measurement system for improvement of power network monitoring using a dynamic multiobjective shortest path algorithm. IEEE Syst J 99:1–12
6. Nikumbh BM (2016) Optimal placement of PMUs considering logical topology of communication medium power system observability (Master's thesis, UiT Norges arktiske university of Norges)
7. Korkali M, Abur A (2011) Transmission system fault location using limited number of synchronized recorders. In: International conference on power system transients proceedings
8. Perkonigg F, Brujic D, Ristic M (2015) Platform for multiagent application development incorporating accurate communications modeling. IEEE Trans Industr Inf 11(3):728–736

BER Analysis of LTE-4G Standard Rayleigh Flat Fading Channel with Adaptive Modulation

Rajeswara Rao Gangula and Sasibhushana Rao Gottapu

Abstract It is a challenging task to improve reliable and high-speed data communication between Transmitter and Receiver. Achieving high data rate using block codes and convolution codes is still questionable through a wireless channel. Turbo codes are a class of high performance forward error correction (FEC) codes with OFDM with adaptive Modulation for 4G and LTE applications. In this paper, BER analysis is carried out for TURBO-coded OFDM data with adaptive modulation mode switching using BPSK, QPSK, 16QAM, and 64QAM. Adaptive modulation scheme is assisted by decision feedback equalizer (DFE) which controls modulation mode. Its output SNR is used as a switching metric. DFE is used to select modulation mode. It is observed that average spectral efficiency (bits per second/Hz) is much higher for adaptive modulation scheme. For higher modulation scheme average spectral efficiency is gradually increases up to 40 dB, that indicates its throughput is much higher in comparison with fixed modulation modes.

Keywords Data communication · Block codes · Convolution codes
Turbo code forward error correction · 16QAM · 64QAM · Adaptive modulation

1 Introduction

Turbo-coded Orthogonal frequency division multiplexing (OFDM) has been introduced to combat frequency selective fading and flat fading experienced by each sub-carrier in an urban environment wireless communications shown in Fig. 1. To transfer high data rates (packet switching) efficiently, Turbo coding is used. In Turbo coding the input bits are channel coded and these serial input bits are converted into parallel form. They are interleaved and adaptive modulated. Theoretical

R. R. Gangula (✉)
G.V.P. College of Engineering (Autonomous), Visakhapatnam, India
e-mail: grajesh197@gmail.com

S. R. Gottapu
Andhra University college of Engineering, Visakhapatnam, India

H. S. Saini et al. (eds.), *Innovations in Electronics and Communication Engineering*,
Lecture Notes in Networks and Systems 33,
https://doi.org/10.1007/978-981-10-8204-7_36

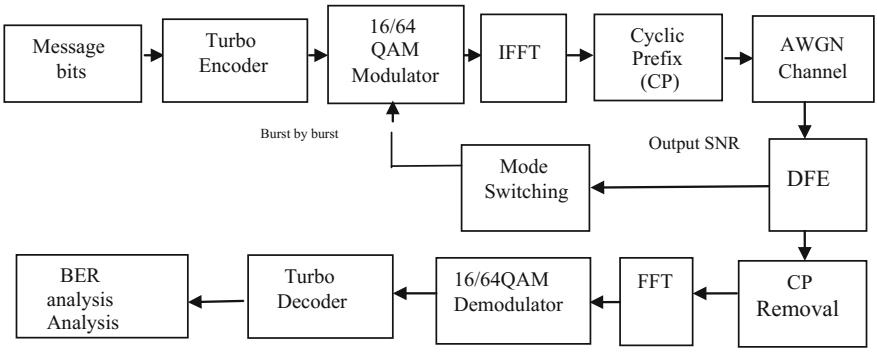

Fig. 1 Block diagram of turbo-coded OFDM with adaptive modulation

maximum for the code rate at which reliable communication is possible depends on specific noise level. Turbo codes are used in 4G mobile communications (e.g., LTE) and in (deep space) satellite communications as well as other applications where designers seek to achieve reliable information transfer over bandwidth constrained communication links in the presence of data-corrupting noise channels.

Adaptive modulation is the scheme in which average spectral efficiency is increased by switching suitable modulation schemes out of QPSK, 16QAM, or 64QAM. Channel quality indicator (CQI) specifies SNR which is mapped to spectral efficiency. This spectral efficiency (γ) decides modulation switching mode.

2 Turbo Encoder

It consists of two rate half Recursive Systematic Convolution (RSC) encoders as shown in Fig. 2. It uses two recursive systematic encoders working parallel on the same information. An inter-leaver is used before the second encoder to shuffle the input bits in a specific pattern. In Turbo encoder, the data block is first encoded by

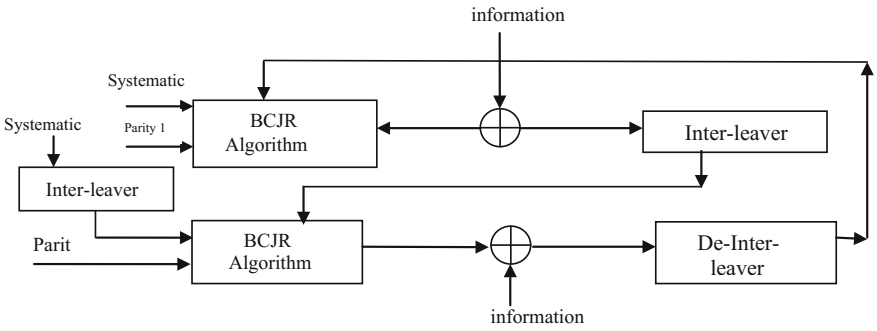

Fig. 2 Turbo encoder

first recursive systematic encoder. The same data block is also interleaved and encoded by second recursive [1] systematic encoder. The main purpose of the inter-leaver is to randomize burst error patterns so that it can be correctly decoded. It also helps to increase the minimum distance of the turbo code. The recursive systematic code can be obtained from a nonsystematic convolution code by adding a feedback loop and setting one of the output bits equal to the input bits.

3 Turbo Decoder

Turbo decoder operation is inverse operation of Turbo encoder. It is an Iterative operation This decoding process improves band width utilization of 16QAM and 64QAM Two and three times higher respectively [2]. Higher order modulations such as 256QAM and above are noisy and require higher S/N. Hence 64QAM is used for cleaner channels and improves BER performance for higher data rate [3]. Turbo decoder is based on the use of BCJR algorithm which is iterative process which leads to error-free output for high data rate applications. In the literature BER Performance of Turbo-coded OFDM is better in comparison with convolution codes [4].

4 OFDM

When the parallel symbol streams are generated, each stream would be modulated and carried at different center frequencies as the traditional FDM scheme. The iterative decoding technique is used in Turbo decoder. The subcarriers centered at frequencies $f_0, f_1, f_2 \ldots f_{N-1}$, must be orthogonal to each other [5].

The definition of the orthogonality is

$$\int_0^T \cos(2\pi f_n t) X \cos(2\pi f_m t) \mathrm{d}t = \delta(n-m), \tag{1}$$

where $\delta(n-m)$ is the Dirac-Delta function. In OFDM modulation, the subcarrier frequency f_n is defined as $f_n = n\Delta f$, Where $\Delta f = \frac{f_n}{N} = \frac{1}{NT}$, Here $f_s = \frac{1}{T}$ is the entire bandwidth, and N is the number of subcarriers. By substituting through the above equations, orthogonality can be justified for all $f_0, f_1, f_2, \ldots f_{N-1}$.

5 Adaptive Modulation

Turbo-coded adaptive modulation scheme assisted by decision feedback equalizer (DFE) is investigated for adaptive modulation. DFE will eliminate most of inter symbol interference (ISI), intercarrier interference (ICI) [4]. The output of DFE is

SINR (BER) which is a mean square error and can be calculated as metric invoked to switch the modulation mode.

Mobile radio channel quality is measured by CQI report (Channel Quality Indicator). Higher the value of CQI measure, higher the modulation order selected from M QAM.

Channel Quality is expressed in terms of BER [6]. It can be estimated with mean square error measured at decision feedback equalizer or by signal-to-interference noise ratio(SNR) selection criteria. This SNR measure is selected in such a way that packet error rate selection while transmission is less than targeted value which reduces frequent retransmissions [7], and the process is shown in Fig. 3.

CQI estimation is performed in two steps

1. SNR estimation: it is a function of decoding bits in the receiver
2. SNR is mapped to a spectral efficiency measure that decides type of modulation to be adapted while transmission that is by selection of number of modulating bits per symbols per symbol. For each SNR measure distinct modulation scheme is chosen from the look-up table [7].

Let G be a optimum equalizer that transmits signal $x(n)$, [8] received signal $y(n)$ and the linear estimate of equalizer signal $\hat{x}(n)$ then the error signal e(n) represented as

Decision feedback estimator (DFE) estimates channel gain by calculating

$$e(n) = \hat{x}(n) - x(n) = Gy(n) - x(n) \tag{2}$$

$e(n)$ and hence signal-to-noise ratio (SNR). SNR is defined as the ratio of transmitted signal power σ_x^2 to the error signal power σ_e^2

$$\text{SNR(indB)} = 10\log_{10}\left(\frac{\sigma_x^2}{\sigma_e^2}\right) \tag{3}$$

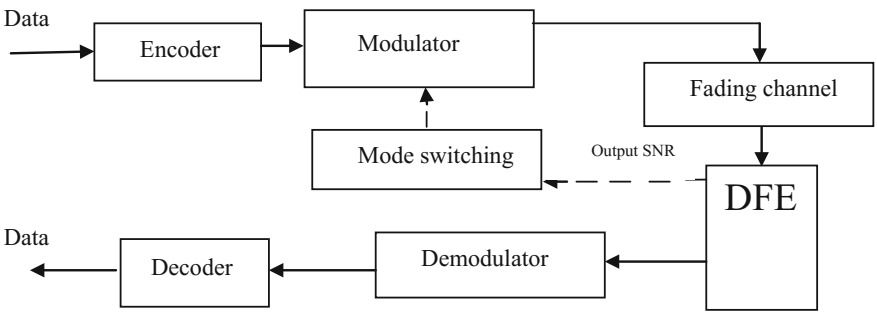

Fig. 3 DFE equalizer's out put SNR used to select suitable modulation mode

SNR value is mapped to spectral efficiency as shown in Table 1. Spectral efficiency is defined as bits per second/Hz of band width. Spectral efficiency γ_{DFE} has range of threshold values for each modulation scheme [7]. Modulation mode switching mechanism depends on this threshold values as shown in Table 2. t_n^c represents modulation switching threshold value (Table 3).

Table 1 Lookup table for mapping SNR estimate to modulation scheme [7]

CQI Index	Modulation	Spectral efficiency γ_{DFE} (bps/Hz)	SNR estimate (in dB)
1	QPSK	0.1523	−6.7
2	QPSK	0.2344	−4.7
3	QPSK	0.3770	−2.3
4	QPSK	0.6016	0.2
5	QPSK	0.8770	2.4
6	QPSK	1.1758	4.3
7	16QAM	1.4766	5.9
8	16QAM	1.9141	8.1
9	16QAM	2.4063	10.3
10	64QAM	2.7305	11.7
11	64QAM	3.3223	14.1
12	64QAM	3.9023	16.3
13	64QAM	4.5234	18.7
14	64QAM	5.1152	21.0
15	64QAM	5.5547	22.7

Table 2 Modulation thresholds

Modulation mode	Spectral efficiency of DFE (γ_{DFE})
No transmission	$\gamma_{DFE} \leq t_1^c$
BPSK	$t_1^c \angle \gamma_{DFE} \leq t_2^c$
QAM	$t_2^c \angle \gamma_{DFE} \leq t_3^c$
16QAM	$t_3^c \angle \gamma_{DFE} \leq t_4^c$
64QAM	$\gamma_{DFE} > t_5^c$

Table 3 Switching threshold values

Threshold	SNR value in dB
t_1^c	−6.3
t_2^c	4.3
t_3^c	5.9
t_4^c	10.3
t_5^c	11.7

6 Results

Through put is measured for BPSK QPSK 16QAM and 64QAM. For BER of 1 and 0.01% in Turbo-coded adaptive modulation scheme. For 25 dB of channel SNR gain can transmit 10^4 BPS using 64QAM. 16QAM needs 15–25 dB for 10^3 BPS

Spectral efficiency is getting saturated for BPSK modulation at 15 dB. Where as 16QAM needs around 20 dB then spectral efficiency is saturated. For QPSK it is 25 dB and, 16QAM it is 30 dB. For adaptive modulation spectral efficiency raises up to 10^8 BPS at power level of 45 dB. More the spectral efficiency higher the data rate.

7 Conclusion

This paper is presented on turbo-coded OFDM signal emphasizes on adaptive modulation schemes. This adaptive modulation improves spectral efficiency and throughput performance with same BER. Future work will investigate spectral efficiency with variable coding rate and switching to modulation modes and hence spectral efficiency.

References

1. Rao KD (2015) Channel coding techniques for wireless communications. Springer, India. ISBN 978-81-322-2291-0
2. Steele R, Webb WT (1991) Variable rate QAM for data transmission over Rayleigh fading channels. In: Wireless'91. IEEE, Calgary, Alberta, pp 1–14
3. Choi K, Liu H (2016) Problem-based learning in communication systems using Matlab and Simulink. ISBN: 9781119060345
4. Zarrinkaub H (2014) Understanding LTE with MATLAB: from mathematical Foundation to simulation, performance evolution and implementation. John Wiley & Sons, Ltd., Hoboken. ISBN: 9781118443415
5. Bahai ARS, Saltzberg (1999) Multi-carrier digital communications: theory and applications of OFDM. Kluwer Acadamic/Plenum Publishers, N.Y.
6. Burr AG, White GP University York, York YO10 5DD, UK email: alister@ohm.york.ac.uk
7. Hanzo L, Wong CH, Yee MS Adaptive wireless transceivers: turbo-coded, turbo- equalised and space-timecoded TDMA, CDMA, MC-CDMA and OFDMSystems
8. Sagias NC, Papaharalabos S, Mathiopoulos PT (2015) Cooperative DVB-SH satellite broadcasting systems with rotated signal constellations. China communications

A Study on the Coverage of Millimeter Wave (MMW) Communication Link for Fifth Generation (5G) Mobile Networks

Umar Farooq and Ghulam Mohammad Rather

Abstract Millimeter wave (MMW) communication is a promising technology to cope up with the ever increasing demand for multi gigabit wireless applications and to alleviate the problems of spectrum scarcity for Fifth generation (5G) mobile communication applications. The coverage distance of the MMW communication system is severely affected due to the various losses such as free space loss, atmospheric loss, and foliage loss. However MMW communication allows the use of smaller antenna size which can facilitate the fabrication of large antenna arrays over small area like a postage stamp which can be used at both transmitter and receiver. This helps in efficient use of the Multi-Input Multi-Output (MIMO) technology in MMW Communication systems which can improve the coverage distance as well as capacity of the system. In this paper, we perform the Mathematical analysis of the coverage distance of MMW communication link and study the effects of different parameters on its performance. A simulation study to examine the effect of the MIMO antenna system for improving the coverage distance of MMW communication links for specific data rates for Line of Sight (LOS) and Non-Line of Sight (NLOS) cases in a highly dense mobile network scenario has been done and results are presented in this paper.

Keywords Millimeter wave communication · 5G · SNR · MIMO
LOS · NLOS

U. Farooq (✉) · G. M. Rather
Department of Electronics and Communication, National Institute
of Technology Srinagar, Srinagar 190006, India
e-mail: umarfarooq232@gmail.com

H. S. Saini et al. (eds.), *Innovations in Electronics and Communication Engineering*,
Lecture Notes in Networks and Systems 33,
https://doi.org/10.1007/978-981-10-8204-7_37

1 Introduction

MMW communication is a key technology to meet the high data rate requirements of Next generation networks [1]. Also due to the exponential growth in the mobile data traffic, next generation or 5G mobile networks are expected to exploit the MMW band to increase the communication capacity and decrease the end to end latency. Hence MMW technology is a key facilitator to address the challenges of 5G cellular network. The main motivation behind this is the worldwide availability of huge unexploited bandwidth in MMW frequency spectrum (30–300 GHz) that can provide high-speed links with throughput of 10's of Gigabits per second (Gbps) [2]. However despite these attractive features, MMW technology has not been fully explored. This is because due to the high carrier frequency, MMW communications suffer from huge propagation loss which limits their operation range [3]. In lower frequency bands signals can propagate for many miles and penetrate through obstacles on the other hand MMW signals can travel only few miles or less and cannot propagate through obstacles. These characteristics are however advantageous in certain applications as it permits more densely packed communication links thus providing very efficient spectrum utilization and enhanced security of communication transmissions in next generation networks. However in those applications where a large coverage distance is required different approaches from the physical layer to the network layer have been proposed to achieve this goal. These include beam switching from a Line of Sight (LOS) path to a Non-Line of Sight Path (NLOS) path [4], relaying, multipath routing, performing handovers between Access Points (APs) and use of high gain antennas [5, 6]. However, every approach has its advantages and shortcomings, and these approaches should be combined in an intelligent way to achieve robust and efficient network performance.

The other alternative scheme is the use of Mult-Input Multi-Output (MIMO) systems [7] to improve the coverage distance and the capacity of the system. Since the antenna size is inversely proportional to the frequency of operation so at MMW frequencies the antenna size is obviously very small which makes it possible to design large antenna arrays over a small area [8]; thus making the MIMO antenna systems inherently a best choice to be used for MMW communications in order to improve the performance of the system. In this paper we mathematically analyze the coverage distance/range of the MMW communication link. Also we examine the effect of MIMO antenna systems for improving the coverage distance of MMW communication links for 5G mobile applications in Line of Sight (LOS) and Non-Line of Sight (NLOS) case scenarios with and without the effect of shadowing. The results are also compared with Single Input Single Output (SISO) and Single Input Multi Output (SIMO) system.

2 Mathematical Analysis of Coverage of MMW Link

Consider a MMW communication link as shown in Fig. 1.

'R' is the distance between transmitter and receiver 'P_{tx}' is the power transmitted; 'G_{tx}' and 'G_{rx}' are the gains of transmitting and receiving antennas respectively.

If P_{rx} is the received signal power and P_n be the receiver noise power, then SNR at input of receiver is given as [9]:

$$\mathrm{SNR}_{in} = \frac{P_{rx}}{P_n} = \frac{P_{rx}}{BN_o}, \tag{1}$$

where 'B' is the bandwidth of data transmission system and 'N_o' is the power spectral density of the AWGN. Since bandwidth is function of center frequency 'f_o' given by:

$$B = \alpha f_o, \tag{2}$$

where α is fractional bandwidth whose value varies from 0.01 to 0.1.

Therefore (1) can be expressed as

$$\mathrm{SNR}_{in} = \frac{P_{rx}}{\alpha f_o N_o} \tag{3}$$

Since the range of the wireless communication system is governed by minimum 'SNR_{min}' required at the receiver which will be a constant. The corresponding power 'P_{rxo}' should be function of 'f_o' as follows:

$$P_{rxo} = \alpha f_o \, N_o \, \mathrm{SNR}_{min} \tag{4}$$

Using Shanaon's Capacity theorem, the achievable capacity 'C' of the channel is given by

$$C = B \log(1 + \mathrm{SNR}_{min}) = \alpha f_o \log(1 + \mathrm{SNR}_{min})$$

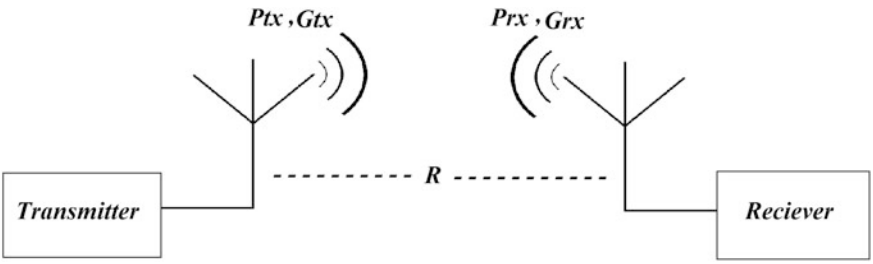

Fig. 1 A general block diagram of a MMW communication link

Thus 'C' is a linear function of the center frequency. Hence the data carrying capacity of the system will increase with increase in the frequency of operation.

If 'λ' be the wavelength of operation and 'c' be the velocity of light and considering the Fig. 1, then according to Friis equation [10] we have

$$\frac{P_{\text{rx}}}{P_{\text{tx}}} = \left(\frac{\lambda}{4\pi R}\right)^2 \cdot G_t \cdot G_r$$

Using this equation the coverage/range can be written as $R_o^2 = \left(\frac{\lambda}{4\pi}\right)^2 \cdot \frac{P_{\text{tx}} \cdot G_{\text{tx}} \cdot G_{\text{rx}}}{P_{\text{rx}}}$. If we put (4) in this equation we can write

$$Ro^2 = \left(\frac{\lambda}{4\pi}\right)^2 \cdot \frac{P_{\text{tx}} \cdot G_{\text{tx}} \cdot G_{\text{rx}}}{\text{SNR}_{\min} \cdot \alpha f_o N_o} = \left(\frac{c}{4\pi f_o}\right)^2 \cdot \frac{P_{\text{tx}} \cdot G_{\text{tx}} \cdot G_{\text{rx}}}{\text{SNR}_{\min} \cdot \alpha f_o N_o} \tag{5}$$

$$\begin{aligned} &\text{or}, R_o^2 = \beta \cdot \frac{1}{f_o^3}, \quad \text{where } \beta \text{ is constant and equal to} \left(\frac{c}{4\pi}\right)^2 \cdot \frac{P_{\text{tx}} \cdot G_{\text{tx}} \cdot G_{\text{rx}}}{\text{SNR}_{\min} \cdot \alpha N_o} \\ &\text{or } R_o = \beta_o \cdot \frac{1}{f_o^{3/2}} \quad \text{where } \beta_o = \sqrt{\beta} \end{aligned} \tag{6}$$

Equation 6 implies that the coverage decreases with increase in frequency of operation as also plotted in Fig. 2. Also if $B = \alpha f_o$ is satisfied then the data rate increases with the increase in frequency as mentioned earlier in this section. So there is tradeoff between the data rate and the coverage with respect to the increase in the frequency of operation.

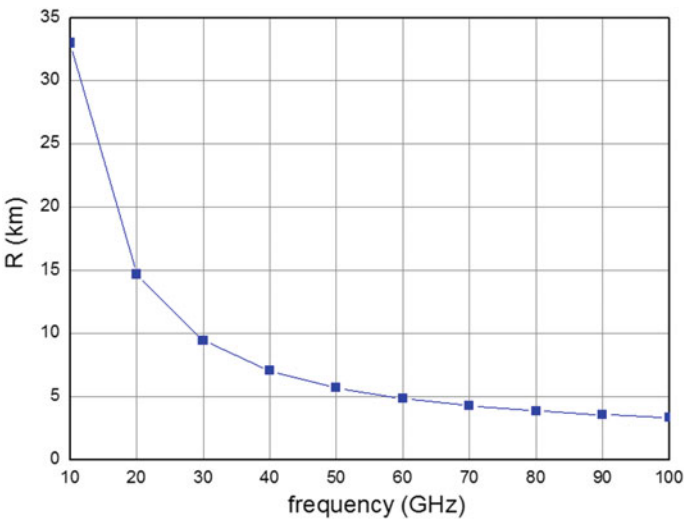

Fig. 2 Range versus frequency (α = 0.01)

3 Performance Analysis of Coverage Using MIMO System

Consider a MMW link in Line of Sight (LOS) and Non-Line of Sight (NLOS) scenario as shown in Fig. 3. The MMW link is simulated and analyzed for coverage distance and data carrying capacity for a MIMO system. The impact of system noise as well as the losses due to various atmospheric factors which affect the performance is also considered.

To obtain the results of 'capacity versus coverage distance' we simulate the MMW link shown in Fig. 3 considering the parameters given in Table 1 [11]:

Assuming the noise to be AWGN, the data carrying capacity of the MMW link using MIMO systems can be easily calculated by the Capacity formulae [12] given by: $C = MB\ \log_2\left(1 + \frac{N}{M}SNR\right)$, where M is the number of antenna elements at transmitter and N is number of antenna elements at receiver end and also $N \geq M$ such that all the transmitted signals can be decoded at the receiver end. The simulation results obtained for various case scenarios are plotted and given in the figures below.

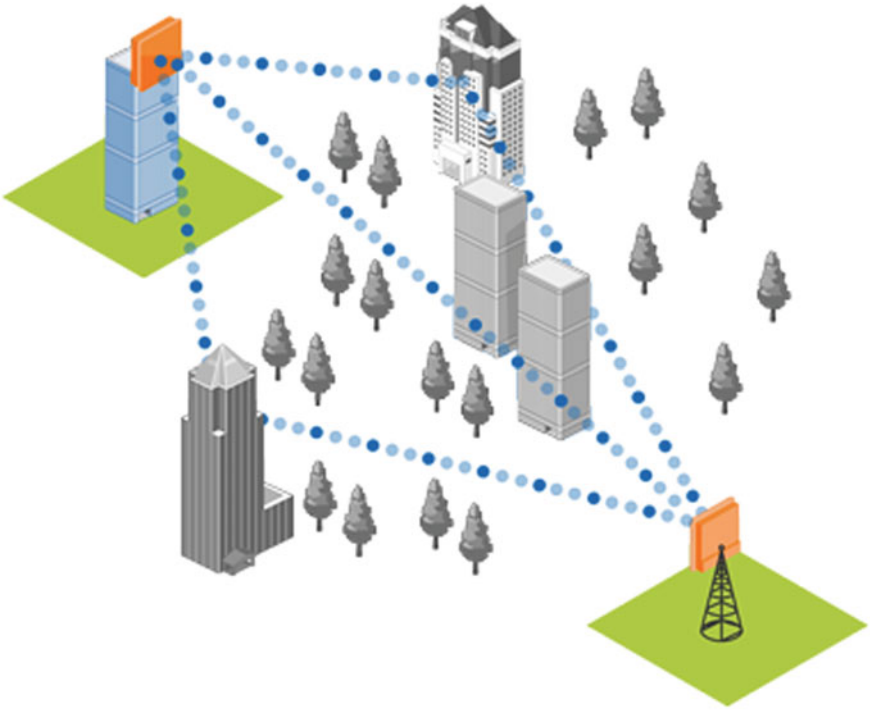

Fig. 3 MMW communication link in LOS and NLOS Scenario

Table 1 Gain due to various components at transmitter and receiver

Component	Gain (dB)	Component	Gain (dB)
Tx feeding network	−5	Tx antenna array	15
Rx feeding network	−5	Rx antenna array	10
Amplifier at receiver	30	Transmitted power	25
LNA at receiver	20	Shadowing (LOS)	−1
Channel selector filter	−5	Shadowing (NLOS)	−5

In Figs. 4 and 5 we show the capacity vs. coverage results for LOS and NLOS scenarios without considering the effect of shadowing and it is clear that the coverage distance is more when MIMO (2 × 2) is used than SIMO (1 × 2) and that of SIMO is more than SISO (1 × 1) for example in LOS case for operating capacity of about 11Gbps the coverage distance using MIMO (2 × 2) system is around 140 meters while that for SIMO is only about 15 meters. In Figs. 6 and 7 we consider the shadowing effect while evaluating the results and again we get similar sort of results.

We increase the number of antennas at the transmitter and the receiver and evaluate the results. As such Figs. 8 and 9 show the results for 2 × 2 and 4 × 4 MIMO systems with and without shadowing effect for both LOS and NLOS case scenarios.

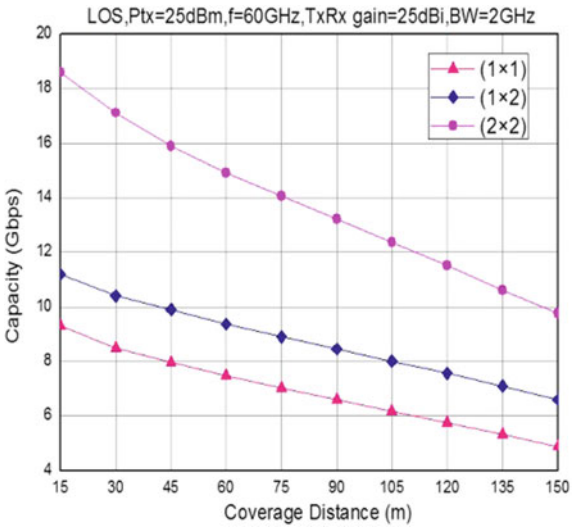

Fig. 4 Capacity versus Coverage (LOS)

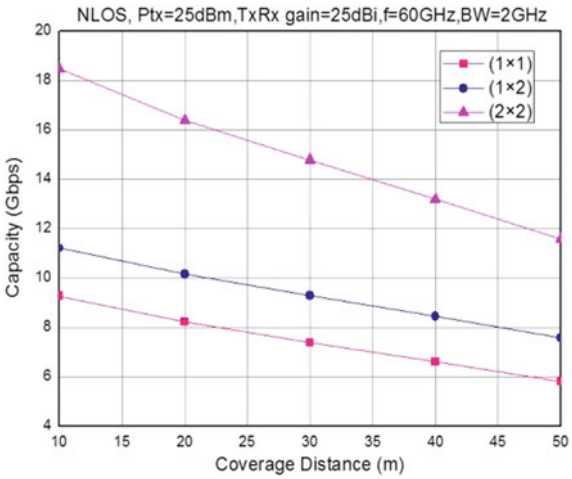

Fig. 5 Capacity versus Coverage (NLOS)

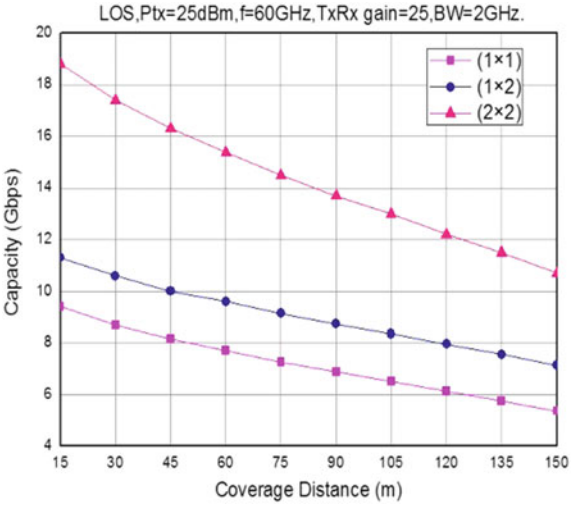

Fig. 6 Capacity versus Coverage (no shadowing)

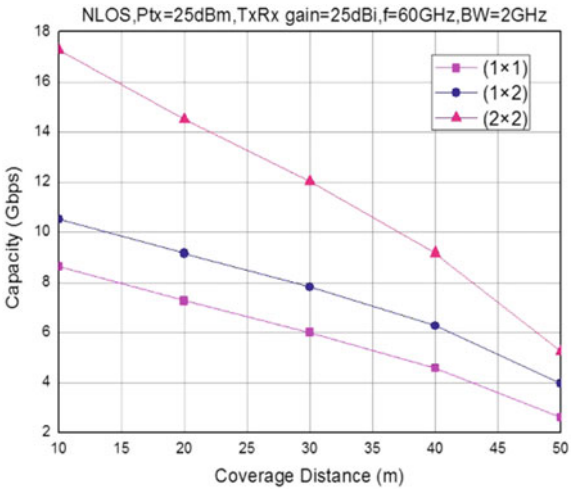

Fig. 7 Capacity versus Coverage (no shadowing)

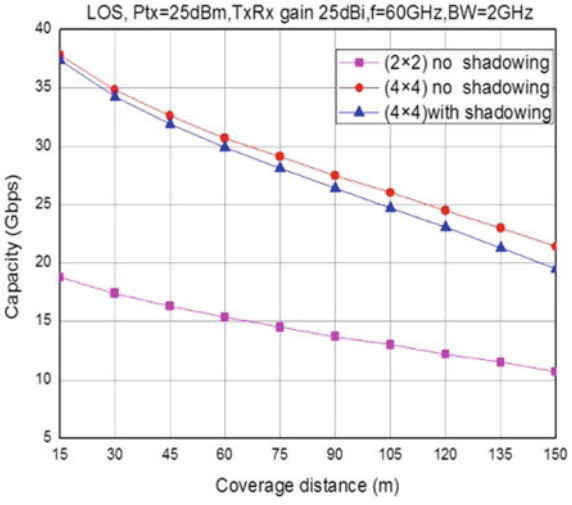

Fig. 8 Capacity versus Coverage for different MIMOs

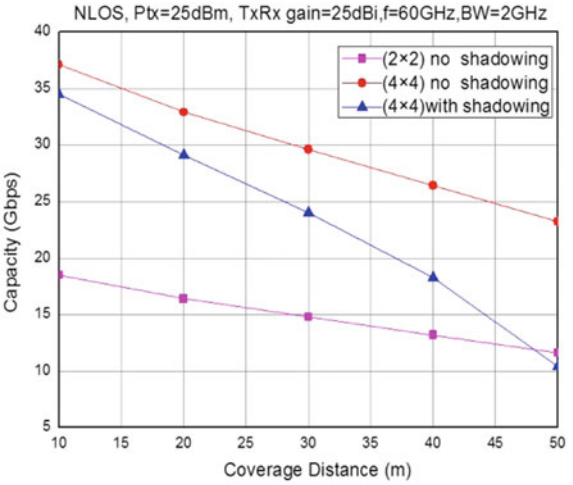

Fig. 9 Capacity versus Coverage for different MIMOs

4 Conclusion

MMW communication has been a great deal of interest from academia, industry and research organizations due to the attractive features of millimeter waves to provide multi-gigabit transmission rate. However due to the various losses such as free space loss, atmospheric loss and foliage loss, the coverage/range of the MMW communication link is highly effected which in turn limits the overall performance of the MMW communication system especially in applications like 5G mobile communication networks. In this paper we perform the Mathematical analysis of the coverage distance for MMW communication link and study the parameters which affect its performance. We also examined the effect of MIMO antenna systems to improve the coverage distance of a MMW communication network for specific data rates for both LOS and NLOS case in a 5G mobile network scenario. It is observed that a there is considerable increase in the coverage distance is achieved with the help of MIMO systems and this improvement increases as we increase the number of transmit and receive antennas, i.e. from 2×2 MIMO system to 4×4 MIMO system and so on. However these improvements are achieved at the cost of increased system complexity which must be sorted out.

References

1. Rangan S, Rappaport TS, Erkip E (2014) Millimeter-wave cellular wireless networks: potentials and challenges. Proc IEEE 102(3):366–385
2. Xia P, Qin X, Niu H, Singh H, Shao H, Oh J, Ngo C (2007) Short range gigabit wireless communications systems: potentials, challenges and techniques. In: *IEEE International Conference on*. pp 123–128

3. Kato A, Sato K, Fujise M, Kawakami S (2001) Propagation characteristics of 60-GHz millimeter waves for ITS inter-vehicle communications. IEICE Trans Commun 84(9):2530–2539
4. An X, Sum CS, Prasad RV, Wang J, Lan Z, Wang J, Niemegeers I (2009) Beam switching support to resolve link-blockage problem in 60 GHz WPANs. In Personal, Indoor and Mobile Radio Communications, pp 390–394
5. Lan Z, Sum CS, Wang J, Baykas T, Gao J, Nakase H, Kato S (2009) Deflect routing for throughput improvement in multi-hop millimeter-wave WPAN system. In: *Wireless Communications and Networking Conference*. pp 1–6
6. Zhang Xu et al (2012) Improving network throughput in 60 GHz WLANs via multi-AP diversity. IEEE, Communications (ICC)
7. Khalid F, Speidel J (2010) Advances in MIMO techniques for mobile communications—a survey. Int J Commun Netw Syst Sci 3(03):213
8. Schwering F, Oliner A (1988) Millimeter-wave antennas. In Antenna Handbook. Springer, US, pp 1135–1282
9. Proakis J, Salehi M (2008) Digital communications, 5th edn. McGraw-Hill, New York
10. Friis HT (1946) A note on a simple transmission formula. Proc IRE 34(5):254–256
11. Huang KC, Edwards DJ (2008) Millimetre wave antennas for gigabit wireless communications: a practical guide to design and analysis in a system context. John Wiley & Sons, Hoboken
12. Goldsmith A (2005) Wireless communications. Cambridge university press, Cambridge

BER Performance Analysis of Wireless Communication System in Flat Fading Environment

O. Ravinder, M. Ravinder and K. Krishna Kumar

Abstract The performance of any wireless communication system mainly depends on the wireless channel environment. Because of huge demand and growth in mobile communication and Internet services the optimization of the wireless communication is critical. If we know the perfect channel characteristics we can easily develop a high bandwidth-efficient wireless communication system. The wireless channel mainly suffers from 3 different modes. They are Reflection, Diffraction, and Scattering. Combination of these three phenomena's is called fading. Fading is fluctuations in the power levels of the signal. In this paper we find the Bit Error Rate (BER) of wireless communication system in Flat Fading environment. At the same time we evaluate the system performance of M-PSK modulation schemes using MATLAB.

Keywords Optimization · Reflection · Diffraction · Scattering
Flat fading · BER · M-PSK

1 Introduction

Wireless communication system performance is mainly depending on channel (wired and wireless) environment [1]. These both types of channel characteristics are unpredictable; so that this makes the analysis of wireless communication system is difficult. Recently with huge demand and growth in mobile communication and Internet services the optimization of the wireless system becomes critical. So the

O. Ravinder (✉) · K. Krishna Kumar
GNITC, Hyderabad, Telangana, India
e-mail: ravinderoranganti@gmail.com

K. Krishna Kumar
e-mail: kkrgnitc@gmail.com

M. Ravinder
KCEA, Nizamabad, Telangana, India
e-mail: ravinder.240684@gmail.com

H. S. Saini et al. (eds.), *Innovations in Electronics and Communication Engineering*,
Lecture Notes in Networks and Systems 33,
https://doi.org/10.1007/978-981-10-8204-7_38

need of discussing a wireless channels will be the strong base for the development of better performance and bandwidth-efficient wireless technology.

The "fading" is the important characteristic of wireless transmission, fading means the variation of any signal amplitude over time and frequency [2]. Generally while transmitting, the additive noise is added so the signal degrades, fading is another phenomenon to degrade signal, i.e. addition of a non-additive noise in the channel. Fading will occur due to two different variations they are multipath propagation or induced fading [3], and shadowing. Shadow fading occurs due to obstacle [4], which affects the propagation of radio wave.

Generally two fading's they are large-scale and small-scale fading [5, 6]. The former one occurs due to mobile moves through a large distance, second one occurs when mobile station moves through short distances [7].

In the last decades there is an enormous growth in Mobile and wireless communications. Wireless channels are defined very random and time-variant. In the received signal arbitrary time dispersion, phase shift and attenuation, are caused by the wireless multipath channel. To concentrate on fading issue, there are lots of diversity techniques such as OFDM, MIMO, and RAKE receiver [7].

In this paper we are transmitting a Gray scale Image or Random data by doing the Gray encoding, Modulation, and corresponding E_b/N_0 through a Flat fading channel in Non-Line-of-Sight environment with a vehicular speed of 20–120 km/hr. Then we are equalizing channel, demodulating and decoding the data [8]. We are estimating the communication system performance based on calculation of probability error of BER [9], Symbol Error Rate (SER) with channel estimation and without channel estimation and also we evaluate the system performance of M-PSK modulation schemes (BPSK, QPSK, 8-PSK) using MATLAB [10].

Rest of the paper is organized is as follows Sect. 2 will discuss about System model and channel model, Sect. 3 will discuss about BER performance of system. Sect. 4 is about Simulation results and Conclusion is given in Sect. 5.

2 System and Channel Model

Figure 1 shows the proposed block diagram; in that first block represent the input data which is Gray scale image or random data. In this each pixel can be represented by 8 number of bits. Each pixel is represented by the possible combination of 2^0–2^8 that is a shade of gray, normally from 0 (black) to 255 (white) [7]. If it is random data, that can be generated by matlab functions.

The Gray coding means like A/D conversion [11]. The purpose is to convert an integer voltage level, into digital form that represented by series of pulses. The properties of gray encoding are, it is a cyclic nature and adjacent words in the Gray code sequence differ in one bit position only.

We have basically three digital modulation techniques they are Amplitude-shift keying (ASK), Frequency-shift keying (FSK) and Phase-shift keying (PSK). In this paper we use M-PSK, the phase is changed to represent the data signal [7]. There

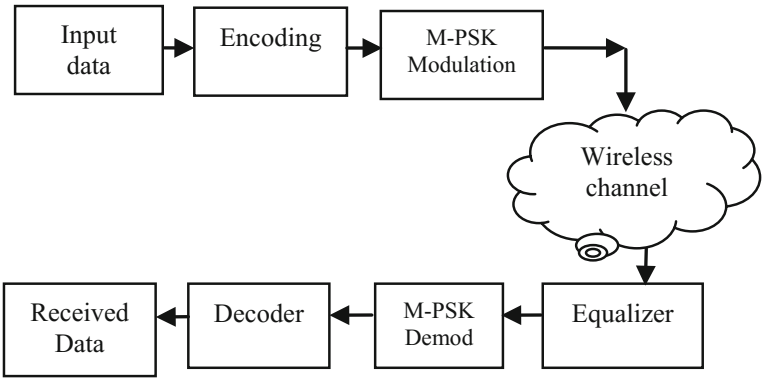

Fig. 1 Proposed block diagram

are two ways to use the phase of a signal; they are coherent and non-coherent detection

Next the signal is transmitted through the wireless channel followed by equalizer. In this paper we are using RLS and LMS equalizers. Finally M-PSK demodulator block, which demodulate the pass-band representation of the modulated signal into equivalent baseband representation.

2.1 Channel model

Here we use fading channel environment. In the process of any radio signal from modulator to demodulator through a wireless channel we need to observe all changes and calculate the gains and losses, these calculations are needed to predict the signal strength at receiver along with the required power margin (Fig. 2).

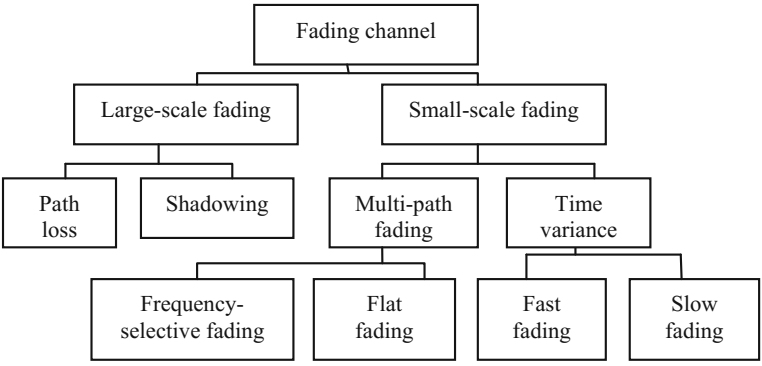

Fig. 2 Fading channel models

In the fading environment, the propagation of signal for any wireless channel focuses on two different ways of communication Line-of-Sight (LOS) or Non Line-of-Sight (NLOS) communication [6]. In the former one the signal follows Rician distribution and in the second one signal follows the Rayleigh distribution [12]. Any received signal in a wireless channel is equal to the sum of the direct and indirect rays. So that by the central limit theorem, the received signal can be considered as a Gaussian random variable.

3 BER Performance of System

PSK uses a finite number of phases; each assigned a unique pattern of binary digits. Under normal condition, each phase is encoded by an equal number of bits in PSK and each pattern of these bits forms the symbol that is represented by the particular phase.

For determining error-rates mathematically [13], we need to define $Q(x)$ function. The $Q(x)$ function means the probability of a random process with mean equal to zero and its variance is equal to unity. It is also called Gaussian or normal PDF with the limit of greater or equal to x [14].

$$\begin{aligned} &\text{i.e} \quad \mathrm{N}(0,1) \quad \text{for } x \geq 0 \\ &Q(x) = \frac{1}{\sqrt{2\pi}} \int_{x}^{\infty} e^{-t^2/2} \mathrm{d}t = \frac{1}{2} \mathrm{erfc}\left(\frac{x}{\sqrt{2}}\right), x \geq 0 \end{aligned} \tag{1}$$

3.1 Binary Phase-Shift Keying (BPSK)

BPSK or 2PSK also called phase reversal keying (PRK), BPSK uses only two phases they are 0° and 180° phase. Because of high noise, for high data rate transmission BPSK modulation is not suitable.

This yields two phases, 0 and π. In generally, binary data is represented by the following signals:

$$\begin{aligned} s_0(t) &= \sqrt{\frac{2E_b}{T_b}} \cos(2\pi f_c t + \pi) = -\sqrt{\frac{2E_b}{T_b}} \cos(2\pi f_c t) \quad \text{for bit “0”} \\ s_1(t) &= \sqrt{\frac{2E_b}{T_b}} \cos(2\pi f_c t) \quad \text{for bit “1”} \end{aligned} \tag{2}$$

Hence, the signal-space can be represented by the single basis function

$$Q(t) = \sqrt{\frac{2}{T_b}\cos(2\pi f_c t)} \tag{3}$$

The probability error for (BER) of BPSK in Additive White Gaussian noise is [15]

$$P_b = Q\left(\sqrt{\frac{2E_b}{N_0}}\right) \tag{4}$$

3.2 Quadrature Phase-shift Keying (QPSK)

If the adjacent symbol is differs by one bit it is known as QPSK, or 4-PSK. So that the data rate of QPSK is twice that of BPSK system, with same bandwidth [16].

$$s_n(t) = \sqrt{\frac{2E_s}{T_s}}\cos\left(2\pi f_c t + (2n-1)\frac{\pi}{4}\right), \quad n = 1, 2, 3, 4 \tag{5}$$

As n = 1, 2, 3 and 4 then four different phase's are possible, i.e., $\pi/4$, $3\pi/4$, $5\pi/4$, and $7\pi/4$. Then the BER probability expression is same for QPSK and BPSK

$$P_b = Q\left(\sqrt{\frac{2E_b}{N_0}}\right) \tag{6}$$

However, in order to achieve the same bit error probability as BPSK, QPSK uses twice the power. The symbol error rate is given by

$$\begin{aligned} P_s &= 1 - (1 - P_b)^2 \\ &= 2Q\left(\sqrt{\frac{E_s}{N_0}}\right) - \left[Q\left(\sqrt{\frac{E_s}{N_0}}\right)\right]^2 \end{aligned} \tag{7}$$

If the *S/N* ratio is high the expression may be approximated as

$$P_s \approx 2Q\left(\sqrt{\frac{E_s}{N_0}}\right) \tag{8}$$

3.3 Higher Order PSK

For the general M-PSK as M is increasing ($M > 4$) the Probability expression for SER is more complex. Probability expression for SER

$$P_s = 1 - \int_{-\frac{\pi}{M}}^{\frac{\pi}{M}} p_{\theta_r}(\theta_r)\, \mathrm{d}\theta_r \tag{9}$$

where

$$\begin{aligned} p_{\theta_r}(\theta_r) &= \frac{1}{2\pi} e^{-2\gamma_s \sin^2 \theta_r} \int_0^{\infty} V e^{-\left(V - \sqrt{4\gamma_s}\cos\theta_r\right)^2/2} \mathrm{d}V \\ V &= \sqrt{r_1^2 + r_2^2} \\ \theta_r &= \tan^{-1}(r_2/r_1) \\ \gamma_s &= \frac{E_s}{N_0} \quad \text{and} \\ r_1 &\sim N\left(\sqrt{E_s}, N_0/2\right) \quad r_2 \sim N(0, N_0/2) \end{aligned} \tag{10}$$

r_1, r_2 are jointly Gaussian normal random variables.

For high M value and high energy bit per noise E_b/N_0 the probability expression is approximated to

$$P_s \approx 2Q\left(\sqrt{2\gamma_s}\sin\frac{\pi}{M}\right) \tag{11}$$

4 Simulation Results

The below Fig. 3a shows the original image, we sent through a fading channel and the received image and adjusted images are shown in Fig. 3b, c for BPSK modulation with Gray encoding and we used LMS Equalization. Figure 3d is drawn between SER and SNR. It consists of two plots, one is for SER without channel estimation and another is for SER with channel estimation. SER will be high without channel estimation due to noise and distortion present in channel. SER will be reducing with increase with SNR values with channel estimation due to

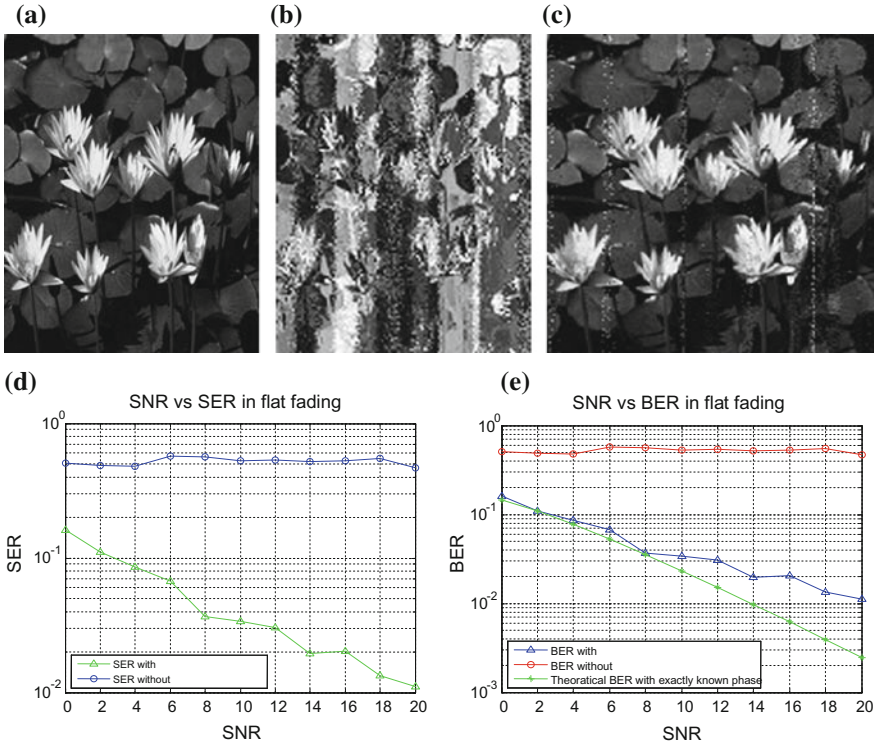

Fig. 3 **a** Original image **b** Received image **c** Adjusted image **d** Graph shows SNR versus SER in flat fading environment with channel estimation **e** SNR versus BER plot in flat fading environment with and without channel estimation

reduction in noise and distortion. From Fig. 3e, the BER will be high without channel estimation. If we estimate the channel characteristics then BER is reduced with increase in SNR.

From Fig. 4d it is clear that SER is high in QPSK than in BPSK due to increase in data rate (i.e., 2 bits/symbol) without channel estimation. So, in the channel with estimation the SER will be comparatively low. From Fig. 4e, it is clear that the BER is very high without channel estimation. So, if we estimate the channel then the BER will be reduced with increase in SNR value.

From above Fig. 5d, e it is clear that as the modulation order increases the SER and BER will be very high without channel estimation. So, with estimation of channel, the SER and BER will be reduced with respect to increase in SNR values.

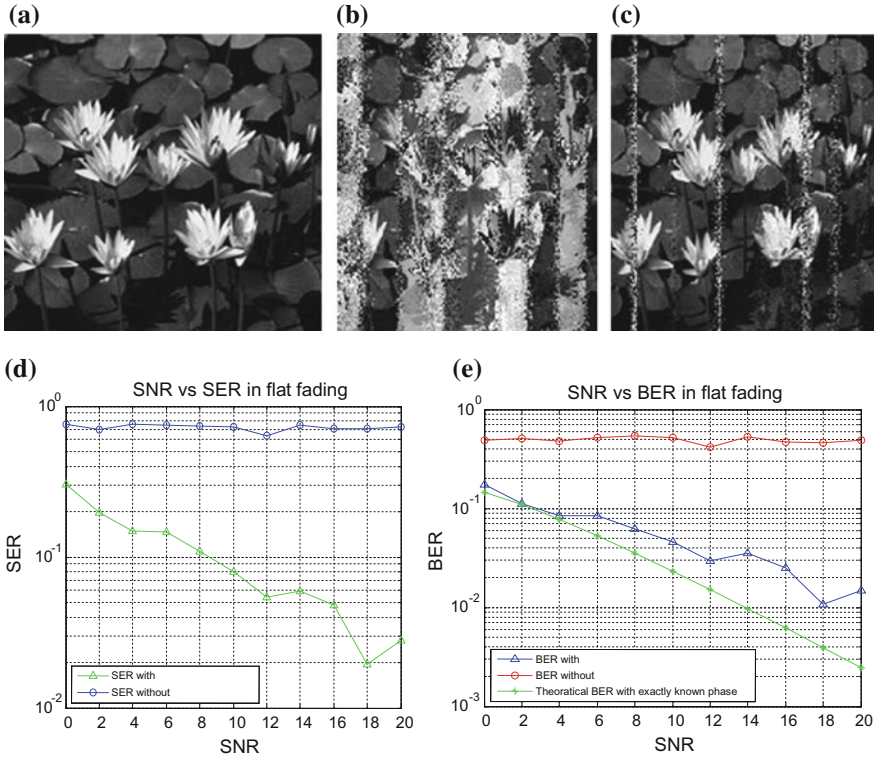

Fig. 4 **a** Original image **b** Received image **c** Adjusted image **d** Graph shows SNR versus SER in flat fading environment with channel estimation **e** SNR versus BER plot in flat fading environment and without channel estimation

In this paper we simulated the different modulation schemes BPSK, QPSK, 8-PSK, with gray encoding in Flat fading environment. We have estimated the BER and SER with and without estimation.

If the modulation order increases BER and SER also increases because of more number of phases. At the same time without channel estimation the BER and SER is also high. As the increase of SNR, BER, and SER decrease. From the above point of view, properly select the Modulation Order and SNR to decrease the BER and SER. For better results use the source encoding also.

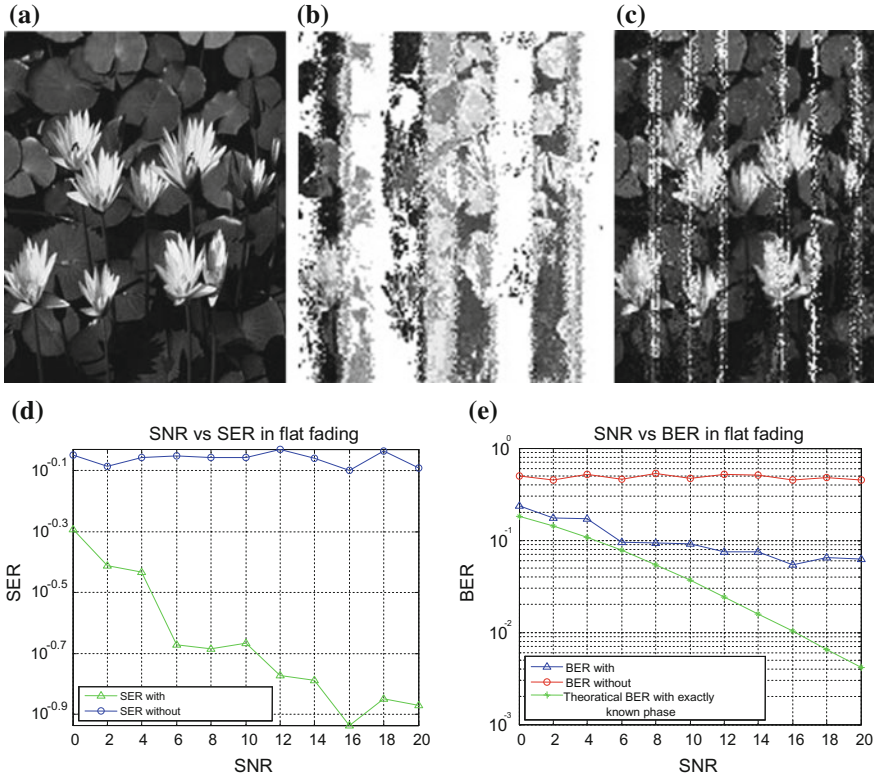

Fig. 5 **a** Original image **b** Received image **c** Adjusted image **d** Graph shows SNR versus SER in flat fading environment with channel estimation **e** SNR versus BER plot in flat fading environment without channel estimation

5 Conclusion

In this paper the comparison was done on the bit error rate (BER) and symbol error rate (SER) of various M-PSK modulations in fading environment. In Rayleigh fading and flat fading mainly the BPSK is compared with QPSK and 8-PSK in terms SER and BER.

References

1. Rappaport TS (2002) Wireless communications: principles and practice, 2nd edn
2. Biglieri E, Proakis J, Shamai S (1998) Fading channels: Information-theoretic and communications aspects. IEEE Trans Inform Theory 44:2619–2692

3. Price R, Green PE (1958) A communication technique for multipath channels. Proc IEEE 46:555–570
4. Foschini GJ (1996) Layered space-time architecture for wireless communication in a fading environment when using multi-element antennas. Bell Labs Tech J 1(2):41–59
5. Yoo D-S, Hafeez A, Stark WE (1999) Trellis-based multiuser detection for DS-CDMA systems with frequency selective fading. In: Wireless communications and networking conference, vol 2. IEEE, pp 829–833
6. Winters JH (1994) The diversity gain of transmit diversity in wireless systems with rayleigh fading. In: ICC '94, pp 1121–1125
7. Proakis JG (2001) Digital communications, 4th edn; Monsen P (1974) Adaptive equalization of the slow fading channel. IEEE Trans 22:1064–1075
8. Crozier S, Falconer D, Mahmoud, S (1989) Shortblock equalization techniques employing channel estimation for fading time dispersive channels. In: IEEE vehicular technology conference, pp 142–146
9. Cimini LJ, Sollenberger NR (1997) OFDM with diversity and coding for high-bit-rate mobile data applications. Mobile Multimedia Communications. Springer, Boston, MA, pp 247–254
10. Simon MK, Divsalar D (1990) Multiple symbol Differential detection of M -PSK. IEEE Trans Commun 38:300–308
11. Bitner JR, Ehrlich G, Reingold EM (1976) Efficient generation of the binary reflected Gray code and its applications. Commun ACM 19(9):517–521
12. Marzetta TL, Hochwald BM (1999) Capacity of a mobile multiple-antenna communication link in Rayleigh flat fading. IEEE Trans Inform Theory 45:139–157
13. Ziv J (1965) Probability of decoding error for random phase and Rayleigh fading channels. IEEE Trans 11:53–61; Pukkila M (2000) Channel estimation modeling
14. Noneaker DL, Pursley MB (1994) Error probability bounds for M-PSK and M-DPSK and selective fading diversity channels. IEEE Trans Veh Technol 43(4):997–1005
15. Proakis J (1968) On the probability of error for multichannel reception of binary signals. IEEE Trans Commun Technol COM-16:68–71
16. Tjhung TT, Loo C, Secord NP (1992) BER performance of DQPSK in slow Rician fading. Electron Lett 28:1763–1765

Part V
Miscellaneous

The Implementation of Rule-Based Early Warning System in Snort Through Email

Aaruni Goel and A. K. Vasistha

Abstract Snort is a network intrusion detection and prevention tool and is used to identify and prevent the different types of attacks on networks. The snort works on the basis of rules enabled or created by the network administrator time to time. In this paper attacks are identified with the help of alert mechanism in the rule set as defined in snort package. The alert notification on email is shown in the form of snapshots. It simply means to deliver the alert in the form of email which makes the flexibility to the administrator to roam anywhere without being taking pain of any missed information related to attacks.

Keywords Intrusion · Snort · Rules · Alert · Swatch and sendmail

1 Introduction

An intrusion detection system (IDS) is a sort of programming or configuration of security software(s) that captures the any type of intrusion detection. An Intrusion Prevention System (IPS) is like the IDS but with the abilities to attempt to stop possible malicious events too. Jointly they are known as IDPS (Intrusion Detection & Prevention Systems) [1].

Snort was developed by Martin Roesch and his group under the umbrella of Sourcefire since December 1998–2013. In 2013 Sourcefire was acquired by Cisco. Snort was created in Language C. Snort performs convention investigation and stuff analyzing to distinguish a range of assaults and tests, for example, buffer overflows, DoS flood attacks, stealth port scans, SMB tests, OS fingerprinting happenings, etc. Snort is accessible in configuration for famous OSs—Windows, Mac OS, Solaris, and Linux.

A. Goel (✉) · A. K. Vasistha
Department of Computer Science and Engineering, Mewar University,
Chittorgarh, Rajasthan, India
e-mail: aaruni.goel@gmail.com

H. S. Saini et al. (eds.), *Innovations in Electronics and Communication Engineering*,
Lecture Notes in Networks and Systems 33,
https://doi.org/10.1007/978-981-10-8204-7_39

1.1 Snort Associates

The architecture and the rules are the important associates of Snort [2]. In continuation of previous work [2], a simple rule is created as [3]:

 # log tcp 10.11.9.234 any -> 160.153.16.37 any (msg: "Miet website is going to be accessed"; priority: 10;)

Here in this scenario: Log type of action will be performed on any TCP data stream packet which originates from local IP address (10.11.9.234) to 'miet.ac.in' college website IP address http://miet.ac.in (160.153.16.37). It is so because in MIET College this experiment is performed by using its all resources. The point to be noted here that in framing this rule it does not concerned about source and destination ports. Any communication between these two IP enabled systems can use any port. Thereby in snort the default syntax here is *any* and is used for both source and destination port addresses. The priority indicates the lowest priority of order 10. The same rule set is applied and demonstrated through the alert mechanism methodology in Sect. 2.

2 Mail Transfer Agents

For alerting the administrator the proposed system uses two important tools Sendmail and Swatch [4, 5].

2.1 Send Mail

In transferring the mail we have used the *sendmail* tool. This tool is written by Eric Allman in 1980s. It is a tool used that finds email routing in an internetworking network environment. It uses SMTP for email transfer. The main motive to use this tool is that it is free for Linux distributions. The command use here to install this tool [5]:

 # apt-get install sendmail mailutils sendmail-bin

Then a directory is created *authinfo* in etc./mail/directory

 # mkdir -m 700/etc./mail/authinfo/

Further in this a new file with name *gmail-auth* is created

 # cd/etc./mail/authinfo/

 # pico gmail-auth

As shown in Fig. 1 the file is opened for making some configurations.

In this file we simply configured typed

AuthInfo: "**U:**root" "**I**:MY_EMAIL ADDRESS"

"**P**: MY_MAIL_PASSWORD".

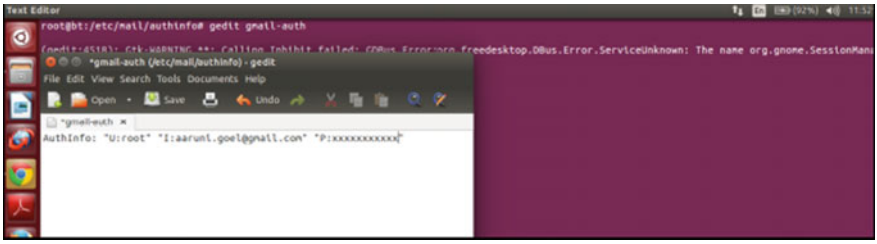

Fig. 1 Accessing gmail_auth file

The bold letters are themselves written on file. Here the email id (aaruni.goel@gmail.com) and its password is typed. In the next step a hash map is created for the above authentication file:

 # makemap hash gmail-auth < gmail-auth

The purpose of the *makemap* program utility is to create the database maps in *sendmail*. The *makemap* command must be used only when we need to create a new database for file like aliases, access, or domain able, mailer table, and virtualize table.

Then a file sendmail.mc is opened at/etc./*mail/*location and some certificate lines are appended as a part of mailing instructions as shown in Fig. 2.

These lines are nothing but the mailer definitions. Now again the configuration of *sendmail* is re-build and reloading it's service. For this purpose the issued command is executed as [4]:

 # make-C/etc./mail

This is the complete installation and configuration of our mail transfer agent), the sendmail. But this configuration is not complete itself since mails take long time to deliver at network administrator's inbox. Then by viewing syslog the answer has found to this problem. In syslog following warning is found:

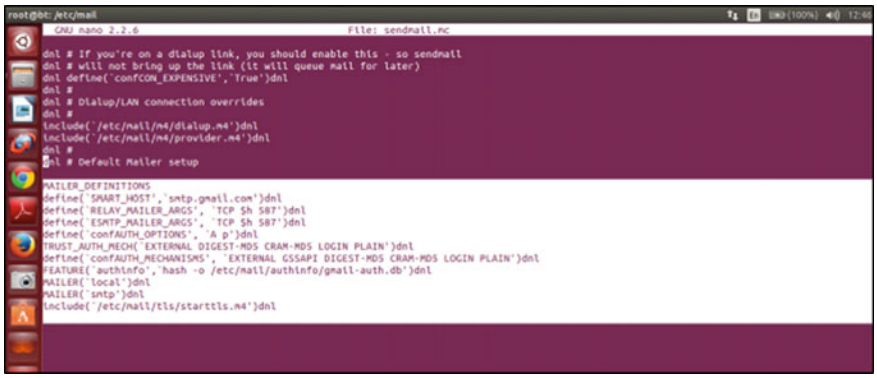

Fig. 2 Adding mailing definitions

"*unqualified hostname unknown; sleeping for retry unqualified hostname*". Due to the said problem the swatch was taking around 2–3 h to deliver the mail to administrator's mailbox.

After going in detailed investigations in syslog the FQDN (frequently qualified domain name) concept was applied and for the same reason the file/etc./hosts was edited in the following manner (see Fig. 3).

It should be clearly mentioned here that in MIET college Dynamic Host Configuration Protocol (DHCP) is implemented for the same reason IP address of machines not remain same throughout the text in this research work.

Here the present system IP address 10.11.9.234 is associated with machine name 'bt' (as the on machine name 'bt' this experiment is performed) in this file. One more thing is that now **127.0.1.1 bt** was commented by **#**. Now it is merely a line with no role on this experiment. Then we restart the installed service *sendmail* and associated parameters by executing following command [5]:

 # /etc./init.d/sendmail reload

The /etc./init.d directory contains various scripts of different services. Basically it is used to activate these services at run time.

2.2 Swatch

In this work the tool *Swatch* is used for this purpose. Swatch simple means 'Simple Watchdog'. Swatch not only helps in central logging but it is also very much beneficial in monitoring the logs on console or through email regularly. The email enabled the administrator to move anywhere. He only needs smart phone; if alert is critical on the basis of priority; he has to just instruct his deputy telephonically to how to resolve the issue. This is the main advantage of Swatch that by receiving timely information network administrators can prevent the network from any

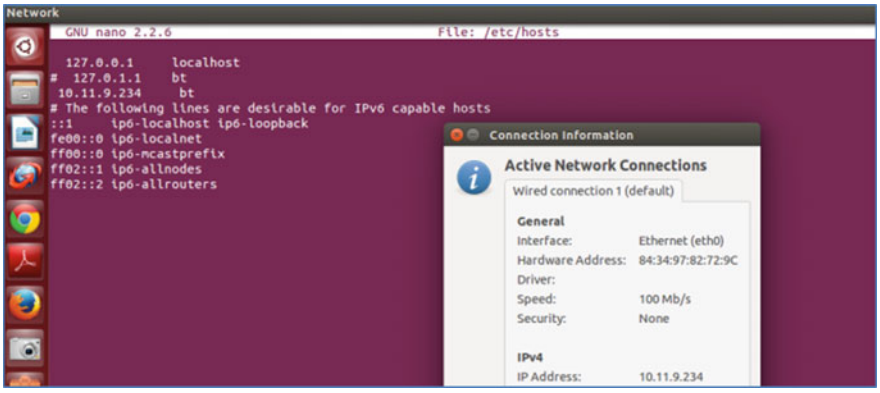

Fig. 3 Altering/etc./hosts file

outside attack or inside security policy violations. Swatch is very much dependent on string or pattern matching facility. Due to this Perl language support is needed. Swatch is divided into three parts: A valid configuration file, Type of actions specified in this file and executing program [5].

The following Fig. 4, portraits the installation part of complete downloaded swatch 3.2.3.tar.gz.

In the Fig. 5, after unzipping the swatch-3.2.3.tar.gz one has to enter in the swatch's directory and make issue the command *cpan*. Basically the *cpan* stands for Comprehensive Perl Archive Network. It contains the various distributions and documentation of softwares written in Perl.

As earlier stated that swatch highly depends on Perl, now further, one has to install date formats (date calculation and manipulation) and file tail script which is

Fig. 4 Installation of swatch

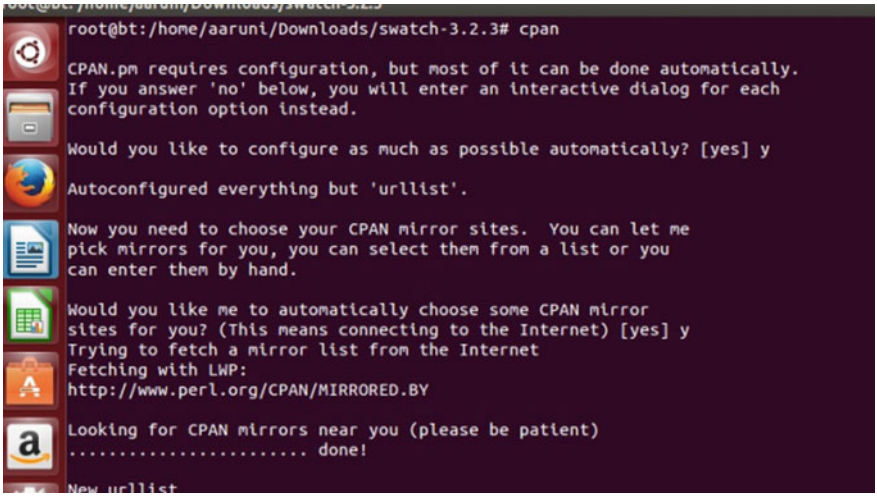

Fig. 5 Nourishing the swatch through *cpan*

responsible to copy and report the new alert on email. So the following command is executed (see Fig. 6) [4].

 # install Date::Calc Date::Manip File::Tail

After this the swatch installation part is completed and one has to exit out the 'cpan' updation. Figure. 7 illustrates the configuration of swatch.txt file which is used to and primarily responsible to send the alert in the form of mail to *aaruni.goel@gmail.com.*

The configuration file is swatch.txt and contains some important syntax like and used in this work to show the color, i.e., green (of text at terminal) and with subject —*Snort IDS Alert*—(refer Fig. 7). The explanation of swatch.txt is described and implemented as under [5]:

- watchfor/snort: /which simply means to watch the logs of Snort at Snort's log folder.
- echo green: Display the alert in green color fonts.

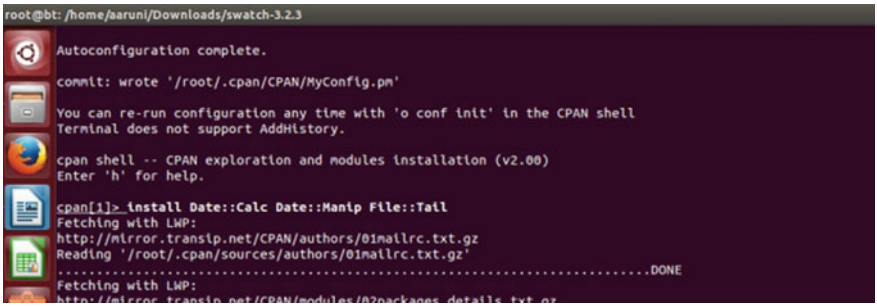

Fig. 6 Installing date and tail package from cpan

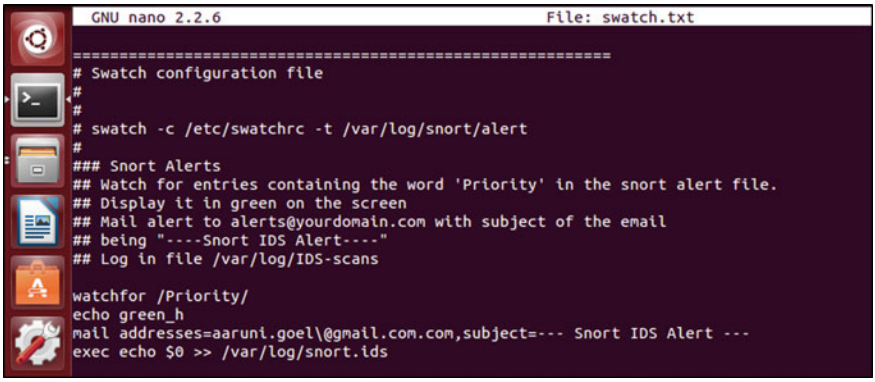

Fig. 7 Swatch configuration file

- mail: TO_MY_EMAIL with a subject— Snort IDS Alert — TO_MY_MAIL is now *aaruni.goel@gmail.com*
- exec echo $0: It means to display the content to console and email whenever new alerts are found in*/var/log/snort.ids*. $0 says that complete line (i.e. tail part) as per the alert received by user to be displayed in email or console.

2.3 *Delivery of Email Alert*

At last we now demonstrated the transfer of mail to network administrators. This is accomplished by first we open the MIET website (www.miet.ac.in). (refer Fig. 8).

Remember in Sect. 2 under rule section we issued the rule to log and identify those traffic packets when any activity is going to access MIET website. In this section the same command with very little (alert in place of log) is used and change as under:

 # alert tcp 10.11.9.234 any -> 160.153.16.37 any (msg: "Miet website is going to be accessed"; priority:10;)

Now Snort IDS command and swatch command are executed in parallel [3, 4, 5]:

 # swatch -c/etc./swatch.txt –script-dir =/etc. –tail-file =/var/log/snort.ids

The swatch command after execution will read swatchch.txt file content (refer Fig. 9) and on this basis it will reflect the contents of snort.ids to console as well as on email.

The snort on other side is running its packet intrusion detection command which tells snort to inspect the packets received from Ethernet adapter (eth0) and check their validity as per policies as for which snort is configured. The Fig. 9 demonstrates the idea of simultaneous execution of both commands [3, 4].

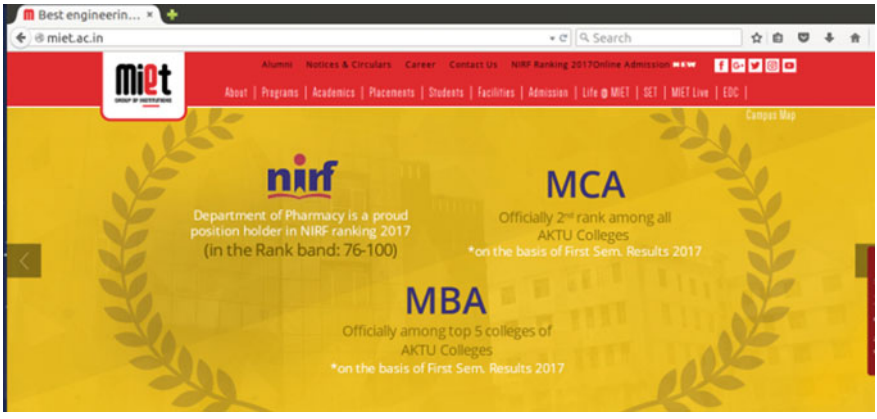

Fig. 8 Miet website homepage

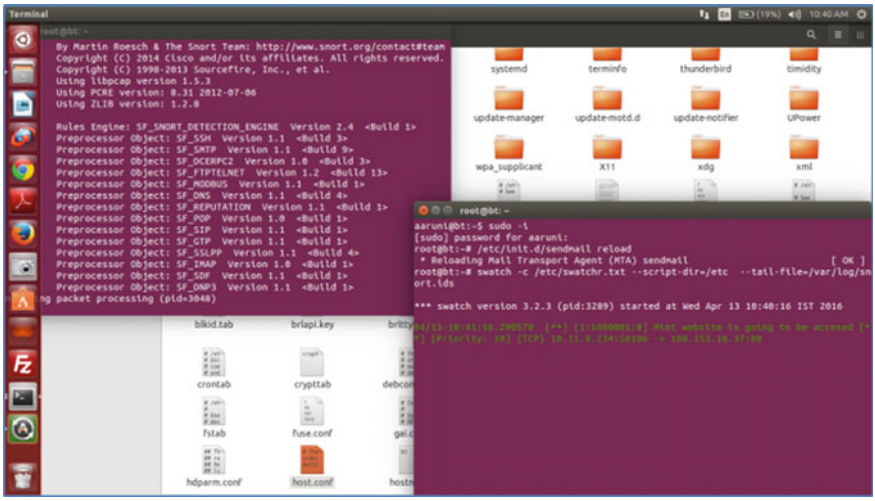

Fig. 9 Snort as an ids and swatch as a mail dispatcher

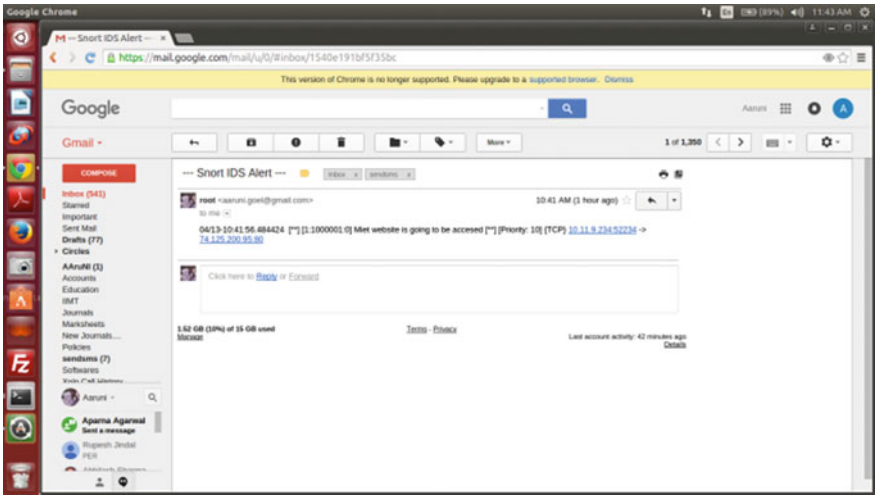

Fig. 10 The received alert mail to administrator's Inbox

 # snort –eth0 –c/etc./snort/snort.conf -l/var/log/snort

The resultant output is that when anybody in the network tries to access https://miet.ac.in. it will alert the email *aaruni.goel@gmail.com*. The output of this last step is demonstrated in Fig. 10.

The Fig. 10 finally identifies the anatomy of email sent to administrator mail and verifies the configuration of Fig. 1. The Fig. 11 depicts the more details of this mail like subject and text body.

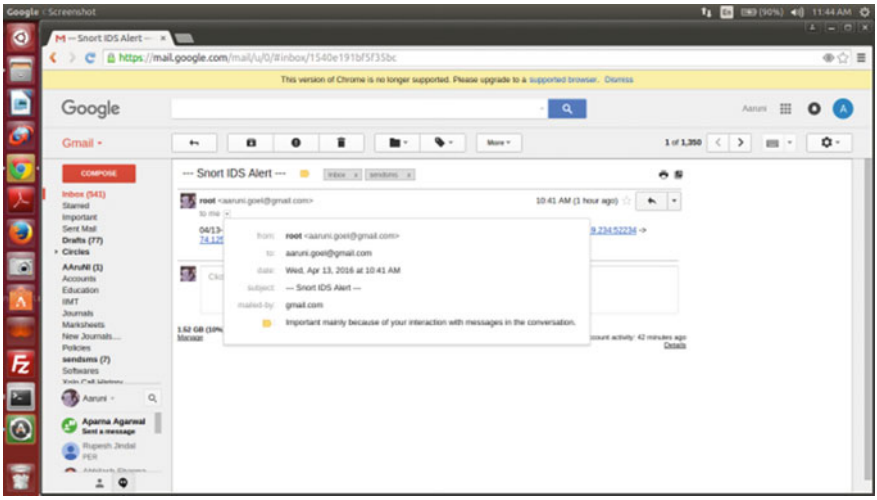

Fig. 11 The anatomy of alert mail

3 Conclusion

In this paper we enjoyed snort but main things, that on which we like to put light are tools. In this very case it is expected from snort designers that they should focus on some proper self-built instant alert reporting tools. However there are some third party tools available but how much they are accountable in terms of compatibility this is again a zigzag puzzle. This is the reason that mail delivery system through swatch and *sendmail* is very slow and we have to configure the FQDN (Fully Qualified Domain Name). After configuring FQDN this problem is solved but still the mail delivery system is still not so strong in terms of speed. So in near future, designers, scientists and authors must put their eyes to alert the administrator instantly on mail on anyhow basis.

References

1. Goel A, Vasistha AK A review on foundation of network intrusion detection and prevention system. Int J Electr Eng 9(1):125–137
2. Goel A, Vasistha AK The implementation and assessment of snort capabilities. Int J Comput Appl 167(13):15–23
3. Sourcefire Inc, Roesch M, Green C (2013) SNORT Users Manual—SNORT Release: snort-2.9.7.2. http://www.snort.org
4. Caswell B, Beale J, Baker A (2007) Snort intrusion detection and prevention toolkit, Syngress. Elsevier
5. Frederick M, Avolio, Paul A (1995) Vixie, Send mail: theory and practice. Digital Press

Robust Secure Routing Protocol for Mobile Ad Hoc Networks (MANETs)

Ravilla Dilli and P. Chandra Sekhar Reddy

Abstract Secure Hash Algorithm (SHA-3) is a next generation security standard used in the world of electronic communications where the digital messages are transformed into "message digest" for creating digital signatures. Any changes in the original message leads to a change in the message digest and it becomes easy to detect the modifications to the original message. Hash functions are used in message authentication. They are also used in routine software upgrades to make sure that the new software has not been tampered with. SHA-3 is a family of functions based on Keccak, some of them can be implemented with minimal additional circuitry on a chip and are very useful alternatives for providing security in small devices. SHA-3 is not a replacement for SHA-2 but it is offered as a backup. So far, there is no procedure that exists to crack the SHA-2 and still remains secure and viable. In this paper, HMAC-SHA-3 standard algorithms were used to address Data Integrity of the message being sent using AODV routing algorithm for MANETs. Message authentication, confidentiality, Integrity were addressed using secure routing. All possible attacks were addressed in AODV using SHA-3 algorithm and the tool used for simulation was Qualnet 7.4.

Keywords Hash function · Secure hash algorithm · Digital signatures HMAC-SHA-3 · Message authentication code · AODV · Qualnet 7.4

R. Dilli (✉)
Department of ECE, Manipal Institute of Technology, Manipal, India
e-mail: dilli.ravilla@gmail.com

P. Chandra Sekhar Reddy
Department of ECE, JNT University, Hyderabad, Andhra Pradesh, India
e-mail: drpcsreddy@gmail.com

H. S. Saini et al. (eds.), *Innovations in Electronics and Communication Engineering*,
Lecture Notes in Networks and Systems 33,
https://doi.org/10.1007/978-981-10-8204-7_40

1 Introduction

Mobile Ad hoc wireless networks (MANETs), because of their quick and low cost deployment, they are used in collaborative and distributed computing, emergency operations, military, wireless sensor, and mesh network architectures. The design, deployment, and performance of a MANETs system are affected by Routing, Security, Medium access scheme, Energy management, Addressing, Scalability, Self-organization, and Deployment considerations [1]. The responsibilities of a routing protocol include the route information exchange, finding a shortest path to a receiver node based on criteria like hop count, minimal power consumption, and link lifetime, collecting information about the link breaks, repair the broken links with by spending minimal processing power [2] and bandwidth. A routing protocol for MANETs must be completely distributed [3] than centralized and adaptive to topology changes frequently due to mobile nodes. Route computation must be loop-free, free from stale routes and less number of nodes should involve in route maintenance. Each node in the network must have local route information and minimum route discovery delay with minimal number of broadcast packets to reduce packet collisions. It is required to have reliable packet transmissions to avoid the occurrence of stale routes and message loss. After the network topology gets stability, the routing protocol must converge to optimal routes and convergence must be faster. Only the stable local topology information must be stored at each node. Based on the applications, quality of service (QoS) and time-sensitive traffic support must be provided [4].

The major security threats [5, 6, 7] that exist in MANETs are Denial of service (DOS), Resource consumption, Energy depletion, Buffer overflow, Host impersonation, Information and disclosure. A malicious node can claim that it has an optimum route to the destination node and make all other nodes to route the packets through it. After receiving the packets from other nodes it simply drop the packets without informing neither source node nor destination node. Gray-hole attack [8, 9, 10] is a variation of black hole attack where the selective packets or packets on probabilistic basis are dropped by a malicious node. An Ad hoc on-demand distance vector (AODV) routing protocol was considered in this paper for validating against various security threats using SHA-3 algorithm. In the initial stage, if the route is not available to the desired destination then the source node sends a Route Request (RREQ) packet in the network using flooding technique. There is a possibility to have more than one route to different destinations from a single RREQ. Any given node updates its route information if and only if the DestSeqNum of the received packet is greater than the DestSeqNum stored at the node.

No local path repairs of a broken link are available in AODV. The link failures are identified using periodical beacons or through link-level acknowledgments (ACKs) and those are informed to the source and destination nodes. Once the sender node realizes about the link failure, it tries to establish the route again to the destination [11]. As long as the source node does not move, the path remains same and it need not to initiate protocol action. The Route Error message (RERR) will be

sent to the sender node if the receiver node or intermediate nodes are moved and this message is initiated by the nodes upstream of the failed link. AODV protocol uses periodic broadcast of hello packets to keep track of neighbors [12].

2 Secure Hash Algorithms

2.1 SHA-3 Algorithm

Using hash functions, it is hard to show $H(m_1) = H(m_2)$ for two different input messages m_1 and m_2. A hash function must be computationally efficient, it means that the processing speed delay must be lower [13]. SHA-3 is a next generation security standard used in the world of electronic communications where the digital messages are transformed into "message digest" for creating digital signatures. Any changes in the original message leads to a change in the message digest and it becomes easy to detect the modifications to the original message. Hash functions are used in routine software upgrades to make sure that the new software has not been tampered with and to have message authentication. SHA-3 is a family of functions based on Keccak, some of them can be implemented with minimal additional circuitry on a chip and are very useful alternatives for providing security in small devices. SHA-3 is not a replacement for SHA-2 [14] but it is offered as a backup. So far, there is no procedure that exists to crack the SHA-2 and still remains secure and viable [15]. SHA-3 offers significantly better performance for hash-based MACs on short messages [16] (Fig. 1).

2.2 Bruteforce Attacks on Hash Functions

First, for a given hash value "*H*", it is difficult to find $H(m_1) = `m_2`$ and this property is called "*Attacking on-wayness*". Second, for a given hash value "*H*", finding any two messages 'm_1', 'm_2' such that $H(m_1) = H(m_2)$ and this property is called "*Attacking collision resistance*". The usage of HMAC with a secure hash functions and as per the specifications (size of the key, and usage of correct output), at present there are no attacks against HMAC in practical (Fig. 2).

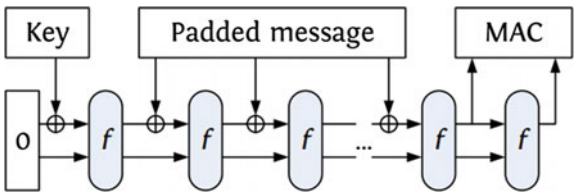

Fig. 1 Message authentication codes using KECCAK or Sponge [16]

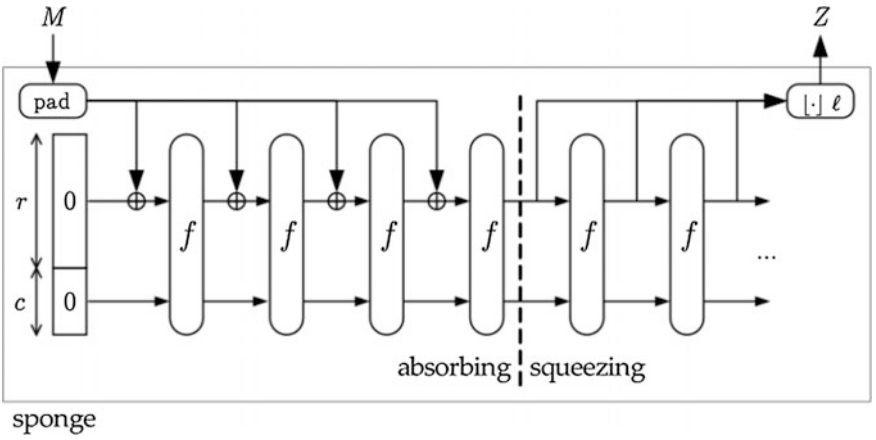

Fig. 2 Sponge structure [16]

The Sponge structure of SHA-3 algorithm consists of two stages called "Absorbing state", "Squeezing state". In the absorbing state, there is initialization, padding, XOR operation with message block and then applying the compression function. There is repetitive XOR operations with the message blocks and applying to the compression function as shown in the Fig. 5. In the second stage, extract the output by applying compression function in repetitive fashion [17] (Tables 1 and 2).

The simulation scenario consisting of 10 CBR connections and AODV routing Protocol that uses SHA-3 algorithm for secure information transmissions in the wireless network.

Table 1 Simulation parameters

Parameter	Value
Simulation time	600 s
Network area	1 km × 1 km
Network size	50 nodes
Channel	Wireless
MAC layer protocol	IEEE 802.11
Mobility model	Random way point
Pause time	30 s
Number of connections	10 CBR (TCP)
Node speed	1–10 m/s
Input data rate	2 Mbits/s

Table 2 Simulation parameters for security protocol

Parameter	Value
Length of hash code	512 bits
Length of digital signature	512 bits
Length of public key	512 bits
HELLO message interval	1.0 s

3 Performance Analysis of AODV Using SHA-3 Algorithm

In this paper, we have used SHA-3 family algorithms in AODV Protocol for MANETs. The analysis of the protocol is performed against various security attacks. First we have addresses the block-hole attack, cooperative block-hole attack, and then Denial-of-Service (DoS) attack in AODV [12, 18, 19]. The nodes send data at rates 2 Mbps for a duration of 600 s and the nodes move as per Random waypoint mobility mode with maximum speed of 10 m/sec. The size of each message is 512 bytes with data rate of 2 Mbps.

The values shown in Figs. 3, 4 and 5 show that the average PDR is higher in SAODV with SHA-3 standard algorithm than conventional AODV at the cost of higher Average End-to-End delay and Average load in the network. The reason behind this is that the computational time or processing time takes at each intermediate nodes to verify the authenticity and integrity taken into account. The routing load increases due to the appending of the hash value along with message being forwarded.

In the worst case scenario, SHA-3 gives 15% better performance than AODV without security features. We have used Qualnet 7.4 Simulator for simulating the performance of SAODV with PDR, End-to-End delay and Average Routing load as metrics. We have addressed all possible attacks including Denial-of-Service (DoS) attack, Black hole attack [20, 21].

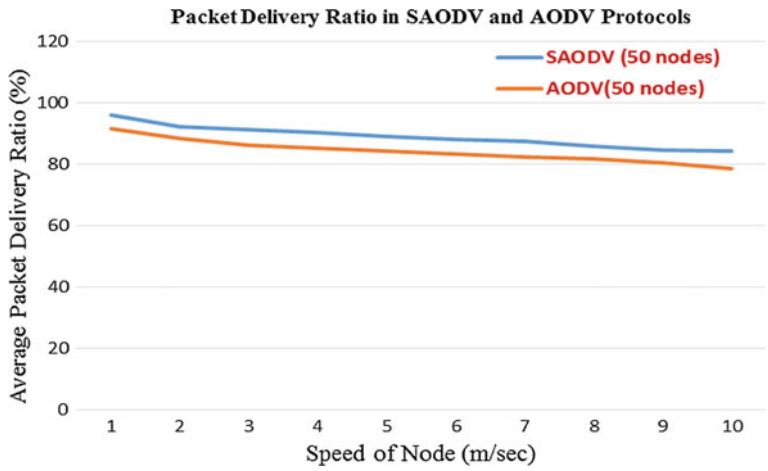

Fig. 3 Comparison of packet delivery ratio (PDR) for AODV and SAODV protocols

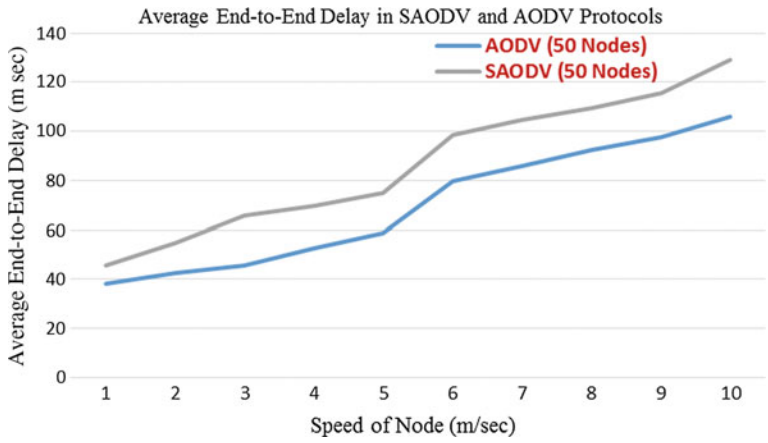

Fig. 4 Comparison of end-to-end delay for AODV and SAODV protocols

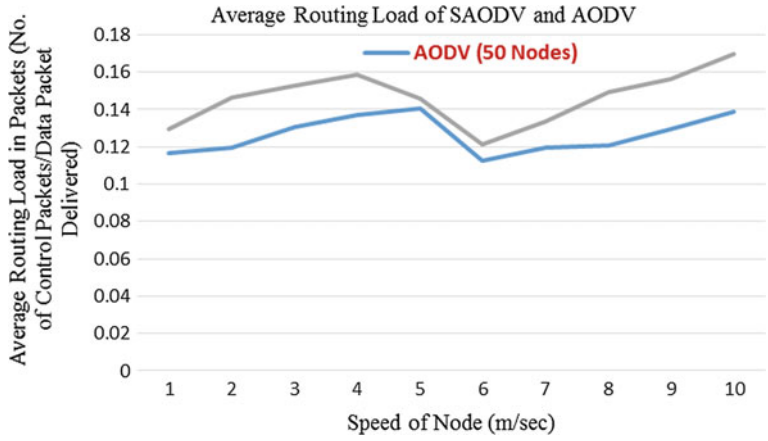

Fig. 5 Comparison of average routing load for AODV and SAODV protocols

4 Conclusions and Future Scope

The performance of AODV against various security attacks are tested using Qualnet 7.4 Simulator. It is shown that introducing SHA-3 standard algorithms further improves the network throughput, packet delivery ratio at the cost of increasing average end-to-end delay and average routing load. Even though, SHA-2 is not broken, but still it is required to provide more security in MANETs. The areas for research and improvements are the different modes of using compression function and use of compression function itself to improve the performance further. Also better techniques to provide trade-off between memory cost and computational time in computing the hash code.

References

1. Govindasamy J, Punniakody S (2017) A comparative study of reactive, proactive and hybrid routing protocol in wireless sensor network under wormhole attack. J Electr Syst Inform Technol. Available online 26 Apr 2017
2. Mazhar N, Farooq M (2011) A hybrid artificial immune system (AIS) model for power aware secure Mobile ad hoc networks (MANETs) routing protocols. Appl Soft Comput 11(8):5695–5714
3. Banoth R, Narsimha G (2016) Trust based certificate revocation for secure routing in MANET. Procedia Comput Sci 92:431–441
4. Murthy CSR, Manoj BS (2004) Ad hoc wireless networks architectures and protocols. Prentice Hall
5. Kim J, Tsudik G (2009) SRDP: secure route discovery for dynamic source routing in MANETs. Ad Hoc Netw 7(6):1097–1109
6. Walikar GA, Rajashekar C (2017) A survey on hybrid routing mechanisms in mobile ad hoc networks. J Netw Comput Appl 77:48–63 (1 Jan 2017)
7. Salehi M, Boukerche A, Amir D (2016) Modeling and performance evaluation of security attacks on opportunistic routing protocols for multihop wireless networks. Ad Hoc Netw 50:88–101 (1 Nov 2016)
8. Sarkar S, Datta R (2016) A secure and energy-efficient stochastic multipath routing for self-organized mobile ad hoc networks. Ad Hoc Netw 37:209–227, Part 2 (Feb 2016)
9. Al-Shurman M, Yoo SM, Park S (2004) Black hole attack in mobile ad hoc networks. In: ACMSE'04, 2–3 April 2004, Huntsville, AL, USA
10. Medadian M, Yektaie MH, Rahmani AM (2009) Combat with black hole attack in AODV routing protocol in MANET. In: 2009 1st Asian Himalayas international conference on internet, 3–5 Nov 2009
11. Lu S, Li L, Lam KY, Jia L (2009) SAODV: a MANET routing protocol that can withstand black hole attack. In: 2009 international conference on computational intelligence and security
12. Tamilselvan L, Sankaranarayanan V (2007) Prevention of blackhole attack in MANET. In: The 2nd international conference on wireless broadband and ultra wideband communications (AusWireless 2007)
13. Stallings W (2012) Cryptography and network security, 5th edn, pp 310–318
14. Dilli R, Chandra Shekar Reddy P (2015) Routing using trust based system with SHA-2 authentication. Procedia Comput Sci 46:1108–1115
15. Dilli R, Chandra Shekar Reddy P (2015) Enhancing the security of MANETs using hash algorithms. Procedia Comput Sci 54:196–206
16. SHA-3 standard: permutation-based hash and extendable-output functions, federal information processing standards publication, FIPS PUB 202. http://nvlpubs.nist.gov/nistpubs/FIPS/NIST.FIPS.202.pdf
17. Siavash B, Mehran MK, Arash RM (2014) Efficient and concurrent reliable realization of the secure cryptographic SHA-3 algorithm. IEEE Trans Comput-Aided Des Integr Circ Syst 33 (7) (July 2014)
18. Ramaswamy S, Fu H, Manohar S, Dixon J, Nygard K (2003) Prevention of cooperative black hole attack in wireless ad hoc networks
19. Perkins CE, Royer EM (2003) Ad hoc on demand distance vector (AODV) routing. https://tools.ietf.org/id/draft-ietf-manet-aodv-02.txt
20. Satoshi K, Hidehisa N, Nei Kato, Abbas J, Yoshiaki N (2007) Detecting blackhole attack on AODV-based mobile ad hoc networks by dynamic learning method. Int J Netw Secur 5 (3):338–346 (Nov 2007)
21. Raj PN, Swadas PB (2009) Dpraodv: a dyanamic learning system against blackhole attack In AODV based MANET. Int J Comput Sci Issues (IJCSI) 1:54–59 (Aug 2009)

Derived Genetic Key Matching for Fast and Parallel Remote Patient Data Accessing from Multiple Data Grid Locations

K. Ashokkumar, P. Saravanan and Rusydi Umar

Abstract In recent years, grid computing has made a fast growth in many scientific experiments and research centers in the area of medicine, scientific computation. Many research works in data grid using replication algorithm and scheduling strategies for managing large data were introduced. However, replication and scheduling strategies pose significant threat when applied in biomedical area due to parallel access limitation in grid. In this paper, Derived Genetic Key Matching (DGKM) technique is introduced for quick parallel accessing of data (heart disease patient data) available in multiple grid locations. The storage key of patient data in multiple grid locations is synchronized to improve data integrity for effective disease diagnosis. DGKM in distributed grid services allows parallel and integrated data accessing with minimal key matching time. Further, Vantage Point (VP) tree indexed Berkeley key model is designed to optimize (patients) data storage at different grid locations. The proposed technique is implemented by GridSim and is tested using Cleveland Clinic Foundation Heart disease dataset. The results showed better performance in improving data access speed by 17.04% and accuracy of integral patient data from corresponding grid location by 15.13% compared to state-of-the-art works.

Keywords Grid computing · Derived genetic · Key matching · Parallel accessing · Gene populations · Parallel computing

K. Ashokkumar (✉) · P. Saravanan
School of Computing, Sathyabama University, Chennai, India
e-mail: ashokkumar.cse@sathyabama.ac.in

R. Umar
Department of Informatics Engineering, Faculty of Industrial Technology,
Ahmad Dahlan University, Yogyakarta, Indonesia
e-mail: rusydi@mti.uad.ac.id

H. S. Saini et al. (eds.), *Innovations in Electronics and Communication Engineering*,
Lecture Notes in Networks and Systems 33,
https://doi.org/10.1007/978-981-10-8204-7_41

1 Introduction

The grid is a combination of hardware and software infrastructure that offers reliable, dependable, pervasive, and economical access to high-end computational capacity. In [1], a dynamic data replication algorithm was introduced to reduce the job execution time with effective network usage. The dynamic data replication algorithm minimized data access time by improving the overall performance of system. Enhanced dynamic hierarchical replication [2] minimized data access time using Weighted Scheduling Strategy (WSS). Virtualization of process for big data in cloud environment [3] was handled using network-related computational resources. A review of grid allocation was performed in [4]. Nash equilibrium was introduced in [5] to improve computational capability while assigning grid by several users. However, in many real scenarios, involving multilingual solutions, accuracy and time for allocation of grid in the field of biomedical have to be suggested. Therefore, key matching indexes (i.e., using the attributes for heart disease diagnosis) based on gene population and vantage point are presented in this paper.

Allocation of grid in cloud computing becomes more and more complicated with the applications and characteristics of multi-server system. In [6], a framework for optimal multi-server configuration was introduced to optimize server speed without compromising quality of service. An adaptive algorithm was introduced in [7] to ensure parallel processing by reducing prediction errors in a significant manner. In [8], multi-objective game theory was introduced to solve fairness and efficiency using communication and storage-aware multi-objective algorithm.

Heterogeneous allocation of resources [9] applied *K*-means clustering algorithm to minimize workload requirements. Efficient data storage and parallel processing in mobile cloud were handled in [10] using k-out-of-n computing. However, biomedical data integrity lacks, which is addressed through synchronization of storage key with grid location in DGKM technique.

Developing incredible parallel computing architectures in [11], parallel computation was performed using Exchanged Cross Cube (ECC) technique. Fuzzy logic for composition optimization [12] was introduced with objective of assigning weights across different geographical locations (grid). Attribute-based solution was introduced in [13] to address scalability and provide fine-grained access control in cloud environment.

In order to perform parallel processing and improve data sharing in cloud, object-centered approach [14] ensures accountability. Continuous aggregation of queries to ensure parallel processing [15] used cost-based query planning. However, the time taken for allocation of grid with respect to biomedical data that helps in diagnosis of disease remained unaddressed. Therefore, reduce time key matching indexes based on derived gene population for heart disease diagnosis in DGKM technique.

A hybrid approach was introduced in [16] to improve the rate of record matching using privacy-preserving partitioning. Saturn [17] reduced the load balancing and

minimizing rate of fault using horizontal and vertical replication. In [18], fault tolerance with distributed systems was introduced to resource allocation problems using Byzantine fault tolerance. Fast allocation of resources using keywords search was performed [19] to reduce query response time. Extended sub-tree [20] improved runtime efficiency by applying distance function. Classification of classical swine flu virus [21] developed potential for new vaccines using antigenic characterization. In [22], a review for treatment of Pilon fracture was presented. Characterization of pseudomonas that inhibits the rice fungal pathogens was introduced for efficient classification of fungal pathogens.

In this paper, with input data drawn from Cleveland Clinic Foundation Heart disease dataset from UCI repository, three strategies are proposed. First, a novel synchronization technique for storage key to grid location that takes into account input attributes and grid location attributes is presented. Second, a novel matching index strategy provides matching between the attributes and its values for heart disease diagnosis, called key matching indexes. The key matching indexes based on derived gene population improves the proposed technique by using a fitness function, which evaluate solution domain leading to heart disease in an efficient manner [23, 24]. Finally, a vantage point tree index improves the data integrity speed rate in an extensive manner.

The rest of this paper is organized as follows: Sect. 2 proposes our Derived Genetic Key Matching (DGKM) technique for heart disease diagnosis. In Sect. 3, experimental settings for DGKM technique are presented. In Sect. 4, discussion of table values and graph form is presented. Finally, Sect. 5 concludes our work.

2 Materials and Methods

The printing area is 122 mm × 193 mm. The text should be justified to occupy the full. The parallel accessing of data grid at different locations needs to be handled properly, to improve the computational and resource efficiency of the grid data environment.

In this section, derived genetic key matching for quick parallel accessing for efficient heart disease diagnosis is presented. For improving grid location identification where factors leading to heart disease are stored, reducing time taken for key matching improves data integrity rate. Those perform better access data from multiple grid locations and improving the data access speed. The architecture of the proposed Derived Genetic Key Matching (DGKM) technique is shown in Fig. 1.

Figure 1 shows the block diagram of DGKM technique with input obtained from heart disease dataset. As shown in the figure, the DGKM technique is divided into three parts. The first part performs efficient synchronization of storage key to grid location for efficient heart disease diagnosis to improve data integrity rate. Key matching indexes using derived gene population are performed, which introduces the features and factors resulting in heart disease in the second part with aiming at reducing time taken for key matching. Finally, vantage point tree index using

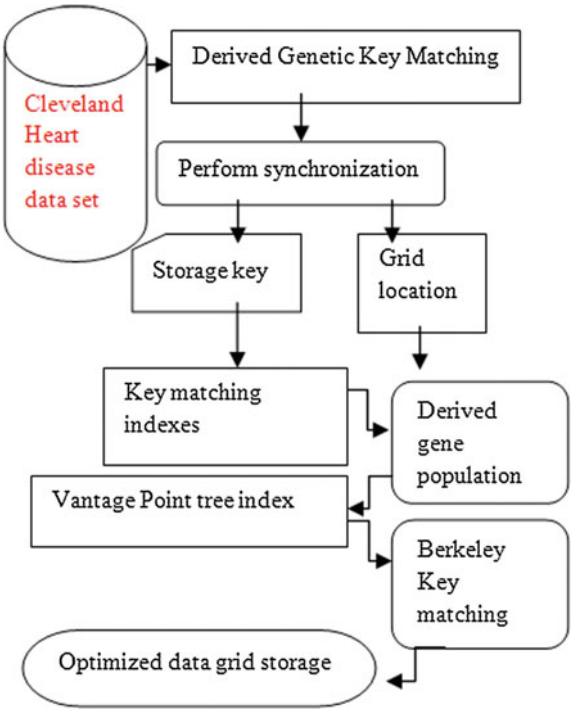

Fig. 1 Block diagram of DGKM technique

Berkeley key matching algorithm results in optimized data grid storage, therefore improving the data grid access rate.

2.1 Synchronization of Storage Key with Grid Location

The first step in DGKM technique is efficient synchronization of storage key to the grid location. The synchronization is performed to identify the request data that cause heart disease for multiple users or patients from different locations and improving the data integrity rate.

Figure 2 shows a given input with multiple users "$\text{User}_i\,\text{User}_1$, $\text{User}_2, \ldots, \text{User}_n$" or patients and "*SK*" storage keys for each patient, with grid locations $\text{GridLoc}_i = \text{GridLoc}_1, \text{GridLoc}_2, \ldots, \text{GridLoc}_n$.

The synchronization of storage key to grid location involves associating storage key to grid location. Multiple users or patients located at different places request for the factors leading to heart disease. A string of features "$SK_1, SK_2, \ldots, SK_n$" that represents the attributes is used to represent each storage key. The mathematical formulation for each feature is as given below:

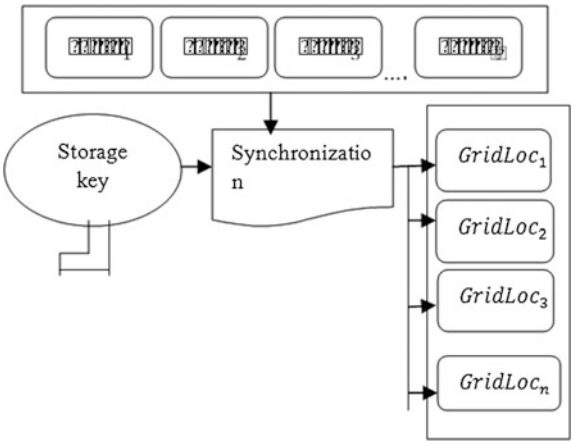

Fig. 2 Block diagram of synchronization of storage key with grid location

$$SK_i = (\text{Key}_{\text{id}}, L_i) \tag{1}$$

From (1), the storage key "SK_i" includes two attributes, where "Key_{id}" represents the key allotted for each user "User_i" (i.e., patient) and "L_i" denotes the length of the storage key, respectively.

The synchronization of storage key to the grid location problem now minimizes to multiple key indexing matchings. Let us consider the input user "$\text{User}_i = \text{User}_1, \text{User}_2, \ldots, \text{User}_n$" with "$|\text{User}_i| = n$ features" where "User_k" is the "kth feature" including attributes as given below:

$$\text{Input Attr}\,(SK_i)(\text{Key}_{\text{id}}(\text{User}_k), L_i(\text{User}_k) \tag{2}$$

Let us consider the grid locators as "$\text{GridLoc}_1, \text{GridLoc}_2, \ldots, \text{GridLoc}_n$", where "$\text{GridLoc}_i = \text{GridLoc}_{i,2}, \ldots, \text{GridLoc}_{i,j}$"; the grid locators include the information relating to the factors resulting in heart disease. For example, a patient with fasting blood sugar > 120 mg/d with maximum heart rate achieved, and exercise-induced angina has highest probability of obtaining heart disease. Here, "$\text{GridLoc}_{i,k}$" is the "kth" input feature of "ith" location comprising attributes as given below:

$$\text{Grid Location Attributes} = \text{Key}_{id}\left(\text{GridLoc}_{i,k}\right), L_i\left(\text{GridLoc}_{i,k}\right) \tag{3}$$

From (2) and (3), after each iteration "$I = I_1, I_2, \ldots, I_n$" corresponds to mapping function "f" from input attributes "InputAttr" with grid location attributes "GridLocationAttributes" which is designed in such a way that the following condition is met:

$$I_m = f(\text{User}_m) = \text{GridLoc}_i \tag{4}$$

Input: users ' $User_i = User_1, User_2, \ldots, Us_t$ ', storage keys '$SK_1, SK_2, \ldots, S$', grid locations '$GridLoc_i = GridLoc_1, GridLoc_2, .., GridLc$',

Output: Efficient synchronization of storage key to grid location

Step 1: **Begin**
Step 2: **For** each user Us
Step 3: Extract features using (1)
Step 4: Evaluate input attributes using (2)
Step 5: Evaluate grid location attributes using (3)
Step 6: Perform synchronization using (4)
Step 7: **End for**
Step 8: **End**

Fig. 3 Algorithms for SKGLS

From (4), synchronization of storage key to the grid location is performed. Significant manner is to identify the request data for multiple users (i.e., patients) at different locations from different hospitals across the region. This in turn improves data integrity rate. The Storage Key Grid Location Synchronization (SKGLS) algorithm works as given below.

The SKGLS algorithm (in Fig. 3) is used to perform efficient synchronization of storage key to grid location with objective of improving the data integrity rate. For each user, the algorithm starts with the extraction of possible features. With the evaluated features, input attributes and grid location attributes are obtained. With the aid of these two attributes, synchronization is performed in an efficient manner.

2.2 *Construction of Key Matching Indexes Based on Derived Gene Populations*

The second step in DGKM technique in distributed grid services allows for parallel and integrated data accessing. With derived gene populations of key matching indexes, aim at reducing the time taken for key matching. In key matching indexes based on derived gene population, efficient matching is performed. Efficient key matching indexes are handled using derived gene population with aid of fitness function to evaluate the solution domain (i.e., key matching indexes).

Figure 4 shows the derived gene populations (i.e., "$\text{User}_1, \text{User}_2, \ldots, \text{User}_n$") of key matching indexes. Efficient key matching indices are performed using fitness function with derived gene population for different patients as given below:

$$\begin{aligned} \text{Fitness} &= \{\ \text{User}_i | f(\text{User}_i) \\ &= SK_i, \text{GridLoc}_{i,m}\} + \{f(\text{User}_i) = SK_j, \text{GridLoc}_{j,n}\} > \alpha \end{aligned} \tag{5}$$

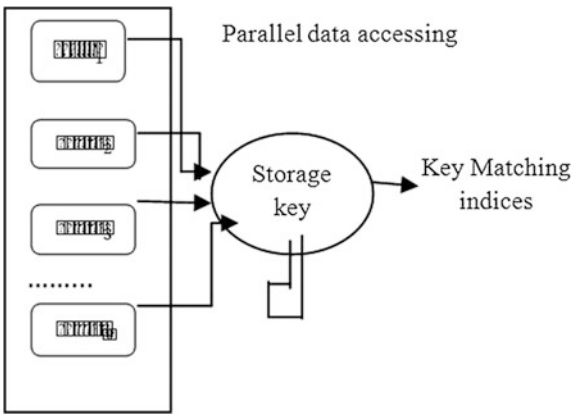

Fig. 4 Block diagram of key matching indexes

From (5), efficient key matching index "KMI" is performed where the first statement marks the storage keys assigned to different users. The second statement marks the features with storage key not matched by function "*f*". The key matching index using Pearson correlation coefficient is as given below:

$$\mathrm{KMI} = \left(\frac{\sum_{i=1}^{n} \mathrm{User}_i, \mathrm{Key}_{id}}{\sum_{i=1}^{n} \mathrm{User}_i} \right) \tag{6}$$

From (6), the key matching indexing "KMI" is evaluated on the basis of similarity between derived gene population "User_i" and storage keys "Key_{id}", respectively. So the storage key that matches with the users are only subjected to key matching which in turn reduces the time for key matching

2.3 *Vantage Point (VP) Tree Indexed Berkeley Key Matching*

In this section, the application of Vantage Point (VP) tree indexed Berkeley key matching algorithm is explained for efficient heart disease diagnosis. The Vantage Point (VP) tree indexed Berkeley key matching algorithm is developed to optimize different data grid storages corresponding to grid server location. Vantage points are used to split the grid storage that includes leading to heart disease in the form of tree structure and performs the process of hierarchical manner. VP tree indexed Berkeley key matching algorithm in DGKM improves the speed of parallel data accessing from distributed grids, which efficiently identifies the cause factor for heart disease from different regions. Tree indexed key matching process is periodically performed from several patients from different regions for data accessing.

Let us discuss the Vantage Point (VP) tree to partition the grid storage around selected vantage points at several levels to form a hierarchical tree structure.

The tree indexed Berkeley key algorithm is then used for effective optimization of grid storage corresponding to grid server location. The major breakthrough is identified in an efficient manner using Vantage Point (VP) tree that consists of a binary tree where the internal node is formulated as given below:

$$\text{Node}_i = (\text{VP}, M_{\text{dis}}, R_{\text{leaf}}, L_{\text{leaf}}) \tag{7}$$

From (7), the internal node "Node$_i$" consists of vantage point "VP", the midpoint distance among all the distances of vantage points represented by "M_{dis}", and pointers to left and right leaf represented by "L_{leaf}" and "R_{leaf}", respectively. Left leaf of the node indexes the vantage points whose midpoint distances from "VP" are less than or equal to "M_{dis}". The right leaf of the node indexes points whose distances from "VP" are greater than or equal to "M_{dis}". In Vantage Point (VP) tree indexed form, instead of pointers to the left and right leaf, references to the data vantage points are used.

For each user "User$_i$" in every internal node, the midpoint "M" is used for partition with respect to the first vantage point "VP$_1$". The medians "M_1" and "M_2" are used in reference with respect to the second vantage point "VP$_2$". The first vantage point, for example, represents the fasting blood sugar (fbs) > 80, second vantage point being fasting blood sugar > 100, and so on.

Figure 5 shows the block diagram of Vantage Point (VP) tree indexed Berkeley key where the leaf node consists of the distances between data points and vantage points of that leaf.

The distances between data points using heart disease dataset represent the various classifications and factors resulting in heart disease, the second vantage point being fasting blood sugar > 100, and so on.

From Fig. 5, "D_1VP$_1$" and "D_2VP$_1$" are the distances between the first and second vantage points, respectively. In heart disease diagnosis example, the first vantage point being fbs > 80 and the second vantage point being fbs > 100.

Figure 6 shows the algorithmic description of VP tree indexed Berkeley key matching. Vantage Point (VP) tree indexed Berkeley key matching algorithm is

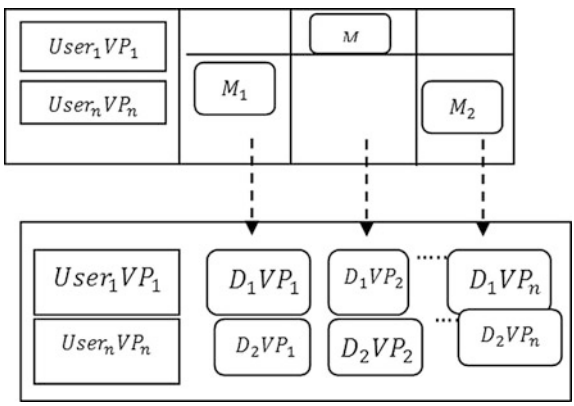

Fig. 5 Block diagram of Vantage Point (VP) tree index

Input: Users ‘ $User_i = User_1, User_2, \ldots, Us_t$ ’, Vantage Points ‘ $VP_i = VP_1, VP_2, \ldots, V$ ’, Finite set of users ‘ ’, Distance ‘ ’, Midpoint ‘ ’, Left Leaf ‘ L_{lt} ’
Output: Optimized data grid storage
Step 1: **Begin** Step 2: **If** ‘ $FS =$ ’ **then** Step 3: Create a tree Step 4: **Else** Step 5: Let Vantage Points be denoted as ‘ ’ Sep 6: **End if** Step 7: **If** Distance($User_i$,) < = **then** Sep 8: Storage is performed at the level ‘ ’ Step 9: **End if** Sep 10: **If** Distance($User_i$,) + > **then** Step11 Storage is continued with the left leaf ‘ L_{lt} ’ Step 12: **End if** Step 13: **If** Distance($User_i$,) + < **then** Step14:Storage is continued with the right leaf ‘ R_{lt} ’ Step 15: **End if** Step 16: **End**

Fig. 6 VP tree indexed Berkeley key matching algorithm

designed with objective of optimizing several data grid storages. The motivation is behind the application of VP tree indexed Berkeley key matching algorithm in DGKM using heart disease dataset and further enhance the parallel data accessing speed from distributed grids. The algorithmic description of VP tree indexed Berkeley key matching is shown in Fig. 6.

In Fig. 6, the tree indexed key matching process is continuously performed in an iterative manner for multiple user requests of data accessing. In this way, any number of patients can access via request to the server and efficiently identifies the factors leading the heart disease. It makes preventive measures accordingly. The performance of DGKM technique is tested with grid file accessing for online data repositories.

3 Experimental Settings

Derived Genetic Key Matching (DGKM) technique is used for quick parallel accessing of data from multiple grid locations, and experiments were conducted based on Gridsim simulator and applied in JAVA using Cleveland heart disease dataset from UCI repository. Cleveland heart disease dataset consists of 76 attributes, whereas the experiments are conducted with the aid of 14 of them. DGKM technique concentrated on attempting to differentiate between the presence of disease by the values 1, 2, 3, and 4 and the absence of disease by the value 0.

Table 1 Dataset description

1	Age	Numerical
2	Sex	Male, Female
3	Chest pain type	1, 2, 3, 4
4	Resting blood pressure	Numerical
5	Serum cholesterol in mg/dl	Numerical
6	Fasting blood sugar > 120 mg/d	Yes, No
7	Resting electrocardiograph results	0, 1, 2, 3
8	Maximum heart rate achieve	Numerical
9	Exercise-induced angina	Yes, No
10	ST depression induced by exercise relative to rest	Numerical
11	Slope of peak exercise	Numerical
12	Number of major vessels colored by fluoroscopy	0–3
13	Thal	Normal, Fixed defect, Reversible defect
14	Disease diagnosis	Presence (1), Absence (0)

The work Derived Genetic Key Matching (DGKM) technique for heart disease diagnosis is compared against the two existing techniques. The experiment is conducted on the factors such as data grid access speed, data integrity rate, time taken for key matching, and accuracy of grid location identification.

The dataset description of Cleveland heart disease dataset from UCI repository is provided in Table 1.

4 Discussion

The result analysis of Derived Genetic Key Matching (DGKM) technique is compared with the existing PDDRA [1] and (EDHR-DG) [2] technique.

4.1 Impact of Data Integrity Rate

Data integrity rate is ensured by checking whether the data is recorded exactly as intended by the patient registered and formulated as given below:

$$\mathrm{DIR} = \sum_{i=1}^{n} \left(\mathrm{User}_i * \mathrm{Data}_{\mathrm{size}}\right) - \left(\mathrm{Data}_{\mathrm{dropped}}\right) \tag{8}$$

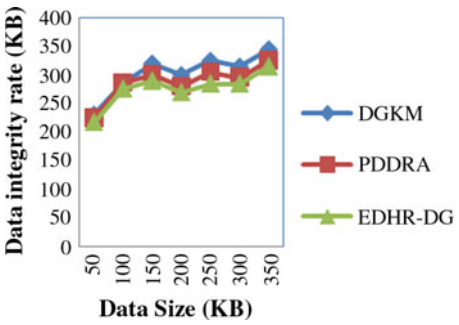

Fig. 7 Measure of data integrity rate

From (8), data integrity rate "DIR" is measured using actual data size "$\text{Data}_{\text{size}}$" and data dropped "$\text{Data}_{\text{dropped}}$" with respect to number of users "User_i". Figure 7 shows the result of data integrity rate that measures the amount of data successfully sent on the basis of the drop rate versus the varying number of data sent in the range of 50–35 KB.

The data integrity rate for different observations made by several patients is performed at different time intervals as shown above. The higher the number of data being sent by different patients from different regions, the more successful the technique required. The results reported here with increase in the number of data being sent by different patients. The data integrity rate efficiency also increases and is repeated in seven different sizes. Figure 7 shows the proposed DGKM technique that performs relatively well when compared to two other methods. The data integrity rate efficiency using DGKM technique is improved with synchronization of storage key with the grid location where data transmission is performed in and out of its neighbors. As a result, by applying mapping function for each user based on the storage key, DGKM technique in data integrity rate efficiency improves by 3.5 and 7.72% compared to PDDRA [1] and EDHR-DG [2], respectively.

4.2 Impact of Time Taken for Key Matching

The time taken for key matching is based on the training and test dataset. The time taken to match the key with respect to total number of patient who are ready for obtaining the information regarding the factors resulting in heart disease is formulated as given below:

$$\text{Time}_{\text{key matching}} = \text{Time}(\text{single user}) * n(9) \tag{9}$$

From (9), the time for key matching "$\text{Time}_{\text{key matching}}$" is obtained using time for single user "Time(single user)" and total number of users "n". In order to reduce the time taken for key matching, different numbers of users are considered. In the experimental setup, the number of user ranges from 10 to 70. The targeting result is

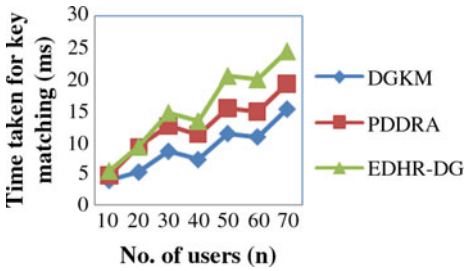

Fig. 8 Measure of time taken for key matching

that the number of users to measure the time taken for key matching using DGKM is compared with two state-of-the-art methods PDDRA and EDHR-DG.

DGKM techniques included key matching indexes based on derived gene population and ensure parallel and integrated data accessing for biomedical data (Fig. 8).

As a result, the time taken for key matching is reduced by 48.88 and 61.12% compared to the PDDRA [1] and EDHR-DG [2], respectively.

4.3 Impact of Data Grid Access Speed

The data grid access speed is rate at which the user is allocated with the grid based on the storage key. It is measured in terms of kilobits per second (KB/s). The data grid access speed rate returned over DGKM technique increases gradually for differing number of users. Figure 9 shows that data grid access speed is improved using the proposed technique DGKM. This is because of the application of vantage point tree index. Vantage point tree index is used to optimize different grid storages.

DGKM technique applies Berkeley key matching algorithm that helps in identifying the data drop rate at an early stage in an extensive manner. This in turn helps in improving the data access speed by 8% compared to PDDRA. In addition, by applying Berkeley key matching algorithm helps in improving the probability of successful data transmission using binary tree, therefore, improving the data grid access speed by 26.08% compared to EDHR-DG.

4.4 Impact of Accuracy of Grid Location Identification

The accuracy of grid location identification is measured on the basis of the number of users who were successfully located with the grid. The accuracy is formulated as given below and is measured in terms of percentage (%):

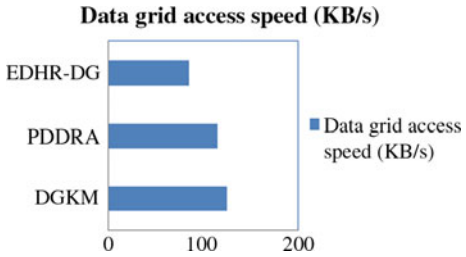

Fig. 9 Measure of data grid access speed

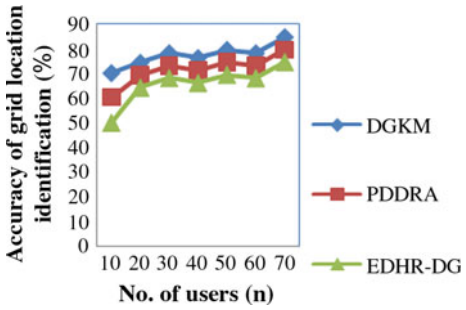

Fig. 10 Measure of accuracy of grid location identification

$$A = \left(\frac{\text{GridLoc}_s}{n}\right) * 100 \tag{10}$$

From (10), the accuracy of grid location identification "A" is measured using the users who were successfully located with the grid "GridLoc_s" to the number of users "n". The higher the accuracy of grid location identification, the more efficient the method is said to be. Figure 10 shows the measure of accuracy of grid location identification. From the figure, the accuracy of grid location identification is improved with the increase in the number of users. However, comparatively, betterment is observed using DGKM technique than PDDRA and EDHR-DG.

This is because of the application of Vantage Point (VP) tree indexed Berkeley key matching algorithm that optimizes several data grid storages with their respective grid server location. This in turn improves the accuracy of grid location identification by 10% compared to PDDRA and 20.26% compared to EDHR-DG, respectively.

5 Conclusion

Derived Genetic Key Matching (DGKM) technique performs efficient parallel processing to reduce time taken for key matching and improve data integrity rate, which applied in the biomedical file for heart disease diagnosis. We then showed how this technique can be extended to incorporate synchronization of storage key. It identifies the factors resulting in heart disease to the grid location where the key factors are stored to improve the data integrity rate based on input attributes and grid location attributes. The synchronization of storage key where the factors related to heart disease to the grid location is also provided efficient mapping. Mapping function for multiple patients at different locations based on the storage key and grid location and hence improved the data integrity rate. Next, the introduced key matching indexes based on derived gene population reduce the time for key matching in an efficient manner for parallel and integrated data accessing. This parallel and integrated data accessing for different patients relating to heart disease from different regions improves the accuracy of grid location identification. Finally, the Vantage Point (VP) tree indexed Berkeley key matching algorithm improves the data grid access speed using vantage point tree index. The experimental results in DGKM technique offer better performance of data integrity rate improved by 5.61% and reduce the time for key matching by 55% compared to PDDRA and EDHR-DG, respectively.

References

1. Saadat N, Rahmani Am (2012) PDDRA: a new pre-fetching based dynamic data replication algorithm in data grids. Elsevier 28(4)
2. Mansouri N, Dastghaibyfard GH (2013) Enhanced dynamic hierarchical replication and weighted scheduling strategy in data grid. Elsevier 73(4):534–543
3. Guan H, Li J, Zhong L, Yu Y, Chapman M (2013) Process virtualization of large-scale lidar data in a cloud computing environment. Elsevier 60:109–116
4. Buyya Rajkumar (2013) Introduction to the IEEE transactions on cloud computing. IEEE Trans Cloud Comput 1(1):3–21
5. Misra S, Das S, Khatua M, Obaidat MS (2014) Qos-guaranteed bandwidth shifting and redistribution in mobile cloud environment. IEEE Trans Cloud Comput 2(2):181–193
6. Cao J, Hwang K, Li K, Zomaya AY (2013) Optimal multi server configuration for profit maximization in cloud computing. IEEE Trans Parallel Distrib Syst (TPDS) 24(6):1087–1096
7. Di S, Wang C-L, Cappello F (2014) Adaptive algorithm for minimizing cloud task length with prediction errors. IEEE Trans Cloud Comput 2(2):194–207
8. Duan R, Prodan R, Li X (2014) Multi-objective game theoretic scheduling of bag-of-tasks workflows on hybrid clouds. IEEE Trans Cloud Comput 2(1):29–42
9. Zhang Q, Zhani MF, Boutaba R, Hellerstein JL (2014) Dynamic heterogeneity-aware resource provisioning in the cloud. IEEE Trans Cloud Comput 2(1):14–28
10. Chen C-A, Won My, Stoleru R, Xie GG (2015) Energy efficient fault-tolerant data storage and processing in mobile cloud. IEEE Trans Cloud Comput 3(1):28–41
11. Li K, Mu Y, Li K, Min G (2013) Exchanged crossed cube: a novel interconnection network for parallel computation. IEEE Trans Parallel Distrib Syst (TPDS) 24(11):2211–2219

12. Dastjerdi AV, Buyya R (2014) Compatibility-aware cloud service composition under fuzzy preferences of users. IEEE Trans Cloud Comput 2(1):1–13
13. Wan Z, Liu J, Deng RH (2012) HASBE: a hierarchical attribute-based solution for flexible and scalable access control in cloud computing. IEEE Trans Inform Forensics Sec 7(2):743–754
14. Sundareswaran S, Squicciarini AC, Lin D (2012) Ensuring distributed accountability for data sharing in the cloud. IEEE Trans Depend Sec Comput 9(4):556–568
15. Gupta R, Ramamritham K (2012) Query planning for continuous aggregation queries over a network of data aggregators. IEEE Trans Knowledge Data Eng (TKDE) 24(6):1065–1079
16. Inan A, Kantarcioglu M, Ghinita G, Bertino E (2012) A hybrid approach to private record matching. IEEE Trans Depend Sec Comput 9(5):684–698
17. Pitoura T, Ntarmos N, Triantafillou P (2012) Saturn: range queries, load balancing and fault tolerance in DHT data systems. IEEE Trans Knowled Data Eng (TKDE) 24(7):1313–1327
18. Balasubramanian B, Garg VK (2013) Fault tolerance in distributed systems using fused data structures. IEEE Trans Parallel Distribu Syst (TPDS) 24(4):1–16
19. Tao T, Cheng S (2014) Fast nearest neighbor search with keywords. IEEE Trans Knowledge Data Eng (TKDE) 26(4):1–13
20. Shahbazi A, Miller J (2014) Extended subtree: a new similarity function for tree structured data. IEEE Trans Knowledge Data Eng (TKDE) 26(4):1–14
21. Wang J-L, Sun Q-W, Dong B-M, Wei F, Chen J-L, Dong Y-K, Wang A-H, Shen Z-Q (2015) Antigenic characterization of the glycosylated E2 proteins of classical swine fever virus. J Pure Appl Microbiol 9(2)
22. Xie S, Dan J, Yu B, Xu Y, Zou Z (2015) Comparison between staged ORIF and EFLIF in treatment of pilon fracture: a systematic review. J Pure Appl Microbiol 9(2)
23. Reddy PK, Reddy MS (2009) Biochemical and PCR-RAPD characterization of pseudomonas fluorescens produced antifungal compounds inhibit the rice fungal pathogens in vitro. J Pure Appl Microbiol
24. Ashok kumar K, Chandrasekar (2015) Influence of vantage point-based dervied genetic key matching for heart disease diagnosis from multiple grid location. J Pure Appl Microbiol. **9** (Spl. Edn. 2):637–646

Enhance Multiple Moving Target Detection in Doppler-Tolerant Radar Using IRAESC Technique

Md. Aleem, R. P. Singh and Syed Jalal Ahmad

Abstract Nowadays, nation's power is gauged in terms of technology to keep an eye on the enemy movements in their vicinity. Hence, there is a need to work for the advancement of detection and tracking technology. For this purpose, the Doppler-tolerant radar fulfills the purpose of detection of multiple moving targets. So such systems needed to be strengthened in terms of precision in detection of multiple moving targets. The art of work of such radars focuses much toward stationary and slow moving targets. In this perspective, abundant work has been done to improve the figure of merit of autocorrelated signal in which transmitted and received signals are operated, thereby increasing the accuracy in detection of multiple moving targets. However, such systems fail to detect multiple moving targets under Doppler shift by suppression of reflection from small moving targets due to noise peaks of the autocorrelated signal. In this paper, we provide a digital coding technique to enhance the probability of target detection by the use of ASCII code to IR system called Indian Radar ASCII EX-OR System Code Technique (IRAESCT). This approach authenticates the position of the target and on the same time, it reduces the noise spikes below the threshold limit, which results in the creation of clear windows to help the multiple moving target detection with respect to desired Doppler. We validate our results using MATLAB.

Keywords Radar · Doppler shift · Target detection · Noise · IR system

Md.Aleem (✉) · R. P. Singh
Research scholar, SSSUTMS, Sehore, MP, India
e-mail: mdaleem80@gmail.com

R. P. Singh
e-mail: vc@sssutms.co.in

S. J. Ahmad
MIET, Jammu, Jammu and Kashmir, India
e-mail: jalal0000@yahoo.com

H. S. Saini et al. (eds.), *Innovations in Electronics and Communication Engineering*,
Lecture Notes in Networks and Systems 33,
https://doi.org/10.1007/978-981-10-8204-7_42

1 Introduction

It has become evident for the nations to improve their technology for monitoring the enemy activities. Radar was the available option at hand to detect and track the targets. However, the existing work concentrates more on the enhancement of stationary target detection probability. For this purpose, various approaches were proposed which enhances the merit factor of sent and reflected signal autocorrelation by increasing the pulse delay or pulse width of the transmitted Doppler pulse which leads to the formation side lobes and due to this reason this approach is more suitable for the stationary target detection and less helpful in detection of multiple small moving targets as the noise spikes of autocorrelated signal suppress the reflections from multiple small moving targets. The certainty of various target detection parameters such as bearing, elevation, and range detection was improved in the existing work. For multiple moving target detections, multiple input and multiple approaches are proposed in which multiple transmitters and multiple receiving antennas are used to enhance the detection probability of multiple moving targets which lead to the employment of Doppler filter bank array. Such contemporary radars for multiple moving target detection use the several unmatched radiating (k) antenna arrays to get sharp and steep autocorrelation response, and thereby the target detection probability is enhanced. Variation of the received parameters like phase and processing of the received echoes which can perform various operations like finding, tracking, etc, which indicates that the degree of freedom for transmitted signal cannot move more than one, whereas the degree of freedom for the received echoes can be more than one; for the simplicity, we can represent by "p". This system can transmit varying signals from "k" unmatched antennas and echoes are collectively processed after received by "p" unmatched receiving antennas. This leads to the improvement of accuracy of multiple moving target detections. However, radiation by multiple antennas results in the requirement of huge power, and also the noise spikes are more due to received echoes from the multiple moving targets. Therefore, slow moving targets are masked by these noise spikes and the range of the radar is also affected by this technique. Therefore, range and power consumption performance is lost at the cost of improving the probability which is not up to the mark comparatively.

In this approach, we are presenting IRAESCT to improve the multiple moving target detections by reducing the noise spikes to create multiple clear windows to show the current position of multiple moving targets with respect to desired Doppler. Our approach works on digital coding technique called IRAESCT having two folds. (***i***) ***IRAESCT by even parity and ii) IRAESCT by odd parity***. The presented approach is very simple but very much effective for multiple moving target detections. Our approach also minimizes the transmission power by sending a simple digital code which discards one major portion of the detection process called the range gates.

The rest of the paper is organized as follows. In Sect. 2, we presented the literature survey. In Sect. 3, we presented our approach and in Sect. 4 we concluded our paper.

2 Literature Survey

Rafiudin and Bangadia [1] proposed that by the use of p1 and p3 polyphase codes along with hyperbolic frequency modulation (HFM), the figure merit of received echo can be enhanced. But this approach has very poor response to delay, and so does not serve the purpose of the multiple moving target detections. Lewis and Kretschmer [2] proved in their proposed approach that bi-phase codes can be used in the place of polyphase codes as one can apply polyphase codes to improve the seamlessness of primary surveillance radar (PSR) by compressing the bits of the transmitted pulses and thereby the security can be enhanced. Moreover, P1 and P2 polyphase codes can be conveniently generated by the use of linear frequency-modulated waveform technique (LFMWT) on step estimation, and bandwidth of the receiver is also improved by this approach. Lewis and Kretschmer [3] proposed additional P3 and P4 codes generated by PFMWT that gives better probability of target detection compared to that of P1 and P2.

Kretschmer and Lewis [4] presented an approach using the same P3 and P4 codes to show the reduction of peak noise spikes and proved that these codes are efficient to improve the probability of moving target detection compared to other polyphase codes. However, use of these codes affects the probability of target detection in the occurrence of Doppler. Lewis [5] proposed a method, known as sliding window technique (SWT), that leads to reduce the effect caused by the range-time noise spikes produced which is evident with polyphase codes. However, this approach is limited to reduce the noise spikes up to certain level, and so have limited application in Doppler-tolerant radars. Kretschmer and Welch [6] presented an approach in which the authors used autocorrelation of polyphase codes to eliminate the noise components present in the signal. However, this particular approach fails to find high-speed targets in the presence of Doppler, as autocorrelation of polyphase codes generates noise spikes near to zero Doppler, and so makes this approach inappropriate for multiple moving target detections. This paper also introduces the use of amplitude weighting function (AWF) employing polyphase codes at the receiver side filter for noise spike deduction. However, there is more power loss in the system observed by comparing sending and receiving power at transmitter and receiver, respectively.

Sahoo and Panda [7] presented compression window technique to lessen the impact of noise spikes in Doppler-tolerant radars. However, this method has increased delay and therefore fails to generate bigger window or increase the quantity of windows to identify the multiple moving targets precisely. Singh et al. [8] proposed a windowing technique in which the authors used Hex coding technique to improve the probability of multiple moving target detections. However,

due to mathematical complexity, it consumes more power and increases delay, so applicable to detect slow moving targets only. Singh et al. [9] improve the probability of target detection by the use of matrix coding technique (MCT), in which they created more number of windows to get a clear picture about the current position of the moving target. This approach is limited to find stationary and slow moving targets only, as the length of the designed code vector is less which decreases the merit factor of the autocorrelated signal and resulted in noise peaks around the zero Doppler.

In this paper, we suggested an approach called Indian Radar ASCII EX-OR System Code (IRAESCT) technique. This not only eliminates the noise peaks but also increases the merit factor of the autocorrelated signal. The proposed system is simple but is very much effective to find the current location of the multiple moving targets. This coding system of target detection also minimizes the power consumption, so save more energy in comparison with the existing approaches

3 Proposed Approach

In this approach, we use ASCII code to generate the primary bits of the code vector, as this code is almost available everywhere in a digital system. Also, we are directly getting seven bits from each alphabet that is used to represent the part of a transmitting code vector to save more energy in comparison with the existing approaches (i.e., Golay, PTM, Hex Coding, Oversampled PTM, and Matrix Coding). For the sake of bit generation code vector, we are using "INDIAN RADAR" as a source of generation of transmitting code word in a matrix form (refer Table 1). Also, a parity bit is adding on both horizontal and vertical directions (i.e., even and odd parities) to help in the code design process.

Table 1 7-bit ASCII code for IR alphabets

IR letters	ASCII code
I	1001001
N	1001110
D	1000100
I	1001001
A	1000001
N	1001110
R	1010010
A	1000001
D	1000100
A	1000001
R	1010010

(A) IRAESCT by even parity

In this method of target detection, an even parity bit is being added on both the row and column directions (refer Table 2) so that the code word can be smoothly used to increase the length of code word using EX-OR operation of the two consecutive bits row-wise (refer Fig. 1). The increased length of the code word not only helps to enhance the merit factor (M.F) of the received signal but also increases the number of clear windows to check the current position of the moving targets through the entire Doppler range. Figure 1 represents how the bits are generated using EX-OR operation that needs to append with the 8-bit code of Table 2 on the right side (refer Table 3), and the EX-OR operation of remaining IR letters will be same as given in Fig. 1. So the complete generated matrix block which is called IRAESCT in our approach is being transmitted toward the target as a row vector to meet the requirements of an ambiguity function in MATLAB. The reflected echo coming from the target is autocorrelated with the transmitted signal to get the clear information about the moving targets.

Table 2 Even parity check bit appended to IR alphabets

IR letters	ASCII code	Even parity check (EPC)
I	1001001	1
N	1001110	0
D	1000100	0
I	1001001	1
A	1000001	0
N	1001110	0
R	1010010	1
A	1000001	0
D	1000100	0
A	1000001	0
R	1010010	1
Even parity check (EPC)	1000001	0

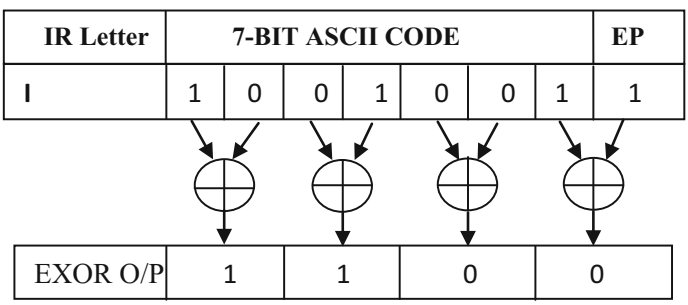

Fig. 1 Generation of bits by EX-OR operation with even parity (EP)

Table 3 Represents a complete code matrix

IR letter	7-bit ASCII code							EPC	Generated bits			
I	1	0	0	1	0	0	1	1	1	1	0	0
N	1	0	0	1	1	1	0	0	1	1	0	0
D	1	0	0	0	1	1	0	0	1	0	0	0
I	1	0	0	1	0	0	1	1	1	1	0	0
A	1	0	0	0	0	0	1	0	1	0	0	1
N	1	0	0	1	1	1	0	0	1	1	0	0
R	1	0	1	0	0	1	0	1	1	1	1	1
A	1	0	0	0	0	0	1	0	1	0	0	1
D	1	0	0	0	1	1	0	0	1	0	0	0
A	1	0	0	0	0	0	1	0	1	0	0	1
R	1	0	1	0	0	1	0	1	1	1	1	1
EPC	1	0	0	0	0	0	1	0	1	0	0	1

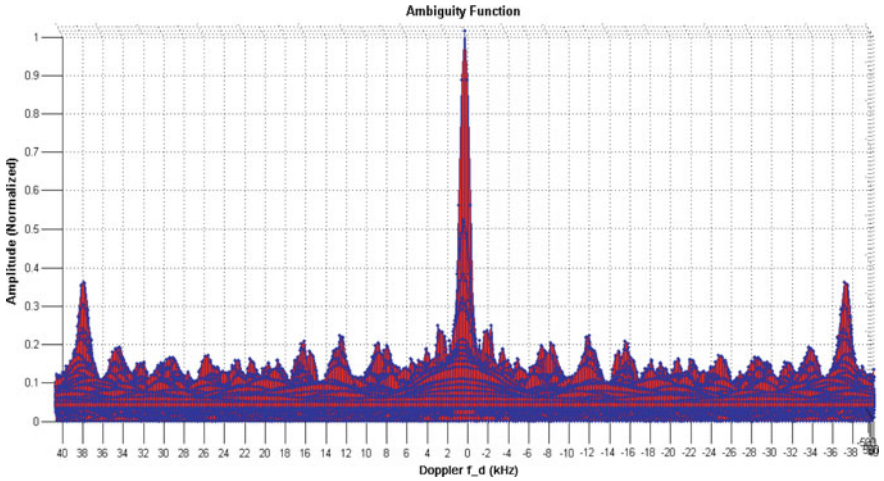

Fig. 2 Variation of Doppler versus amplitude (normalized)

Figures 2 and 3 represent the variation of Doppler versus amplitude, delay using MATLAB, and from the figures we observe that number of clear windows (i.e., 3–8, 10–11, 13–15, 18–38, and −3 to −8, −10 to −11, −13 to −15, −18 to −38) can be achieved by using IRAESCT even parity. However, some portion of the Doppler has still affected by noise spikes, and so to eliminate these noise spikes another method is being used called IRAECT odd parity.

(B) IRAESCT by odd parity

In this method of target detection, an odd parity bit is being added in both the row and column directions (refer Table 4), so that the varied code word can be used

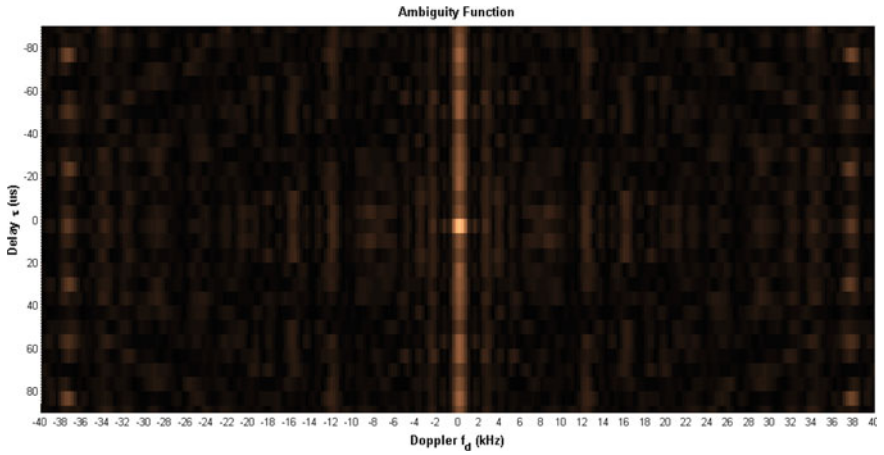

Fig. 3 Variation of Doppler versus delay (um)

Table 4 Odd parity check bit appended to IR alphabets

IR letters	ASCII code	Odd parity check
I	1001001	0
N	1001110	1
D	1000100	1
I	1001001	0
A	1000001	1
N	1001110	1
R	1010010	0
A	1000001	1
D	1000100	1
A	1000001	0
R	1010010	0

to increase the length of code word using EX-OR operation of the two consecutive bits row-wise (refer Fig. 4). The increased length of the code word unlike previous one not only helps to enhance the merit factor (M.F) of the received signal, but also increases the number of clear windows to check the current position of the moving targets through the entire Doppler range better than the previous code. Figure 4 represents how the bits are generated using EX-OR operation that needs to append with the 8-bit code of Table 4 on the right side (refer Table 5), and the EX-OR operation of remaining IR letters will be same as given in Fig. 4. So the complete generated matrix block which is called IRAESCT in our approach is being transmitted toward the target as a row vector. The reflected echo coming from the target is autocorrelated with the transmitted signal to get the clear information about the moving targets.

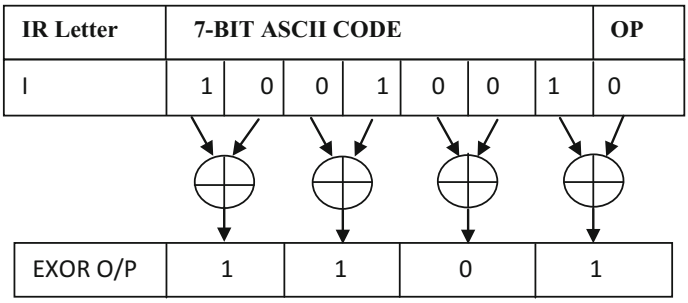

Fig. 4 Generation of bits by EX-OR operation with odd parity check bit

Table 5 Represents a complete code matrix

IR letter	7-bit ASCII code							OPC	Generated bits			
I	1	0	0	1	0	0	1	0	1	1	0	1
N	1	0	0	1	1	1	0	1	1	1	0	1
D	1	0	0	0	1	1	0	1	1	0	0	1
I	1	0	0	1	0	0	1	0	1	1	0	1
A	1	0	0	0	0	0	1	1	1	0	0	0
N	1	0	0	1	1	1	0	1	1	1	0	1
R	1	0	1	0	0	1	0	0	1	1	1	0
A	1	0	0	0	0	0	1	1	1	0	0	0
D	1	0	0	0	1	1	0	1	1	0	0	1
A	1	0	0	0	0	0	1	0	1	0	0	1
R	1	0	1	0	0	1	0	0	1	1	1	0
OPC	0	1	1	1	1	1	0	0	1	0	0	0

Figures 5 and 6 show the variation between Doppler versus amplitude, delay. From the figure, we observe that huge window has been created from 4 to 38, −4 to −38 by using IRAESCT by odd parity.

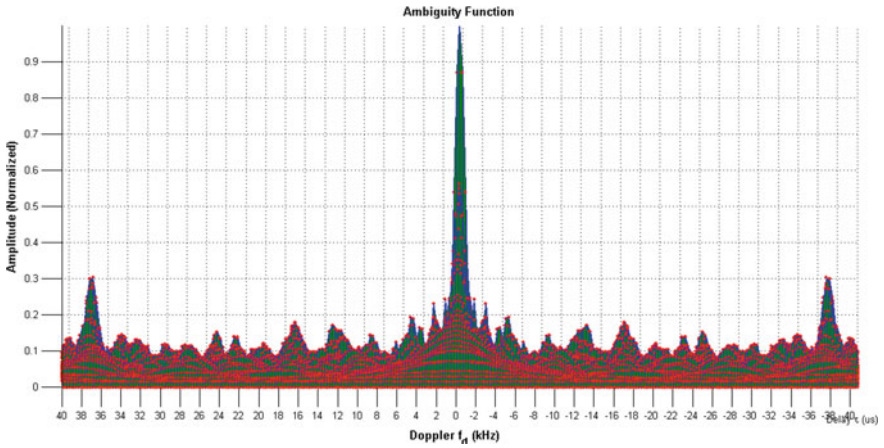

Fig. 5 Variation of Doppler versus amplitude (normalized)

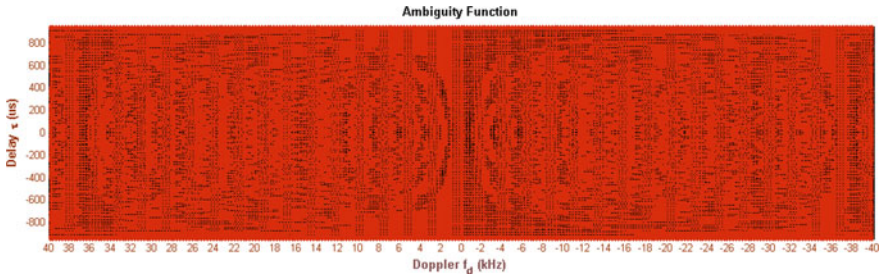

Fig. 6 Variation of Doppler versus delay (um)

4 Conclusion and Future Scope

The presented approach is very simple as far as the generation of the code word is concerned. Also, the given approach reduces design complexity as all the digital system hardwares readily consist of ASCII encoder. Multiple and huge window sizes have been created to enhance the probability of multiple fast-moving targets by reducing the noise spikes that can hinder the probability of multiple moving target detections. The two output devices such as two A-Scope and PPI (plan position indicator) can visualize the moment of the target continuously by using approaches. However, still one noise spike at 38 kHz still present which can reduce the probability of target detection after some instant. This noise spike will be taken into consideration in the next part of this paper using modified version of the existing approach. The future scope of the model is to reduce the noise spikes below 0.1 amplitude, so that moving target can be more accurately judged.

References

1. Rafiuddin SSA, Bhangdia VK (2013) Empirical analysis on Doppler tolerant radar codes. Int J Sci Eng Res 4(5):1579–1582
2. Lewis BL, Jr. Kretschmer FF (1981) A new class of polyphase pulse compression codes and techniques. IEEE Trans Aerosp Electron Syst AES-17(3):364–372
3. Lewis BL, Kretschmer Jr FF (1982) Linear frequency modulation derived polyphase pulse compression codes. IEEE Trans Aerosp Electron Syst AES-18(5):637–641
4. Kretschmer FF Jr, Lewis BL (1983) Doppler properties of polyphase pulse compression waveforms. IEEE Trans Aerosp Electron Syst 19(4):521–531
5. Lewis BL (1993) Range-time-sidelobe reduction technique for FM-derived polyphase PC codes. IEEE Trans Aerosp Electron Syst AES-29(3):834–840
6. Kretschmer Jr FF, Welch LR (2000) Sidelobe reduction techniques for polyphase pulse compression codes. In: IEEE international radar conference, pp 416–421, May 2000
7. Sahoo AK, Panda G (2011) Doppler tolerant convolution windows for radar pulse compression. Int J Electron Commun Eng 4(1):145–152
8. Singh RK, Rani DE, Ahmad SJ (2016) RSBHCWT: re-sampling binary hex code windowing technique to enhance target detect. Indian J Sci Technol 9(47):1–5
9. Singh RK, Rani DE, Ahmad SJ (2017) HQECMT: hex quadratic residue EX-OR coded matrix technique to improve target detection in Doppler tolerant radar. Int J Sci Res (PONTE) 73(1): 21–28

Prediction of Acute Myeloid Leukemia Subtypes Based on Artificial Neural Network and Adaptive Neuro-Fuzzy Inference System Approaches

Etee Kawna Roy and Subrata Kumar Aditya

Abstract The proposed technique involves designing and implementing an acute myeloid leukemia sub-type prediction system based on artificial neural network and adaptive neuro-fuzzy inference system approaches. The dataset of 600 possible cases (patients) of acute myeloid leukemia is used. After training the system with 540 input–output dataset of patients having AML-M0, AML-M1, AML-M2, AML-M3, and AML-M4 types of leukemia, it is tasted with 60 data for validation. The method is implemented to predict these five types of acute myeloid leukemia based on the characteristics of four complete blood count (CBC) parameters, namely leukocytes, hemoglobin, platelets, and blasts of the patients. The neural network performed well than the adaptive neuro-fuzzy inference system when test data was considered, where the average mean squared error (MSE) for each system was 0.0433 and 0.2089, respectively. The adaptive neuro-fuzzy inference system showed better performance than artificial neural network when training data was considered, where the mean squared error (MSE) for each system was 0.0017 and 0.0044, respectively.

Keywords Acute myeloid leukemia · Inference system · Perceptron Epoch · Hematology · Membership function

1 Introduction

Acute myeloid leukemia (AML) is a cancer that originates from the myeloid lineage and hampers the growth of normal blood cells by rapid production of abnormal white blood cells in the bone marrow and blood [1]. According to the classification

E. K. Roy (✉) · S. K. Aditya
Department of Electrical and Electronic Engineering, University of Dhaka, Dhaka 1000, Bangladesh
e-mail: kawnaroy@gmail.com

S. K. Aditya
e-mail: aditya@du.ac.bd

H. S. Saini et al. (eds.), *Innovations in Electronics and Communication Engineering*, Lecture Notes in Networks and Systems 33,
https://doi.org/10.1007/978-981-10-8204-7_43

done by a group of French, American, and British leukemia experts in 1970s, AML can be divided as undifferentiated acute myeloblastic leukemia (AML-M0), acute myeloblastic leukemia with minimal maturation (AML-M1), acute myeloblastic leukemia with maturation (AML-M2), acute promyelocytic leukemia (AML-M3), acute myelomonocytic leukemia (AML-M4), acute myelomonocytic leukemia with eosinophilia (AML-M4eos), acute monocytic leukemia (AML-M5), acute erythroid leukemia (AML-M6), and acute megakaryoblastic leukemia (AML-M7) [2].

Two methods are used to predict the first five acute myeloid leukemia subtypes. They are artificial neural network (ANN) approach and adaptive neuro-fuzzy inference system (ANFIS) approach. In ANN approach, a feed-forward neural network also called multilayer perceptron is trained using a backpropagation learning algorithm [3]. They are supervised neural networks. A desired response pattern is used to train such networks. To design the ANFIS network, some parameters have to set initially to start training. For this paper, three types of membership functions are used during the course of network training such as Gaussian curve membership function, generalized bell-shaped membership function, and triangular-shaped membership function. Adaptive neuro-fuzzy inference system embeds the fuzzy inference model within the framework of an adaptive network and uses Takagi–Sugeno fuzzy inference technique to combine fuzzy logic decision-making capability with artificial neural network's learning ability. By training itself with training data, ANFIS computes initial membership functions and afterward adjusts membership functions using either a backpropagation algorithm or a hybrid-learning algorithm (a combination of backpropagation and least squares method) to minimize the error measure.

Artificial neural networks were used and are still used in many parts of biomedical science, such as in detecting breast cancer [4–7], prostate cancer [8–12], coronary artery disease [13], Alzheimer's disease [14, 15], brain disease [16], diabetes [17], optic nerve disease [18], ovarian cancer [19], pancreatitis and pancreatic cancer [20], to classify heart disease [21], to construct risk classification model of cervical cancer [22], dermatologic diagnosis [23], and so on.

In this paper, we focus on the prediction of the first five subtypes (AML-M0 to AML-M4) of acute myeloid leukemia with the help of artificial neural network and adaptive neuro-fuzzy inference system approaches and comparing them.

2 Experimental Details

From the blood tests of acute myeloid leukemia patients, it is seen that for all types of AML, significant changes occur in the amount of four hematological parameters from their normal ranges. These parameters are leukocytes, hemoglobin, platelets, and blasts. They are taken as input parameters to the system. The output is any one

Table 1 Ranges for CBC parameters for AML subtypes [24]

Hematological parameters	Acute myeloid leukemia (AML) subtypes				
	M0	M1	M2	M3	M4
Leukocytes $\times 10^9$/l	1.2–189.0	3.1–266.0	2.2–8.3	2.1–55.9	2.1–100.0
Hemoglobin/deciliter	5.8–15.1	8.0–9.2	4.3–11.1	1.6–10.0	3.5–11.6
Platelets $\times 10^9$/l	8.0–129.0	4.0–253.0	5.0–77.6	10.0–26.0	12.0–257.0
% blasts	60.0–93.0	23.0–97.0	13.0–20.0	2.0–98.0	5.0–73.0

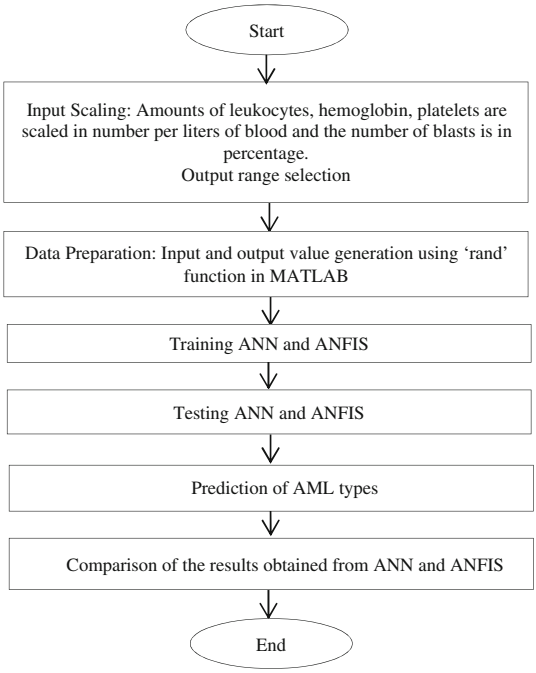

Fig. 1 Flowchart for prediction of AML types using ANN and ANFIS network

of the five types of AML. Table 1 shows the input parameters along with their ranges for these five types of AML. The flowchart in Fig. 1 describes the procedure for predicting the acute myeloid leukemia subtypes using both artificial neural networks and adaptive neuro-fuzzy inference system. We selected the output ranges as follows: from values 0.0–0.2 for AML-M0, 0.2–0.4 for AML-M1, 0.4–0.6 for AML-M2, 0.6–0.8 for AML-M3, and 0.8–1.0 for AML-M4.

3 Results and Discussion

3.1 *Training and Performance Evaluation with Artificial Neural Network*

The flowchart shown in Fig. 2 describes the procedure of predicting the AML types using artificial neural network.

Table 2 gives a comparison of training errors (in mean squared error, MSE) for "trainlm" training function at different numbers of epochs and hidden neurons. The hidden layer and output layer transfer functions are tan-sigmoid and log-sigmoid, respectively.

After completing the assigned epoch values (500 in this case), the performance (in MSE) is obtained as shown in Fig. 3.

The optimum network is tested with a dataset of 60 patients. Test error is calculated using

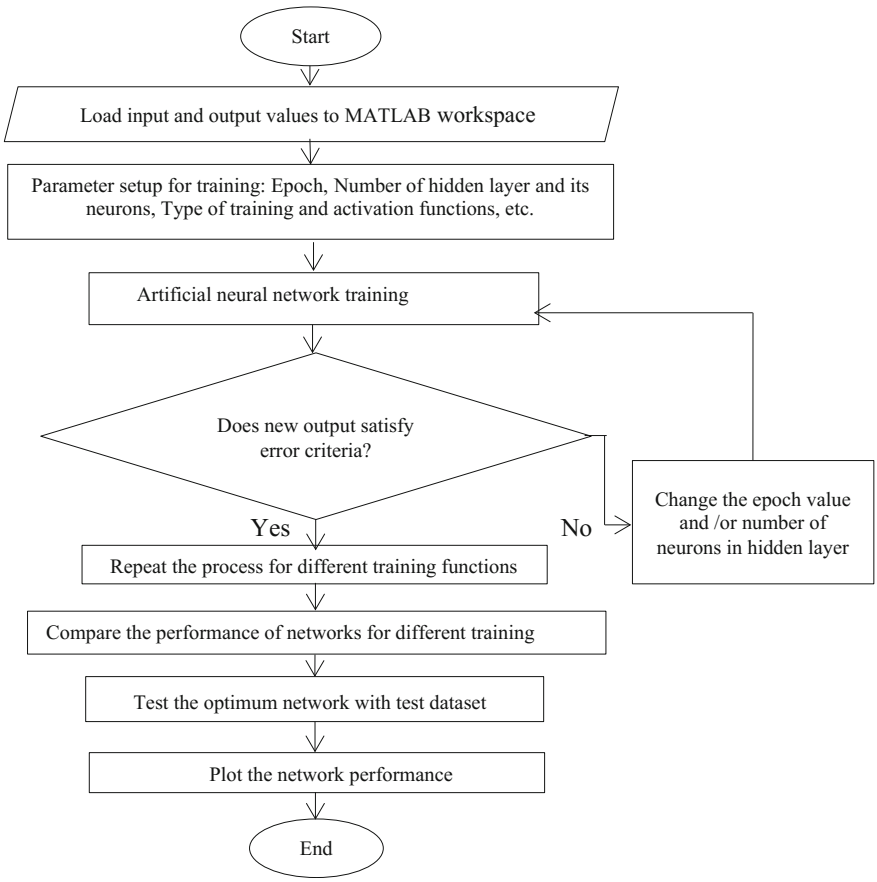

Fig. 2 Flowchart for designing artificial neural network

Table 2 Artificial neural networks with different training errors, number of hidden neurons, and epochs for "trainlm" training function

Training function: trainlm			
Network	Number of neurons in hidden layer	Training error (MSE)	Number of epochs
ANN 1	10	0.0106	100
ANN 2	12	0.0086	500
ANN 3	14	0.0072	500
ANN 4	16	0.0068	300
ANN 5	18	0.0052	500
ANN 6	20	0.0069	554
ANN 7	22	0.0061	500
ANN 8	*24*	*0.0044*	*500*
ANN 9	26	0.0045	500
ANN 10	28	0.0048	500

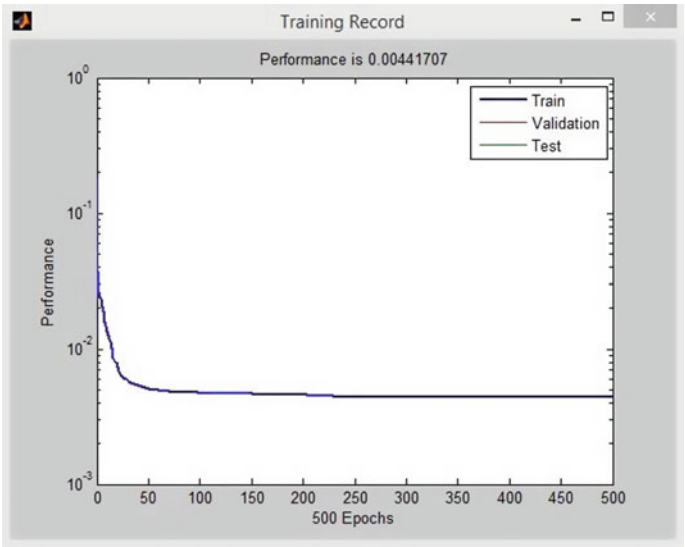

Fig. 3 Performance of the trained neural network

$$e_i = V_p \sim D_m, \quad i = 1, 2, 3, \ldots \tag{1}$$

where e_i—test error, D_m—desired response from ANN or ANFIS, and V_p—output predicted by ANN or ANFIS.

$$\text{Squared error}, E = \sum_i e_i^2 \tag{2}$$

Mean squared error,

$$\text{MSE} = \frac{E}{n} = \frac{\sum_i e_i^2}{n} \tag{3}$$

where $n = \sum i$, root mean squared error,

$$\text{RMSE} = \sqrt{\frac{E}{n}} = \sqrt{\frac{\sum_i {e_i}^2}{n}} \tag{4}$$

According to the linear regression analysis of the network, the coefficient of determination is $R^2 \approx 0.94255$, which means approximately 94% variation in the model response is explained by regression on target outputs (Fig. 4).

3.2 *Training and Performance Evaluation with Adaptive Neuro-Fuzzy Inference System*

The flowchart in Fig. 5 describes the procedure of predicting the AML types using adaptive neuro-fuzzy inference system. Table 4 shows the performance for different membership functions.

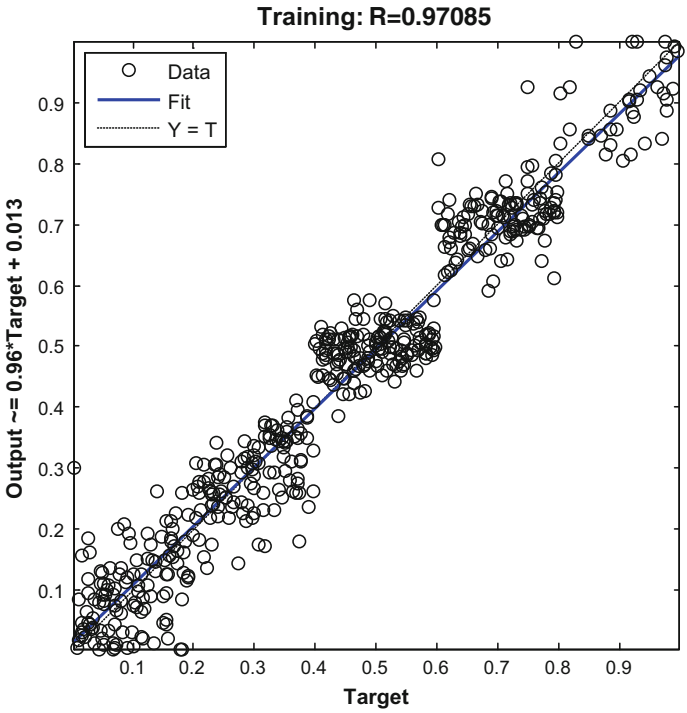

Fig. 4 Regression analysis plot

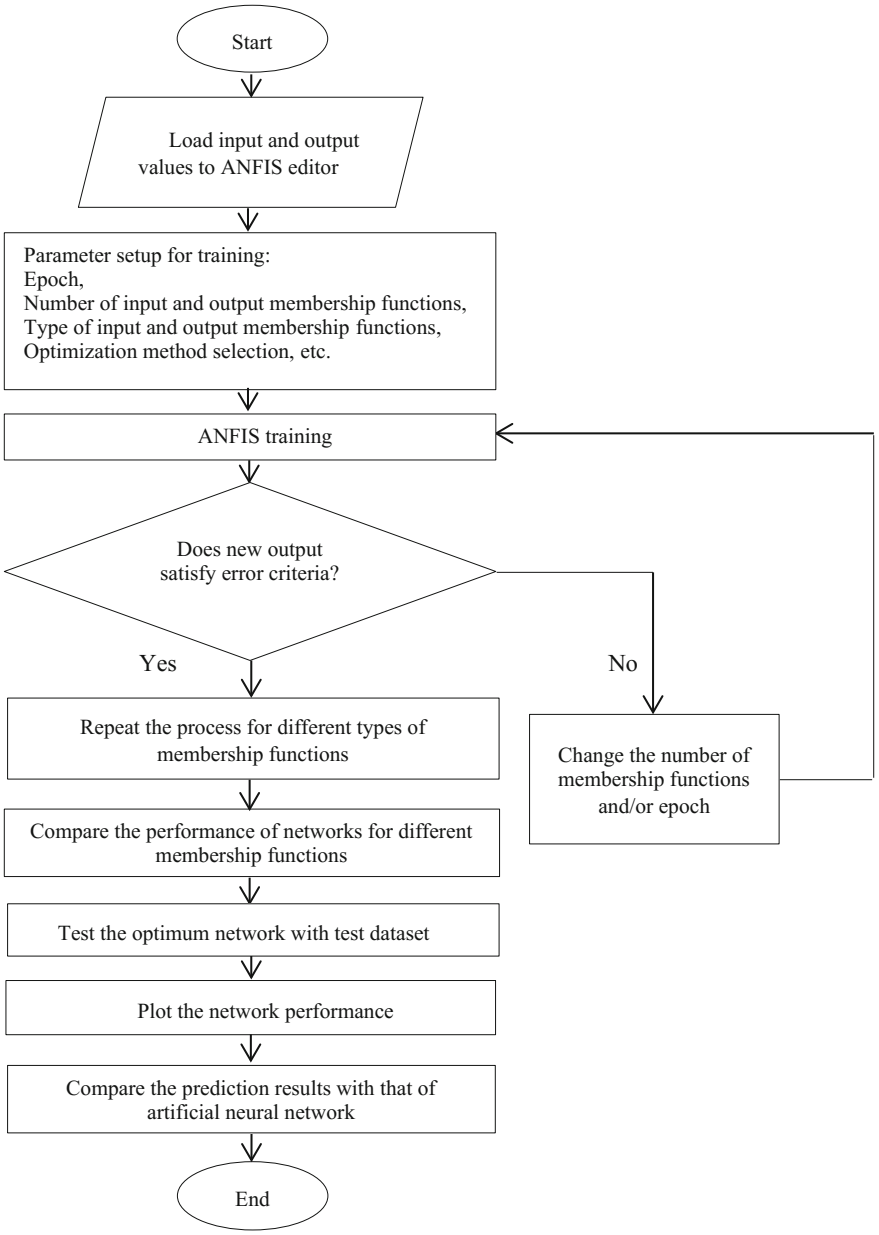

Fig. 5 Flowchart for designing an adaptive neuro-fuzzy inference system

From Table 4, it is shown that minimum training error (in terms of root mean squared error, RMSE) is obtained by Gaussian membership function at epochs of 50. The ANFIS generated membership functions (in Fig. 6i–iv) by analyzing the data fed to it for training.

In Fig. 7, it is seen that for a set of input parameter values, an output value of 0.202 is generated which belongs to the range (0.2–0.4). This indicates that the dataset is for AML-M1 patients. Figure 8 shows that the training error decreases gradually as the number of epoch increases. At epochs of 30, the minimum error is reached and it is 0.041379.

The system test error and the accuracy are calculated using Eqs. (1)–(4). The results are given in Table 5.

Table 3 Analysis results for AML subtypes using artificial neural network

Acute myeloid leukemia subtypes	Test set	Predicted case	Prediction failure	Test error (MSE)
AML-M0	14	14	0	0.0433
AML-M1	14	14	0	
AML-M2	14	12	2	
AML-M3	14	11	3	
AML-M4	4	3	1	

Table 4 Training errors of different adaptive neuro-fuzzy inference system models

ANFIS system	Membership function	Epochs	Training error (RMSE)
ANFIS 1	gaussmf	30	0.041682
ANFIS 2	*gaussmf*	*50*	*0.041379*
ANFIS 3	gbellmf	30	0.045994
ANFIS 4	gbellmf	50	0.042127
ANFIS 5	trimf	10	0.057602
ANFIS 6	trimf	30	0.047242

Table 5 Analysis results for AML subtypes using ANFIS

Subtypes	Test set	Predicted case	Prediction failure	Test error (MSE)
AML-M0	14	12	2	0.2089
AML-M1	14	14	0	
AML-M2	14	14	0	
AML-M3	14	13	1	
AML-M4	4	2	2	

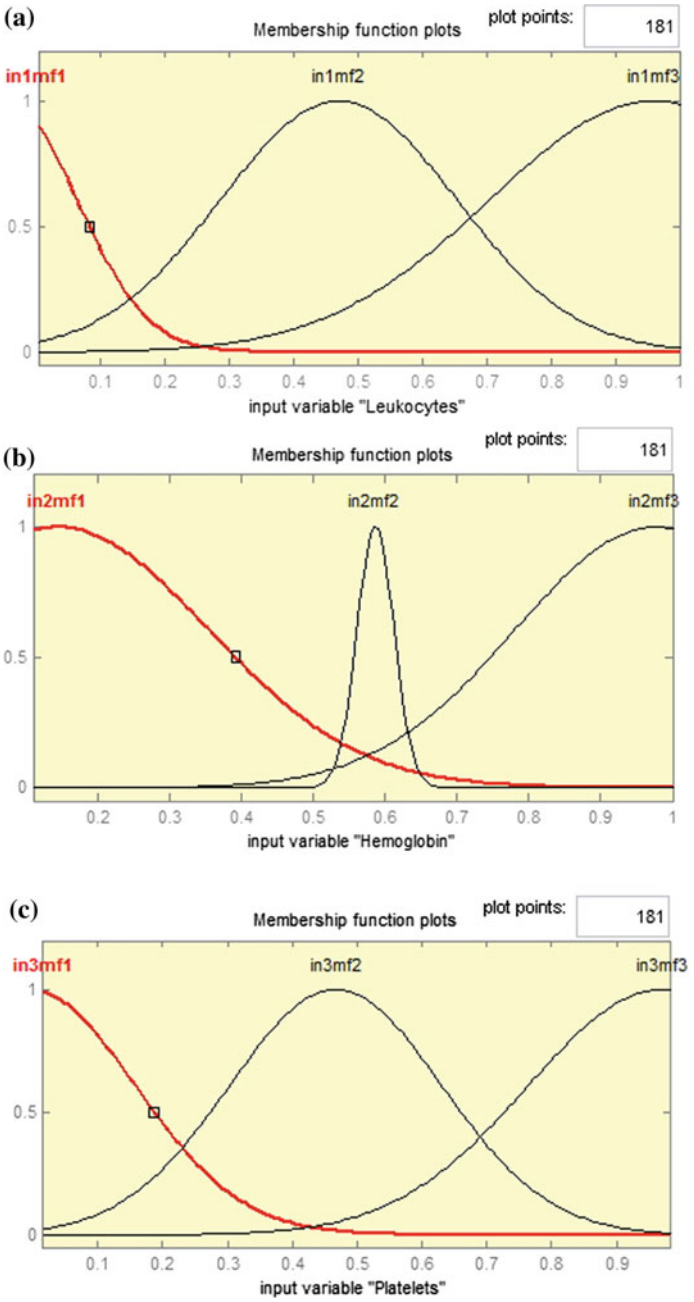

Fig. 6 (i) Generated membership function for leukocytes after training ANFIS, (ii) generated membership function for hemoglobin after training ANFIS, (iii) generated membership function for platelets after training ANFIS, (iv) generated membership function for blasts after training ANFIS

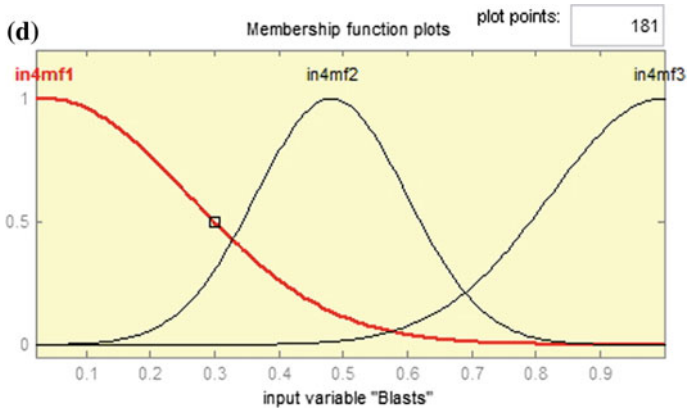

Fig. 6 (continued)

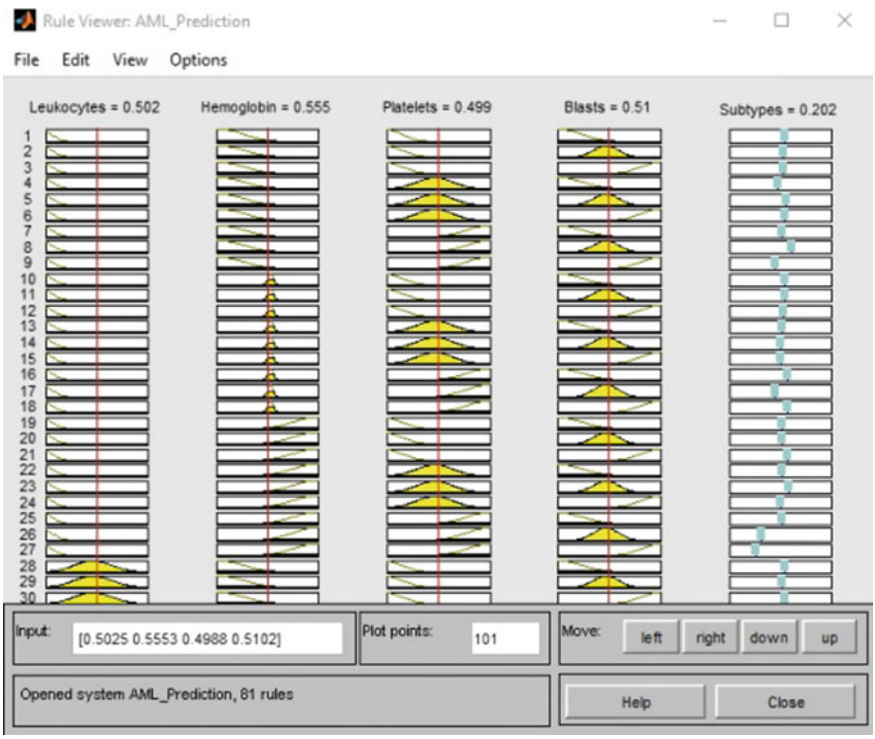

Fig. 7 Rule viewer window

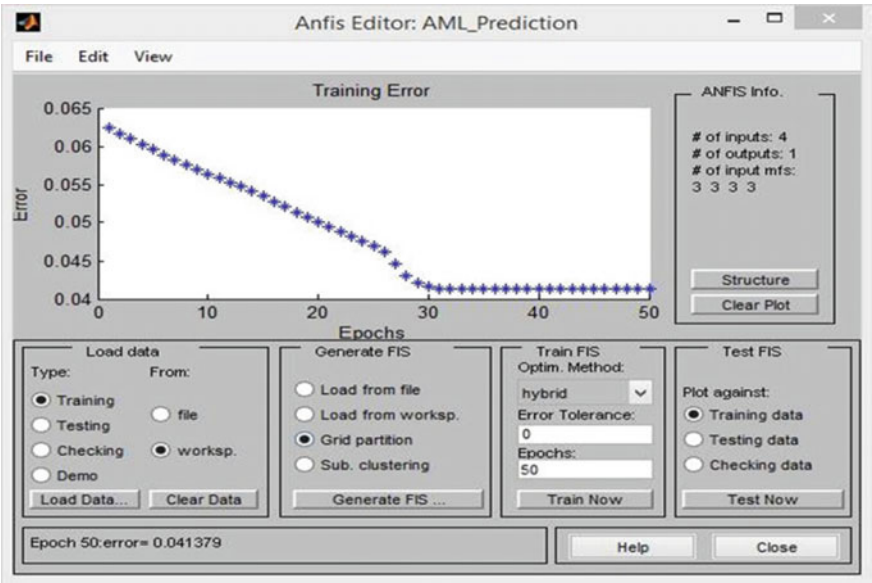

Fig. 8 Changes of training error with epochs

Table 6 Comparison between the developed artificial neural network and adaptive neuro-fuzzy inference system

Networks	Subtypes	Training error (MSE)	Average test error (MSE)
ANN	AML-M0	0.0044	0.0433
	AML-M1		
	AML-M2		
	AML-M3		
	AML-M4		
ANFIS	AML-M0	0.0017	0.2089
	AML-M1		
	AML-M2		
	AML-M3		
	AML-M4		

3.3 Comparison Between Developed Artificial Neural Network and Adaptive Neuro-Fuzzy Inference System Approaches

Using Tables 2, 3, 4, and 5, the developed neural network and adaptive neuro-fuzzy inference system model can now be compared (Table 6).

4 Conclusions

Artificial neural network approach showed that a simple multilayer perceptron with one hidden can be effectively used for prediction purposes. With 24 hidden neurons and 500 epochs, the desired network performance is obtained with "trainlm" training function. The mean squared training error is 0.0044. The performance plot is observed and it is seen that the network meets the validation criteria. Then, the network is tested with 60 test datasets. According to the linear regression analysis of the network, the coefficient of determination is $R^2 \approx 0.94255$, which means approximately 94% variation in the model response is explained by regression on target outputs.

In the second approach, an adaptive neuro-fuzzy inference system (ANFIS) is developed using the same training and test dataset. The error criterion is satisfied with Gaussian curve membership function and with hybrid optimization method at epochs of 50. The training error for ANFIS is 0.0017 (MSE).

To test the system against the test data, the rule base is viewed and finally, results of training and testing are compared with that of the neural network. Average test errors for ANN and ANFIS are 0.0433 (MSE) and 0.2089 (MSE), respectively. That means for this research, the neural network performance is better than the ANFIS when test dataset is considered. On the other hand, the ANFIS shows better performance when training data is considered. During training the ANFIS, the surface change was also observed, which shows the relationship between outputs and inputs. It is seen that there is no considerably large flat area touching the ground grid, which means the system responds well to all the four inputs. A larger dataset can be used for training and testing the systems. In this case, care should be taken in selecting the number of hidden neurons and other parameters to avoid overfitting.

References

1. Pouls RK, Shamoon RP, Muhammed NS (2012) Clinical and hematological parameters in adult AML patients: a four year experience at Nanakaly Hospital for blood diseases. Zanco J Med Sci 16:199–203
2. American Cancer Society, https://www.cancer.org/cancer/acute-myeloid-leukemia/detection-diagnosis-staging/how-classified.html. Accessed 18 Apr 2017
3. Negnevitsky M (2011) Artificial intelligence: a guide to intelligent systems. Pearson Education Ltd., England
4. Karabatak M, Ince CM (2009) An expert system for detection of breast cancer based on association rules and neural network. Expert Syst Appl 36:3465–3469
5. Übeyli ED (2007) Implementing automated diagnostic systems for breast cancer detection. Expert Syst Appl 33:1054–1062
6. Tan TZ, Quek C, Ng GS et al (2007) A novel cognitive interpretation of breast cancer thermography with complementary learning fuzzy neural memory structure. Expert Syst Appl 33:652–666

7. Lisboa PJ, Etchells TA, Jarman IH et al (2008) Time-to-event analysis with artificial neural networks: an integrated analytical and rule-based study for breast cancer. Neural Netw 21:414–426
8. Stephan C, Cammann H, Meyer HA et al (2008) An artificial neural network for five different assay systems of prostate specific antigen in prostate cancer diagnostics. BJU Int 102:799–805
9. Stephan C, Xu C, Finne P et al (2007) Comparison of two different artificial neural networks for prostate biopsy indication in two different patient populations. Urology 70:596–601
10. Kattan WM (2008) Editorial comment on: development, validation, and head-to-head comparison of logistic regression-based nomograms and artificial neural network models predicting prostate cancer on initial extended biopsy. Eur Urol 54:611 (epub January 15)
11. Kawakami S, Numao N, Okubo Y et al (2008) Development, validation, and head-to-head comparison of logistic regression-based nomograms and artificial neural network models predicting prostate cancer on initial extended biopsy. Eur Urol 54:601–611 (epub January 15)
12. Chun FKH, Graefen M, Briganti A et al (2007) Initial biopsy outcome prediction head-to-head comparison of a logistic regression-based nomogram versus artificial neural network. Eur Urol 51:1236–1243
13. Kurt I, Ture M, Kurum AT (2008) Comparing performances of logistic regression, classification and regression tree, and neural networks for predicting coronary artery disease. Expert Syst Appl 34:366–374
14. Mucke L Strategies to prevent neural network dysfunction in Alzheimer. Alzheimer's Dementia 4(Supp 1):T102–T103
15. Luca, MD, Grossi E, Borroni B et al (2005) Artificial neural networks allow the use of simultaneous measurements of alzheimer disease markers for early detection of the disease. J Transl Med 3
16. Uğuz H, Öztürk A, Saraçoğlu R et al (2008) A biomedical system based on fuzzy discrete hidden markov model for the diagnosis of the brain diseases. Expert Syst Appl 35:1104–1114
17. Mataria M, Janech GM, Almeida J et al (2008) Prediction of progression of diabetic nephropathy in a small set of patients by artificial neural networks and proteomic analysis. Am J Kidney Dis 51:B67–B67
18. Polata K, Karab S, Güvenc A et al (2008) Utilization of discretization method on the diagnosis of optic nerve disease. Comput Methods Programs Biomed 91:255–264
19. Tan TZ, Quek C, Ng SG et al (2008) Ovarian cancer diagnosis with complementary learning fuzzy neural network. Artif Intell Med 43:207–222
20. Săftoiu A et al (2008) Neural network analysis of dynamic sequences of EUS elastography used for the differential diagnosis of chronic pancreatitis and pancreatic cancer. Gastrointest Endosc 68:1086–1094
21. Ari S, Saha G (2009) In search of an optimization technique for artificial neural network to classify abnormal heart sounds. Appl Soft Comput 9:330–340
22. Qiua X, Taob N, Tana Y et al (2007) Constructing of the risk classification model of cervical cancer by artificial neural network. Expert Syst Appl 32:1094–1099
23. Chang CL, Chena CH (2009) Applying decision tree and neural network to increase quality of dermatologic diagnosis. Expert Syst Appl 36:4035–4041
24. Noronha EP et al (2011) Immunophenotyping characterization of acute leukemia at a public oncology reference center in Maranhão, Northeastern, Brazil. Sao Paulo Med J 129

Detection of Chronic Kidney Disease by Using Artificial Neural Networks and Gravitational Search Algorithm

S. M. K. Chaitanya and P. Rajesh Kumar

Abstract Chronic Kidney Disease (CKD) is a universal health issue attacking around 10% of the populace worldwide. This disease can be detected using Artificial Neural Networks approach along with optimizing technique called as Gravitational Search Algorithm. These networks are periodically used as strong classifiers during the diagnosis of a disease. The data has been collected from the UCI Machine Learning Repository, which is an MR image. From the collected data, 80% of it is used for training the neural networks and 20% is used for the testing purpose. In this paper, the algorithms like Artificial Neural Network with Gravitational Search Algorithm (ANN+GSA), Artificial Neural Network with Genetic Algorithm (ANN+GA), and K-nearest neighbor are used. The intent of this paper is to compare the performance of these two algorithms on the basis of accuracy, sensitivity, and specificity.

Keywords ANN FFBP algorithm · Feature extraction · GSA · UCI Machine Learning Repository

1 Introduction and Literature Review

Chronic kidney diseases have become major health problem. They are the main reason for mortality in India accounting 60% of deaths worldwide. CKD also called as Chronic Renal Disease is known for its reduction in regular functioning of kidney over a period of time. Around 5–10% of the world population has been infected by this disease.

S. M. K. Chaitanya (✉)
Department of ECE, G. V. P. College of Engineering (Autonomous), Visakhapatnam, Andhra Pradesh, India
e-mail: Chaitry1084@gmail.com

P. Rajesh Kumar
Department of ECE, Andhra University College of Engineering (Autonomous), Visakhapatnam, Andhra Pradesh, India

H. S. Saini et al. (eds.), *Innovations in Electronics and Communication Engineering*, Lecture Notes in Networks and Systems 33,
https://doi.org/10.1007/978-981-10-8204-7_44

Vital et al. [1] have explained neural network approach for classification of kidney disease datasets collected from Visakhapatnam, AP, India. By considering 50 attributes such as age, height, blood pressure, water intake, calcium, food habits, blood sugar, and so on and for classification, they used backpropagation algorithm.

Panwong et al. [2] have explained the predicting transitional interval of kidney disease stages 3–5 using data mining methods. Naïve Bayes and ANN were used to elicit knowledge and for classification with the selected set of attributes. They compare the performance on the basis of accuracy among the different algorithms.

Pourghahestani et al. [3] have explained object detection in images using ANN and binary GSA [3]. Detection of objects in set of objects by using the Artificial Neural Networks along with Gravitational Search Algorithm here, watershed algorithm is used to segment image and extract the objects.

Chakraborty et al. [4] have explained training FFNN using hybrid flower pollination-GSA to minimize the error in feed-forward network algorithm. Here, training of feed-forward network is introduced by meta-heuristic optimization algorithm.

Kumar et al. [5] have explained ANN for detection of Kidney Stones Disease. Here classifier as ANN and consider the 1000 instances with 8 attributes and trained to network, and they used three types of algorithms, namely, LVQ, FFBN, and RBF, where FFBN gives the highest accuracy.

Ramya et al. [6] have explained Diagnosis of chronic kidney disease using machine learning algorithms. For diagnosis, backpropagation neural network, random forest algorithms are used for classification, and calculation of accuracy is also done in this paper.

Vijayarani et al. [7] have explained data mining classification algorithms for kidney disease prediction. The Algorithms are used for classification of CKD, Naïve Bayes and support vector machine and concluded that SVM is better than the Naïve Bayes classifier algorithm on the basis of accuracy.

2 Proposed Method

In the current paper, ANN, Gabor filter, FFBP, and GSA are used for the classification of an image.

2.1 Input Image

The dataset for diagnosis of chronic kidney disease is obtained from UCI Machine Learning Repository, which is an MR image. There are 33 MR images out of which 27 images are abnormal images and the remaining 6 are normal images. Based on the trained dataset, we classify the test image (Fig. 1).

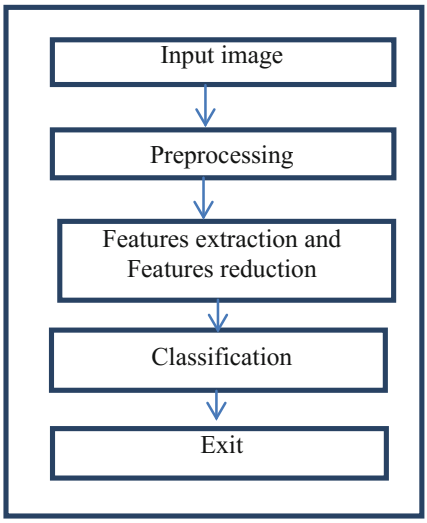

Fig. 1 The block diagram for classification of kidney images

Steps involved in this application

2.2 Preprocessing

Due to the problem of initial collection of data, processing was required. During preprocessing, conversion of an image into a gray scale image takes place.

2.3 Features Extraction

We cannot train the original image to the Artificial Neural Networks. So the requirement of main features in the image is important, which is done in this step.

In order to define a class of an image, the uniqueness in the kidney image is represented by selecting the features. In this methodology, the 5-level Wavelet decomposition is considered. At each and every level, mean, seven moment invariant and covariance features were extracted. Further, for the horizontal and vertical details, the Gabor features were extracted for four different wavelengths and six different orientations. The two-dimensional discrete wavelet transform (2D-DWT) has been used to represent an image for multi-resolution analysis. The image is first represented by LH (Horizontal), HL (Vertical), and HH (Diagonal) sub-bands in which the image details are encoded in three directions, and an LL sub-band provides an approximation of it. The LL sub-band is again considered for further decomposition levels.

Dennis Gabor named Gabor filter in image processing. This filter is used for edge detection and for features extraction. Frequency (wavelength (pixels/cycle))

and orientation (degree) representations of Gabor filters are analogous to the human visual system and it has been appropriate for the texture representation and image discrimination. So, we should calculate the mean and variance and moments for those coefficients. Probabilistic Principal Component Analysis (PPCA) is used to get the dominant features. Thus, as a result, 90 (i.e., $5 * 2(H, V) * \begin{pmatrix} \text{mean} + \text{variance} + \\ (\psi_1 + \psi_2 \ldots \psi_7) \end{pmatrix}$) features were extracted.

2.4 Classification Using Artificial Neural Networks

This step involves the classification of an image if it is a normal or an abnormal image. ANN often called as the "neural networks" is the mathematical model based on biological neural networks. The machine learning algorithms such as FFBN with GSA is implemented as classification task for accurate diagnosis of CKD based on different performance evaluation measures such as accuracy, specificity, sensitivity, and precision.

2.5 Feed-Forward Backpropagation with GSA

A meta-heuristic optimization algorithm called as Gravitational Search Algorithm (GSA) is introduced by Rashedi et al. It obeys Newton's laws of linear motion and depends on Newton's law of gravity and relative motion of masses (Fig. 2).

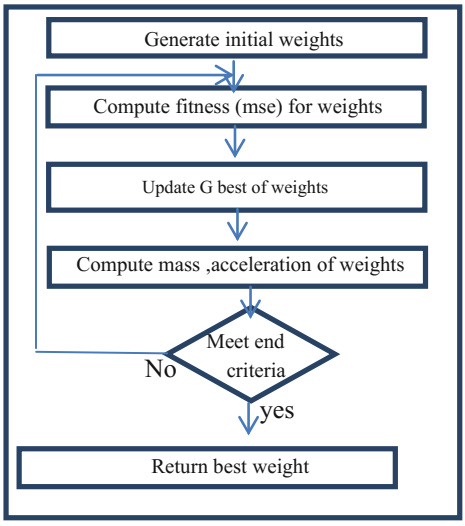

Fig. 2 Flowchart of GSA

In GSA, there are N agents in an isolated system where each agent is a candidate solution which is described as

$$X_i = x_i^1, x_i^2, \ldots, x_i^d \tag{1}$$

where x_i^d depicts the location of the ith agent in dth dimension. The complete number of dimensions or parameters to be enhanced are represented by n. Each agent can be initialized by the generation of an arbitrary number in a given dimension. The same method is carried out for the whole populace.

$$q_{i(t)} = \frac{\text{fit}_i(t) - \text{worst}(t)}{\text{best}(t) - \text{worst}(t)} \tag{2}$$

$$M_{i(t)} = \frac{q_{i(t)}}{\sum_{j=1}^{N} q_{j(t)}} \tag{3}$$

After evaluating the fitness for entire population, the best and worst fitness of the population and also the fitness of the corresponding agent are used for calculating the weight of each probable solution. This is estimated according to Eqs. (2) and (3). Here, $\text{fit}_i(t)$ represents the fitness of the ith agent, and $M(t)$ gives its respective weight. The best and worst fitness of population are given as best(t) and worst(t), respectively. There is a linear decreasing function called gravitational constant G that relies on the initial value Go as well as the repetitions shown in (4).

$$G(t) = G_{0(t)\left(1-\frac{t}{7}\right)} \tag{4}$$

Here, t shows the maximum no. of repetitions.

Velocity is used to improve the position for everybody. It is calculated by determining the net gravitational force of an agent, acceleration of the body, and the velocity of the body according to (5)–(8), respectively.

$$F_{ij^d} = G(t)\frac{M_{i(t)} \times M_{j(t)}}{R_{ij(t)+\varepsilon}}\left(x_j^d(t) - x_i^d(t)\right) \tag{5}$$

$$F_i^d = \sum_{j=1, i\neq 1}^{N} \text{rand}_j F_{ij}^d(t) \tag{6}$$

$$a_i^d(t) = \frac{F_{i^{d(t)}}}{\mu_{i(t)}} \tag{7}$$

$$V_i^d(t+1) = \text{rand}_i \times V_i^d(t) + a_i^d(t) \tag{8}$$

At last, the particle's position in a given dimension is depicted as follows:

$$x_i^d(t+1) = x_i^d(t) + v_i^d \tag{9}$$

2.5.1 Training Feed-Forward Backpropagation Neural Network with GSA

Here, to train the feed-forward multilayer NN, we use the proposed GSA. In general, the meta-heuristic algorithm is used to train NNs in different means like detecting the best solution or determining the best merging of weights and biases to ensure that they give the least error value. Here, with the aim to minimize mean square error in various classification issues, we use a maximizing technique to find the best combination of weights and biases. The dimension of the problem depends on the attributes like the number of features and classes present in a dataset.

3 Performance Evaluation

Accuracy, sensitivity and specificity are mostly used attributes to describe a diagnostic test.

Accuracy: It is the amount of true results, one or the other true positive or the negative in a population. It estimates the degree of precision of a test based on a condition.

$$\text{Accuracy} = \frac{\text{TP} + \text{TN}}{\text{TP} + \text{FP} + \text{TN} + \text{FN}}$$

Here, TP—true positive, TN—true negative, FP—false positive, and FN—false negative.

Sensitivity: It is also known as the true positive rate. It estimates the amount of positives which are accurately identified. The possibility of a positive test shows that patient is ill.

$$\text{Sensitivity} = \frac{\text{TP}}{\text{TP} + \text{FN}}$$

Specificity: It is also known as the true negative. It estimates the amount of negatives that are accurately identified. The probability of negative test shows that the patient is well.

$$\text{Specificity} = \frac{\text{TN}}{\text{TN} + \text{FP}}$$

4 Results

For the purpose of analyzing and evaluating, MR images from UCI Machine Learning Repository dataset are used (Fig. 3).

While analyzing the classification accuracy values, the proposed GSA–ANN provides 78%, GA–ANN gives 56%, and KNN gives 67% only (Fig. 4).

In the case of specificity, the proposed GSA–NN and KNN algorithms give 85%, which is better than the remaining techniques. Whereas the GA-based ANN offers values less than 60% (Fig. 5).

It is clear that the sensitivity is 100% for the techniques like GA–ANN algorithms, thus showing the better classification effectiveness of the proposed method. Whereas the KNN offers null sensitivity and 50% sensitivity is attained for the GSA-based ANN method.

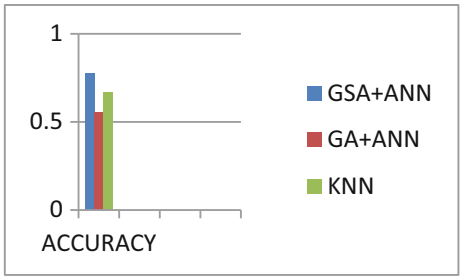

Fig. 3 Comparison plot of accuracy for proposed versus existing techniques

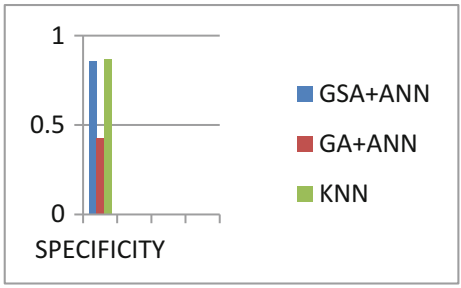

Fig. 4 Comparison plot of specificity for proposed versus existing techniques

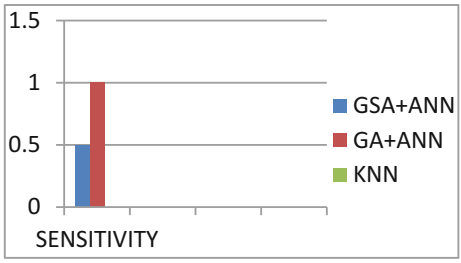

Fig. 5 Comparison plot of sensitivity for proposed versus existing techniques

5 Conclusion

Prediction of chronic kidney disease is one of the main aspects in medical diagnosis. In this paper, three algorithms are used, namely, Artificial Neural Network along with Gravitational Search Algorithm (GSA+ANN), Genetic Algorithm along with ANN (GA+ANN), and K-Nearest Neighbor (KNN). They are used to assess the training performance of classification accuracy. The Gravitational Search Algorithm enhances the classification accuracy of neural networks by skipping the local minima and converging to global minima. The main goal to estimate the performance of the algorithm over kidney disease dataset is Accuracy. Comparing these three algorithms, (GSA+ANN) gives better accuracy, sensitivity, and with equal specificity which are very important metrics in a medical report. I expect that this methodology is extended to enhance the implementation in any engineering up gradation problem.

6 Future Scope

Gravitational Search Algorithm with some modifications that are oppositional-based Gravitational Search Algorithm (OGSA) and advanced Gravitational Search Algorithm will give better results than GSA-based ANN.

References

1. Vital TP, Nagesh MYV, Anuradha T, Samanthula AR (2016) A neural network approach for classification of kidney disease dataset collected from Visakhapatnam of A.P., India. Int J Innovative Res Sci Eng 2(2)
2. Panwong P, lam-On N (2016) Predicting transitional interval of kidney disease stages 3 to 5 using data mining method. In: 2016 second Asian conference on defence technology (ACDT)
3. Pourghahestani FA, Rashedi E (2015) Object detection in images using artificial neural network and improved binary gravitational search algorithm. In: 2015 4th Iranian joint congress on fuzzy and intelligent systems
4. Chakraborty D, Saha S, Maity S (2015) Training feedforward neural networks using hybrid flower pollination-gravitational search algorithm. In: 2015 1st international conference on futuristic trend in computational analysis and knowledge management (ABLAZE-2015)
5. Kumar K, Abhishek B Artificial neural networks for diagnosis of kidney stones disease. Published Online July 2012 in MECS https://doi.org/10.5815/ijitcs
6. Ramya S, Radha N Diagnosis of chronic kidney disease using machine learning algorithms. https://doi.org/10.15680/ijircce.2016.0401049
7. Vijayarani S, Dhayanand S (2015) Data mining classification algorithms for kidney disease prediction. Int J Cybern Inform (IJCI) 4(4)

Design and Placement of a Conformal Microstrip Antenna on a Vehicular Structure for SATCOM Applications

B. Ebenezer Abishek, Arun Raaza, K. Leelaram, S. Jerritta and V. Rajendran

Abstract Various applications utilized in vehicles like GPS reception, GSM communication, AM, FM, automated tolling, television, keyless entry, etc., use different antennas, which need to be incorporated at different positions in the outer structure of the vehicles. Thus, finding the location in different positions and the placement of the antennas in these positions is a challenging task. The antenna placed should be functional in the given location as well as the position of these antennas should not affect the aesthetic of the vehicle design. Conforming the antenna over the vehicular structure is the best solution for the above task. The first step to achieve the solution for the above problem is to analyze the radiation characteristics of the antenna along with the vehicular platform. Designing of such an antenna requires a complex procedure and also requires more computational resources to determine the electromagnetic radiation surrounding the vehicular structure. In this research, a circularly polarized conformal microstrip patch antenna on a vehicular structure for SATCOM application in Ku band using both HFSS and FEKO tool is designed and simulated, and a comparative study is done with linearly polarized planar and conformal antenna used for vehicular communication.

Keywords Conformal antenna · Vehicular platform · Coaxial probe feed Circular polarization · Ku band

B. Ebenezer Abishek (✉) · A. Raaza · K. Leelaram · S. Jerritta · V. Rajendran
Vels University, P.V. Vaithiyalingam Road, Pallavaram, Chennai 600117, Tamil Nadu, India
e-mail: abishek.se@velsuniv.ac.in

A. Raaza
e-mail: arunraaza@gmail.com

K. Leelaram
e-mail: bram8230@gmail.com

S. Jerritta
e-mail: jerritta.se@velsuniv.ac.in

V. Rajendran
e-mail: hodece@velsuniv.ac.in

H. S. Saini et al. (eds.), *Innovations in Electronics and Communication Engineering*, Lecture Notes in Networks and Systems 33,
https://doi.org/10.1007/978-981-10-8204-7_45

1 Introduction

High-speed voice/data communication in fast-moving vehicles has been achieved by transmission and reception through satellite because of the reliability and large footprint [2]. This makes it essential to develop SATCOM antennas which can be conformed with the different types of fast-moving vehicle thereby beneficial to both the vehicle manufacturers and travelers [7]. Different antennas have been tried by researchers and the microstrip patch antenna has been found to be advantageous in many cases due to its increased efficiency, less complexity and less expensiveness.

In this research work, both planar and conformal microstrip patch antenna were designed and studied for fast-moving vehicular communication [5]. Based on the performance metrics obtained, the conformal microstrip patch antenna with circular polarization was used for SATCOM reception on a moving car. The circular polarization was achieved by truncating the corners of a rectangular patch [11]. The designed antenna was placed on the roof of the moving vehicle and results indicate increased coverage area with low side lobe patterns during the moving vehicle trial.

2 Methodology

The planar and conformal microstrip patch antenna used in this work was designed using FEKO tool. The design steps are illustrated in Fig. 1.

The dimensions were calculated using the design equations as in [12]. The RT Duroid 5880 material of thickness 0.79 mm is given as substrate. The dielectric constant of this material is 2.20. The resonating frequency is set as 12.2 GHz as the antenna is for SATCOM reception.

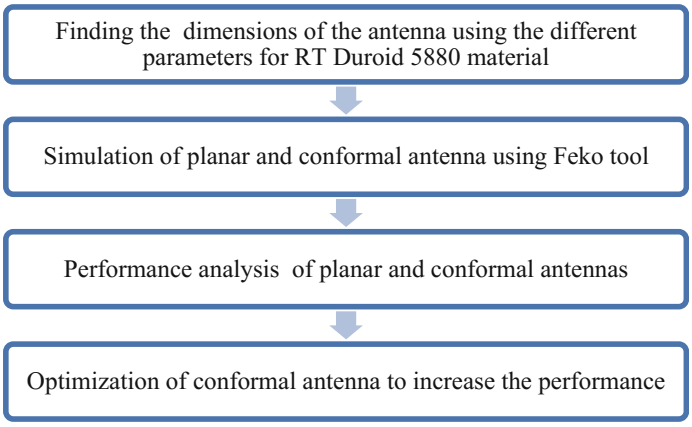

Fig. 1 Flow diagram of the design steps

2.1 Microstrip Planar Linearly Polarized Antenna

The microstrip patch antenna, as in Fig. 2, consists of a very thin metallic patch which is placed above the dielectric substrate that is placed above the ground plane. The length of a conventional microstrip patch antenna is less than half the resonating wavelength. As the antenna has to be designed for a vehicle, the flexible RT Duroid 5880 material is used with coaxial probe feed. The geometry of the microstrip planar linearly polarized antenna is shown in Fig. 2.

2.2 Microstrip Conformal Linearly Polarized Patch Antenna

Conformal antennas can be of any geometry, although the main structures investigated so far are cylindrical, spherical, and conical [1, 5, 7]. Due to their electrical and mechanical attractive characteristics, conformal microstrip antennas and their arrays are suitable for installation in a wide variety of structures such as aircrafts, missiles, satellites, ships, vehicles, base stations, etc. When mounted on a surface these antennas do not cause extra drag and are less visible to the human eye. Moreover, they are low weight, easy to fabricate and can be integrated with PCB's. The geometry of the microstrip conformal linearly polarized antenna is shown in Fig. 3.

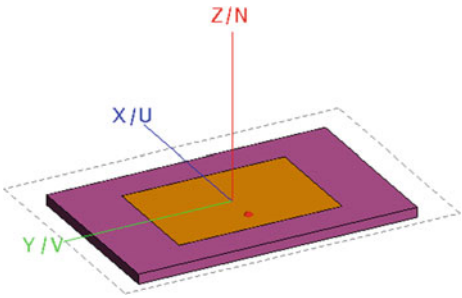

Fig. 2 Geometry of the microstrip planar linearly polarized antenna

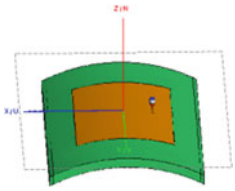

Fig. 3 Geometry of the microstrip conformal linearly polarized antenna

2.3 Microstrip Conformal Circular Polarized Patch Antenna

Circular polarization can be achieved using a single feed or multiple feeds. Single feed does not need phase shifters or power dividers and uses small feed network with low profile [4, 9]. Truncation technique introduced by Hsu and Chang was used in this work. Thus, method coverts the rectangular patch into a square patch by making the width of the patch equal to the length of the patch. The corners located across the diagonal are then cut off. The feed position is located in the middle one of the edges. Therefore, one mode gets excited directly and the others are excited by the irregularity in the square patch. The geometry of the microstrip planar circularly polarized antenna is shown in Fig. 4.

The antenna was then conformed to be placed on the top of a car. The geometry of the base model or platform in which the antenna is to be conformed is shown in Fig. 5, and the conformal antenna placed on the roof of the car base model is shown in Fig. 6.

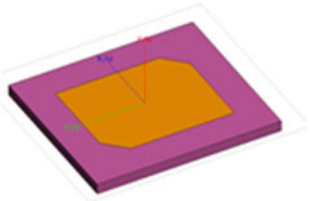

Fig. 4 Geometry of the microstrip planar circularly polarized

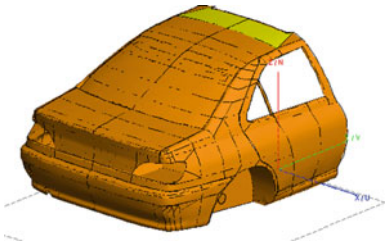

Fig. 5 Geometry of the base model or platform in which the antenna is to be conformed

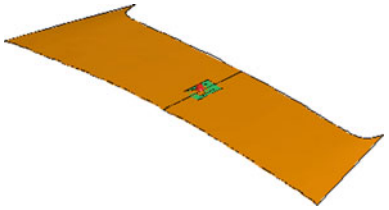

Fig. 6 Conformal antenna placed on the roof of the car base model

3 Results and Discussion

The design is simulated using FEKO tool. A correct meshing size is not selected to avoid the overload of computational recourses. Multilevel Fast Multipole Method (MLFMM) is selected for simulating or solving the design [3]. The characteristic impedance of the patch (Z0) of the simulated design is 50 Ω. Figure 7 shows the Cartesian graph showing S_{11} parameter versus frequency of linearly polarized planar patch antenna, linearly polarized conformal patch antenna, and circularly polarized conformal patch antenna, respectively. S_{11} should be less than −10 dB in the operating bandwidth [10] for the antenna to work efficiently which is achieved (−34.0661, −14.75, −17.75) for linearly polarized planar patch antenna, linearly

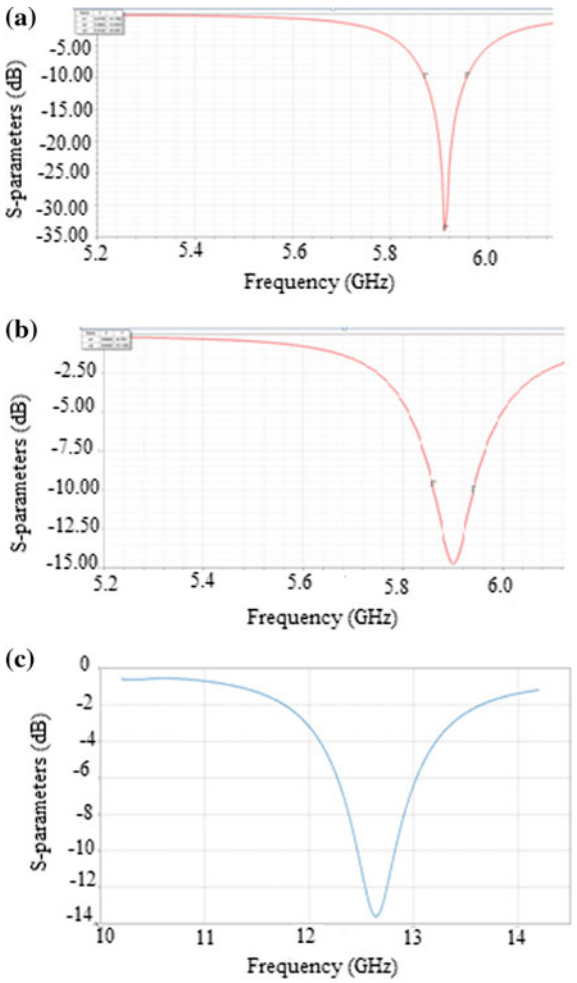

Fig. 7 Cartesian graph showing S_{11} parameter versus frequency. **a** Microstrip planar linearly polarized antenna. **b** Microstrip conformal linearly polarized antenna. **c** Microstrip conformal circularly polarized antenna

polarized conformal patch antenna, and linearly polarized conformal patch antenna, respectively, in this research work for all the antennas.

Figure 8 shows the Cartesian graph showing VSWR parameter versus frequency of linearly polarized planar patch antenna, linearly polarized conformal patch antenna, and circularly polarized conformal patch antenna, respectively. In this

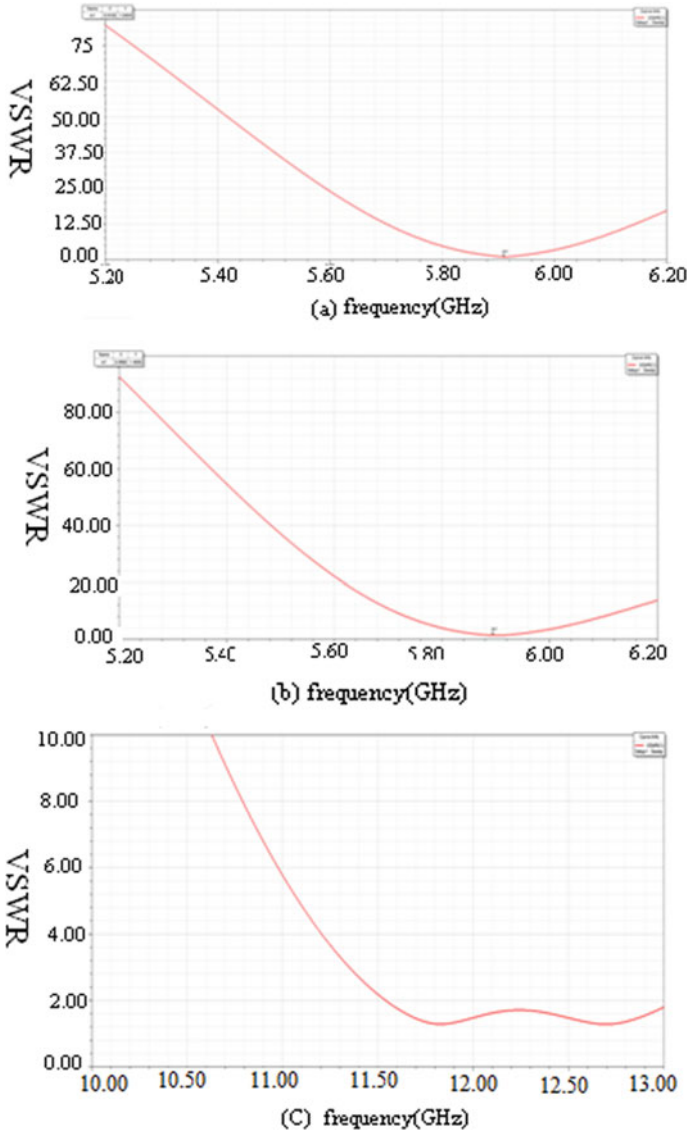

Fig. 8 Cartesian graph showing VSWR parameter versus frequency. **a** Microstrip planar linearly polarized antenna. **b** Microstrip conformal linearly polarized antenna. **c** Microstrip conformal circularly polarized antenna

work, a VSWR of 1.0404, 1.4555, and 1.2 has been achieved for the planar linear, conformal linear and conformal circular polarized antennas, indicating that they are well in the operating bandwidth.

Figure 9 shows the polar graph showing the gain of linearly polarized planar patch antenna, linearly polarized conformal patch antenna, and circularly polarized conformal patch antenna, respectively. Gain for the designed linearly polarized antenna for both planar and conformal is shown in the figure below and is more than 7 dB for both the elevation angle and azimuthal angle. For circular polarization in conformal antenna, the difference between the gain of co pole (LHCP) and cross pole (RHCP) component is 17 dB, which is more than the minimum requirement of 15 dB. This indicates that the circular polarized antenna on the top of a car is fully functional and can be used for SATCOM applications.

Circularly polarized conformal patch antenna is tabulated in Table 1. The metrics of the linearly polarized planar patch antenna has the lowest value of S_{11}, VSWR and high gain. However, this antenna cannot be used for SATCOM applications because of its orientation. Circular polarization of conformal antenna also has higher value of gain similar to planar antenna. S_{11} and VSWR are less than planar but higher than linearly polarized conformal antenna.

The simulation study also shows that the reduction in S_{11} parameter performance in conformal patch antenna is less. However, there is a tremendous reduction in the low side lobe patterns. Furthermore, this antenna also provides an increased coverage area and hence can be advantageous for fast-moving vehicular communication [6, 8].

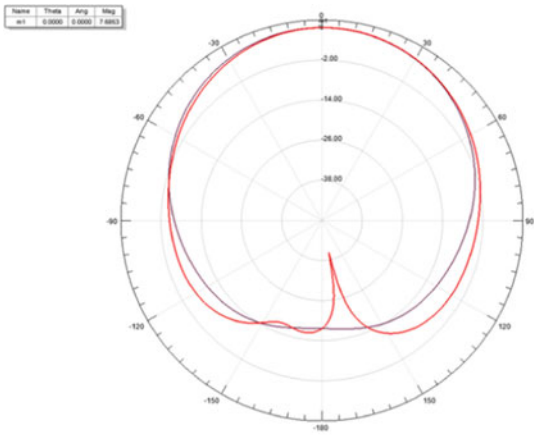

(a) Linearly Polarized Planar Patch Antenna

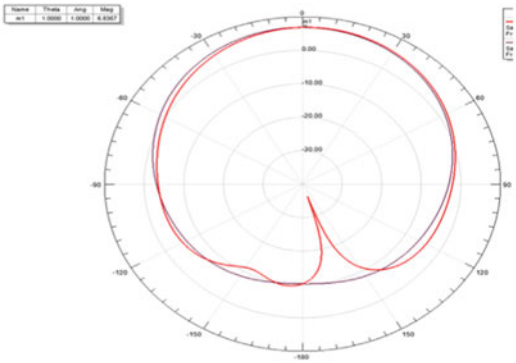

(b) Linearly Polarized Conformal Patch Antenna

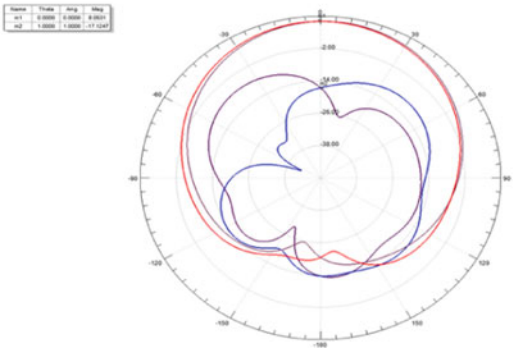

(c) Circularly Polarized Conformal Patch Antenna

Fig. 9 Polar graph showing gain

Table 1 Circularly polarized conformal patch antenna

Radiation characteristics	Linearly polarized planar patch antenna	Linearly polarized conformal patch antenna	Circularly polarized conformal patch antenna
S_{11}	−34.0661	−14.75	−17.75
VSWR	1.0404	1.4555	1.2
Gain (dB)	8	7	8

4 Conclusion

In this work, a conformal circular polarized antenna is found to be efficient with low side lobe patterns and more coverage area. The analysis of three types of antennas, namely, microstrip planar linearly polarized antenna, microstrip conformal linearly polarized antenna, and microstrip conformal circularly polarized antenna for fast-moving vehicular communication, indicates that the conformal circular polarized microstrip antenna is best suited for the above application.

References

1. Braaten BD, Roy S, Irfanullah I, Nariyal S, Anagnostou DE (2014) Phase-compensated conformal antennas for changing spherical surfaces. IEEE Trans Antennas Propag 62 (4):1880–1887
2. Cianca E, Rossi T, Yahalom A, Pinhasi Y, Farserotu J, Sacchi C (2011) EHF for satellite communications: the new broadband frontier. Proc IEEE 99(11):1858–1881. https://doi.org/10.1109/JPROC.2011.2158765
3. Ergül Ö, Güre L (2014) The multilevel fast multipole algorithm (MLFMA) computational problems. Wiley, p 460
4. Harchandra B, Singh R (2014) Analysis and design of Bowtie antenna with different shapes and structures. Int J Eng Trends Technol (IJETT) 18(4):171–175
5. Josefsson L, Persson P (2006) Conformal array antenna theory and design. IEEE Press Series on Electromagnetic Wave Theory. http://doi.org/10.1109/MAP.2007.4395313
6. Khairnar VD, Kotecha K (2013) Performance of vehicle-to-vehicle communication using IEEE 802.11p in vehicular ad-hoc network environment. Int J Netw Secur Appl 5(2):143–170. http://doi.org/10.5121/ijnsa.2013.5212
7. Kumari P (2016) Performance analysis of microstrip conformal antenna array and effect of mutual coupling for different curvature. Int J Comput Appl 135(9):30–35
8. Papadimitratos P, De La Fortelle A, Paristech M, Evenssen K, Asa Q (2009) Vehicular communication systems: enabling technologies, applications, and future outlook on intelligent transportation. IEEE Commun Mag 84–95. http://doi.org/10.1109/MCOM.2009.5307471
9. Roy J, Themal M (2008) Design of a circularly polarized microstrip antenna for WLAN. Prog Electromagnet Res M 3:79–90

10. Sujimol MR, Acharya R, Singh G, Gupta RK (2015) Rain attenuation using Ka and Ku band frequency beacons at Delhi Earth Station. Indian J Radio Space Phys 44(March):45–50
11. Taha İmeci AS (2010) Corners truncated microstrip patch antenna. Aces 02:760–765
12. Afridi MA (2015) Microstrip patch antenna—designing at 2.4 GHz frequency, biological and chemical research. Science Signpost Publishing, pp 128–132

Statistical Analysis of Path Length in Optical Networks

Mihir Malladi, V. Mithun, K. B. N. Naveen, N. Punith, Jyoti M. Roogi, Mrinal J. Sarma and Sudhir K. Routray

Abstract Optical networks are the main traffic carriers of all the modern communications. All the core and regional networks are very much optical these days. Even in the metro and access area networks, we now have a lot of presence of optical fibers. With the growth of traffic, the complexities of management and control aspects of the optical networks increase. In optical networks, shortest path and the minimum hop paths are not the only choices when the network operates at its optimum capacity level. Rather, several other paths are chosen for routing and traffic management, which are neither the shortest nor minimum hop path lengths. So, there is a requirement to understand the statistics of these paths. In this paper, we analyze the path lengths of 35 real optical transport networks (OTNs). For this study, we used 65 different statistical distributions. We found that both Wakeby and Johnson S_B distributions are very much suitable for the modeling of path lengths in OTNs. The validity of our statistical measurements was checked using

M. Malladi (✉) · V. Mithun · K. B. N. Naveen · N. Punith · J. M. Roogi · M. J. Sarma
Department of Electronics and Communication Engineering, CMR Institute of Technology, Bengaluru, India
e-mail: mima13ec@cmrit.ac.in; mihirmal@udel.edu

V. Mithun
e-mail: minv13ec@cmrit.ac.in

K. B. N. Naveen
e-mail: nabn13ec@cmrit.ac.in

N. Punith
e-mail: puth13ec@cmrit.ac.in

J. M. Roogi
e-mail: jyoti.r@cmrit.ac.in

M. J. Sarma
e-mail: mrinal.js@cmrit.ac.in

S. K. Routray
Department of Telecommunication Engineering, CMR Institute of Technology, Bengaluru, India
e-mail: sudhirkumar.r@cmrit.ac.in

H. S. Saini et al. (eds.), *Innovations in Electronics and Communication Engineering*, Lecture Notes in Networks and Systems 33,
https://doi.org/10.1007/978-981-10-8204-7_46

Kolmogorov–Smirnov statistic (KSS). For both Wakeby and Johnson S_B distributions, all the KSS values obtained are valid at 95% confidence interval for all 35 networks.

Keywords Optical transport network · Path lengths · Statistical model for path lengths · Wakeby distribution · Johnson S_B distribution

1 Introduction

Network science is a new branch of science and engineering which has pervasive uses across several disciplines. Its impact is everywhere around us from searching websites to social networking, from designing drugs to metabolic engineering, from security analysis to managing organizations [1]. Telecommunication sector has undergone drastic changes due to the evolution of the Internet and the World Wide Web. Due to this tremendous growth, the traffic has been growing very rapidly since last several decades. This also leads to the increase in demand for various resources such as bandwidth and transmit power. Performance enhancements in effective routing, compensation techniques, and advanced data transmission too have been better [2]. These complexities of networks can be explained using network science [3].

Optical networks are the main traffic carrier of modern telecommunications [2]. They tend to play fundamental roles in the current and future telecommunication infrastructures. Due to the popularity of the Internet, the roles of optical networks have become very much critical in global communication networks. The technology and architecture of modern telecommunications continue to evolve. Broadly, the optical transport network (OTN) topologies are survivable in nature [4]. OTNs are robust and they ensure a high level of integrity, privacy, and security [2]. These optical networks are becoming increasingly capable of delivering flexible bandwidths wherever and whenever needed [5]. Optical networks are nowadays becoming increasingly capable of providing the required channel capacity due to availability of compensation techniques [2]. The channel capacities provided by these OTNs are becoming larger than the capacities provided by any other networks including wireless networks and copper cable-based networks. An OTN provides a common infrastructure over which a variety of services can be delivered [2]. Over the last three decades, optical networking has become the preferred medium for provision of major infrastructure for voice, video, and data transmission [3]. Network traffic is becoming larger with every passing year due to the significant increase in the number of users and smart devices connected to the Internet. Also due to the increased use of web-based applications such as streaming, sharing, and broadcasting of multimedia contents through cloud computing the popularity is enhanced [2]. Optical networking technologies have been evolved to meet the growing demands for efficient, cost-effective, worldwide communications [2]. Business companies too are relying on high-speed networks to conduct their

businesses. These networks are used to interconnect multiple locations within a company as well as between companies for business-to-business transactions [2]. Hence, early stage planning and cost estimation are needed for network investors [3]. These include expenses for capital equipment (CAPEX), operating expense (OPEX), and management expenditure (MANEX) [3]. Therefore, these networks must be studied systematically from their structure and behavior points of views. Statistical analysis and modeling of the network parameters form integral parts in studying the behavior and the structural point of view [5–8]. The CAPEX, OPEX, and MANEX are important parameters for the operators to improve the efficiency and performances of the OTNs [6–8]. From the research on statistical analysis of the shortest path lengths, it was found that Johnson S_B is the best fit [5]. In [5], 40 real optical networks were studied and analyzed for the shortest path lengths. The model developed can be applied to estimate the type of signal modulation formats, compensation methods, and several CAPEX parameters required in transparent OTNs. Statistical analysis has been performed on the link lengths in optical networks [6] and it has been found that the general extreme value (GEV) ranks as the best fit for the real optical networks. In [7], a network global expectation model has been presented. In this work, the network expectation parameters have been estimated with just the partial information. Several expressions have been developed in these works which are used in the fast estimation of network needs and dimensioning. In [8], fast estimation formulas have been developed for mesh optical networks. These formulas can be used for network dimensioning and performance analysis. In [8], an approximate expression for average path length has been developed using empirical information of the network. In [9], a Weibull model has been proposed for the shortest path lengths of random networks. This model can be applied to the networks that exhibit random network characteristics. Very few optical networks may come in this category. In [10], optical path routing has been used for OFDM-based elastic optical networks. This work uses optical path lengths for dynamic routing.

In this paper, we analyze all possible path lengths in optical networks using 35 real topologies of [4]. We found that Wakeby and Johnson S_B distributions are the best fit for the optical networks. We use these two distributions for characterizing the path lengths of optical networks.

The remaining part of the paper has been arranged in the next three sections. Section 2 of the paper talks about how the possible path lengths were measured and computed and also how the data collected were analyzed using EasyFit. Section 3 gives a brief description about the EasyFit software and the rankings of the distribution fits for 35 networks.

2 Statistical Analysis of All Possible Path Lengths

Statistics is the study of the collection, analysis, interpretation, presentation, and organization of data. Statistics continues to be an area of active research and development for network science. It provides the theory and methods of extracting

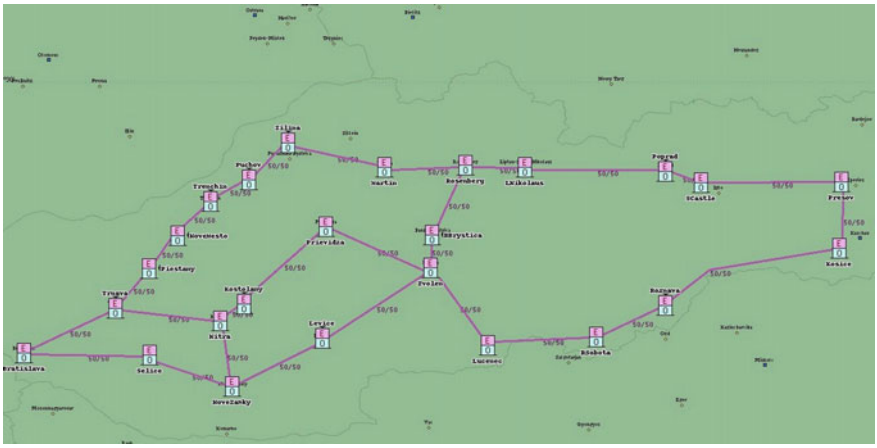

Fig. 1 An example of an optical network used in this study (SANET, Slovenia)

information from observational data for solving real-world problems. Statistical features of communication networks play important roles in the designing and evaluation of the performance of these networked systems. We analyzed 35 real topologies from [4] to study the shortest path lengths in optical networks. In Fig. 1, we present the topology of an optical network [4]. SANET is the research and educational optical network in Slovenia. It has 28 links and 25 nodes.

2.1 Measurement of the Lengths Between Two Nodes and All Possible Path Lengths

For the measurement of link lengths and path lengths, Google Earth was used. We find out the great circle link lengths of the real optical networks. All these real OTNs can be found in [4]. The path lengths were computed manually by adding up the associated link lengths measured using the above mentioned methods.

2.2 Analysis of All Possible Path Lengths

All possible path lengths were calculated for 35 networks. These path lengths were analyzed using EasyFit (a statistical analysis software from www.mathwave.com). It has been observed from the analysis of these 35 optical networks that Johnson S_B and Wakeby do not fail for any network at 95% confidence interval (CI) which indicates the significance level = 0.05.

3 Analysis of the Distributions

3.1 The Statistical Analysis of the Paths Computed

The possible path lengths were analyzed and their statistical properties were studied for 35 real OTNs. From the analysis, we found out that for most of the networks, the best distributions are Wakeby and Johnson S_B. We measure the validity or the goodness to fit for 40 distributions in terms of the Kolmogorov–Smirnov statistic (KSS value). The CI for the KSS values is set to 0.95 (=95%). The rankings are given in Table 1.

In Table 1, we show the rankings of top 15 best fitting distributions for 35 real optical networks. These rankings are based on the average KSS values of the respective distributions (averaged over 35 optical networks). Out of the 65 distributions analyzed for 35 real Optical Networks, Wakeby has the least KSS value, and Johnson S_B has the next least.

Though Wakeby ranks as the best fit among the total 65 distributions, this distribution has several drawbacks. It does not adapt to the bimodal cases of the path length distributions. Also, it needs five input parameters. Furthermore, it is generally expressed in terms of its quartile functions as the expression for the probability density function is not well defined (quartile function specifies for a given probability in the probability distribution of random variable). Johnson S_B which is the second best can be taken into consideration for the practical path length modeling. We calculate the average path lengths and medians of the real

Table 1 Best fitting distributions and their ranks according to the average KSS values (from the largest to the smallest)

Rank	Distribution	Avg. KSS	Max. KSS	Min. KSS
1	Wakeby	0.0414	0.1245	0.0088
2	Johnson S_B	0.0522	0.1973	0.01,372
3	Error	0.0593	0.1292	0.01949
4	Gen Pareto	0.0597	0.1245	0.02698
5	GEV	0.0613	0.1693	0.01497
6	GenGamma (4P)	0.0642	0.2331	0.01515
7	Beta	0.0656	0.1559	0.02202
8	Weibull (3P)	0.0694	0.2176	0.01614
9	Uniform	0.0730	0.1445	0.03806
10	Log-Logistic (3P)	0.0734	0.1751	0.0249
11	LogPearson3	0.0745	0.2018	0.02893
12	Lognormal (3P)	0.0760	0.1855	0.0133
13	Normal	0.0761	0.1793	0.02008
14	GenLogistic	0.0788	0.1939	0.02799
15	Gamma (3P)	0.0804	0.2158	0.01736

optical networks as shown in Table 2. We have collected the data related to the convex area of the networks from [5]. From the regression analysis between the square root of the convex area, the average path lengths, and median we obtain linear trends.

Table 2 The values of average path length, median and square root of area for 35 real OTNs analyzed

Network	Average path length (in km)	Area (in km^2)	Square root of area (in km)	Median (in km)
Arpanet	5450	5,975,012	2444	5387
Memorex	1040	253,850	504	1068
Omnicom	3282	2,596,279	1611	3309
EON	4383	5,800,056	2408	4303
CESNET	394	45,957	214	475
LONI	580	68,008	261	527
Hibernia	2555	1,257,762	1121	2607
CANARIE	6192	3,462,688	1861	6198
PIONIER	618	194,178	441	594
Metrona	757	158,837	399	712
KAREN	778	349,015	591	735
California	797	168,087	410	835
LEARN	818	183,296	428	735
Optosunet	950	122,980	351	983
SANREN	1620	508,348	713	1620
ITALY	1357	436,577	661	1507
SINET	1380	406,969	638	1301
RENATER	1402	462,096	680	1438
BELNET	289	17,466	132	277
RNP	2502	1,814,676	1347	2412
Global AD	594	95,108	308	599
AARNET	3148	7,591,320	2755	3171
ERNET	2906	2,382,858	1544	2961
BREN	356	42,196	205	319
SANET	391	24,336	156	375
LambdaRail	4903	6,899,337	2627	4922
Abilene	5160	5,698,507	2387	5196
MZIMA	5256	6,805,153	2609	5377
NEWNET	5283	7,033,452	2652	5319
ARNES	155	12,641	112	156
CompuServ	5793	5,442,148	2333	6321
NSFNET	5885	6,007,605	2451	5897
vBNS	6018	6,279,993	2506	6190
Germany	618	196,675	444	609
VIA	2239	1,267,876	1126	2312.5

In Fig. 2, we show the best fitting Wakeby distribution for Bulgaria network whose topology can be found in [5]. In this case, the best fitting distribution is Wakeby. In Fig. 3, we show another instance of best fitting distribution in which Johnson S_B the best fitting. Therefore, both these distributions can be considered as the candidates for path length modeling.

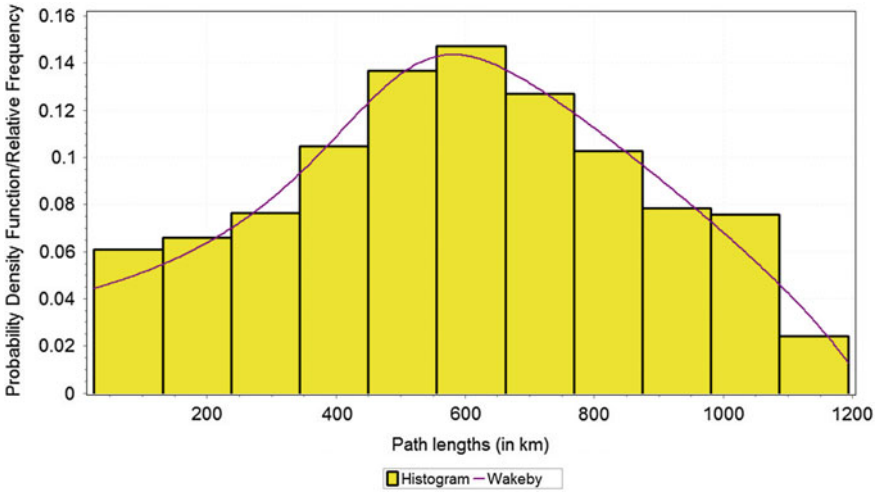

Fig. 2 Possible path length distribution of Bulgaria (Global Communication Net Ad) histogram fitted with Wakeby distribution

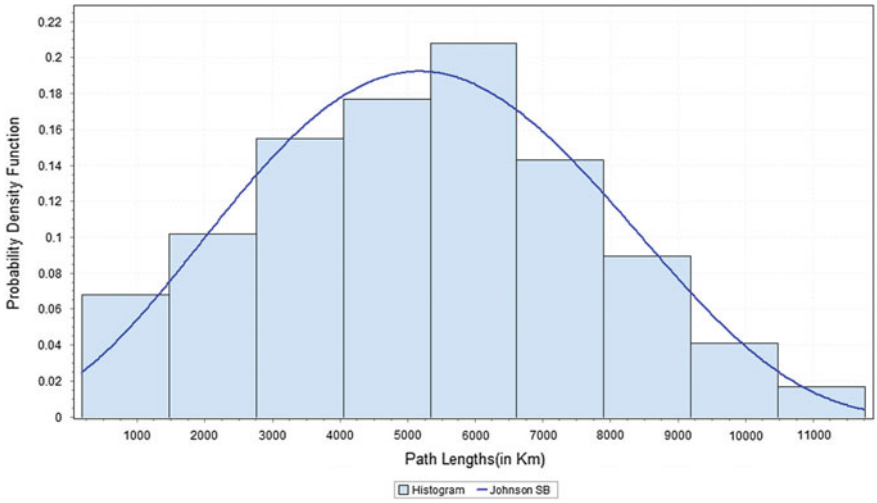

Fig. 3 Possible path length distribution of NEWNET (histogram) fitted with Johnson S_B distribution

4 Conclusion

Optical networks are a set of optical network elements, connected by optical fiber links. The links carry information from one node to another. The statistical analysis of the path lengths can determine planning and cost estimation of OTNs.

The path lengths between the node pairs of 35 real optical networks were found to follow Wakeby and Johnson S_B distributions. However as mentioned before, Johnson S_B is considered a better choice than other distributions, because in addition to yielding low KSS values for all networks, it also accommodates both unimodal and bimodal PDFs. Either of these two distributions is fine for the path length modeling in OTNs. We have also found out that linear correlation exists between the average path lengths and the square root of the convex area of the networks. The data is shown in Table 2 which also shows similar trends with the median of the path lengths.

References

1. Barabási AL (2013) Network science. Philos Trans Roy Soc A 371(1987):1–3
2. Ramaswamy R, Shivrajan K, Sasaki G (2010) Optical networks: a practical perspective, 2nd edn. Morgan Khufman, San Fraccisco, CA, USA
3. Routray SK et al (2015) Statistical analysis and modelling of optical transport networks: characterization and application. In: Proceedings of international conference on telecommunication (ConfTele), Aveiro, Portugal, September 2015
4. Reference Optical Networks (last updated: 23 Jan 2015). [Online]. Available: http://www.av.it.pt/anp/on/refnet2.html
5. Routray SK, Sahin G, da Rocha JRF, Pinto AN (2015) Statistical analysis and modeling of shortest path lengths in optical transport networks. IEEE/OSA J Opt Commun Netw 33 (13):2791–2801
6. Routray SK, Morais RM, da Rocha JRF, Pinto AN (2013) Statistical model for link lengths in optical transport networks. J Opt Commun Netw 5(7):762–773
7. Korotky SK (2004) Network global expectation model: a statistical formalism for quickly quantifying network needs and costs. IEEE/OSA J Lightwave Technol 22(3):703–722
8. Labourdette JF, Bouillet E, Ramamurthy R, Akyamac AA (2005) Fast approximate dimensioning and performance analysis of mesh optical networks. IEEE/ACMJ Trans Netw 3(4):906–917
9. Bauckhage C, Kersting K, Rastegarpanah B (2013) The weibull as a model of shortest path distributions in random networks. In: Proceedings of ACM international workshop on mining learning graphs, Chicago, IL, USA
10. Zhu Z, Lu W, Zhang L, Ansari N (2013) Dynamic service provisioning in elastic optical networks with hybrid single-/multi-path routing. J Lightwave Technol 31(1):15–22

A Survey on Conventional and Secure Routing Protocols in Wireless Sensor Networks

A. L. Sreenivasulu and P. Chenna Reddy

Abstract Wireless sensor networks are one of the emerging fields. This has been supported by advanced technologies and smart sensor nodes that are cost-effective and easily deployable. Our survey is concentrated on conventional routing techniques and security routing protocols in WSNs. The review provides the knowledge about different routing protocols in terms of energy efficiency, location awareness, and security. This paper aims to help the researchers entering into the field of wireless sensor networks by providing the complete understanding of the recent developments.

Keywords Sensor nodes · Energy · Security · Wireless sensor networks Routing

1 Introduction

Wireless sensor networks (WSNs) play a crucial role in the communication technology. WSNs contain sensor nodes that are distributed geographically. The utilization of WSNs is extended to the field of resource monitoring [1, 2], structural monitoring [3, 4], environmental monitoring [5–7], health monitoring [8, 9], and animal tracking [10, 11]. The sensor nodes collect the data from the environment and forwards to the base stations. The sensor nodes work with the battery power. Therefore, they work for a limited time. Figure 1 shows the composition of WSNs.

WSNs are composed of major challenges such as to minimize the energy consumption and to increase the node lifetime. The efficient routing mechanisms are

A. L. Sreenivasulu (✉) · P. Chenna Reddy
Department of Computer Science and Engineering, JNTUA,
Anantapuramu, Andhra Pradesh, India
e-mail: intellseenu@gmail.com

P. Chenna Reddy
e-mail: pcreddy1@rediffmail.com

H. S. Saini et al. (eds.), *Innovations in Electronics and Communication Engineering*,
Lecture Notes in Networks and Systems 33,
https://doi.org/10.1007/978-981-10-8204-7_47

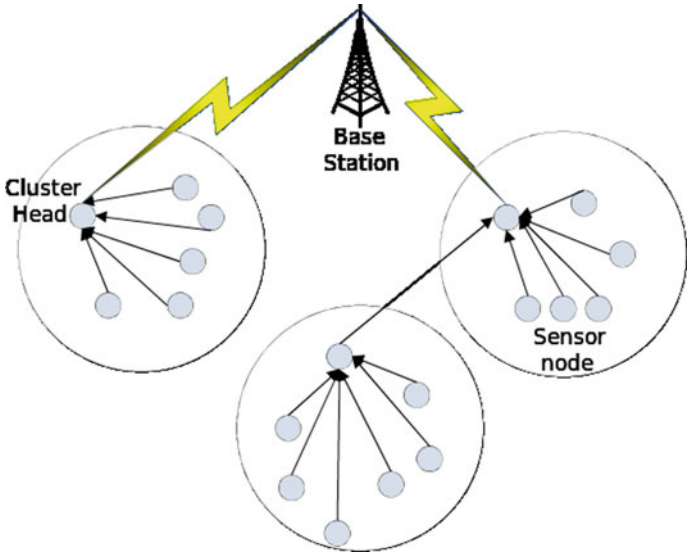

Fig. 1 Organization of wireless sensor network

needed to increase the data accuracy, to decrease the cost, to increase the throughput, and to provide the security in sensor networks.

2 Characteristics of WSNs

At the time of routing, the node properties decide the characteristics of networks which are given below. In [12], the network cost is defined as the organized cost of the path from source to destination. In [13], the clustering coefficient is measured by using the localized connection of the nearer nodes. In [14], the authors define the degree of the node by calculating the direct connections of the source node.

2.1 Energy Efficient Protocols in WSNs

In WSNs, energy management of the nodes is treated as an important issue. In [15], authors proposed the dynamic power management routing protocol to handle the energy management in sensor networks. This protocol automatically turns off the nodes that are in idle state to preserve the battery power. In [16], Jing-hui Zhong made an attempt to increase the lifetime of the network by preserving the energy using the Local Wake-up Scheduling (LWS). A bioinspired approach called as ant colony optimization is used to achieve the energy optimization. In the LWS, the

network is divided into two groups. One group is in active mode and another group is in sleep mode. If the nodes in the active group drain their energy, then the nodes automatically go to the sleep state, and the nodes in the other group come alive.

In [17], sleep scheduling algorithm is proposed for multiple target tracking in sensor networks (SSMTT). For every node, the scheduling time is in the dynamic nature, i.e., based on the network condition. If the nodes are in the active state, the sleep time is scheduled, and if the nodes are in the sleep state, the wake-up time is initiated. SSMTT is more useful in conserving the energy of the sensor nodes.

In [18], the authors made a contribution by proposing the medium reservation preamble-based MAC protocol (MRPM). The nodes in the network are contended for the channel allocation within the duration period. When the nodes are in the active state, they contend for the channel; otherwise, they simply ignore the period of contention. The authors also made some modifications by shortening the contention period using the combination of both SYNC and RTS packets.

With the combination of ACO and SSMTT, a better resource allocation protocol is designed by the authors in [19]. This protocol makes the sleep nodes active with less energy consumption. In [20], a low power state routing protocol was designed to schedule the activities to the nodes when they are in active or sleep states. The nodes consume more energy when they need to change the states from sleep to active. It is more than the energy consumed for the packet transfer. Therefore, the nodes having the less energy will be kept in idle state, where they can listen to the packet, but they cannot transfer or receive the packet. The proposed protocol is efficient in covering the sensor region and also the connectivity of the network.

In [21], the TEEM protocol is designed by combining the RTS into a single packet. The TEEM protocol is faster when compared to the S-MAC, and also, it minimizes the energy consumption and maximizes the lifetime of the sensor network. The node listening period is minimized.

In [22], the authors made an attempt to minimize the energy consumption by implementing the ant colony-based AODV (EACAODV) method. The performance of the proposed model is tested with the packet delivery ratio and energy consumption of the network. The results proved that EACAODV is efficient in reducing the network energy.

3 Conventional Routing Protocols in WSNs

The nodes in the sensor network are dedicated to collect the data from the deployed environment and to forward the data to the base station with the help of intermediate nodes. The collected data is forwarded through the access points or gateways to the outer region. The properties of the gateways or access points may be static or dynamic.

The network layer plays a major role in managing the path routing from source to destination. The network layer follows the properties which are as follows:

- Energy management is the threatening issue in the WSNs. Therefore, the energy management protocols are necessary to manage the acquired resources.
- Multi-hop routing is followed by the network layer to establish the connection between source nodes to the base station.
- Data redundancy is another major issue in the WSN, the data duplicates cannot be avoided by the sensor nodes. Therefore, to reduce the data redundancy, suitable protocols need to be designed.

In [23], the authors proposed many protocols by considering the above factors. Among them, some of the protocols are classified as follows:

- Hierarchical routing protocols,
- Data-centric routing protocols, and
- Location-based routing protocols.

3.1 Hierarchical Routing Protocols

These protocols are more popular in preserving the energy of the nodes. It implements the clustering mechanism to organize the group of sensor nodes in the network. The sensor node which is having the more residual energy is selected as the cluster head, and it is responsible for forwarding the data from the source node to the base station.

- Power Efficient Gathering in Sensor Information Systems (PEGSIS) [24]:

The PEGSIS protocol is an energy management protocol where the nearby nodes are used for data exchange and also these nodes will form a chain. The communication establishment between the nodes is done by the traditional algorithms. This PEGSIS has the higher functionality compared to the LEACH. In PEGSIS, there are no policies for selecting the cluster head, energy of the nodes, and location of the nodes. The major drawback for the PEGSIS is data redundancies caused by clustering procedure.

- Power-Aware Clustered TDMA (PACT) [25]:

PACT is one of the efficient hierarchical protocols where the cluster head is selected based on the passive election model. The nodes which have the maximum residual energy are selected as cluster heads. The communication to the base station is established through the source nodes and cluster heads. In AODV routing protocol, the gateways and the cluster head are used to transfer to the data to improve the forwarding efficiency in the MANETs [26].

- Low Energy Adaptive Clustering Hierarchy (LEACH) [27]:

LEACH is one type of adaptive protocol having the highest preference in the hierarchical group. It follows the random selection procedure to elect the cluster head. Later it changes the cluster head over time. The selection of cluster head in the next stages is carried by calculating the distance between the sensor nodes and the cluster head. The major disadvantage of the LEACH is it not suitable for the larger networks and also the network overhead caused by the random selection procedure for cluster head.

- Shortest Hop Routing Tree Protocol [28]:

The shortest path routing protocol works on the principle of collecting only the useful data from the sensor nodes. This will minimize the energy waste in the sensor nodes. The cluster head selection of the proposed routing protocol is based on the highest battery power of the nodes.

- Extending Lifetime of the Cluster Head (ELCH) [29]:

In ELCH protocol, the cluster head selection process is carried by using the voting policy. The cluster head is selected based on the highest polls voted by the sensor nodes. The ELCH Protocol has the self-configurable and hierarchal properties.

- Tree-based Efficient Protocol for Sensor Information [30]:

The tree-based routing protocol adapts the tree structure to transfer the sensed data. In general, there are two methods to construct the tree model. One model is to compute the cost of each path from source node to the base station, and the second one is to find the local algorithm for each sensor node. Here, the local algorithm is implemented using the tree traversal algorithm.

- Threshold Sensitive Energy Efficient (TEEN) [31]:

This protocol has the special properties that can adjust to any unexpected situations in the wireless sensor networks. The major thing in the network is quick response to the critical applications such as environmental disasters. The architecture of the proposed protocol follows the hierarchical routing. The major drawback of the TEEN protocol is it consumes more energy.

3.2 Data-Centric Routing Protocols

Data-centric routing protocols are also referred with query-based routing protocols and it works on the principle of gathering the data by the sensor nodes based on the query processing. The protocols define the set of sensor nodes and process the data aggregation. For connection establishment, data-centric routing protocols follow the on-demand routing.

- Flooding and Gossiping [32]:

Flooding is the mechanism where the sensor nodes gather the data and forward to the nearest nodes until it reaches the sink node. The major drawback of the flooding is it causes collisions, requires more energy, and produces data redundancy. The gossiping is the technique where the sensor nodes gather the data and forward to the random nodes. The major drawback for gossiping is delay.

- Data Diffusion [33, 34]:

Data diffusion is defined as the process of dividing the sensor nodes into groups based on the data generated. When the query is posted in the network, all the nodes gather the data for aggregation process. As a next step, the aggregated data is forwarded to the base station. The base station checks the aggregated data and sends to the neighboring nodes. The nodes verify the received data and collect the data accordingly. The major drawback of this protocol is data redundancy.

- Sensor Protocols for Information via Negotiation [32]:

This protocol is efficient in terms of reducing redundancy and preserving the energy. The protocol predicts that all the nodes in the neighboring region may contain the similar data. Therefore, the protocol compares the aggregated data with received data from the base station. The nodes with low redundant data are selected and forwards to the base station. This protocol is efficient and simpler to implement.

3.3 Location-Based Routing Protocols

In general, WSNs consists of thousands of sensor nodes, and they are not organized with any IP-based addressing scheme. Therefore, to locate the sensor nodes, their location information is considered. The location-based routing protocols use global positioning system (GPS) to collect the location information of the sensor nodes, but this process leads to the energy consumption [35].

- Minimum Energy Communication Network (MECN) [36]:

MECN is the efficient routing mechanism in location-based routing protocols. This protocol discards the weak nodes and reconfigures the network by regrouping. MECN utilizes minimum energy for data forwarding and also it finds the relay nodes in the network to transfer the data instead of direct transmission.

- Small Minimum Energy Communication Network (SMECN) [37]:

SMECN is the advanced version of the MECN, where it contains minimum number of sensor nodes to form the group. SMECN consumes less energy compared to the MECN due to the smaller network, but the network overhead will be high for searching the subnetwork with limited number of sensor nodes.

- Geographic and Energy-Aware Routing (GEAR) [38]:

GEAR is a major routing protocol in WSNs and it is treated as the alternative to the GPS usage in location prediction. The major motive of the proposed protocol is to decrease the energy consumption of the network and increase the network lifetime. The function of the GEAR is to collect the data from the sensor nodes according to the query and sends the data to the particular location where the data is required.

- Geographic Adaptive Fidelity(GAF) [39]:

GAF is practically designed for routing in the MANETs, and then it is extended to use in the WSNs. The basic principle of GAF is to create the virtual grid based on the nodes location information. This protocol utilizes the GPS location of the sensor nodes for cluster formation. GAF preserves the energy of the network by making the idle nodes into inactive state, and also, it increases the lifetime of the sensor nodes. It uses the dynamic resource routing in WSNs.

4 Secure Routing in WSNs

In WSNs, the sensor nodes are deployed in different regions to collect information, and this information is sent to the sink nodes where it can be used by the application [40]. This type of sensor nodes generally gathers the information and transfers to the base station. This type of information gathering in the distributed environment is called as data aggregation and requires aggregation of data from same occurrences. The major motive of data aggregation is to maximize the network lifetime with the help of minimizing the resource utilization of the nodes such as bandwidth, energy consumption, and battery power. To achieve the increment in network lifetime, an efficient routing protocol is necessary. The routing protocols should address the QoS metrics such as fault tolerance, latency, data accuracy, and security.

In the data aggregation process, the design of architecture for WSNs plays a crucial role. There are a number of protocols which provides routing and data aggregation at the same time. These protocols are divided into two types: cluster-based routing protocols and tree-based routing protocols. In [41, 42], the authors made contributions by developing the shortest path tree-based structures. But the disadvantages are not addressing the resource constraints of WSN. In [43], the data aggregation protocol is presented along with the security enhancement. This is because malicious nodes can compromise the data aggregation results.

In WSNs, security is one of the major requirements to protect the nodes from malicious attacks. Some of the characteristics of sensor nodes will compromise the security features when they are deployed in remote environments. The wireless medium is the primary target of the attackers, which is open to everyone. The attackers had the advantage to access the transmitted packets easily by compromising the sensor nodes. The second one is, sensor nodes which are deployed in the WSN environment have limited resources, and therefore it is difficult to implement robust security mechanisms [44–46].

In recent years, some of the secure data aggregation routing protocols are presented. These protocols are not completely sufficient to address the vulnerabilities of the WSN, but they will provide an overview of possible mechanisms for securing data aggregation.

In [47], Jacques et al. proposed the end-to-end encryption mechanism for secure data aggregation which uses the smaller key size and elliptic curve cryptography. This approach restricts the usage of two same texts for the cryptography and also does not allow the usage of a large number of operations over the ciphertext. The major advantage of this encryption scheme is it allows the small asymmetric encrypted keys that are crucial for sensor nodes. The drawback of the end-to-end encryption mechanism is time delay between the packet deliveries which will ultimately affect the network performance.

In [48], Prakash et al. presented the data aggregation model along with privacy-preserving scheme. The approach is simply called as cluster-based private data aggregation. The main feature of this protocol is to preserve the security at the time of data aggregation. This approach will provide less communication overhead over the WSN. The proposed method does not guarantee the fault tolerance, which is a primary concern for secure data aggregation.

In [49] Saut et al. presented the authentication and aggregation model for sensor motes (DAA). This model integrated the functionalities of authentication, data aggregation, and false data detection. The data aggregator node performs the data aggregation and performs data validation with authentication codes for their corresponding nodes. This approach follows the data confidentiality among the nodes by sending the encrypted data. Due to the utilization of encrypted keys, the network overhead is high in this approach.

Roy et al. [50] surveyed the problem of security in WSNs. One compromised sensor node will render the whole network useless and untruthful. They developed secure data aggregation protocols are strong against the intruders and the public key compromises. But the major issue in this protocol is that every time the size of the aggregated data is expanded when it was forwarded to the intermediate nodes.

Othman et al. [51] developed a secure data aggregation protocol to manage the queries over the data collected by the sensor nodes. The proposed protocol is designed especially for securing the computation at the time of data aggregation. However, this protocol manages to provide the data authentication. But still, the data sent from the sensor nodes to the data aggregator is a plaintext. It means the protocol fails to provide security at the time of data transmission.

Rezvani et al. [52] proposed the protocol to address the collusion attacks in WSNs. This protocol follows the iterative filtering algorithm to restrict the unwanted traffic in the network. The proposed protocol is robust against the collusion attacks, but the communication overhead is high in the network. Ouada et al. [53] developed lightweight-based authentication protocol for preserving the energy and providing the security in the wireless sensor networks. This protocol uses identity-based encryption in order to reduce the energy from the public key certificate management. This protocol achieved satisfying results in providing the security. The drawback of this protocol is it concentrates on the energy

Table 1 .

Protocols	Encryption approach	Data confidentiality	Data integrity	Drawbacks
Prakash et al. [48]	End-to-end symmetric	Yes	No	Does not have fault tolerance approach
Jacques et al. [47]	End-to-end symmetric	Yes	Yes	Time delay between the packet deliveries
Suat and Hasan [49]	End-to-end symmetric	Yes	Yes	Network overhead is high
Roy et al. [50]	Hop-to-hop	Yes	Yes	Size of the aggregated data is more
Othman et al. [51]	End-to-end symmetric	Yes	Yes	Lack of security at the time of data transmission
Rezvani et al. [52]	No	Yes	Yes	Communication overhead is high
Ouada et al. [53]	No	Yes	Yes	No encryption mechanism is applied for the data transfer

consumption and the data encryption is not employed to preserve the security. The comparison of secure data aggregation protocols is given in Table 1.

By observing the above-discussed protocols, it can be stated that the behavior of the sensor networks makes the sensor nodes prone to the different type of attacks. Therefore, an efficient data aggregation scheme is necessary to address the data security, energy consumption, data accuracy, and propagation delay.

5 Conclusion

Routing in wireless sensor networks is a new research filed with increasing set of research results with limited flexibility. In this paper, we made a comprehensive survey on conventional routing mechanisms as well as secure routing mechanisms. All the routing mechanisms have the common motive of extending the lifetime of the nodes, while not compromising the security parameters. Overall, the routing mechanisms are classified into three categories such as hierarchical, location-based, and data-centric routing protocols. We highlighted the challenges and future scope of each routing techniques. Although all the routing protocols promising in the sensor networks, still there is need to address many challenges.

References

1. Jiang X, Dawson-Haggerty S, Dutta P, Culler D (2009) Design and implementation of a high-fidelity ac metering network. In: The 8th ACM/IEEE international conference on information processing in sensor networks, San Francisco, California, USA, pp 253–264

2. Kim Y, Schmid T, Charbiwala ZM, Friedman J, Srivastava MB (2008) Nawms: nonintrusive autonomous water monitoring system. In: 6th ACM conference on embedded networked sensor systems, Raleigh, North Carolina, USA, pp 309–322
3. Ceriotti M, Mottola L, Pietro G, Murphy AL, Gun S (2009) Monitoring heritage buildings with wireless sensor networks: the torreaquila deployment. In: ACM/IEEE international conference on information processing in sensor networks, San Francisco, California, USA, pp 277–288
4. Xu N, Rangwala S, Chintalapudi KK, Ganesan D (2004) A wireless sensor network for structural monitoring. In: Conference on embedded networked sensor systems, Baltimore, MD, USA, pp 13–24
5. Beutel J, Gruber S, Hasler A, Lim R, Meier A, Plessl C, Talzi I, Thiele L, Tschudin C, Woehrle M, Yuecel M (2009) Permadaq: a scientific instrument for precision sensing and data recovery in environmental extremes. In: The 8th ACM/IEEE international conference on information processing in sensor networks, San Francisco, USA, pp 265–276
6. Tolle G, Polastre J, Szewczyk R, Culler D, Turner N, Tu K, Burgess S, Dawson T, Buonadonna P, Gay D, Hong W (2005) A macroscope in the redwoods. In: 3rd international conference on embedded networked sensor systems, San Diego, California, USA, pp 51–63
7. Werner-Allen G, Lorincz K, Johnson J, Lees L, Welsh M (2006) Fidelity and yield in a volcano monitoring sensor network. In: The 7th USENIX symposium on operating systems design and implementation, Seattle, Washington, pp 381–396
8. Cerpa A, Elson J, Estrin D, Girod L, Hamilton M, Zhao J (2001) Habitat monitoring: application driver for wireless communications technology. In: 2001 ACM SIGCOMM workshop on data communications
9. Hu W, Bulusu N, Chou CT, Jha S, Taylor A, Tran VN (2009) Design and evaluation of a hybrid sensor network for cane toad monitoring. ACM Transac Sensor Netw 5(1):4:1–4:29
10. Zhang P, Sadler CM, Lyon SA, Martonosi M (2004) Hardware design experiences in zebranet. In: Conference on embedded networked sensor systems, Baltimore, MD, USA, pp 227–238
11. Blough DM, Santi P (2002) Investigating upper bounds on network lifetime extension for cell-based energy conservation techniques in stationary ad hoc networks. In: The 8th international conference on mobile computing and networking, Atlanta, Georgia, US, pp 183–192
12. Kodialam M, Lakshman TV (2000) Minimum interference routing with applications to mpls traffic engineering. In: Nineteenth annual joint conference of the IEEE computer and communications societies, vol 2, pp 884–893. Tel Aviv, Israel, IEEE
13. Watts JD, Strogatz HS (1998) Collective dynamics of small-world networks, Nature © Macmillan Publishers, New York, USA, vol 393, pp 440–442, June 1998
14. Diestel R (2010) Graph theory. Springer-Verlag, Berlin, Heidelberg, Electronic Edition, 4th edn, vol 173
15. Lin C et al (2006) An energy efficient dynamic power management in wireless sensor networks. In: Proceedings of the 5th international symposium on parallel and distributed computing, IEEE 2006
16. Zhong JH, Zhang J (2011) Energy-efficient local wake-up scheduling in wireless sensor networks. In: 2011 IEEE congress on evolutionary computation (CEC), pp 2280–2284, 5–8 June 2011. https://doi.org/10.1109/cec.2011.5949898
17. Jiang B, Ravindran B, Cho H (2008) Energy efficient sleep scheduling in sensor networks for multiple target tracking. In: Distributed computing in sensor systems, lecture notes in computer science, vol 5067, pp 498–509
18. Sthapit P, Pyun JY (2013) Medium reservation based sensor MAC protocol for low latency and high energy efficiency. Telecomm Syst 52:2387–2395. https://doi.org/10.1007/s11235-011-9551-z
19. Fulkar S, Kapgate D (2014) Energy efficient resource allocation in wireless sensor networks. Int J Comput Sci Mob Comput 3(5):887–892, May 2014

20. Parvatkar S, Gore D (2014) Energy efficient protocol for heterogeneous wireless sensor network using ant colony optimization. (IJCSIT) Int J Comput Sci Inf Technol 5(3): 3454–3456
21. Heidemann J, Silva F, Intanagonwiwat C, Govindan R, Estrin D, Ganesan D (2001) Building efficient wireless sensor networks with low-level naming. In: Proceedings of the Symposium on Operating Systems Principles, Lake Louise, Banff, Canada, Oct 2001
22. Luo Z, Zhang Y, Pang Z (2013) Research on energy-efficient intelligent method for WSN. J Convergence Inf Technol (JCIT) 8(1), Jan 2013. https://doi.org/10.4156/jcit.vol8.issue1.12
23. Niculescu D (2005) Communication paradigms for sensor networks. IEEE Comm Mag
24. Lindsey S, Raghavendra CS (2002) PEGASIS: power-efficient gathering in sensor information systems. In: Proceeding of IEEE aerospace conference, vol 3, pp 1125–1130
25. Pei G, Chien C (2001) Low power TDMA in large wireless sensor networks. In: Military communications conference (MILCOM 2001), vol 1, pp 347–351, Vienna, VA, Oct 2001
26. Gerla M, Kwon T, Pei G (2000) On demand routing in large ad hoc wireless networks with passive clustering. In: Proceedings of IEEE WCNC 2000, Chicago, Illinois, Sept 2000
27. Heinzelman WR, Chandrakasan A, Balakrishnan H (2002) An application specific protocol architecture for wireless microsensor networks. IEEE Wireless Comm 1(4):660–670
28. Yang Y, Wu H, Chen H (2006) SHORT: shortest hop routing tree for wireless sensor networks. In: Proceedings of the IEEE international conference on communications, Istanbul, Turkey, pp 3450–3454
29. Lotf J, Bonab M, Khorsandi S (2008) A novel cluster-based routing protocol with extending lifetime for wireless sensor networks. In: Proceedings of the 5th international conference on wireless and optical communications networks, Surabaya, India, pp 1–5
30. Satapathy SS, Sarma N (2006) TREEPSI: tree based energy efficient protocol for sensor information. In: Wireless and optical communications networks 2006, IFIP international conference, pp 11–13, Apr 2006
31. Manjeshwar A, Agrawal DP (2001) TEEN: a routing protocol for enhanced efficiency in wireless sensor networks. In: Parallel and distributed processing symposium (IPDPS'01), San Fransisco, USA, pp 2009–2015
32. Heinzelman W, Kulik J, Balakrishnan H (1999) Adaptive protocols for information dissemination in wireless sensor networks. In: The 5th annual ACM/IEEE international of the first workshop on sensor networks and applications (WSNA). Altlanta, GA, USA
33. Sohrabi K, Gao J, Ailawadhi V, Pottie G (2000) Protocols for self-organization of a wireless sensor network. IEEE Personal Communication 7(5):16–27
34. Su W, Sankarasubramaniam Y, Cayirci E, Akyildiz IF (2002) A survey on sensor networks. IEEE Comm Mag 102–114
35. Gerla M, Kwon T, Pei G (2000) On demand routing in large ad hoc wireless networks with passive clustering. In: Proceedings of IEEE WCNC 2000, Chicago, Illinois, Sept 2000
36. Rodoplu V, Meng TH (1999) Minimum energy mobile wireless networks. IEEE J Sel Areas Commun 17(8):1333–1344
37. Li L, Halpern JY (2001) Minimum-energy mobile wireless networks revisited. Proceedings IEEE ICC'01. Helsinki, Finland, pp 278–283
38. Yu Y, Govindan R, Estrin D (2001) Geographical and energy aware routing: a recursive data dissemination protocol for wireless sensor networks. Technical Report UCLA/CSD-TR-01–0023, UCLA Computer Science Department, May 2001
39. Xu Y, Heidemann J, Estrin D (2001) Geography-informed energy conservation for ad-hoc routing. In: Proceedings ACM/IEEE MobiCom'01, Rome, Italy, pp 70–84, July 2001
40. Peter S, Westhoff D, Castelluccia C (2010) A survey on the encryption of converge cast traffic with in-network processing. IEEE Trans Dependable Secure Comput 7(1):20–34
41. Zheng J, Xu X, Wang G (2011) Energy efficient data aggregation scheduling in wireless sensor networks. In: IEEE 10th international conference on trust, security and privacy in computing and communications, pp 1662–1667
42. Chaudhary S, Singh N, Pathak A (2012) Energy efficient techniques for data aggregation and collection in WSN energy. IJCSEA 2(4):37–47

43. Maraiya K, Kant K, Gupta N (2011) Wireless sensor network: a review on data aggregation. Int J Sci Eng Res 2(4):1–6
44. Sethi H, Prasad D, Patel RB (2012) EIRDA: an energy efficient interest based reliable data aggregation protocol for wireless sensor networks. IJCA 22(7):20–25
45. Nithyakalyani S, SureshKumar S (2012) Optimal clustering algorithm for energy efficient data aggregation in WSN. Eur J Sci Res 78(1):146–155
46. Mathapati BS, Patil SR (2012) A reliable data aggregation forwarding protocol for wireless sensor networks. IJCSNS 12(5):90–95
47. Jacques MB, Christophe G, Abdallah M (2010) Efficient and robust secure aggregation of encrypted data in sensor networks. In: 10th proceeding of the 2010 4th international conference on sensor technologies and applications, (SENSORCOMM), Washington, DC, USA
48. Prakash GL, Thejaswini M, Manjula SH, Venugopal KR, Patnaik LM (2009) Secure data aggregation using clusters in sensor networks: world academy of science. Eng Technol 51:32–35
49. Suat O, Hasan C (2010) Integration of false data detection with data aggregation and confidential transmission in wireless sensor networks. IEEE/ACM Trans Netw 18(3):736–749
50. Roy S, Conti M, Setia S, Jajodia S (2012) Secure data aggregation in wireless sensor networks. IEEE Trans Inf Forensics Secur 7(3):1040–1052
51. Othman SB, Trad A, Youssef H, Alzaid H (2013) Secure data aggregation in wireless sensor networks. In: Ad Hoc networking workshop (MED-HOC-NET), 2013 12th annual mediterranean, pp 55–58. IEEE, 2013
52. Rezvani M, Ignjatovic A, Bertino E, Jha S (2015) Secure data aggregation technique for wireless sensor networks in the presence of collusion attacks. IEEE Trans Dependable Secure Comput 12(1):98–110
53. Ouada FS, Omar M, Bouabdallah A, Tari A (2016) Lightweight identity-based authentication protocol for wireless sensor networks. Int J Inf Comput Secur 8(2):121–138

Neural-Based Hit-Count Feature Extraction Method for Telugu Script Optical Character Recognition

M. Swamy Das, Kovvur Ram Mohan Rao and P. Balaji

Abstract The recognition accuracy and efficiency of any OCR system greatly depend on the feature extraction methods. There are several feature extraction methods each has its own characteristics. These methods differ in terms of the number features that they extract and the complexity. With less number of features, the recognition accuracy may be low, and with more number of features, the recognize time may be more. The features are to be selected in such a way that they could distinguish one character from other with minimum comparisons and gives less false positives and false negatives. The accuracy of an OCR can be improved by changing the feature extraction methods. Telugu is called Italian of the east. But it is surprising that there are not many OCRs that could detect Telugu characters with fairly good accuracy. The accuracy of OCRs available in the market are either highly objectionable or the price is very high. To address this issue, we took up this project. Other problems include the segmentation of overlapped characters and right feature extraction. We tried to solve these issues, by taking a segmented character from a word and check to find a correct match for it or tell that the character does not exist so that the particular character can be re segmented. In this work, a hit-count-based feature extraction method with neural networks is used for the fast recognition even though the training time is more. The experimental results show that the proposed hit-count-based feature method greatly reduces the time by maintaining the recognition accuracy.

Keywords OCR · Hit-count · Segmentation · Feature extraction
Blob · PyBrain · Neural network · Skeleton · Skew · Backpropagation

M. Swamy Das (✉) · P. Balaji
CSE Department, CBIT, Hyderabad, India
e-mail: msdas@cbit.ac.in

P. Balaji
e-mail: balaji.polakampally@gmail.com

K. R. M. Rao
IT Department, Vasavi College of Engineering, Hyderabad, India
e-mail: krmrao@staff.vce.ac.in

H. S. Saini et al. (eds.), *Innovations in Electronics and Communication Engineering*,
Lecture Notes in Networks and Systems 33,
https://doi.org/10.1007/978-981-10-8204-7_48

1 Introduction

There are currently millions of books available from libraries, universities and other organizations. They can be made available on the Internet by digitization. This can be achieved by a process called Optical Character Recognition (OCR) and the tools are called Optical Character Recognition Systems. This can be achieved by a process called Optical Character Recognition (OCR) and the tools are called Optical Character Recognition Systems. There are several applications of OCR systems like as a reading tool for blind people, sorting postal mails, scanning bank cheques, library catalogues, creating indexes, checking for grammar, etc. It is a common method of converting digitized printed text documents into electronically editable text documents. So that they can be searched, stored more compactly, displayed online. They can also be used in machine applications for translating from one language to another, text-to-speech, key data, text mining. OCR is a field of research in pattern recognition, artificial intelligence and computer vision [1, 2].

Any typical OCR system consists of several steps as shown in Fig. 1. These steps include the text image acquisition, preprocessing, segmentation, features extraction, features selection and recognition. The input for the system is the machine printed or handwritten image documents. These documents are scanned and digitized by a scanner to produce a digitized image and stored in different file formats like .bmp, . jpeg, .png, .png., tiff, .gif, etc. The input image may be in colour or greyscale. To save memory space and computational cost we convert them into black and white (binary) form. We used Otsu method for this conversion [3, 4].

The input image document may contain noise included in the input images due to several reasons like paper quality, scanner resolution (dpi), etc. It may also have

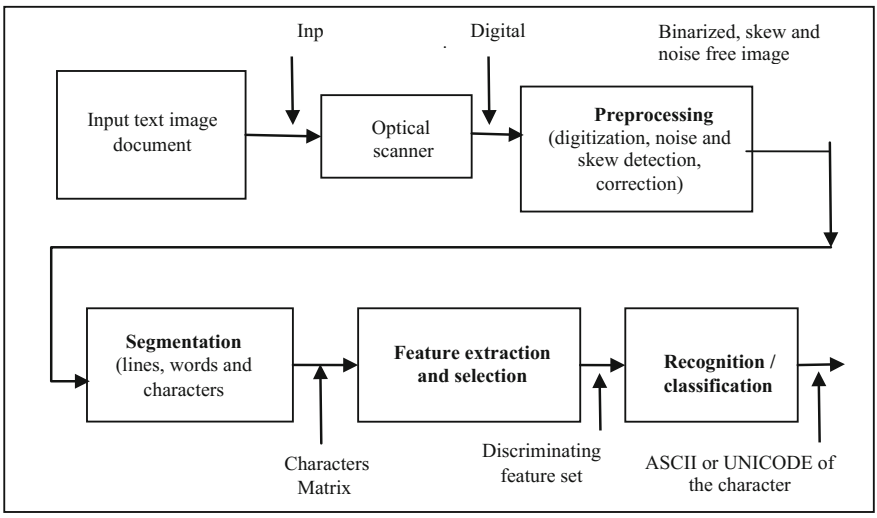

Fig. 1 Block diagram of a typical OCR System

skew due to the manual feeding of the document to the scanner. For noise removal, low-pass filters can be used. The noise and skew-free image are thinned (*skeletonization) to* reduce unnecessary information. The segmentation module segment the binary image into lines, words and then into characters. Each character image can be represented as a matrix of pixels. The size of this matrix depends on the complexity of the character shape and vocabulary involved, resolution of a digitized character used to achieve speed and accuracy. The character matrix is then given as input to the feature extraction module. The feature extraction module then extracts the features useful for distinguishing each character from the other characters. From the literature, we can find several features extraction methods. These methods include *template-based*, *statistical-based* and *structural-based*. In template-based methods where each pixel may be treated as a feature. Once the characters are recognized, then the recognized character may be stored as an editable ASCII or UNICODE file on which we can do post-processing tasks like spell checking, grammar checking, indexing, etc [5].

There are many OCRs available in the market both commercial and free. The accuracy of the OCRs varies widely depending on several factors like script type, algorithms used for segmentation and feature extraction, etc.

Telugu is a language that is widely spoken. It has nearly 80 million speakers across the globe. It is also called Italian of the East. The Telugu script differs from Latin script by a vast amount. In fact, there is no resemblance between these two scripts. So, we cannot use the OCRs targeted for Latin script for Telugu language. The development of OCR for Telugu script is also a complex task. This is because the letters in this script are formed by combining symbols and modifiers resulting in very large number of characters. Due to all these reasons, the accuracy of OCRs for Telugu script is comparatively pretty low and worst if the input image is not of good quality. So there is a scope to improve the accuracy of Telugu OCR systems [6].

2 Existing Methods, Tools and Technologies

In this work, we used the *Tesseract* and the PyBrain of *Python.* The following sections givens the information about these two tools/technologies.

2.1 Tesseract

It is an open source OCR engine. The Tesseract engine can accept different image format document and convert into editable text documents in more than 60 languages. It is available under Apache License. It can be used directly or using an API. Tesseract does not have a built-in GUI but several third parties provide it. It can be installed on Linux, Mac OSX and Windows. Most of the Tesseract project was developed using C and some using C++. It provides the Standard

Template Library (STL). It is portable and efficient but sometimes it may lead to segmentation errors as it uses lists and difficult to debug. However, we used it for the segmentation purpose.

For character classification, the polygon approximation for segmenting the characters as features did not provide satisfactory results. The reasons for taking a new approach for classification rather than the Tesseract approach are as follows:

- The features in the unknown data need not be same as the features in the training data.
- In the segmentation phase, features of small and fixed length extracted from the outline and matched with many-to-one against the clustered prototype features of the training data.

So the classification in this work is done in two steps:

- A pruner class created a shortlist of characters that the unknown might match.
- Each feature of the unknown looks up a bit vector of prototypes of the given class that it might match, and the actual similarity between them is computed.

2.2 Python's PyBrain

The Python's PyBrain module encapsulates different data processing algorithms. This module allowed us to makes our implementation task simple where only we need to adjust the free parameters through some machine learning approaches. This module contains an input, an output buffer and the corresponding error buffers. It uses backpropagation algorithm for the training process. All the inputs are to be assembled into objects of the class '*Network*'. The objects are then connected using connection objects that results in a directed acyclic graph. The parameters are to be tuned for determining the correct weights by trial-and-error method.

The neural network is created by using the buildNetwork(p,q,r) method imported from the pybrain.tools.shorcuts library. P: number of input, q: no. of neurons in the hidden layer, r: no. of neurons in the output layer. Then, it is activated using the `activate ()` method. The dataset is created using the package named '*pybrain.dataset*' and the class '*SupervisedDataset*' to build supervised dataset. The method used to add sample is '*addsample*()'. PyBrain also provides trainers `BackpropTrainer()` and `Trainer.train()`, for the convergence of the solution, `trainUntilConvergence()` method is used.

3 Proposed Dictionary-Based Hit-Count Method

This method is associated with two classes named *Dictio* and *hitcount* class. The *Dictio* class builds the dictionary from the trained data stored in a file and it can create multiple dictionaries. As the skeletons are grouped together into classes and

each class has a separate fixed width and height, it is important that all the grouped skeletons are assigned to one dictionary, e.g. all the skeletons of group A are used to create dictionary A and so on. A dictionary is a <*key*, *value*> pair which uniquely maps a key to a value. It should be noted that the keys should be unique whereas the values need not be. The keys in our dictionaries are pixel locations and the values are list of skeletons which have that pixel location as a foreground pixel. By using the above procedure, multiple dictionaries are created.

Hit-count method *superimposes* skeletons on the segmented image and gives the *hitcoun*t. The *hitcount* is just an integer value that tells us the number of foreground pixels a skeleton and a character have in common. This superimposing skeleton process on the character image is not done serially rather it is *parallel*. The *hitcount* class takes the dictionaries created by the *Dictio* class and used them to superimpose skeletons on the character image. Since each dictionary is created using more than one skeleton, when we use a dictionary, it is concurrently superimposed with multiple skeletons. Now that all the skeletons are superimposed and the *hitcounts* are temporarily stored.

```
hitcount = Hits(dict1, dict2, ...)
```

Classify: The *classify* class takes the temporarily stored *hitcounts*. Our method is to use the max of an array, it means the *hitcounts* are of a character image are taken into an array and the skeleton corresponding to the maximum *hitcount* is found. Since each skeleton uniquely identifies a particular character, we can recognize the character image as the character of the skeleton using multi-layer perceptron network. Then the recognized character is written into a text file using UTF-8 format.

4 Implementation

A sample dataset with 48 Telugu characters is created and stored as an image. The preprocessing and segmentation tasks are carried out in Python using the Tesseract-based methods. The segmented characters are then skeletonized to remove redundant pixels as shown in Fig. 2. With the proposed hit-count-based method, the hit-counts for each character skeleton are extracted to form the feature datasets. A neural topology is created and trained using the PyBrain class and also tested.

Figure 3 is a sample input and its corresponding output text file produced by our proposed hit-count-based OCR system. The output shows that there are four misrecognized characters. The character '*tha*' is recognized as '*dha*' that means the

Fig. 2 Sample skeletonized character with 1-pixel thickness

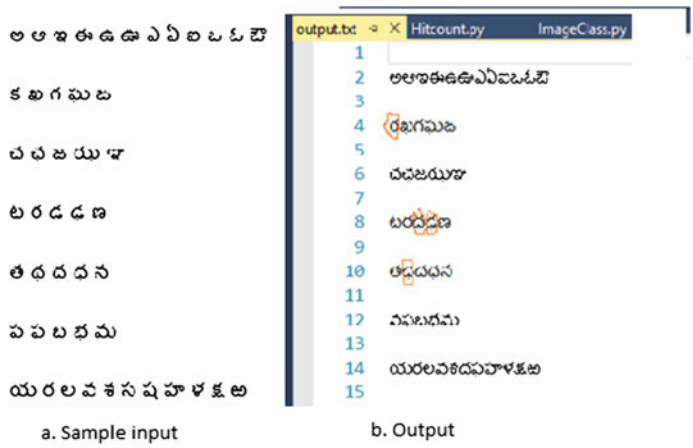

Fig. 3 Screenshot with a sample input and output

blotch in the middle of the character image is not recognized. When we are creating skeletons, we used a mask of size 3 * 3, since the blotch that should be in the middle is smaller than the mask it did not contribute to the output. The errors can be corrected by using methods like confusion table, etc., and the complete experimental results tested with three different kinds of variations are shown in Table 1 and Graph 1.

Table 1 Experimental results with various fonts and font types

Dataset type	Dataset description	Accuracy (%)	Remarks
Tl	Same font, size as that of training set	91.21	Most of the characters are identified correctly. The misidentified characters are confusing characters
T2	Same font, different size as that of training set	83.33	With small font sizes, most of the characters are misrecognized. Resize is also not very effective
T3	Different font than the training set	50.11	Accuracy dropped because of great differences in their skeletons. Similar fonts may give similar accuracies

Graph 1 Dataset type versus accuracy

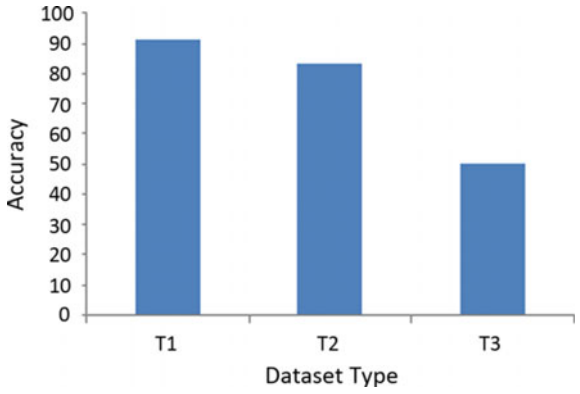

5 Conclusions and Future Work

In order to improve the speed and the accuracy of Telugu script OCR, a hit-count-based feature extraction method is proposed and successfully implemented using the Python's PyBrain neural network class. In this process, a dataset of with 48 Gauthami font Telugu characters created and using proposed method features are created. With these features, MLPN is trained and tested successfully. Finally, an OCR system is built, and experiments are conducted with three different datasets by varying the font size, font types. From the experimental results, it is understood that the system accuracy is high with the same font and font size of those training sets and less with other font types. However, the proposed method-based system could not detect the characters with small font size and confusing characters. The accuracy may be improved by using KNN or SVM classifiers.

References

1. Krishnan P, Jawahar C et al (2014) Towards a robust OCR system for indic scripts. DAS
2. Singh A, Bacchuwar K et al (2012) A survey of OCR applications. IJMLC 2(3)
3. Sankaran N, Jawahar C (2013) Devanagari text recognition: a transcription based formulation. ICDAR
4. Gonzalez RC, Woods RE (2001) Digital image processing. Addison-Wesley Longman Publishing Co., Inc., Boston, MA, USA
5. Borovikov E (2014) A survey of modern optical character recognition techniques. AMS 2004, arXiv:1412.4183v1 [cs.CV] Dec 2014
6. Varalaxmi A, Negi A et al (2012) DataSet generation and feature extraction for Telugu hand-written recognition. IJCST 3(2):57–59
7. http://dli.iiit.ac.in

8. http://www.archive.org/details/millionbooks
10. http://www.tesseract.org/
11. http://www.wikipedia.org/OCR

Oversampled PTM Sequencing for Sidelobe Suppression in Radar

Ravi Kishore Singh, D. Elezebeth Rani and Bandella Deepika Chowdary

Abstract Detecting fast moving targets by radar has become an issue due to Doppler shift in the frequency of the return signal. This issue attracted the research community to enhance the quality of detection in radar system. Current literature is mainly focusing to increase the power spectral density of the main lobe, which also minimizes the effect of sidelobes to some extent. However, the effect of sidelobes still exists, which makes detection very difficult at all Doppler shifts. Most of the existing research assumed Doppler filter bank followed by range gates to detect the range and speed of the targets. In this paper, we pay much attention to present oversampling PTM sequencing for sidelobe suppression which is a better solution than earlier methods to remove the effect of sidelobes over large extent by creating windows at regular Doppler frequencies to enhance detection. The detection of the targets will be done in range through the Doppler windows giving excellent signal-to-noise ratio. The transmission code may be oversampled to get the requested Doppler clearance.

Keywords Ambiguity · Golay pairs · Doppler · Oversampled PTM sequencing

1 Introduction

It is evident that the radar signal received by the receiver is very weak due to the two-way transmission making it mandatory to use very sensitive receivers to detect the targets. The return signal is auto-correlated (Matched Filtering) to get best

R. K. Singh (✉) · B. D. Chowdary
ECE, Guru Nanak Institutions Technical Campus, Hyderabad, India
e-mail: ad.rk@gniindia.org

B. D. Chowdary
e-mail: deepikachoudary2@gmail.com

D. E. Rani
GITAM University, Vizag, India
e-mail: hod_ei@gitam.edu

H. S. Saini et al. (eds.), *Innovations in Electronics and Communication Engineering*,
Lecture Notes in Networks and Systems 33,
https://doi.org/10.1007/978-981-10-8204-7_49

possible signal-to-noise ratio. Many attempts have been made in the past to design radar codes to nullify the effect of the Doppler on the signal-to-noise ratio. Doppler shift is also not constant but a factor of the hit angle, the phase at which the beam hits the target and finally the target speed makes it difficult to predict for the same target. Many researchers have used barker codes, minimum peak sidelobe codes, ternary codes, etc., to get very good signal-to-noise ratio [1]. However, most of these codes are not Doppler tolerant and the sidelobes are uncontrolled even with moderate Doppler shifts. Doppler-tolerant radar codes like frank, $P1$, $P2$, $P3$, $P4$, hyperbolic, etc., are not easy to transmit due to pulse-to-pulse changing amplitudes [2]. Attempts were made to transmit Golay codes. These codes gave excellent thumbtack output with no side lobes at all. However when the targets are moving the output no longer remains thumbtack due to Doppler caused by the moving targets and the side lobe with high amplitude appears. These side lobes due to Doppler of moving target may mask the output of small real targets which could be dangerous in the battle field [3]. Another problem with the Golay codes is two complementary codes have to be transmitted in two pulses, each code is auto-correlated and then added to give the desired results.

PTM codes [4] transmission resulted in giving a small window in the delay versus Doppler graph at zero-Doppler making detection possible for slow-moving targets, which can be used for battlefield surveillance radars where the Doppler is not much. Golay codes transmitted as [5] PTM codes were reported to give better window at zero-Doppler and windows at other Doppler which can be used for detection. In this paper, we propose oversampled PTM codes which give good autocorrelation at various Doppler windows. The detection is based on Doppler windows giving very high signal-to-noise ratio in the selected Doppler window. The delay versus Doppler graph from the ambiguity function gives a clear range from minimum range to maximum range of the radar. Oversampled PTM codes give windows at various Doppler in the delay versus Doppler graph depending on the oversampled ratio. Simulation is done for the total length of 256 codes where in oversampling is done at two, four, six and so on.

2 Related Work

Golay code is the binary code which has the property to suppress the sidelobes. Golay code is a pair of two complementary codes, code-x and code-y, each having length of M, where M is a positive integer.

Golay codes have a remarkable property that addition of autocorrelation of the two complementary codes results in zero sidelobes. These complimentary codes have properties conducive to use in radar and communication system [4, 6]. The sum of autocorrelations of each of a Golay code pair represents a delta function. This property can be used for the complete suppression of sidelobes from radar signals, by transmitting each code, correlating the received signals and combining them [7]. The codes have to be transmitted separately in different pulse repetition frequency (PRFs)

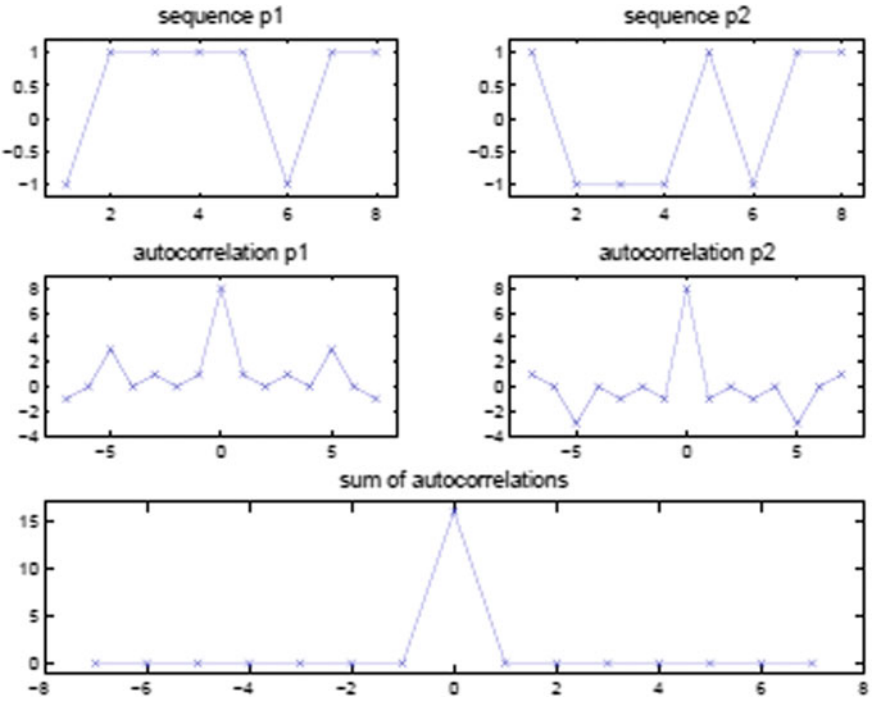

Fig. 1 Golay complimentary code sequence output

and separate autocorrelation of the two pulses are to be added delaying the output of the first pulse by one PRT in the delay line. This code has interesting properties, which facilitate the removal of sidelobes and optimization of phase and frequency [8]. Figure 1 shows that the Golay complimentary code sequence output.

Two discrete binary sequences of length M, $q1(n)$ and $q2(n)$, are termed Golay complementary sequences and the correlation with the received signal with $qi1(n)$ is termed as $Rq1(n)$ [9] and similarly, correlation with the received signal with $q2(n)$ is termed as $Rq2(n)$. The sum of their autocorrelations is zero except at zero lag, i.e. (Fig. 1).

$$Rq1(k) + Rq2(k) = 2M\delta(k)$$

3 PTM Introduction

The Prouhet–Thue–Morse (P.T.M) sequence can be defined as $\mathcal{P} = (P_n)_{n \geq 0}$ over [0, 1] by the following recursion:

$$P_0 = 0$$

$$P_{2n} = P_n$$

$$P_{2n+1} = \bar{\mathrm{P}}_n = 1 - P_n, \text{ for all } n > 0, \text{ where } \bar{\mathrm{P}}1 - P.$$

A P.T.M sequence can be explained by the set $P = \{0, 1, 2, \ldots, 7\}$, which can be divided into two subsets as $S_0 = \{0, 3, 5, 6\}$ and $S_1 = \{1, 2, 4, 7\}$ whose elements satisfy $(0^m + 3^m + 5^m + 6^m) - (1^m + 2^m + 4^m + 7^m) = 0$, for $m = 1, 2\ldots$ This can be also shown as $\sum_{\rho \in so} \mathrm{p}^m = \sum q \in \mathrm{s}1q^m$ [4].

For example, the P.T.M sequence of length 16 is $P = (P_n)_{n=0}^{15} =$ 0101001100100110.

The P.T.M pulse train, when transmitted, clears out the sidelobes in a Doppler interval around zero-Doppler axes. The P.T.M pulse train sequence of length 2^{M} has the following ambiguity functions:

$$G(k, \theta) = \mathrm{e}^{j(2M-1-1)\theta} \frac{\sin(2M\theta/2)}{\sin(\theta/2)} L\delta k, 0 + \frac{1}{2}\left(\Pi_{m=0}^{m-1}\left(1 - \mathrm{e}^{\mathrm{j}2\mathrm{m}\theta}\right)\right)[Cx(k)$$

$$Cy(K)] = e^{j(2M-1-1)\theta} \frac{\sin(2M\theta/2)}{\sin(\theta/2)} L\delta k, 0 + \frac{1}{2}\left[(-j)^M 2^{M(M-1)/2}\theta^M + \mathrm{O}\left(\theta^{M+1}\right)\right]$$

$$[Cx(K) - CY(k)]$$

Proof

$$Sp(\theta) = \sum_{n=0}^{2M} (-1)^{pn}\, \mathrm{e}^{jn\theta}$$

$$= \sum_{n0=0}^{1} \cdots \sum_{nM-1=0}^{1} (-1)^{n0+\cdots+nM-1} \mathrm{e}^{j(n020+n121+\cdots+nM-12M-1)\theta}$$

$$= \prod_{M-o}^{m=0} (1 - \mathrm{e}^{j2m\theta}) = \prod_{m=0}^{M-1} \wedge m(\theta) \quad \text{Where } \wedge_m(\theta) = 1 - \mathrm{e}^{j2m\theta}$$

Since, $\Lambda m(0) = 0$, we have $S_p^{\mathrm{l}}(0) = 0$, if $\ell < M$
and $S_p^m(0) = M! \prod_{m=0}^{m-1} \wedge(0) = (-j)^M 2^{M(M-1)/2} M!$

4 Oversampled PTM

It has been reported that the P.T.M sequence can clear out sidelobes only around zero-Doppler axis, to clear out sidelobes in other Doppler intervals we can oversample P.T.M sequence which is called as oversampled P.T.M. The *k*-oversampled

P.T.M sequence of length $2^N k$ produces an Nth-order null at $\Theta = 2\ \pi l/k$ for all co-primes l and k.

Consider bi-phase sequences whose spectrum has higher order null frequencies other than zero-Doppler. Consider Taylor expansion of spectrum

$$Sp(\theta) = \sum_{t=0}^{\infty} \frac{1}{n!} f_p^t(\theta_0)(\theta - \theta_0)t, \text{ around } \Theta = \Theta_0 \neq 0$$

where

$f_p^t(\theta_0)$ can be given as follows:

$$f_p^t(\theta_0) = \left[\frac{\mathrm{d}_t}{\mathrm{d}\theta} Sp(\theta)\right]\theta = \theta_0 = j^t \sum_{n=0}^{N-1} n^t p_n \mathrm{e}^{njt\theta}, \text{ for } t = 0,\ 1,\ 2\ldots.$$

Consider a sequence P so that $f_p^t(\theta_0) = 0$, for all $t = 0, 1, \ldots..M$ Rational Doppler shift is considered at $\theta_0 = 2\pi l/k$, where $l \neq 0$ and $k \neq 1$ are co-prime integers. Assume the length of P is $N = kq$ for some integer q. If we express $0 \leq n \leq N - 1$ as $n = rk + i$, where $0 \leq r \leq q - 1$ and $0 \leq i \leq l - 1$, then using the binomial expansion for $nt = (rk + i)t$ we can write

$$f_p^t(\theta_0) = j^t \sum_{u=0}^{t} \binom{t}{u} k^u \sum_{i=0}^{k-1} i^{t-u} \mathrm{e}^{j\frac{2\pi li}{k}} \sum_{r=0}^{q-1} r^u p_{rk+i}$$

A length-q sequence is defined by $\{b_r\}_{r=0}^{q-1}$ as $b_r = P_{rk+i}, 0 \leq r \leq q-1$. If $\{b_r\}_{r=0}^{q-1}$ satisfies

$$\sum_{r=0}^{q-1} r^u b_r = 0 \quad \text{for all } 0 \leq u < t \tag{1}$$

Then, the coefficient $f_p^t(\theta_0)$ will be zero. It follows that the zero-forcing condition in (1) will be satisfied if $\{b_r\}_{r=0}^{q-1}$ is the PTM sequence of length $2t$. We note that $f_p^N(\theta_0)$ is zero as $\sum_{i=0}^{m-1} \mathrm{e}^{j\frac{2\pi li}{k}} = 0$. To zero-force the derivatives $f_p^t(\theta_0)$ for $t \leq N$, it is enough to select $P = \{pn\}_{n=0}^{2Nk-1}$ of length $2L$ PTM sequence. Such sequence can be called as $(2N, k)$-PTM sequence which has length $2N \times k$. The length-2N PTM sequence can be written by repeating each 1 and −1 in the PTM sequence n times, that is by oversampling the PTM sequence by a factor n. Then, the spectrum $S_P(\theta)$ of P has Nth-order nulls at all $\theta_0 = 2\pi l/k$ where $l \neq 0$ and $k \neq 1$ are co-prime integers as mentioned earlier.

5 Output

Figure 2 represents the output for a PTM sequence of length 256 where in only the practical Doppler frequencies are considered from 0 to 50 KHz. It is seen that the amplitude of noise is around 0.1 and window for transmission is available

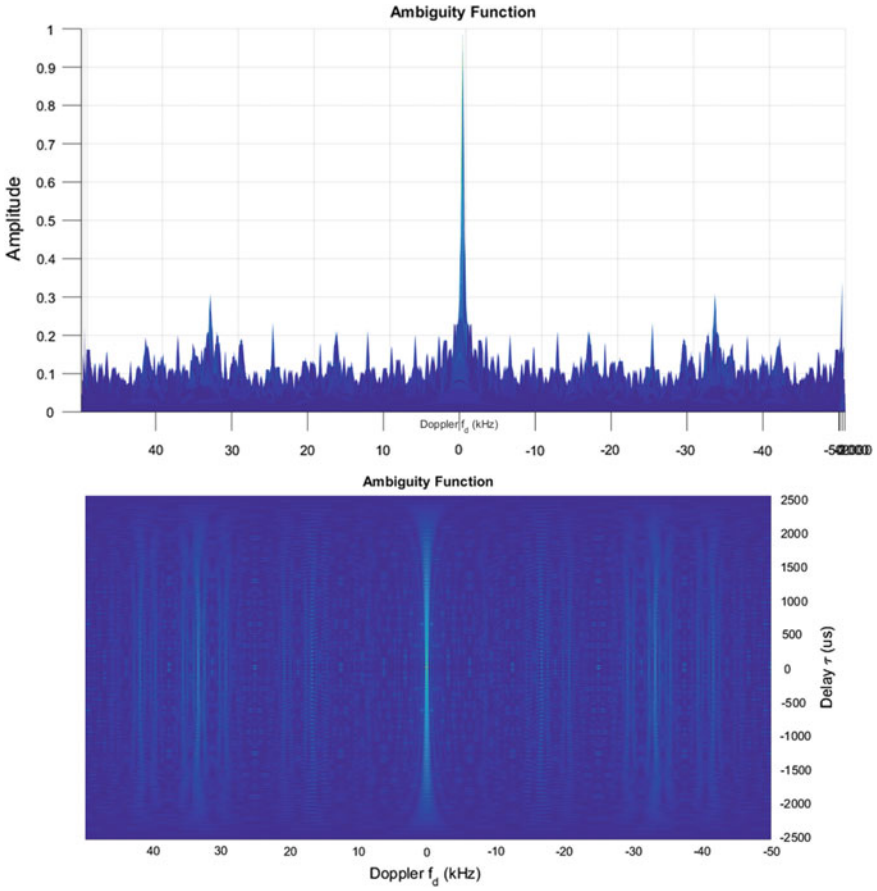

Fig. 2 Normal PTM sequence of length 256

considering the noise levels of 0.2 as optimum. Noise levels are high only in range of 30–40 KHz.

Figure 3 gives output for PTM sequence of 128 bit repeated twice to give fixed length of 256 bit. The transmission is possible in all frequencies where noise levels are below 0.2 of normalized amplitude gives on Y axis. The windows where transmission is recommended is also given.

Figures 4, 5 and 6 also gives output for PTM sequence 64 bits repeated 4 times, 32 bits eight times and 16 bits repeated 16 times. The windows where transmission is possible is also given. It is seen that both window size and the noise levels increase as the PTM sequence is reduced and repeated.

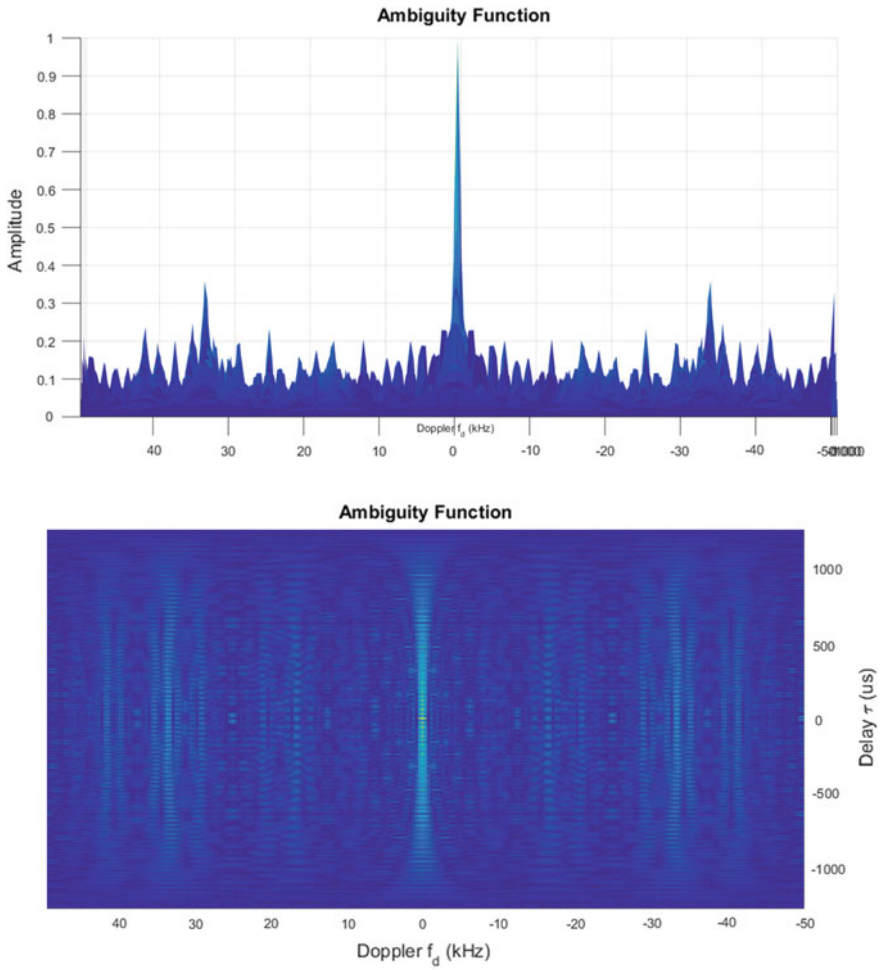

Fig. 3 PTM sequence oversampled 2 times which is represented as (256, 2) where 256 is the length of PTM sequence

Window-1	Window-2	Window-3	Window-4
2.6 to 12.5	12.6 to 25.56	25.57 to 34.48	35.2 to 50
−2.6 to −12.5	−12.6 to −25.56	−25.57 to −34.48	−35.2 to −50

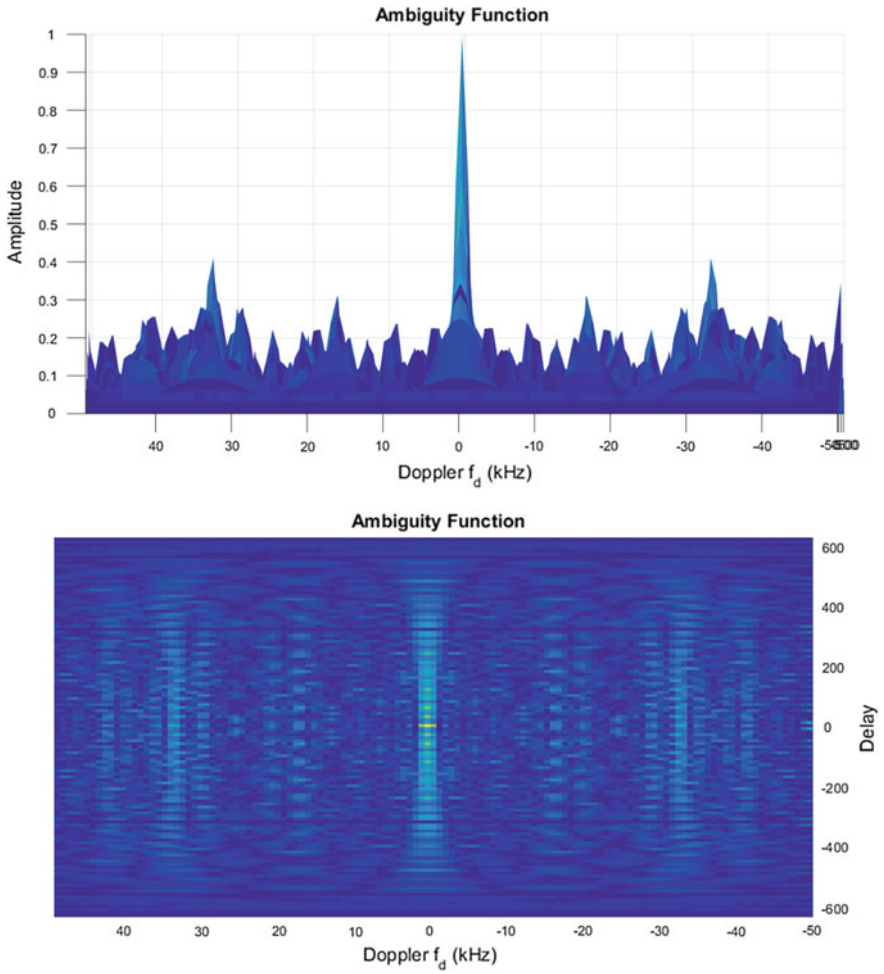

Fig. 4 PTM sequence oversampled 4 times which is represented as (256, 4), where 256 is the length of PTM sequence

Window-1	Window-2	Window-3	Window-4	Window-5
7.1 to 12.35	12.45 to 18.52	18.6 to 24.52	25.2 to 44.5	
−3.25 to −12.3	−12.4 to −18.52	−18.6 to −24.52	−25.2 to −38.52	−39.1 to 50

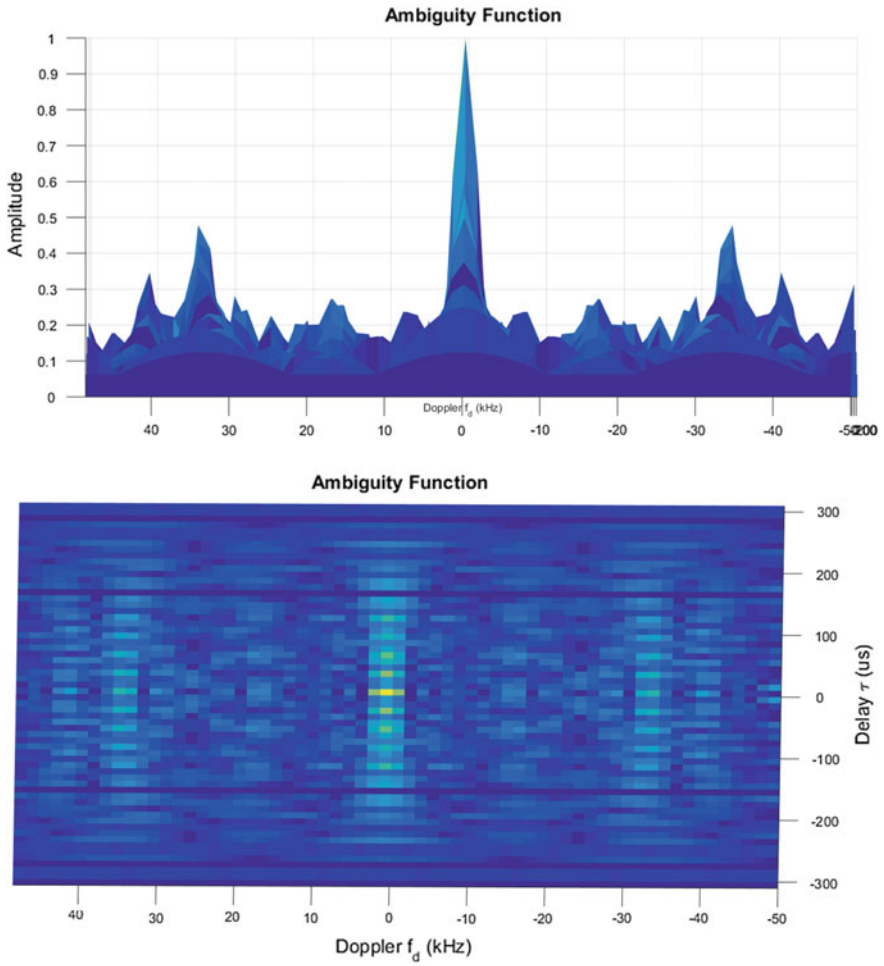

Fig. 5 PTM sequence oversampled 8 times which is represented as (256, 8) where 256 is the length of PTM sequence

Window-1	Window-2	Window-3	Window-4
7.86 to 16.78	17.12 to 34.56	35.21 to 50	
−0.56 to −8.45	−8.6 to −17.65	−17.82 to −29.6	−30.15 to −50

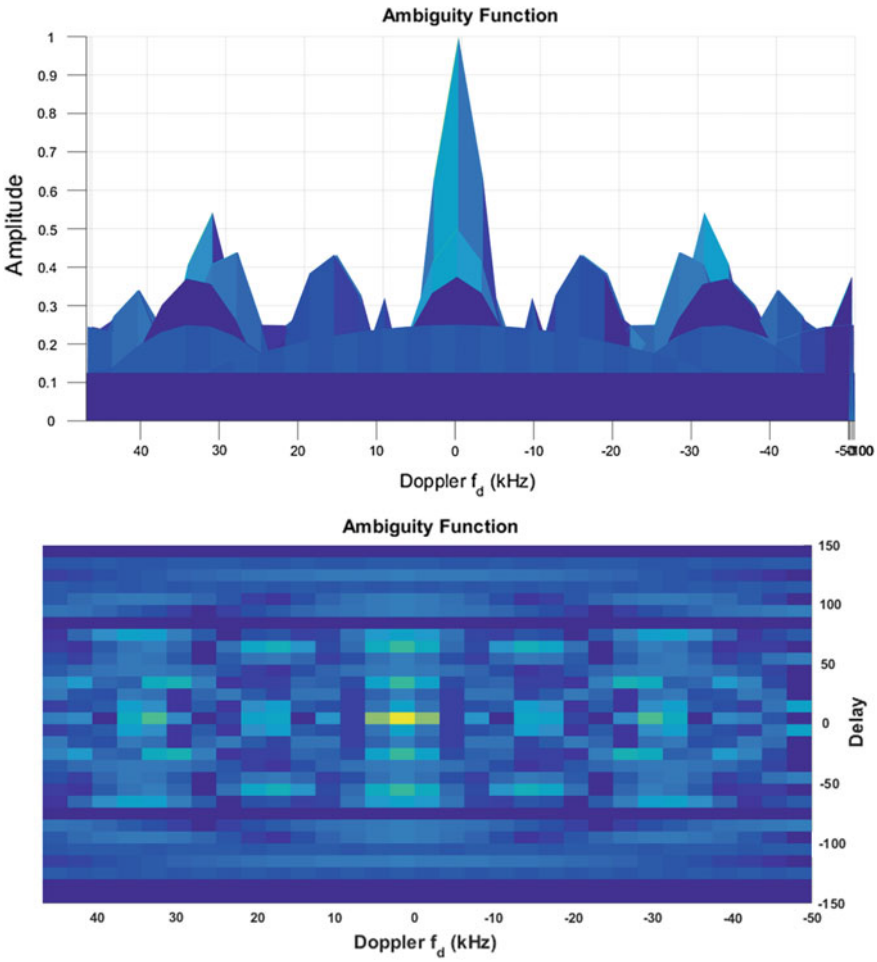

Fig. 6 PTM sequence oversampled 16 times which is represented as (256, 16) where 256 is the length of PTM sequence

Window-1	Window-2	Window-3
0.45 to 15.6	15.7 to 28.6	29.12 to 48.56
−0.45 to −15.6	−15.7 to −28.6	−29.12 to −48.56

6 Conclusion

Through this paper, different techniques are proposed using methods like Linear Block Coding Complimentary Oversampled ExOR Technique, and Re-Sampling Binary Hex Coding Technique (RSBHCT) to create windows for all possible targets which need to be detected by the radar. These techniques can detect multiple moving targets at various Doppler by the radar simultaneously without interference by other radars or targets. By increasing the number and size of the windows and creating the window at desired Doppler, we can easily detect the multiple moving targets. As in radar transmission, enhanced Quality of Service (QOS) can be obtained by decreasing the noise levels in these windows. This can be achieved by increasing the size and the number of the windows. The presented approaches not only increased the number, but also increased the size of the windows over a large extent to get the desired Doppler. The various approaches presented in this thesis easily detect the multiple moving targets by creating a huge number of windows at various Doppler's. Our approaches are very simple to operate and the probability of detection of the target is enhanced in comparison with binary codes discussed so far, Golay and PTM codes. The presented approaches also increase the size of the window, so the probability of detection of the moving targets is increased up to large extent we explain that by oversampling PTM sequence at different sampling rates we can produce suppressed sidelobe waveform over different Doppler intervals and trace weak targets which are masked by the sidelobes.

References

1. Golay MJE (1961) Complementary series. IRE Trans Inform Theory 7(2):82–87
2. Welti GR (1960) Quaternary codes for pulsed radar. IRE Trans Inform Theory 6(3):400–408
3. Levanon N, Mozeson E (2004) Radar signals. Wiley
4. Allouche JP, Shallit J (1999) The ubiquitous ProuhetThue-Morse sequence. In: Helleseth T, Ding C, Niederreiter H, (eds) Sequences and their applications, Proceedings of SETA'98, Springer Verlag, pp 1–16
5. Turyn RJ (1963) Ambiguity functions of complementary sequences. IEEE Trans Inform Theory 9:46–47
6. Prouhet E (1851) Mèmoire sur quelques relations entre les puissances des nombres. C. R. Acad. Sci. Paris Sèr., vol I 33, p 225
7. Pezeshki A, Calderbank R, Moran W, Howard SD (2007) Doppler resilient waveforms with perfect autocorrelation. IEEE Trans Inform Theory. available at arXiv.org:cs/0703057
8. Gerlach K, Kretschmer FF (1998) General forms and properties of zero cross-correlation radar waveforms. IEEE Trans Aerosp Electron Syst 28(1):98–104
9. Sivaswami R (1982) Self-clutter cancellation and ambiguity properties of subcomplementary sequences. IEEE Trans Aerosp Electron Syst 18(2):163–181

Author Index

H. S. Saini et al. (eds.), *Innovations in Electronics and Communication Engineering*,
Lecture Notes in Networks and Systems 33,
https://doi.org/10.1007/978-981-10-8204-7